

UNCLASSIFIED

AD NUMBER
AD878776
NEW LIMITATION CHANGE
TO Approved for public release, distribution unlimited
FROM Distribution authorized to U.S. Gov't. agencies and their contractors; Critical Technology; OCT 1970. Other requests shall be referred to Air Force Flight Dynamics Laboratory, Attn: FBE, Wright-Patterson AFB, OH 45433.
AUTHORITY
AFFDL ltr, 12 Nov 1971

THIS PAGE IS UNCLASSIFIED

AFFDL-TR-70-10  
Volume I, Part I

3

# LOW ALTITUDE ATMOSPHERIC TURBULENCE LO-LOCAT PHASE III

Volume I, Part I, Data Analysis

*J. W. JONES, R. H. MIELKE, G. W. JONES, et al*

*THE BOEING COMPANY*

TECHNICAL REPORT AFFDL-TR-70-10, VOLUME I, PART I

NOVEMBER 1970

DDC  
RECEIVED  
JAN 20 1971  
STANDARD

This document is subject to special export controls and each transmittal to foreign governments or foreign nationals may be made only with prior approval of the Air Force Flight Dynamics Laboratory (FBL), Wright-Patterson Air Force Base, Ohio, 45433.

AIR FORCE FLIGHT DYNAMICS LABORATORY  
AIR FORCE SYSTEMS COMMAND  
WRIGHT-PATTERSON AIR FORCE BASE, OHIO

AD 878776

AD No. \_\_\_\_\_  
DDC FILE COPY

455

**Best  
Available  
Copy**

NOTICE

When Government drawings, specifications, or other data are used for any purpose other than in connection with a definitely related Government procurement operation, the United States Government thereby incurs no responsibility nor any obligation whatsoever; and the fact that the Government may have formulated, furnished, or in any way supplied the said drawings, specifications, or other data, is not to be regarded by implication or otherwise as in any manner licensing the holder or any other person or corporation, or conveying any rights or permission to manufacture, use, or sell any patented invention that may in any way be related thereto.

This document is subject to special export controls and each transmittal to foreign governments or foreign nationals may be made only with prior approval of the Air Force Flight Dynamics Laboratory (FFDL), Wright-Patterson Air Force Base, Ohio, 45433.

The distribution of this report is limited because it contains information that would significantly diminish the technological lead time of the United States and friendly foreign nations by revealing formulas, processes, or techniques having a potential strategic or economic value not generally known throughout the world.

GROUP	WHITE SECTION	<input type="checkbox"/>
NO.	DIFF. SECTION	<input checked="" type="checkbox"/>
CLASSIFIED		<input type="checkbox"/>
EXPIRES		
BY		
DISTRIBUTION/AVAILABILITY CODES		
REST.	AVAIL.	SPECIAL
2		

Copies of this report should not be returned unless return is required by security considerations, contractual obligations, or notice on a specific document.

**LOW ALTITUDE ATMOSPHERIC TURBULENCE**  
**LO-LOCAT PHASE III**

**Volume I, Part I, Data Analysis**

*J. W. JONES, R. H. M'ELKE, G. W. JONES, et al*

This document is subject to special export controls and each transmittal to foreign governments or foreign nationals may be made only with prior approval of the Air Force Flight Dynamics Laboratory (FBE), Wright-Patterson Air Force Base, Ohio 45433.

## FOREWORD

This is the final report on the Low-Low Altitude CAT research work conducted under Contract Number F33615-68-C-1468 (LO-LOCAT Phase III). The report was prepared by The Boeing Company, Wichita Division, for the Air Force Flight Dynamics Laboratory, Wright-Patterson Air Force Base, Ohio.

The LO-LOCAT Phase III project was part of Advanced Development Program 682E (ALLCAT) and was under the direction of ADP 682E Program Director, Mr. E. Brazier, and the Technical Coordinator, Mr. Neal V. Loving. Mr. Jan Garrison, FBZ, was the Air Force Project Engineer.

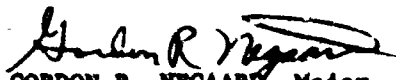
The research effort was conducted under the Boeing supervision of Mr. F. K. Atnip, Program Manager. Mr. C. F. Peterson was the Project Pilot. Mr. D. B. Marshall was in charge of instrumentation, Mr. H. H. Depew directed the data processing effort, Mr. J. D. Gault was in charge of data analysis, and Mr. W. B. Moreland (Boeing-Seattle) directed the meteorological forecasts and analysis. Airplane maintenance and inspection were the responsibility of Mr. J. Strain and Mr. J. Bonawitz, respectively.

Mr. Gerald A. Comstock piloted the observer airplane over the Peterson Field, Colorado, high mountain route and was also backup pilot for this program. While acting in this latter capacity during a data gathering flight over the Griffiss AFB, New York route, Mr. Comstock was fatally injured in a forced landing following an engine flameout.

Authors of this report, other than those shown on the cover, were Messrs D. E. Gunter and K. R. Monson.

The report was submitted by the authors 17 August 1970. It was reviewed by Mr. Jan Garrison and Dr. T. Swaney (Boeing) who made many constructive comments and suggestions.

This technical report has been reviewed and is approved.

  
GORDON R. NEGAARD, Major, USAF  
Chief, Design Criteria Branch  
Structures Division  
Air Force Flight Dynamics Laboratory

## ABSTRACT

This report presents procedures, analysis methods, and final results pertaining to the LO-LOCAT Phase III program. Approximately 150 hours of low altitude (100 - 1000 feet) turbulence and associated meteorological data were recorded from 16 August 1968 through 30 June 1969. The original program was curtailed by approximately six weeks due to the crash of the T-33 research airplane. A model of the turbulence environment at low-level is presented in terms of gust velocity primary peaks, level crossings, amplitude samples, rms values, and gust maxima, as well as derived equivalent gusts, turbulence scale lengths, and power spectra. Mathematical expressions for turbulence spectra, scale length and primary peak statistics are shown. Correlations between atmospheric gust velocities and meteorological and geophysical phenomena are evaluated. It was found that gust velocity magnitude at low altitude is most affected by atmospheric stability and terrain. Gust velocity rms values above 1.5 fps may be approximated by truncated Gaussian distributions. For wavelengths less than 15,000 feet, turbulence spectra are best represented by the von Karman mathematical expressions. The turbulence, sampled for 4-1/2 minute intervals over a distance of approximately 32 miles at absolute altitudes below 1,000 feet, was found to be basically stationary, isotropic, and homogeneous. A high percentage of Phase III data were recorded over high mountains since very little high mountain data were recorded under contour flight conditions at low level during Phases I and II. Phase III data are compared with data from Phases I and II and with data from other low altitude programs.

This report consists of two volumes with each volume divided into two parts. Parts I and II of Volume I give the techniques and results of data analysis. Part I of Volume II provides the details pertaining to data acquisition, instrumentation, calibrations and checks, data processing, and data quality. Data tabulations and plots and a log of pertinent information concerning the program are also presented in Volume II Part I. Part II of Volume II contains the power spectral density and other frequency data plots.

(Distribution of this abstract is unlimited.)

TABLE OF CONTENTS  
VOLUME I DATA ANALYSIS  
PART I

		<u>PAGE NO.</u>
SECTION I	INTRODUCTION	1
	1. Instrumentation	3
	2. Data Categorization Technique	4
	3. Data Analysis	5
	4. Data Gaps in the Turbulence Model	7
SECTION II	SUMMARY	12
SECTION III	GUST VELOCITY TIME FUNCTION	17
	5. Run Test for Stationarity	17
	6. Ensemble Averaging	19
	7. Gaussian Distribution Check	30
	8. Primary Peak Count	32
	9. Amplitude Count	50
	10. Level Crossings Count	56
	11. Comparison of Counting Techniques	62
	12. Correlation of Peak Distributions with Geophysical Category	87
SECTION IV	GUST VELOCITY INTENSITY	104
	13. Gust Velocity RMS Statistical Analysis	104
	14. Gust Velocity RMS versus Inflight Measured Wind Velocity	149
	15. Maximum Derived Equivalent Gust Velocities	183
	16. Maximum Gust Velocity During Each Sample	189
	17. Severe and Extreme Turbulence Samples	190
	18. Gust Velocity Magnitude versus Temperature Correlations	263
SECTION V	GUST VELOCITY SPECTRA	272
	19. Instrumentation Anomalies, Low Intensity Turbulence Levels	272
	20. Statistical Confidence and Independency	275
	21. Homogeneity	280
	22. Isotropy	288
	23. Normalized Spectra	296
	24. Cross Spectra	317
	25. Truncated Standard Deviations	332



TABLE OF CONTENTS

	<u>PAGE</u> <u>NO.</u>	
SECTION V	GUST VELOCITY SPECTRA (Contd.)	
	26. Gust Velocity Distance History Power Spectra	336
	27. Spectra During High Speed Flight	342
	28. Experimental/Mathematical Spectra Comparison	347
	29. Recommended Spectra Shape	354
	30. Turbulence Scale Length	356
	31. Turbulence Microscales	399
REFERENCES	VOLUME I	408
VOLUME I DATA ANALYSIS		
PART II		
SECTION VI	GEOPHYSICAL CHARACTERISTICS	1
	32. Terrain Profiles	1
	33. Wind Speed	22
	34. Viscous Dissipation Rate	53
SECTION VII	TURBULENCE FORECASTING	60
	35. Meteorological Data Sampling	60
	36. Forecast Evaluations	67
	37. Case Studies - Phases I and II	76
	38. Case Studies - Phase III	111
	39. Richardson Number	143
	40. Stability Ratio	152
SECTION VIII	EREN TOWER, THUNDERSTORM, AND WAKE TURBULENCE INVESTIGATIONS	160
	41. EREN Tower Flyby	160
	42. Thunderstorm Turbulence	173
	43. Wake Turbulence	192
SECTION IX	COMPARISON OF LO-LOCAT PHASES I AND II WITH PHASE III DATA	249
	44. Gust Velocity RMS Values	249
	45. Peak Count	268
	46. Power Spectra	282
	47. Scale Lengths	287
	48. Relationships Between Turbulence and Meteorological Data	294

TABLE OF CONTENTS

	<u>PAGE</u> <u>NO.</u>
SECTION X      COMPARISON OF LO-LOCAT (PHASES I, II, AND III) WITH OTHER LOW ALTITUDE TURBULENCE DATA	313
49.    Peak Count	313
50.    Power Spectra Comparison	320
SECTION XI     ADDITIONAL RESEARCH	349
51.    Gust Acceleration	352
52.    Wind Spectra	394
53.    High Intensity Gust Program Re-Evaluation	413
SECTION XII    CONCLUSIONS	450
REFERENCES    VOLUME I	453

VOLUME II DATA ACQUISITION AND PROCESSING,  
DATA PLOTS, AND TABULATIONS

PART I

APPENDIX I    AIRPLANE MODIFICATION AND INSTRUMENTATION DETAILS	1
I.1    Airplane Modification	1
I.2    Gust Boom and Probe Design	2
I.3    Airplane Instrumentation	3
I.4    Mobile Ground Station	14
APPENDIX II   CALIBRATIONS AND CHECKS	25
II.1    Calibrations in the Laboratory and at the Airplane	25
II.2    Wind Tunnel Static Calibration of the Gust Probe	25
II.3    Wind Tunnel Dynamic Calibration of the Gust Probe	27
II.4    Dynamic Calibration of the Gust Probe Installed on the Airplane	28
II.5    Inflight Calibration of Angles of Attack and Sideslip Differential Pressures	29
II.6    Inflight Calibration of the Gust Probe and Airplane Airspeed Systems	31
II.7    Gust Probe and Boom Natural Frequency Determination	32
II.8    Outside Air Temperature Calibration	33
II.9    Radiometer (Ground Surface Temperature) Calibration	34

TABLE OF CONTENTS

	<u>PAGE NO.</u>
APPENDIX II CALIBRATIONS AND CHECKS (Contd.)	
II.10 Radar Altimeter Check	37
II.11 Ground Speed Calibration Verification	37
APPENDIX III DATA QUALITY	53
III.1 Evaluation of Transducer Inaccuracies	53
III.2 Bias Error Corrections	54
III.3 Frequency Response Compensation	55
III.4 Instrumentation Noise Removal	56
III.5 Evaluation of Instrumentation Noise Not Removed	57
III.6 Drift Analysis	59
III.7 Evaluation of Interchangeable Variables	63
III.8 Probe Motion Removal Evaluation	55
III.9 Overall Quality of Gust Velocity Calculations	66
III.10 Digital Filtering Application and Evaluation	67
APPENDIX IV DATA ACQUISITION OPERATION	103
IV.1 Operations	103
IV.2 Flight Operations	104
IV.3 Ground Operations	105
APPENDIX V DATA PROCESSING	113
V.1 Ground Station Data Processing	113
V.2 Computer Programs	116
V.3 Multiple Regression	135
APPENDIX VI TEST LOG	143
APPENDIX VII GUST VELOCITY PEAK, AMPLITUDE, AND LEVEL CROSSINGS COUNT DATA	182
APPENDIX VIII DATA TABULATIONS	268
REFERENCES VOLUME II	338

VOLUME II FREQUENCY DATA PLOTS

PART II

APPENDIX IX GUST VELOCITY POWER SPECTRA AND ASSOCIATED DATA	1-457
---	-------

LIST OF ILLUSTRATIONS

VOLUME I, PART I

<u>FIGURE NO.</u>	<u>TITLE</u>	<u>PAGE NO.</u>
3.1	Primary Editing Sequence	6
4.1	Data Gaps	8
6.1	Power Spectra and Associated Data of Ensemble Average Time Function for High Mountain, 250 Feet, Stable Category	21
6.2	Power Spectra and Associated Data of Ensemble Average Time Function for High Mountain, 250 Feet, Neutral Category	22
6.3	Power Spectra and Associated Data of Ensemble Average Time Function for High Mountain, 250 Feet, Unstable Category	23
6.4	Power Spectra and Associated Data of Ensemble Average Time Function for High Mountain, 750 Feet, Stable Category	24
6.5	Power Spectra and Associated Data of Ensemble Average Time Function for High Mountain, 750 Feet, Neutral Category	25
6.6	Power Spectra and Associated Data of Ensemble Average Time Function for High Mountain, 750 Feet, Unstable Category	26
6.7	Power Spectra and Associated Data of Ensemble Average Time Function for Plains, 250 Feet, Unstable Category	27
6.8	Power Spectra and Associated Data of Ensemble Average Time Function for Plains, 750 Feet, Unstable Category	28
6.9	Scale Length Comparison	29
7.1	Chi-Square Test for Statistical Normality	31
8.1	Primary Peak Count Example	39
8.2	Peak Count Extrapolation Technique	40
8.3	Gust Velocity Peak Count Probability Distribution for an Individual Turbulence Sample	41

LIST OF ILLUSTRATIONS

VOLUME I, PART I

<u>FIGURE NO.</u>	<u>TITLE</u>	<u>PAGE NO.</u>
8.4	Gust Velocity Peak Count Probability Density Distribution	42
8.5	Gust Velocity Peak Distribution	43
8.6	Longitudinal Gust Velocity Peak Count Distribution with 99% Confidence Limits	44
8.7	Lateral Gust Velocity Peak Count Distribution with 99% Confidence Limits	45
8.8	Vertical Gust Velocity Peak Count Distribution with 95% Confidence Limits	46
8.9	Longitudinal Gust Velocity Peak Count Distribution with 95% Confidence Limits	47
8.10	Lateral Gust Velocity Peak Count Distribution with 95% Confidence Limits	48
8.11	Vertical Gust Velocity Peak Count Distribution with 95% Confidence Limits	49
9.1	Amplitude Count Example	51
9.2	Gust Velocity Amplitude Count Cumulative Distribution for an Individual Turbulence Sample	52
9.3	Gust Velocity Amplitude Count Cumulative Probability Distribution for an Individual Turbulence Sample	53
9.4	Gust Velocity Amplitude Count Probability Density Distribution for an Individual Turbulence Sample	54
9.5	Amplitude Count Cumulative Probability Distributions	55
10.1	Level Crossings Count Example	58
10.2	Gust Velocity Level Crossing Distribution for an Individual Turbulence Sample	59
10.3	Gust Velocity Level Crossing Probability Distribution for an Individual Turbulence Sample	60

LIST OF ILLUSTRATIONS

VOLUME I, PART I

<u>FIGURE NO.</u>	<u>TITLE</u>	<u>PAGE NO.</u>
10.4	Gust Velocity Level Crossing Probability Density Distribution for an Individual Turbulence Sample	61
11.1	Longitudinal Gust Velocity Distributions for an Individual Turbulence Sample	66
11.2	Lateral Gust Velocity Distributions for an Individual Turbulence Sample	67
11.3	Vertical Gust Velocity Distribution for an Individual Turbulence Sample	68
11.4	Comparison of Peak and Level Crossing Count Distributions - Longitudinal Gust Velocity	69
11.5	Comparison of Peak and Level Crossing Count Distributions - Lateral Gust Velocity	70
11.6	Comparison of Peak and Level Crossing Count Distributions - Vertical Gust Velocity	71
11.7	Longitudinal Gust Velocity Probability Distributions for an Individual Turbulence Sample	72
11.8	Lateral Gust Velocity Probability Distributions for an Individual Turbulence Sample	73
11.9	Vertical Gust Velocity Probability Distributions for an Individual Turbulence Sample	74
11.10	Longitudinal Gust Velocity Probability Distribution for LO-LOCAT Phase III	75
11.11	Lateral Gust Velocity Probability Distribution for LO-LOCAT Phase III	76
11.12	Vertical Gust Velocity Probability Distribution for LO-LOCAT Phase III	77
11.13	Longitudinal Gust Velocity Probability Density Distributions for an Individual Turbulence Sample	78
11.14	Lateral Gust Velocity Probability Distributions for an Individual Turbulence Sample	79

LIST OF ILLUSTRATIONS

VOLUME I, PART I

<u>FIGURE NO.</u>	<u>TITLE</u>	<u>PAGE NO.</u>
11.15	Vertical Gust Velocity Probability Distributions for an Individual Turbulence Sample	80
11.16	Longitudinal Gust Velocity Probability Density Distribution	81
11.17	Lateral Gust Velocity Probability Density Distribution	82
11.18	Vertical Gust Velocity Probability Density Distribution	83
11.19	Comparison of Longitudinal Gust Velocity Standard Deviations Calculated by Different Techniques	84
11.20	Comparison of Lateral Gust Velocity Standard Deviations Calculated by Different Techniques	85
11.21	Comparison of Vertical Gust Velocity Standard Deviations Calculated by Different Techniques	86
12.1	Terrain Effects on Longitudinal Gust Velocity Peaks	89
12.2	Terrain Effects on Lateral Gust Velocity Peaks	90
12.3	Terrain Effects on Vertical Gust Velocity Peaks	91
12.4	Altitude Effects on Longitudinal Gust Velocity Peaks	92
12.5	Altitude Effects on Lateral Gust Velocity Peaks	93
12.6	Altitude Effects on Vertical Gust Velocity Peaks	94
12.7	Stability Effects on Longitudinal Gust Velocity Peaks	95
12.8	Stability Effects on Lateral Gust Velocity Peaks	96
12.9	Stability Effects on Vertical Gust Velocity Peaks	97
12.10	Time of Day Effects on Longitudinal Gust Velocity Peaks	98

LIST OF ILLUSTRATIONS

VOLUME I, PART I

<u>FIGURE NO.</u>	<u>TITLE</u>	<u>PAGE NO.</u>
12.11	Time of Day Effects on Lateral Gust Velocity Peaks	99
12.12	Time of Day Effects on Vertical Gust Velocity Peaks	100
12.13	Location Effects on Longitudinal Gust Velocity Peaks	101
12.14	Location Effects on Lateral Gust Velocity Peaks	102
12.15	Location Effects on Vertical Gust Velocity Peaks	103
13.1	Gust Velocity RMS Cumulative Probability	112
13.2	Gust Velocity RMS Cumulative Probability Associated with Type of Terrain	113
13.3	Gust Velocity RMS Cumulative Probability Associated with Absolute Altitude	114
13.4	Gust Velocity RMS Cumulative Probability Associated with Atmospheric Stability	115
13.5	Gust Velocity RMS Cumulative Probability Associated with Time of Day	116
13.6	Gust Velocity RMS Cumulative Probability Associated with Geographic Location	117
13.7	Season Effects on Gust Velocity RMS Values - Peterson	118
13.8	Terrain Effects on Gust Velocity RMS Values - 250 Feet, Very Stable	119
13.9	Terrain Effects on Gust Velocity RMS Values - 750 Feet, Very Stable	120
13.10	Terrain Effects on Gust Velocity RMS Values - 250 Feet, Stable	121
13.11	Terrain Effects on Gust Velocity RMS Values - 750 Feet, Stable	122



LIST OF ILLUSTRATIONS

VOLUME I, PART I

<u>FIGURE NO.</u>	<u>TITLE</u>	<u>PAGE NO.</u>
13.12	Terrain Effects on Gust Velocity RMS Values - 250 Feet, Neutral	123
13.13	Terrain Effects on Gust Velocity RMS Values - 750 Feet, Neutral	124
13.14	Terrain Effects on Gust Velocity RMS Values - 250 Feet, Unstable	125
13.15	Terrain Effects on Gust Velocity RMS Values - 750 Feet, Unstable	126
13.16	Altitude Effects on Gust Velocity RMS Values - High Mountains, Very Stable	127
13.17	Altitude Effects on Gust Velocity RMS Values - High Mountains, Stable	128
13.18	Altitude Effects on Gust Velocity RMS Values - High Mountains, Neutral	129
13.19	Altitude Effects on Gust Velocity RMS Values - High Mountains, Unstable	130
13.20	Altitude Effects on Gust Velocity RMS Values - Plains, Very Stable	131
13.21	Altitude Effects on Gust Velocity RMS Values - Plains, Stable	132
13.22	Altitude Effects on Gust Velocity RMS Values - Plains, Neutral	133
13.23	Altitude Effects on Gust Velocity RMS Values - Plains, Unstable	134
13.24	Atmospheric Stability Effects on Gust Velocity RMS Values - 250 Feet, High Mountains	135 o
13.25	Atmospheric Stability Effects on Gust Velocity RMS Values - 750 Feet, High Mountains	136
13.26	Atmospheric Stability Effects on Gust Velocity RMS Values - 250 Feet, Plains	137

LIST OF ILLUSTRATIONS

VOLUME I, PART I

<u>FIGURE NO.</u>	<u>TITLE</u>	<u>PAGE NO.</u>
13.27	Atmospheric Stability Effects on Gust Velocity RMS Values - 750 Feet, Plains	138
13.28	Terrain Effects on Gust Velocity RMS Values - 250 Feet	139
13.29	Terrain Effects on Gust Velocity RMS Values - 750 Feet	140
13.30	Altitude Effects on Gust Velocity RMS Values - High Mountains	141
13.31	Altitude Effects on Gust Velocity RMS Values - Low Mountains	142
13.32	Altitude Effects on Gust Velocity RMS Values - Desert	143
13.33	Altitude Effects on Gust Velocity RMS Values - Plains	144
13.34	Comparison of Vertical Gust Velocity RMS Values from Various Research Programs	145
13.35	Longitudinal Gust Velocity RMS Cumulative Proba- bility Distribution Shape	146
13.36	Lateral Gust Velocity RMS Cumulative Probability Distribution Shape	147
13.37	Vertical Gust Velocity RMS Cumulative Probability Distribution Shape	148
14.1	Gust Velocity RMS Values versus Wind Speed at 250 Feet over High Mountains	153
14.2	Gust Velocity RMS Values versus Wind Speed at 750 Feet over High Mountains	154
14.3	Gust Velocity RMS Values versus Wind Speed at 250 Feet over Low Mountains	155
14.4	Gust Velocity RMS Values versus Wind Speed at 750 Feet over Low Mountains	156

LIST OF ILLUSTRATIONS

VOLUME I, PART I

<u>FIGURE NO.</u>	<u>TITLE</u>	<u>PAGE NO.</u>
14.5	Gust Velocity RMS Values versus Wind Speed at 250 Feet over Desert	157
14.6	Gust Velocity RMS Values versus Wind Speed at 750 Feet over Desert	158
14.7	Gust Velocity RMS Values versus Wind Speed at 250 Feet over Plains	159
14.8	Gust Velocity RMS Values versus Wind Speed at 750 Feet over Plains	160
14.9	Correlation of Gust Velocity RMS Values with Wind Speed as a Function of Terrain and Altitude	161
14.10	Effect of Wind Speed on Gust Velocity RMS Values - High Mountains	162
14.11	Effect of Wind Speed on Gust Velocity RMS Values - Low Mountains	163
14.12	Effect of Wind Speed on Gust Velocity RMS Values - Desert	164
14.13	Effect of Wind Speed on Gust Velocity RMS Values - Plains	165
14.14	Correlation Between Longitudinal Gust Velocity RMS Values and Wind Speed with Respect to Wind Direction - Leg 5 at Peterson	166
14.15	Correlation Between Lateral Gust Velocity RMS Values and Wind Speed with Respect to Wind Direction - Leg 5 at Peterson	167
14.16	Correlation Between Vertical Gust Velocity RMS Values and Wind Speed with Respect to Wind Direction - Leg 5 at Peterson	168
14.17	Correlation Between Longitudinal Gust Velocity RMS Values and Wind Speed with Respect to Wind Direction - Leg 6 at Peterson	169

LIST OF ILLUSTRATIONS

VOLUME I, PART I

<u>FIGURE NO.</u>	<u>TITLE</u>	<u>PAGE NO.</u>
14.18	Correlation Between Lateral Gust Velocity RMS Values and Wind Speed with Respect to Wind Direction - Leg 6 at Peterson	170
14.19	Correlation Between Vertical Gust Velocity RMS Values and Wind Speed with Respect to Wind Direction - Leg 6 at Peterson	171
14.20	Correlation Between Longitudinal Gust Velocity RMS Values and Wind Speed with Respect to Wind Direction - Leg 7 at Peterson	172
14.21	Correlation Between Lateral Gust Velocity RMS Values and Wind Speed with Respect to Wind Direction - Leg 7 at Peterson	173
14.22	Correlation Between Vertical Gust Velocity RMS Values and Wind Speed with Respect to Wind Direction - Leg 7 at Peterson	174
<del>14.23</del>	Correlation Between Longitudinal Gust Velocity RMS Values and Wind Speed with Respect to Wind Direction - Leg 3 at Peterson	175
14.24	Correlation Between Lateral Gust Velocity RMS Values and Wind Speed with Respect to Wind Direction - Leg 8 at Peterson	176
14.25	Correlation Between Vertical Gust Velocity RMS Values and Wind Speed with Respect to Wind Direction - Leg 8 at Peterson	177
14.26	Effects of Wind Direction on the Correlation Between Gust Velocity RMS Values and Wind Speed - Leg 5 at Peterson	178
14.27	Effects of Wind Direction on the Correlation Between Gust Velocity RMS Values and Wind Speed - Leg 6 at Peterson	179
14.28	Effects of Wind Direction on the Correlation Between Gust Velocity RMS Values and Wind Speed - Leg 7 at Peterson	180

LIST OF ILLUSTRATIONS

VOLUME I, PART I

<u>FIGURE NO.</u>	<u>TITLE</u>	<u>PAGE NO.</u>
14.29	Effects of Wind Direction on the Correlation Between Gust Velocity RMS Values and Wind Speed - Leg 8 at Peterson	181
14.30	Correlation of Gust Velocity RMS Values with Wind Speed as a Function of Terrain and Atmospheric Stability	182
15.1	Cumulative Probability of Maximum Absolute Gust Velocity and $U_{de}$ - All Categories	185
15.2	Cumulative Probability of Maximum Absolute Gust Velocity and $U_{de}$ as a Function of Terrain	186
15.3	Cumulative Probability of Maximum Absolute Gust Velocity and $U_{de}$ as a Function of Altitude	187
15.4	Cumulative Probability of Maximum Absolute Gust Velocity and $U_{de}$ as a Function of Time of Day	188
17.1	Time History of Severe Turbulence Encounter - Edwards	192
17.2 thru 17.71	Time History of Severe Turbulence Encounter - Peterson	193-262
18.1	Coherency of Vertical Gust Velocity with Outside Air and Ground Surface Temperatures	265
18.2	Coherency of Vertical Gust Velocity with Outside Air and Ground Surface Temperatures	266
18.3	Coherency of Vertical Gust Velocity with Outside Air and Ground Surface Temperatures	267
18.4	Coherency of Vertical Gust Velocity with Outside Air and Ground Surface Temperatures	268
18.5	Slope of GSF Spectra versus Ground Speed	269
18.6	Power Spectrum of Total Air Temperature Measurement over Plains Leg	270
18.7	Ground Surface Temperature Standard Deviation versus Gust Velocity Standard Deviation	271

LIST OF ILLUSTRATIONS

VOLUME I, PART I

<u>FIGURE NO.</u>	<u>TITLE</u>	<u>PAGE NO.</u>
19.1	Gust Velocity Power Spectra of a Data Sample Containing Instrumentation Irregularities	273
19.2	Gust Velocity Power Spectra of a Data Sample Having Low Signal-to-Noise Ratio	274
20.1	Confidence Bands Associated with Pooled Samples	278
20.2	Average Coherency	279
21.1	Homogeneity Characteristics for LO-LOCAT Phase III	282
21.2	Cumulative Probability Distribution of Power Spectra Ratio Mean Values - Homogeneous Sample Only	283
21.3	Variation of Homogeneity Characteristics with Terrain	284
21.4	Variation of Homogeneity Characteristics with Absolute Altitude	285
21.5	Variation of Homogeneity Characteristics with Atmospheric Stability	286
21.6	Variation of Homogeneity Characteristics with Time of Day	287
22.1	Isotropy Based on von Karman Expressions	290
22.2	Isotropy Characteristics - All Categories	291
22.3	Isotropy Characteristics for Different Altitudes	292
22.4	Isotropy Characteristics for Different Terrain	293
22.5	Isotropy Characteristics for Different Atmospheric Stabilities	294
22.6	Isotropy Characteristics for Different Times of Day	295
23.1	Longitudinal Power Spectrum Variation with Terrain	298

LIST OF ILLUSTRATIONS

VOLUME I, PART I

<u>FIGURE NO.</u>	<u>TITLE</u>	<u>PAGE NO.</u>
23.2	Lateral Power Spectrum Variation with Terrain	299
23.3	Vertical Power Spectrum Variation with Terrain	300
23.4	Power Spectrum of Differential Sideslip Pressure	301
23.5	Lateral Power Spectrum	302
23.6	Lateral Power Spectrum	303
23.7	Longitudinal Power Spectrum Variation with Altitude	304
23.8	Lateral Power Spectrum Variation with Altitude	305
23.9	Vertical Power Spectrum Variation with Altitude	306
23.10	Vertical Power Spectrum	307
23.11	Longitudinal Power Spectrum Variation with Stability	308
23.12	Lateral Power Spectrum Variation with Stability	309
23.13	Vertical Power Spectrum Variation with Stability	310
23.14	Longitudinal Power Spectrum Variation with Time of Day	311
23.15	Lateral Power Spectrum Variation with Time of Day	312
23.16	Vertical Power Spectrum Variation with Time of Day	313
23.17	Representative Scatter Bands for Categorized Longitudinal Power Spectra	314
23.18	Representative Scatter Bands for Categorized Lateral Power Spectra	315
23.19	Representative Scatter Bands for Categorized Vertical Power Spectra	316
24.1	Schematic of Eddies Arranged Contiguously next to Ground	318

LIST OF ILLUSTRATIONS

VOLUME I, PART I

<u>FIGURE NO.</u>	<u>TITLE</u>	<u>PAGE NO.</u>
24.2	Gust Velocities Encountered when Passing Through Contiguous Eddies Below Center	318
24.3	Gust Velocities Encountered when Passing Through Contiguous Eddies Above Center	318
24.4	Cross, Co, and Quadrature Power Relationship for Lateral - Longitudinal Gust Velocity, Test 28, Leg 6, Category 412224	319
24.5	Cross, Co, and Quadrature Power Relationship for Lateral - Vertical Gust Velocity, Test 28, Leg 6, Category 412224	320
24.6	Cross, Co, and Quadrature Power Relationship for Longitudinal - Vertical Gust Velocity, Test 28, Leg 6, Category 412224	321
24.7	Cross, Co, and Quadrature Power Relationship for Lateral - Longitudinal Gust Velocity, Test 51, Leg 3, Category 323231	322
24.8	Cross, Co, and Quadrature Power Relationship for Lateral - Vertical Gust Velocity, Test 51, Leg 3, Category 323231	323
24.9	Cross, Co, and Quadrature Power Relationship for Longitudinal - Vertical Gust Velocity, Test 51, Leg 3, Category 323231	324
24.10	Cross, Co, and Quadrature Power Relationship for Lateral - Longitudinal Gust Velocity, Test 66, Leg 2, Category 312331	325
24.11	Cross, Co, and Quadrature Power Relationship for Lateral - Vertical Gust Velocity, Test 66, Leg 2, Category 312331	326
24.12	Cross, Co, and Quadrature Power Relationship for Longitudinal - Vertical Gust Velocity, Test 66, Leg 2, Category 312331	327
24.13	Cross, Co, and Quadrature Power Relationship for Lateral - Longitudinal Gust Velocity, Test 66, Leg 6, Category 113331	328



LIST OF ILLUSTRATIONS

VOLUME I, PART I

<u>FIGURE NO.</u>	<u>TITLE</u>	<u>PAGE NO.</u>
24.14	Cross, Co, and Quadrature Power Relationship for Lateral - Vertical Gust Velocity, Test 66, Leg 6, Category 113331	329
24.15	Cross, Co, and Quadrature Power Relationship for Longitudinal - Vertical Gust Velocity, Test 66, Leg 6, Category 113331	330
24.16	u to w Quad-Spectra Trends	331
25.1	Truncated Standard Deviation Variation with Phase - Low Mountains	334
25.2	Truncated Standard Deviation Variation with Phase - Plain	335
26.1	Time History - Distance History Power Spectra Comparison, Test 40, Leg 4	338
26.2	Time History - Distance History Power Spectra Comparison, Test 46, Leg 4	339
26.3	Time History - Distance History Power Spectra Comparison, Test 46, Leg 6	340
26.4	Time History - Distance History Power Spectra Comparison, Test 87, Leg 7	341
27.1	High Speed Flight Gust Velocity Power Spectra	344
27.2	Average Isotropy for High Speed Flight Samples	345
27.3	Average Coherency for High Speed Flight Samples	346
28.1	Comparison of Experimental and von Karman Power Spectra	350
28.2	Comparison of Experimental and Dryden Power Spectra	351
28.3	Comparison of Experimental Power Spectra with Lumley-Panofsky and Busch-Panofsky Power Spectra	352
28.4	Comparison of Agreement Between Mathematical and Experimental Power Spectra	353

LIST OF ILLUSTRATIONS

VOLUME I, PART I

<u>FIGURE NO.</u>	<u>TITLE</u>	<u>PAGE NO.</u>
30.1	Example Longitudinal Gust Velocity Autocorrelation Function Plot	368
30.2	Example Lateral Gust Velocity Autocorrelation Function Plot	369
30.3	Example Vertical Gust Velocity Autocorrelation Function Plot	370
30.4	Comparison of von Karman and Autocorrelation Function Derived Longitudinal Scale Lengths	371
30.5	Comparison of von Karman and Autocorrelation Function Derived Longitudinal Scale Lengths	372
30.6	Comparison of von Karman and Autocorrelation Function Derived Longitudinal Scale Lengths	373
30.7	Comparison of von Karman and Autocorrelation Function Derived Longitudinal Scale Lengths	374
30.8	Comparison of von Karman and Autocorrelation Function Derived Longitudinal Scale Lengths	375
30.9	Comparison of von Karman and Autocorrelation Function Derived Longitudinal Scale Lengths	376
30.10	Comparison of von Karman and $1/k$ Derived Longitudinal Scale Lengths	377
30.11	Comparison of von Karman and $1/k$ Derived Longitudinal Scale Lengths	378
30.12	Comparison of von Karman and $1/k$ Derived Longitudinal Scale Lengths	379
30.13	von Karman Longitudinal Scale Length Cumulative Probability	380
30.14	von Karman Longitudinal Scale Length Cumulative Probability Associated with Terrain Type	381
30.15	von Karman Longitudinal Scale Length Cumulative Probability Associated with Absolute Altitude	382

LIST OF ILLUSTRATIONS

VOLUME I, PART I

<u>FIGURE NO.</u>	<u>TITLE</u>	<u>PAGE NO.</u>
30.16	von Karman Longitudinal Scale Length Cumulative Probability Associated with Atmospheric Stability	383
30.17	von Karman Longitudinal Scale Length Cumulative Probability Associated with Time of Day	384
30.18	Effects of Time of Day on Cumulative Probability of Gust Velocity RMS Values Used in Scale Length Calculations	385
30.19	Effects of Terrain Type on Cumulative Probability of von Karman Longitudinal Scale Lengths from Data Recorded at 250 Feet	386
30.20	Effects of Terrain Type on Cumulative Probability of von Karman Longitudinal Scale Lengths from Data Recorded at 750 Feet	387
30.21	Effects of Atmospheric Stability on Cumulative Probability of von Karman Longitudinal Scale Lengths from Data Recorded at 250 Feet	388
30.22	Effects of Atmospheric Stability on Cumulative Probability of von Karman Longitudinal Scale Lengths from Data Recorded at 750 Feet	389
30.23	Effects of Absolute Altitude on Cumulative Probability of von Karman Longitudinal Scale Lengths from Data Recorded Over High Mountains	390
30.24	Effects of Absolute Altitude on Cumulative Probability of von Karman Longitudinal Scale Lengths from Data Recorded Over Low Mountains	391
30.25	Effects of Absolute Altitude on Cumulative Probability of von Karman Longitudinal Scale Lengths from Data Recorded Over Plains	392
30.26	Variations of Mean von Karman Longitudinal Scale Length with Absolute Altitude and Terrain Type	393
30.27	Variations of Mean von Karman Longitudinal Scale Length with Absolute Altitude and Atmospheric Stability	394

LIST OF ILLUSTRATIONS

VOLUME I, PART I

<u>FIGURE NO.</u>	<u>TITLE</u>	<u>PAGE NO.</u>
30.28	Dryden Longitudinal Scale Length Cumulative Probability	395
30.29	Cumulative Probability of Lumley-Panofsky Scale Parameter, $C$ , as Calculated from the Longitudinal Component	396
30.30	Cumulative Probability of Busch-Panofsky Scale Parameter, $C_v$ , as Calculated from the Lateral Component	397
30.31	Cumulative Probability of Busch-Panofsky Scale Parameter, $C_v$ , as Calculated from the Vertical Component	398
31.1	Variation of Taylor Microscale for Time of Day	401
31.2	Variation of Taylor Microscale for Altitude and Atmospheric Stability	402
31.3	Variation of Taylor Microscale for Plains and Mountain Terrain	403
31.4	Variation of Kolmogorov Microscale for Time of Day	404
31.5	Variation of Kolmogorov Microscale for Altitude and Stability	405
31.6	Variation of Kolmogorov Microscale for Plains and Mountain Terrain	406
31.7	Variation of Taylor Microscale with Altitude	407
31.8	Variation of Kolmogorov Microscale with Altitude	407

LIST OF TABLES

VOLUME I, PART I

<u>TABLE NO.</u>	<u>TITLE</u>	<u>PAGE NO.</u>
4.1	Statistics of Gust Velocity Intensity ( $\sigma_t$ ) with Respect to Season and Location During Phases I and II	10
4.2	Number of IFR Days	11
4.3	Number of Thunderstorm Days	11
II.1	Basic LO-LOCAT Information	14
5.1	Percent of Turbulence Samples Accepted as Stationary at the 0.02 Level of Significance	19
8.1	Number of Low Intensity Turbulence Samples in Each Category for Statistical Analysis of Peak, Amplitude, and Level Crossings Count	35
8.2	Total Number of Turbulence Samples in Each Combined Category Distribution and the Number of Low Intensity Samples Included - Peak, Amplitude, and Level Crossings Count	37
8.3	P and b Values for Peak Count Cumulative Probability Distribution Functions	38
11.1	Comparison of Characteristic Frequencies Calculated from Power Spectra, Peak Count and Level Crossings Data	64
13.1	Total Number of Samples and Numbers of Low Intensity Turbulence Samples Included in Gust Velocity RMS Analysis	109
13.2	LO-LOCAT Gust Velocity RMS Ratios Compared to Those Recommended by Reference 13.1	110
13.3	Gust Velocity RMS Distribution Constants	111
14.1	Wind Direction Categorization	151
15.1	$U_{ds}$ Equations and Equation Constants	184
17.1	Tabulation of Samples and Components Equal to or Exceeding 50 FPS	191
26.1	Comparison of Distance History and Time History Standard Deviations	337

LIST OF TABLES

VOLUME 1, PART I

<u>TABLE NO.</u>	<u>TITLE</u>	<u>PAGE NO.</u>
27.1	Turbulence Samples Recorded at High Speed	343
30.1	LO-LOCAT Phase III Scale Lengths for von Karman Expressions Compared to Those Recommended by MIL-F-008785A (USAF)	363
30.2	LO-LOCAT Phase III Scale Length for Dryden Expressions Compared to Those Recommended by MIL-F-008785A (USAF)	363
30.3	LO-LOCAT Phase III Scale Length Ratios Compared with Those Recommended by Reference 13.1	364
30.4	LO-LOCAT Phase III Scale Lengths Compared to Those Recommended by AFFDL-TR-67-122	366
30.5	LO-LOCAT Phase III Average Scale Lengths	367
31.1	Average Taylor and Kolmogorov Microscales	400

## SYMBOLS

Infrequently used symbols are defined after the equation in which they are used.

### Symbols and Abbreviations:

A	Regression coefficient.
A thru H, J, K	Angle of attack equation coefficients.
A' thru H', J', K'	Angle of sideslip equation coefficients.
A(n)	Complex finite transform.
$\bar{A}(n)$	Complex conjugate of A(n).
a	"Universal Constant" in the longitudinal gust velocity component spectrum expression; shape parameter used in spectra mathematical expressions; constant in gust velocity rms distribution equation.
B	Air stability ratio.
b	Constant in gust velocity rms distribution equation.
b <sub>1</sub> , b <sub>2</sub>	Constants in the analytical expressions of the peak count probability distributions.
C	Constant in the Lumley-Panofsky equation.
CC	Cloud cover (percent).
CDT	Central Daylight Time.
C <sub>L</sub>	Airplane lift curve slope (radians) <sup>-1</sup> .
C <sub>v</sub>	Constant in the Busch-Panofsky equations.
c	Length of mean aerodynamic chord (feet).
c.g.	Airplane center of gravity.
cpf	Cycles/foot.
cps	Cycles/second.
DOY	Day of year.
d	Degrees of freedom; distance traveled (statute miles); differential.

## SYMBOLS

### Symbols and Abbreviations:

$E_i$	Normalized standard error of a regression coefficient
$E_\alpha$	Total crossings of the level $\alpha$ .
$e$	Base of natural logarithms (2.71828).
$F$	F-ratio or F-test of significance in regression analysis.
$F(x)$	Cumulative probability distribution function.
$f$	Frequency (cycles/second); function.
$f(r)$	Longitudinal correlation function.
$f_b$	Frequency of occurrence in band $b$ .
$f_c$	Cutoff frequency of a low-pass filter (cycles/second).
$f_N$	Nyquist or folding frequency (cycles/second).
$f_s$	Sampling frequency (samples/second).
GMT	Greenwich Mean Time.
$G_s$	Ground speed (feet/second).
$g$	Earth's gravitational constant at sea level $(32.174 \text{ feet/second})^2$ .
$g(r)$	Lateral or vertical correlation function.
$H$	Altitude above the earth's surface (feet); true altitude (feet).
$H_c$	Calibrated pressure altitude (feet).
$H(f)$	Filter transfer function.
Hg	Symbol for the element mercury.
$H_I$	Indicated reading of tower altimeter (feet).
$H_I, H_1$	Indicated pressure altitude (feet).
$\overline{H}_N(f)$	Constrained filter transfer function.



## SYMBOLS

### Symbols and Abbreviations:

$H_p$	Pressure altitude (feet).
$H_t$	Terrain elevation (feet).
$h$	True heading (degrees).
$h_m$	Magnetic heading (degrees).
$h_n$	Filter weights at time $t \pm n \Delta t$ .
$\bar{h}_n$	Constrained filter weights.
$h(t, r)$	Time domain weighting function.
$h_0$	Constant in empirical scale length equation.
$i$	Counter; time series sample.
IAS	Indicated airspeed.
IRIG	Inter-range Instrumentation Group.
$j$	Square root of minus one.
$K_{a,b}$	Constants.
KIAS	Knots indicated airspeed.
$K_c$	Gust alleviation factor.
$K_r$	Ram recovery factor for OAT probe.
$k$	Spatial frequency (cycles/foot); order of the derivative of the transfer function $H(f)$ ; indicates number of records.
$L$	Turbulence scale length (feet).
$L_n$	Constant in empirical scale length equation.
$M$	True Mach number.
$n$	Maximum lag ( $f_0/\Delta f$ ); slope of a line; number of functions of the input variables; and meters.
mb	Millibar.
mm	Millimeter.

## SYMBOLS

### Symbols and Abbreviations:

N	Total number of conditions, data points, samples, peaks, bands, or filter weights.
NBPM	Narrow band frequency modulation.
$N_0$	Characteristic frequency from power spectral density (cycles/foot).
$N_{0L}$	Number of zero level crossings.
$N_p$	Total number of peaks per mile obtained using extrapolation technique (characteristic frequency).
$N_{pe}$	Total number of peaks obtained using extrapolation technique.
$N_\alpha$	Crossings per mile of the level $\alpha$ .
n	Acceleration in g units; counter; number of data points; shape parameter in spectra mathematical expressions.
OAT	Outside air temperature (degrees Fahrenheit).
$O_n$	Run test observation of the mean.
$O_n^2$	Run test observation of the mean square.
PSD	Power spectral density.
PST	Pacific Standard Time.
$P_s$	Static pressure (inches of mercury).
$P_{s_i}$	Indicated static pressure (inches of mercury).
$P_0$	Standard atmospheric pressure at sea level (29.921 inches of mercury).
$P_1, P_2$	Intercepts of the exponential curves for the analytical expressions of the peak count probability distributions.
Q	Number of independent variables in the regression equation.
$Q_c$	Calibrated impact pressure (inches of mercury).

## SYMBOLS

### Symbols and Abbreviations:

$q_I$	Indicated impact pressure (inches of mercury).
$R_A$	Radar altitude (feet).
$R$	Richardson number.
$[R]$	Rotation matrix used to transform measurements from the airplane reference axes to the earth reference axes.
$R_1$	Value of rms gust velocity at a given wind speed as read from least square line (feet/second).
$R(i)$	Autocorrelation function.
$R_{xy}(i)$	Cross correlation function.
rms	Root mean square.
$R(\tau)$	Gust velocity covariance function.
$R(\tau)/R(0)$	Gust velocity autocorrelation function where $\tau = 0 \dots \tau_L$ .
$r$	Distance (feet).
$r_c$	Value of $r$ at which the autocorrelation function crosses zero.
$S$	Airplane planform wing area (feet <sup>2</sup> ); horizontal distance - miles.
$S_{SE}$	Sine of solar elevation.
$T_a$	Ambient air temperature (degrees Rankine).
$T_{filt.}$	Time width of filter weight function.
$T_0$	Ground surface temperature (degrees Fahrenheit).
$T_1$	Calibrated outside air temperature (degrees Rankine).
$T_s$	Temperature at sea level under standard conditions (518.69 degrees Rankine).
$T_s$	Air temperature at the surface (degrees centigrade).

## SYMBOLS

### Symbols and Abbreviations:

T <sub>A1</sub>	Temperature at 250 feet (degrees Fahrenheit).
T <sub>A2</sub>	Temperature at 750 feet (degrees Fahrenheit).
T <sub>A3</sub>	Temperature at 1000 feet (degrees Fahrenheit).
T <sub>A4</sub>	Temperature at flight altitude plus 1000 feet (degrees Fahrenheit).
T <sub>A7</sub>	Temperature at flight altitude (degrees Fahrenheit).
T <sub>D2</sub>	Dew point at 750 feet (degrees Fahrenheit).
T <sub>D3</sub>	Dew point at 1000 feet (degrees Fahrenheit).
T <sub>D4</sub>	Dew point at flight altitude plus 1000 feet (degrees Fahrenheit).
T <sub>D5</sub>	Dew point at 850mb (degrees centigrade).
TOD	Time of day.
t	Time (seconds); standardized variable.
U <sub>de</sub>	Derived equivalent gust velocity (feet/second).
u	Longitudinal gust velocity (feet/second); positive-aft.
V	True airspeed or ground speed (feet/second).
V <sub>e</sub>	Equivalent airspeed (feet/second).
V <sub>T</sub>	True airspeed (feet/second).
{V}	Represents the matrix of true airspeed components corrected for pitch and yaw.
v	Lateral gust velocity (feet/second), positive to the right.
W	Airplane weight (pounds); wind speed (feet/second).
WA	Angle between airplane ground track and wind vector (degrees) positive - wind vector from the left, zero degrees - direct tail wind.
W <sub>A4</sub>	Wind direction at flight altitude plus 1000 feet (degrees azimuth).

## SYMBOLS

### Symbols and Abbreviations:

$W_D$	Wind direction (degrees azimuth).
$\bar{W}_E$	Average easterly winds (feet/second).
$\bar{W}_N$	Average northerly winds (feet/second).
$W_S$	Wind speed at the surface (knots).
$W_6$	Wind speed at 700mb (knots).
$v$	Vertical gust velocity (feet/second), positive - upward.
$x$	Amplitude.
$x_b$	Mid-band value.
$x_1$	1 <sup>th</sup> value of $x$ ; predictors; coefficient of simple linear correlation; value of gust velocity rms at a given wind speed (feet/second).
$x_a$	Level of gust velocity (feet/second).
$x_k(t_1)$	$k^{\text{th}}$ record included in the ensemble averaging scheme.
$x(t)$	Sampled value of time series.
$Y$	Dependent variable; regression function.
$\alpha$	Angle of attack (degrees), positive - nose above relative wind; levels of gust velocity used in level crossing procedures; confidence limit.
$\beta$	Angle of sideslip (degrees), positive - nose left of relative wind.
$\Gamma$	Standard lapse rate (0.00356 degrees Fahrenheit/foot), positive - temperature decrease with increasing altitude.
$\Gamma_d$	Dry adiabatic lapse rate (0.0055 degrees Fahrenheit/foot).
$\gamma$	Ratio of specific heats for air (1.40).
$\gamma^2(k)$	Coherency function.

## SYMBOLS

### Symbols and Abbreviations:

$\Delta$	Incremental or difference.
$\Delta f$	Change in frequency (cycles/second); frequency range spanned by filter roll-off; frequency interval between adjacent PSD data points.
$\Delta H$	Distance above or below reference point (feet); difference in terrain elevation (feet).
$\Delta h$	Static pressure error (feet).
$\Delta N_{ZCG}$	Incremental load factor (acceleration units).
$\Delta P_s$	Static pressure position error (inches of mercury).
$\Delta P_s/q_I$	Pressure coefficient (dimensionless).
$\Delta P_\alpha$	Angle of attack differential pressure (inches of mercury).
$\Delta P_\beta$	Angle of sideslip differential pressure (inches of mercury).
$\Delta T_{z_z}$	Vertical temperature gradient (degrees Fahrenheit/foot).
$\Delta T_H$	Horizontal temperature gradient (degrees Fahrenheit/mile).
$\Delta T_s$	Atmospheric stability (degrees Fahrenheit/1000 feet), positive - temperature increase with increasing altitude.
$\Delta t$	Time interval between data samples (seconds).
$\Delta W_{D_z}$	Vertical wind direction gradient (degrees/foot).
$\Delta W_H$	Horizontal wind gradient (feet/second/mile).
$\Delta W_{HEW}$	Horizontal east-west wind gradient (feet/second/mile).
$\Delta W_z$	Vertical wind velocity gradient (feet/second/foot).

## SYMBOLS

### Symbols and Abbreviations:

$\delta$	Drift angle (degrees), positive to the right.
$\epsilon$	Viscous dissipation rate (feet <sup>2</sup> /second <sup>3</sup> ); emissivity factor; filter empirical error bounds (percent).
$\eta$	Kolmogorov microscale (feet).
$\theta$	Pitch angle (degrees), positive - nose up.
$\dot{\theta}$	Rate of pitch (degrees/second), positive - nose moving up.
$\lambda$	Taylor turbulence microscale length (feet); characteristic wavelength (feet); terrain wavelength (feet).
$\mu$	Air viscosity (pound second/feet <sup>2</sup> ); mean value; air-plane mass ratio.
$\mu_2, \mu_3$	Constant in gust velocity rms distribution equation.
$\mu_x(t)$	Ensemble average time function.
$\nu$	Kinematic viscosity (feet <sup>2</sup> /second); degrees of freedom.
$\pi$	3.1416. . . .
$\rho$	Air density (slugs/foot <sup>3</sup> ).
$\rho_0$	Standard air density at sea level (0.002378 slugs/foot <sup>3</sup> ).
$\sigma$	Standard deviation of a statistical sample; standard deviation (fps) from gust velocity spectra between 0.0416 and 10 cps; Stefan-Boltzman constant.
$\sigma_D$	Standard deviation about a least square line.
$\sigma_L$	Standard deviation of level crossing distribution.
$\sigma_N$	Standard deviation of noise.
$\sigma_{pe}$	Standard deviation of primary peaks obtained using extrapolated value of $N_{pe}$ .
$\sigma_R$	Standard deviation of recorded data.
$\sigma_T$	Standard deviation obtained from the truncated gust velocity spectra (feet/second).

## SYMBOLS

### Symbols and Abbreviations:

$\sigma_t$	Standard deviation of the gust velocity time series (feet/second).
$\sigma_{tr}$	Standard deviation of terrain roughness (feet).
$\sigma_a$	Standard deviation of angle of attack differential pressure (inches of mercury).
$\sigma_\beta$	Standard deviation of sideslip differential pressure (inches of mercury).
$\sigma_e$	Standard deviation (dispersion of the distribution) of gust velocity rms (feet/second).
$\sigma_1$	Standard deviation of the derivative of the time function divided by $2\pi V$ (cps for gust velocity).
$\sigma_2, \sigma_3$	Constant used in rms gust velocity distribution equation.
$\tau$	Lag time for the weighting operation convolution (seconds).
$\Phi$	One-dimensional gust velocity power spectral density.
$\Phi(k)$	Power spectral estimates.
$\Phi(n)$	Raw estimate of power spectral density.
$\Phi'(n)$	Averaged estimate of power spectral density.
$\Phi_{xy}(n)$	Estimate of cross power spectral density.
$\Phi_{90}$	Power spectra 90 per cent confidence interval.
$\phi$	Roll angle (degrees), positive - right wind down.
$\dot{\phi}$	Rate of roll (degrees/second), positive - right wing moving down.
$\chi$	Chi statistic.
$\psi$	Yaw angle (degrees), positive - nose right.
$\dot{\psi}$	Rate of yaw (degrees/second), positive - airplane nose moving right.
$\omega$	Frequency (radians/second).



## SYMBOLS

### Subscripts and Superscripts:

b	Band number.
D	Based on the Dryden equation.
e	Extrapolated value.
filt.	Filtered value.
H	Horizontal.
i	Sample number.
N	Noise.
n	Counter.
K	Based on the von Karman equation.
max	Indicates maximum value.
min	Indicates minimum value.
P	Peak count; based on the Lumley-Panofsky equation.
T	Truncated; obtained from tower.
t	From the gust velocity time series.
u	From the longitudinal gust velocity component.
v	From the lateral gust velocity component.
w	From the vertical gust velocity component.
x	Longitudinal.
y	Lateral.
z	Vertical.
o	Initial value.
I	Pertaining to quadrant 1; indicates LO-LOCAT Phases I and II.
II	Pertaining to quadrant 2.
III	Pertaining to quadrant 3; indicates LO-LOCAT Phase III.

## SYMBOLS

### Subscripts and Superscripts:

- IV            Pertaining to quadrant 4.  
              Related to level crossing count.
- Primes indicate Handed estimates unless otherwise noted.
- Overbars depict time means.
- 2             Refers to starting point of leg.  
3             Refers to ending point of leg.  
32            Refers to difference between start and end.

### Weather Chart Symbols

#### Surface Charts:

——— 1018 Sea level pressure (millibars)

----- 50 Temperature (° F.)

#### Cloud Cover:

- |                |                |
|----------------|----------------|
| ○ Clear        | ⊙ 6/10         |
| ⊙ ≤ 1/10       | ⊙ 7/10 or 8/10 |
| ⊙ 2/10 or 3/10 | ⊙ 9/10         |
| ⊙ 4/10         | ● Overcast     |
| ⊙ 5/10         | ⊗ Sky obscured |

#### Wind:

- |              |              |
|--------------|--------------|
| ⊙ Calm       | └─○ 10 Knots |
| —○ ≤ 2 Knots | └─○ 15 Knots |
| └─○ 5 Knots  | └─○ 50 Knots |

Tail points in the direction from which the wind is blowing.

SYMBOLS

Weather Chart Symbols (Contd.)

Surface Charts (Contd.):

Precipitation:

.. Rain

\*\* Snow

,' Drizzle

≡ Fog

∇ Rain shower

∇\* Snow shower


↘ Freezing rain

⊥ Thunderstorm

Fronts:

 Cold front

 Warm front

 Stationary front

Upper Air Charts

— 1540 Height of pressure surface (meters)

---- 1530 Intermediate height values (meters)

## SECTION I

### INTRODUCTION

Knowledge of the characteristics, causes, and effects of atmospheric turbulence has become increasingly important during the last few years. Indications are that the need for this knowledge will continue to increase in the future. This is due to several factors. Many economic and safety considerations are related to increased aircraft life through decreased fatigue failure. The effects of atmospheric turbulence on the handling and ride qualities of airplanes have become increasingly significant as the demand for improved performance has increased.

Older generation aircraft, due to their relatively slow speeds, operated well into the inertial subrange of atmospheric turbulence. As a result, they had to cope mainly with the low power, high frequencies of turbulence. Requirements for high performance have brought about the use of highly flexible structures in aircraft design. Increased speed has caused airplanes to be responsive to the higher power long wavelength turbulence components while increased flexibility has decreased structural response frequencies. As a result, aircraft rigid body and structural response frequencies are coincident with frequencies of atmospheric turbulence which are capable of significant driving forces. It appears that future aircraft may be responsive to turbulence frequencies in the frequency range where atmospheric turbulence power spectral density, in theory, remains at a large constant value with further decreases in frequency. The detailed definition of turbulence characteristics in this realm has, therefore, become increasingly pertinent.

Military missions include terrain contour flight at low altitude to avoid radar detection. In this region of the atmosphere, near ground level, there is a frequent occurrence of high magnitude turbulence. Therefore, detailed knowledge of the atmospheric environment at low altitudes has become particularly important. The Air Force has long recognized this fact and in their continuing efforts to design better aircraft, contracted The Boeing Company to participate in an extensive investigation of low altitude turbulence. The research program was designated LO-LOCAT (Low-Low Altitude Critical Atmospheric Turbulence). LO-LOCAT was established as part of an overall program known as ALLCAT (Reference I.1). ALLCAT was devised to define a model of atmospheric turbulence over a wide range of altitudes as follows:

<u>Program</u>	<u>Altitude (Feet)</u>
TOICAT	0 - 250
LO-LOCAT	250 - 1,000
LOCAT	1,000 - 20,000
MEDCAT	20,000 - 40,000
HICAT	40,000 - 70,000
HI-HICAT	70,000 - 200,000

Research of the lower atmosphere had been accomplished in the past. These programs were worthwhile contributions, but the data were limited in quantity and/or resolution of long turbulence wavelengths. Advances of instrument technology and calibration techniques following these programs made the measurement of lower frequencies possible. Improved computers made the accomplishment of a turbulence research program based on statistical analysis of large quantities of data feasible.

The purpose of the IO-LOCAT Program was to determine the turbulence environment below 1,000 feet above the ground. This was done by utilizing statistically representative samples of turbulence data obtained over a wide range of meteorological, topographical, seasonal, and time of day conditions. Basically, the following general items were studied:

- Probabilities of encountering given levels of turbulence intensity.
- Frequency analysis of atmospheric turbulence utilizing the power spectral method.
- Correlation of atmospheric turbulence with meteorological and geophysical conditions, and associated forecasting techniques.

The IO-LOCAT Program consisted of three phases. Phases I and II, which are discussed in Reference I.2, involved the use of four C-131B aircraft as instrumentation platforms. Each of these aircraft was stationed at a different base within the United States, and was flown over a specific route laid out near the base. The routes were located in New York, Kansas, Colorado, and California and were established to provide a wide range in topographical and climatological conditions. Data were gathered for approximately 15 months.

The C-131B aircraft were flown at an average airspeed of approximately 330 fps. The instrumentation had adequate frequency response down to approximately 0.04 cps; therefore, wavelengths up to 8,000 feet were investigated.

Phase III of the IO-LOCAT Program was accomplished in order to extend the statistical definition of the turbulence environment and investigate longer wavelengths. A T-33A airplane was utilized and was flown at an average speed of approximately 630 fps. This higher speed, with the same basic instrumentation used during Phases I and II, made possible the measurement of turbulence wavelengths up to 15,500 feet.

The Phase III data were recorded over approximately a 10-month period. Data were gathered at the same geographical locations as during Phases I and II.

A specific route for the airplane to follow was laid out at each base. Each route consisted of eight straight legs approximately 45 statute miles long. All legs were traversed in the same direction on each flight. Four and one-half minutes of data, recorded while flying over each leg, constituted a turbulence sample. Prior to flying each leg, meteorological

data were obtained at 100 and 1,000 feet above the terrain. These data were obtained in the same vertical air mass at the beginning of each leg, and were used to compute vertical gradients of temperature, pressure, and wind.

Flights were scheduled nearly every week day not required for routine maintenance of the airplane and instrumentation. Three missions were scheduled each flight day; one at dawn, one at mid-morning, and one in the afternoon. The airplane was maintained and flown by Boeing personnel. Two specific altitudes, 250 feet and 750 feet above the terrain, were used for the gust data gathering portion of the flights. Only one altitude was flown on a given day. The pilot followed the terrain contour, as closely as safety allowed, using a radar altimeter to maintain a constant absolute altitude.

This report primarily covers the results of the research conducted under Phase III of the program. Results from additional research of the long wavelengths of turbulence and a comparison of Phase III data with the data from Phases I and II and other turbulence programs are also included. Volume I is divided into two parts and gives the techniques and results of data analysis. Volume II is also divided into two parts. Part I provides the details pertaining to data acquisition, instrumentation, calibrations and checks, data processing, and data quality. Data tabulations and plots, and a log of pertinent information concerning the program are also presented in Volume II Part I. Part II of Volume II contains the power spectral density and other frequency data plots.

Pertinent data obtained during LO-LOCAT Phase III were recorded on magnetic tape. These tapes were delivered to the Air Force Flight Dynamics Laboratory.

## 1. INSTRUMENTATION

The T-33A airplane was instrumented to measure meteorological and gust velocity data. A radar altimeter, Doppler radar system, radiometer, and outside air temperature probe comprised the basic instrumentation used to obtain meteorological data. Atmospheric turbulence was sensed by instrumentation contained in a Boeing-designed gust probe mounted on the end of a nose boom. Probe data were supplemented by airplane attitude and roll rate information obtained at the boom base. Instrumentation contained inside the gust probe sensed the following:

- Sideslip and attack angles
- Vertical, lateral, and longitudinal accelerations
- Static and impact pressures
- Pitch and yaw rates

Fine and coarse measurements were provided, in some instances, to improve resolution. Also, the temperature of each transducer was maintained at 135° F by thermostatically controlled heaters.

Details of the instrumentation are presented in Appendix I.

## 2. DATA CATEGORIZATION TECHNIQUE

All data were categorized with respect to selected geophysical conditions under which they were obtained. This forms a common basis for comparison of the data, points out specific effects of some of the more important category parameters, and provides a systematic method of analysis. At the beginning of the IO-LOCAT Program, six general categories were chosen in an anticipated order of significance. These include type of terrain, altitude above the terrain (absolute altitude), atmospheric stability, time of day, season of the year, and geographic location. These general areas were divided into the components indicated in the following list:

### Type of Terrain

1. High Mountain
2. Low Mountain
3. Desert
4. Plains
5. Swamp (not used)
6. Water

### Absolute Altitude

1. 250 Feet
2. 750 Feet

### Atmospheric Stability

- |                |  |   |
|----------------|--|---|
| 1. Very stable |  | $\Delta T_s > -2^\circ\text{F}/1000 \text{ ft.}$    |
| 2. Stable      | $-2^\circ\text{F}/1000 \text{ ft.} \geq$ | $\Delta T_s > -5^\circ\text{F}/1000 \text{ ft.}$    |
| 3. Neutral     | $-5^\circ\text{F}/1000 \text{ ft.} \geq$ | $\Delta T_s > -6^\circ\text{F}/1000 \text{ ft.}$    |
| 4. Unstable    |  | $\Delta T_s \leq -6^\circ\text{F}/1000 \text{ ft.}$ |

### Time of Day

	TAKEOFF TIMES - LOCAL TIME $\pm$ 30 MINUTES		
	Summer	Spring-Fall	Winter
1. Dawn	Sunrise	Sunrise	Sunrise
2. Mid-morning	0900	0930	1000
3. Mid-afternoon	1500	1430	1400

### Season of the Year

1. Spring - March 21 to June 20
2. Summer - June 21 to September 20
3. Fall - September 21 to December 20
4. Winter - December 21 to March 20

### Geographic Location

1. Edwards Air Force Base, California
2. Griffiss Air Force Base, New York
3. Peterson Field, Colorado
4. McConnell Air Force Base, Kansas

The number beside each category component, or element, was used as a code for that particular element. All data recorded during a turbulence sample were then categorized by the appropriate six-digit number. The following example illustrates this method:

Category No. 422324

- 4 - Terrain Feature, Plains
- 2 - Altitude, 750 Feet
- 2 - Atmospheric Stability, Stable
- 3 - Time of Day, Afternoon
- 2 - Season, Summer
- 4 - Location, McConnell AFB

Some of the data within different categories were pooled when the data showed like characteristics. This was done to improve statistical analyses by increasing sample sizes. For example, suppose that data within category 422324 shows the same characteristics as data within categories 422124 and 422224, i.e., time of day showed no effect on the data. Then all the data were put together within the category 422024, where the 0 indicates that all times of day are included.

All category numbers, except stability, were assigned prior to data processing. The number for atmospheric stability was assigned after the vertical temperature gradient had been computed for each turbulence sample.

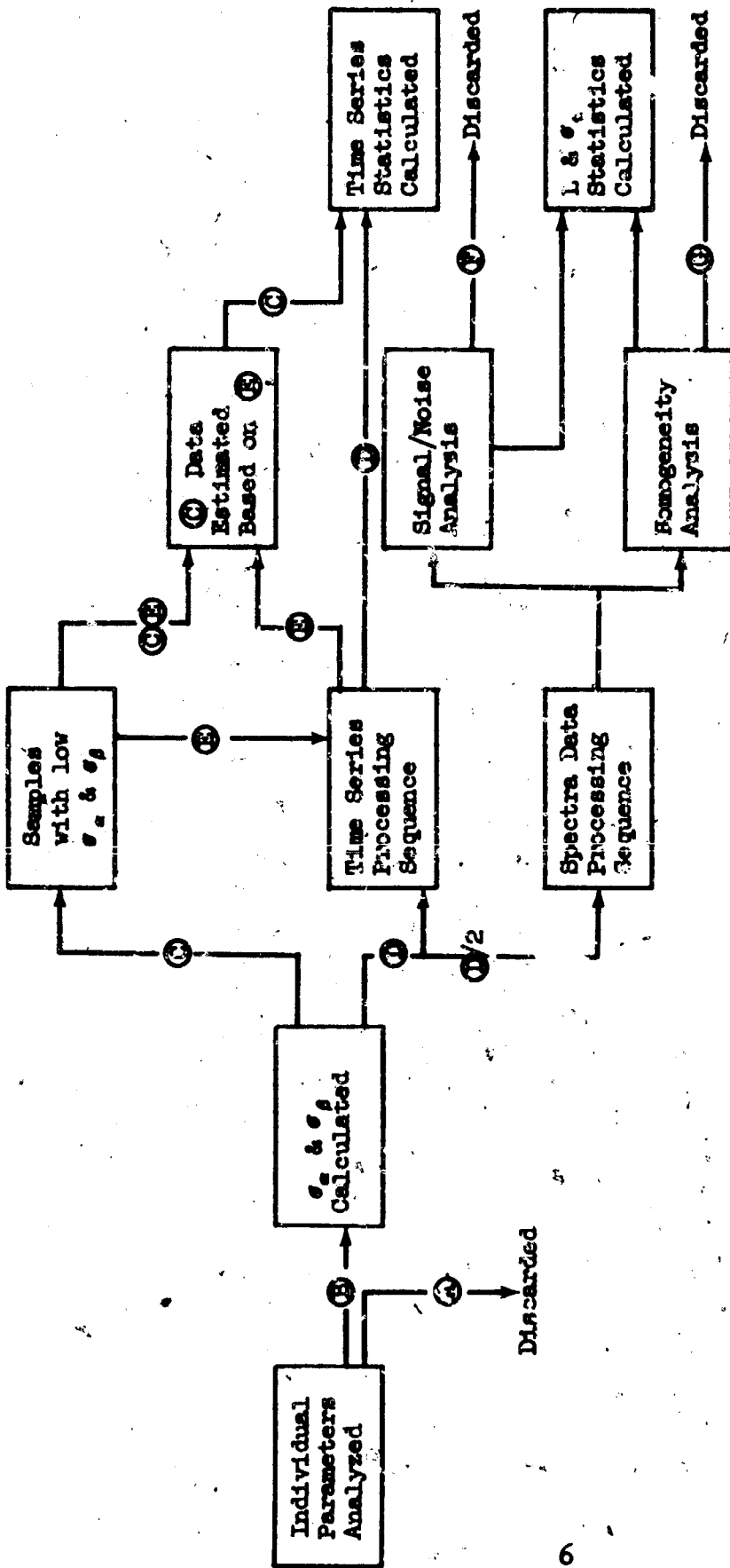
### 3. DATA ANALYSIS

The IO-LOCAT Phase III data were edited in a number of ways depending on the statistic being analyzed. The various methods of editing and analysis are discussed in each section of this document along with the particular type of data involved. Time histories of individual parameters measured during each test were evaluated to determine if instrumentation malfunctions occurred. Data involving malfunctions were eliminated for all analyses. The time series standard deviations of angle of sideslip and angle of attack measurements were computed for each sample. When these values indicated a low signal to noise ratio for particular turbulence samples, the turbulence samples were case handled to conserve computer time. They were not eliminated from statistical calculations.

A schematic showing the primary steps involved in the data processing, editing, and analysis functions is presented in Figure 3.1.

Gust velocity statistics were determined based on primary peaks, amplitude, and level crossing counts. The distributions of gust velocity peak and amplitude values were compared to normal distributions. The level crossing data were compared to Rice's equation (Reference 3.1). Values of characteristic frequency calculated from peak and level crossing count data were compared with those calculated from the power spectral density. Frequency of exceedance and the probability of exceeding given levels of gust velocity were determined.





- ① Turbulence data involving instrumentation malfunctions
- ② Turbulence data showing no instrumentation malfunctions
- ③ Turbulence data with  $\sigma_a < 0.07$  or  $\sigma_\beta < 0.05$  in.Hg.
- ④ Turbulence data with  $\sigma_a > 0.07$  and  $\sigma_\beta > 0.05$  in.Hg.
- ⑤ Representative low intensity samples (Ref. Section 13)
- ⑥ Spectra data distorted by low signal/noise (Ref. Section 19)
- ⑦ Spectra data from non homogeneous turbulence samples (Ref. Section 21)

Figure 3.1 Primary Editing Sequence

Gust velocity standard deviations, determined from peak, amplitude, and level crossings count data were compared. The cumulative probability of these data was calculated.

Power spectral densities of the gust velocity components were calculated and plotted for those turbulence samples recorded over the even numbered legs on the even numbered flights and for those recorded over the odd numbered legs on the odd numbered flights.

The spectra were normalized by the gust velocity variance  $\sigma_t^2$  and also by  $L\sigma_t^2$ . Mathematical representation of the spectra was investigated by comparing the experimental spectra with the commonly used mathematical expressions as suggested by von Karman, Dryden, and others. The integral scale of turbulence, essential to the representation of the spectra by mathematical expressions, was analyzed. Turbulence qualities such as homogeneity and isotropy were also evaluated.

Although important parameters are included in the category components, there were other possible parameters which might affect the turbulence intensity. The turbulence recorded during Phase III was compared to some of these parameters. They included wind speed, wind direction, stability ratio, Richardson number, air temperature, ground surface temperature, and other meteorological parameters obtained from rawinsonde equipment, ground observers, and synoptic charts.

Analysis of the data by category required a pooling of data showing like characteristics. Obviously, many combinations of the category components were possible. If all possible combinations were used, only a small amount of data would be in each combination. Therefore, the data were pooled for category components which had the smallest effects in order to determine reliable statistics of the data.

Peak count, gust velocity power spectra, turbulence scale length, and gust velocity rms data obtained during Phase III were compared to corresponding data obtained during Phases I and II. Corresponding data from the various phases could not be indiscriminately pooled together because of differences in the conditions under which they were obtained as discussed in Section IX.

#### 4. DATA GAPS IN THE TURBULENCE MODEL

LO-LOCAL Phases I and II data can be used to define a turbulence model for all terrain types except high mountain, for all times of day except nighttime, for various weather conditions except storms, for contour flight at altitudes of 250 and 750 feet, and for at least four locations.

Turbulence data were not recorded under contour flight conditions at low level over the high mountain terrain at the Peterson route during Phases I and II as shown in Figure 4.1. Turbulence data were not recorded at nighttime nor during periods of inclement weather. Although the data were recorded at each location during all seasons, the climatology for that particular year may not have been representative of the average. It was the purpose of Phase III to extend the statistical definition obtained during Phases I and II and to define longer wavelengths.

HM LM DE PL WA High Mountains, Low Mountains, Desert, Plains, Water  
 SP SU FA WI Spring, Summer, Fall, Winter  
 ED PE CR MC Edwards AFB, Peterson Field, Griffiss AFB, McConnell AFB

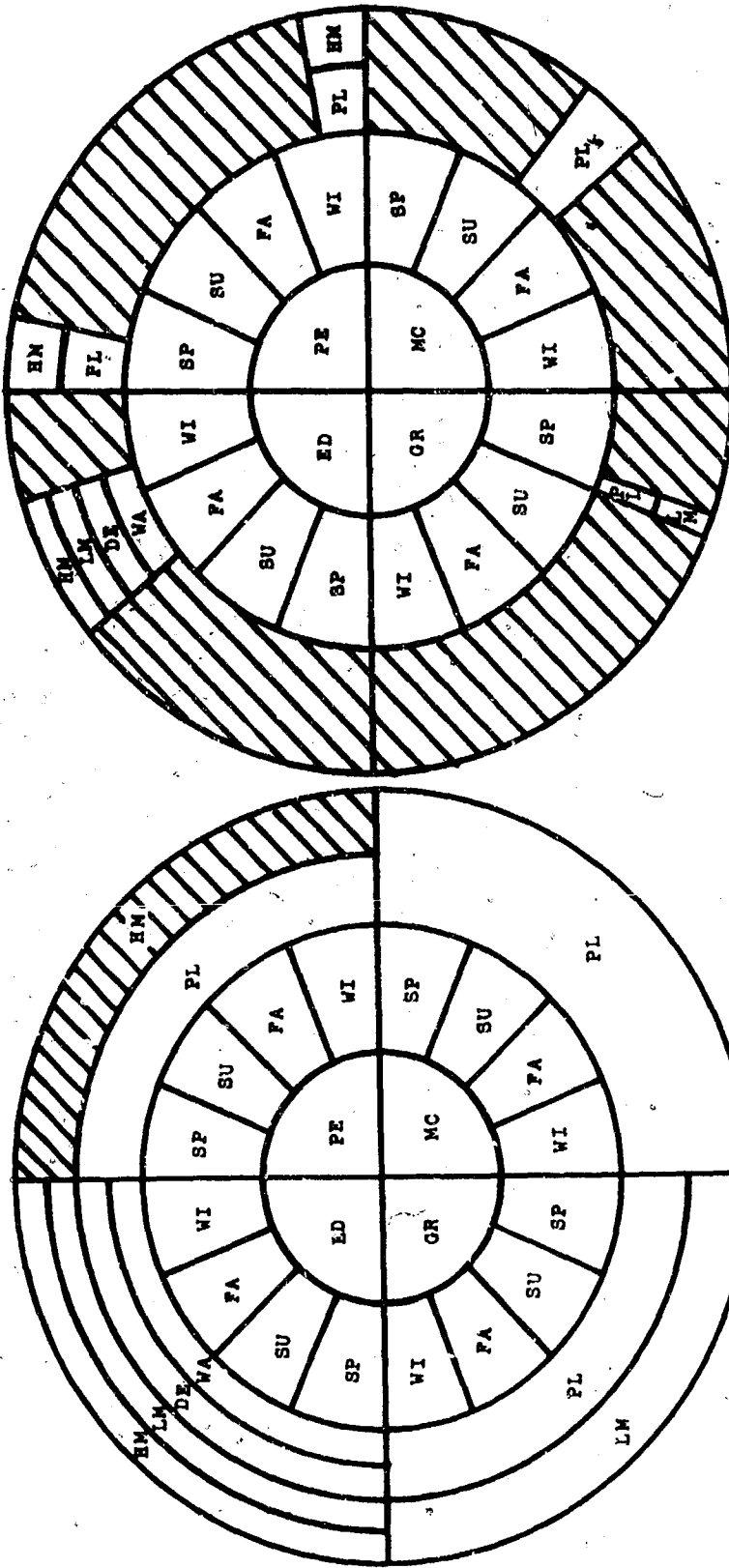


Figure 4.1 Data Gaps

Segments of data significant to the normal atmospheric system, for which adequate samples for a statistical model were not obtained are defined as data gaps.

The best method to develop a turbulence model based on IO-LOCAT data would be to:

- Evaluate the variation of Phases I and II data with season. These statistics are shown in Table 4.1.
- Assume that corresponding seasonal variations would have occurred during Phase III and expand the data (with the exception of high mountain data) accordingly.
- Evaluate the relationship between high mountain data at Peterson and pertinent climatology which existed at the time it was gathered. The geophysical situation during Phase III is discussed in Section VI.
- Estimate the Peterson high mountain data in the gap based on the climatology which normally would exist during the time period of the gap. Records of normal climatology are available from the U.S. Weather Bureau.

Once the Phase III data have been applied, other considerations must be made. These include:

- How well the geophysical situations encountered during IO-LOCAT match those for the development of a particular model.
- The compatibility of the range of turbulence wavelengths measured with that of an airplane being designed.
- The effects of not gathering data under storm conditions during IO-LOCAT.

Of the three other considerations mentioned, the first is probably the least significant. The IO-LOCAT Program was designed to cover a large number of geophysical situations. Chances are, the geophysical conditions under which it is desired to develop a turbulence model may be well matched. Not a great amount of data were obtained over water but from all indications, low altitude atmospheric turbulence over water at wavelengths less than 15,000 feet is relatively insignificant.

The difference between the range of turbulence wavelengths measured and the range to which an airplane being designed would respond is a highly significant consideration. It is necessary to extrapolate the data available in an attempt to arrive at an estimate for the range in question. Effects of shifting the wavelength window through which the turbulence is viewed is discussed throughout this report.

TABLE 4.1

**STATISTICS OF GUST VELOCITY INTENSITY ( $\sigma_g$ ) WITH  
SEASON AND LOCATION DURING PHASES I AND II**

Category	Gust Velocity Component					
	u (fps)		v (fps)		v (fps)	
	$\mu$ (fps)	$\sigma$ (fps)	$\mu$ (fps)	$\sigma$ (fps)	$\mu$ (fps)	$\sigma$ (fps)
100011	3.14	0.93	3.38	0.95	3.61	1.04
100021	3.21	1.32	3.59	1.53	3.13	1.09
100031	2.93	1.29	3.17	1.33	3.00	1.38
100041	2.78	1.31	3.05	1.37	2.74	1.28
200011	2.78	0.88	3.09	0.97	3.20	1.00
200021	2.74	0.92	2.77	1.09	3.22	1.12
200031	2.52	1.15	2.83	1.29	2.71	1.25
200041	2.69	1.14	3.07	1.28	2.72	1.17
300011	2.72	0.99	2.90	1.02	3.20	1.22
300021	2.32	1.01	2.17	1.00	2.92	1.28
300031	1.64	0.86	1.90	0.92	1.91	1.11
300041	1.55	0.70	1.91	0.79	1.83	1.00
600011*	0.93	0.41	1.00	0.30	0.82	0.31
600021*	0.56	0.18	0.72	0.23	0.65	0.27
600031	0.89	0.52	1.08	0.56	0.90	0.56
600041*	0.61	0.25	0.82	0.26	0.59	0.26
200012	3.76	1.46	4.10	1.68	3.76	1.28
200022	3.03	1.07	3.22	1.17	3.21	1.11
200032	3.00	1.28	3.31	1.47	2.99	1.10
200042	3.21	1.32	3.59	1.53	3.13	1.09
400012	3.67	1.49	4.07	1.60	3.43	1.27
400022	2.78	0.93	2.82	0.92	2.76	0.94
400032	2.81	1.25	3.02	1.27	2.61	1.04
400042	3.08	1.31	3.39	1.44	2.81	1.05
400013	2.46	1.05	2.95	1.23	2.71	1.33
400023	2.14	0.96	2.48	1.03	2.40	1.20
400033	1.89	0.86	2.21	1.00	1.84	0.91
400043	2.43	0.94	2.77	1.00	2.40	1.00
400014	2.80	1.19	2.98	1.24	2.73	1.11
400024	2.08	0.84	2.05	1.05	2.15	0.91
400034	2.30	1.02	2.49	1.04	2.22	0.93
400044	2.79	1.08	3.02	1.15	2.48	0.97

\* Less than 30 samples involved

NOTE:  $\mu$  = mean of the standard deviations

$\sigma$  = standard deviation of the gust velocity time series  
standard deviations

The third consideration is also important. If a complete model is being developed, the data must be adjusted to account for the fact that IO-LOCAT data were not measured during adverse weather. The extent of the adjustment required is given in Tables 4.2 and 4.3. These data were taken from Reference 4.1. Turbulence data used in the adjustment must come from programs other than IO-LOCAT. Two such sources are References 4.2 and 4.3.

A multiplicity of types of data were obtained and analyzed during IO-LOCAT. These data may be applied in numerous ways to the evaluation of atmospheric turbulence at low altitude, depending on the application. Examples of applications and adjustments that may be made are shown in Sections IX and X of this report. In these sections, the IO-LOCAT Phase III data are analyzed with data from Phases I and II and with data from other low altitude turbulence programs.

TABLE 4.2

NUMBER OF IFR WEATHER DAYS

Location	Spring Days	Summer Days	Fall Days	Winter Days	Maximum Yearly Days (%)
McConnell	<9	<9	<9	9 - 18	45 (12.3)
Edwards	9 - 18	9 - 36	9 - 18	9 - 27	99 (27.1)
Peterson	<9	<9	<9	<9	36 (9.85)
Griffiss	9 - 18	<9	9 - 27	18 - 27	81 (22.2)

TABLE 4.3

NUMBER OF THUNDERSTORM DAYS

Location	Spring Days	Summer Days	Fall Days	Winter Days	Maximum Yearly Days (%)
McConnell	10	20	10	1 - 5	45 (12.3)
Edwards	1	1	1	1	4 (1.1)
Peterson	10	30	5	0 - 1	46 (12.6)
Griffiss	5	10	1 - 5	0 - 1	21 (5.75)

## SECTION II

### SUMMARY

It was found, based on primary peak, amplitude, and level crossing counts and rms values that gust velocity magnitude becomes larger as the terrain becomes rougher, as altitude above the terrain is decreased, and as the atmosphere becomes less stable. Statistical distributions of gust velocity primary peak, amplitude, and level crossing data were found to be in reasonable agreement with each other. (See Figures 11.10 through 11.12). The distributions of the primary peaks were found to be definable by an equation using the component Gaussian process. The distribution of the gust velocity rms values was also defined by using the combination of two Gaussian equations (see Figures 13.35 through 13.37).

Gust velocities in excess of 70 feet per second were encountered. The maximum value for vertical gust velocity was 74.5 fps and occurred over leg 3 of the Edwards route. The maximum gust velocity for longitudinal and lateral components were 71.0 and 76.9 fps, respectively, and occurred over leg 5 of the Peterson route. The probability distribution of the maximum derived equivalent vertical gust velocity agreed well with that of the maximum true vertical gust velocity.

The nondimensionalized power spectral density of atmospheric turbulence did not show any variation which might be associated with different geophysical or meteorological phenomena. Good agreement between nondimensionalized von Karman and measured spectra was exhibited. The von Karman spectra, however, did slightly underestimate the power of the measured spectra at the low values of  $kL$ , the nondimensionalized spatial frequency. The average value of the measured scale lengths was 600 feet; this average, however, is more representative of the turbulence found around the high mountains over the Peterson route in Colorado than of turbulence in general.

Forecasting of low altitude turbulence intensity was most successful when based on vertical wind gradient and lapse rate. It was found that the greatest chance of encountering significant turbulence exists when the Richardson number is in the  $\pm 0.2$  range. As the Richardson number increases, the chance of high intensity turbulence decreases rapidly. The stability ratio was found to provide a good indication of turbulence intensity, but did not, as suggested by other investigators, provide any advantages over the Richardson number.

Taylor and Kolmogorov microscales and viscous dissipation rates and stability ratios were evaluated. They were compared to values obtained by other investigators.

LO-LOCAT Phases I, II, and III data were compared. Basic information concerning the three phases is shown in Table II.1. The Phase III data tended to have higher turbulence magnitudes. This increased magnitude is attributed to the measurement of longer wavelength turbulence and measurement of turbulence over high mountains. An example of measuring longer wavelength turbulence is shown in Figure 17.1 where the vertical gust velocity component contains a wavelength of approximately 14,300 feet with a magnitude

exceeding 74.0 fps. The wavelength appears at a frequency of approximately 0.04 cps in the time history. This same long wavelength turbulence, if encountered during Phases I and II, would have appeared at a frequency of 0.02 cps due to the lower speed at which the C-131 airplanes were flown. Phases I and II gust velocity measurements in this frequency realm would have been attenuated approximately 80 per cent by the data filtering techniques used to alleviate the effect of drift. This is illustrative of the fact that there is turbulence, some of which is significantly high in intensity, that contains wavelengths longer than 7000 feet.

LO-LOCAT data were compared to that from other low altitude turbulence programs. Because of the variety of filtering techniques used, only those samples which were most agreeable to Kolmogorov's theory were used. Based on the method of selecting the spectra, it was concluded that the spectra of turbulence at low altitudes from various independent researchers are consistent in that their shape can be approximated by the von Karman mathematical expressions with scale lengths generally less than 1000 feet.

During the course of this program, three additional turbulence investigations were accomplished. These were the BREN Tower Flyby, Thunderstorm Turbulence Investigation, and the Wake Turbulence Investigation. The BREN Tower Flyby investigation was accomplished to compare turbulence data recorded from an instrumented airplane and an instrumented tower. Although the turbulence levels were slightly different, the normalized spectra were in good agreement. The Thunderstorm Turbulence Investigation was accomplished to investigate turbulence near thunderstorms and convective clouds. Unfortunately, no severe thunderstorms developed in the area during the period of investigation. It was found that turbulence intensities near convective clouds were low and that the power spectra of turbulence near convective clouds exhibits a  $-5/3$  logarithmic slope relationship between power density and spatial frequency. Air temperature changes near cumulus clouds occurred, in some instances, when turbulence was encountered. The Wake Turbulence Investigation consisted of flying the Phase III airplane behind formations of C-141 airplanes in an effort to qualitatively evaluate the wake turbulence environment generated by these airplanes. The maximum gust velocity encountered was 63 fps and the estimated size of the vortices varied from 19 to 41 feet in diameter. Although high gust velocities were encountered, the time duration of the gusts were so short that the T-33 airplane did not respond to the turbulence and the pilot reported very little turbulence.

Since the major findings of LO-LOCAT Phase III were the significant influences on atmospheric turbulence statistics of the longer wavelengths of turbulence and turbulence over high mountains in Colorado, additional research was accomplished. Gust accelerations and wind velocities were calculated and analyzed to determine if the longer wavelengths could be better resolved. The most pertinent of extreme gust data obtained during the High Intensity Gust Investigation was reprocessed using techniques developed during the LO-LOCAT program to see if the new techniques would alter the results originally obtained.

Spectra of longitudinal and lateral wind components showed indications of isotropy for the two components. Integral scale lengths were found to be



on the order of 6000 feet. A technique was developed whereby the statistics of gust velocities can be determined using gust accelerations. This technique proved to have two distinct advantages. The gust accelerations require less high-pass filtering due to their low power at low frequencies. The technique also requires considerably less computer effort since filtering may be performed in the frequency rather than the time domain. Analysis of the reprocessed High Intensity Gust Investigation data showed that the original results were effected very little by the IO-LOCAT processing techniques.

It is believed that enough statistical information on low altitude turbulence is available from various programs such that adequate gust criteria can be established for aircraft which are sensitive to wavelengths less than 15,000 feet. In the application of these data to gust criteria for the mission requirements of a given airplane the following should be considered:

- The difference in speed at which the IO-LOCAT data were obtained and that associated with the mission. Turbulence data recorded at higher speeds will usually have the longer wavelengths better defined. This causes the gust velocity probability distributions, average scale lengths, etc. to vary as a function of speed.
- The geophysical conditions under which the data were obtained. Turbulence data for wavelengths less than 8,000 feet were obtained during Phases I and II for all seasons at different locations, for all terrain types except the high mountain, for a wide range of meteorological conditions except those involving precipitation and storms, and for all times of day excluding darkness. Phase III data were not recorded during all seasons at each of the route locations.

TABLE II.1

BASIC IO-LOCAT INFORMATION

	Phases I & II	Phase III
Aircraft used to obtain data	4 C-131's	1 T-33
Flight period	9-15-66 - 12-20-67	8-16-68 - 6-30-69
Number of turbulence data flights	1,244	299
Low altitude turbulence samples	8,871	1,938
BRNN tower samples	0	8
Thunderstorm turbulence samples	0	55
Wake turbulence samples	0	46

TABLE II.1 (Contd.)

BASIC IO-LOCAT INFORMATION

	Phases I & II	Phase III
Turbulence sample average length	21 mi.	32 mi.
Turbulence sample average time interval	5.5 min.	4.5 min.
Average turbulence PSD wavelength band	33 - 7,980 feet	63 - 15,100 feet
Aircraft average ground speed	332 fps	630 fps
$\sigma_t$ bandwidth*	0 - $\infty$ cps	0 - $\infty$ cps
$\sigma_T$ bandwidth	0.33 - 10 cps	.66 - 10 cps
$\sigma$ bandwidth	0.04 - 10 cps	0.04 - 10 cps
Hot wire data bandwidth	5 - 500 cps	N/A
u time series samples analyzed statistically	6,553	1,730
v time series samples analyzed statistically	6,270	1,709
w time series samples analyzed statistically	6,508	1,716
u non-contour samples	1,113	0
v non-contour samples	1,091	0
w non-contour samples	1,118	0
u rms values analyzed statistically	7,670	1,762
v rms values analyzed statistically	6,621	1,740
w rms values analyzed statistically	7,630	1,746
Gust velocity samples for which spectra were calculated	1,775	904

\* Influenced below 0.046 and above 10.0 cps by high and low pass filters.

TABLE II.1 (Concluded)

BASIC LO-LOCAT INFORMATION

	Phases I & II	Phase III
u spectra eliminated due to irregularities**	296	313
v spectra eliminated due to irregularities**	514	380
w spectra eliminated due to irregularities**	306	408
Homogeneous u spectra analyzed	1,272	591
Homogeneous v spectra analyzed	1,061	524
Homogeneous w spectra analyzed	1,259	496
u spectra obtained during non-contour flight	207	0
v spectra obtained during non-contour flight	200	0
w spectra obtained during non-contour flight	210	0
Gust velocity time series samples per turbulence sample	33,000	27,000
Time interval - spectra calculations	0.01 sec.	0.02 sec.
Gust velocity samples in spectra calculations	33,000	13,500
Frequency interval - spectra calculations	0.0416 cps	0.0416 cps
Nyquist frequency	50 cps	25 cps
Number of frequency estimates - PSD	1,200	600
Miles covered recording acceptable turbulence data	135,900	55,750
Hours of acceptable turbulence data	600	130
Spectrum degrees of freedom - Individual samples	55	45

\*\* Low signal/noise, high airplane motion effects, low turbulence homogeneity, etc.

### SECTION III

#### GUST VELOCITY TIME FUNCTION

##### 5. RUN TEST FOR STATIONARITY

One of the assumptions normally made in the analysis of turbulence data is that it is stationary. Stationarity generally means that statistical properties computed over a short interval of time do not vary more than would be expected due to normal sampling variations.

In order to verify that the stationarity assumption was valid, it was necessary to perform a test for stationarity on each turbulence sample. During LO-LOCAT Phase III, the run test procedure for stationarity, as described in Reference 5.1, was used. Two separate run tests, one on the gust velocity mean values and one on the mean-square values, were performed for each turbulence sample. The use of mean-square values was suggested in Reference 5.2. Run test observations were obtained using the following equations:

$$O_n = \frac{1}{135} \sum_{i=a}^b x_i \quad (\text{Mean}) \quad (5.1)$$

$$O'_n = \frac{1}{135} \sum_{i=a}^b x_i^2 \quad (\text{Mean-Square}) \quad (5.2)$$

where:

$$a = 135n - 134$$

$$b = 135n$$

$$n = 1, 3, 5, \dots, 199$$

A total of 100 observations were made for each run test. Each observation ( $O_n$  or  $O'_n$ ) was compared with the observation mean and assigned a sign: plus when above and minus when below the mean. The number of runs is defined as the number of sets with like signs. The number of runs and whether or not the sample was accepted as stationary at the 0.02 level of significance for both run test methods was then determined. This was done by comparing the actual number of runs to the expected number of runs at a given level of significance.

The expected number of runs at a level of significance of 0.02 was determined using the following equations:

$$\mu = \frac{2N_1N_2}{N_1 + N_2} + 1 \quad (5.3)$$

$$\sigma = \left[ \frac{2N_1N_2(2N_1N_2 - N_1 - N_2)}{(N_1 + N_2)^2(N_1 + N_2 - 1)} \right]^{1/2} \quad (5.4)$$

where:

$N_1$  = Total number of plus values ( $O_n$  or  $O'_n$ )

$N_2$  = Total Number of minus values ( $O_n$  or  $O'_n$ )

Using the above information, the expected number of runs ( $E$ ) was then calculated:

$$E = (\mu \pm 2.326 \sigma) - 0.5$$

where 2.326 corresponds to the 0.02 level of significance.

When the actual number of runs fell between the two values of  $E$ , the stationarity hypothesis was accepted at the 0.02 level of significance.

Run test data were obtained for all turbulence samples recorded after Flight Number 177. Due to a computer programming problem, run tests were obtained for only some of the flights prior to Number 178. Run tests were, however, performed on a total of 802 turbulence samples.

The results for both run tests performed during IO-LOCAT Phase III are shown in Table 5.1. This table shows that over 80 per cent of the turbulence samples tested by a run test of the means were accepted as stationary. The mean-square test accepted from 60 to 70 per cent of the samples depending upon the component of gust velocity being tested. This indicates that the mean-square test is the more stringent. The average of these tests for all components indicate that 77 per cent of the samples may be accepted as stationary.

When a table such as the one in Reference 5.1 is used to determine the expected number of runs corresponding to a given level of significance, the assumption that  $N_1 = N_2$  in Equations 5.3 and 5.4 is made. The results of making this assumption are illustrated in Table 5.1. As shown, the percentage of turbulence samples accepted as stationary is reduced by using the  $N_1 = N_2$  assumption. The mean-square test is affected much more than the test of the means.

A number indicating the degree of stationarity for each turbulence sample was not computed. However, since homogeneity is the property which in space coordinates corresponds to the stationarity property in time coordinates, these two properties may be considered similar. Numerical values indicating the degree of homogeneity were computed for turbulence samples for which power spectra were computed and are presented in Section 21 and in Appendix VIII.

TABLE 5.1

PERCENT OF TURBULENCE SAMPLES ACCEPTED AS STATIONARY  
AT THE 0.02 LEVEL OF SIGNIFICANCE

	Test of Means			Test of Mean Squares		
	u	v	w	u	v	w
Analytical Method	85.1	80.7	88.3	77.4	60.1	70.7
Table Method	77.0	71.2	79.0	42.0	28.5	45.5

## 6. ENSEMBLE AVERAGING

A random process may be classed as either nonstationary, stationary, or stationary and ergodic. Atmospheric turbulence, over long periods of time, must be considered to be nonstationary. Stationarity implies that statistical properties computed over short time intervals do not vary more than would be expected due to normal sampling variations. The fact that turbulence is nonstationary is seen by comparing mean square values computed from turbulence samples for different days. Also, in mountainous regions where the terrain is not homogeneous and the wind currents vary considerably, mean square values for adjacent 4.5 minute turbulence samples have been found to vary from 3 to 75 (fps)<sup>2</sup>.

Over a small area and a short time interval, turbulence can usually be considered to be stationary. Atmospheric turbulence cannot be considered to fall into the stationary and ergodic class since ergodicity implies that each record of an ensemble is statistically equivalent to every other record and that ensemble averages over a large number of records at fixed times may be replaced by corresponding time averages on a single representative record of the ensemble.

Reference 6.1 indicates that to obtain a well defined statistical representation of a random process that is nonstationary or stationary and not ergodic, ensemble averages should be computed. Since atmospheric turbulence could fall into either class, ensemble averages were calculated for several categories of data. This averaging of a number of samples gave high statistical confidence, as discussed in Section 20.

Ensemble averaging was accomplished by taking an ensemble (group) of records and averaging the ensemble at corresponding times. Individual points of the ensemble average time function  $\mu_x(t)$  were calculated by:

$$\mu_x(t_i) = \frac{1}{N} \sum_{k=1}^N x_k(t_i) \quad (6.1)$$

Each of the 270-second records used were considered to be self stationary.

Ensemble average time functions were computed for each of the eight following category combinations:

High mountain, 250 foot, stable (112000)

High mountain, 250 foot, neutral (113000)

High mountain, 250 foot, unstable (114000)

High mountain, 750 foot, stable (122000)

High mountain, 750 foot, neutral (123000)

High mountain, 750 foot, unstable (124000)

Plains, 250 foot, unstable (414000)

Plains, 750 foot, unstable (424000)

Power spectra and coherency functions were calculated for the ensemble average time functions. Isotropy and homogeneity characteristics were evaluated and the spectra were compared to the von Karman mathematical expressions. These data are presented in Figures 6.1 through 6.8. Isotropy, homogeneity, and coherency checks gave essentially the same results as those from the principle analyses (Section V). The observed spectra agreed well with the von Karman spectra. The scale lengths from the ensemble time function, with the exception of two points, agreed fairly well with those representing the average of the scale lengths for the individual samples. These data are presented in Figure 6.9. The ensemble average scale lengths varied with category in the same way that individual sample scale lengths varied. That is, generally speaking, scale lengths increase with increasing terrain roughness, increasing altitude and decreasing stability.

It was concluded that short, relatively self-stationary segments of turbulence data can be accurately evaluated statistically without resorting to ensemble averaging techniques.

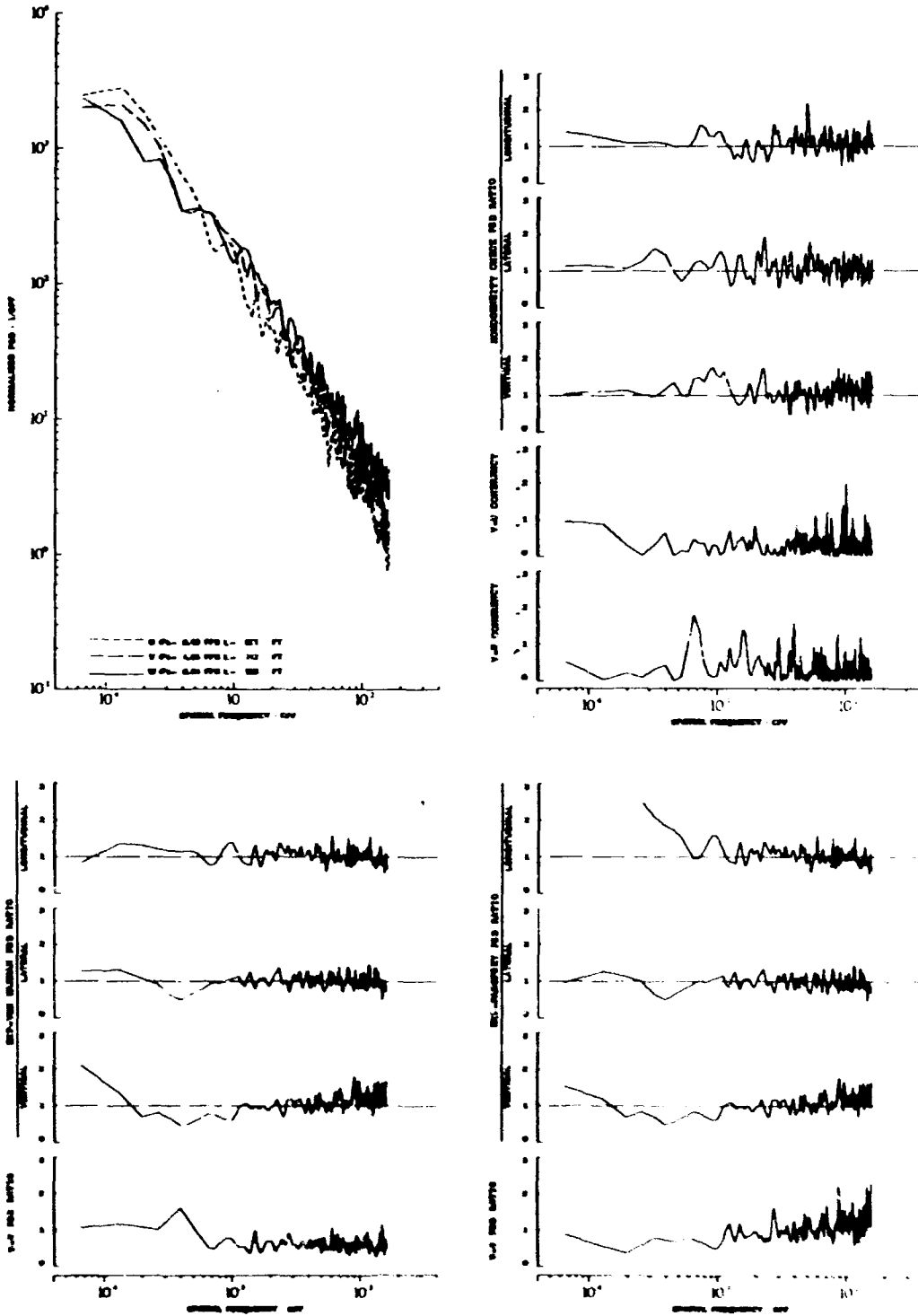


Figure 6.1 Power Spectra and Associated Data of Ensemble Average Time Function for High Mountain, 250 Feet, Stable Category



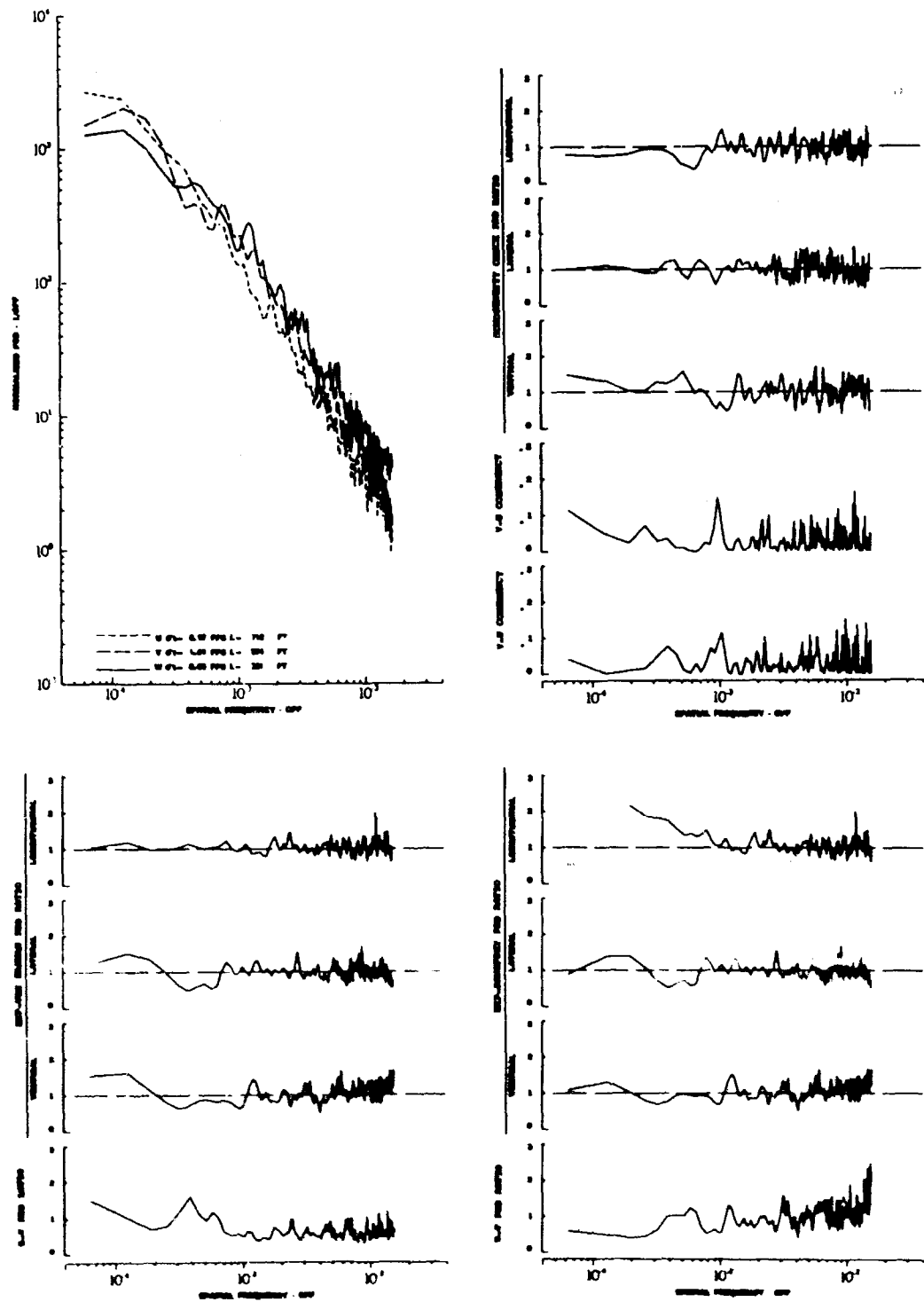


Figure 6.2 Power Spectra and Associated Data of Ensemble Average Time Function for High Mountain, 250 Feet, Neutral Category

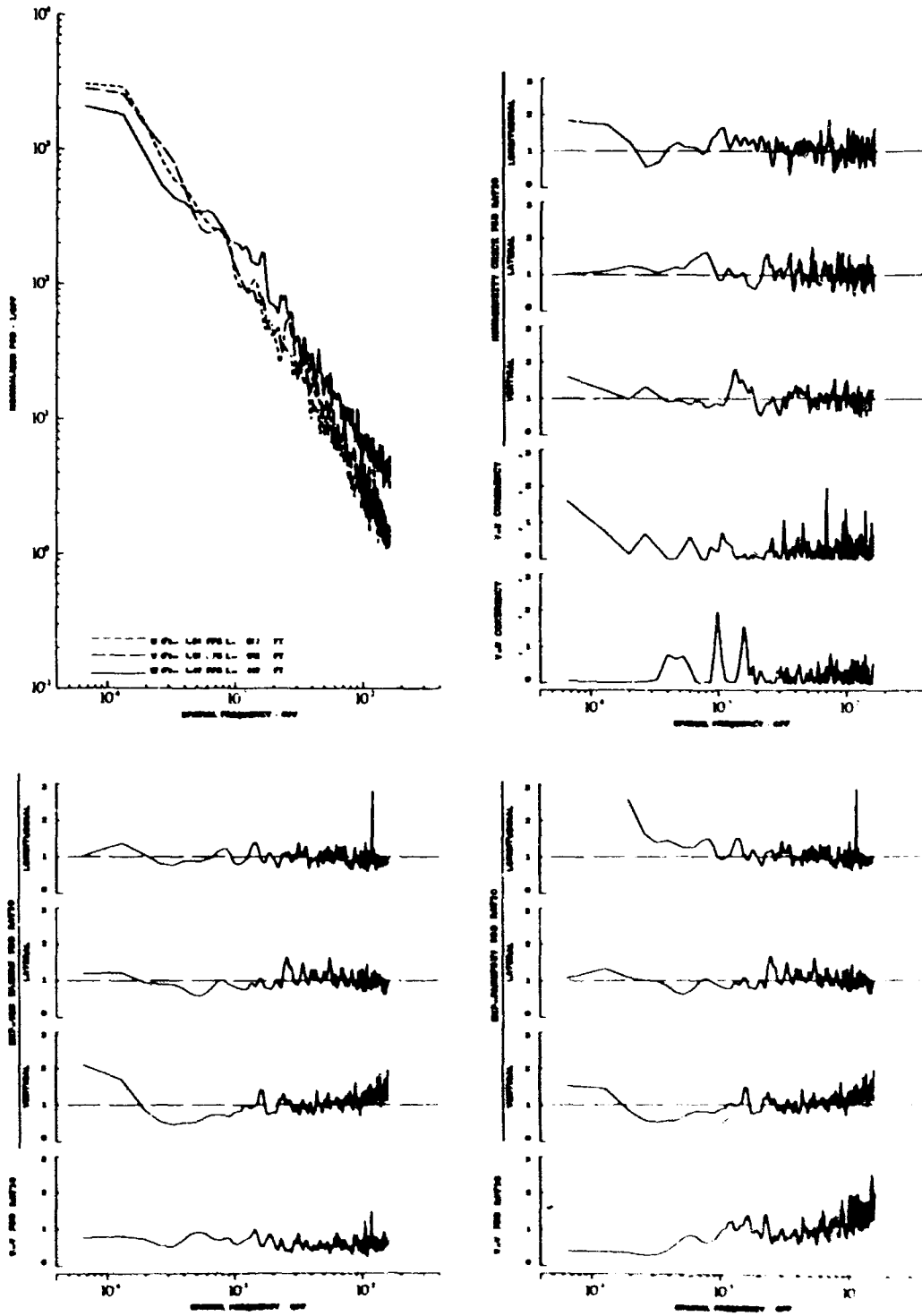


Figure 6.3 Power Spectra and Associated Data of Ensemble Average Time Function for High Mountain, 250 Feet, Unstable Category

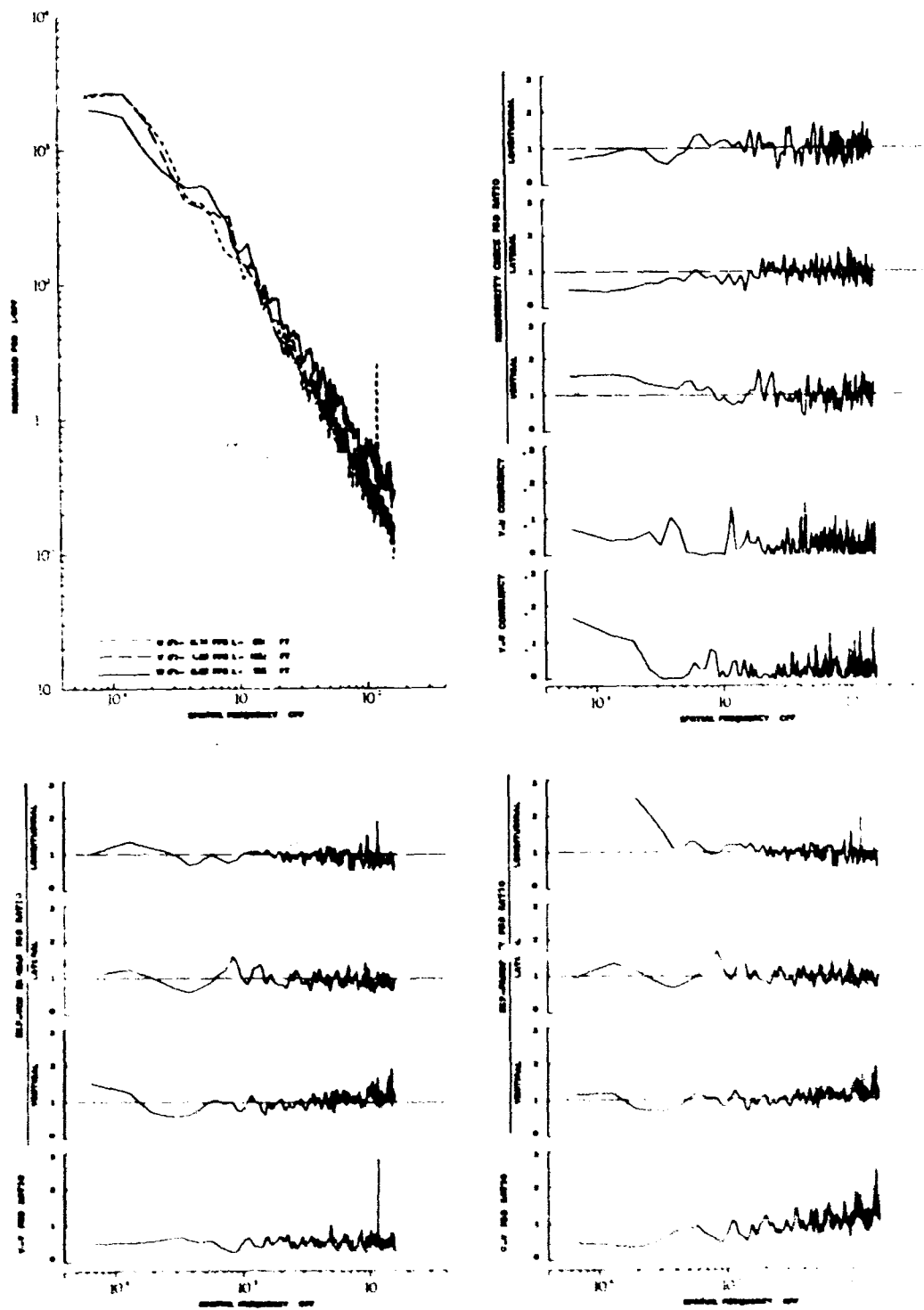


Figure 6.4 Power Spectra and Associated Data of Ensemble Average Time Function for High Mountain, 750 Feet, Stable Category

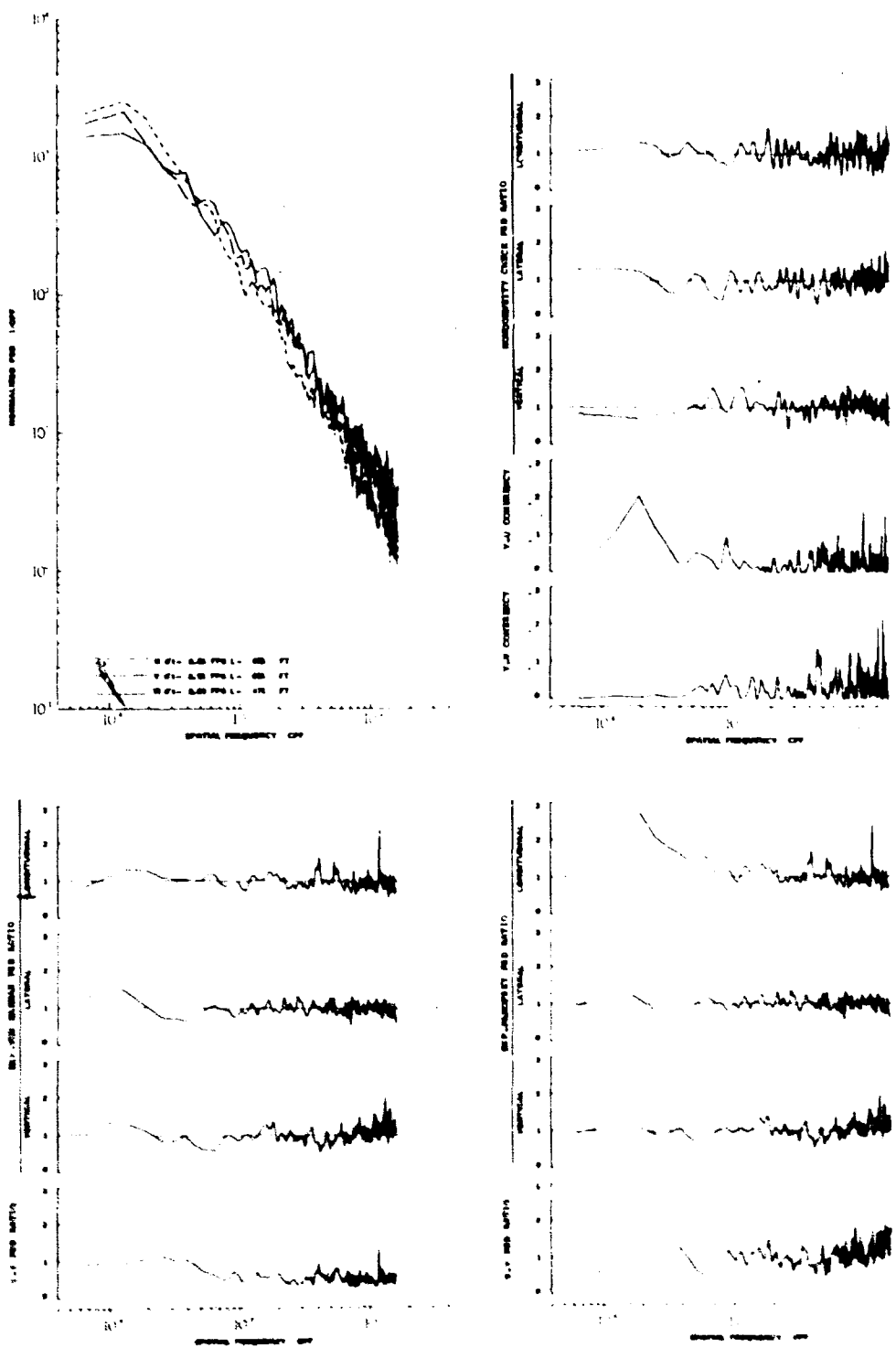


Figure 6.5 Power Spectra and Associated Data of Ensemble Average Time Function for High Mountain, 750 Feet, Neutral Category

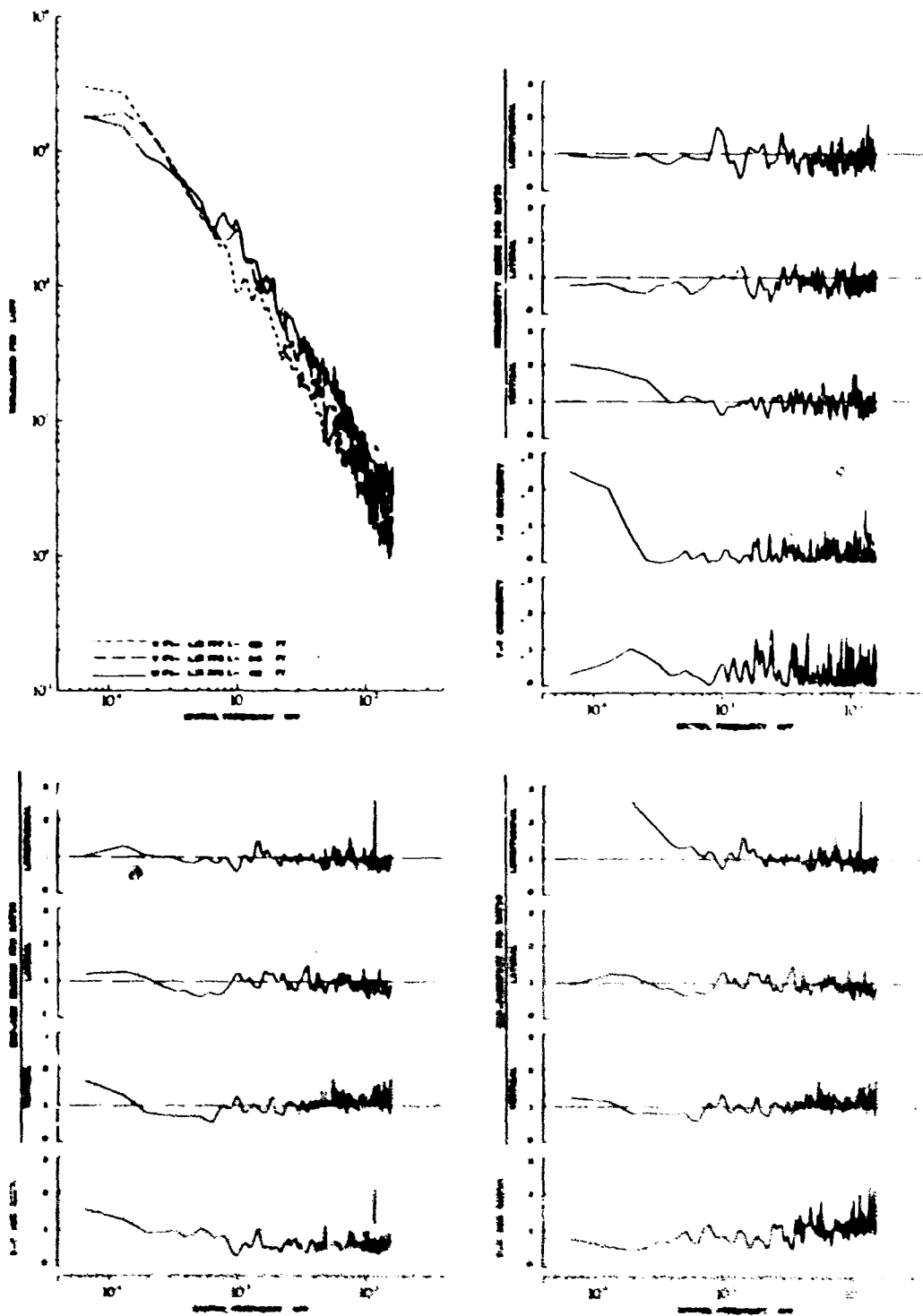


Figure 6.6 Power Spectra and Associated Data of Ensemble Average Time Function for High Mountain, 750 Feet, Unstable Category

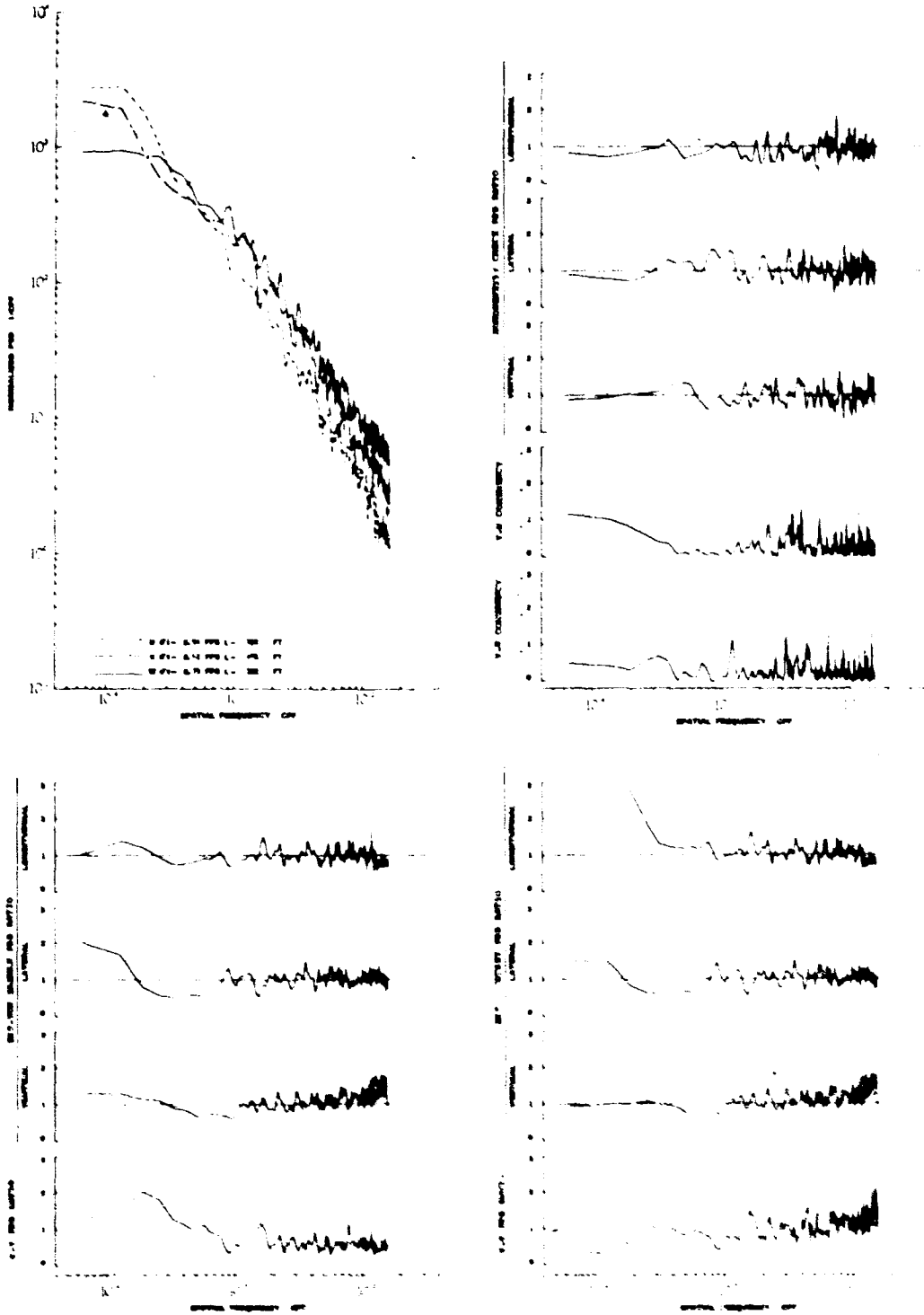


Figure 6.7 Power Spectra and Associated Data of Ensemble Average Time Function for Plains, 250 Feet, Unstable Category

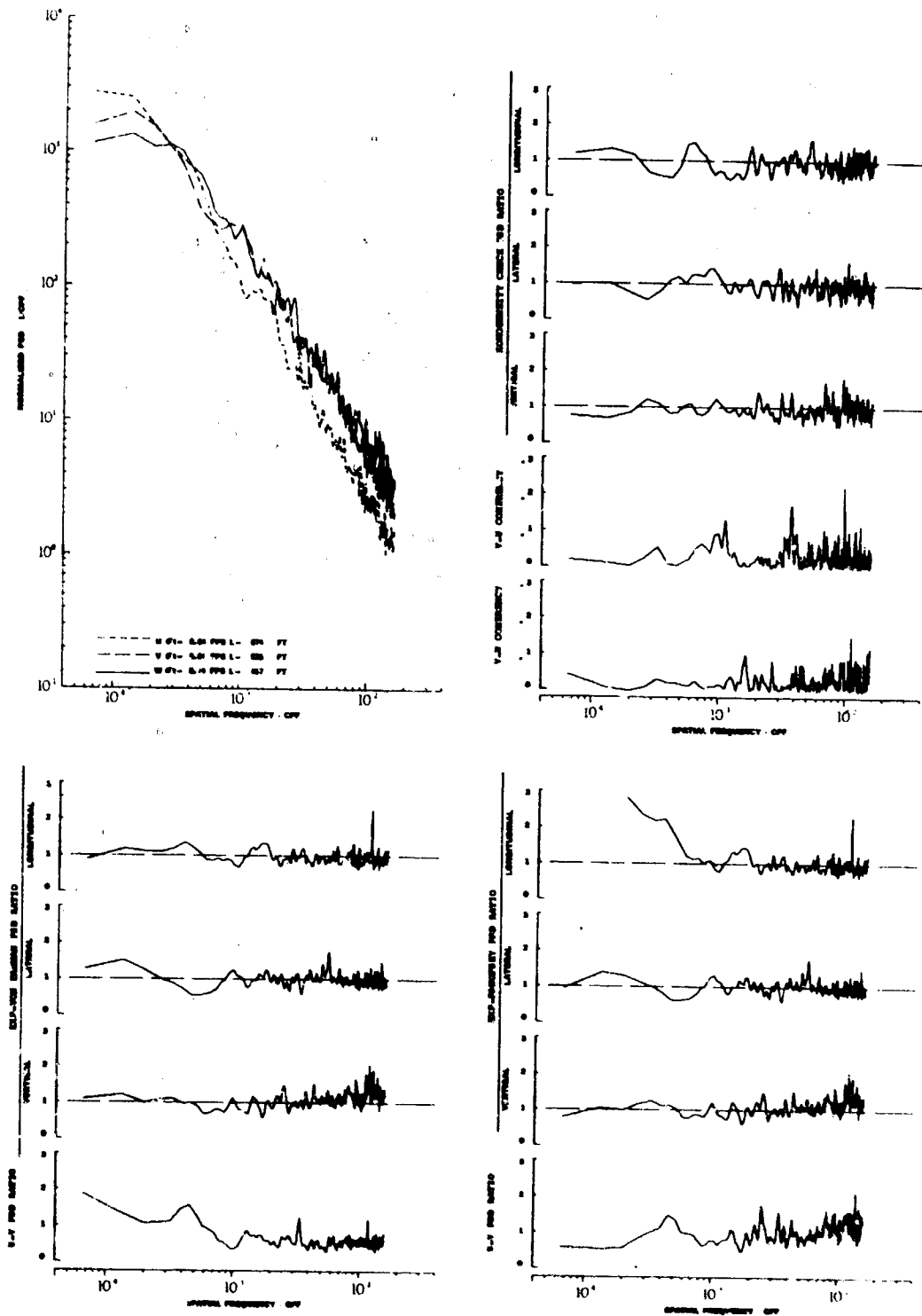


Figure 6.8 Power Spectra and Associated Data of Ensemble Average Time Function for Plains, 750 Feet, Unstable Category

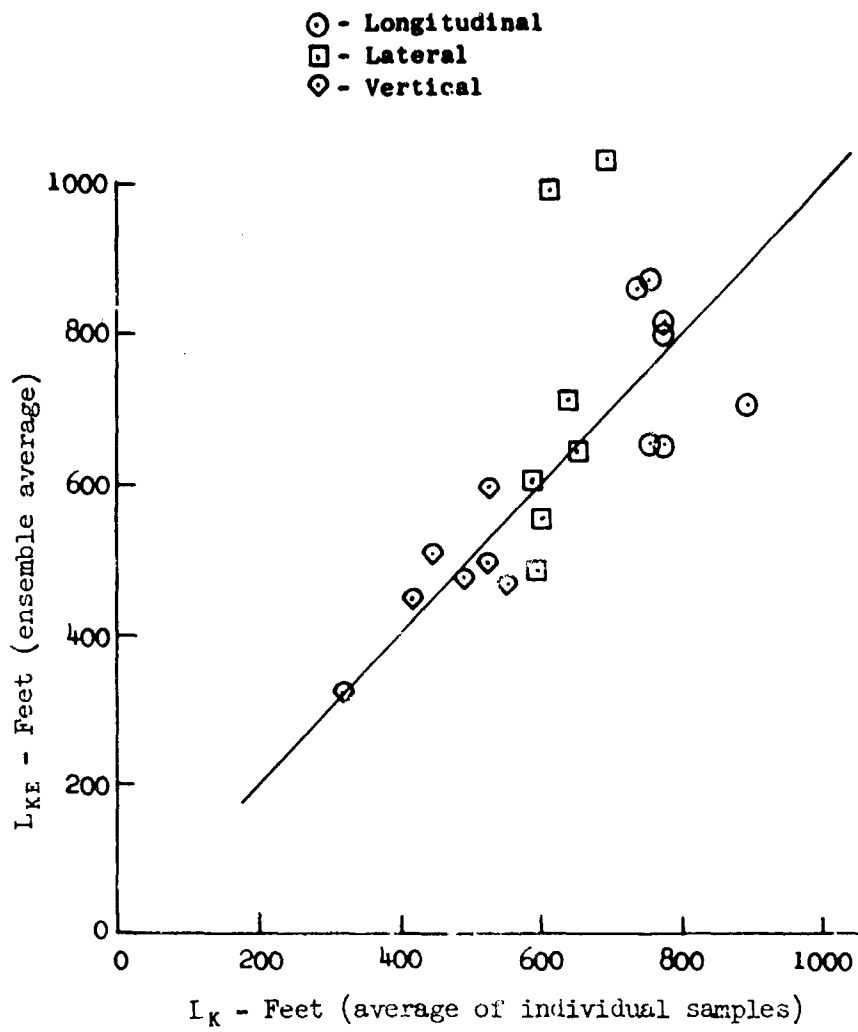


Figure 6.9 Scale Length Comparison



## 7. GAUSSIAN DISTRIBUTION CHECKS

Gust velocity amplitude values computed for each turbulence sample were checked for normality using the chi-squared goodness-of-fit test. This test compares the actual distribution with a normal distribution.

A chi-squared test was performed on each four and one-half minute turbulence sample using 28 bands ( $N_b$ ) with widths of constant probability. The degrees of freedom for each sample were ( $N_b-1$ ). Two hundred ( $N$ ) gust velocity amplitude values were used in the calculations of  $\chi^2$  values by equation 7.1:

$$\chi^2 = \sum_{b=1}^{N_b} \frac{(f_b - F_b)^2}{F_b} \quad (7.1)$$

where:

$f_b$  = observed frequency

$F_b$  = theoretical frequency

Since:

$$\sum_{b=1}^{N_b} f_b = N, \quad \sum_{b=1}^{N_b} F_b = N, \quad F_b = \frac{N}{N_b};$$

$$\chi^2 = .14 \sum_{b=1}^{28} f_b^2 - 200 \quad (7.2)$$

A cumulative probability distribution of the chi-square values for all IO-LOCAT Phase III data is shown in Figure 7.1. Levels of significance based on the number of degrees of freedom for these data are shown. Inspection of this figure shows that approximately 87 per cent of the vertical, 88 per cent of the longitudinal, and 89 per cent of the lateral gust velocity samples were accepted as Gaussian at the 0.02 level of significance. Approximately 10 per cent more samples were accepted during Phases I and II (Ref. I.2). This is attributed to the fact that turbulence samples were taken over a 60 per cent longer distance (approximately 32 miles) during Phase III.

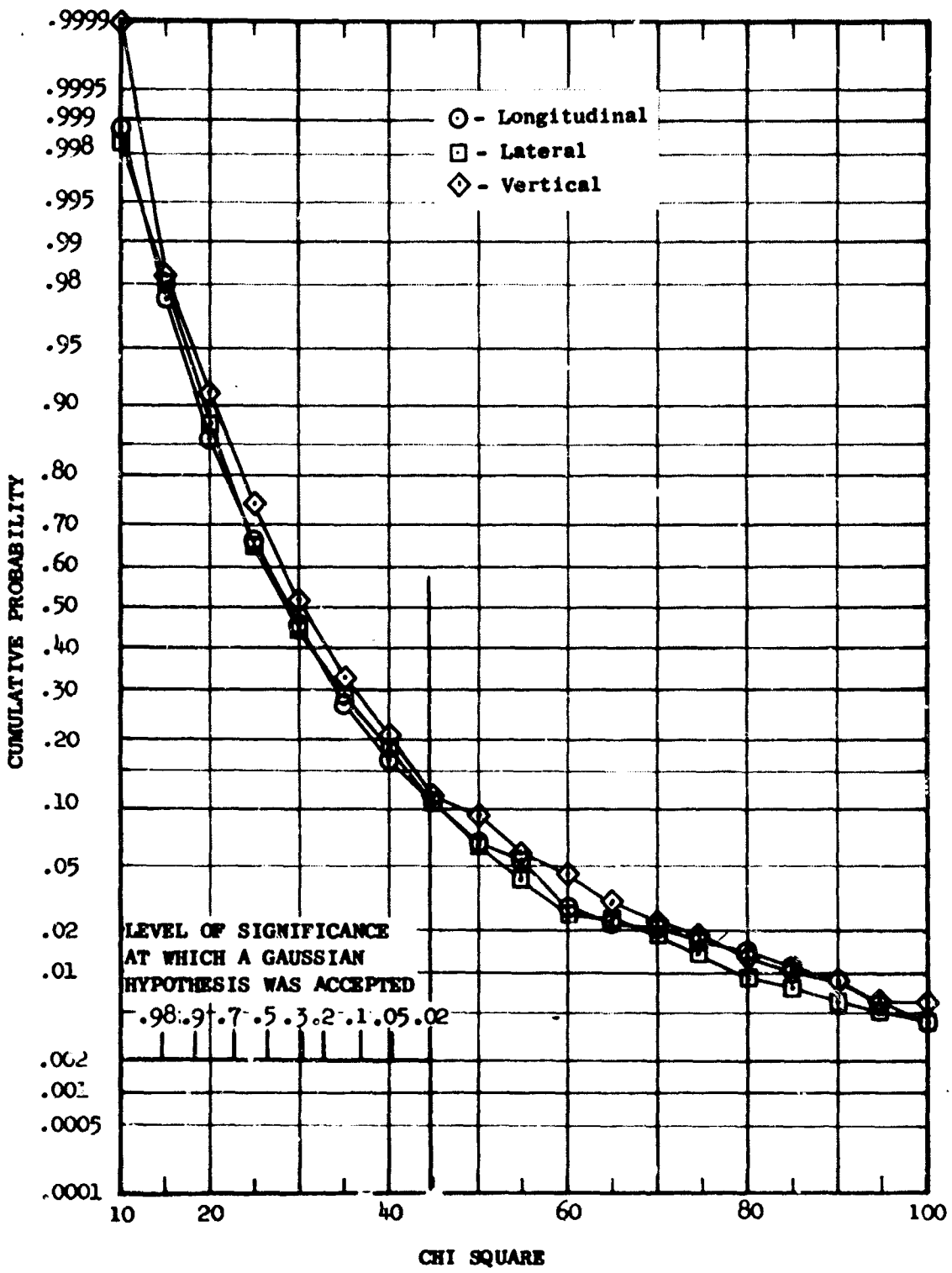


Figure 7.1 Chi-Square Test for Statistical Normality

## 8. PRIMARY PEAK COUNT

In the peak count procedure each maximum positive or negative excursion of a gust velocity time history, between adjacent crossings of the mean, is defined as a primary peak. A graphical illustration of this procedure is presented in Figure 8.1. As shown in this figure secondary peaks are not considered, and only the primary peaks which fall within each 2 fps wide band are counted.

In this procedure, high frequency, low amplitude data are counted as primary peaks in the lowest band. Figure 8.2 shows a peak count distribution plotted on semi-logarithmic scales and illustrates how it was extrapolated to obtain the peaks in the lowest band. The shaded points indicate the cumulative number of peaks in the lowest band as they were originally counted. The unshaded points at zero gust velocity are the extrapolated values. The extrapolation technique had the effect of compensating the error induced by not counting the secondary peaks and thereby adjusted the cumulative probability of the peak count data to be more compatible with that of the level crossings data.

The extrapolation was performed by fitting a curve through the data points using the least square method. The curve fitting was accomplished by computer and consisted of fitting the general polynomial (Equation 8.1) to the distribution.

$$Y_1 = A_0 + A_2 X_1^2 \quad (8.1)$$

The coefficients  $A_0$  and  $A_2$  were determined such that the following quantity was a minimum:

$$\sum e_1^2 = \sum_{i=1}^N W_i \left[ Y_1 - A_0 - A_2 X_1^2 \right]^2 \quad (8.2)$$

where:

$X_1 = (x_1 + 20)$  in fps, where  $x_1$  is the gust velocity

$Y_1 = \log (F_{b_1})$ , where  $F_b$  is the cumulative number of peaks per mile occurring in a given band

$W_1$  = The weight applied to each  $Y_1$ . For this application the following  $W_1$  values were used:

$$W_1 = 0$$

$$W_6 = 6$$

$$W_2 = 20$$

$$W_7 = 4$$

$$W_3 = 15$$

$$W_8 = 2$$

$$W_4 = 10$$

$$W_9 \text{ through } W_{L_0} = 1$$

$$W_5 = 8$$

$e$  = error or difference between observed and analytical values of  $Y$

$N$  = Number of data points being fitted

$A_0, A_2$  = Constants

The following equations were obtained by taking the partial derivatives of  $f(x)$  with respect to each coefficient:

$$A_0 \sum_{i=1}^N W_i + A_2 \sum_{i=1}^N W_i X_i^2 - \sum_{i=1}^N W_i Y_i = 0 \quad (8.3)$$

$$A_0 \sum_{i=1}^N W_i X_i^2 + A_2 \sum_{i=1}^N W_i X_i^4 - \sum_{i=1}^N W_i X_i Y_i = 0 \quad (8.4)$$

Simultaneous solution of these equations yields values of the coefficients for use in Equation 8.1. The coefficient  $A_0$  is the extrapolated  $\log(K_{pe})$ . Details of the least squares curve fit are given in References 8.1 through 8.3.

After positive and negative peaks were added for each band and accumulated, cumulative peaks per mile were calculated by dividing the cumulative number of peaks in each band by the miles traveled while obtaining the turbulence sample. Cumulative probability was calculated by dividing the cumulative number of peaks for each band by the cumulative number of peaks for the lowest band (for peak count, this is an extrapolated value). The probability density is the change in probability from one band to the next higher one divided by the band width.

Figure 8.2 is an example of a peak count cumulative distribution for a particular turbulence sample. The curves shown on this plot represent those fitted by computer to the data points. The characteristic frequency of the peak count data,  $N_{pe}$ , is defined as the cumulative peak per mile value determined by extrapolating the cumulative distribution curve to zero gust velocity. Figures 8.3 and 8.4 are examples of peak count cumulative probability distribution and probability density distribution for the same turbulence sample as shown in Figure 8.2.

The turbulence samples on which the peak count was performed all had means which had been set to zero. A standard deviation was calculated about this mean for each gust velocity sample using the grouped data technique discussed in Reference 8.4. Standard deviation values, presented in Section 11, were computed from the following equation:

$$\sigma_{pe} = \left[ \sum_{b=1}^n \frac{f_b(x_b)^2}{N_{pe}} \right]^{1/2} \quad (8.5)$$

The subscript  $e$  denotes that an extrapolated value for cumulative peaks, as discussed previously, was used in this calculation.

Those turbulence samples set aside from the normal data processing routine because of low signal to noise ratio (discussed in Appendix III, Section III.5) were included in the gust velocity peak count distributions so that the effects of low intensity turbulence would be present in the final analysis. Inclusion of these turbulence samples was accomplished in the following manner. (1) The category number associated with each of these turbulence samples was determined (Table 8.1 is a list of the number of samples involved with respect to category number). (2) One low signal to noise sample was processed for each different category number to obtain peak count data representative of that category. (3) The representative data, multiplied by a factor equal to the number of samples involved in each category (Table 8.1), were added to the peak count distributions initially computed in the normal data processing routine.

Figure 8.5 is a plot of the peak distribution for the overall category. The shaded points illustrate the effect of including low intensity turbulence samples. Only the points at zero gust velocity were changed a noticeable amount; all other points were essentially unchanged. Also, the inclusion of the low intensity turbulence samples slightly lowered the cumulative probability distribution curves of those data in the categories involved. Figure 8.5 also compares the peak count distribution curves for the gust velocity components for the overall category. Lateral gust velocity has the highest distribution curve and longitudinal the lowest with vertical crossing over between them. The relationship between components of gust velocity for all categories analyzed is shown in Appendix VII. Those categories which contain high mountain data show a relationship between components similar to that for the overall category. Categories which do not contain high mountain data generally show a closer comparison between lateral and vertical distributions with longitudinal always slightly lower. The reason lateral is higher for the high mountain data is probably due to the effects of flying parallel to and on the leeward side of high mountain ridges.

The distributions of the three components, for the categories other than high mountain, agreed much more closely during Phase III than they did during Phases I and II. High-pass filtering attenuates the long wavelength amplitudes of the longitudinal component more than the vertical or lateral because the longitudinal component contains higher power at the long wavelengths. The attenuation of these long wavelengths was less severe during Phase III than during Phases I and II. This occurred because the Phase III data were recorded using a higher speed airplane which made possible the measurement of longer wavelengths as discussed elsewhere in this report.

TABLE 8.1

NUMBER OF LOW INTENSITY TURBULENCE SAMPLES INCLUDED  
IN EACH CATEGORY FOR STATISTICAL ANALYSIS OF  
PEAK, AMPLITUDE, AND LEVEL CROSSINGS COUNT

Category Number	Number of Samples	Category Number	Number of Samples
321131	1	611241	1
411124	6	611331	5
421113	1	611341	1
421124	15	621131	6
421134	8	621141	2
421234	3	621231	5
422234	1	621241	3
424124	1	621331	4
611141	2	621341	1

The peak count, amplitude count, and level crossings count distributions obtained for each turbulence sample were compiled on a master computer tape as they were processed. These distributions were recorded on the master tape according to category number. For IO-LOCAT Phase III, data were stored in 260 out of a possible 1920 different categories on this tape. Some of these categories contained many samples, others had only one. In order to obtain distributions which were statistically reliable, it was necessary to combine categories so that none contained fewer than 30 samples.

The master tape data were processed through a computer program which had the capability of combining categories in any selected combinations. Those samples not categorized with respect to atmospheric stability because of invalid outside air temperature data could not be handled by the computer program and therefore, were not included on the master tape, nor included in the statistical analysis. The combined category distributions obtained from this program were then plotted. Table 8.2 lists those categories which contained 30 or more samples. The total number of samples included in each category, as well as the number of low intensity turbulence samples included in the total are also included in Table 8.2. Plots and listings of peak count distributions and probability distributions for these categories are given in Appendices VII and VIII, respectively.

Analytical expressions of the peak count probability distributions were determined for each of those categories involving individual category components as well as the all data category. These expressions were determined using a technique similar to that described in References 8.5 and 8.6. This technique involved the selection by least-squares fit techniques, of two exponential curves which, when added together, would result in a curve representing the distribution in question. This expression takes the following form:

$$F(x) = P_1 \exp\left(-\frac{x}{b_1}\right) + P_2 \exp\left(-\frac{x}{b_2}\right) \quad (8.6)$$

where:

$F(x)$  = Cumulative probability distribution function

$P_1, P_2$  = Intercepts of the exponential curves

$1/b_1, 1/b_2$  = Slopes of the exponential curves on semi-logarithmic paper

$x$  = Gust velocity amplitude

Table 8.3 shows the values of  $P_1, P_2, b_1,$  and  $b_2$  for the above mentioned categories. The values are valid out to the maximum gust velocity value measured for each category as given in Appendix VIII. Experimental data corresponding to the fitted curves is given in Appendix VII.

Confidence limits were computed for the categorized primary peak count cumulative distribution functions. Since each distribution analyzed contained many turbulence samples, each point on the distribution curve is representative of the mean at that point of all samples contained in the category. The central limit theorem states that for large samples, mean values are distributed normally without consideration of the underlying distribution. The confidence limits were therefore calculated using the procedure for a normal population with unknown standard deviation, as described in Reference 8.4. Peak count distributions and their confidence limits for all categories analyzed are given in Appendix IX. Figures 8.6 through 8.11 illustrate the relationship of the 99 and 95 per cent confidence limits to the distribution of all of Phase III data.

An analysis of the peak count data with respect to those categories involving individual category components as well as the all data category is contained in Section 11. A comparison of the various counting techniques is also contained in that section.

TABLE 8.2

TOTAL NUMBER OF TURBULENCE SAMPLES IN EACH COMBINED  
CATEGORY DISTRIBUTION AND THE NUMBER OF LOW  
INTENSITY TURBULENCE SAMPLES INCLUDED -  
PEAK, AMPLITUDE, AND LEVEL CROSSINGS COUNT

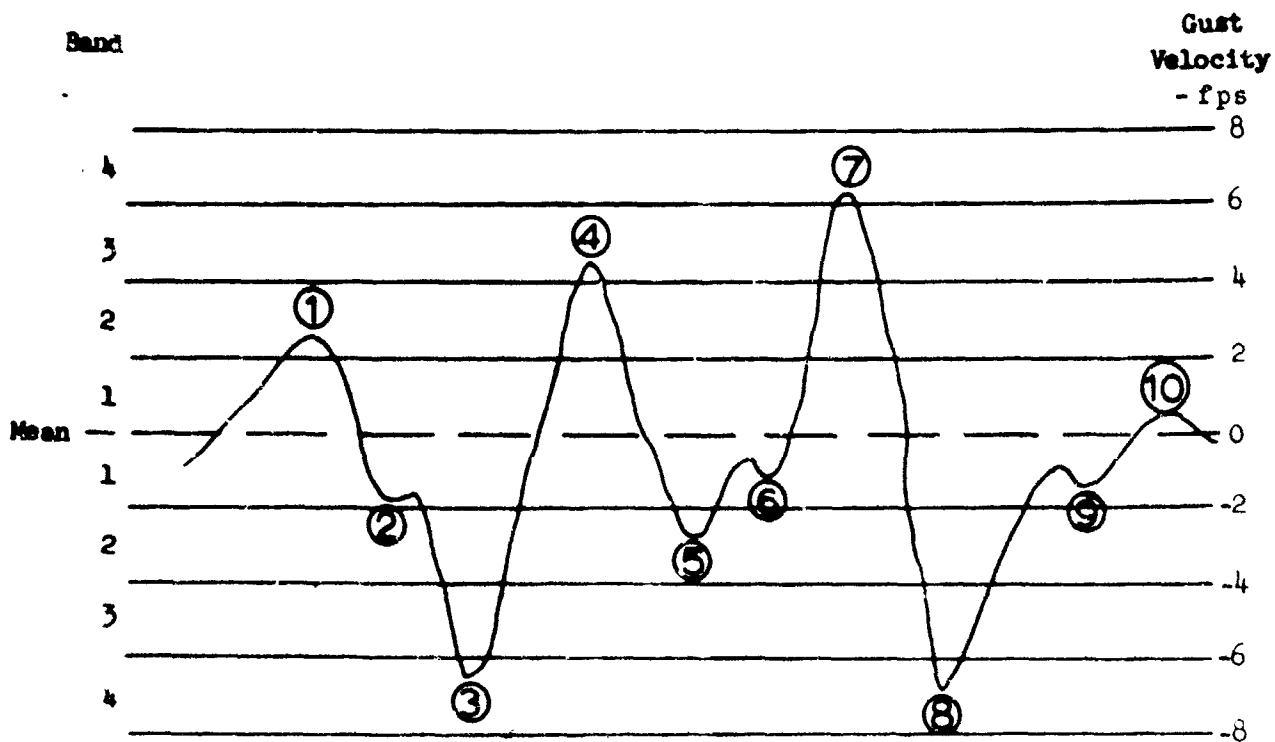
Category	Total Number of Samples			Number of Low Turbulence Samples
	u	v	w	
000000	1730	1709	1716	66
100000	846	841	846	0
200000	297	297	297	0
300000	115	115	115	1
400000	396	380	382	35
600000	76	76	76	30
010000	899	887	891	15
020000	831	822	825	51
001000	561	558	560	64
002000	479	475	477	1
003000	393	387	390	0
004000	297	289	289	1
000100	465	462	465	42
000200	644	637	639	13
000300	621	610	612	11
000001	599	599	599	31
000002	135	134	135	0
000003	743	736	742	1
000004	253	240	240	34
111000	109	108	109	0
112000	140	140	140	0
113000	129	128	129	0
114000	64	64	64	0
121000	112	112	112	0
122000	147	146	147	0
123000	95	94	95	0
124000	50	49	50	0
211000	60	60	60	0
212000	31	31	31	0
213000	33	33	33	0
214000	33	33	33	0
221000	65	65	65	0
312000	31	31	31	0
411000	52	51	52	6
412000	39	39	39	0
413000	57	54	55	0
414000	50	44	44	0
421000	55	54	54	27
422000	33	30	31	1
423000	39	38	38	0
424000	71	70	69	1
621000	32	32	32	21



TABLE 8.3  
P AND b VALUES FOR PEAK COUNT CUMULATIVE PROBABILITY DISTRIBUTION FUNCTIONS

CATEGORY	00000	10000	20000	30000	40000	60000	010000	020000	001000	002000	
Longitudinal	P1	0.89834	0.79466	0.99602	0.77279	0.99748	0.98454	0.87892	0.74711	0.98692	0.72763
	b1	2.26164	2.76646	2.68262	1.22354	2.11600	0.73180	2.32707	2.25176	1.71590	2.64255
	P2	0.09055	0.20536	0.00395	0.02721	0.00242	0.01542	0.12107	0.05285	0.01302	0.07233
	b2	6.18505	6.25127	5.60192	2.54267	4.45536	2.26177	6.04953	6.54838	6.07773	6.83023
Lateral	P1	0.90197	0.77362	0.99992	0.94829	1.00433	0.88682	0.88880	0.74745	0.99361	0.89889
	b1	2.51345	2.98231	2.89267	1.31182	2.35630	0.58961	2.61682	2.63770	2.22727	2.72840
	P2	0.09802	0.22640	0.0	0.03173	0.0	0.11260	0.11120	0.05254	0.00823	0.10109
	b2	7.00041	7.03901	0.0	2.55757	0.0	1.55766	6.98913	7.60860	8.01288	7.39998
Vertical	P1	0.85077	0.64837	0.99603	0.99991	0.99876	0.83059	0.89379	0.88253	0.98869	0.89749
	b1	2.27930	2.29740	2.60459	1.54145	2.16538	0.49453	2.61929	2.28519	1.86096	2.77033
	P2	0.14022	0.35166	0.00392	0.00005	0.00084	0.16936	0.10821	0.11538	0.01123	0.10218
	b2	5.46880	5.49476	6.41905	13.64360	4.82243	1.32566	5.83392	5.62643	6.43224	6.24360
CATEGORY	003000	004000	000100	000200	000300	000001	000002	000003	000004		
Longitudinal	P1	0.68899	0.65136	0.93845	0.93340	0.90858	0.97735	*	0.79537	*	
	b1	3.02619	2.47833	1.74384	2.53698	2.68864	1.84266	1.84266	2.81293		
	P2	0.11102	0.14867	0.06154	0.06659	0.09142	0.02262	0.20465	0.20465		
	b2	6.23914	6.38375	6.61730	6.54498	6.11534	5.43430	6.28688			
Lateral	P1	0.90611	0.93329	0.91992	0.92262	0.92080	0.93610	1.03733	0.77189	0.99158	
	b1	5.26164	5.01555	2.07610	2.72576	2.95688	1.85882	3.11968	2.99616	1.94265	
	P2	0.09388	0.09473	0.07611	0.07733	0.07920	0.06379	0.0	0.22813	0.00345	
	b2	7.41389	7.45566	7.77154	7.09544	7.06916	4.34628	0.0	7.05635	3.36834	
Vertical	P1	0.70534	0.80884	0.87166	0.94899	0.87488	0.99669	1.00008	0.54950	0.99988	
	b1	2.48306	2.63024	1.64787	3.00482	2.71874	2.21775	2.75463	2.30585	1.92721	
	P2	0.29467	0.19116	0.11264	0.05096	0.12510	0.00319	0.0	0.45053	0.00306	
	b2	5.03957	5.53334	5.88692	6.39510	5.48802	2.77914	0.0	5.20379	9.45753	

\* Not available



Band No.	Gust Velocity (fps)	Plus Peak Ident.	Minus Peak Ident.	Cumulative Peaks	Cumulative Peaks per Mile*	Cumulative Probability	Probability Density
1	0	⑩		7	35	1.0000	.0714
2	2	①	⑤	6	30	.8571	.1428
3	4	④		4	20	.5714	.0715
4	6	⑦	③ ⑧	3	15	.4285	.2143

NOTE: This is only an illustration and should not be considered as typical of turbulence data.

② ⑥ ⑨ = Secondary Peaks - Not Counted

\* For this example, assume 0.2 statute miles is the length of the above record.

Figure 8.1 Primary Peak Count Example

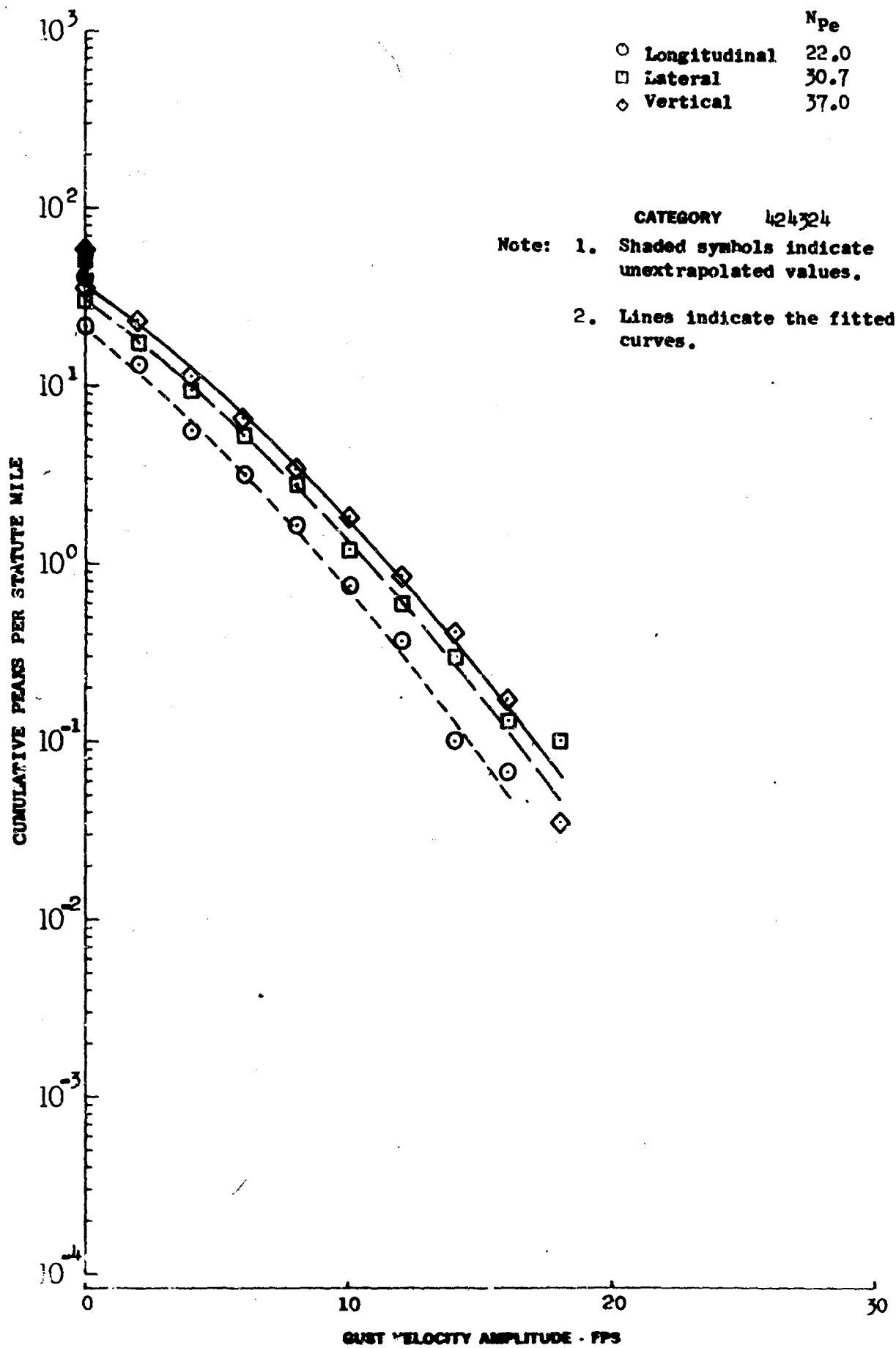


Figure 6.2 Peak Count Extrapolation Technique

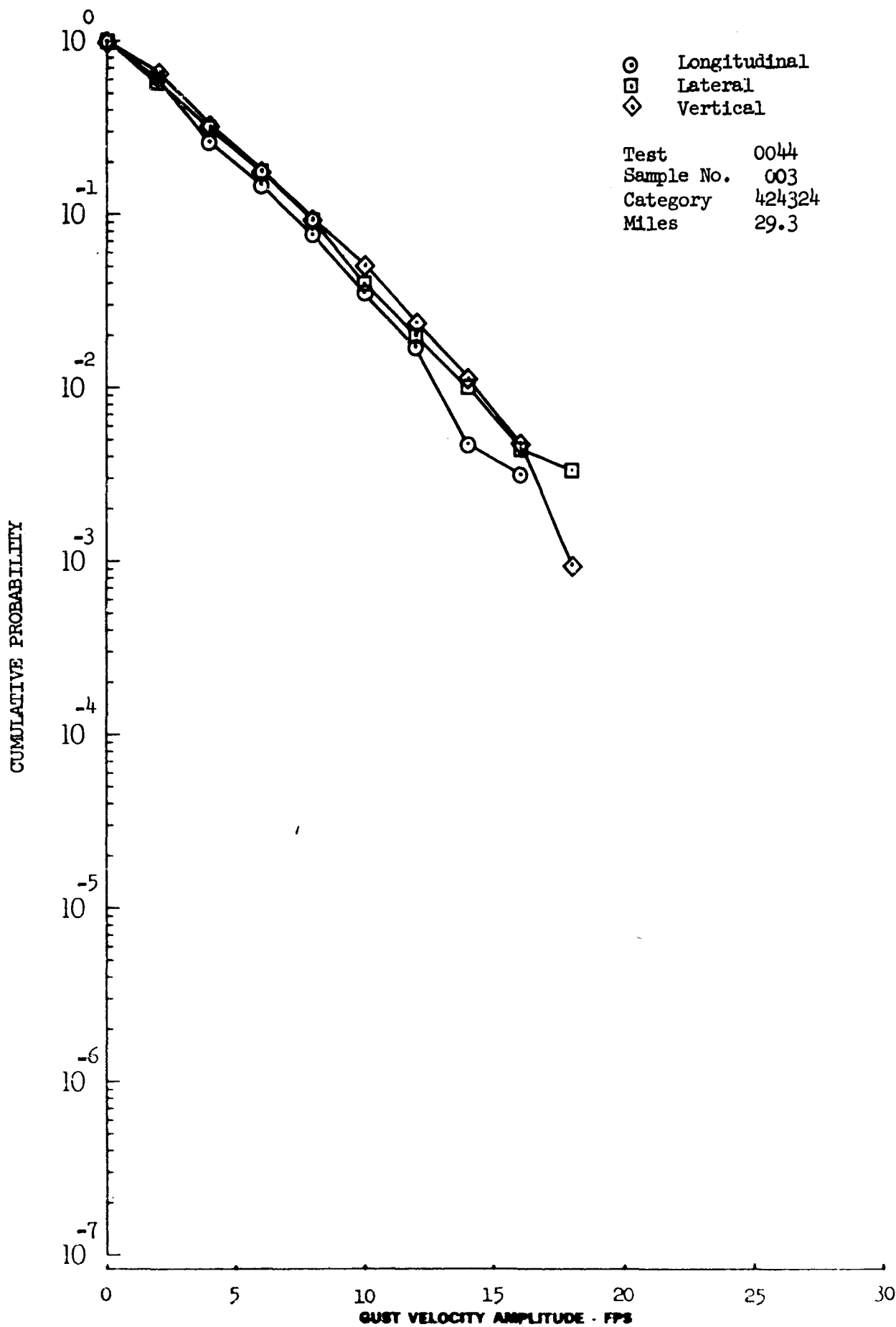


Figure 8.3 Gust Velocity Peak Count Probability Distribution for an Individual Turbulence Sample

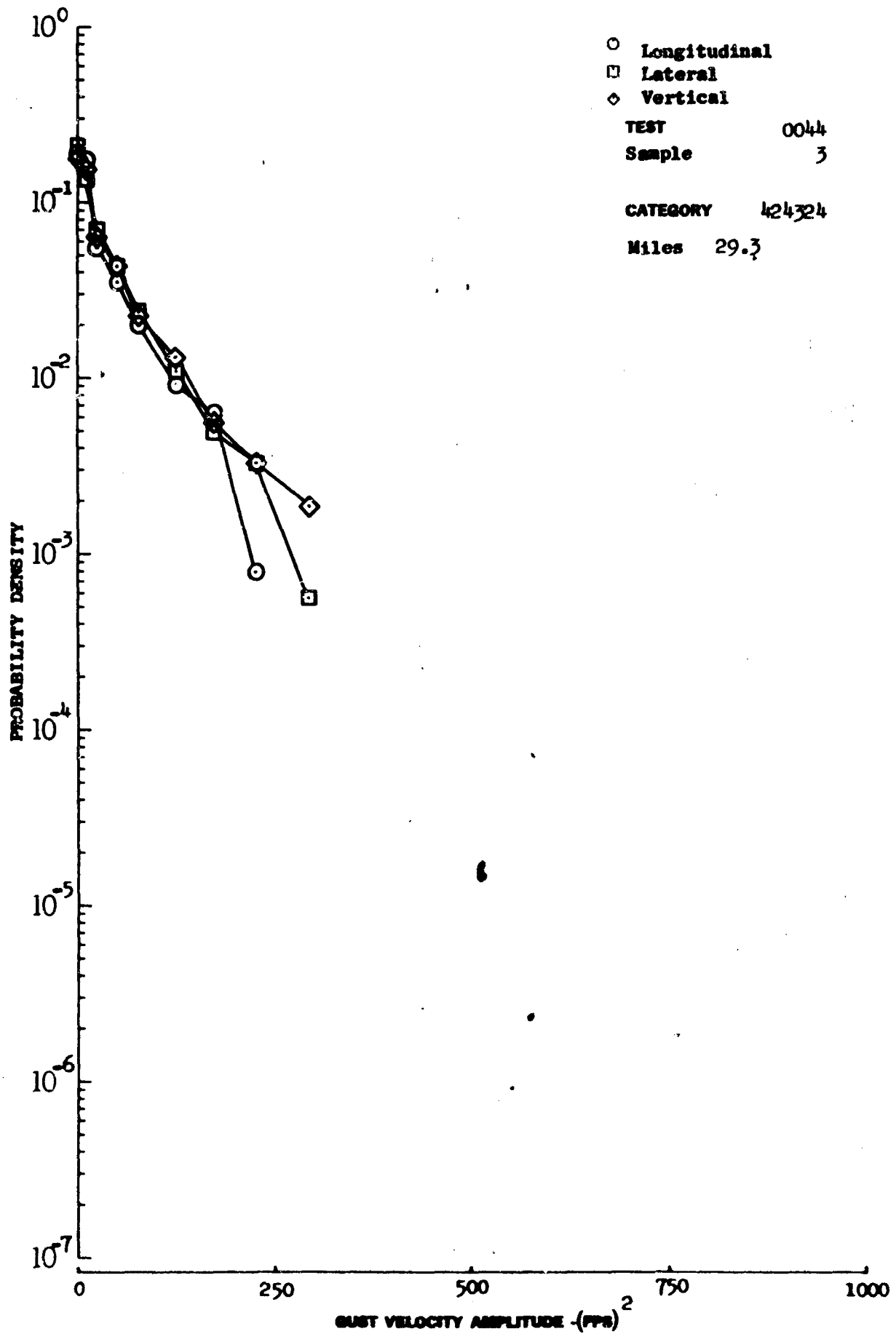


Figure 8.4 Gust Velocity Peak Count Probability Density Distribution

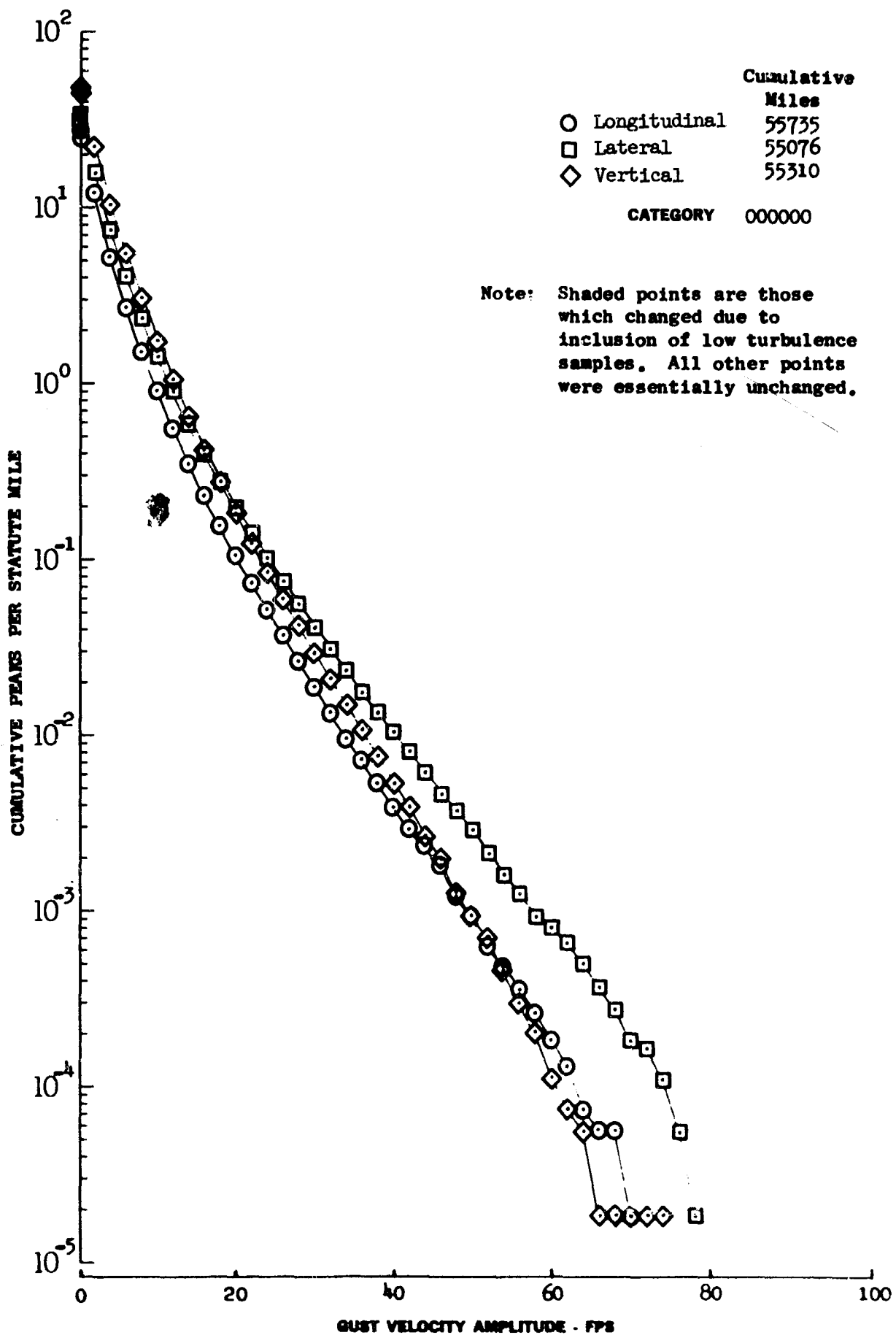


Figure 8.5 Gust Velocity Peak Distribution

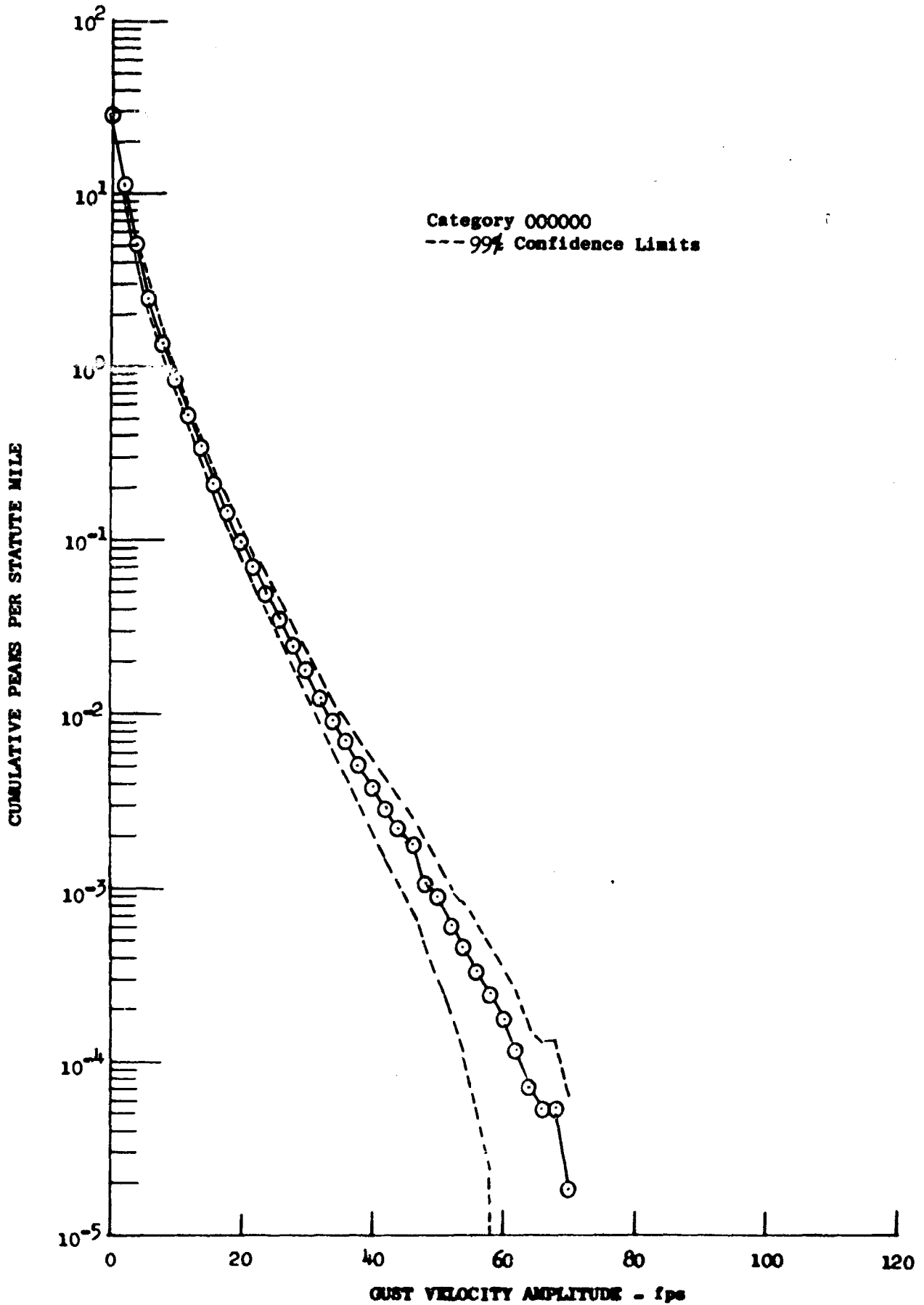


Figure 8.6 Longitudinal Gust Velocity Peak Count Distribution with 99% Confidence Limits

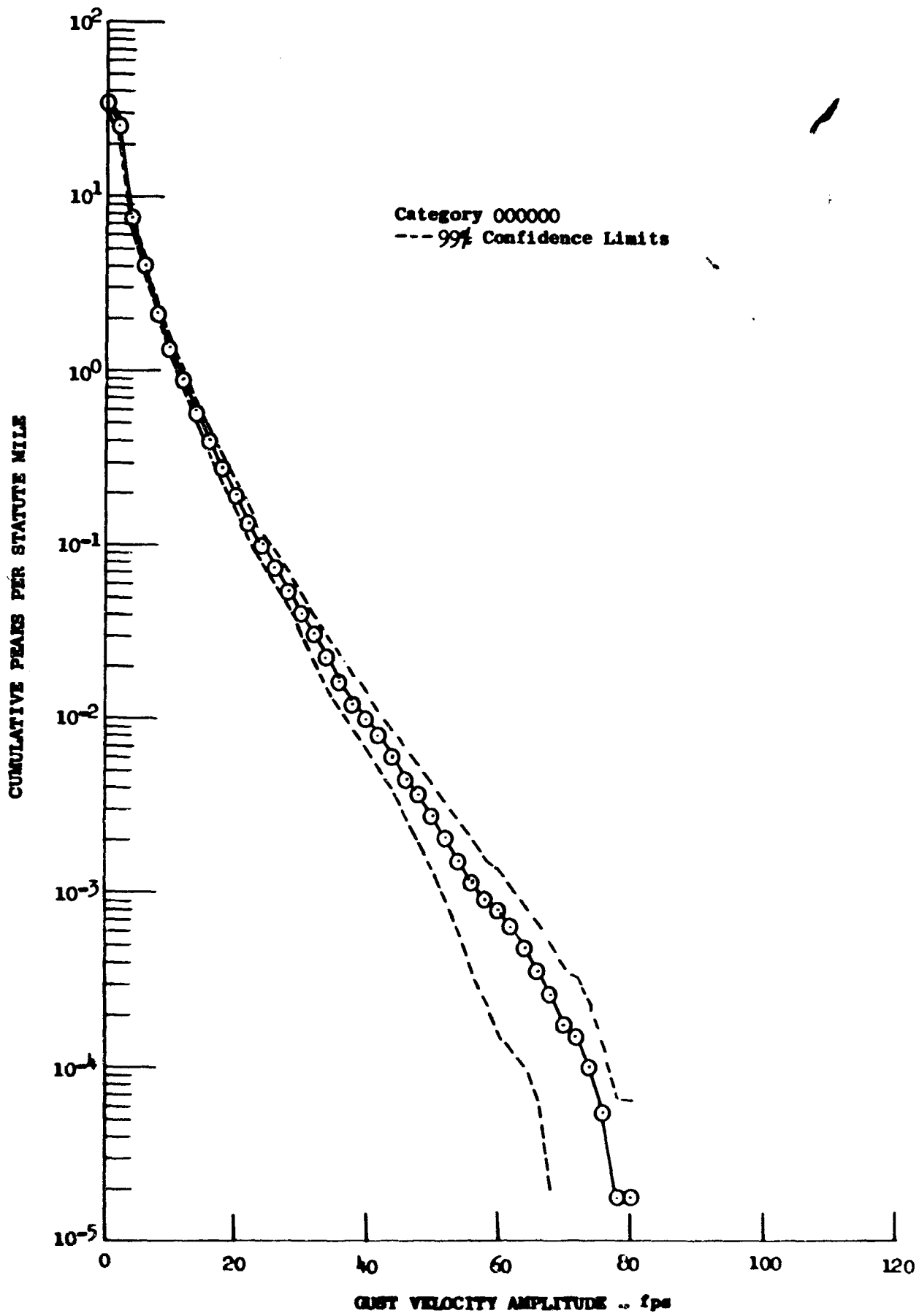


Figure 8.7 Lateral Gust Velocity Peak Count Distribution with 99% Confidence Limits



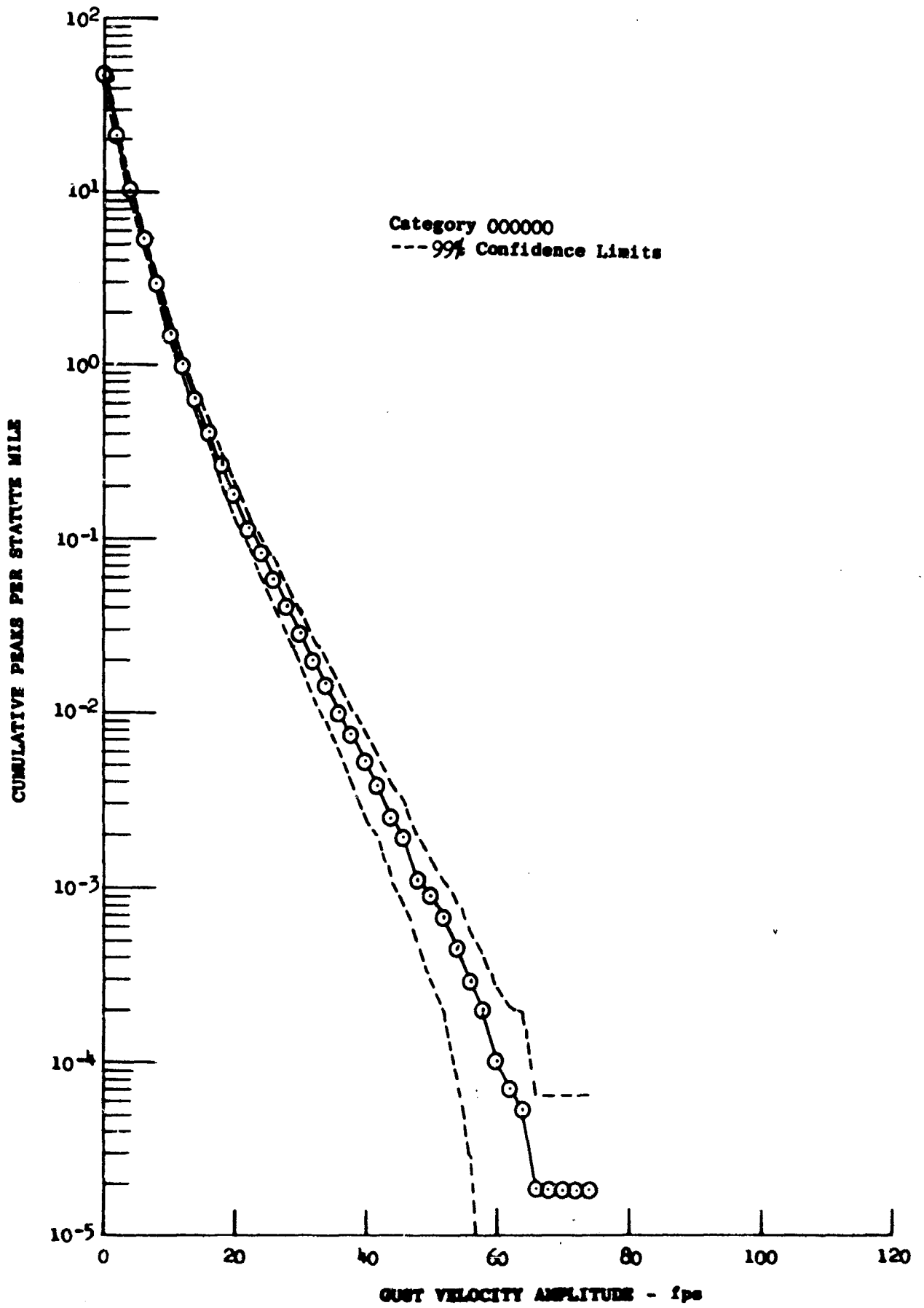


Figure 8.8 Vertical Gust Velocity Peak Count Distribution with 99% Confidence Limits

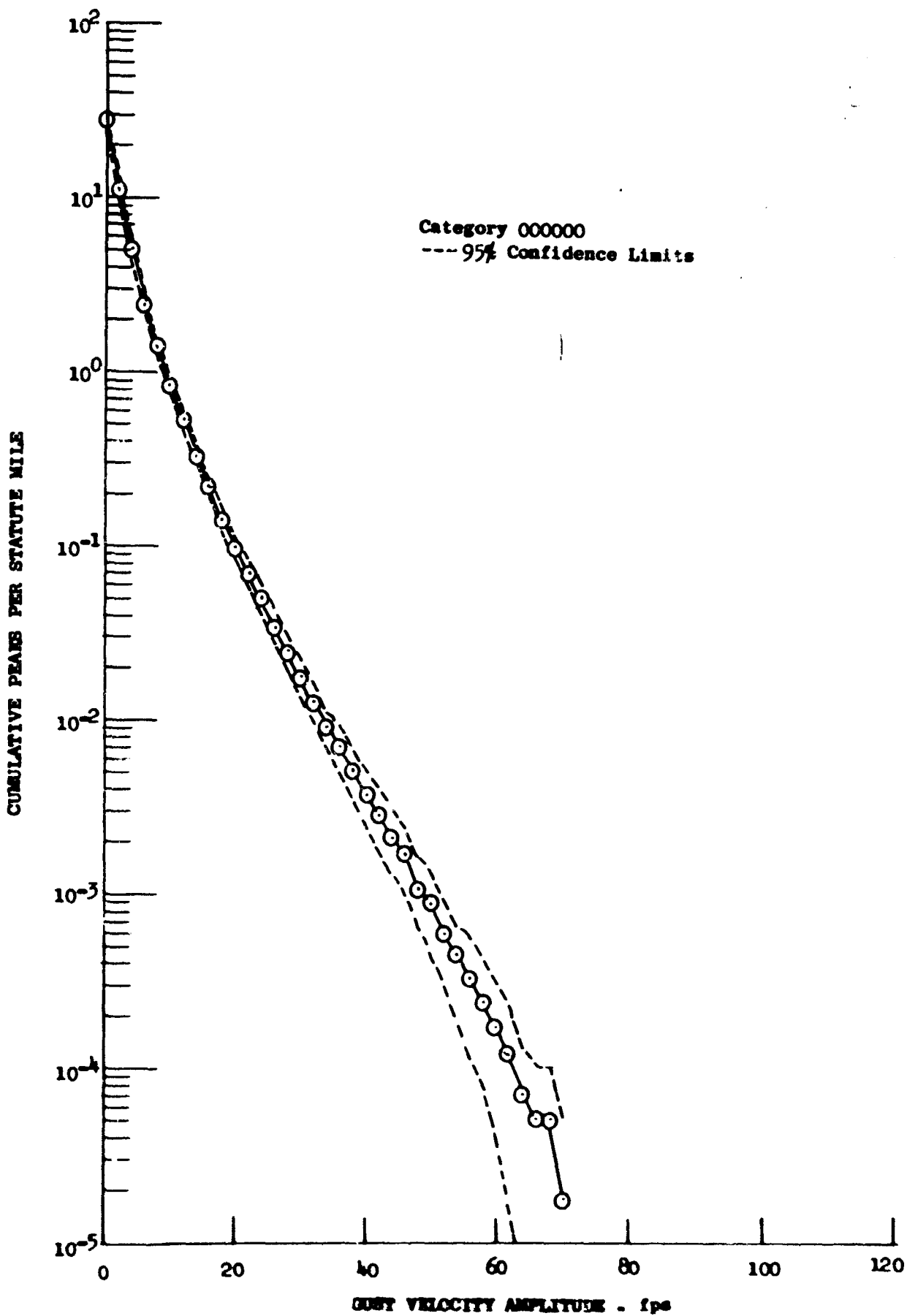


Figure 8.9 Longitudinal Gust Velocity Peak Count Distribution with 95% Confidence limits

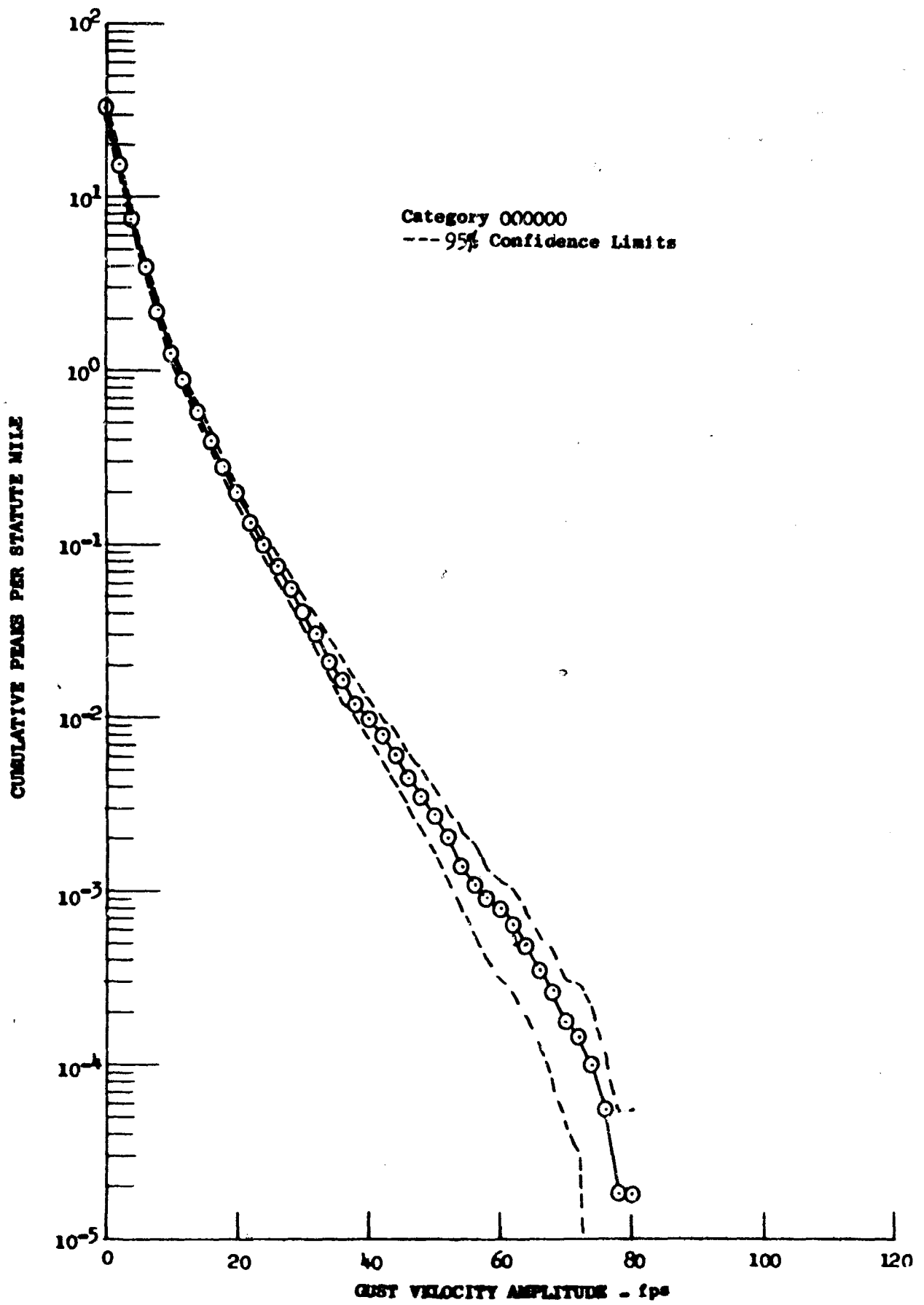


Figure 8.10 Lateral Gust Velocity Peak Count Distribution with 95% Confidence Limits

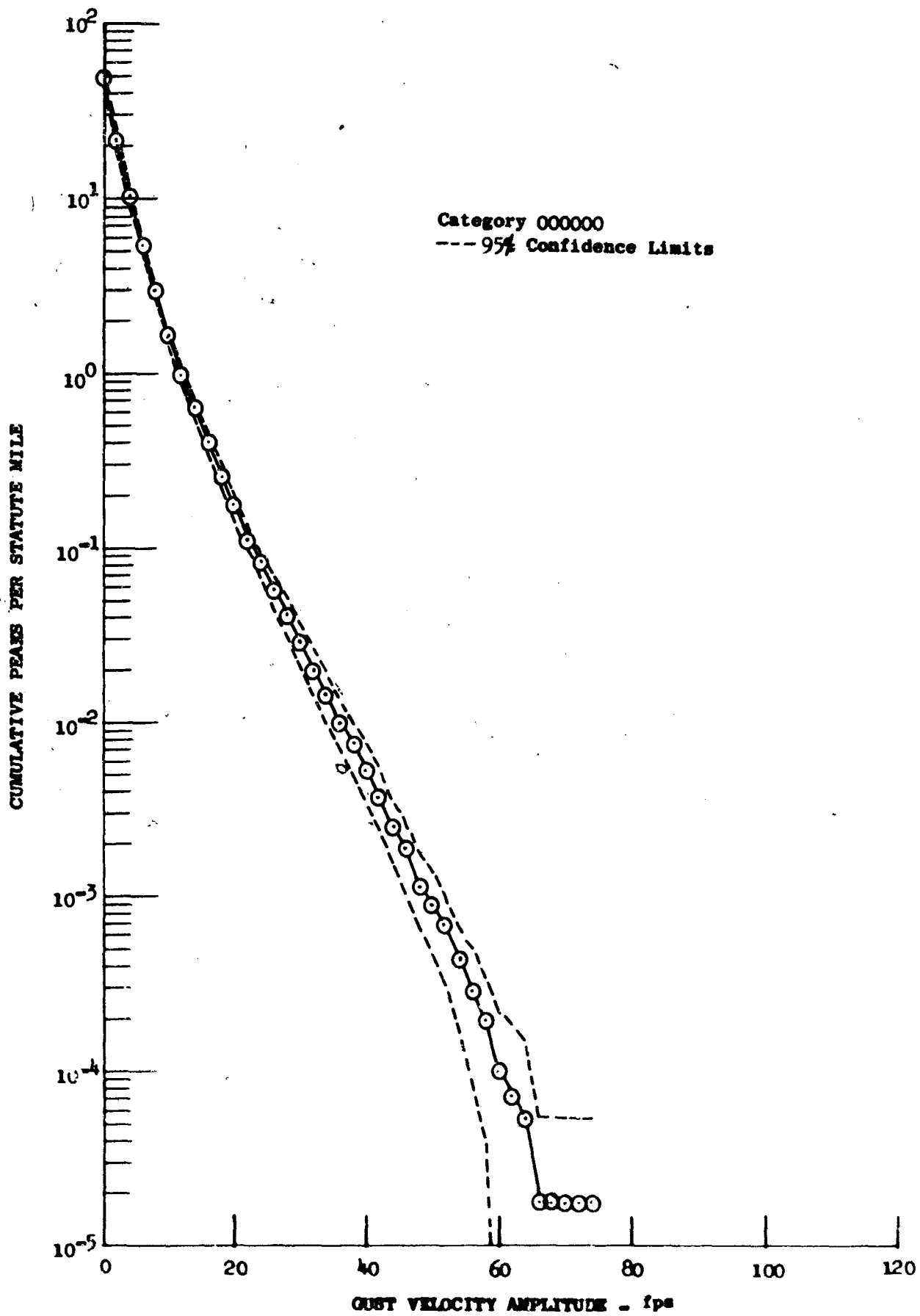


Figure 8.11 Vertical Gust Velocity Peak Count Distribution with 95% Confidence Limits

## 9. AMPLITUDE COUNT

The amplitude count technique of analysis was used on the time series of the gust velocity components. Values for each component were computed by the gust velocity program (Appendix V) at 100 samples per second. In this procedure, amplitude bands 2 fps wide were placed on either side of the zero mean. The number of samples contained in each band was determined and the samples in the corresponding positive and negative bands were added together. This procedure is illustrated in Figure 9.1. Amplitude data were used to compute cumulative distributions, cumulative probability distributions and probability density distributions. The technique used to calculate these distributions is also shown in Figure 9.1. The time series standard deviation ( $\sigma_t$ ) for each gust velocity component was computed from the following equation:

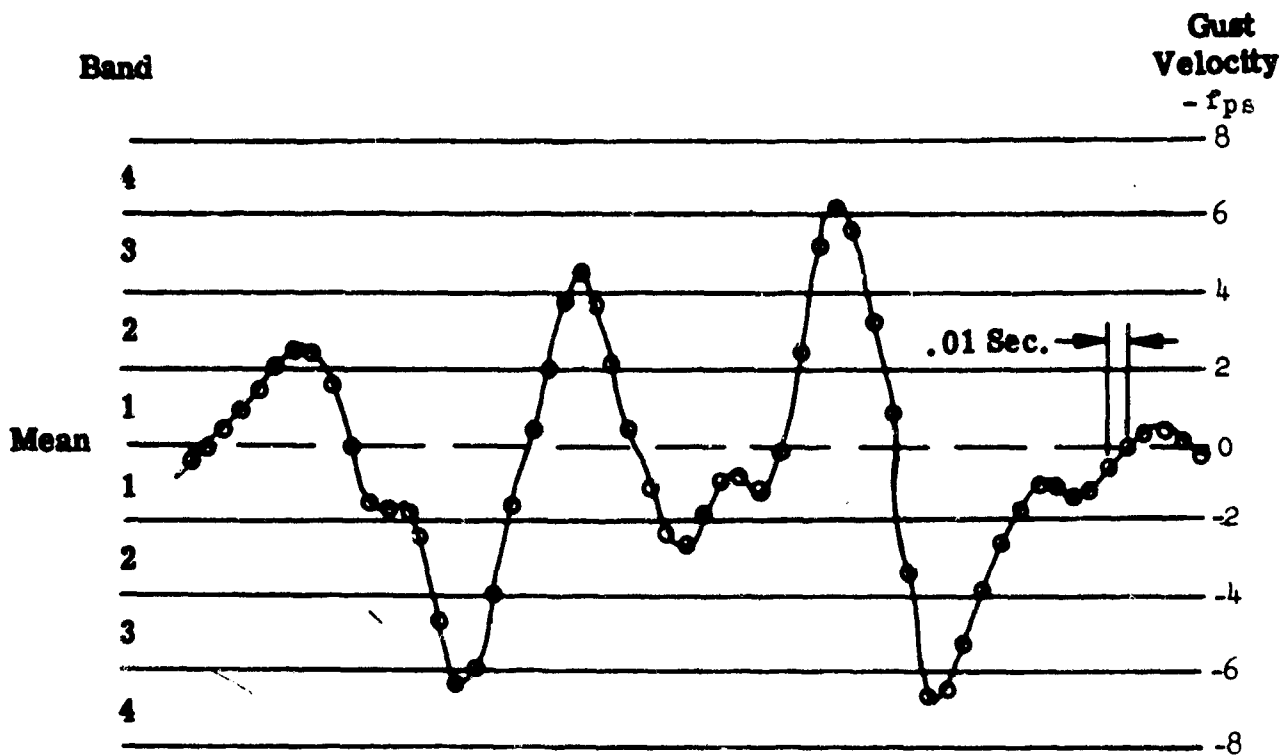
$$\sigma_t = \left[ \frac{1}{N} \sum_{i=1}^N (x_i - \bar{x})^2 \right]^{1/2} \quad (9.1)$$

Examples of amplitude count cumulative distribution, cumulative probability distribution, and probability density distribution for an individual turbulence sample are shown in Figures 9.2, 9.3, and 9.4, respectively.

Amplitude data were combined for the same categories shown in Table 8.2 and the data from turbulence samples of low intensity were accounted for in the same manner as described in Section 8.

Amplitude count cumulative probability distribution plots for the Phase III data are shown in Figure 9.5. Plots for the 42 categories of Table 8.2 are shown in Appendix VII and listings of these data are presented in Appendix VIII.

Comparisons of peak, amplitude, and level crossings count are made in Section 11.



Band No.	Gust Velocity (fps)	Plus Occurrences	Minus Occurrences	Cumulative Occurrences	Cumulative Probability	Probability Density*
1	0	12	19	57	1.0000	.2720
2	2	9	7	26	.4561	.1404
3	4	3	3	10	.1754	.0526
4	6	1	3	4	.0702	.0351

NOTE: This is only an illustration and should not be considered as typical of turbulence data.

Figure 9.1 Amplitude Count Example

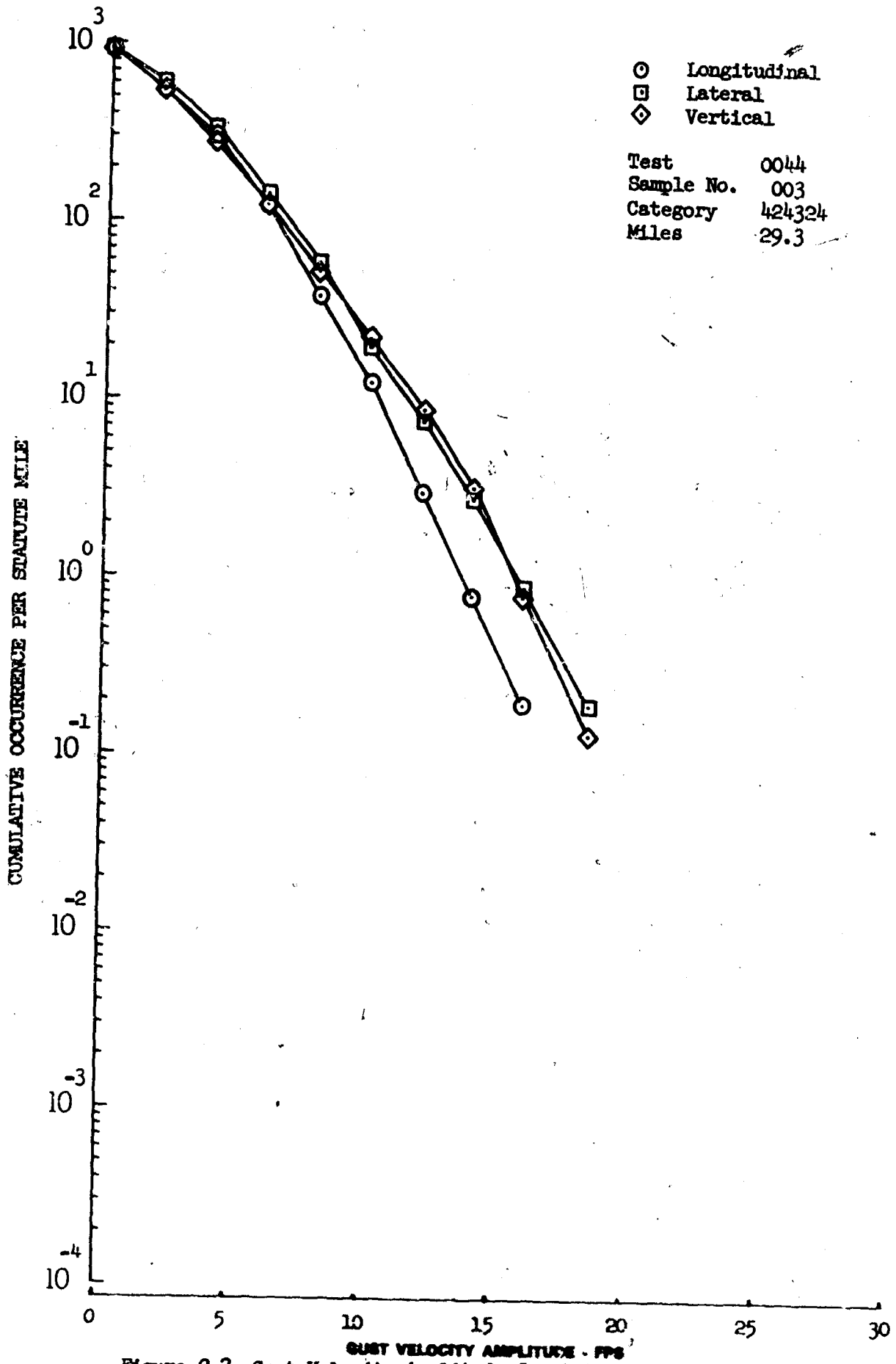


Figure 9.2 Gust Velocity Amplitude Count Cumulative Distribution for an Individual Turbulence Sample

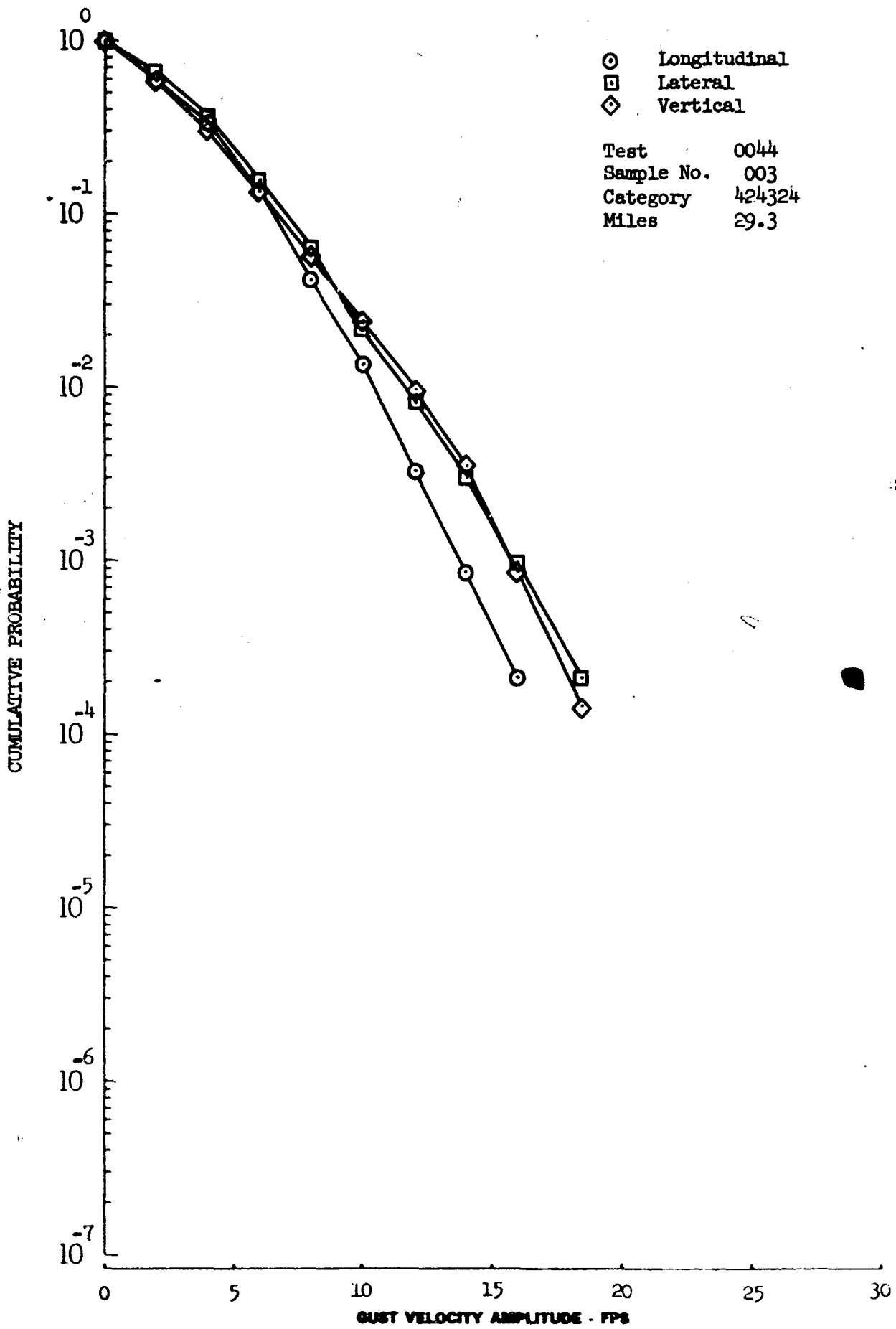


Figure 9.3 Gust Velocity Amplitude Count Cumulative Probability Distribution for an Individual Turbulence Sample



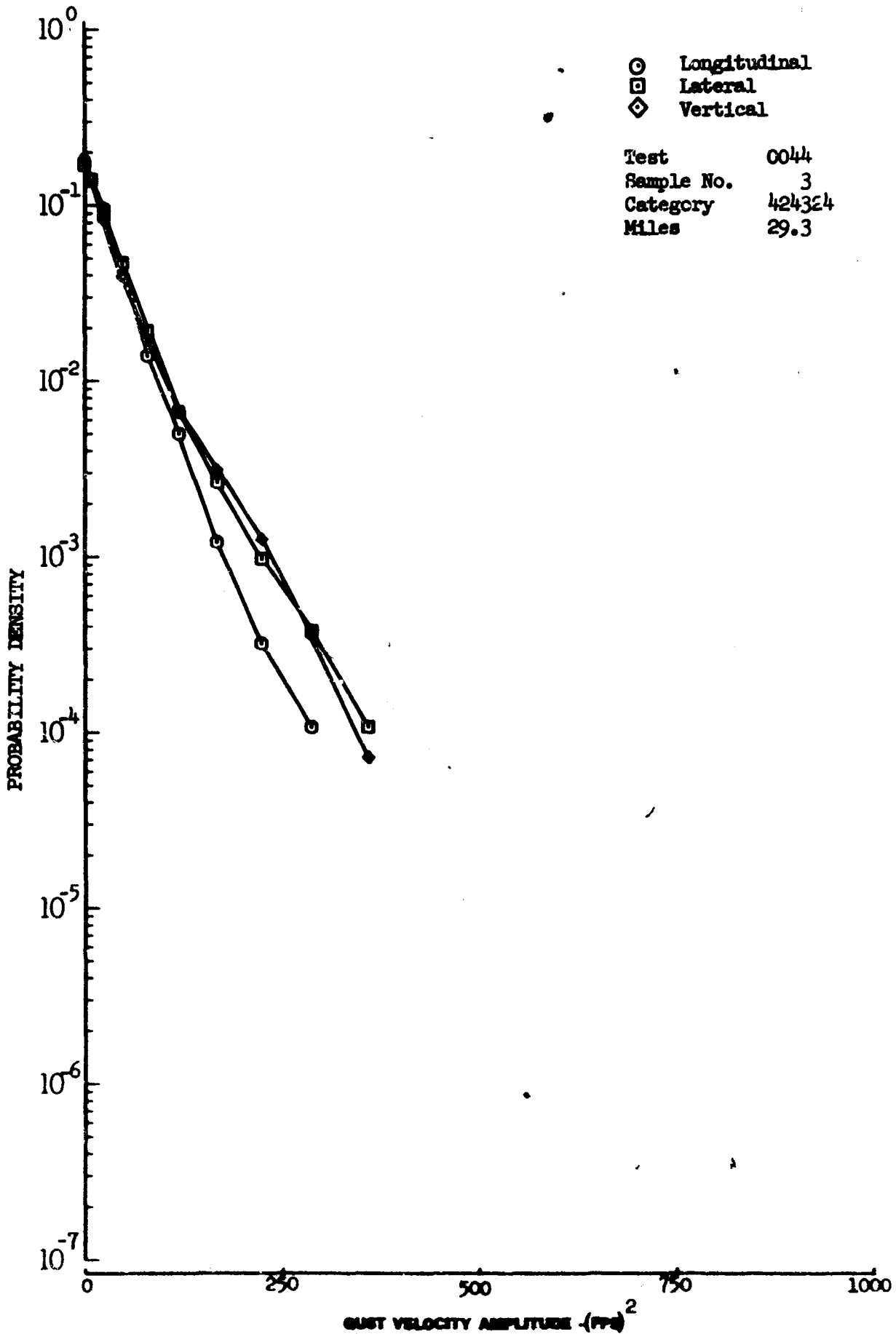


Figure 9.4 Gust Velocity Amplitude Count Probability Density Distribution for an Individual Turbulence Sample

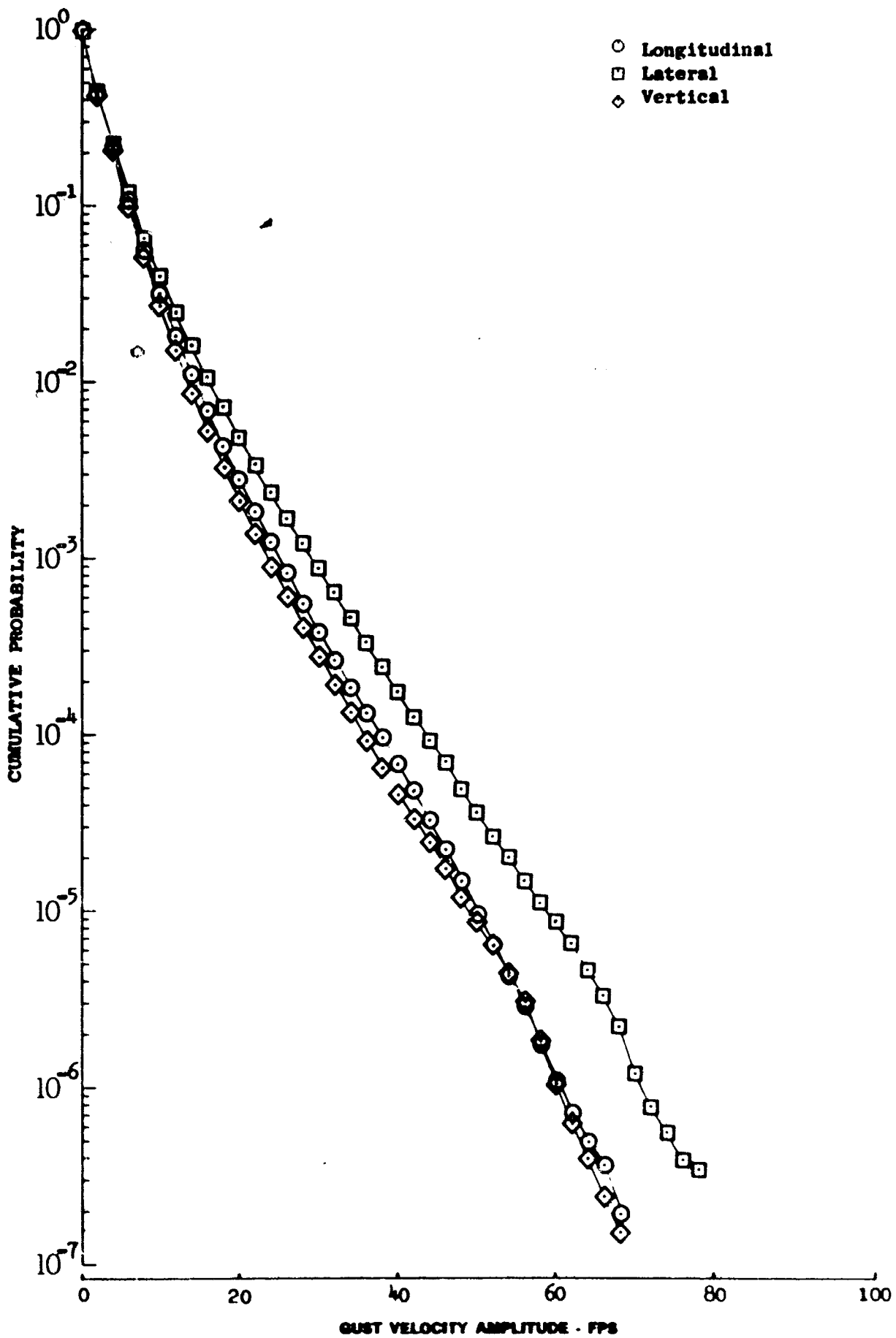


Figure 9.5 Amplitude Count Cumulative Probability Distributions

## 10. LEVEL CROSSINGS COUNT

Another method of gust velocity amplitude analysis was the level crossing technique. Levels of gust velocity were established at 2 fps intervals from the zero mean. Crossings with a positive slope were counted. Figure 10.1 illustrates the level crossings technique. This figure shows how crossings of corresponding positive and negative levels were combined. Crossings of the zero level were a special case and were doubled to account for crossings with both positive and negative slopes. The number of level crossings per mile, probability of exceedance, and probability density distributions were calculated as shown in Figure 10.1. Detailed discussions of the level crossings analysis technique can be found in References 10.1 and 10.2.

A level crossings standard deviation ( $\sigma_L$ ) was calculated using the following equation:

$$\sigma_L = \left[ \sum_{i=1}^N \frac{E_a x_a^2}{N_{OL}} \right]^{1/2} \quad (10.1)$$

According to Rice (Reference 3.1), level crossings count provides a description of a stationary Gaussian process. The level crossings distributions obtained for each turbulence sample were compared with a distribution obtained from Equation 10.2 (Rice's equation).

$$N(x) = N_{OL} \exp(-x_a^2 / 2\sigma_t^2) \quad (10.2)$$

where:

$N(x)$  = Expected number of crossings per mile of a given positive and negative level

$N_{OL}$  = Total number of zero crossings with positive and negative slopes per mile

$x_a$  = Level of gust velocity in ft./sec.

$\sigma_t$  = Standard deviation of time series (Equation 9.1)

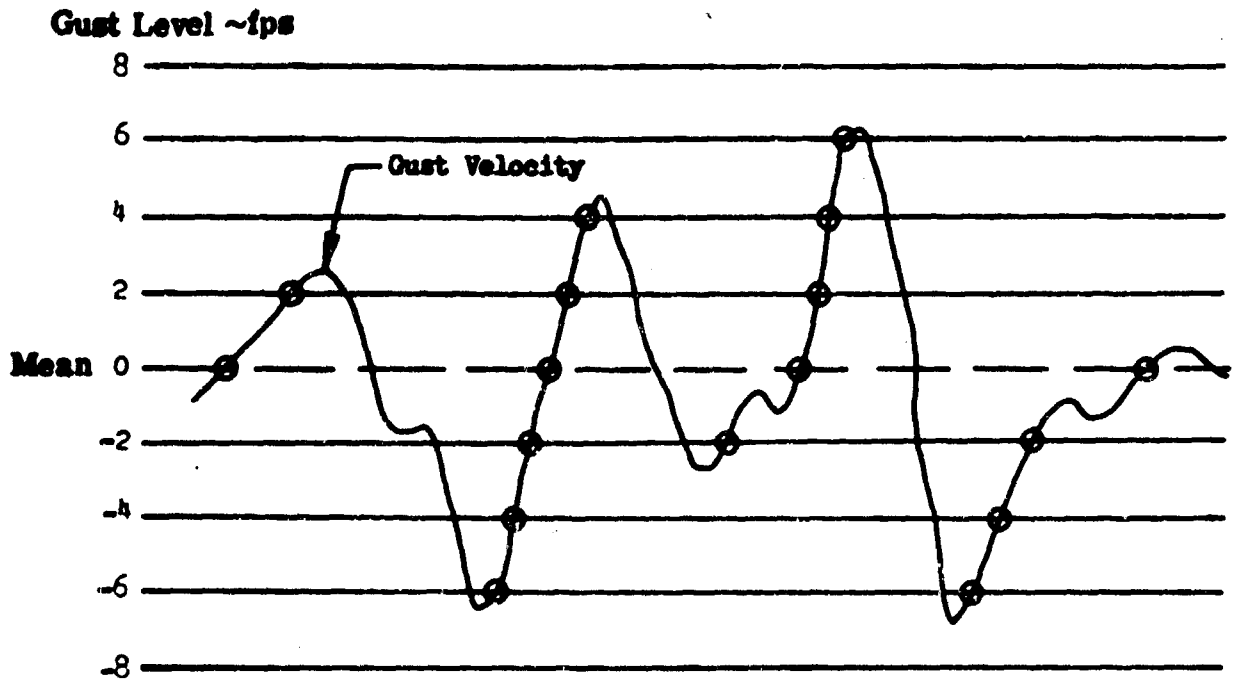
Figure 10.2 is an example level crossing distribution plot. The curves shown on these plots represent a distribution obtained from Rice's equation. Agreement between LO-LOCAT data and Rice's equation was found to be best for the longitudinal component. Rice's equation underestimated nearly every LO-LOCAT sample measured. For a further discussion of Rice's equation, see Section 51.

Figures 10.3 and 10.4 are level crossings probability distribution and probability density distribution plots, respectively, of the same turbulence sample as shown in Figure 10.2. The probability distribution, Figure 10.3, shows a higher probability of occurrence of the smaller gust velocity values than the probability distributions obtained from either

the peak count data (Figure 8.3) or the amplitude count data (Figure 9.3). This is also shown in Figure 10.4 where the probability density is lower at one than it is at nine feet squared per second squared.

Low intensity turbulence samples were accounted for in the same manner as described in Section 8. Also, samples were categorized using the same technique as discussed in Section 8.

Comparison of the peak, amplitude, and level crossings count are given in Section 11. The distributions and probability distributions of the level crossings count data for those categories shown in Table 8.2 are plotted in Appendix VII and listed in Appendix VIII.



Gust Level (fps)	Number of Crossings	Level	Folded Number of Crossings	Number of Crossings per Mile*	Probability of Exceedance	Probability Density
8	0	0	8	40	1.0000	.1250
6	1	2	6	30	.7500	.1250
4	2	4	4	20	.5000	.0625
2	3	6	3	15	.3750	.1875
0	4					
-2	3					
-4	2					
-6	2					
-8	0					

\* For this example, assume 0.2 statute miles is length of above record.

NOTE: This is only an example and should not be considered as typical of turbulence data.

Figure 10.1 Level Crossings Count Example

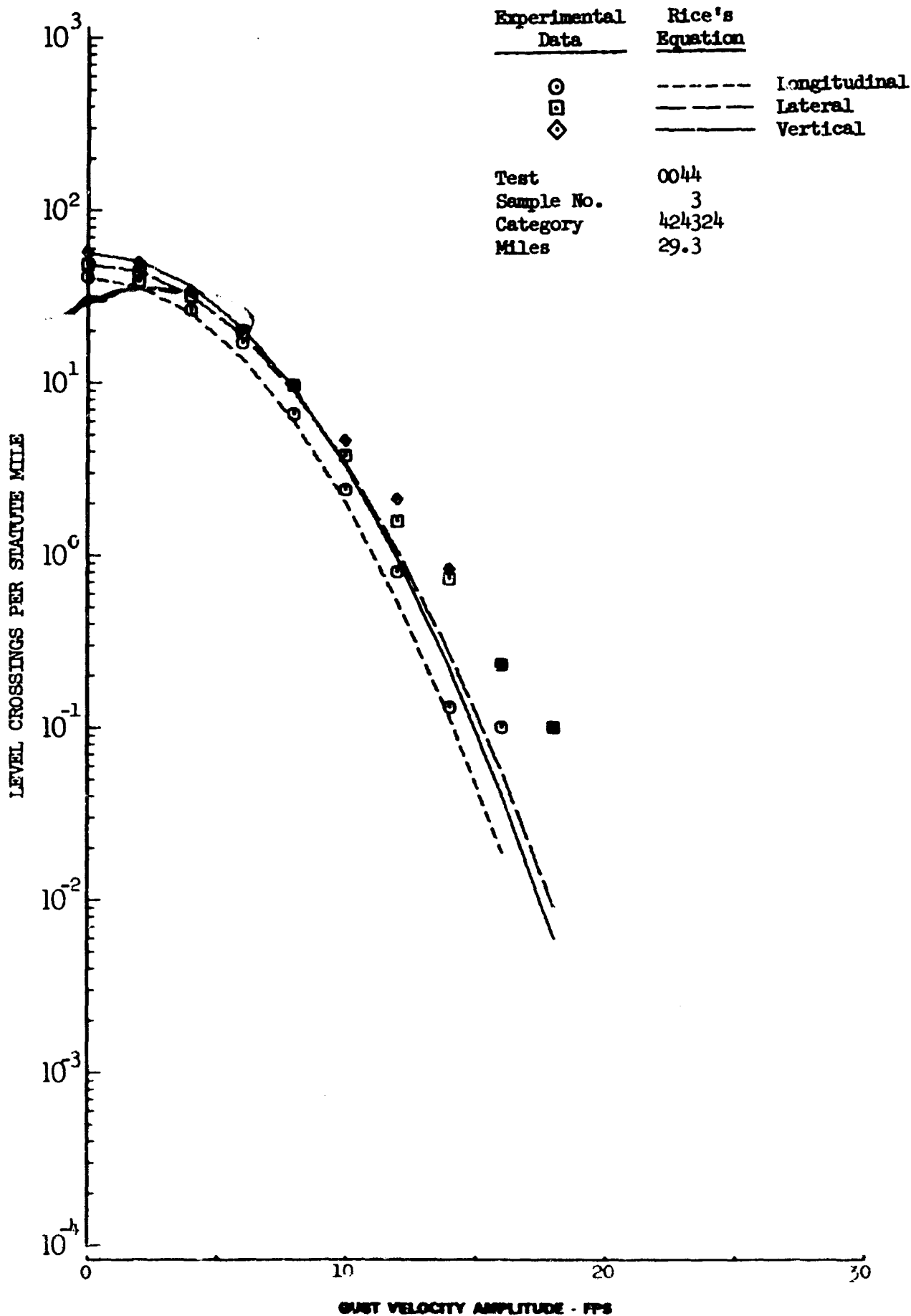


Figure 10.2 Gust Velocity; Level Crossing Distribution for an Individual Turbulence Sample

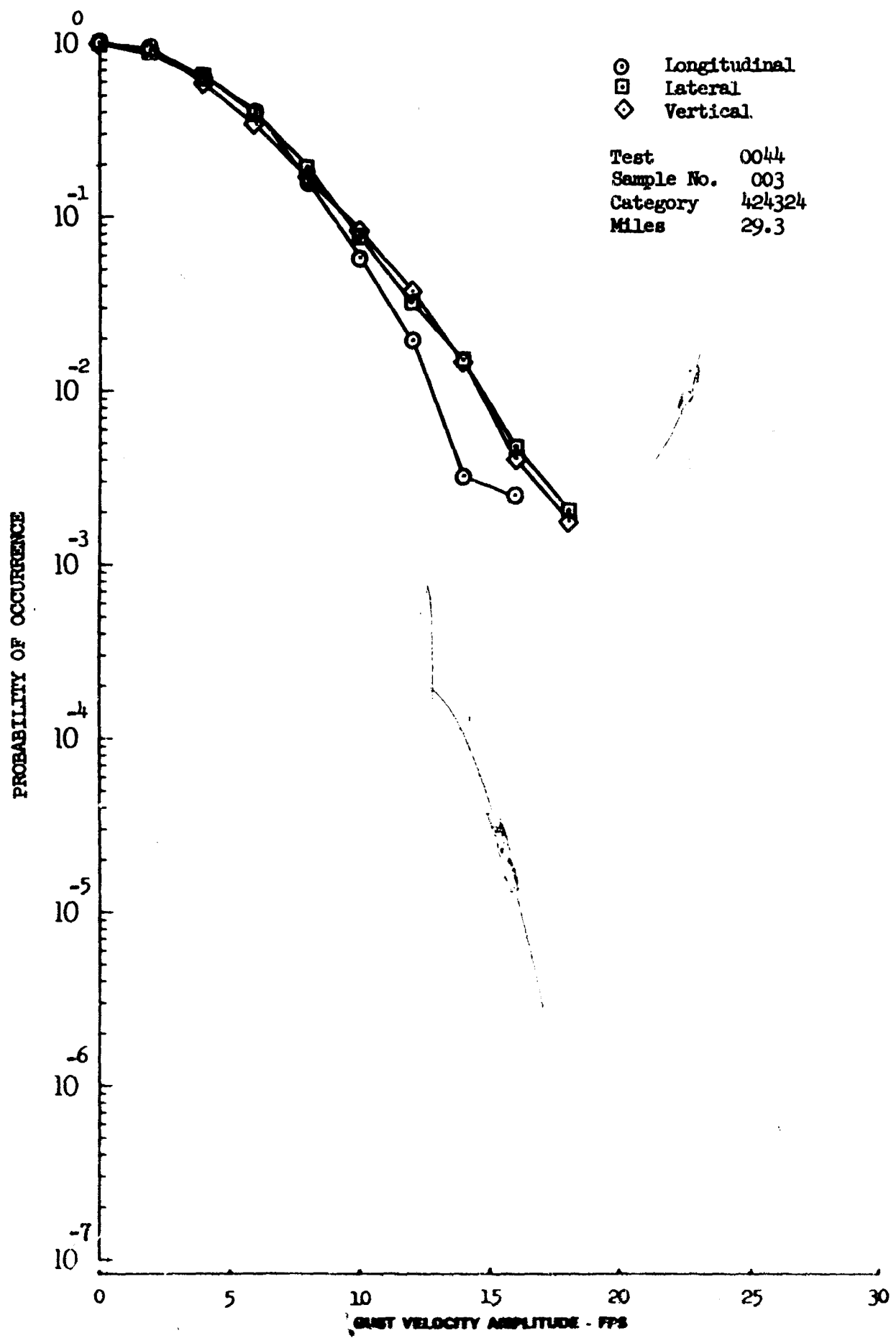


Figure 10.3 Gust Velocity Level Crossing Probability Distribution for an Individual Turbulence Sample

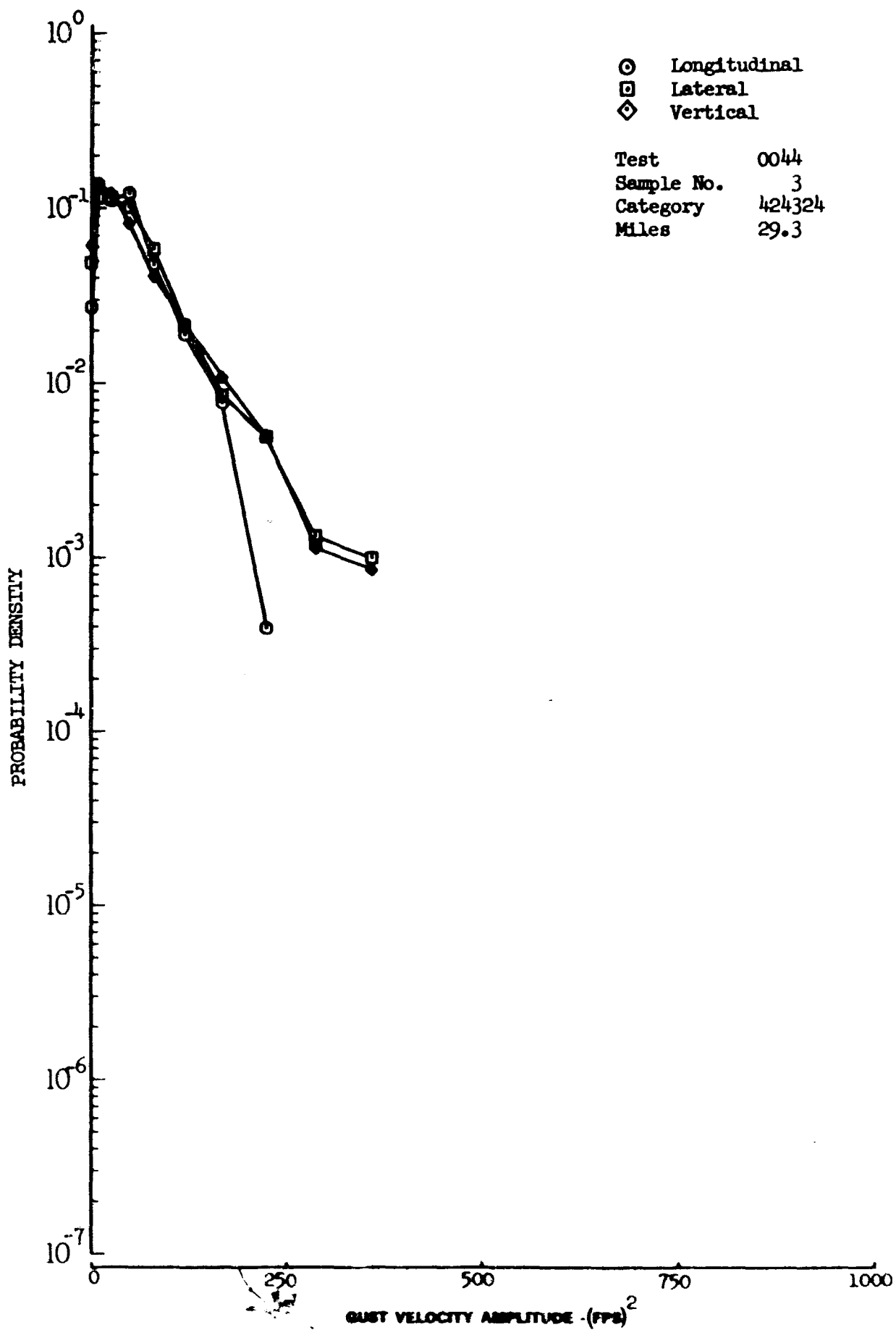


Figure 10.4 Gust Velocity Level Crossing Probability Density Distribution for an Individual Turbulence Sample



## 11. COMPARISON OF COUNTING TECHNIQUES

The peak, amplitude, and level crossings count techniques used for analyzing gust velocity time series data were compared. Data for an individual turbulence sample and the all data category are shown here to illustrate the relationship between counting techniques. This relationship is similar for all categories so they will not be shown. Plots and listings for all the categories investigated are available in Appendix VII and VIII, respectively.

Occurrences per mile of peaks and level crossings for a single turbulence sample are compared in Figures 11.1 through 11.3. These plots show that generally a greater frequency of occurrence of level crossings than of peaks above a given gust velocity can be expected for all three components of gust velocity. Figures 11.4 through 11.6 provide a comparison of peaks and level crossings per mile for the all data category. These figures show a relationship very similar to that shown for a single turbulence sample.

The cumulative number of peaks in the first band should agree with the number of level crossings counted in the first band. This is because the peak count technique counts the positive and negative peak excursions following a crossing of the zero mean and the level crossings technique doubles the number of crossings of the zero mean with a positive slope. Therefore, it should be noted that the unextrapolated peak count cumulative occurrences per mile equal the level crossings occurrences per mile at zero gust velocity. This may be seen by comparing the unextrapolated peak count values of Figure 8.2 with the level crossings count values of Figure 10.2 at the zero gust velocity level.

Probabilities of encountering a gust velocity equal to or greater than a given value for the three counting techniques are shown in Figures 11.7 through 11.12. Figures 11.7 through 11.9 show these comparisons for a single turbulence sample. Figures 11.10 through 11.12 show the comparison for the all data category.

The relationship between the counting techniques is very similar for both the single sample and the all data category. Also, there is little variation from one component of gust velocity to another. In general, the amplitude count distributions are lower and the level crossings are highest. The peak count probability curve approximates the amplitude count curve at the lower gust velocity values and approaches the level crossings curve at the higher gust velocities.

Probability density distributions, obtained from a single turbulence sample using the three counting techniques, are shown in Figures 11.13 through 11.15 for the three gust velocity components. Figures 11.16 through 11.18 show the same information for the all data category. The amplitude count probability density distribution curve is lower than for peak count for the single turbulence sample, as shown in Figures 11.13 through 11.15. The level crossings density curve has a hump near zero gust velocity and a slope somewhat steeper than the others. This is representative of the level crossings probability density curve for an individual sample with a maximum gust velocity greater than approximately 10 fps. For a sample

with a maximum gust less than approximately 10 fps, the density curve is shaped very much like the peak and amplitude count curves. The reason for the difference in curve shape is due to the increased number of zero crossings for those turbulence samples of low intensity. Figures 11.16 through 11.18 show that generally level crossings have the highest probability density curve and amplitude count the lowest with peak count in between. The differences between the three curves are small and their shape is generally the same. There is no hump in the level crossings curve as there was for some individual samples. This is due to the combining of many turbulence samples of both high and low intensity into this category.

Gust velocity standard deviations from amplitude count, peak count, and level crossings were calculated as shown by Equations 8.5, 9.1, and 10.1. Figures 11.19 through 11.21 show comparisons of the cumulative distributions of these standard deviations for the three gust velocity components. All 10-LOCAT Phase III data are included.

The level crossings standard deviations show a higher probability of occurrence than for peak count or amplitude count. This relationship is similar for all three components of gust velocity, except the peak count distribution is higher relatively for the vertical component.

It should be noted that the characteristic frequency,  $N_0$ , as referred to in this report is not the actual characteristic frequency of the turbulence but is equivalent to the intercept of the peak count cumulative distribution function. Measurement of the actual characteristic frequency of the turbulence would require calculation out to very high frequencies (around 30,000 cps).

Values of the characteristic frequency were obtained by these different methods. In the first method,  $N_0$  (in cycles per foot) was obtained from PSD data using Equation 11.1.

$$N_0 = \sigma_1 / \sigma \text{ cycles per foot} \quad (11.1)$$

$N_0$  was converted to cycles per mile and multiplied by two to obtain occurrences per mile.

In the second method,  $N_p$  (peaks per mile) was determined by extrapolation of the peak count distribution curve as previously described in Section 8.

A third characteristic frequency,  $N_{OL}$  (crossings per mile), was calculated from level crossings data using Equation 11.2.

$$N_{OL} = 19.55 \frac{E_z}{V} \quad (11.2)$$

where:

$E_z$  = Total number of crossings of zero level with both positive and negative slope.

$V$  = Average speed during turbulence sample.

Average values for each method are given in Table 11.1.

TABLE 11.1

COMPARISON OF CHARACTERISTIC FREQUENCIES CALCULATED FROM  
POWER SPECTRA, PEAK COUNT, AND LEVEL CROSSINGS DATA

Characteristic Frequency	Longitudinal	Lateral	Vertical
$N_0$ (occurrences/mile)	25.09	30.19	35.08
$N_p$ (peaks/mile)	25.34	31.44	45.85
$N_{OL}$ (crossings/mile)	55.79	47.18	63.31

These averages represent Phase III data. Power spectra and  $N_0$  values were calculated for approximately 50 per cent of the data processed. In addition, characteristic frequency values were not calculated for irregularly shaped spectra (i.e. nonhomogeneous turbulence or turbulence samples having low signal-to-noise ratios).  $N_p$  and  $N_{OL}$  values were calculated for all turbulence samples processed. Extraneous  $N_p$  and  $N_{OL}$  values defined as those which deviated more than four standard deviations from the mean were removed before averaging.

The characteristic frequency of the longitudinal component is the smallest and vertical is the largest. This is true for both  $N_0$  and  $N_p$ . Comparison of corresponding  $N_0$  and  $N_p$  values shows reasonable agreement between the two methods of computation, except for vertical where  $N_0$  is significantly less than  $N_p$ . This is believed to be due to the removal from analysis of a higher proportion of the  $N_0$  than  $N_p$  data. These  $N_0$  values were removed primarily because of distortion of the spectra at higher frequencies.

The values of characteristic frequency obtained using level crossings data are considerably larger than those obtained from peak count. This is because the level crossings values correspond to what the peak count values would have been had they not been extrapolated. The reason for extrapolating to obtain the characteristic frequencies from peak count data is explained in Section 8.

It should be noted that the characteristic frequencies obtained using the peak count and level crossings method are dependent upon the frequency range of turbulence being investigated. During LO-LOCAT Phases I and II, the C-131B test airplanes were flown at an average speed of approximately 330 feet per second while gathering gust velocity data. These gust velocity data were filtered so that only the frequency band from approximately 0.04 to 10 cps was retained. This frequency band corresponds to a range of gust velocity wavelengths ranging from 7980 to 33 feet. During LO-LOCAT Phase III, the T-33A test airplane was flown at an average speed of approximately 630 feet per second. The same band of frequencies was passed during data processing as for Phases I and II. With the higher airplane speed and the same filtering bands, the new range of gust velocity wavelengths obtained ranged from 15,100 to 63 feet. The segment of the turbulence spectrum investigated during LO-LOCAT Phase III was therefore shifted toward longer wavelengths from that of Phases I and II.

The average values of  $N_p$  obtained during Phases I and II were 50 peaks per mile for the longitudinal components and 60 for lateral and vertical components. Comparison of these values with those obtained during Phase III shows the difference between them to be a factor of approximately 2. This difference is due to the high frequency of occurrence per mile of the 33-63 foot wavelength gusts which were measured during Phases I and II. Wavelengths less than 60 feet were not measured during Phase III.

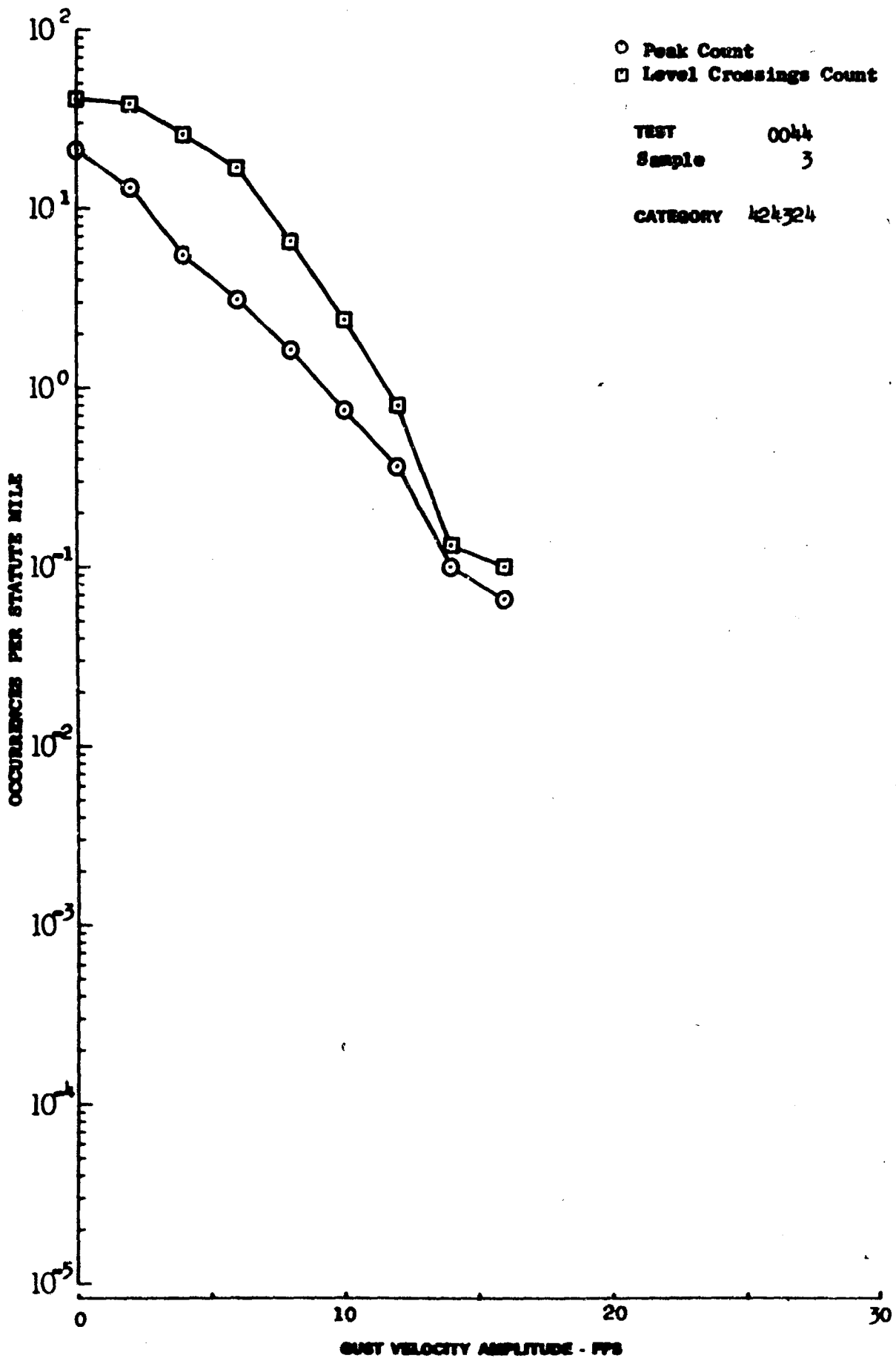


Figure 11.1 Longitudinal Gust Velocity Distributions for an Individual Turbulence Sample

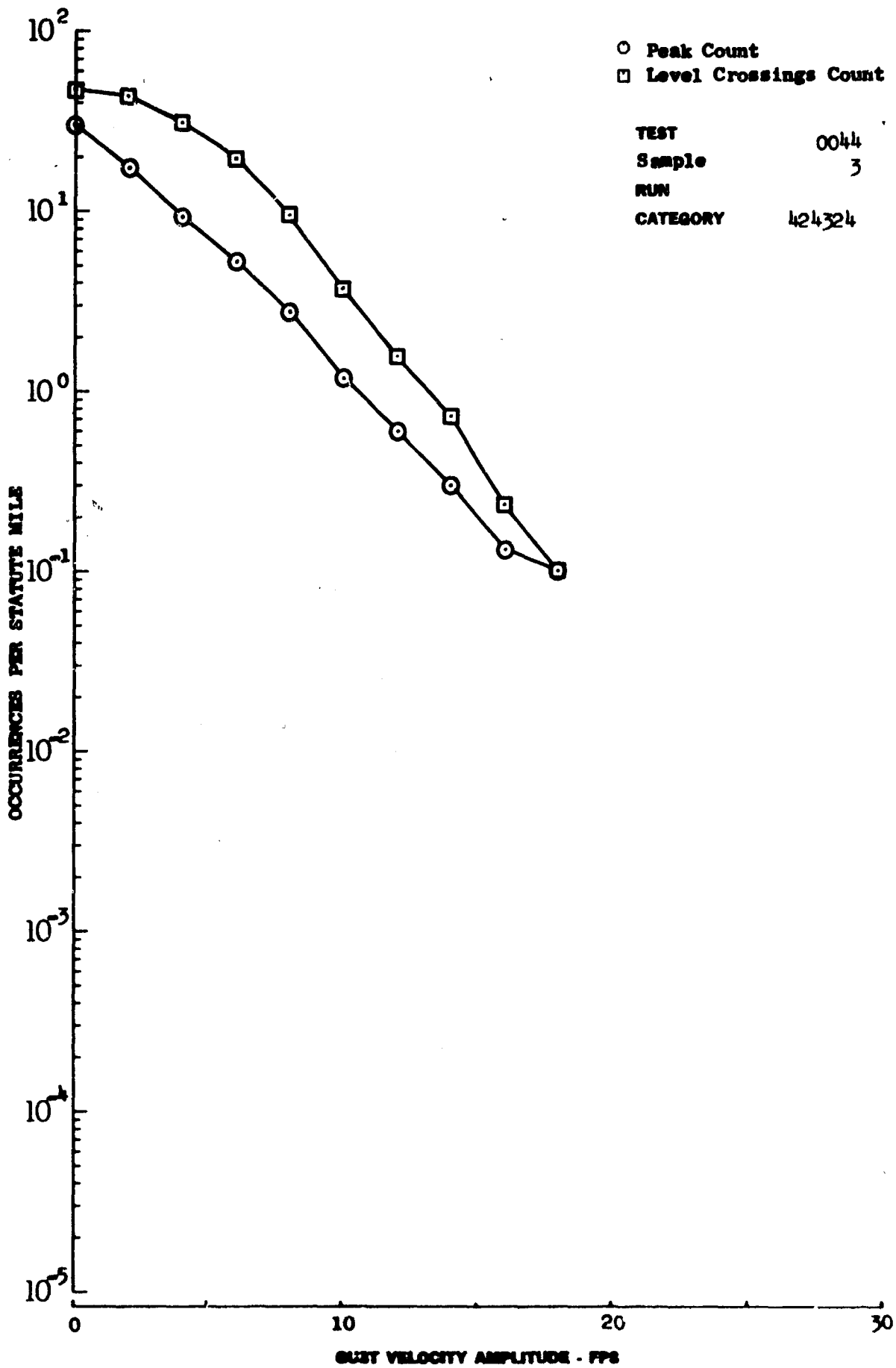


Figure 11.2 Lateral Gust Velocity Distributions for an Individual Turbulence Sample

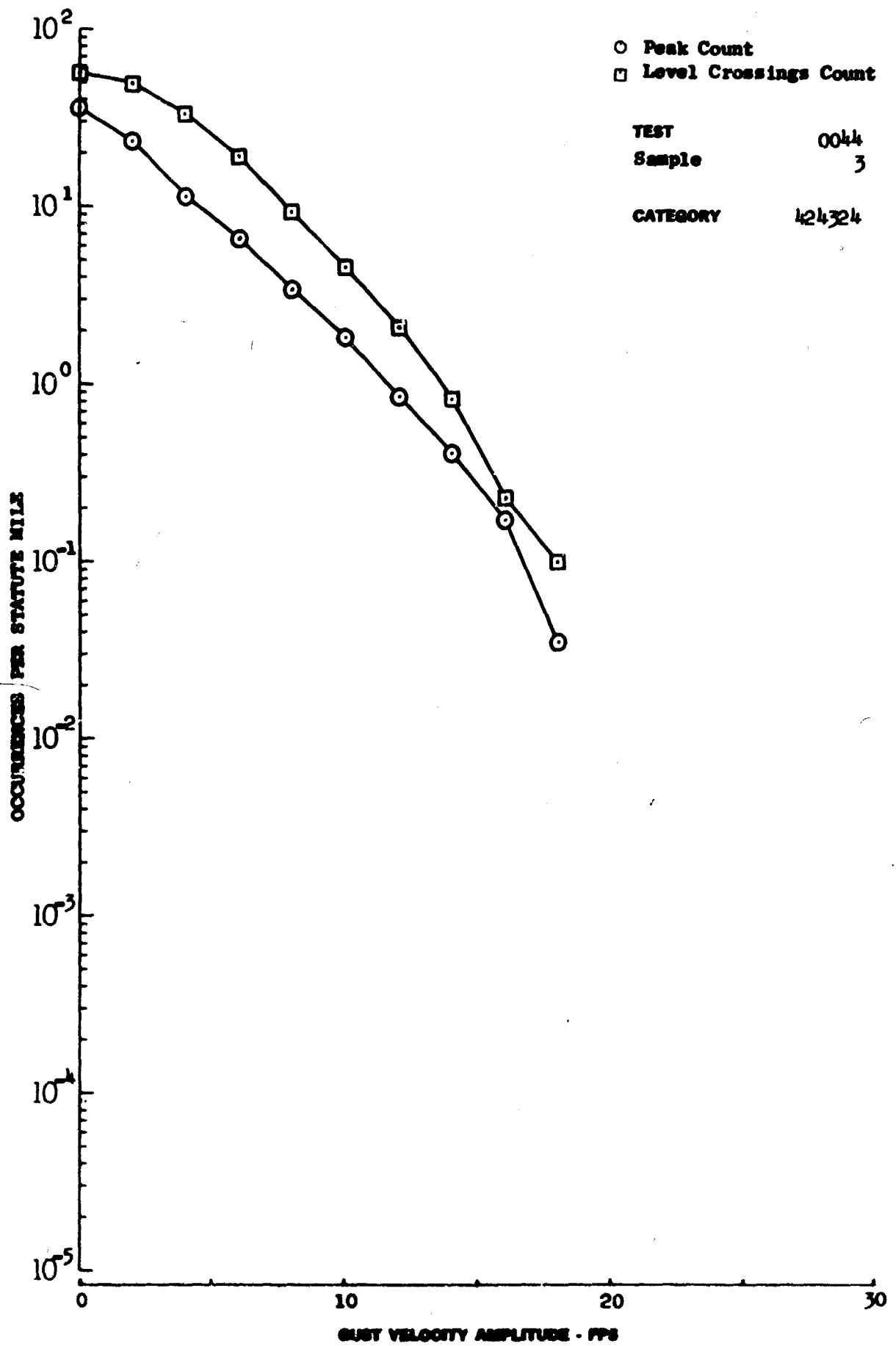


Figure 11.3 Vertical Gust Velocity Distribution for an Individual Turbulence Sample

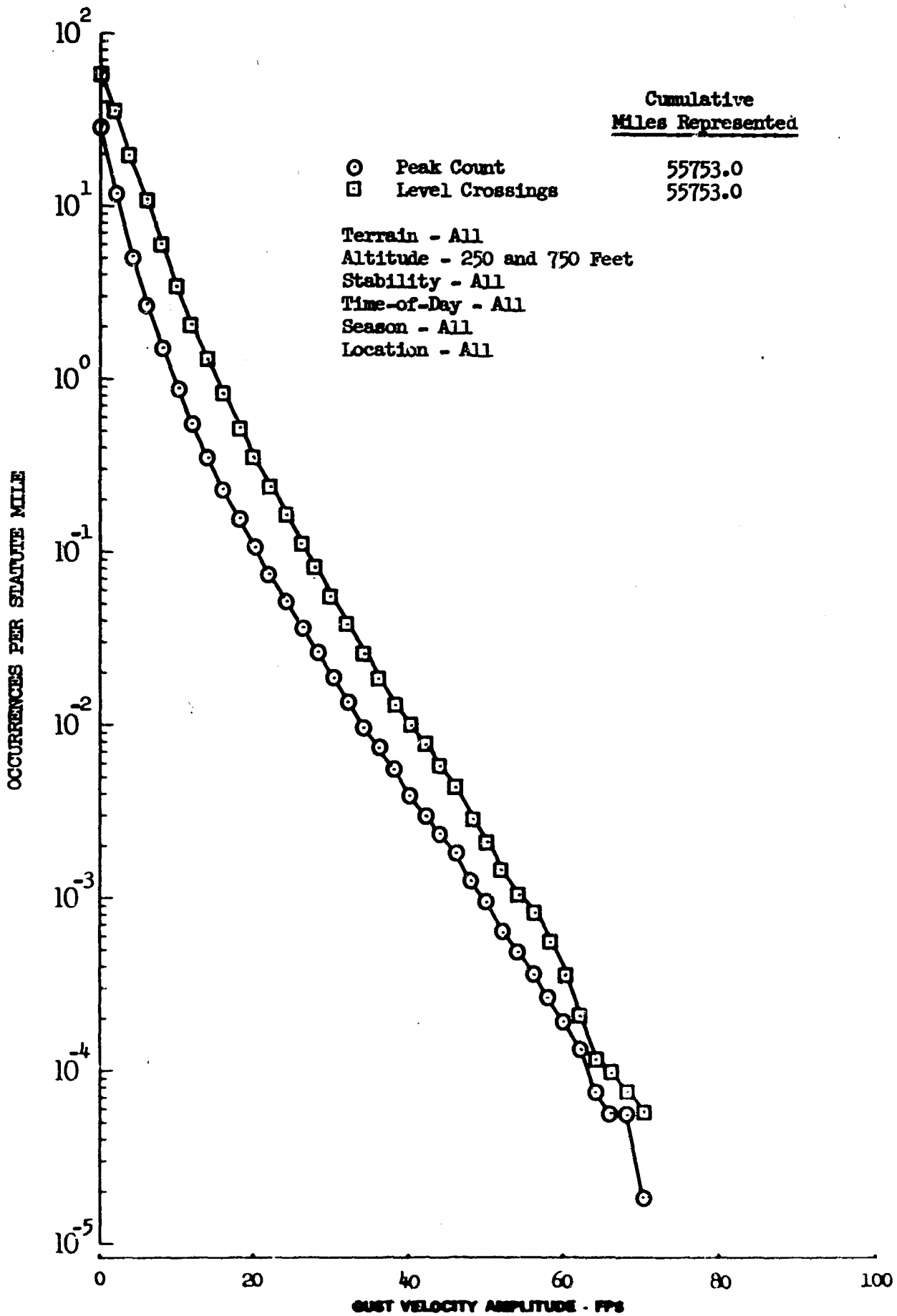


Figure 11.4 Comparison of Peak and Level Crossing Count Distributions - Longitudinal Gust Velocity



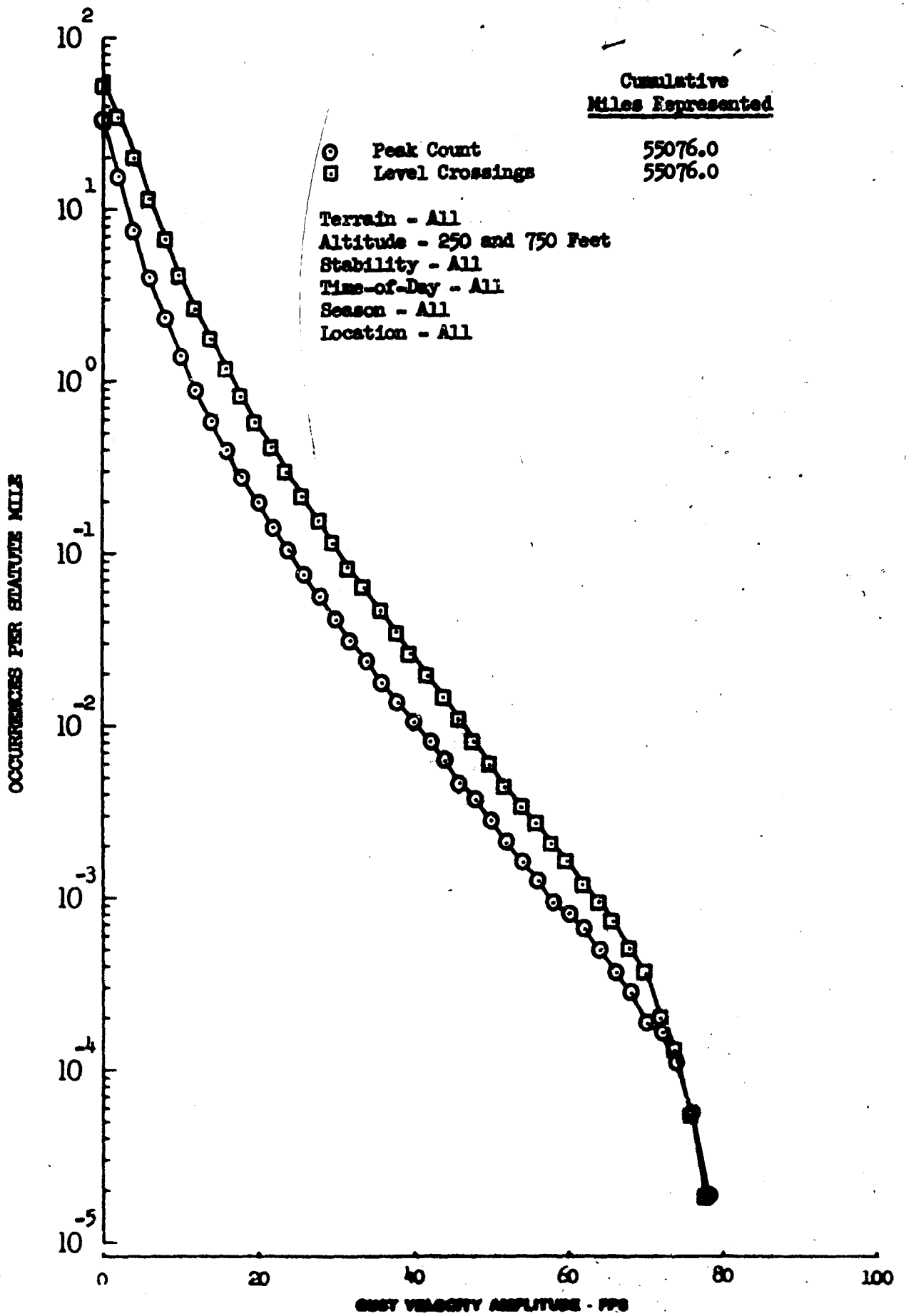


Figure 11.5 Comparison of Peak and Level Crossing Count Distributions - Lateral Gust Velocity

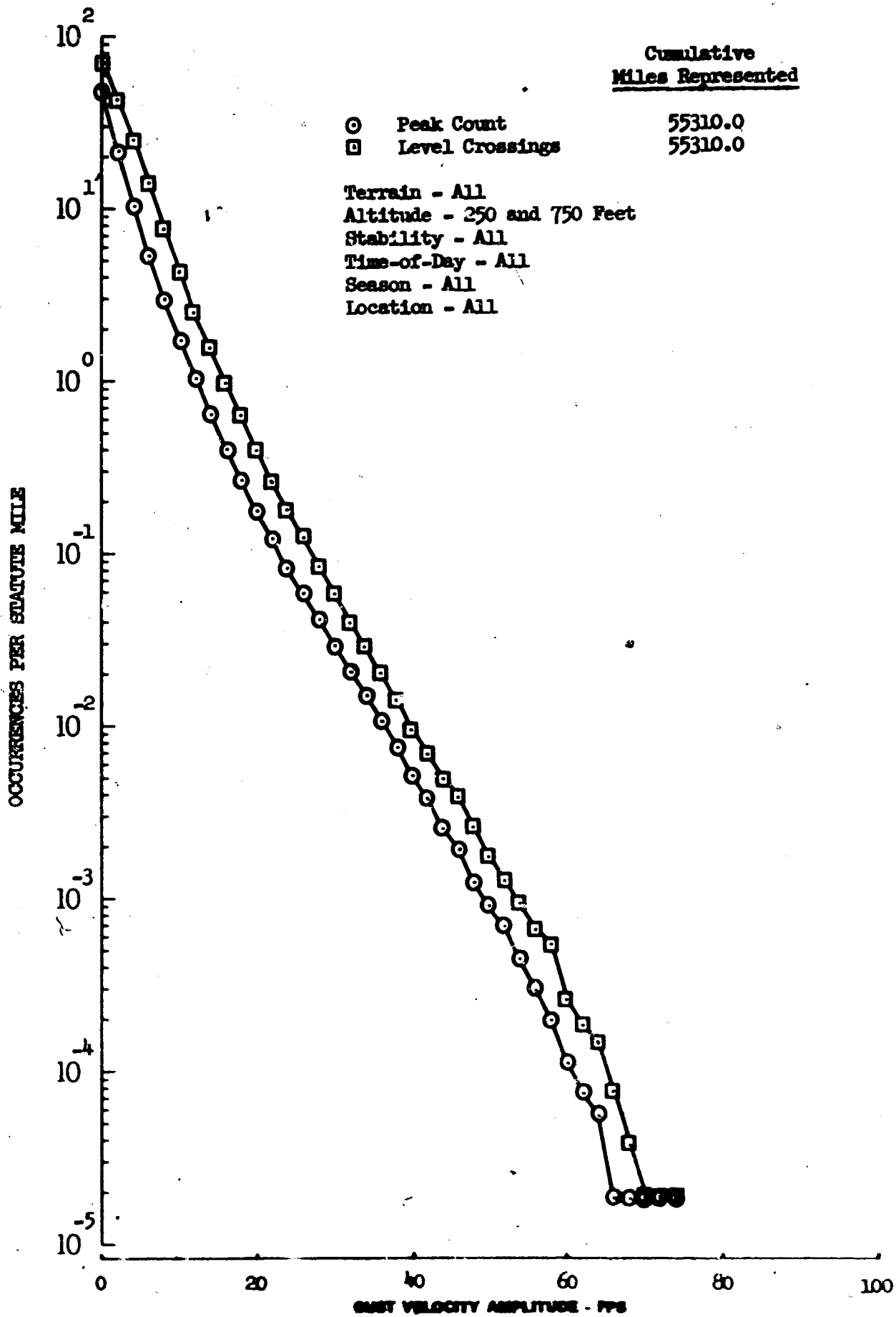


Figure 11.6 Comparison of Peak and Level Crossing Count Distributions - Vertical Gust Velocity

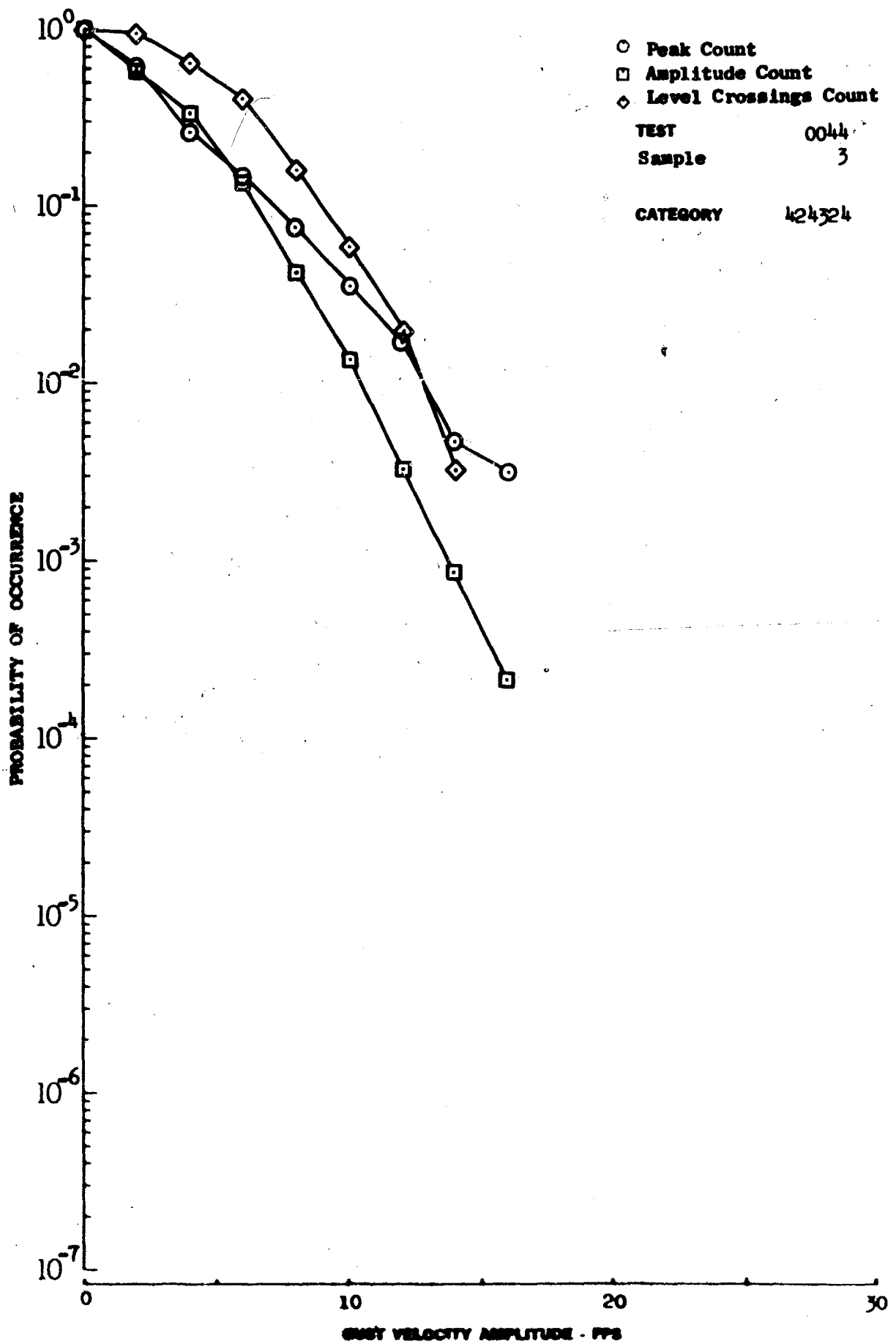


Figure 11.7 Longitudinal Gust Velocity Probability Distributions for an Individual Turbulence Sample

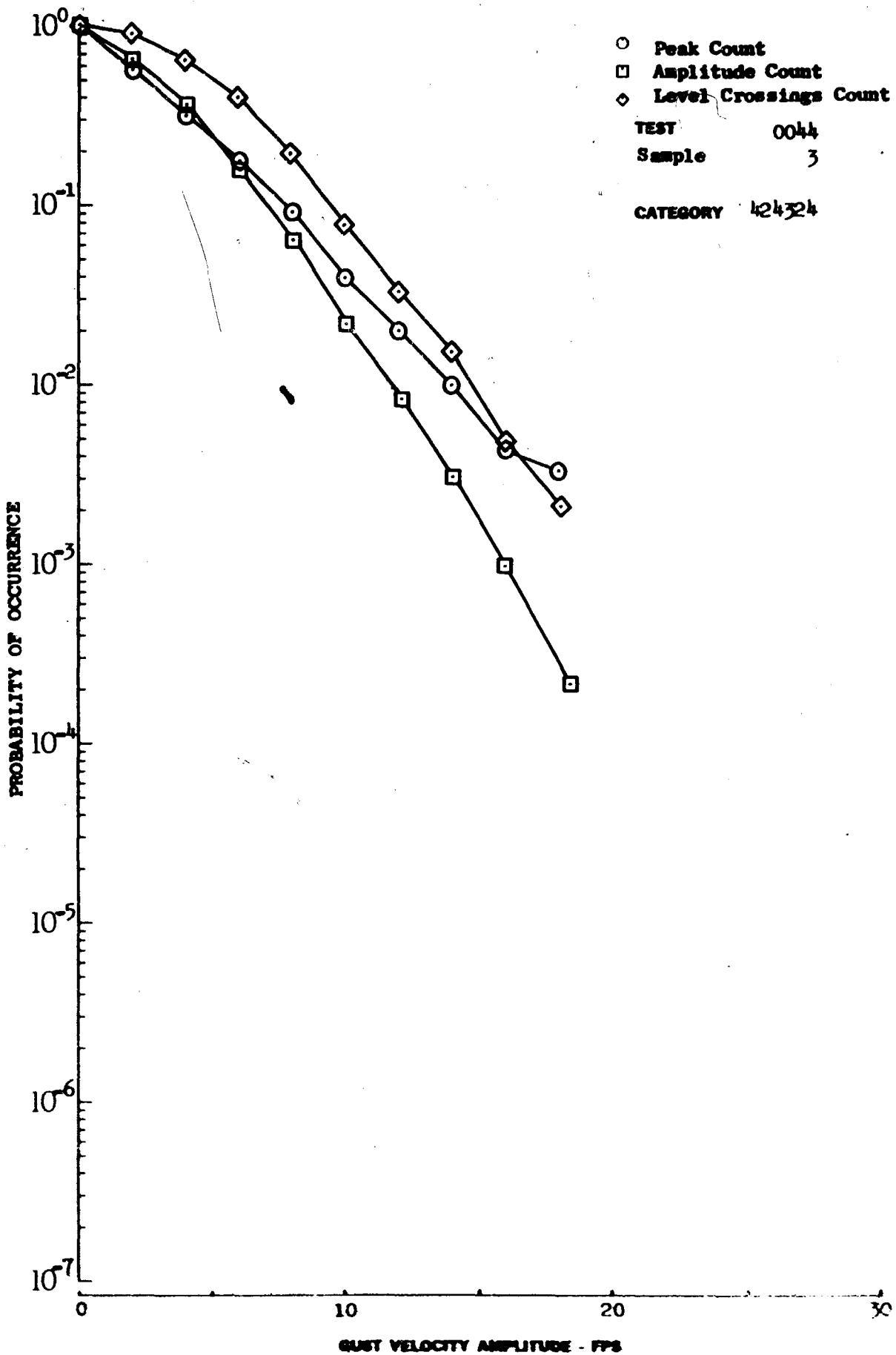


Figure 11.8 Lateral Gust Velocity Probability Distributions for an Individual Turbulence Sample

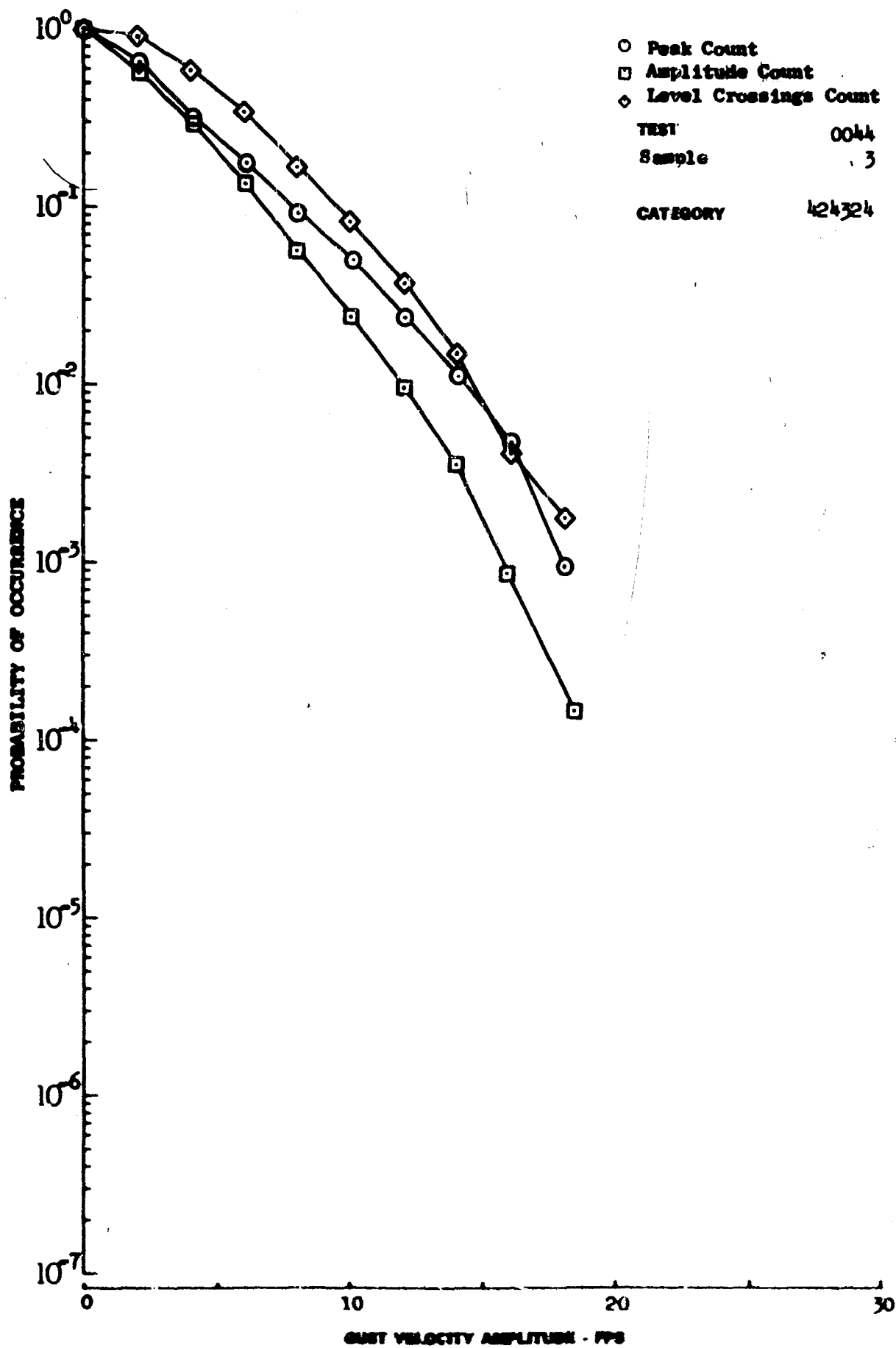


Figure 11.9 Vertical Gust Velocity Probability Distributions for an Individual Turbulence Sample

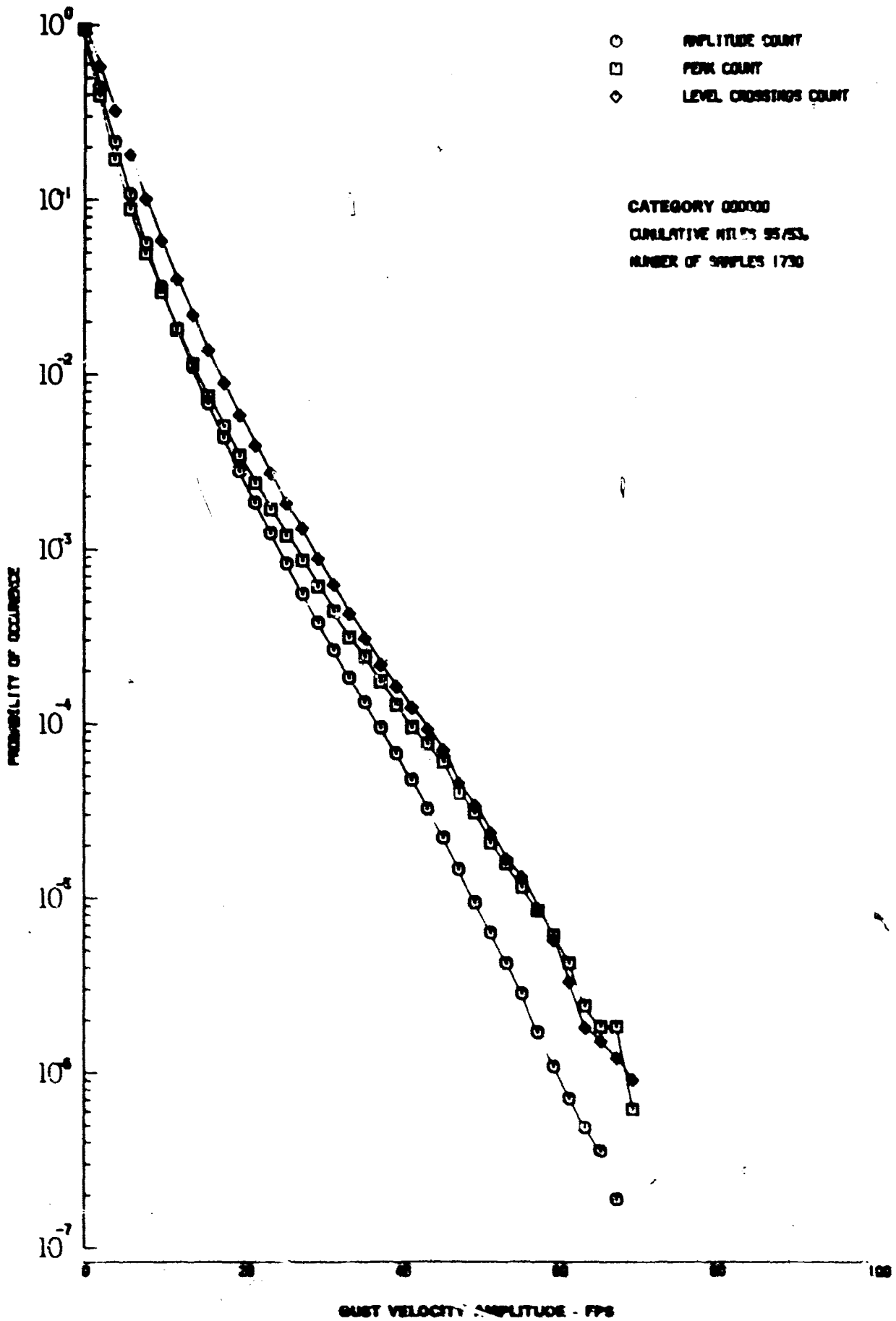


Figure 11.10 Longitudinal Gust Velocity Probability Distribution for LO-LOCAT Phase III

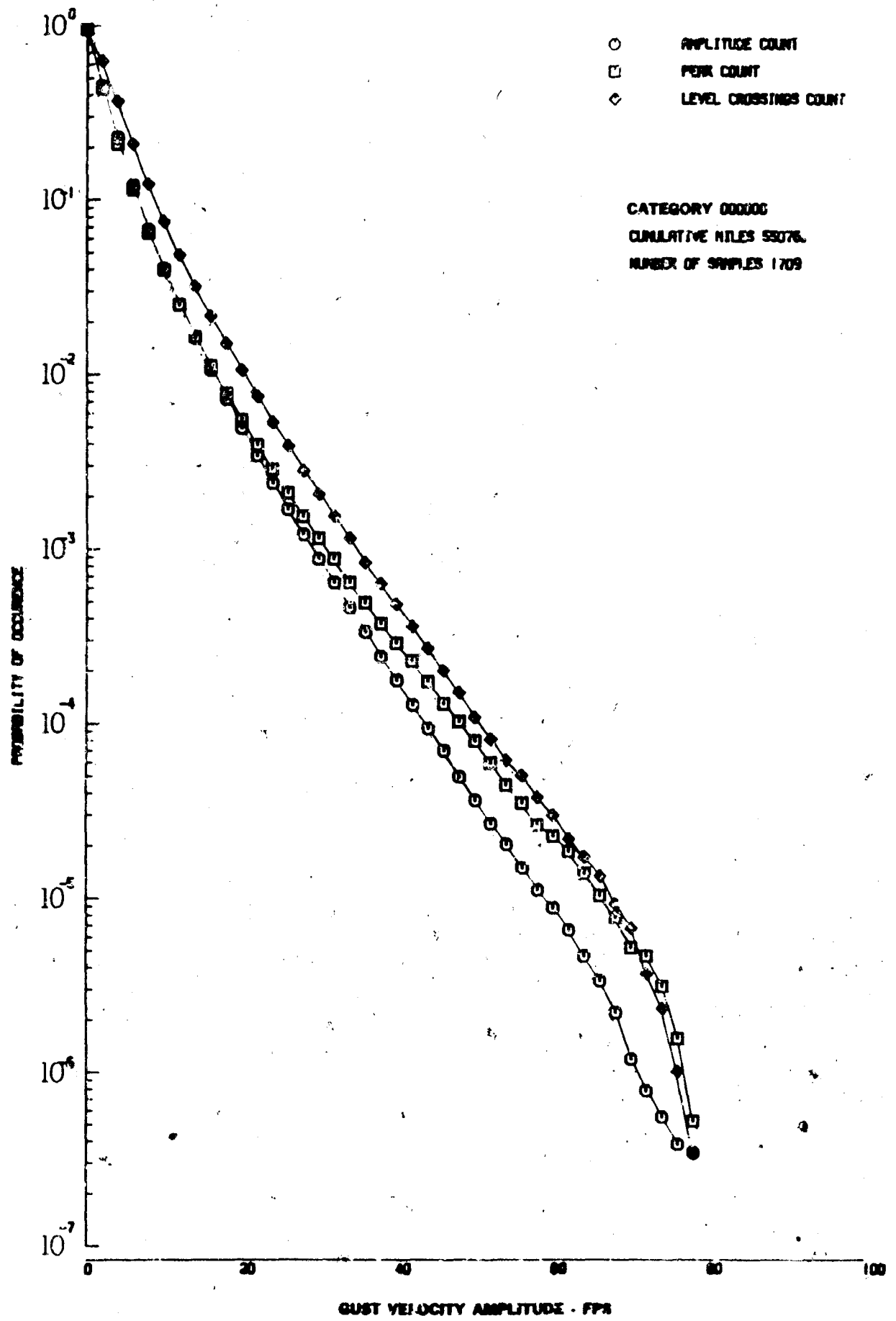


Figure 11.11 Lateral Gust Velocity Probability Distribution for LO-LOCAT Phase III

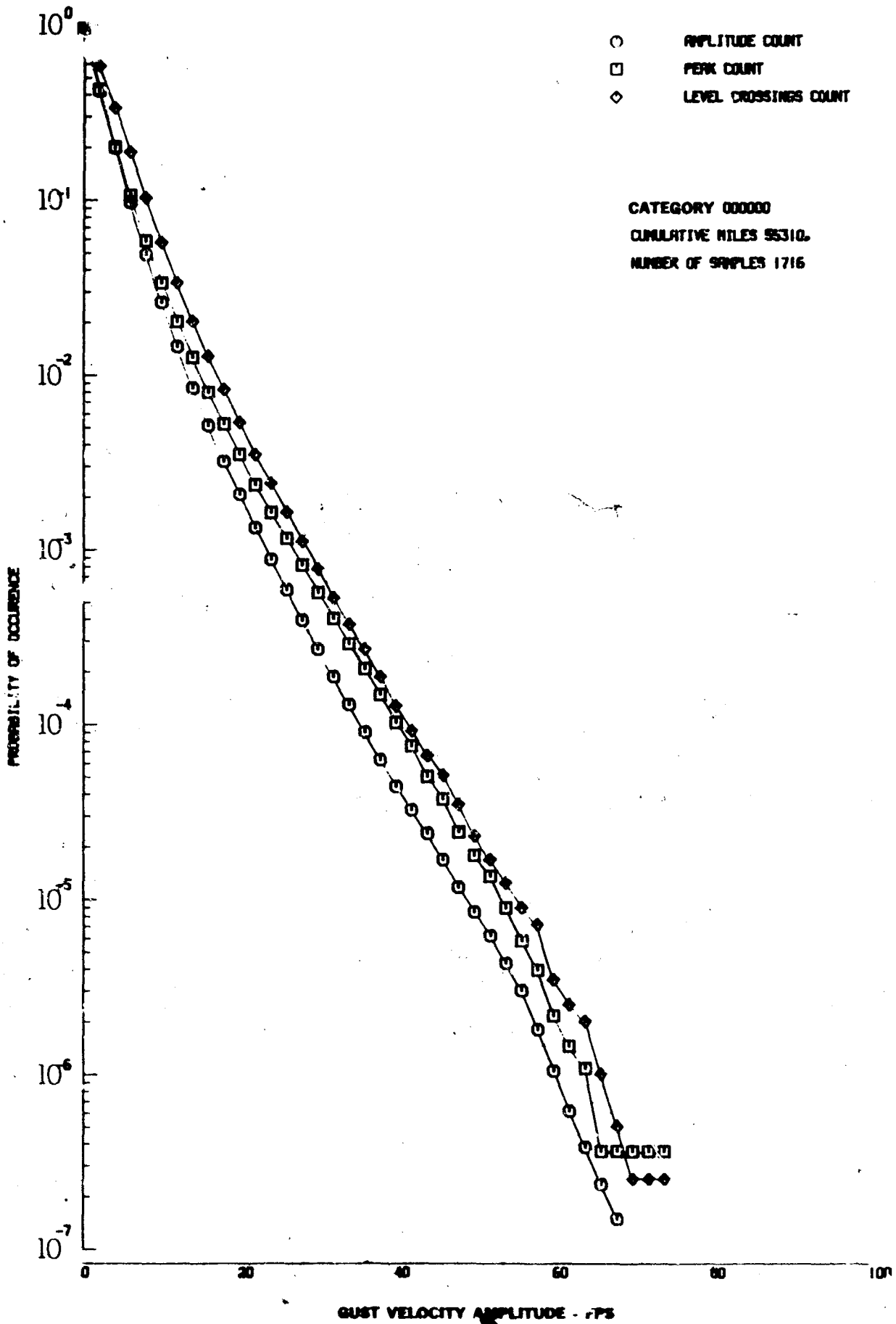


Figure 11.12 Vertical Gust Velocity Probability Distribution for LO-LOCAT Phase III



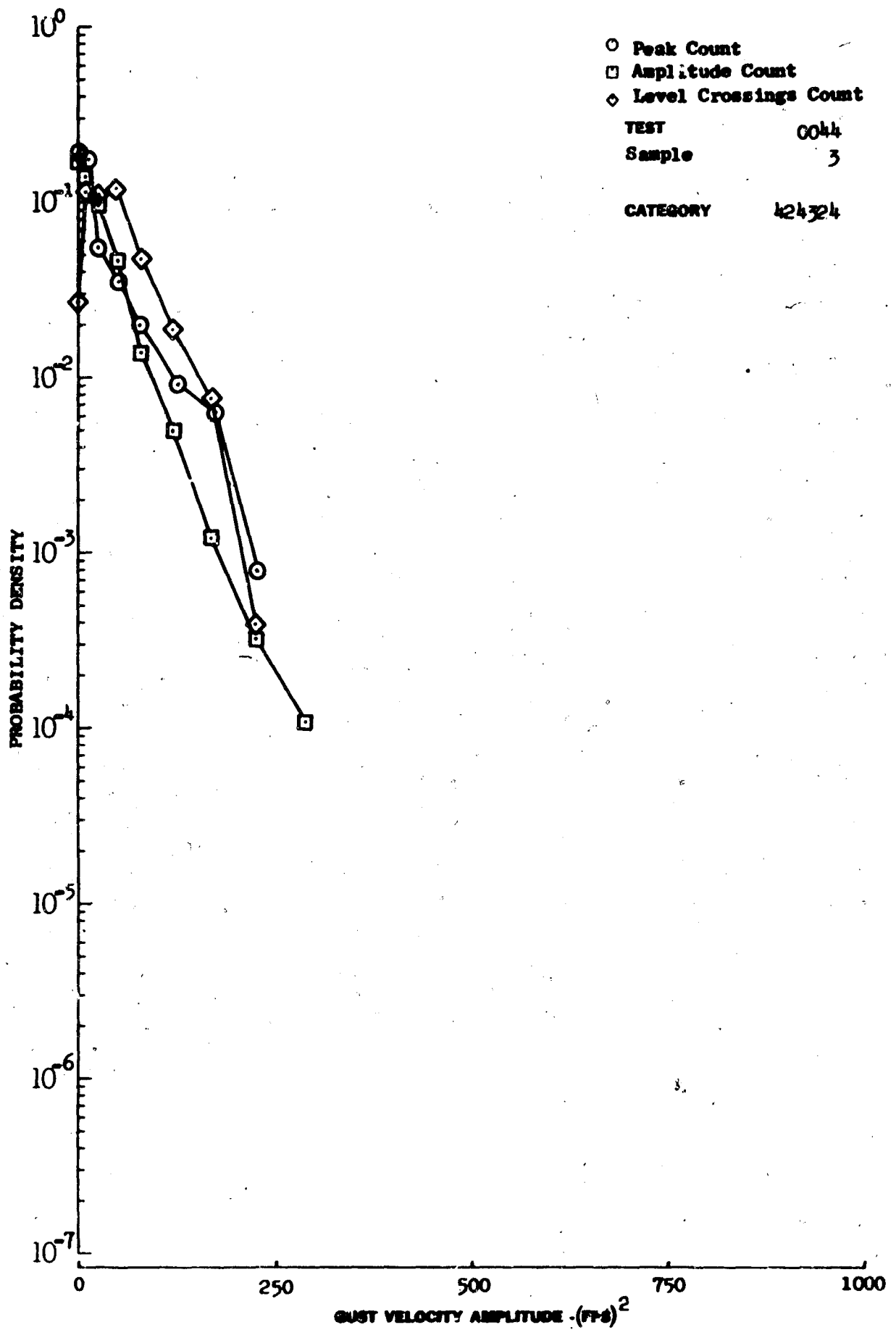


Figure 11.13 Longitudinal Gust Velocity Probability Density Distributions for an Individual Turbulence Sample

S

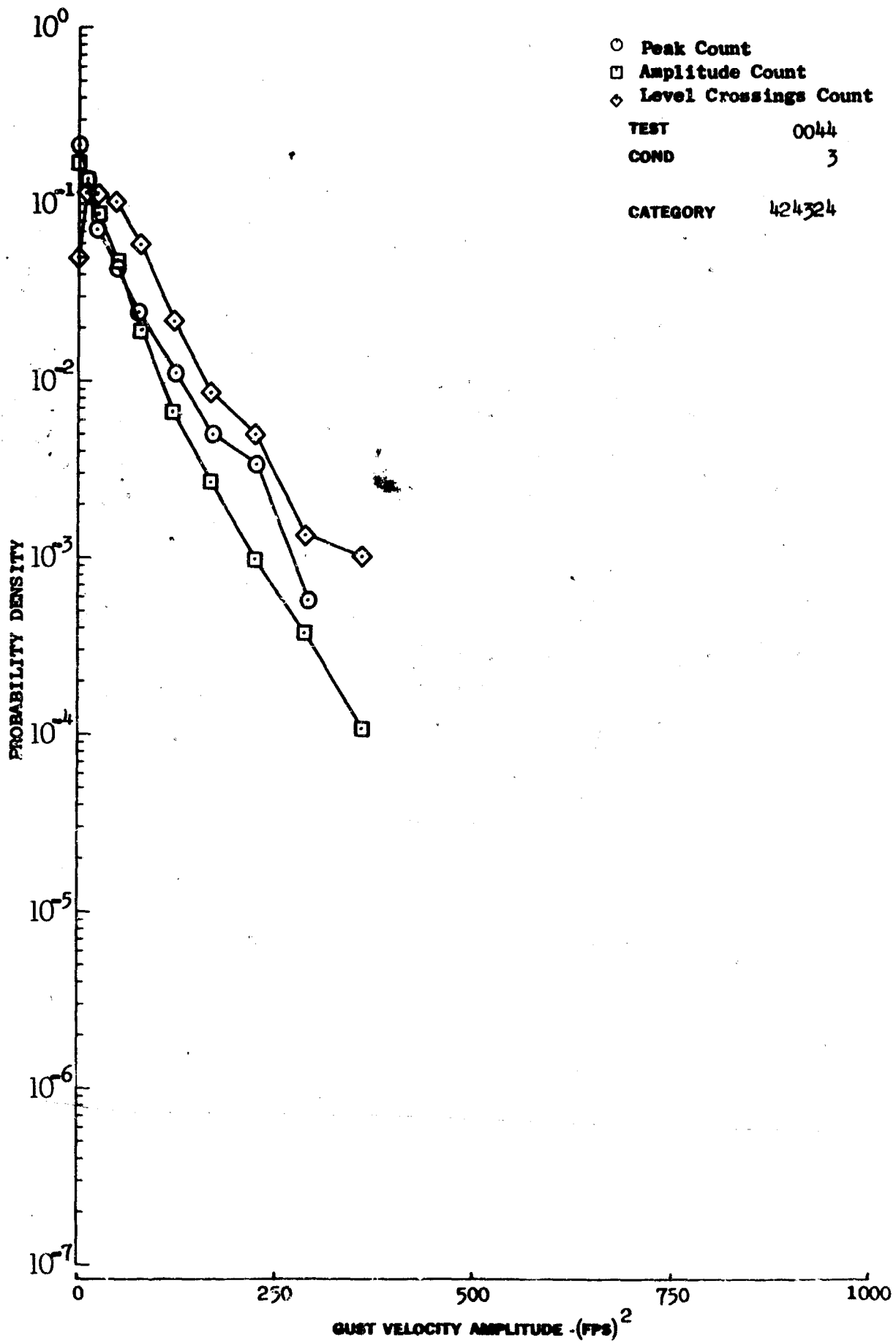


Figure 11.14 Lateral Gust Velocity Probability Density Distributions for an Individual Turbulence Sample

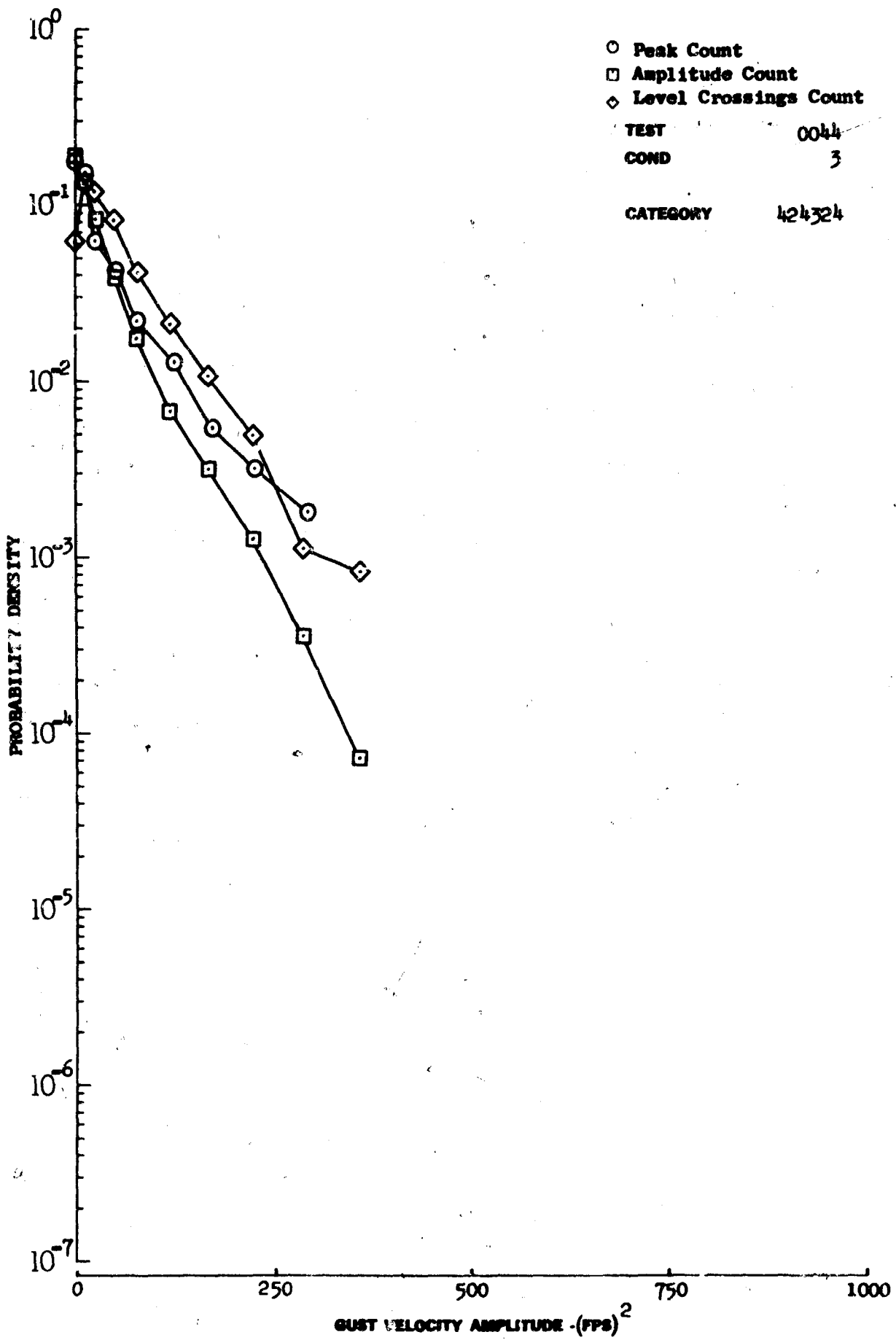


Figure 11.15 Vertical Gust Velocity Probability Density Distributions for an Individual Turbulence Sample

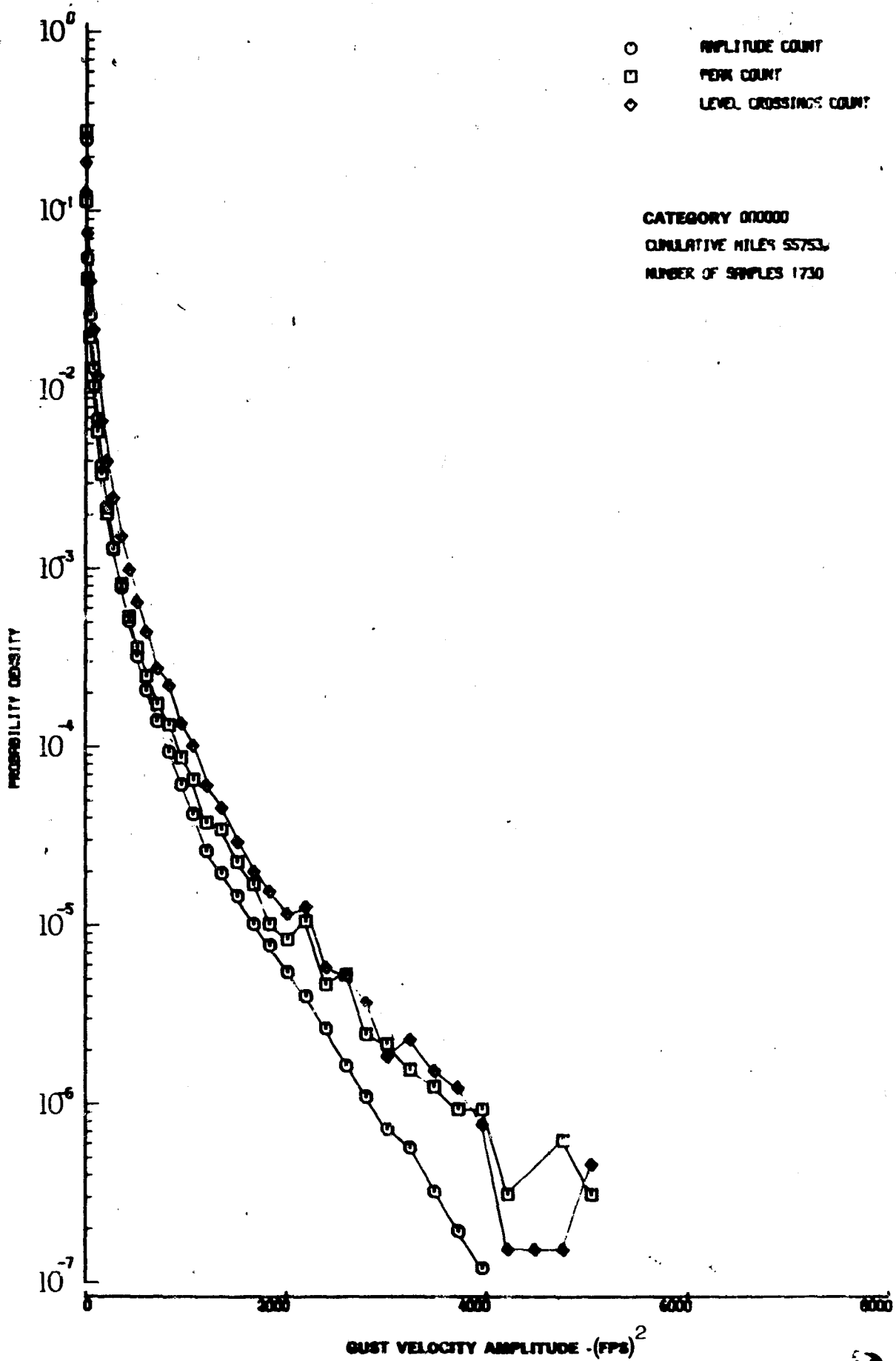


Figure 11.16 Longitudinal Gust Velocity Probability Density Distribution

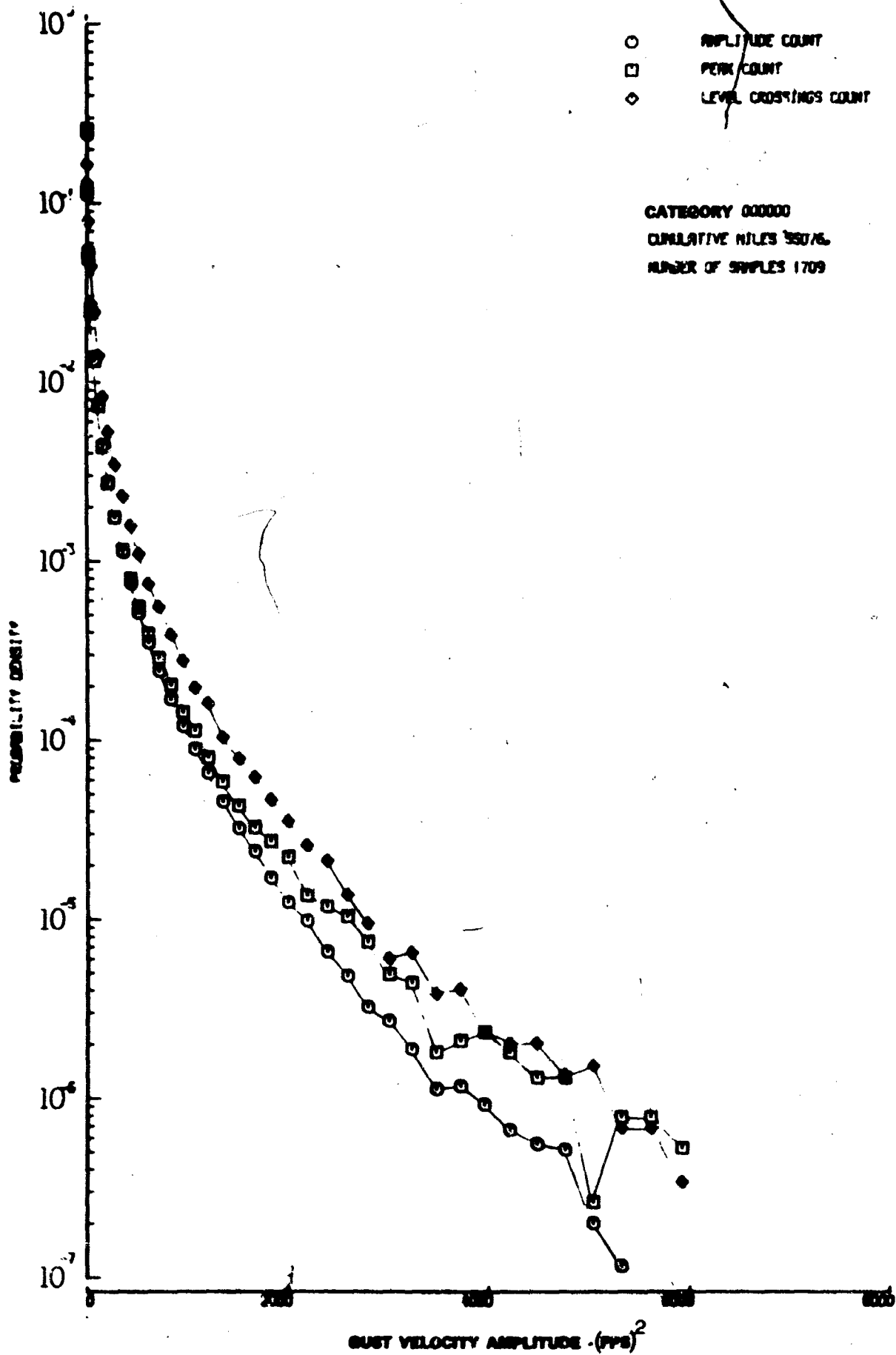


Figure 11.17 Lateral Gust Velocity Probability Density Distribution

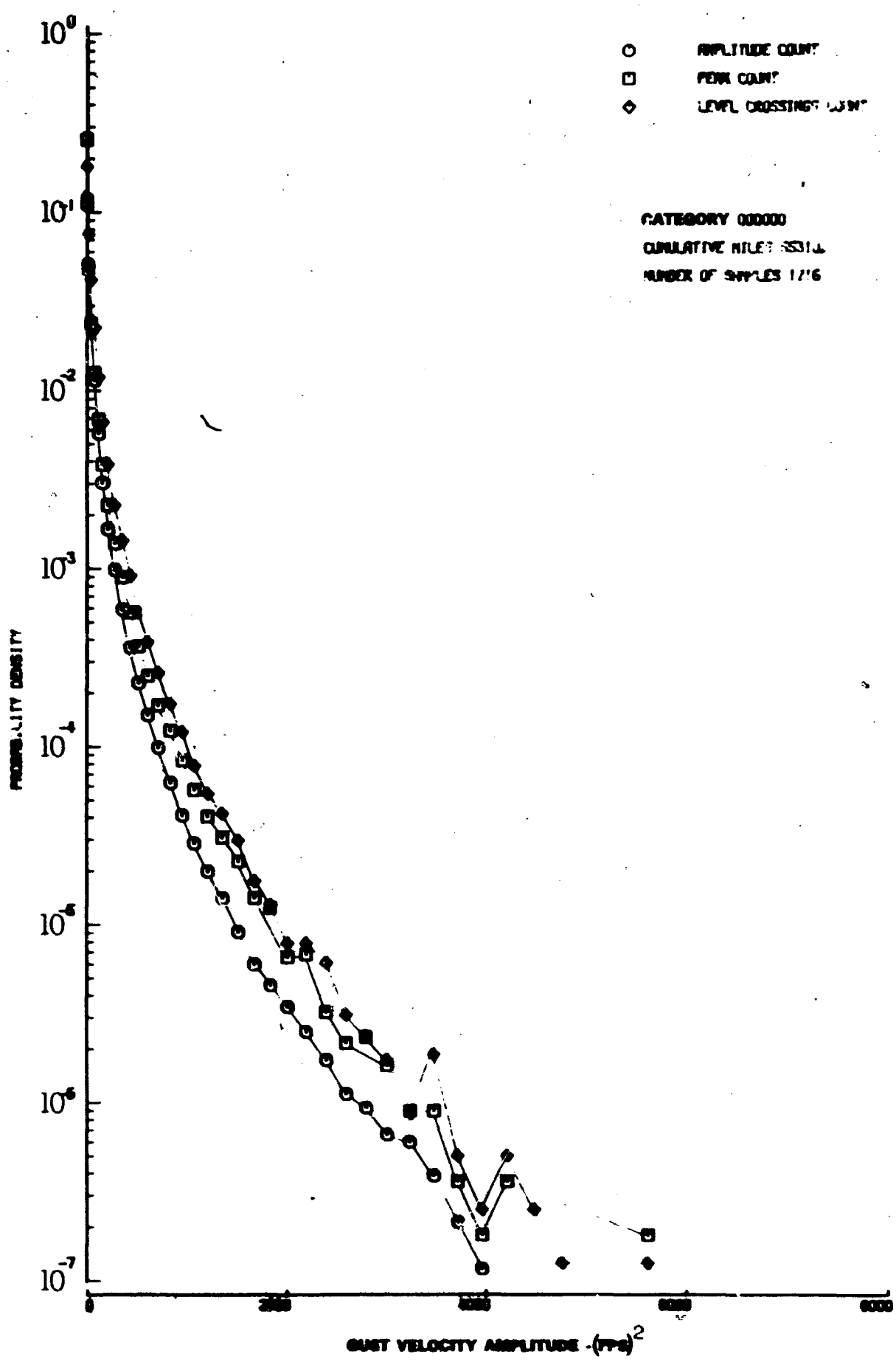


Figure 11.18 Vertical Gust Velocity Probability Density Distribution

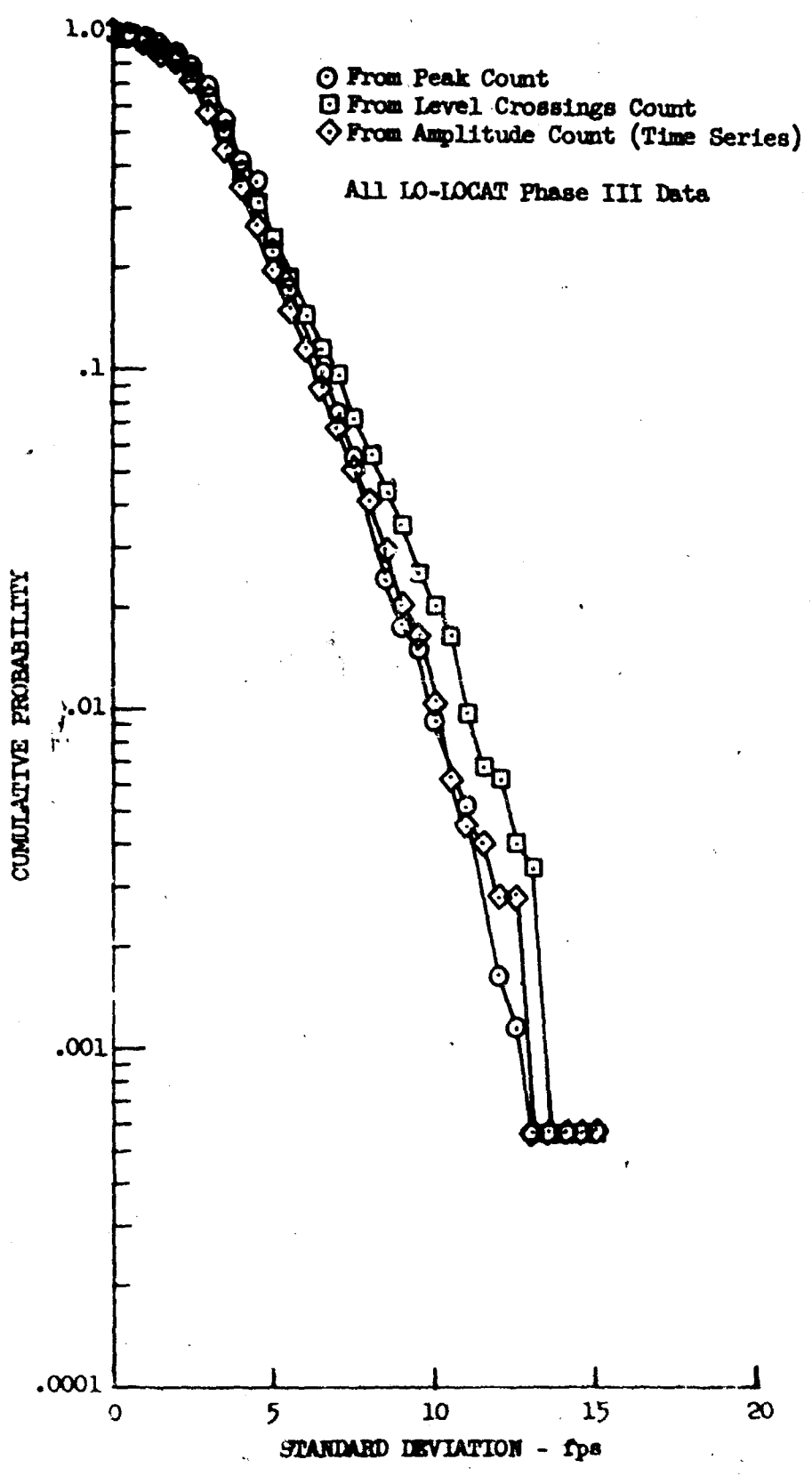


Figure 11.19 Comparison of Longitudinal Gust Velocity Standard Deviations Calculated by Different Techniques

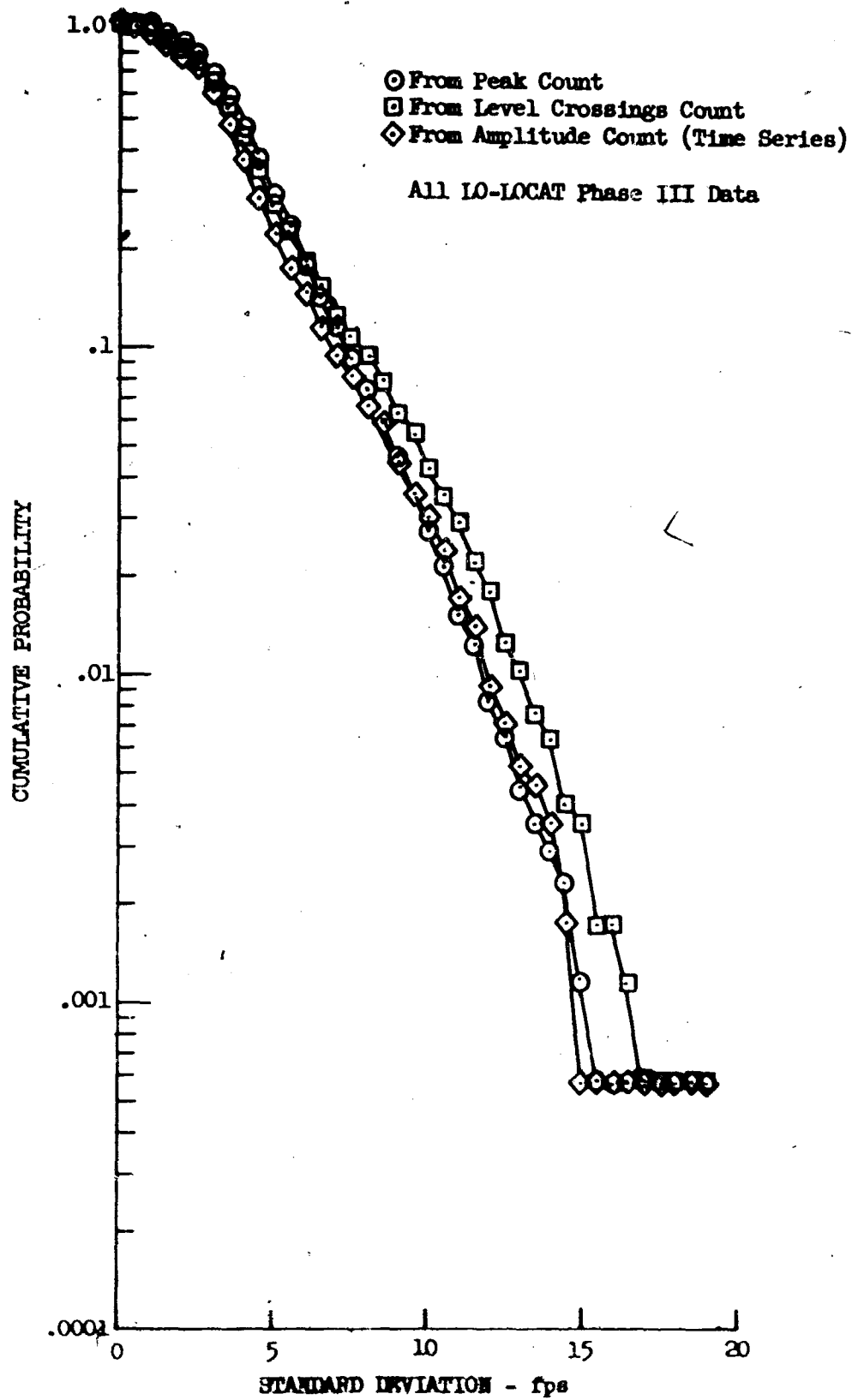


Figure 11.20 Comparison of Lateral Gust Velocity Standard Deviations Calculated by Different Techniques



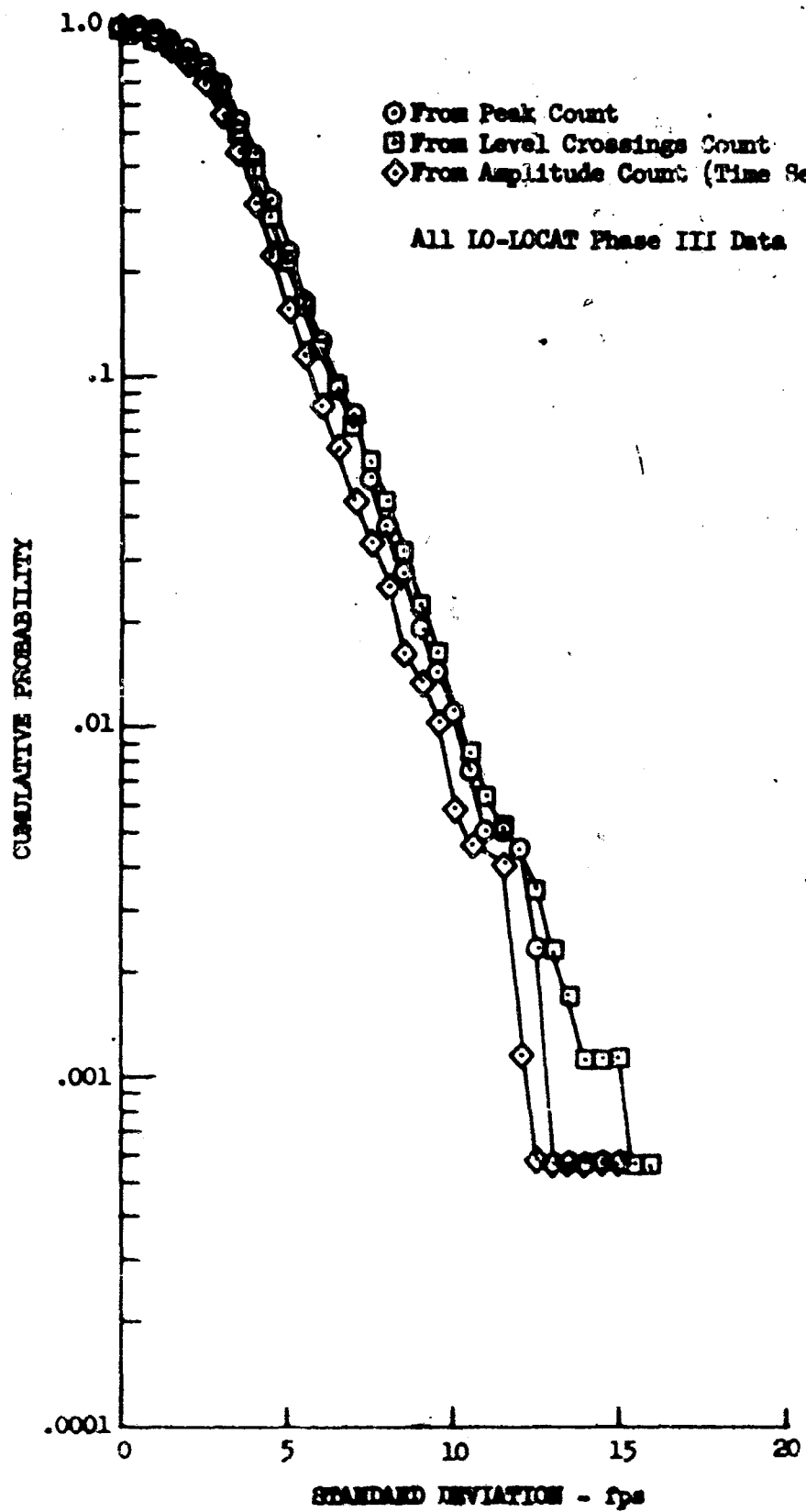


Figure 11.21 Comparison of Vertical Gust Velocity Standard Deviations Calculated by Different Techniques

## 12. CORRELATION OF PEAK DISTRIBUTIONS WITH GEOPHYSICAL CATEGORY

Peak, amplitude, and level crossings count distributions are very similar in the way they vary with different geophysical phenomena. Therefore, only the peak count distributions are used in this document to illustrate these variations. Plots and listings of data from all three counting techniques are presented in Appendices VII and VIII.

Figures 12.1 through 12.3 show the terrain effects on peak count distributions of the three gust velocity components. These plots show that the number of peaks per mile exceeding given values are, in general, larger for high mountain data and decrease for low mountains, plains, desert, and water in that order.

Peak probabilities of the plains data are higher than that of the desert data, even though the average desert terrain was rougher than that of the plains. This was probably caused by the fact that higher wind velocities were recorded over the plains resulting in a higher percentage of mechanically generated turbulence.

A distinct change was seen in the distribution curves for terrain effects between the Phase III Interim Report (Reference 12.1) and this report. There was no change in water and desert distribution curves since no additional data were obtained for these categories. The plains, low mountain, and high mountain distribution curves were raised considerably. This was due primarily to the effects of the more turbulent air encountered over the Peterson route. These effects were not included in Reference 12.1.

Figures 12.4 through 12.6 present the altitude effects on peak count distributions. These figures show greater frequencies of occurrence of gust velocity peaks at 250 feet than at 750 feet.

Figures 12.7 through 12.9 show the effect of atmospheric stability on peak count distributions. In general, very stable air has the lowest distribution, whereas, the distributions of data obtained in stable, neutral, and unstable air are nearly the same. This was not the case for the Phase III Interim Report data where the difference between distributions for the very stable and other stabilities was not so distinct. The distribution curves for all four stabilities were raised above what they were for the interim analysis. But, the curves for stable, neutral, and unstable were raised considerably more than the very stable curve. This was probably due to the fact that a much smaller percentage of the very stable data, as compared to the other three stabilities, came from the Peterson route.

Figures 12.10 through 12.12 show the effect of time of day on peak count distributions. These plots show that the distributions do not vary significantly with time of day. The only distinguishable characteristic is that the distribution for dawn starts out below the others at small gust velocities, but crosses over at about 30 fps and generally is higher from there on. This is probably due to the effects of the high percentage of the low intensity turbulence samples that were included in the dawn category. Forty-two of the 66 low intensity turbulence samples (Table 8.2) were obtained at dawn. Also, the effects of very stable samples should be considered, since

68 per cent of the dawn data was very stable. The curve for dawn data was lower at the smaller gust velocities, however, due to the effects of the higher intensity turbulence samples obtained at Peterson, the curve is higher at the larger gust velocities.

Figures 12.13 through 12.15 show the variation of peak count distributions with geographical location. The distribution for the Peterson route was the highest. This is due to the high mountain terrain and the season of the year during which this route was flown. The Edwards distribution is the lowest at the smaller gust velocities due to the effects of the water and desert legs, but increases rapidly with increasing velocity due to the effects of the mountain legs. The distribution for the Griffiss route is somewhat higher than for the McConnell route due to the effects of low mountain legs at Griffiss.

It will be noted that the lateral component for the Peterson route exhibits a higher distribution than that of the vertical component, while, for the Edwards route, the vertical component is higher than the lateral. This is due to location of those legs with respect to the more rugged terrain characteristics. The legs at Peterson paralleled the ridge lines while at Edwards the legs crossed over the ridge lines. Thus, higher lateral than vertical gust velocities would be experienced over the Peterson route and higher vertical than lateral gust velocities would be experienced over the Edwards route.

The variation of peak count distributions with season was not determined during Phase III, since the airplane was not flown over each route for a full year.

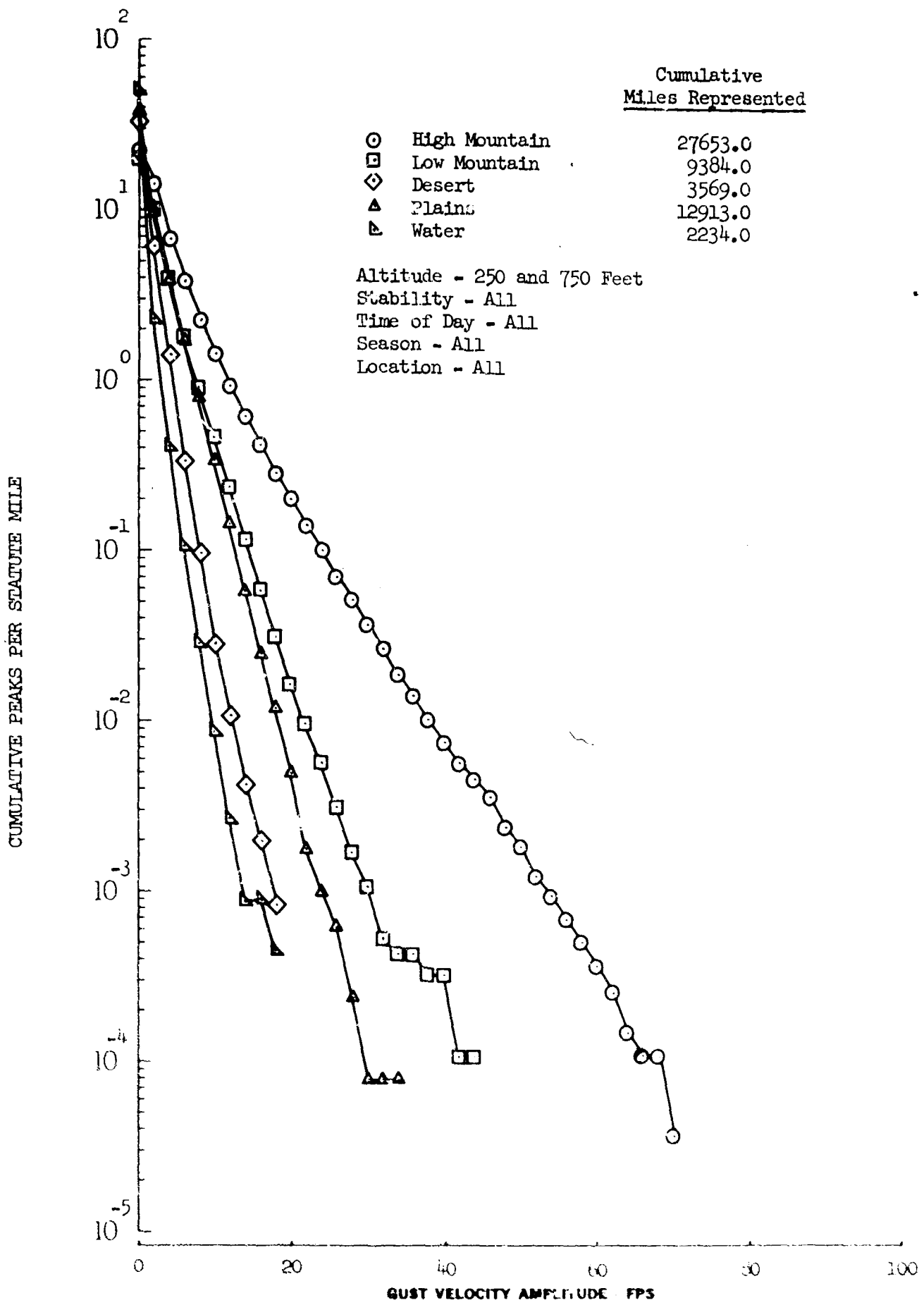


Figure 12.1 Terrain Effects on Longitudinal Gust Velocity Peaks

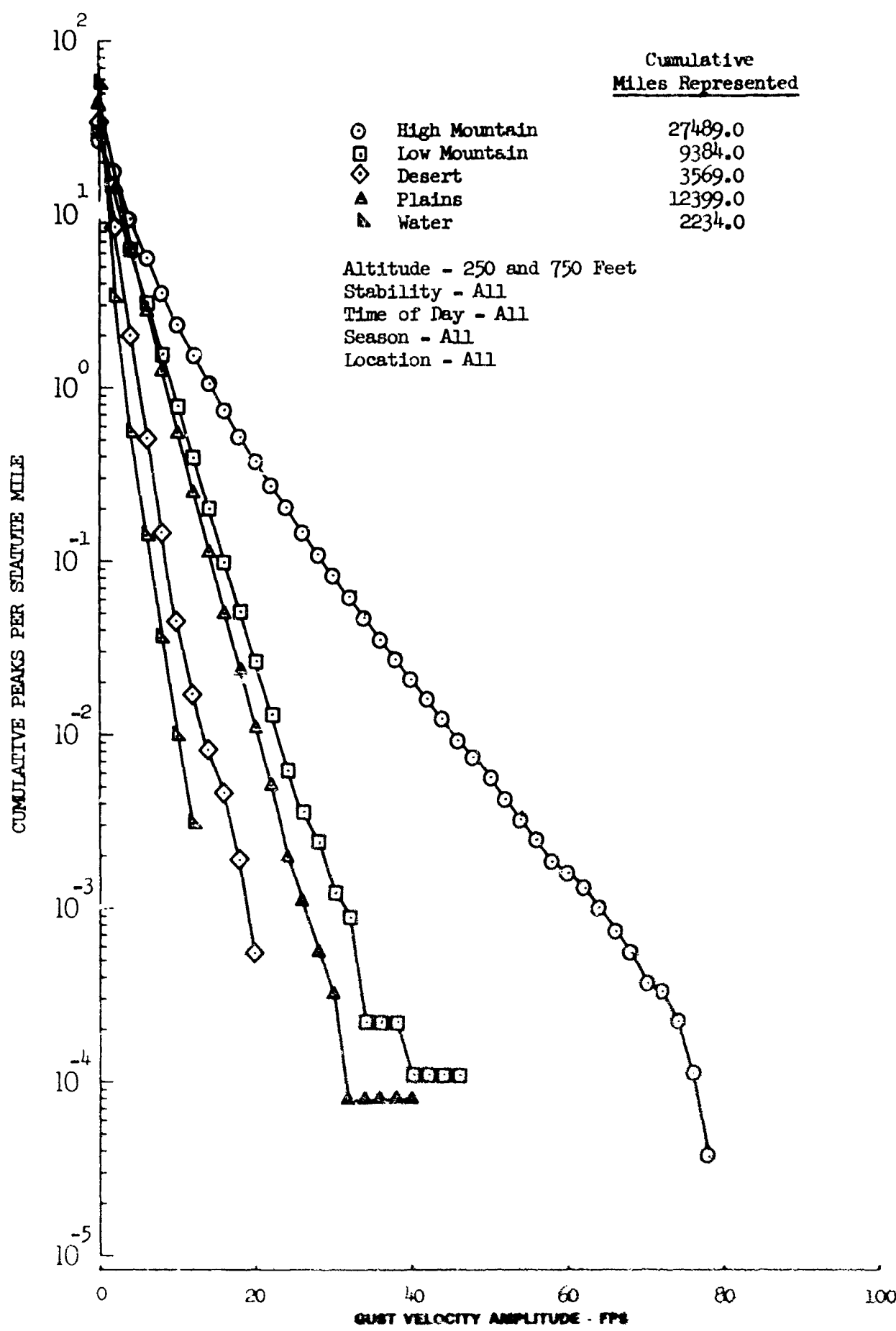


Figure 12.2 Terrain Effects on Lateral Gust Velocity Peaks

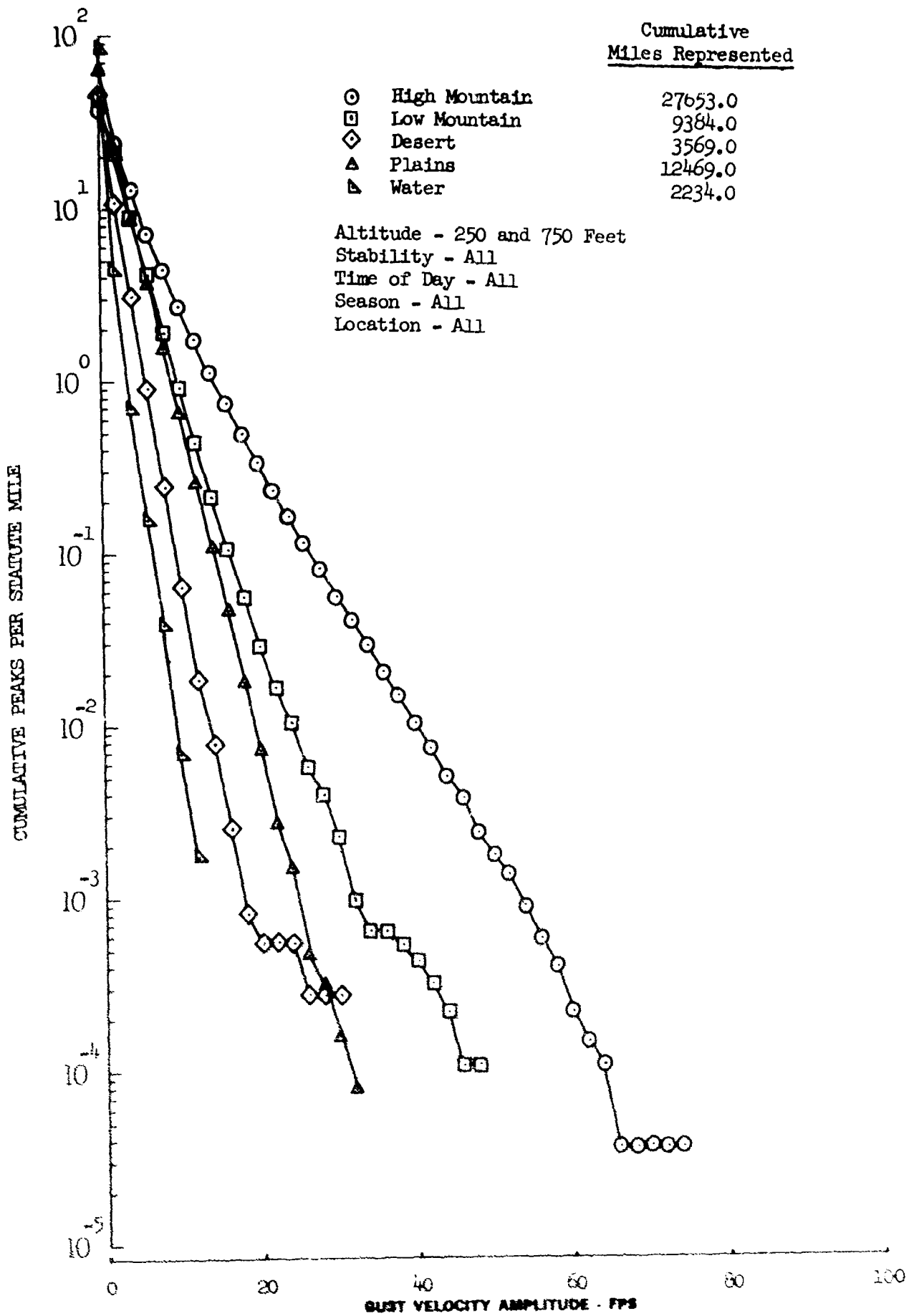


Figure 12.3 Terrain Effects on Vertical Gust Velocity Peaks

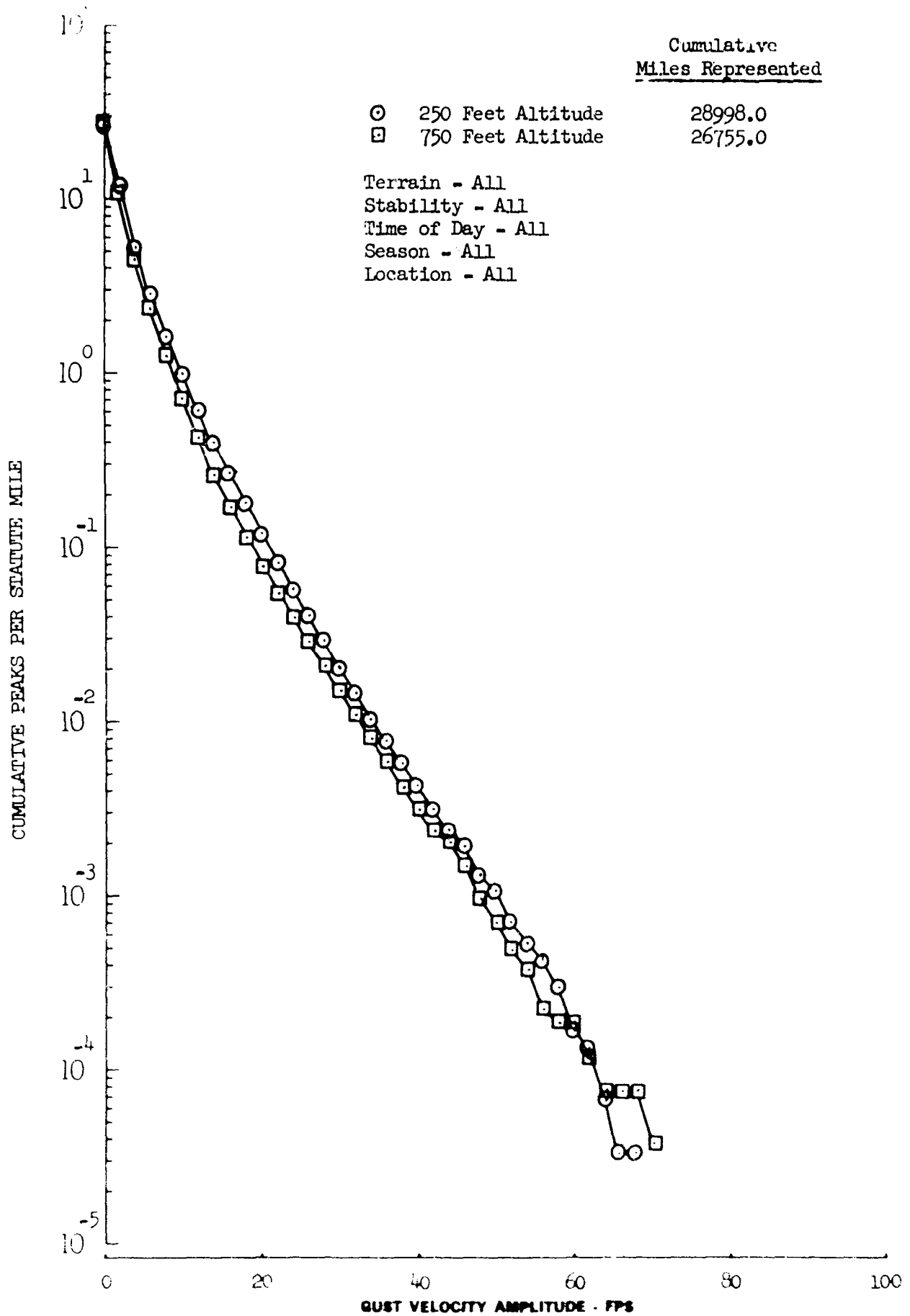


Figure 12.4 Altitude Effects on Longitudinal Gust Velocity Peaks

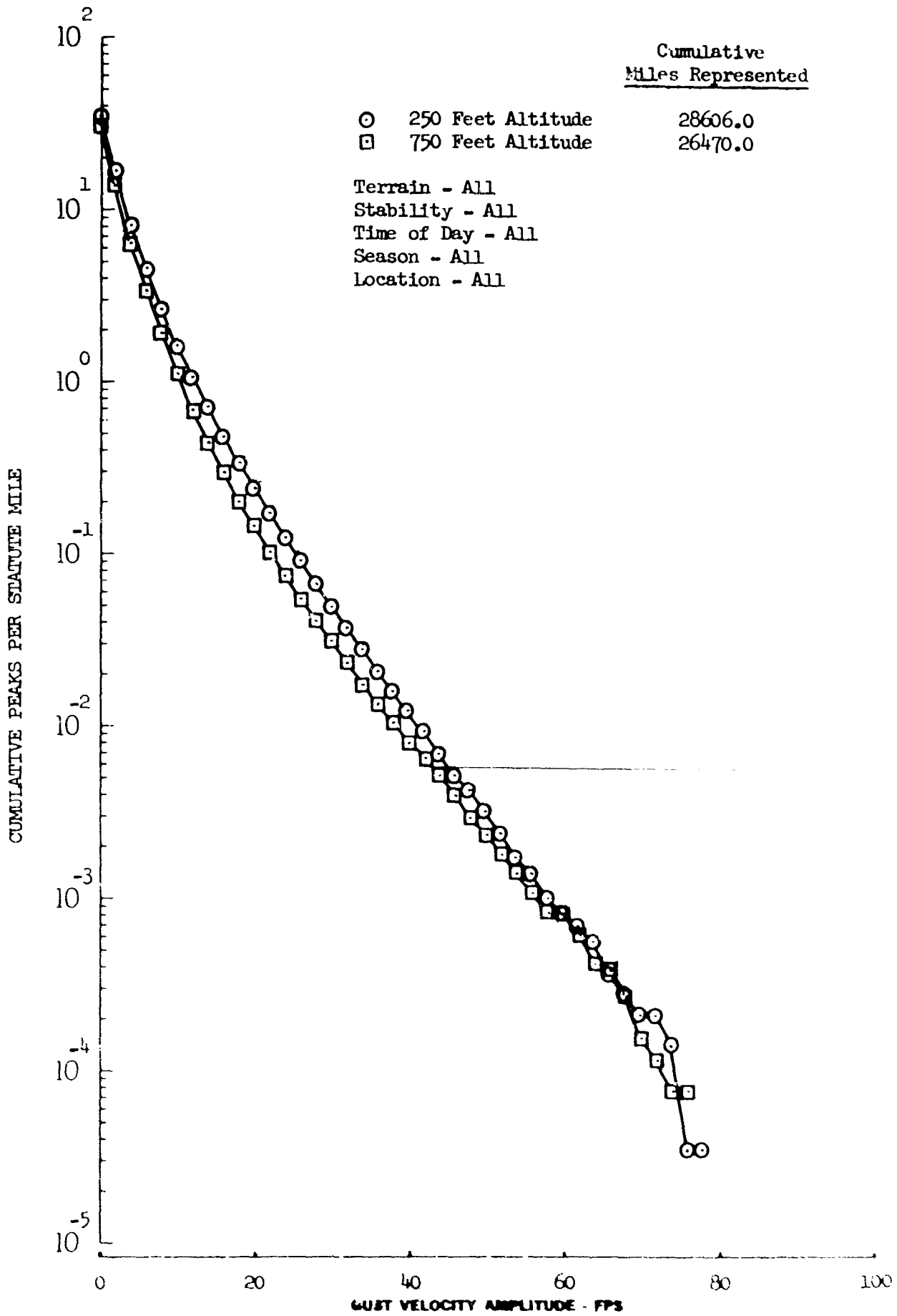


Figure 12.5 Altitude Effects on Lateral Gust Velocity Peaks



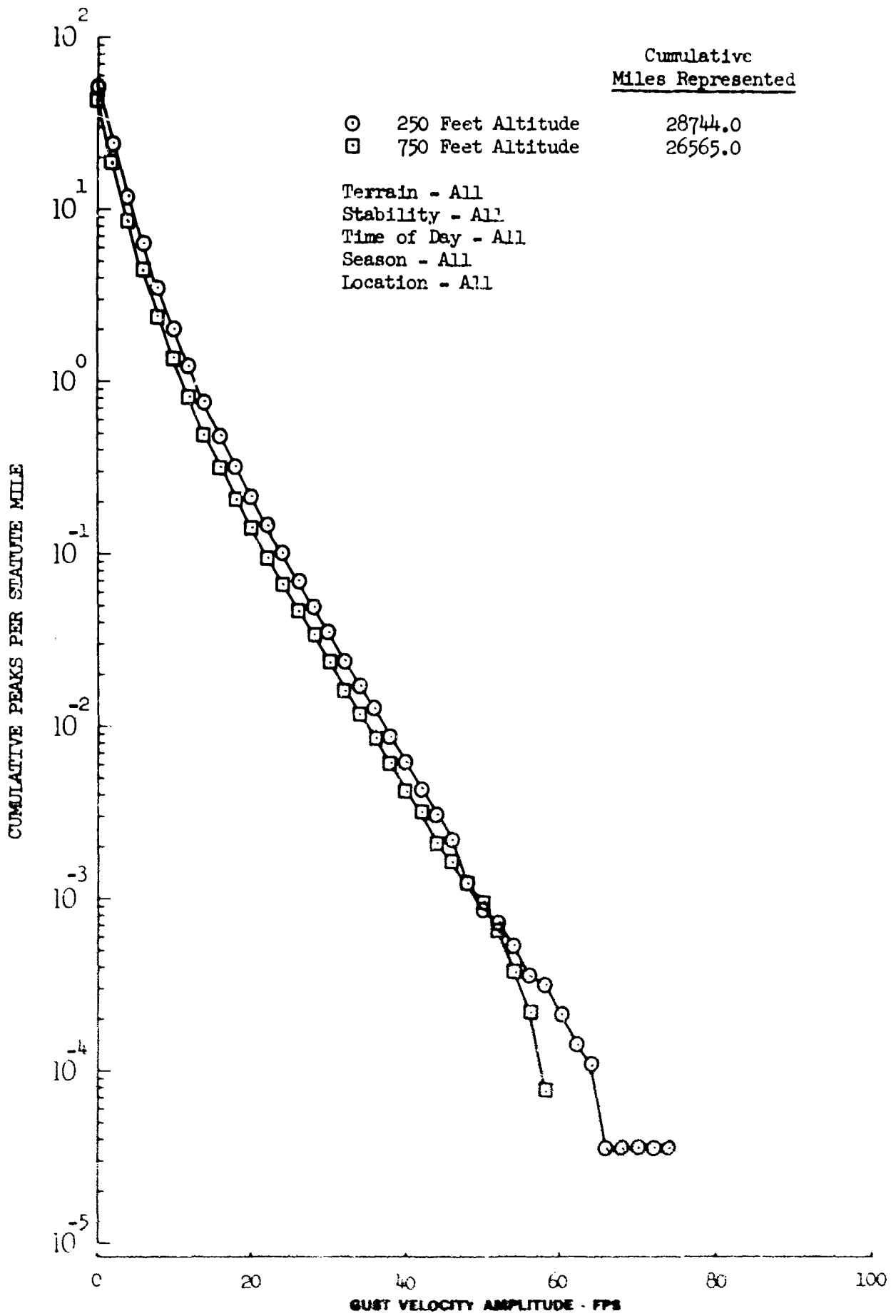


Figure 12.6 Altitude Effects on Vertical Gust Velocity Peaks

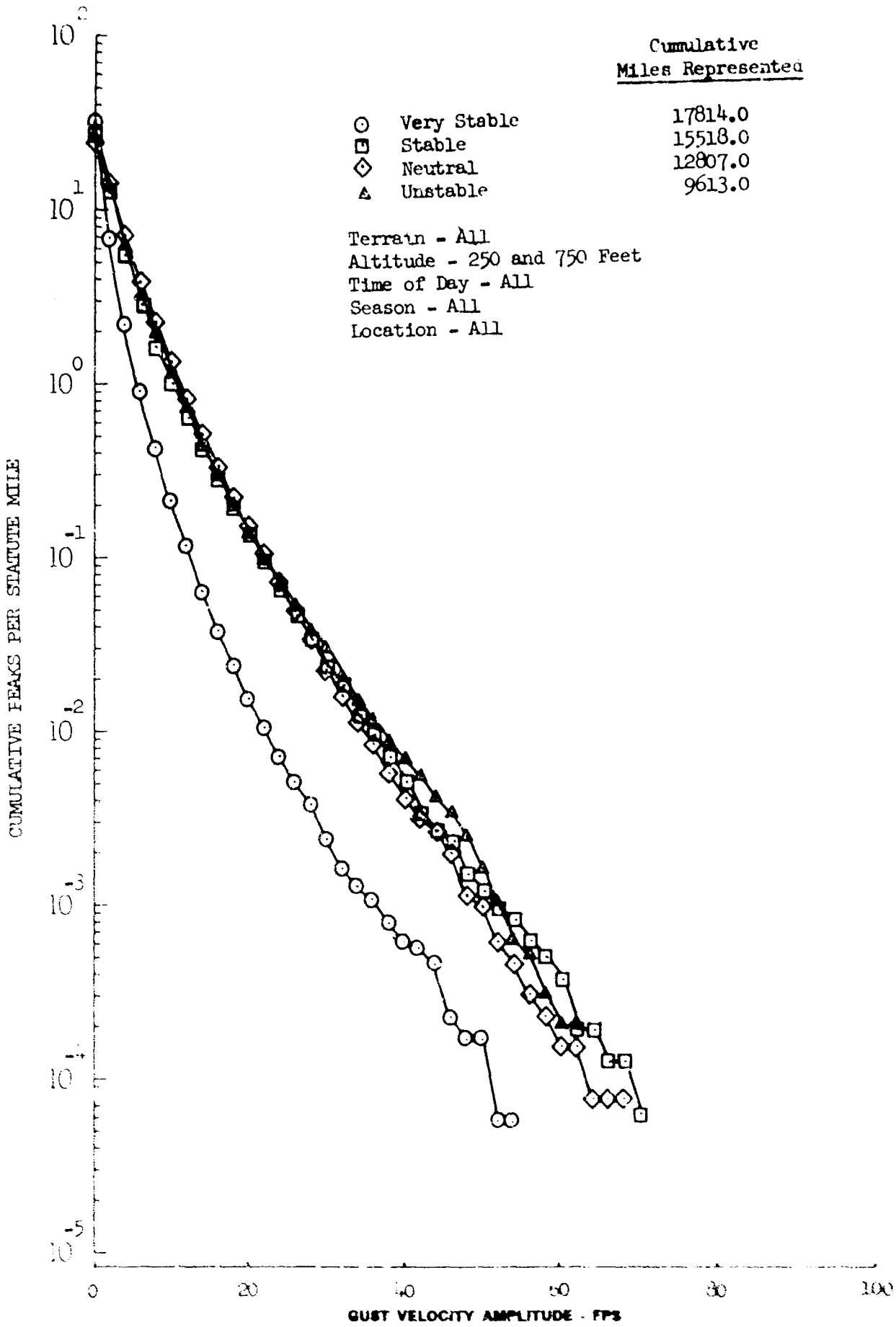


Figure 12.7 Stability Effects on Longitudinal Gust Velocity Peaks

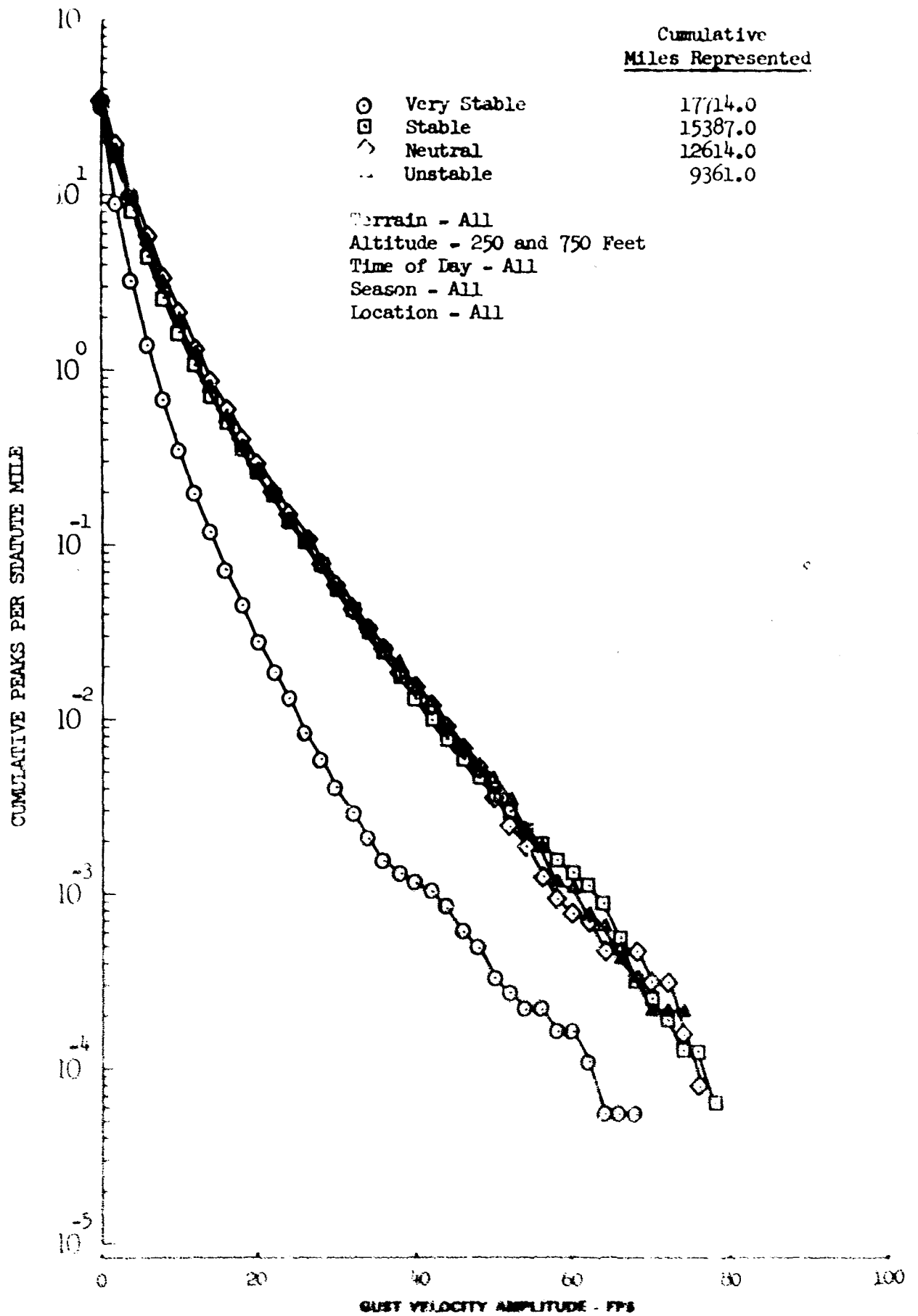


Figure 12.8 Stability Effects on Lateral Gust Velocity Peaks

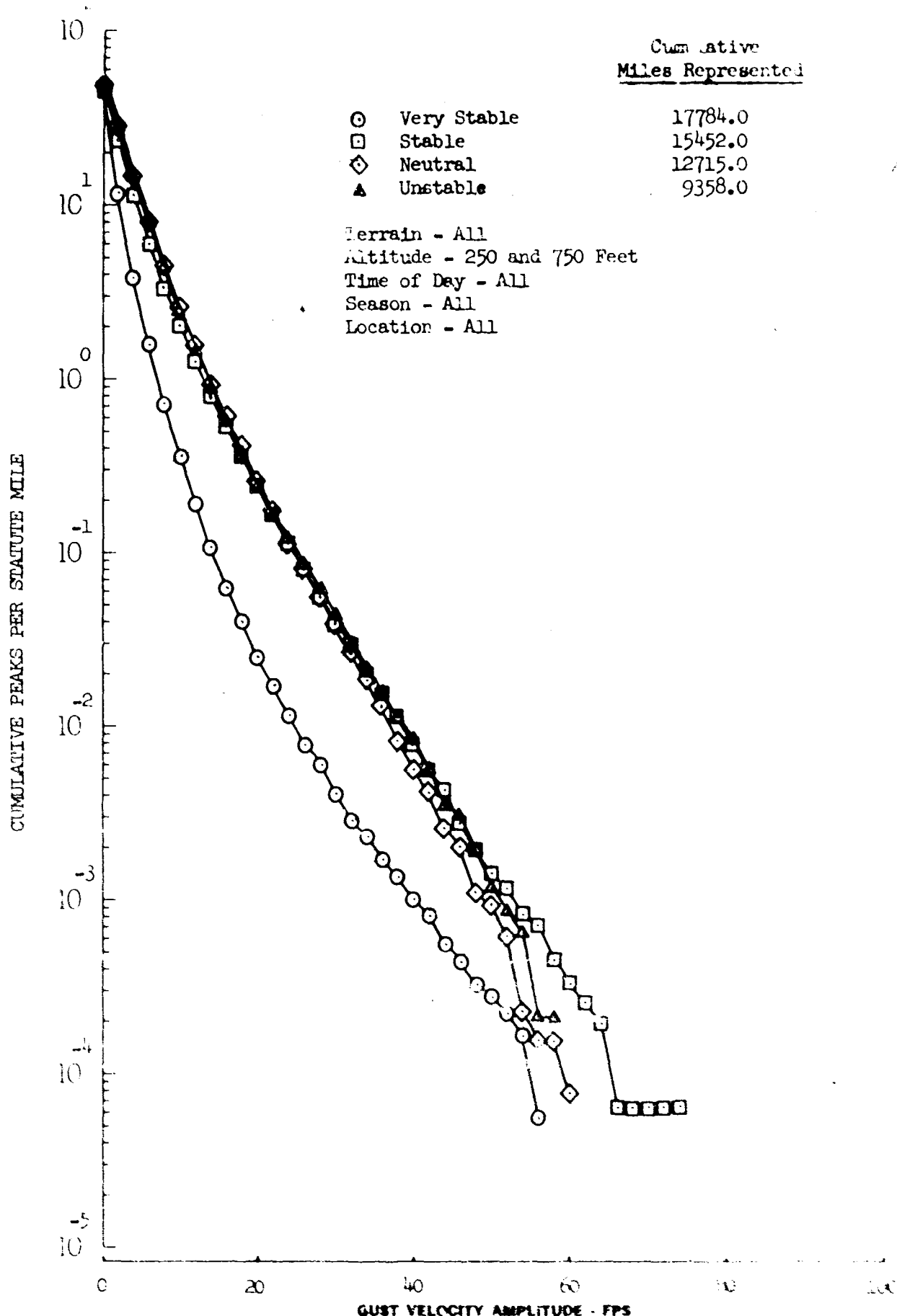


Figure 12.9 Stability Effects on Vertical Gust Velocity Peaks

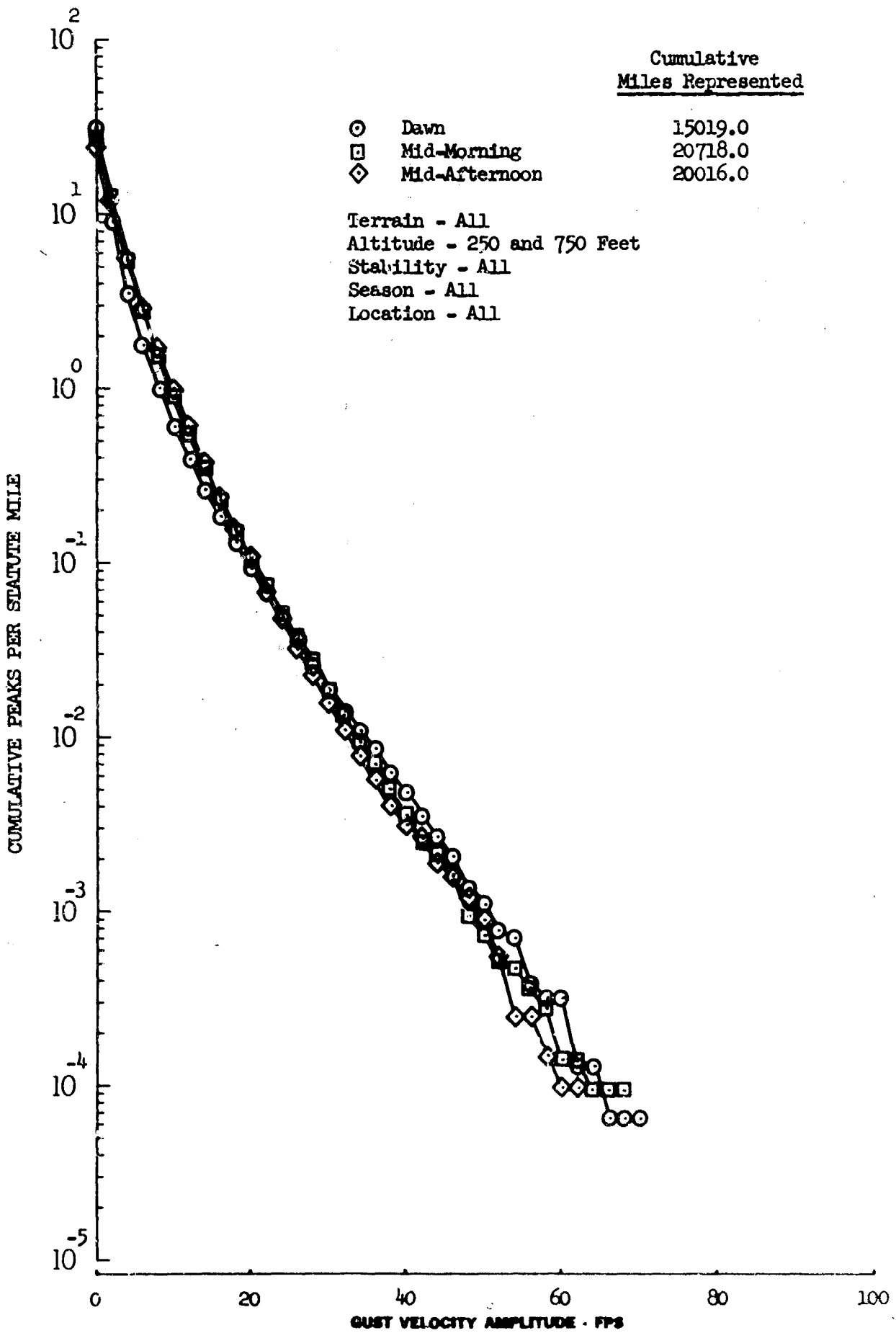


Figure 12.10 Time of Day Effects on Longitudinal Gust Velocity Peaks

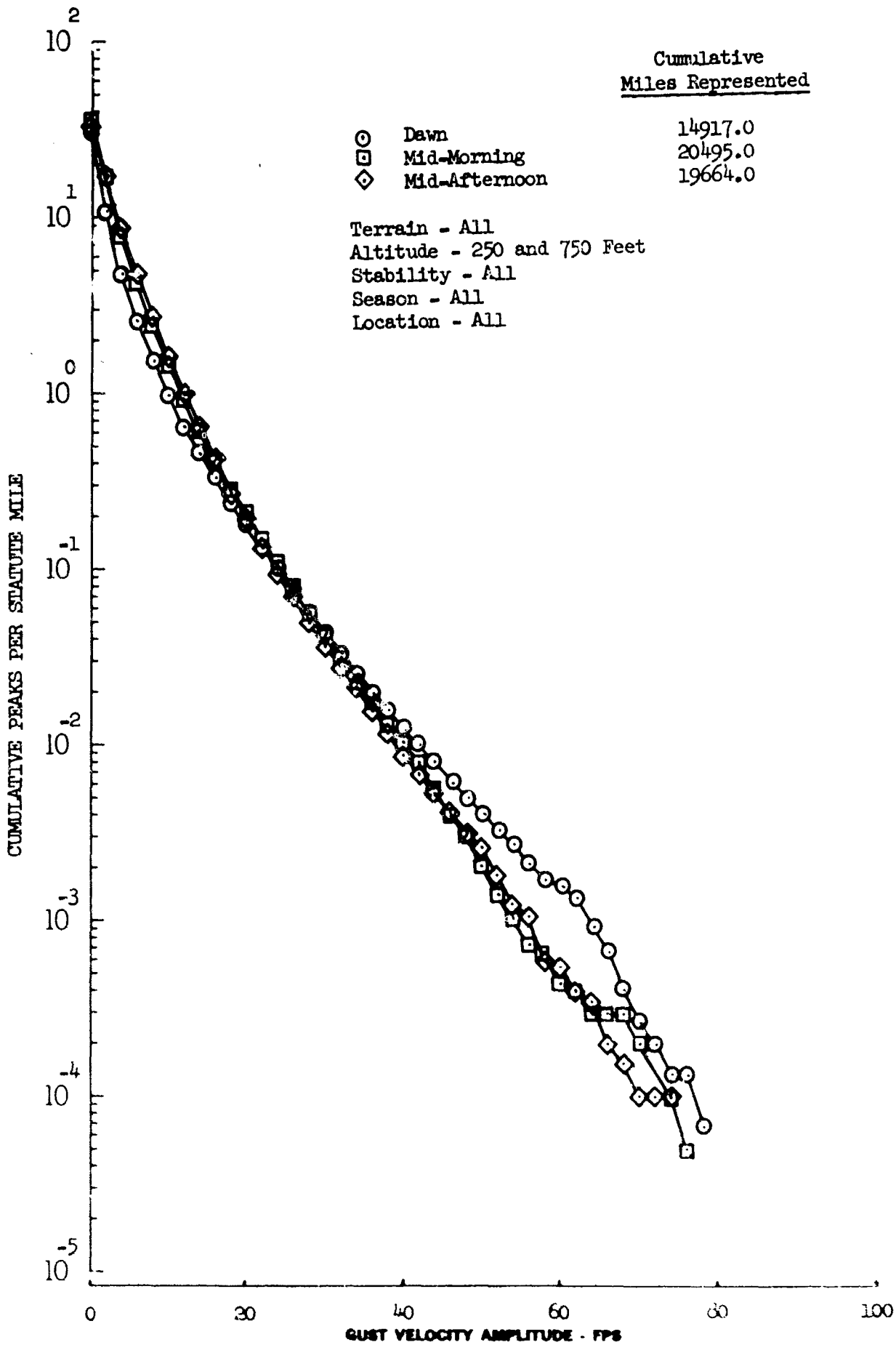


Figure 12.11 Time of Day Effects on Lateral Gust Velocity Peaks

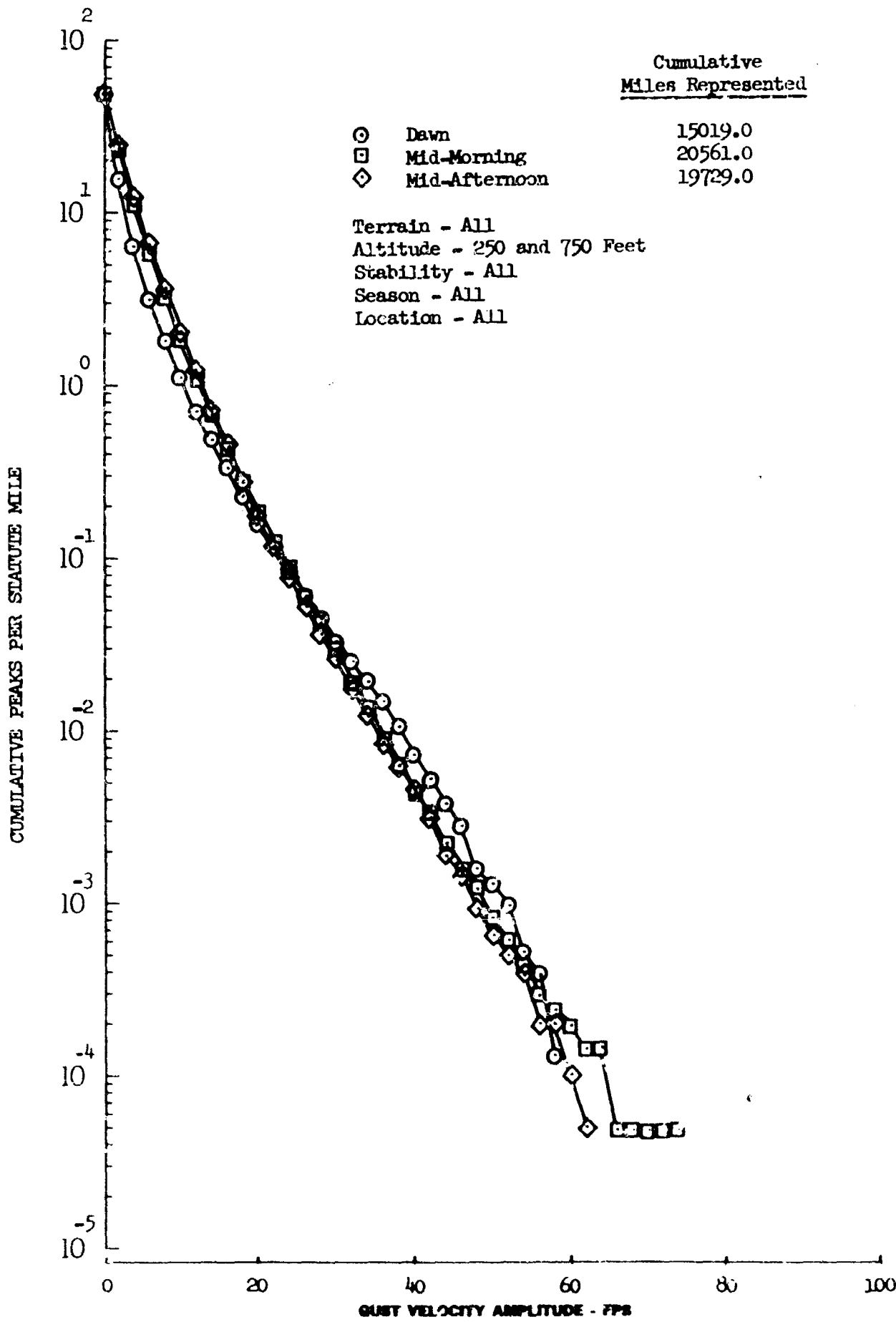


Figure 12.12 Time of Day Effects on Vertical Gust Velocity Peaks

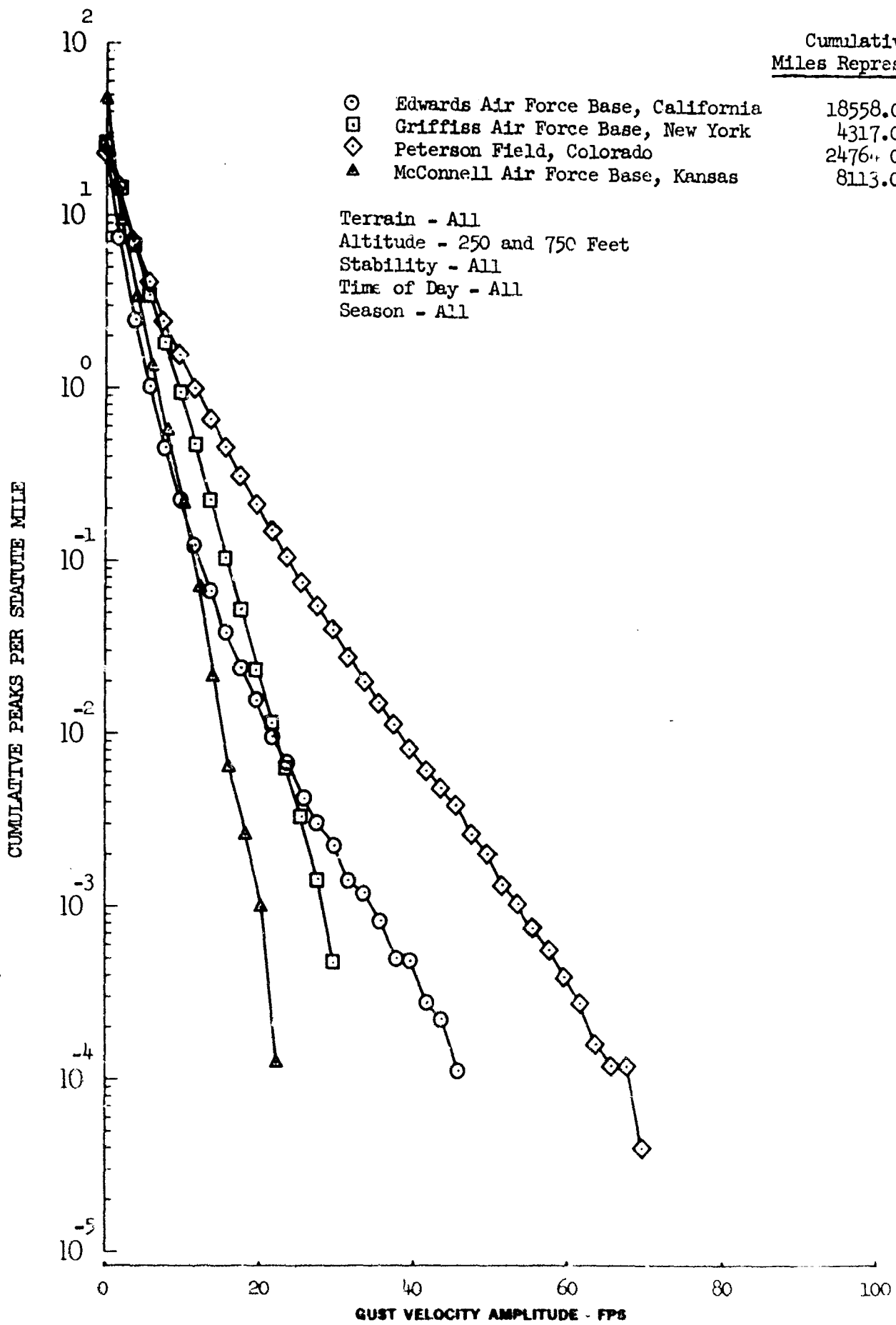


Figure 12.13 Location Effects on Longitudinal Gust Velocity Peaks



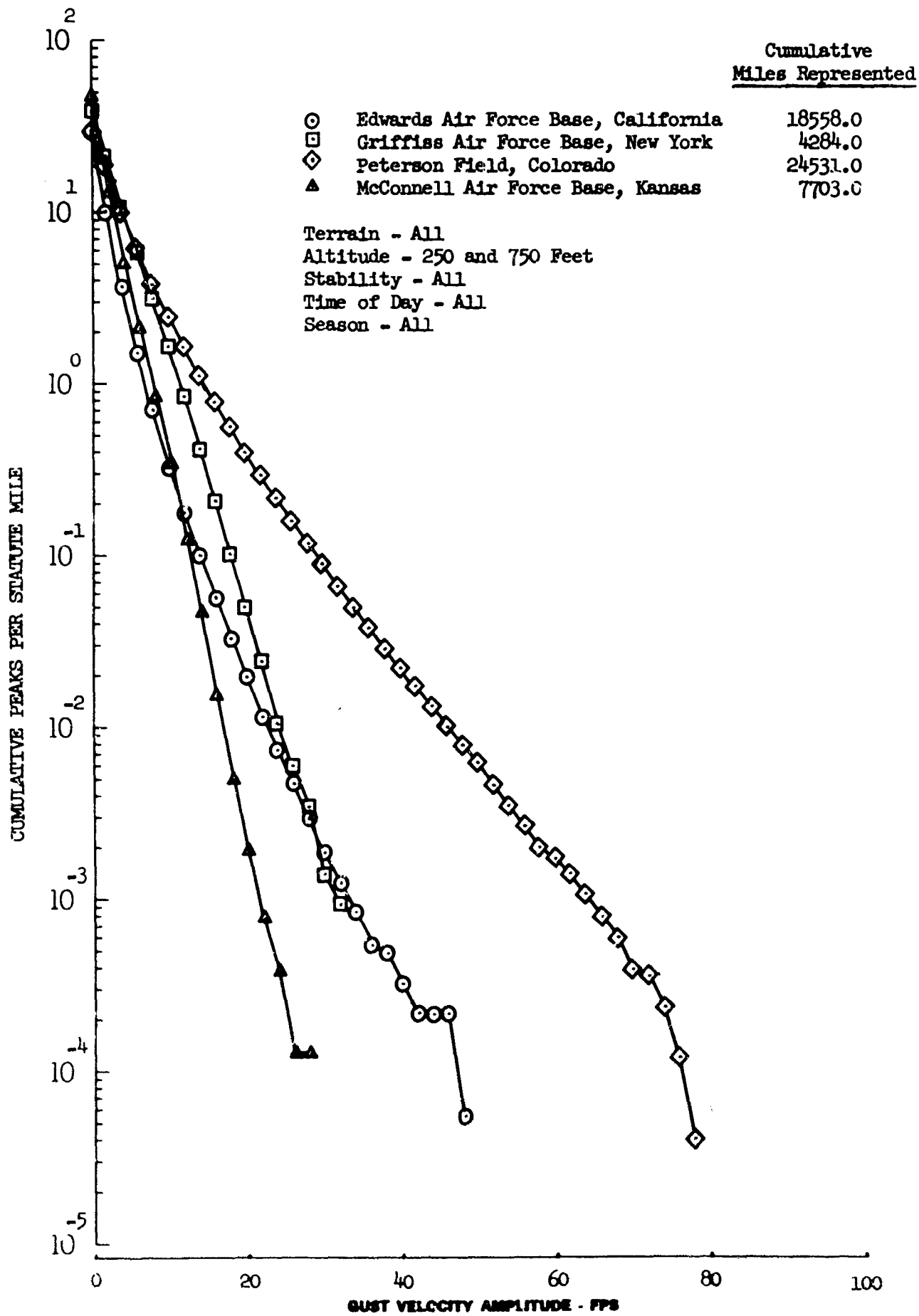


Figure 12.14 Location Effects on Lateral Gust Velocity Peaks

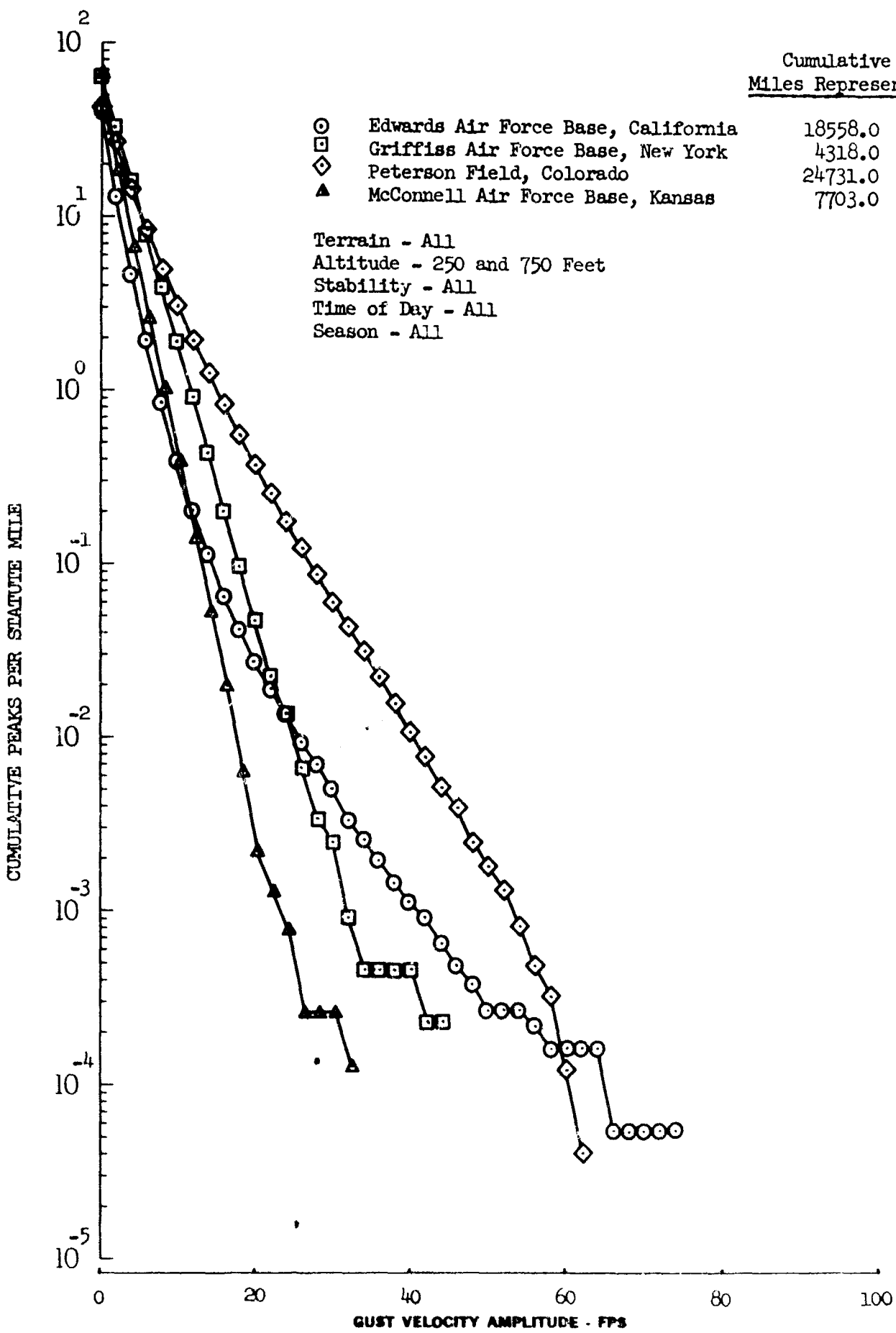


Figure 12.15 Location Effects on Vertical Gust Velocity Peaks

## SECTION IV

### GUST VELOCITY INTENSITY

The time series standard deviation ( $\sigma_t$ ) of each of the three gust velocity components was calculated by the following equation:

$$\sigma_t = \left[ \frac{1}{N} \sum_{i=1}^N (x_i - \bar{x})^2 \right]^{1/2} = \text{rms (with } \bar{x} = 0) \quad (9.1)$$

The values for  $x_i$  were taken from the time histories of gust velocities which were computed at the rate of 100 samples per second giving 27,000 values for each four and one-half minute turbulence sample. Therefore, for this particular calculation,  $N = 27,000$ . The mean gust velocity value is indicated by  $\bar{x}$ .

Since the mean value,  $\bar{x}$ , is made essentially equal to zero by high-pass filtering, the standard deviation is actually equal to the root-mean-square (rms) value as shown. The two terms are used interchangeably in this report.

### 13. GUST VELOCITY RMS STATISTICAL ANALYSIS

The rms values were grouped into amplitude bands of 0.5 fps and the cumulative probability distribution (CPD) was calculated. These CPD values give the probabilities of a gust velocity rms value being equal to or greater than a given value. The cumulative probabilities determined for all data recorded during the Phase III program are shown in Figure 13.1.

The cumulative probability distribution curve for lateral rms gust velocity is higher than for longitudinal since a high percentage of the turbulence data were obtained while flying parallel to mountain ridge lines. The curve for vertical rms gust velocity was lower than for longitudinal due to the compression of the vertical eddies near the ground.

For categories which did not contain any high mountain data the cumulative probability distribution curves for longitudinal and lateral rms gust velocity were in general nearly the same.

The CPD of rms values for various geophysical categories was calculated. In order to assure a good statistical sampling, a minimum of 30 data samples per category was established as the criteria necessary for a valid analysis.

The gust velocity rms distributions are shown as functions of terrain type, absolute altitude, atmospheric stability, time of day, and geographic location in Figures 13.2 through 13.6. As can be seen, the results are similar for all three gust velocity components.

The highest gust velocity rms values were recorded over the high mountain legs and the lowest over the water (Figure 13.2). In general, the gust velocity rms cumulative probabilities are larger at a given rms value for data recorded over the rougher terrain. The only exception occurs for data recorded over the plains and desert. Larger gust velocity rms values were recorded over the plains, even though the desert terrain was somewhat rougher (see Section 32). This is attributed to the fact that the winds were significantly greater over the plains (Section 33).

The data were recorded at the two nominal altitudes of 250 and 750 feet above the terrain. Resultant gust velocity rms probabilities are shown in Figure 13.3; and, as can be seen, the rms values are greater at the lower altitude.

The effect of atmospheric stability on gust velocity rms values is shown in Figure 13.4. The lowest rms values were recorded when the atmospheric stability was classified as very stable. The cumulative probability increases with decreasing atmospheric stability, although the differences between these values for the stability classifications of stable, neutral, and unstable are very small.

As the time of day during which the data were recorded varies from dawn to mid-morning, to mid-afternoon, the cumulative probability of encountering a gust rms of a given magnitude increases. This is shown in Figure 13.5.

Gust velocity rms CPDs are shown as a function of the four geographic locations. The greatest gust velocity rms values are associated with the Peterson and Griffiss routes, as shown in Figure 13.6. As mentioned previously, Peterson was the only location where data were obtained over more than one season. These winter and spring data are shown in Figure 13.7. The cumulative probability is greater for a given gust velocity rms value during the winter season.

Based on the findings of Phases I and II and on the data in Figures 13.2 through 13.6, it appears that combinations of terrain, altitude, and stability are primary factors in the determination of gust velocity rms cumulative probability distributions. The distributions for the combinations of the three category components are shown in Figures 13.8 through 13.27. In each of these figures, only one of these category components is varied, while the other two are held constant. Only data obtained over high mountains and plains are analyzed in this manner. Combinations of these three category components involving data obtained over the other types of terrain did not generally contain a sufficient number of turbulence samples. Likewise, the data obtained over the plains, at 750 feet, during the condition of very stable atmospheric stability did not contain the necessary 30 samples and is not shown in Figures 13.8 through 13.27. However, these figures show the effects of variations in the geophysical parameters for rough and smooth types of terrain.

The data in Figures 13.8 through 13.27 indicate approximately the same results as were indicated in Figures 13.2 through 13.6. Gust velocity rms values are greater over the rougher terrain, at the lower altitude, and for atmospheric stability conditions other than very stable.

The data obtained over the low mountains, desert, and water were not sufficient to permit an extensive investigation of geophysical effects. However, these data were analyzed as a function of altitude and type of terrain (Figures 13.28 through 13.33). The high mountain and plains data are also shown for comparative purposes. In general, it was found that for the various combinations of terrain, altitude, and atmospheric stability, gust velocity rms cumulative probability becomes greater, for a given rms value, as terrain becomes rougher, altitude decreases, and atmospheric stability becomes more unstable.

It has been found that the effects of noise are significant at the smaller gust velocity rms magnitudes. According to theory for normal distributions:

$$\sigma_R^2 = \sigma_t^2 + \sigma_N^2 \quad (13.1)$$

where:

$\sigma_t$  = standard deviation of the turbulence

$\sigma_N$  = standard deviation of the noise

$\sigma_R$  = standard deviation of the recorded data

If  $\sigma_N$  is assumed constant for a given category, this value becomes a greater and greater percentage of  $\sigma_R$  as  $\sigma_t$  becomes smaller and smaller. Therefore, at lower turbulence intensities the distribution is distorted by the high percentage of noise content in the data where the noise has a greater effect on the distribution than does the turbulence.

During the LO-LOCAT Phase III Program, gust velocities were not computed for turbulence samples when the level of turbulence and hence, the signal-to-noise ratio, was known to be small. The criteria used to determine the level of turbulence were the values of the angles of attack and sideslip differential pressures as sensed by the gust probe pressure ports. Gust velocities were calculated only for turbulence samples where the standard deviation of both the angle of attack differential pressure ( $\sigma_\alpha$ ) and angle of sideslip differential pressure ( $\sigma_\beta$ ) were greater than 0.07 and 0.05 inches of Hg, respectively. This is discussed further in Appendix III, Section III.5.

Because of the low signal-to-noise ratio of some turbulence samples, the cumulative probability distributions have not been plotted below a gust velocity rms value of 1.5 fps, since this is the lowest band limit which is greater than the minimum valid gust velocity rms value of 1.4 fps. The number of turbulence samples having rms values below 1.5 feet per second were used to compute the probabilities for the data above 1.5 fps. The number of turbulence samples not processed due to the  $\sigma_\alpha$  and  $\sigma_\beta$  criteria were assumed to have gust velocity rms values below 1.5 fps and were included in the cumulative probability distribution calculations by being added into the total number of turbulence samples within the category being investigated. For example, the following distribution which excludes those samples not meeting the  $\sigma_\alpha$  and  $\sigma_\beta$  criteria but includes those having a  $\sigma_t$  less than 1.5 fps and meeting the  $\sigma_\alpha$  and  $\sigma_\beta$  criteria.

<u>Band (fps)</u>	<u>No. of Samples</u>	<u>Cumulative Distribution</u>	<u>Cumulative Probability</u>
0 - 0.5	0	200	$\frac{200}{200} = 1.000$
0.5 - 1.0	10	200	$\frac{200}{200} = 1.000$
1.0 - 1.5	20	190	$\frac{190}{200} = 0.950$
1.5 - 2.0	40	170	$\frac{170}{200} = 0.850$
2.0 - 2.5	80	130	$\frac{130}{200} = 0.650$
2.5 - 3.0	40	50	$\frac{50}{200} = 0.250$
3.0 - 3.5	10	10	$\frac{10}{200} = 0.050$

Suppose that, because of the  $\sigma_a$  and  $\sigma_b$  criteria, 50 samples were not processed. Then the following tabulation illustrates the method used to account for these 50 samples when calculating the gust velocity rms probability distributions.

<u>Band (fps)</u>	<u>No. of Samples</u>	<u>Cumulative Distribution</u>	<u>Cumulative Probability</u>
0 - 0.5	0 + *	250	$\frac{250}{250} = 1.000$
0.5 - 1.0	10 + *	-	-
1.0 - 1.5	20 + *	-	-
1.5 - 2.0	40	170	$\frac{170}{250} = 0.680$
2.0 - 2.5	80	130	$\frac{130}{250} = 0.520$
2.5 - 3.0	40	50	$\frac{50}{250} = 0.200$
3.0 - 3.5	10	10	$\frac{10}{250} = 0.040$

\* Unknown parts of 50

It should be pointed out that this procedure was only necessary for categories which included data obtained over plains, desert, and water legs. It was over these types of terrain where the data having low signal-to-noise ratios was gathered. Categories consisting exclusively of data obtained over high or low mountains were not involved. The number of low turbulence samples within the categories pertaining to the peak count, amplitude count, and level crossing data analysis are shown in Tables 8.1 and 8.2. The number of samples included in those tables is not entirely applicable to the gust velocity rms value analysis because of the following reasons.

- Peak count, amplitude count, and level crossings data were put on a master tape, as explained in Section III. The program by which this was accomplished was designed to put the data on tape in the order of the six-digit category. The atmospheric stability category component was not defined for some of these low turbulence samples because of instrumentation malfunctions. Therefore, these particular samples could not be used in the peak count, amplitude count, and level crossings data. The gust velocity rms values were not constrained by this six-digit category number. Thus, even though stability was not defined for some low turbulence samples, these samples were still included in category combinations including components other than stability.
- When the gust velocity rms values were being individually reviewed it was noticed that a number of values obtained over the water leg at Edwards were less than 1.0 fps. These data, questionable because of their low signal-to-noise ratios, were treated as low intensity turbulence samples in the gust velocity rms analysis.

Table 13.1 shows the number of low intensity turbulence samples and the corresponding total number of samples included in the category combinations utilized in the gust velocity rms analysis. A tabulation of all valid  $\sigma_c$  values is presented in Appendix VI. The number of low intensity turbulence samples consists of those not processed due to  $\sigma_u$  and  $\sigma_\beta$  criteria and those low intensity samples recorded over the water legs as mentioned above.

According to the theory of isotropic turbulence,  $\sigma_{t_u} = \sigma_{t_v} = \sigma_{t_w}$ . Reference 13.1 suggests that this relationship does not hold true for turbulence up to about 1000 feet above the terrain. This reference proposes that the relationship between the rms values of the three components is a function of atmospheric stability and absolute altitude.

For very stable, stable, and neutral atmospheric conditions:

$$\frac{\sigma_{t_u}}{\sigma_{t_v}} = \frac{\sigma_{t_v}}{\sigma_{t_w}} = 1.2 - 0.00017 H \quad (13.2)$$

TABLE 13.1

TOTAL NUMBER OF SAMPLES AND NUMBER OF LOW INTENSITY  
TURBULENCE SAMPLES INCLUDED IN GUST VELOCITY RMS ANALYSIS

Category	Total Number of Samples			Number of Low Intensity Turbulence Samples
	u	v	w	
000000	1762	1740	1746	113
100000	853	851	853	0
200000	297	297	297	0
300000	115	115	115	1
400000	415	395	401	50
600000	83	83	81	62
010000	909	894	900	37
020000	853	846	846	76
001000	570	564	568	35
002000	450	477	478	7
003000	394	389	391	0
004000	296	289	288	0
000100	491	485	490	67
000200	648	641	642	24
000300	623	614	614	22
000001	601	607	605	62
000002	135	134	135	0
000003	751	747	750	1
000004	270	253	257	50
000043	397	395	396	0
000013	354	352	354	1
111000	114	113	114	0
112000	140	140	140	0
113000	129	129	129	0
114000	64	64	64	0
121000	114	114	114	0
122000	147	147	147	0
123000	95	94	95	0
124000	50	50	50	0
411000	51	46	51	6
412000	40	40	40	0
413000	58	55	56	0
414000	50	44	44	0
421000	56	56	56	28
422000	33	30	31	0
423000	39	38	38	0
424000	71	70	69	1
110000	447	446	447	0
120000	406	405	406	0
210000	157	157	157	0
220000	140	140	140	0
310000	64	64	64	0
320000	51	51	51	1
410000	199	185	191	6
420000	214	208	208	11
610000	42	42	41	31
620000	41	41	40	31



For unstable atmospheric conditions:

$$\frac{\sigma_{tu}}{\sigma_{tv}} = \frac{\sigma_{tv}}{\sigma_{tv}} = 1.3 - 0.00058 H \quad (13.3)$$

Values from Equations 13.2 and 13.3 are compared to IO-LOCAT Phase III data in Table 13.2.

TABLE 13.2

IO-LOCAT GUST VELOCITY RMS RATIOS COMPARED TO THOSE RECOMMENDED BY REFERENCE 13.1

Absolute Altitude (H) ~ Ft.	Atmospheric Stability	Values Predicted by Equations 13.2 and 13.3	IO-LOCAT Phase III Data	
			$\frac{\sigma_{tu}}{\sigma_{tv}}$	$\frac{\sigma_{tv}}{\sigma_{tv}}$
250	Very Stable, Stable, and Neutral	1.16	1.07	1.13
250	Unstable	1.15	1.11	1.14
750	Very Stable, Stable, and Neutral	1.07	1.05	1.15
750	Unstable	0.86	0.99	1.06

The data show approximately the same magnitudes as predicted by the equations. At the 750 foot altitude, smaller ratios occur for unstable than for very stable, neutral, and unstable conditions.

Reference 13.1 also presents the vertical gust velocity rms cumulative probability distributions from several different turbulence research programs, as well as a distribution recommended for data at an absolute altitude of 500 feet. The data from the IO-LOCAT Phase III Program are compared to those distributions in Figure 13.34.

The gust velocity rms cumulative probability distributions for all three components can be closely represented by portions of two normal distributions, i.e.:

$$F(x) = \frac{1}{\sqrt{2\pi}} \left[ \frac{1}{\sigma_2} \int_{1-1.5}^a \exp. - \frac{1}{2} \left( \frac{x_1 - \mu_2}{\sigma_2} \right)^2 dx + \frac{1}{\sigma_3} \int_{b-a}^b \exp. - \frac{1}{2} \left( \frac{x_2 - \mu_3}{\sigma_3} \right)^2 dx \right] \quad (13.4)$$

where:

$$x = \sigma_t$$

$\sigma$  = dispersion of the distributions

$\mu$  = mean of the distributions

and: subscript 2 refers to that portion of the probability distribution between rms values from 1.5 to a, and subscript 3 refers to that portion of the distribution between rms values from a to b.

The constants for Equation 13.4 are shown in Table 13.3 for each component. The agreement between the distribution of the recorded data and the distributions represented by the equation is shown in Figures 13.35, 13.36, and 13.37.

TABLE 13.3

GUST VELOCITY RMS DISTRIBUTION CONSTANTS

Constant	Gust Velocity Component		
	u	v	w
a	4.79	4.75	5.30
$\mu_2$	3.35	3.46	3.23
$\sigma_2$	1.70	1.65	1.70
$\mu_3$	1.79	0.98	0.65
$\sigma_3$	3.59	4.79	3.79
b	14.00	17.00	14.00

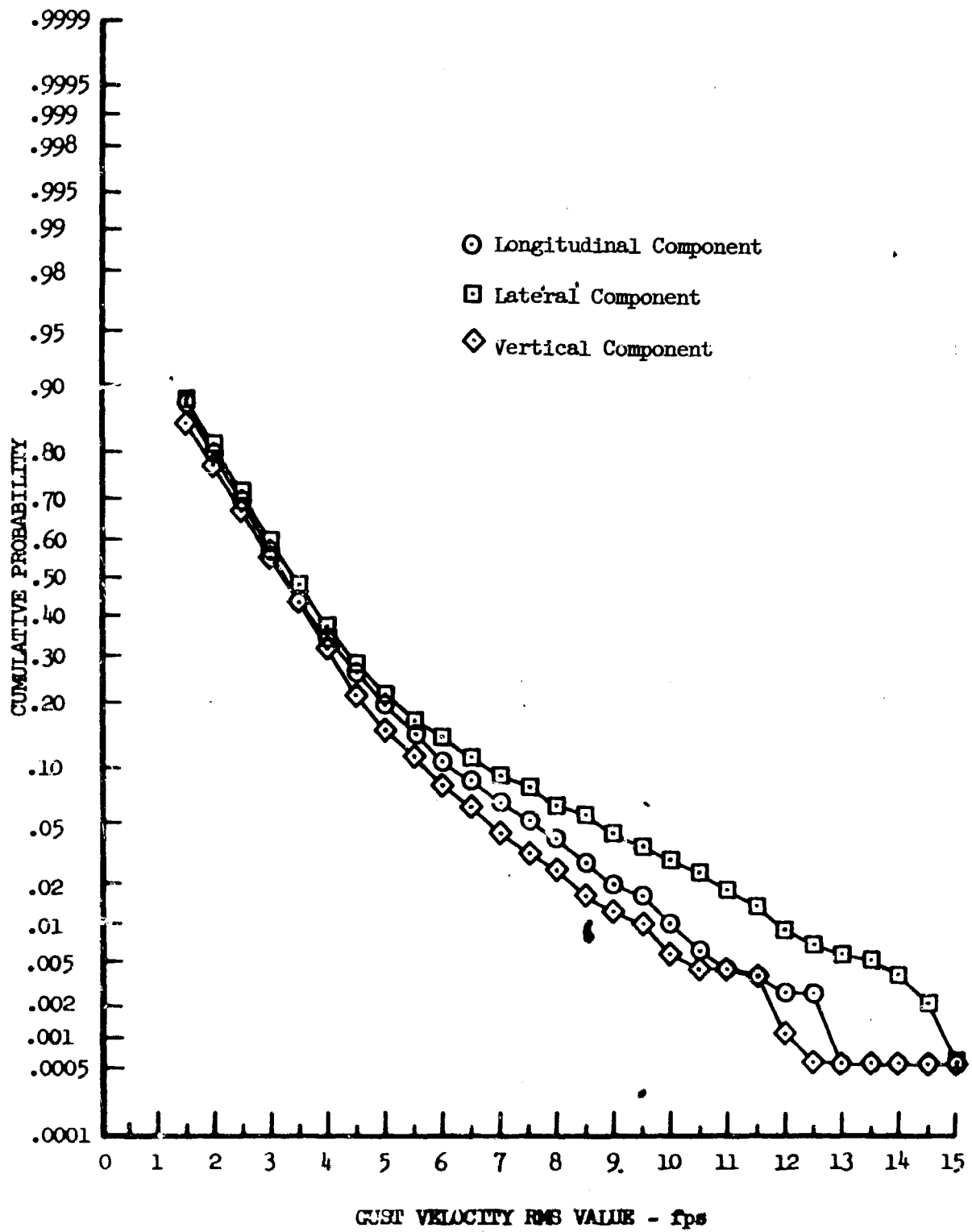


Figure 13.1 Gust Velocity RMS Cumulative Probability

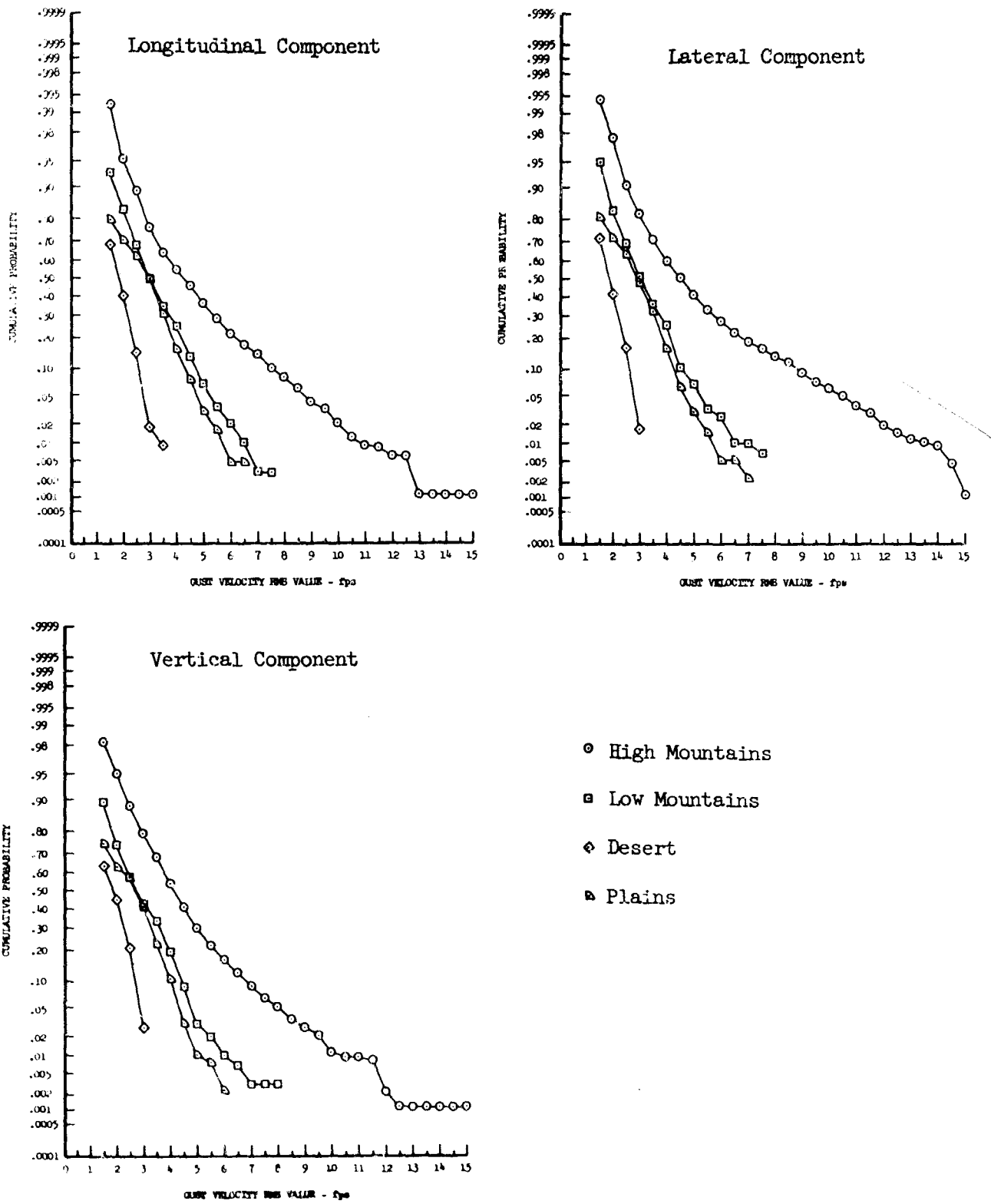
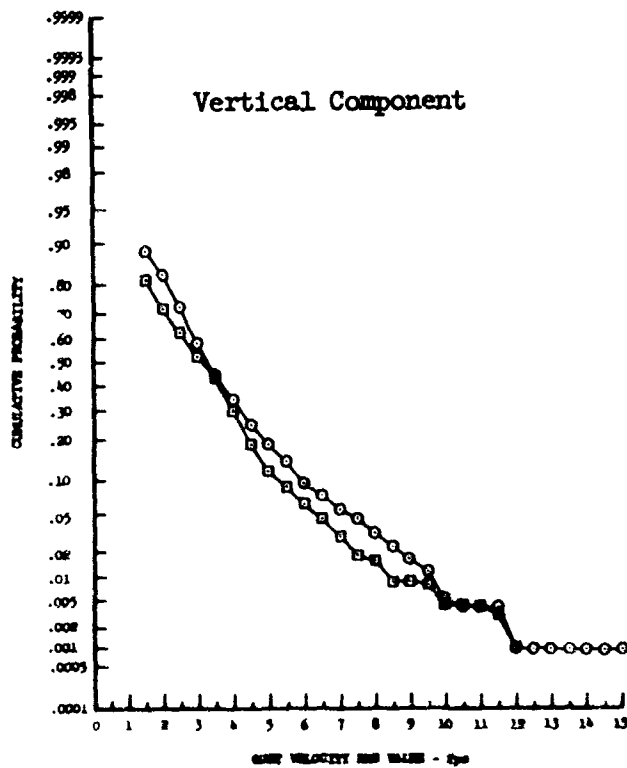
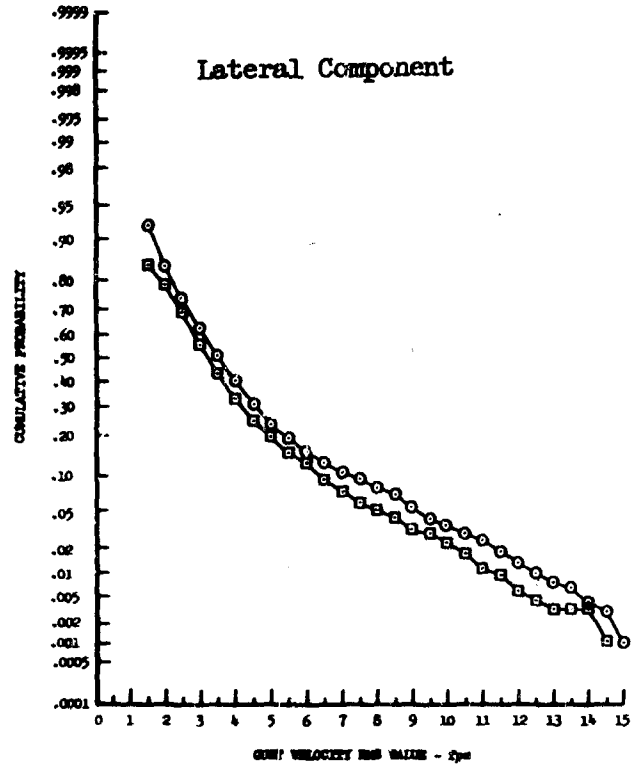
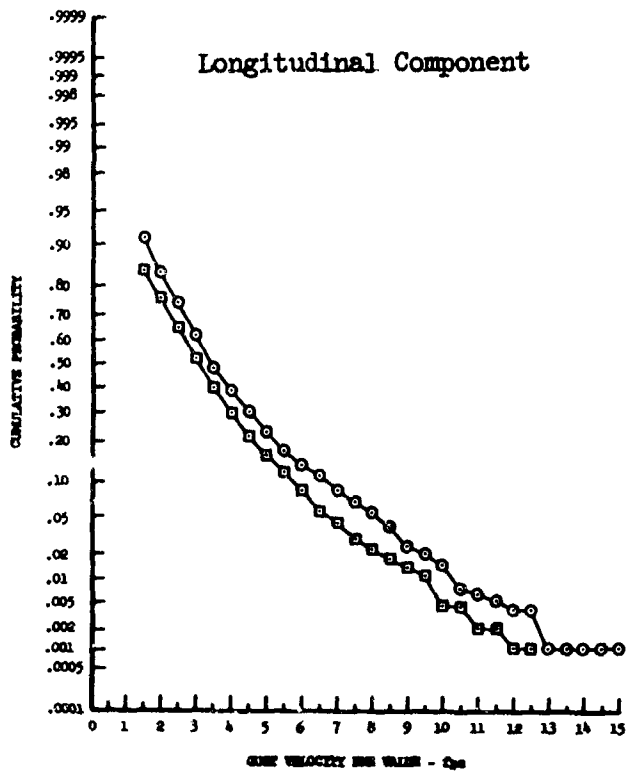
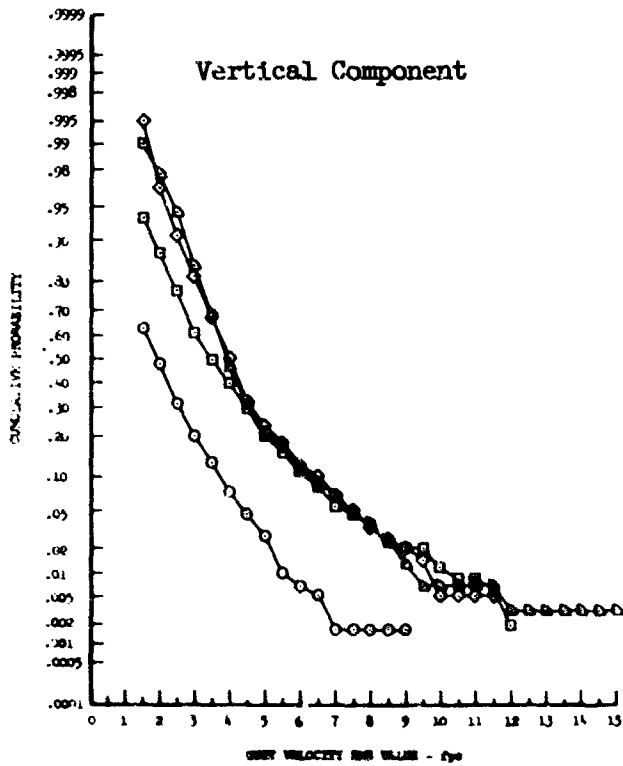
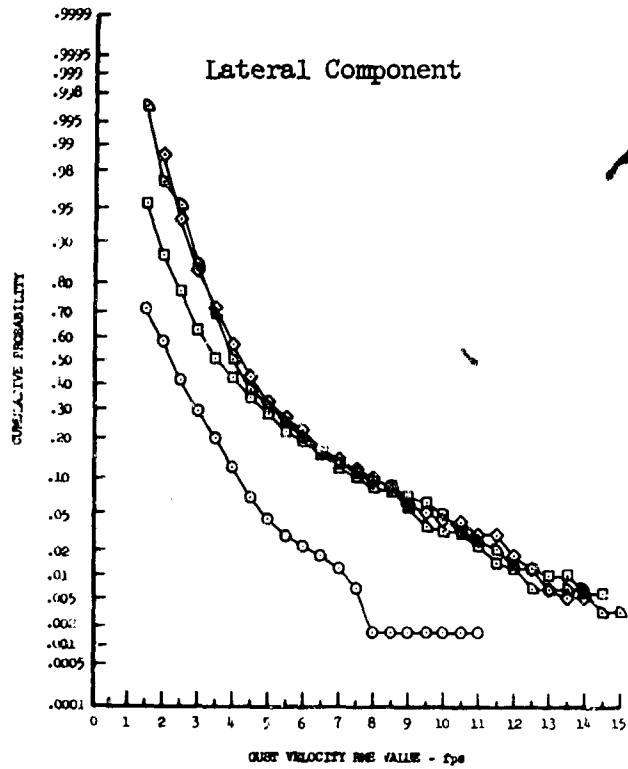
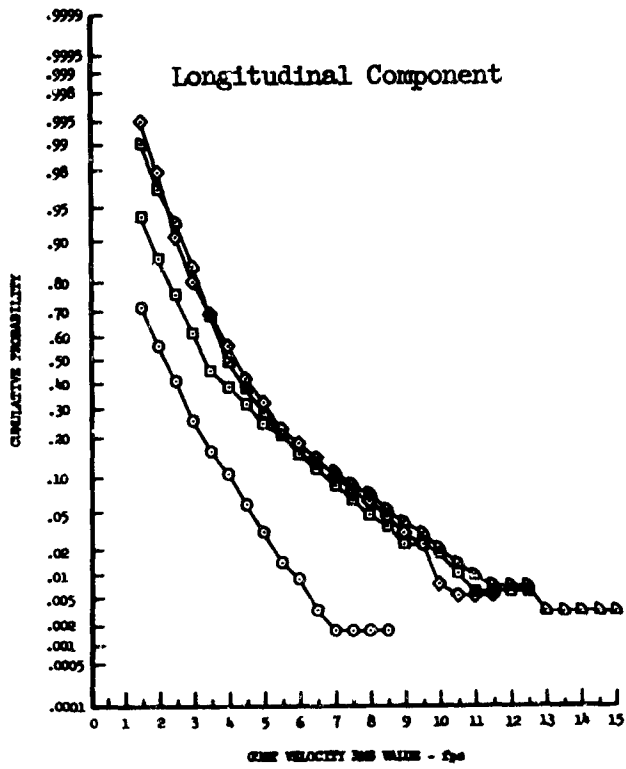


Figure 13.2 Gust Velocity RMS Cumulative Probability Associated with Type of Terrain



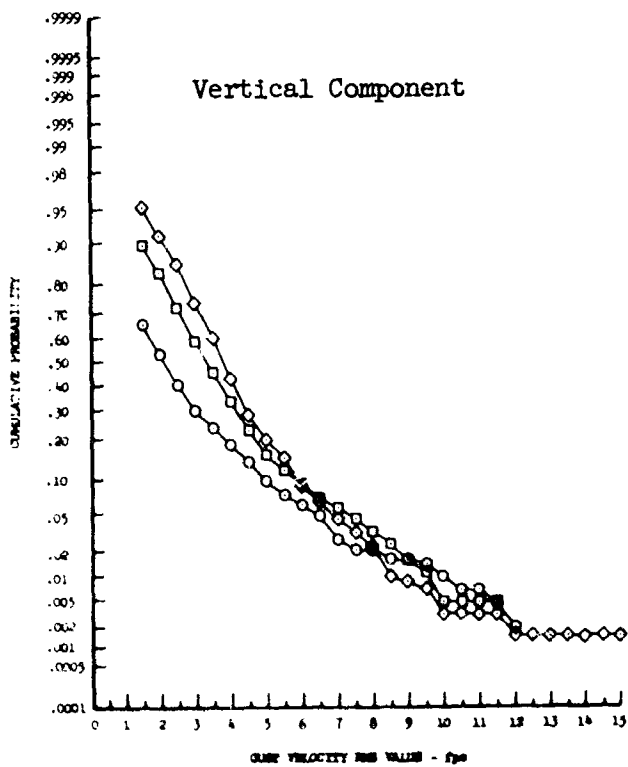
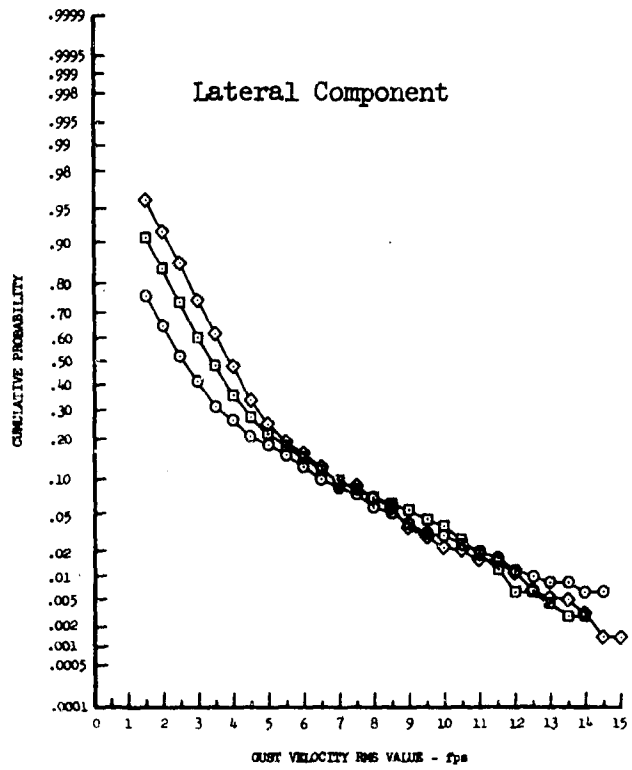
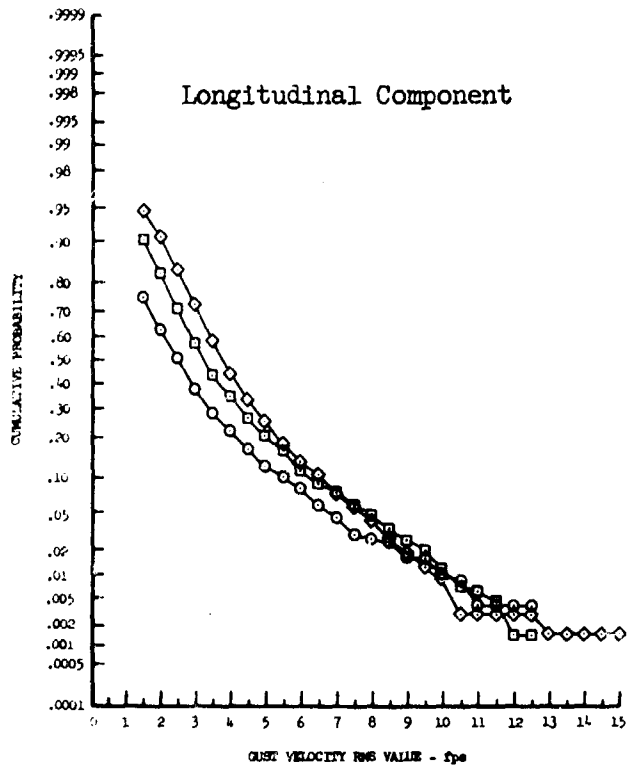
- 250 Feet
- 750 Feet

Figure 13.3 Gust Velocity RMS Cumulative Probability Associated with Absolute Altitude



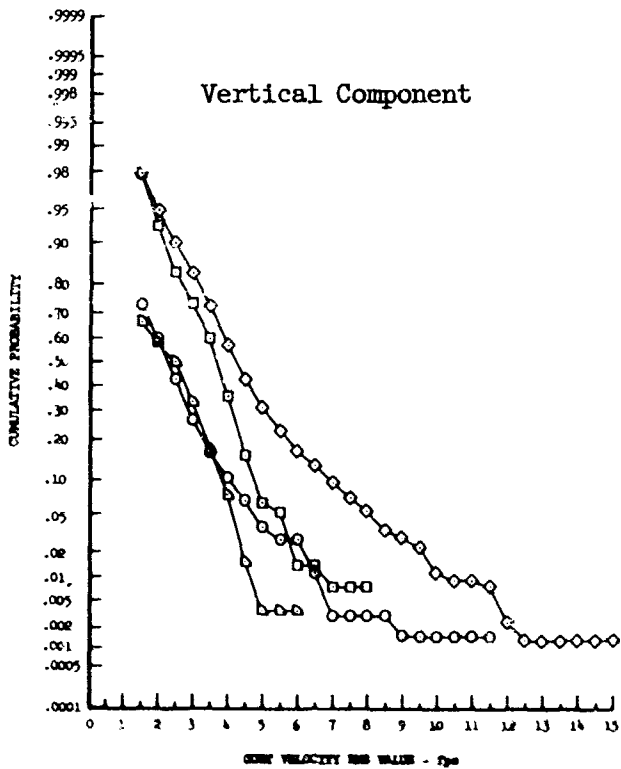
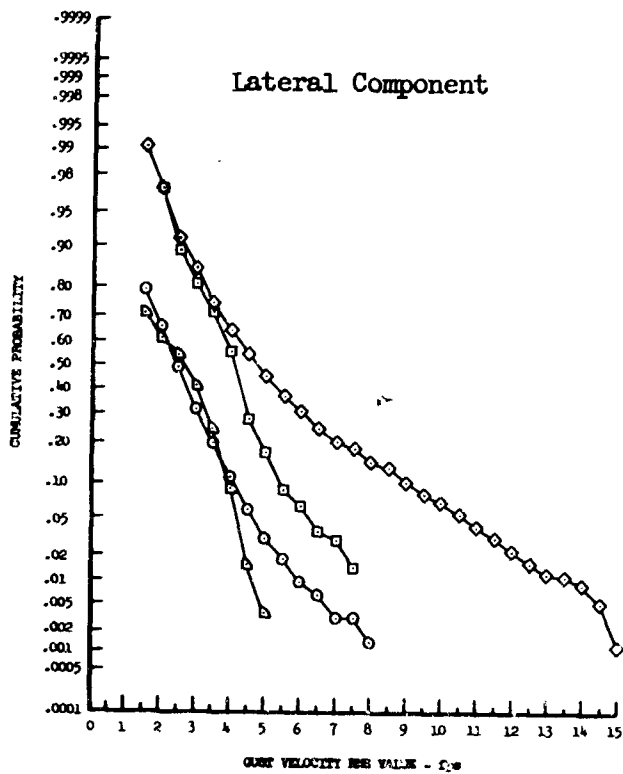
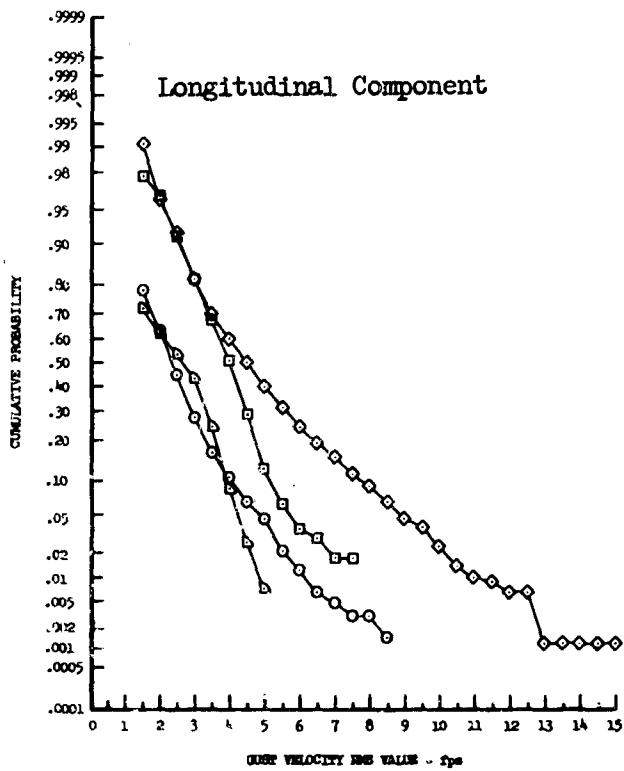
- Very Stable
- Stable
- ◇ Neutral
- Unstable

Figure 13.4 Gust Velocity RMS Cumulative Probability Associated with Atmospheric Stability



- Dawn
- Mid-Morning
- ◇ Mid-Afternoon

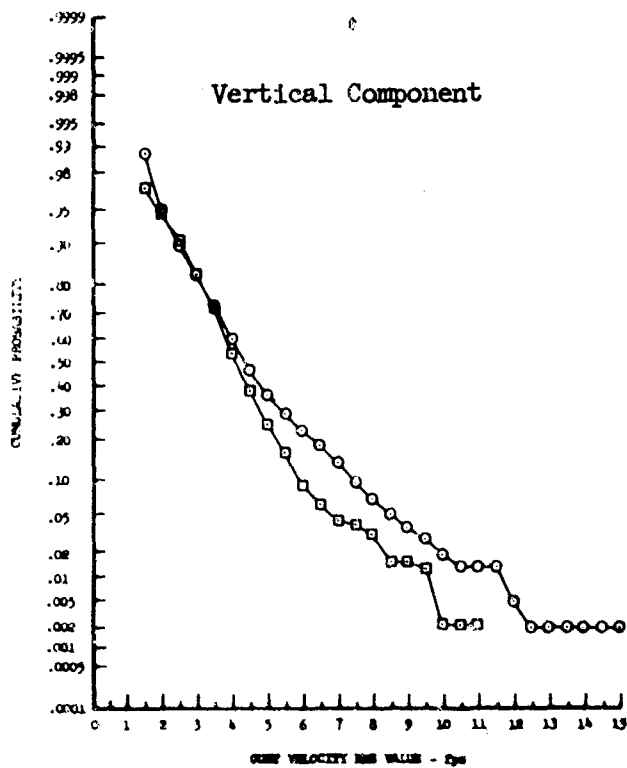
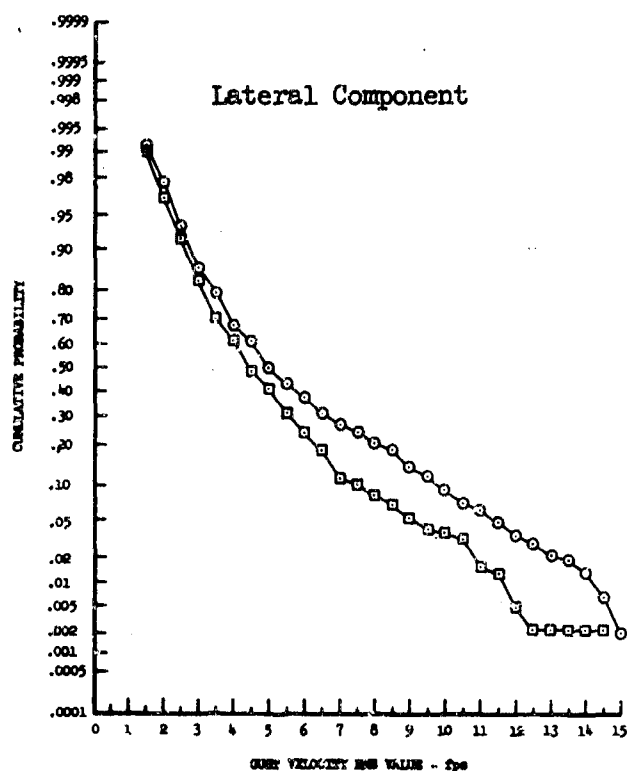
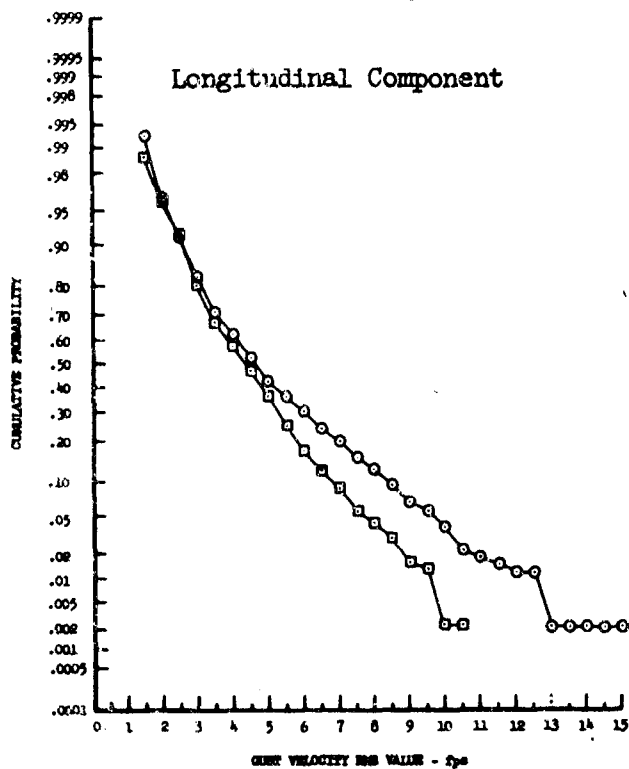
Figure 13.5 Gust Velocity RMS Cumulative Probability Associated with Time of Day



- Edwards
- Griffiss
- ◇ Peterson
- ▲ McConnell

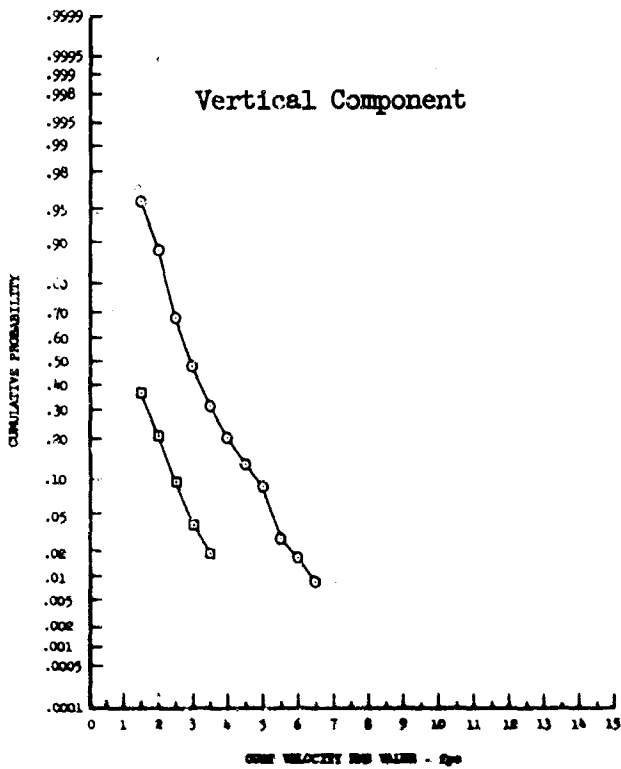
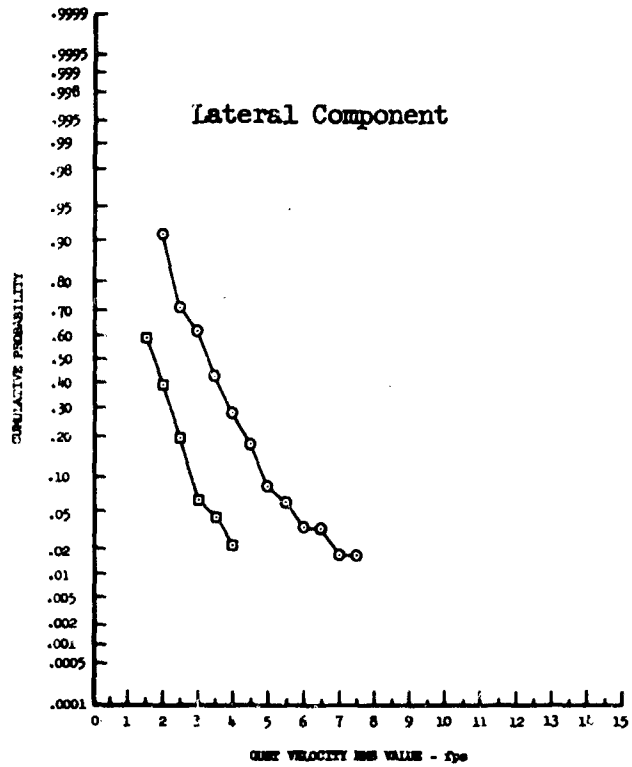
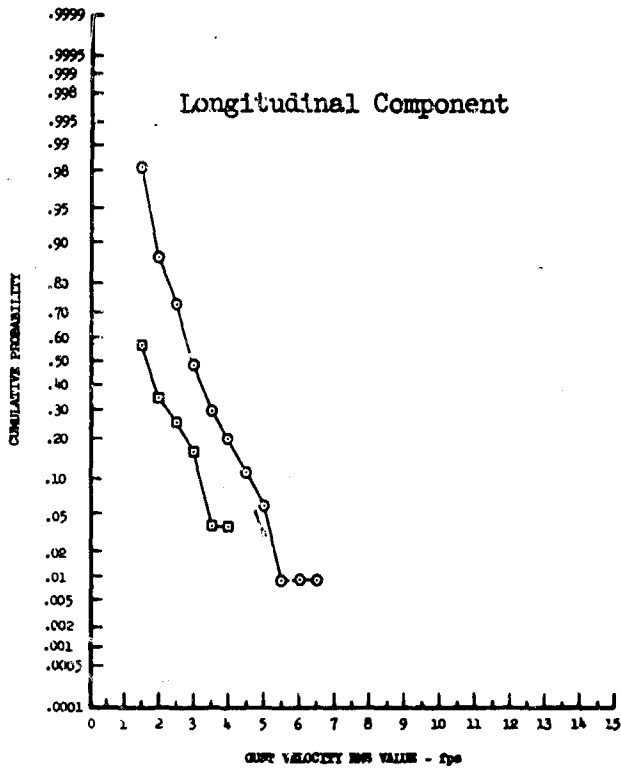
Figure 13.6 Gust Velocity RMS Cumulative Probability Associated with Geographic Location





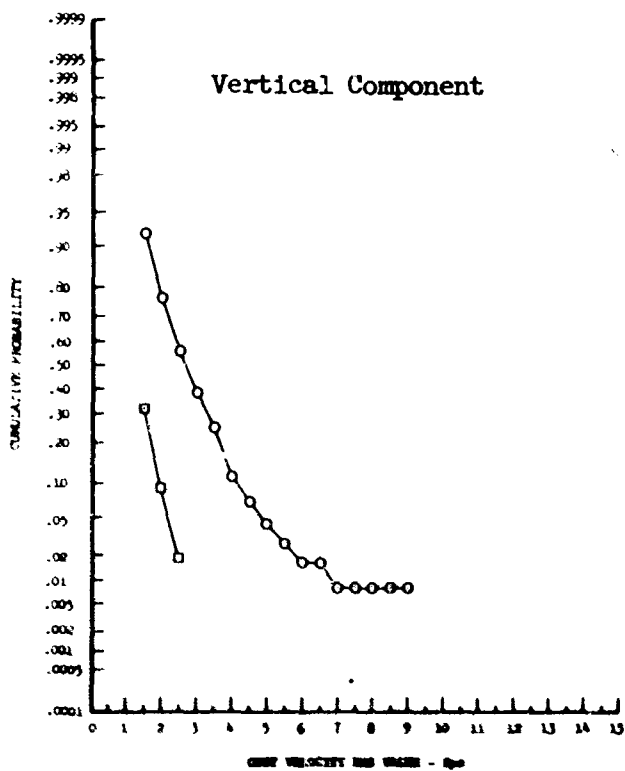
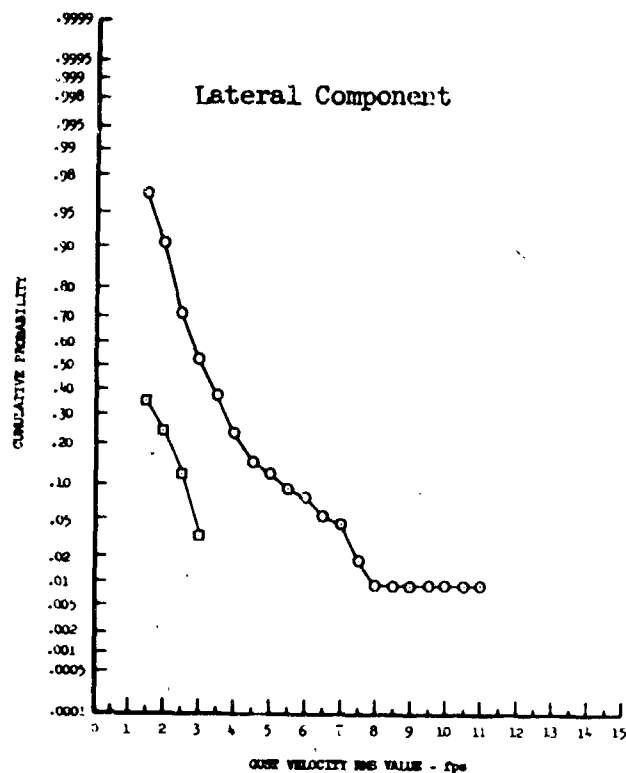
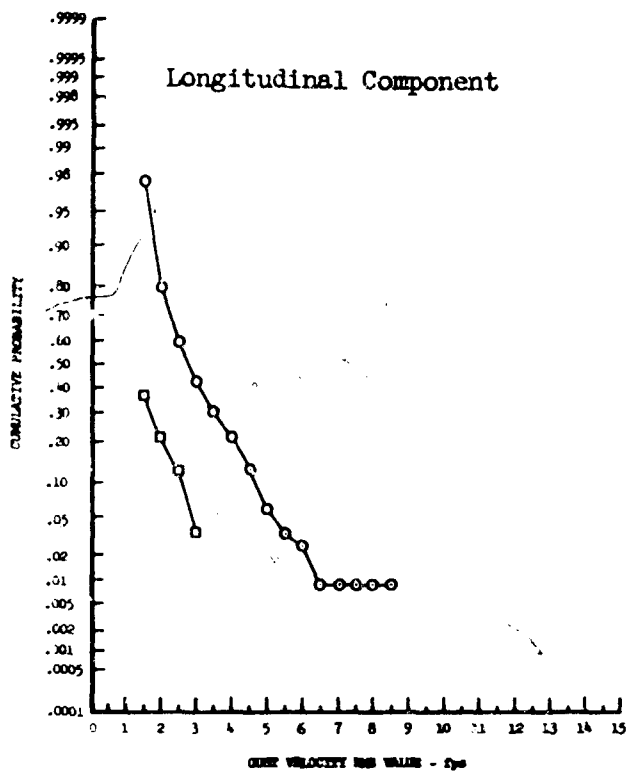
○ Winter  
 ■ Spring

Figure 13.7 Season Effects on Gust Velocity RMS Values - Peterson



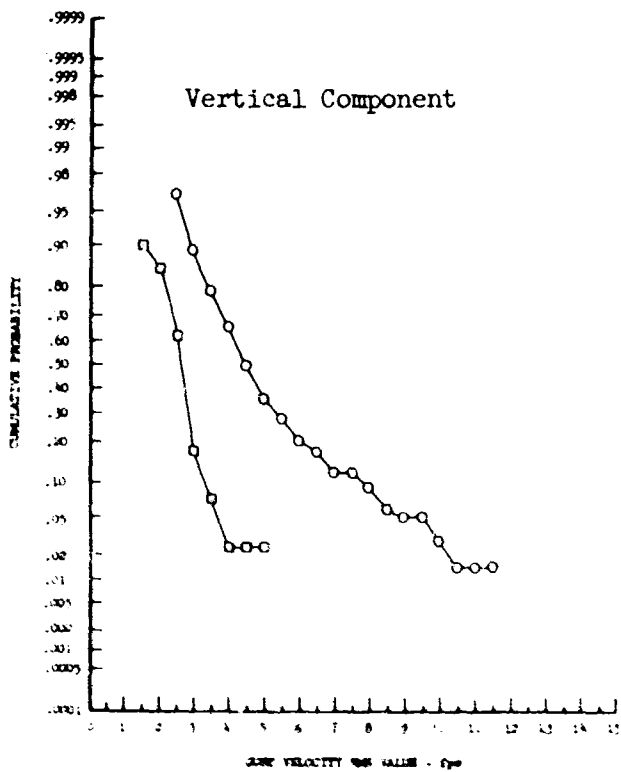
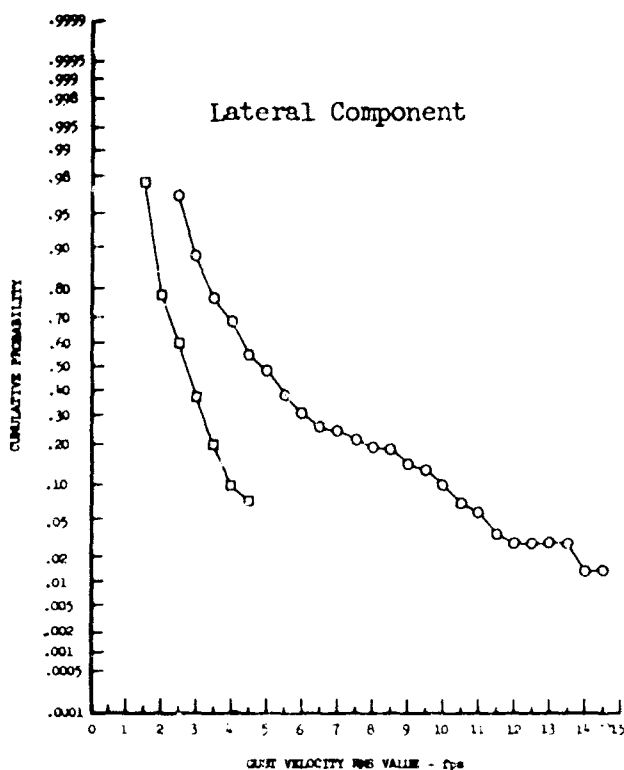
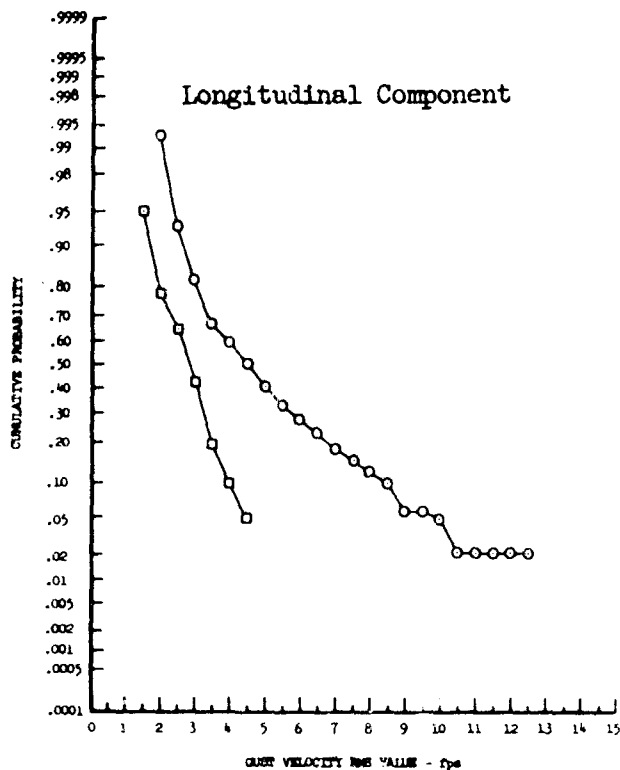
- High Mountains
- Plains

Figure 13.8 Terrain Effects on Gust Velocity RMS Values - 250 Feet, Very Stable



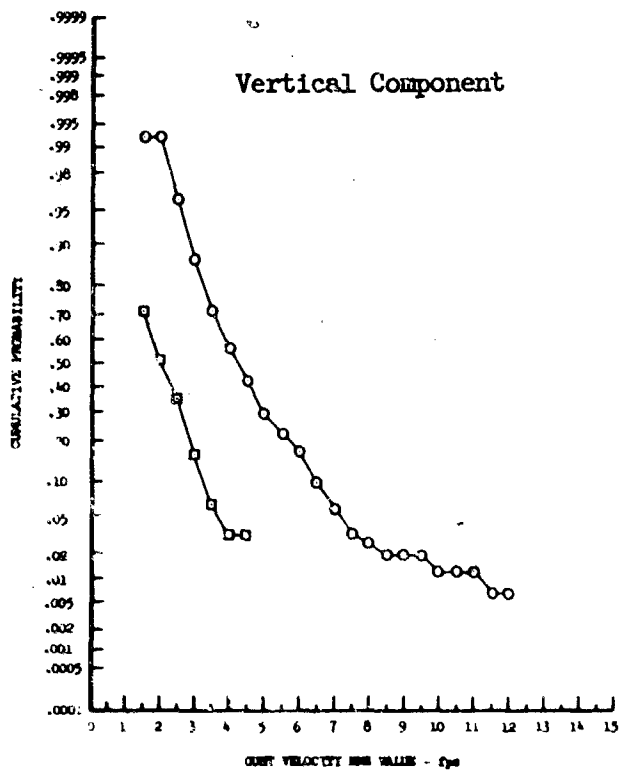
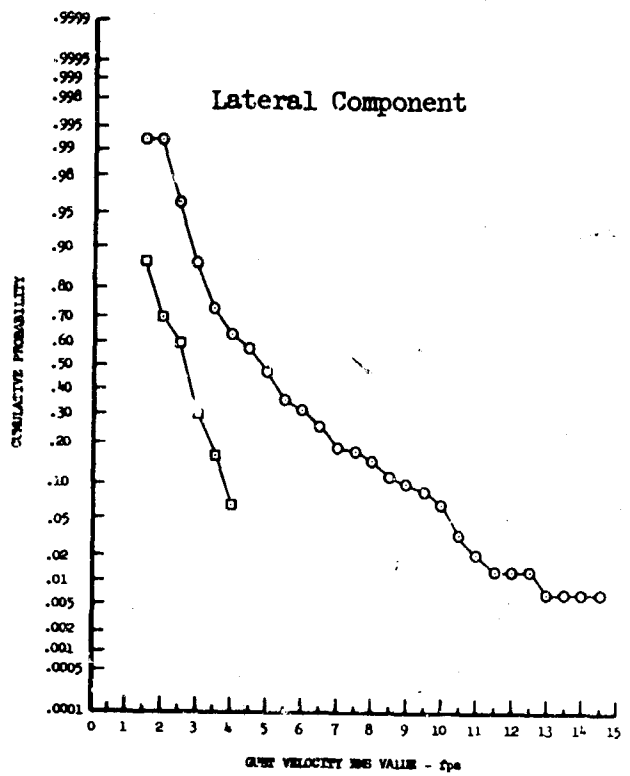
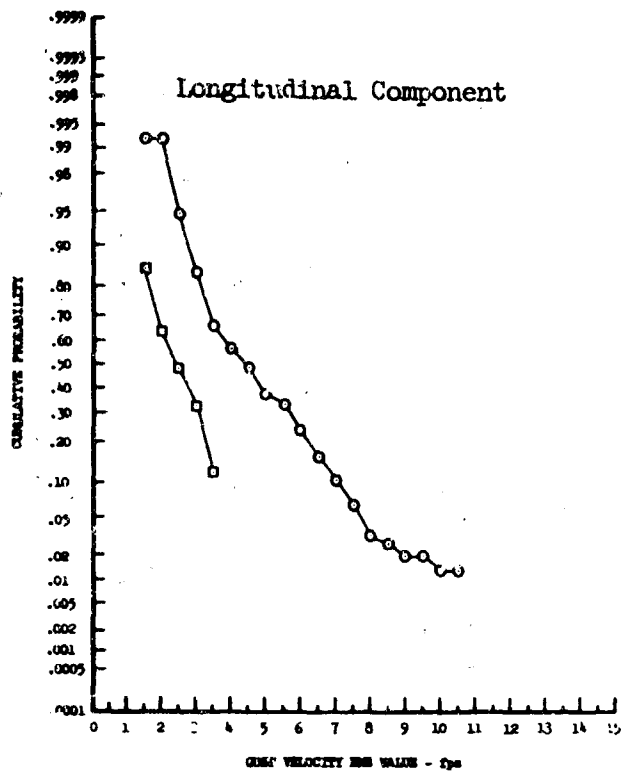
- High Mountains
- Plains

Figure 13.9 Terrain Effects on Gust Velocity RMS Values - 750 Feet, Very Stable



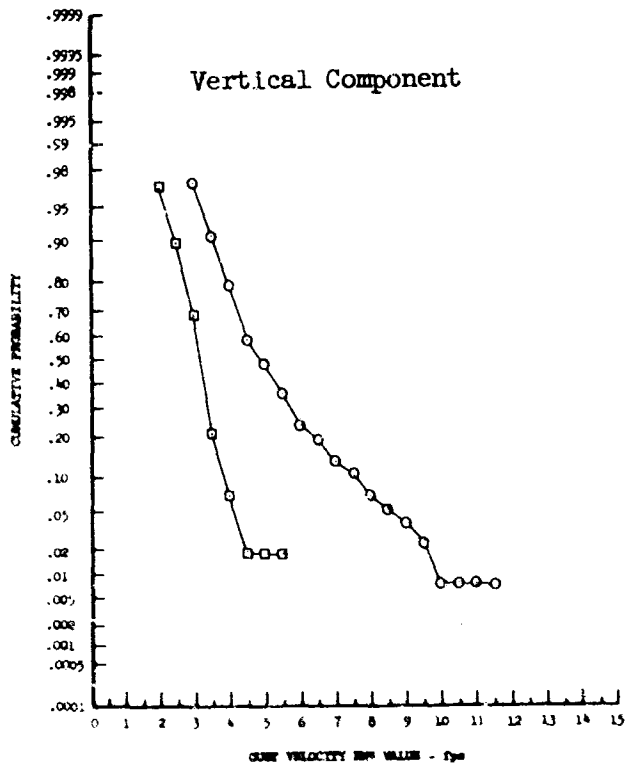
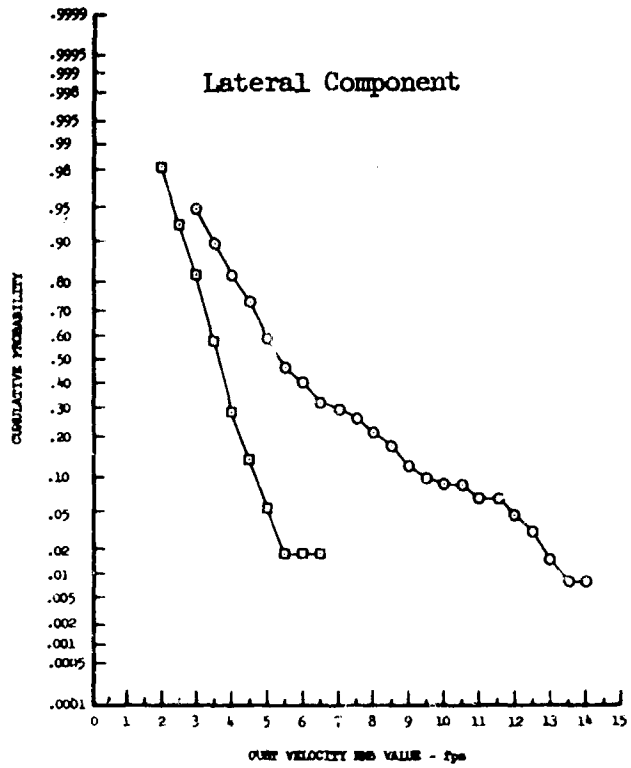
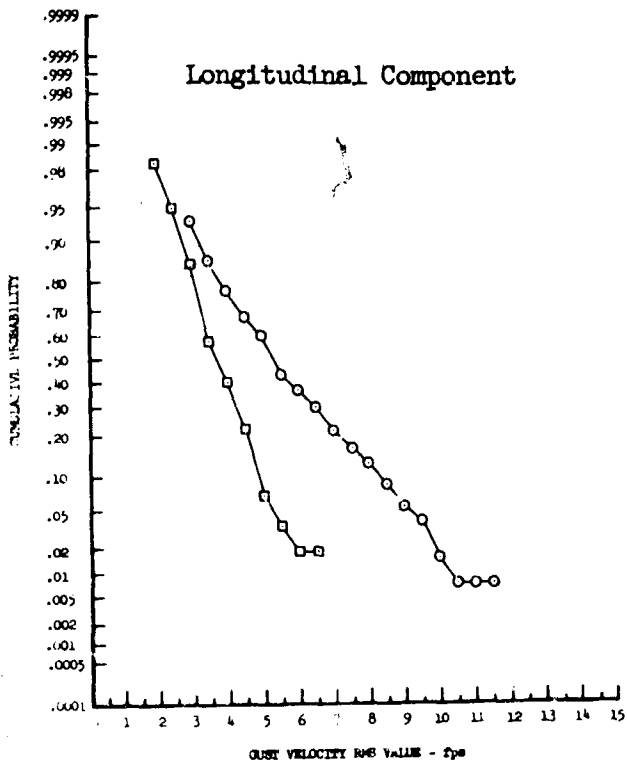
- High Mountains
- Plains

Figure 13.10 Terrain Effects on Gust Velocity RMS Values - 250 Feet, Stable



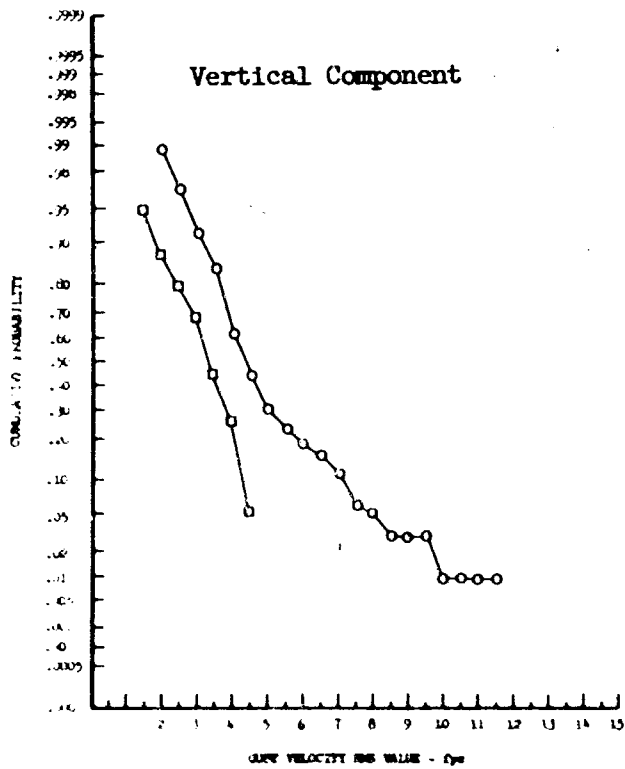
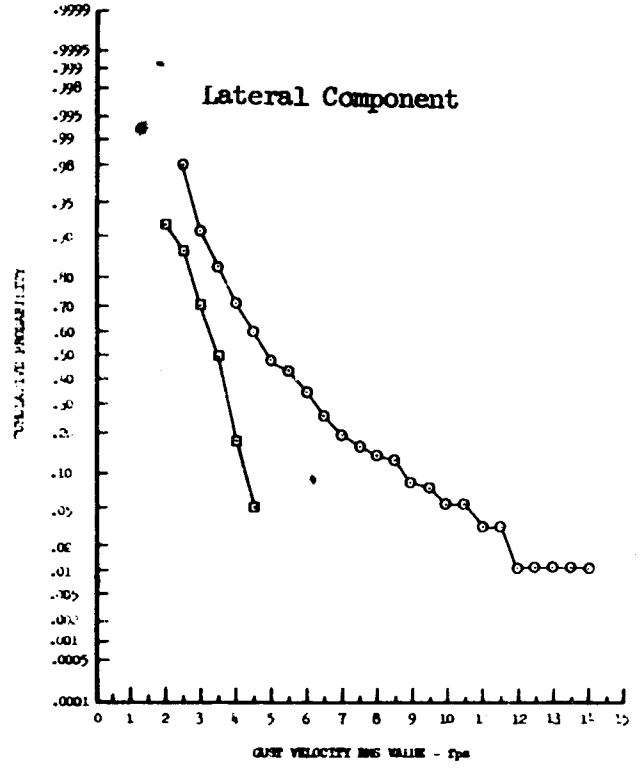
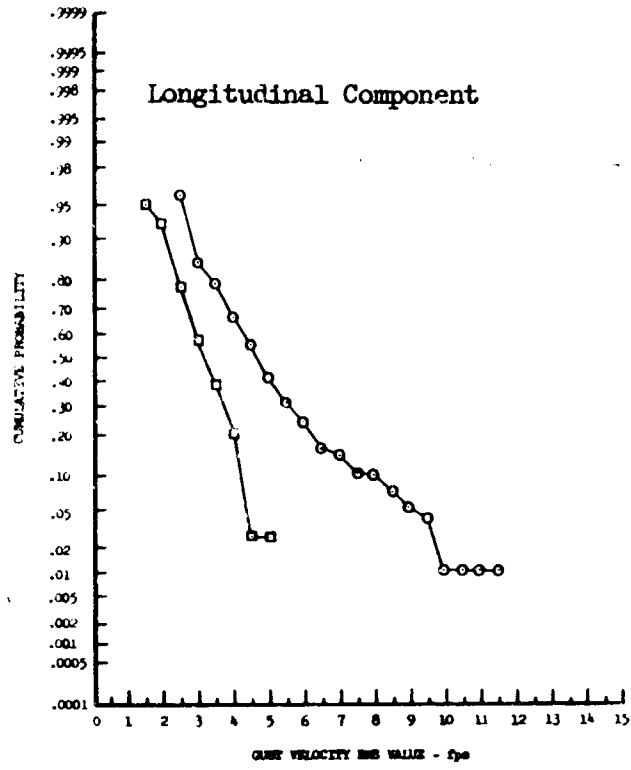
○ High Mountains  
 ■ Plains

Figure 13.11 Terrain Effects on Gust Velocity RMS Values - 750 Feet, Stable



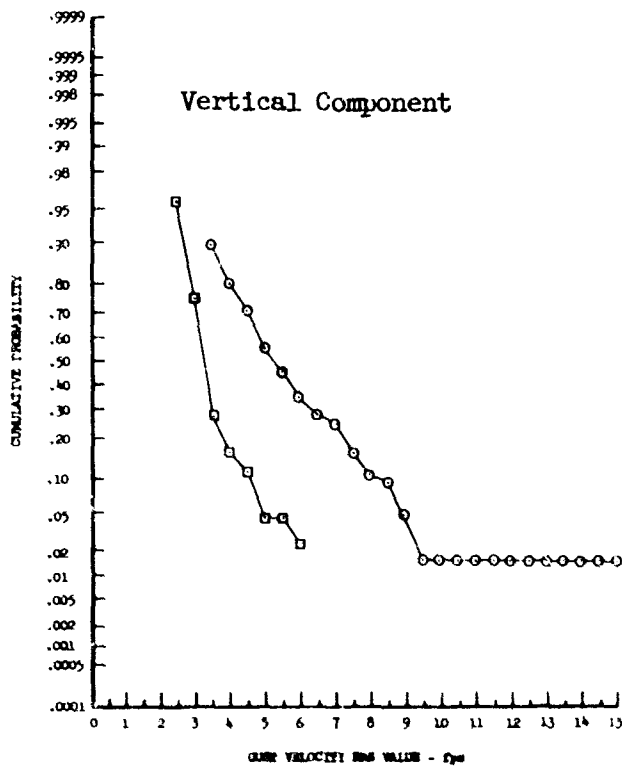
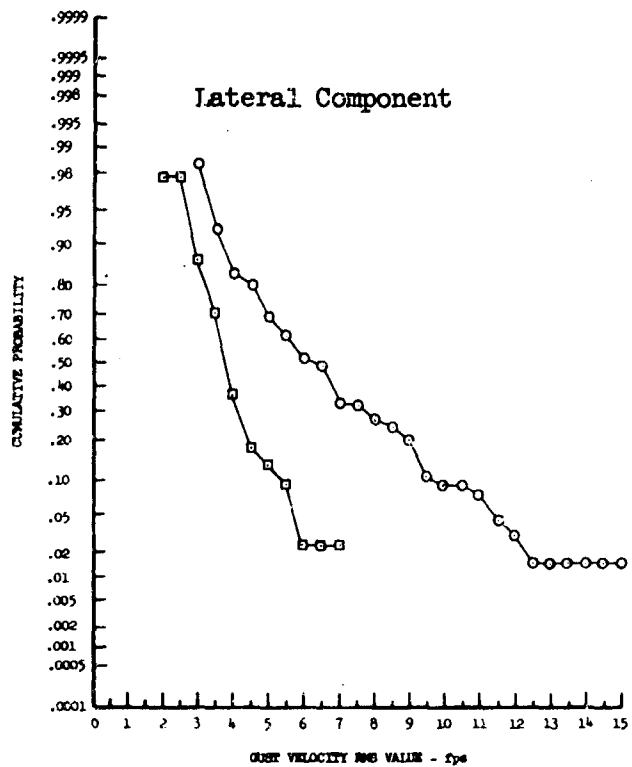
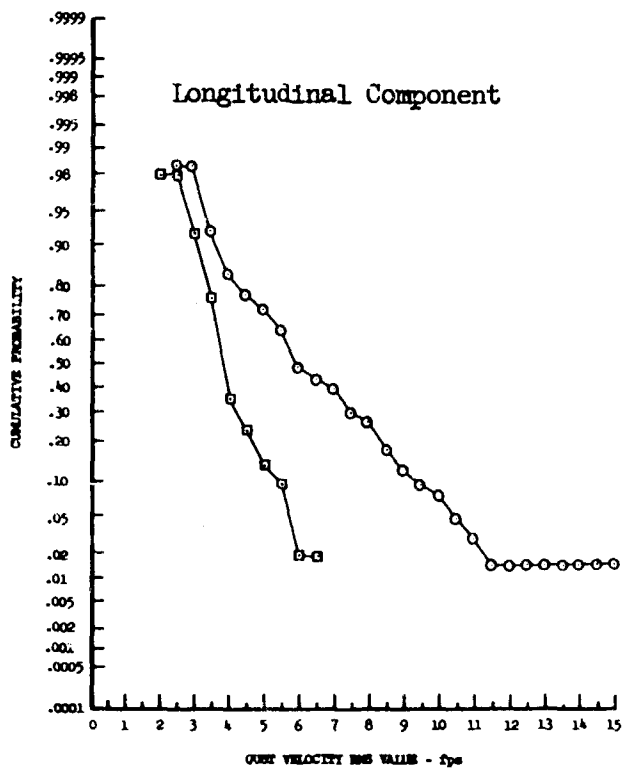
- High Mountains
- Plains

Figure 13.12 Terrain Effects on Gust Velocity RMS Values - 250 Feet, Neutral



- High Mountains
- Plains

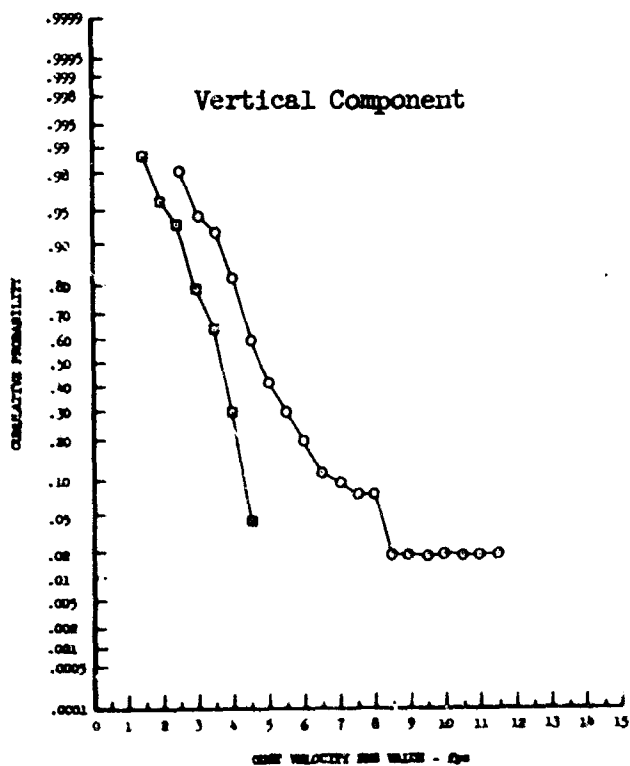
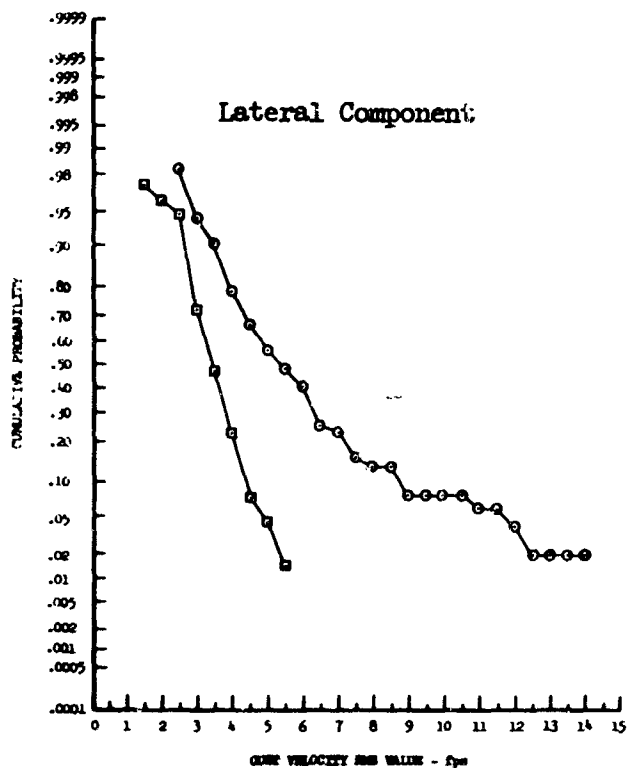
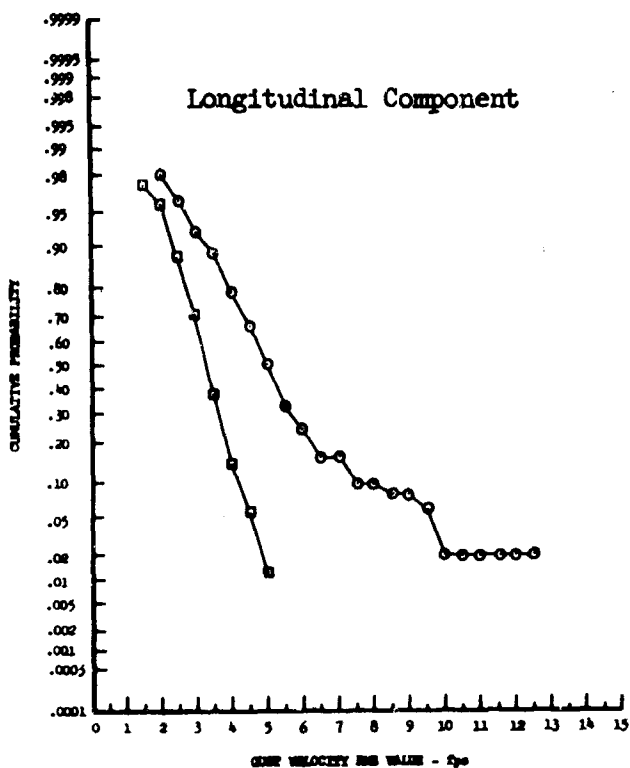
Figure 13.13 Terrain Effects on Gust Velocity RMS Values - 750 Feet, Neutral



- High Mountains
- Plains

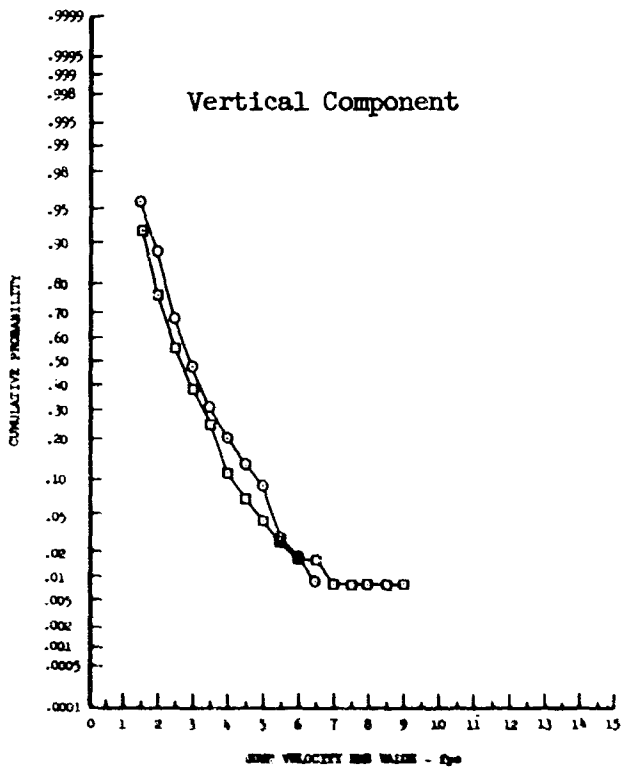
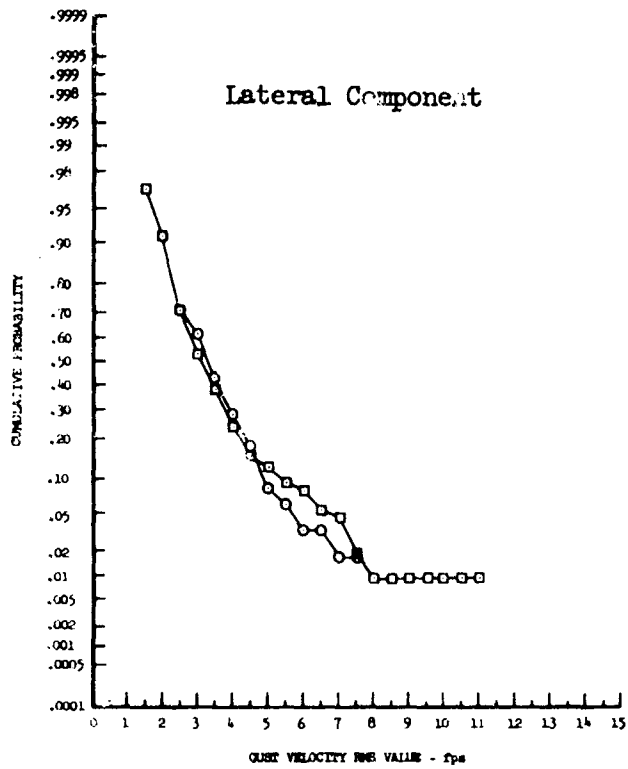
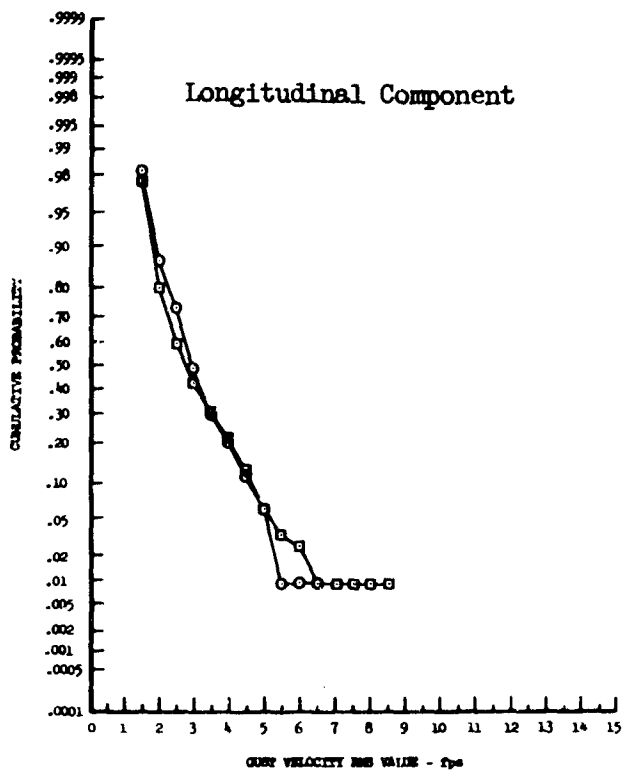
Figure 13.14 Terrain Effects on Gust Velocity RMS Values - 250 Feet, Unstable





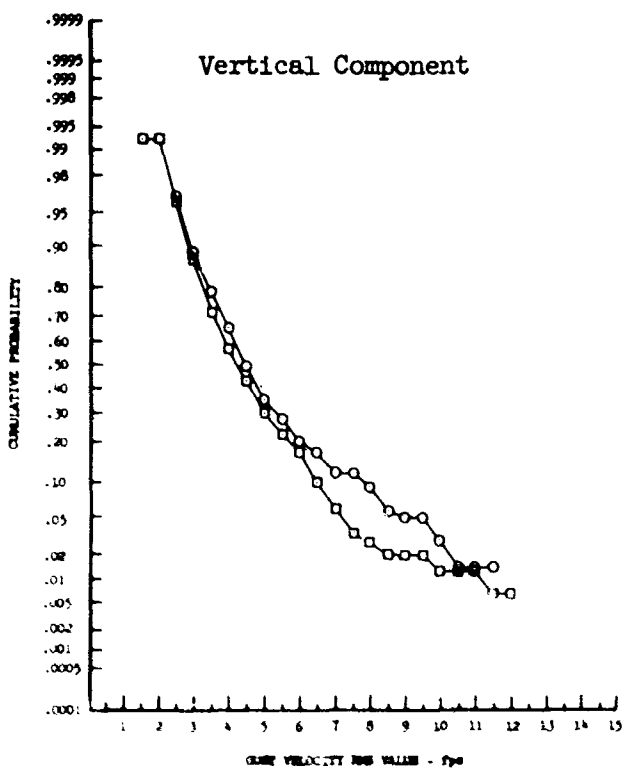
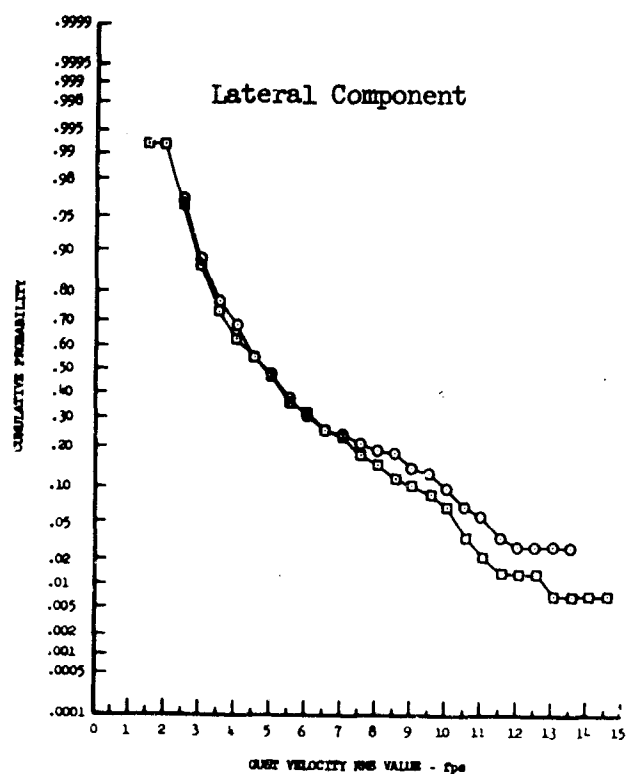
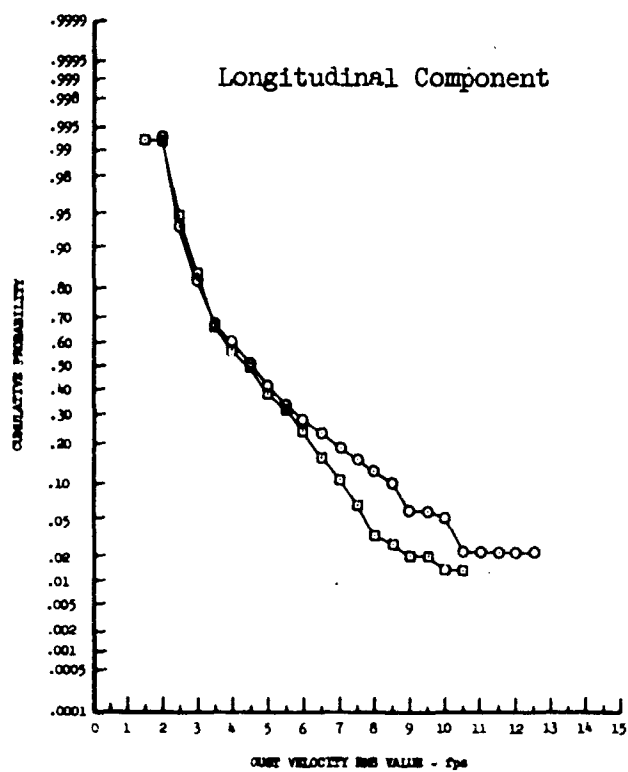
- High Mountains
- Plains

Figure 13.15 Terrain Effects on Gust Velocity RMS Values - 750 Feet, Unstable



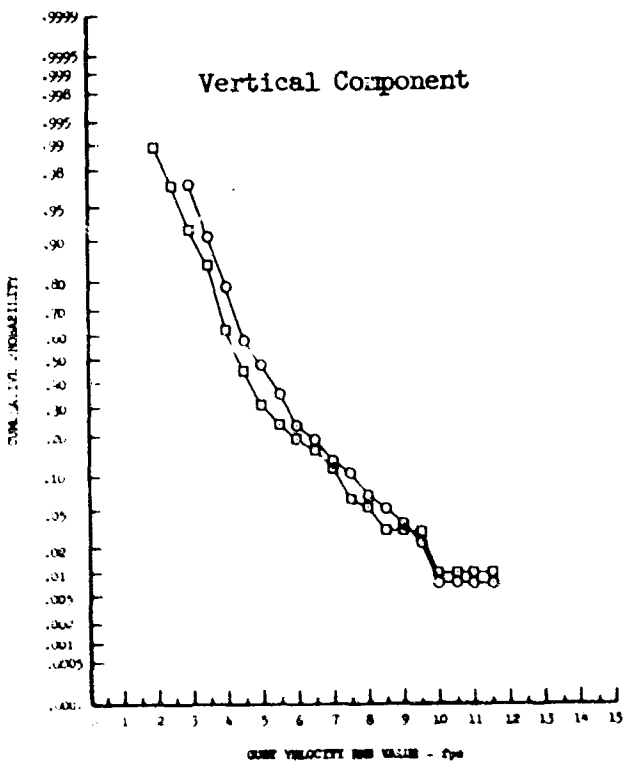
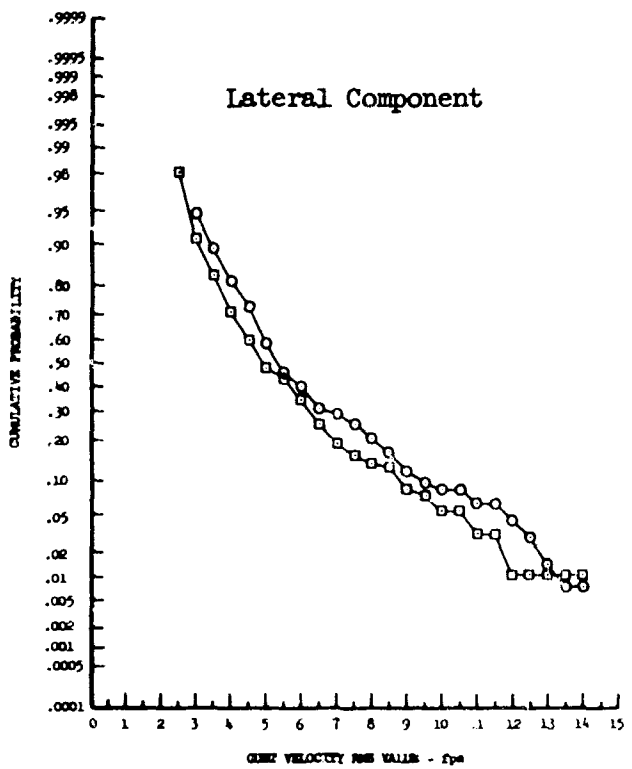
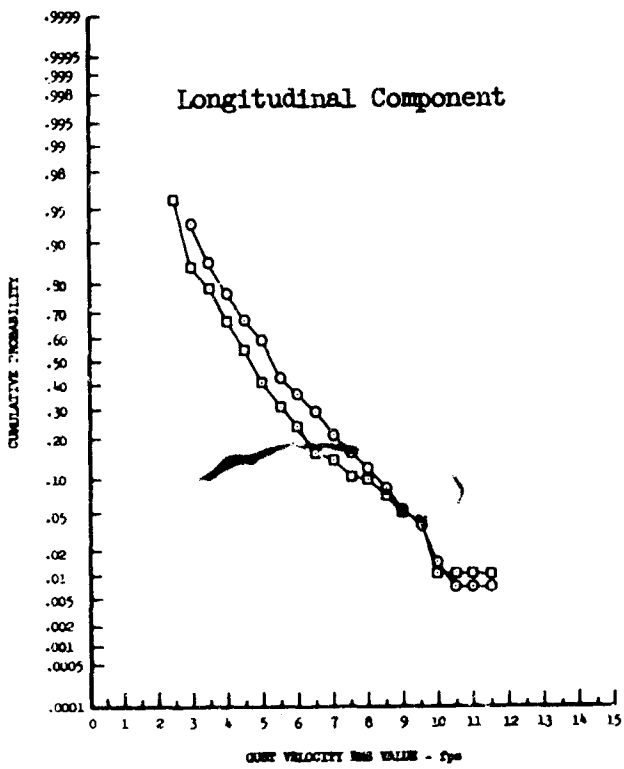
● 250 Feet  
 ■ 750 Feet

Figure 13.16 Altitude Effects on Gust Velocity RMS Values  
 - High Mountains, Very Stable



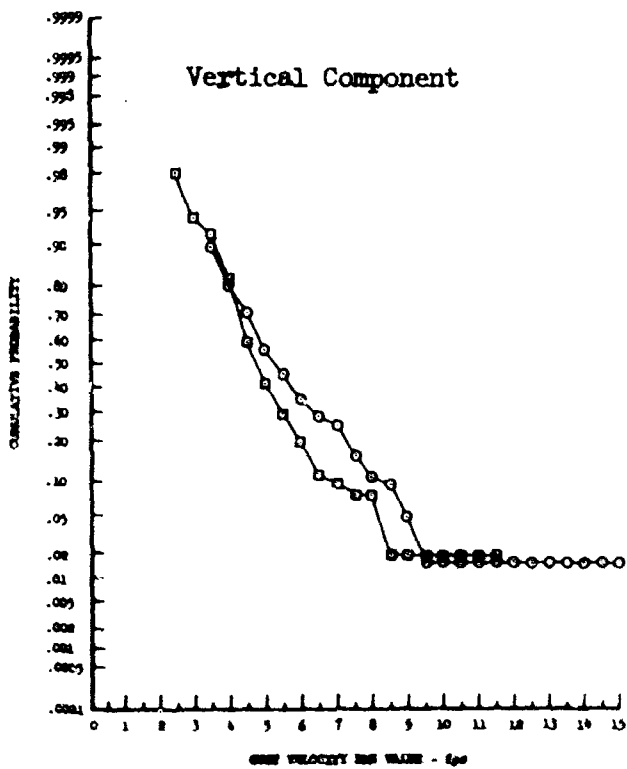
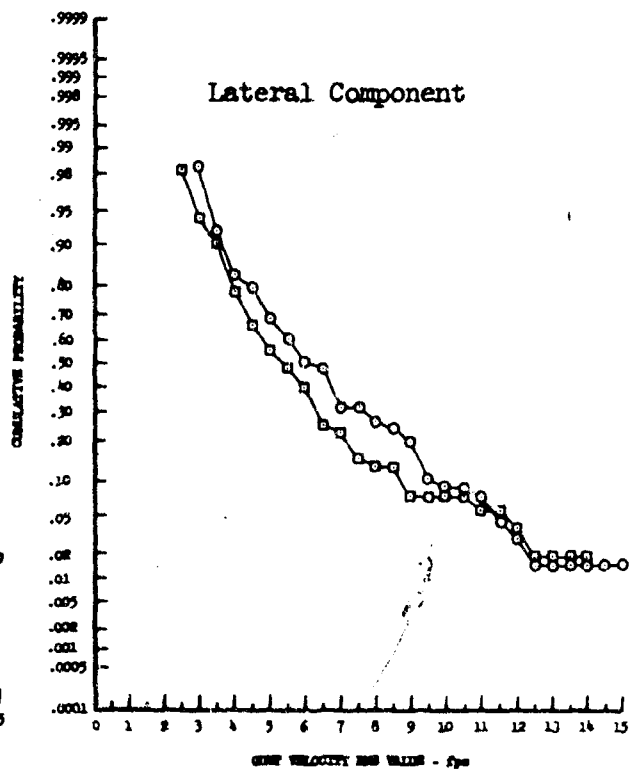
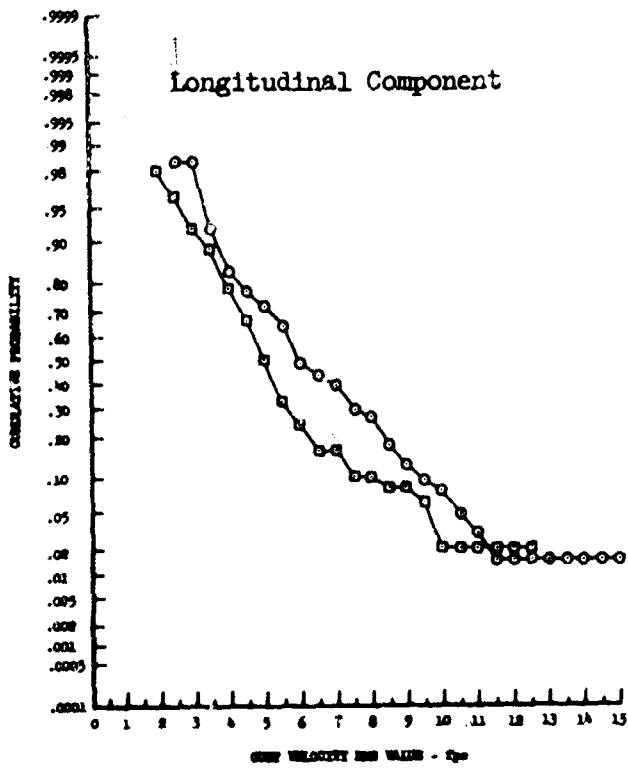
- 250 Feet
- 750 Feet

Figure 13.17 Altitude Effects on Gust Velocity RMS Values - High Mountains, Stable



- 250 Feet
- 750 Feet

Figure 13.18 Altitude Effects on Gust Velocity RMS Values - High Mountains, Neutral



● 250 Feet

■ 750 Feet

Figure 13.19 Altitude Effects on Gust Velocity RMS Values - High Mountains, Unstable

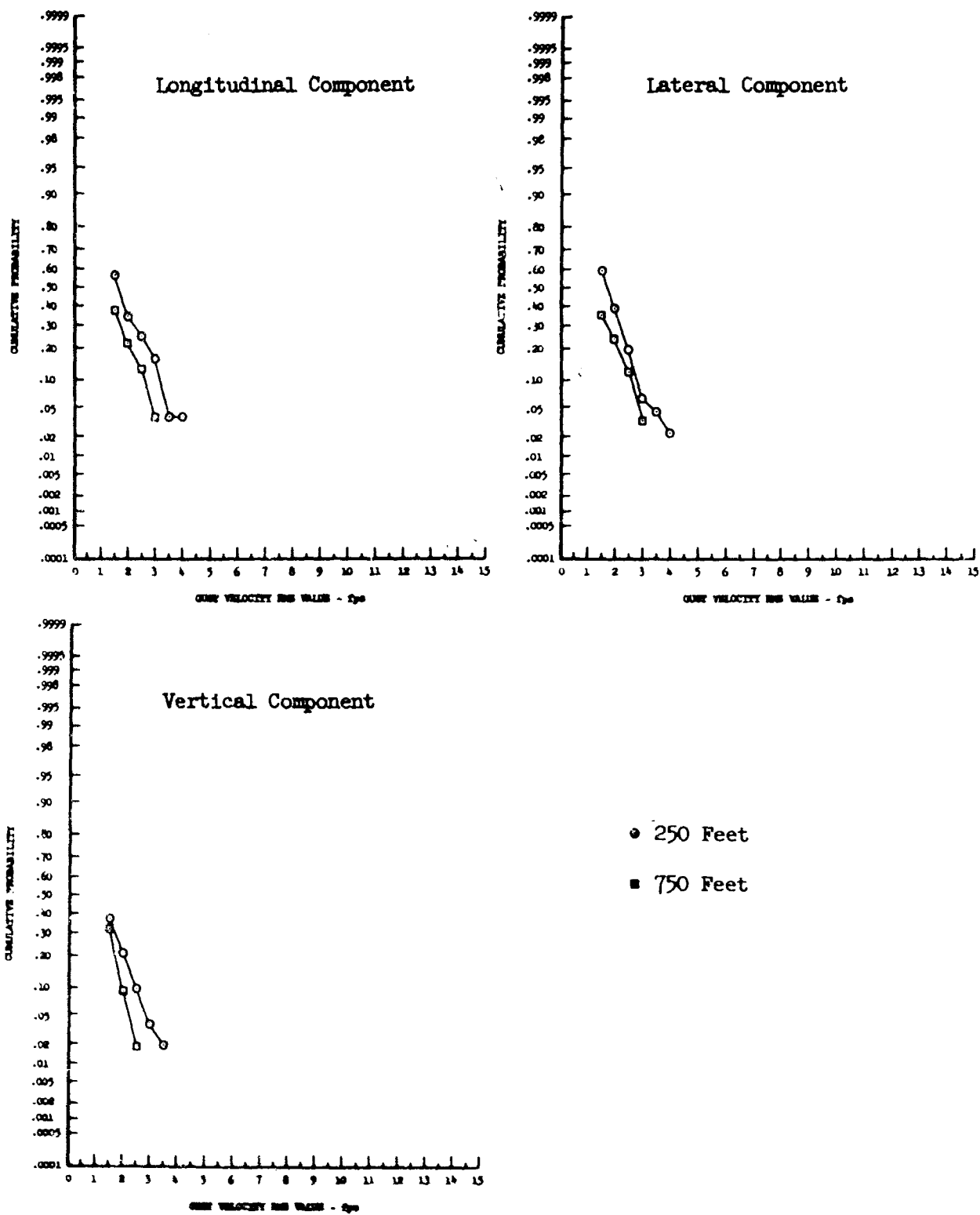
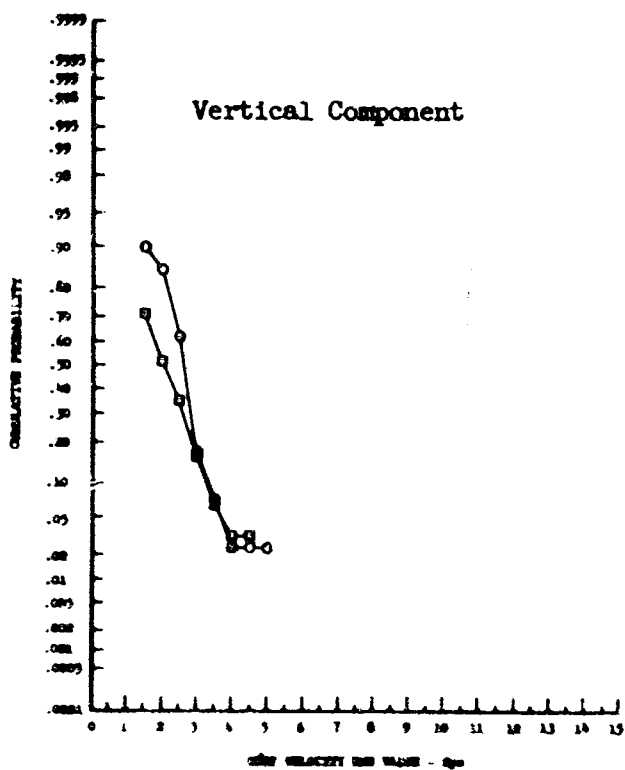
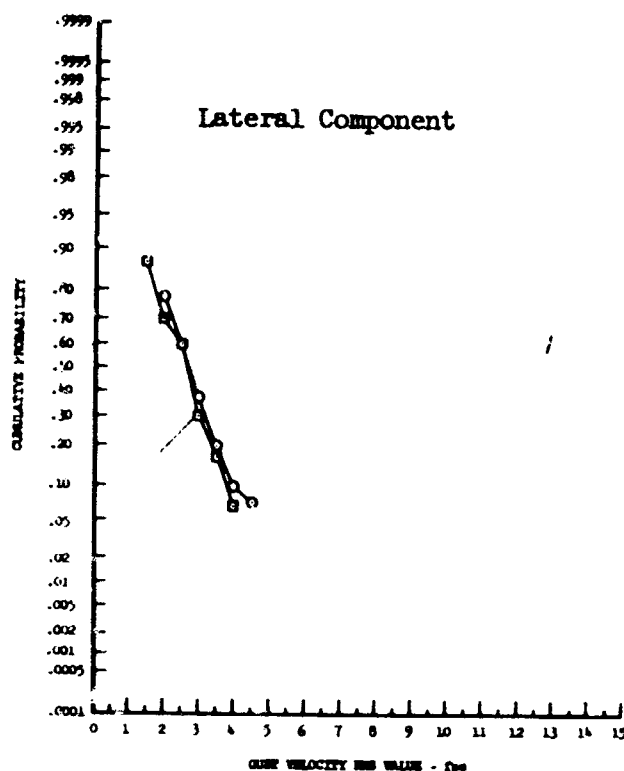
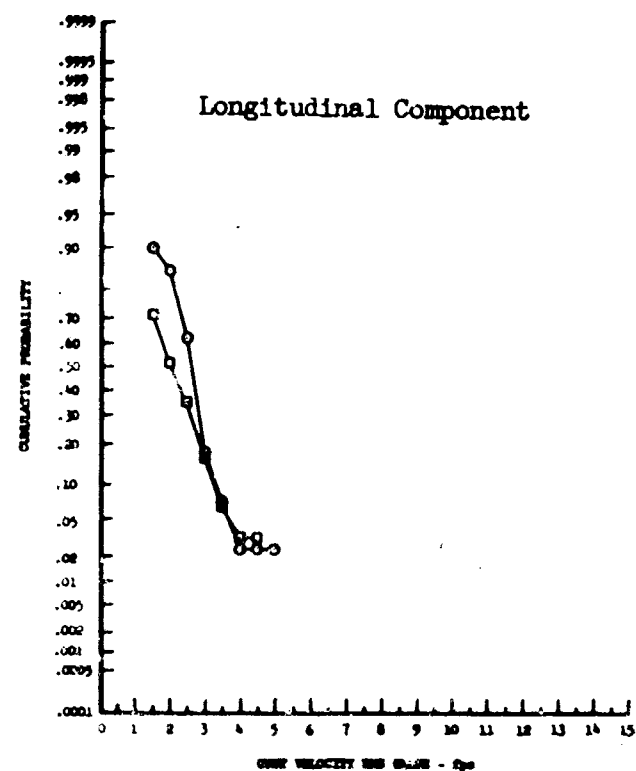
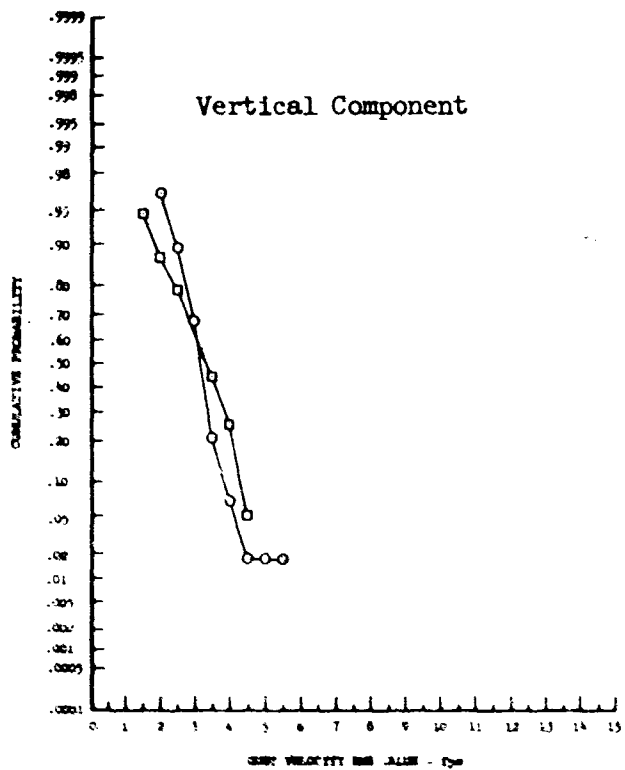
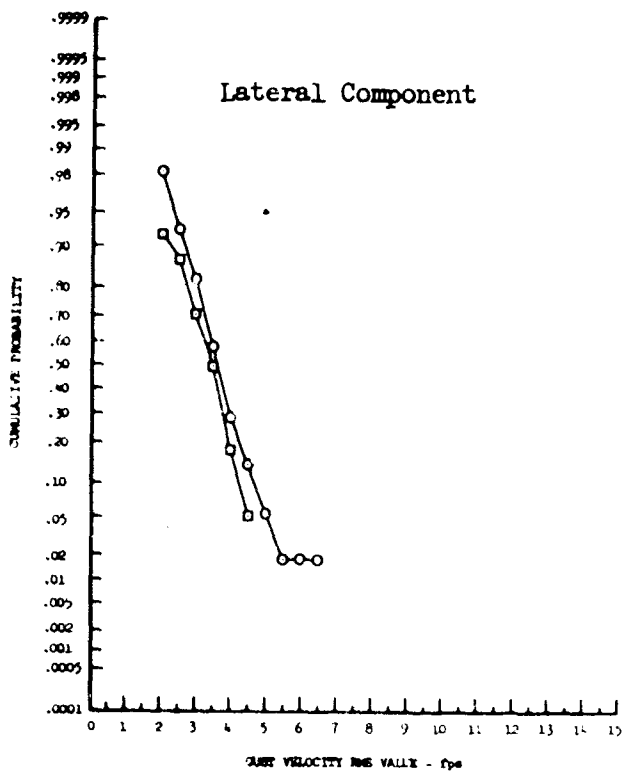
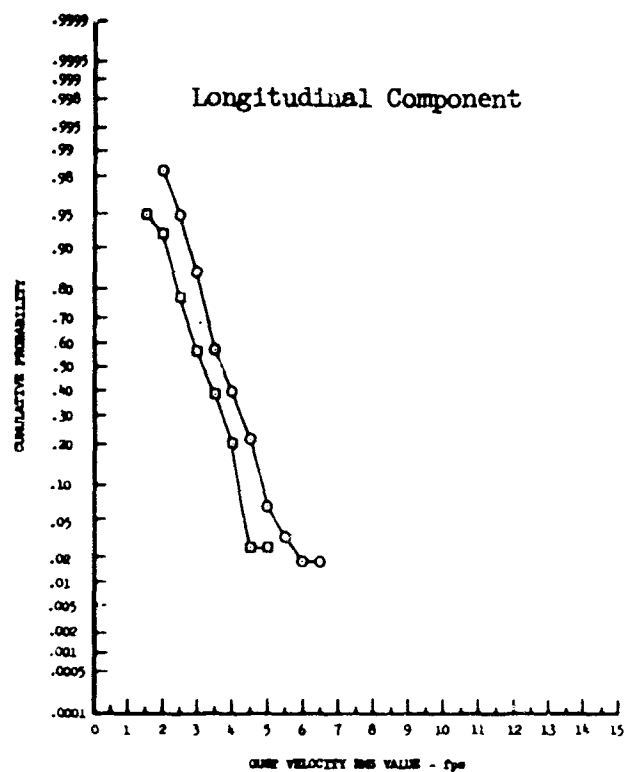


Figure 13.20 Altitude Effects on Gust Velocity RMS Values - Plains, Very Stable



- 250 Feet
- 750 Feet

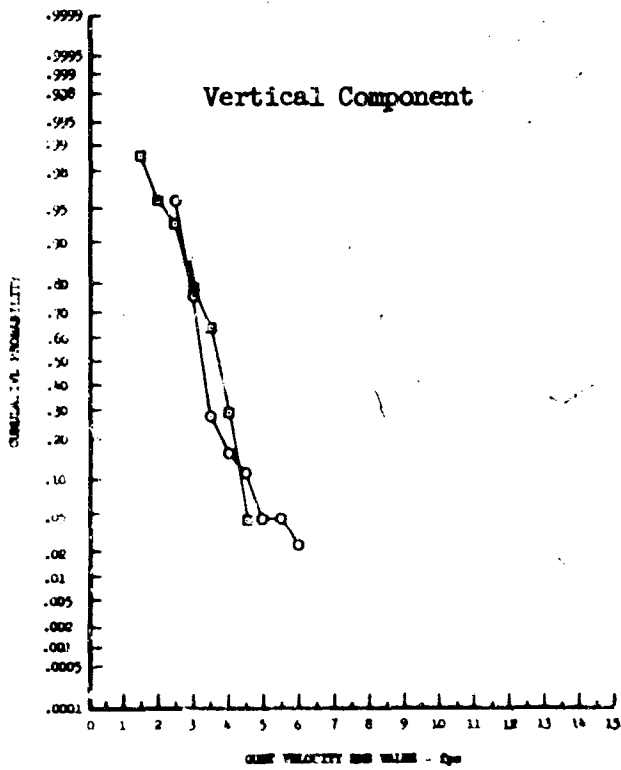
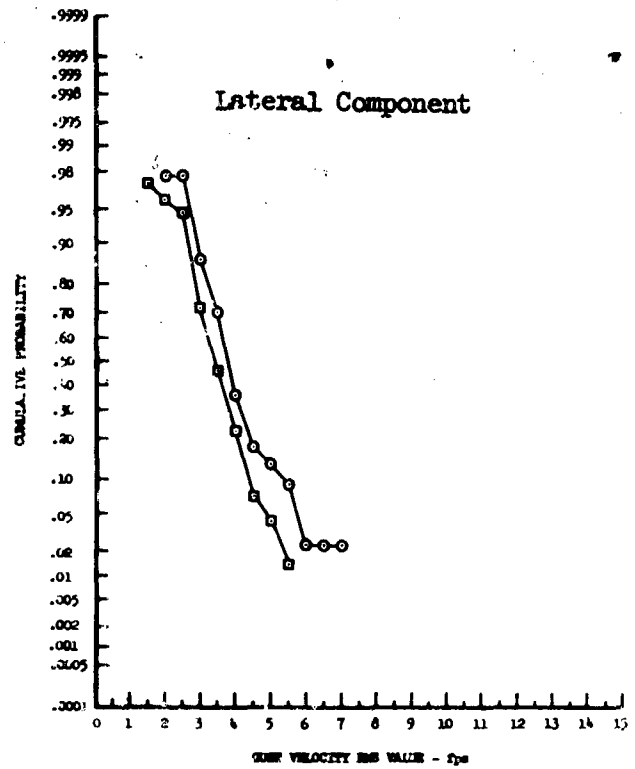
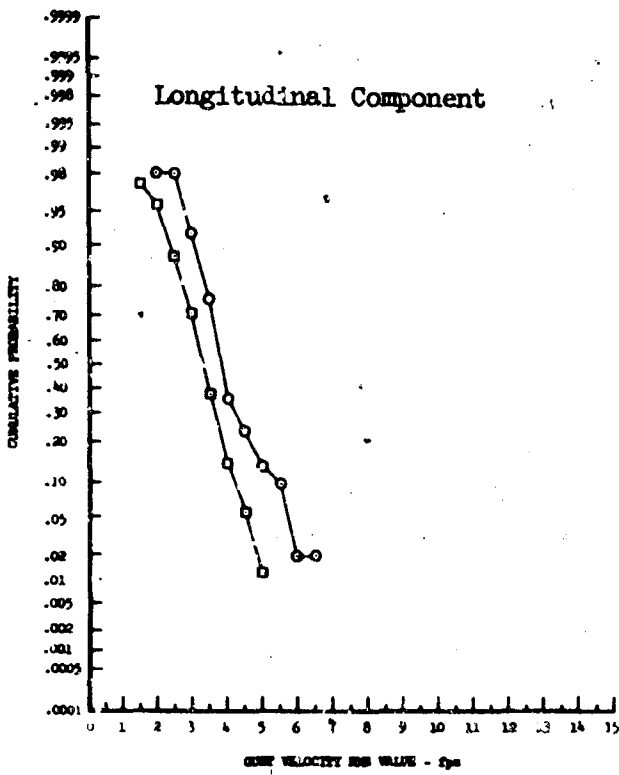
Figure 13.21 Altitude Effects on Gust Velocity RMS Values - Plains, Stable



- 250 Feet
- 750 Feet

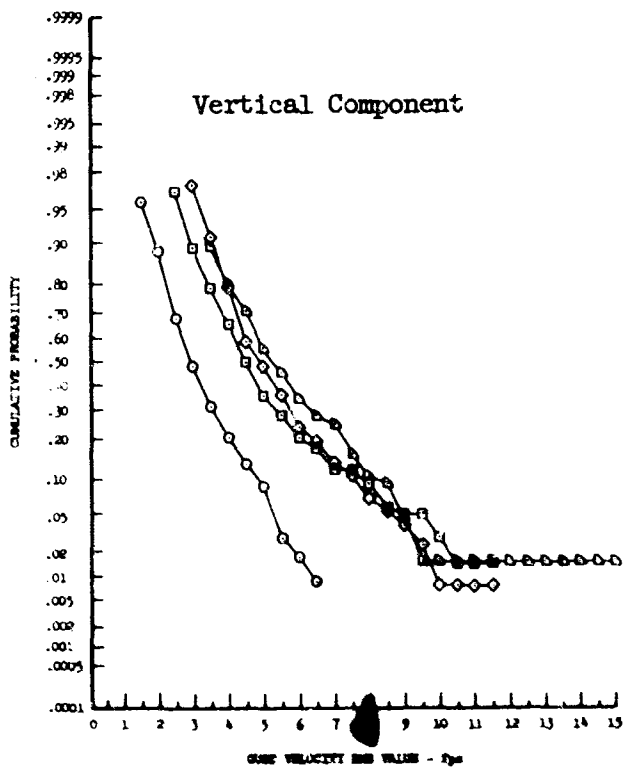
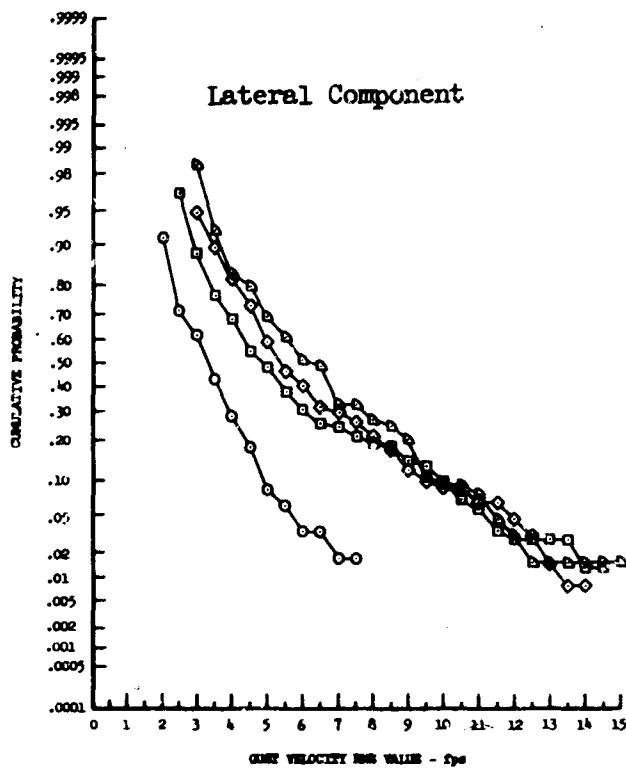
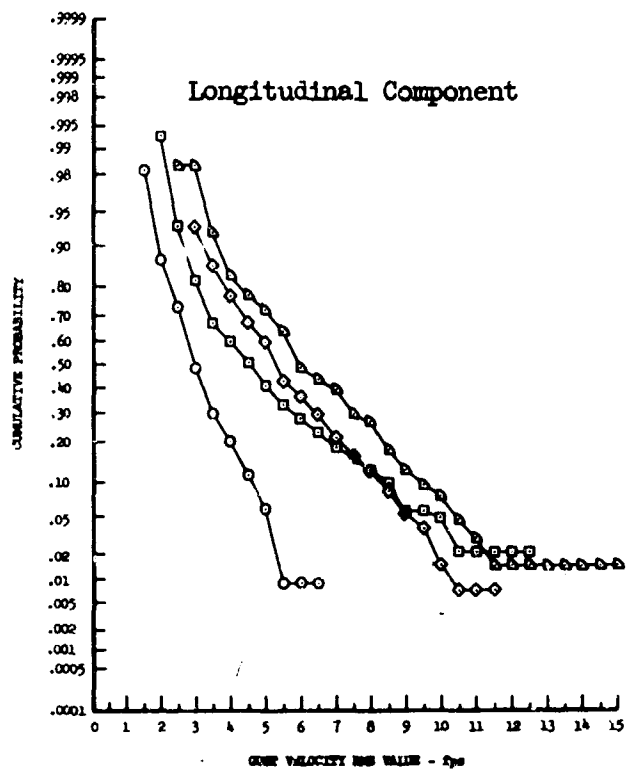
Figure 13.22 Altitude Effects on Gust Velocity RMS Values - Plains, Neutral





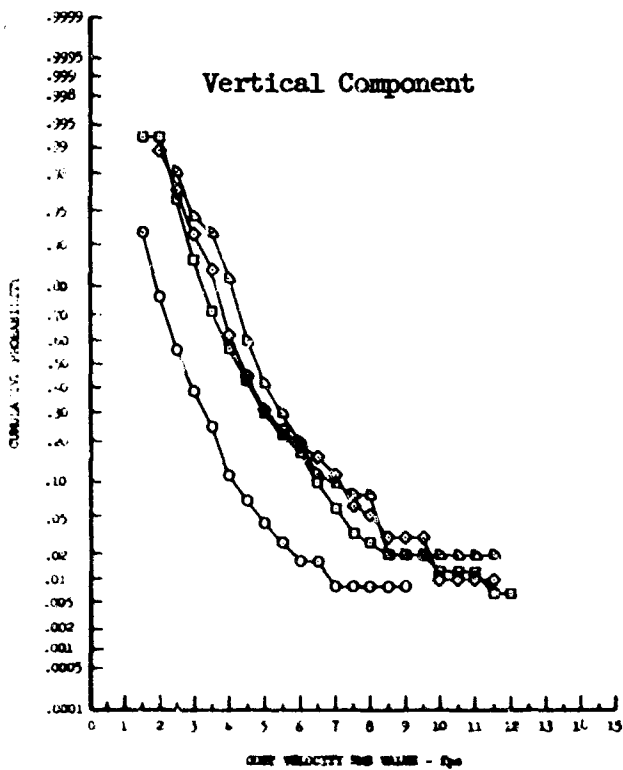
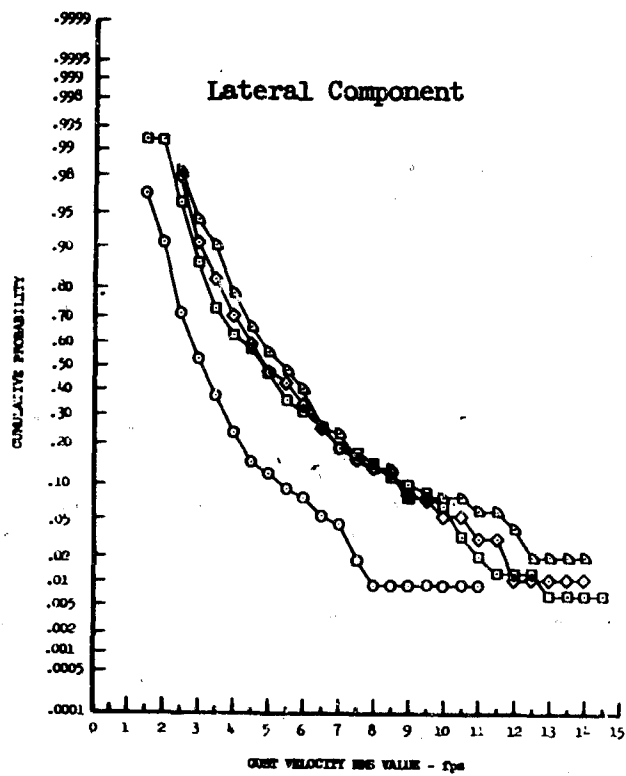
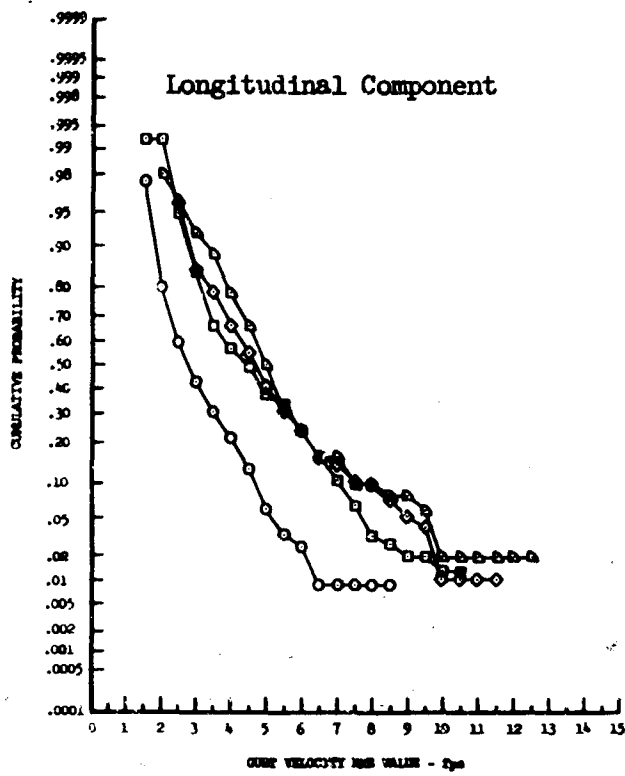
- 250 Feet
- 750 Feet

Figure 13.23 Altitude Effects on Gust Velocity RMS Values - Plains, Unstable



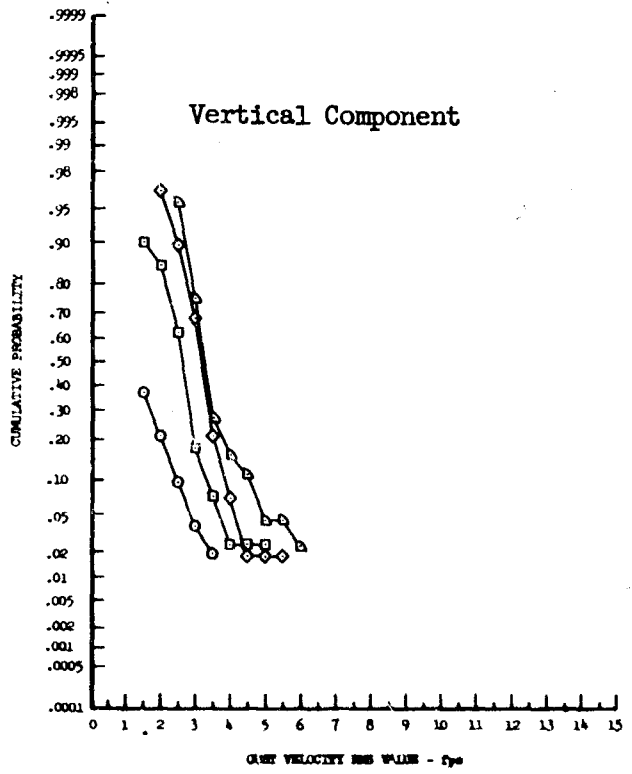
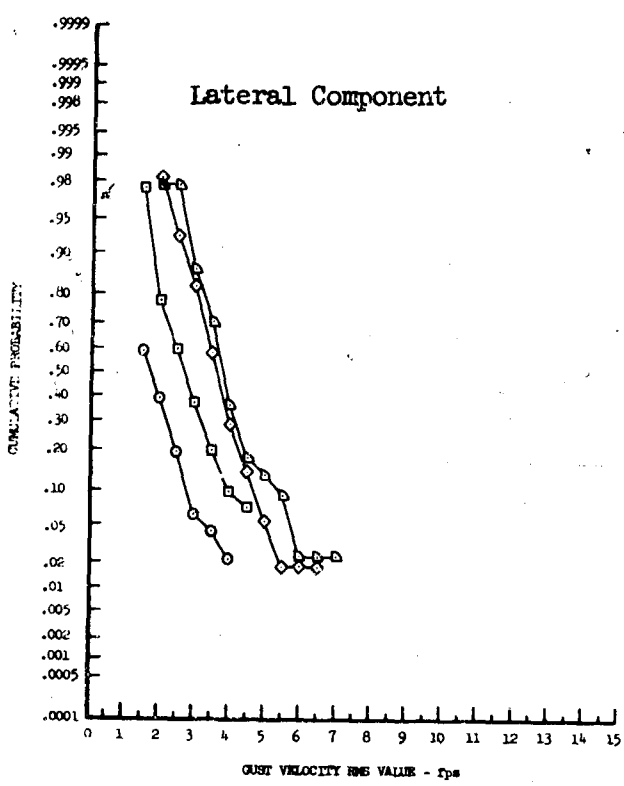
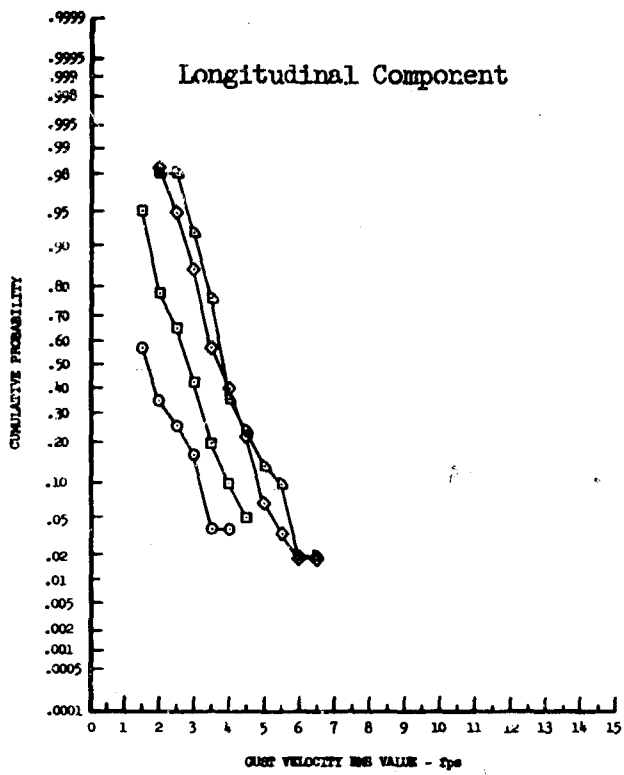
- Very Stable
- Stable
- ◆ Neutral
- ▲ Unstable

Figure 13.24 Atmospheric Stability Effects on Gust Velocity RMS Values - 250 Feet, High Mountains



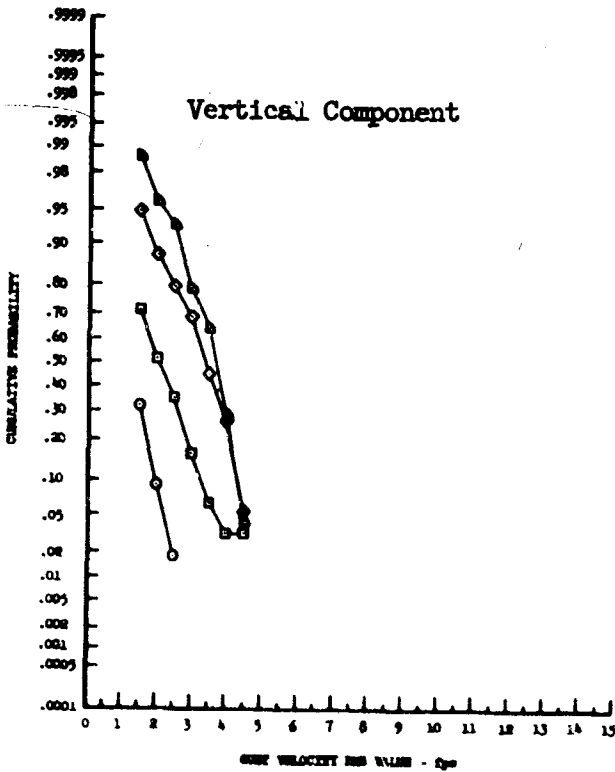
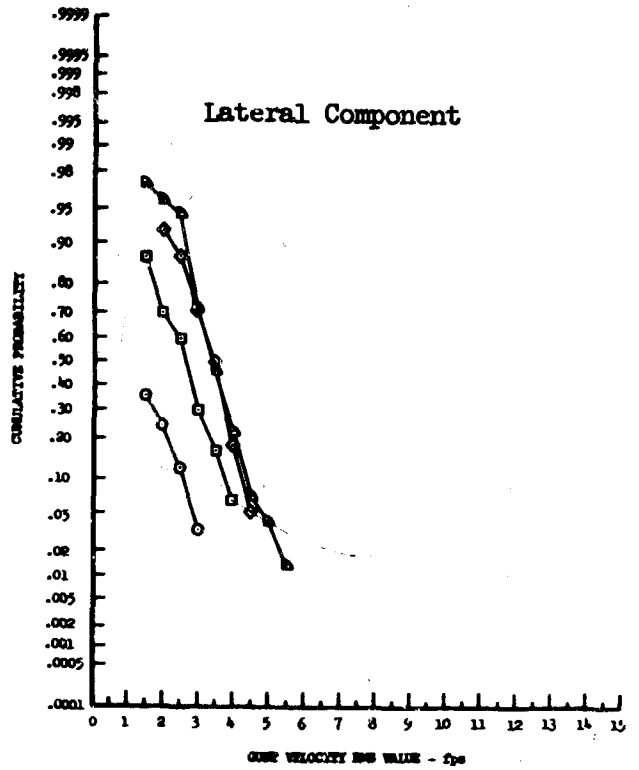
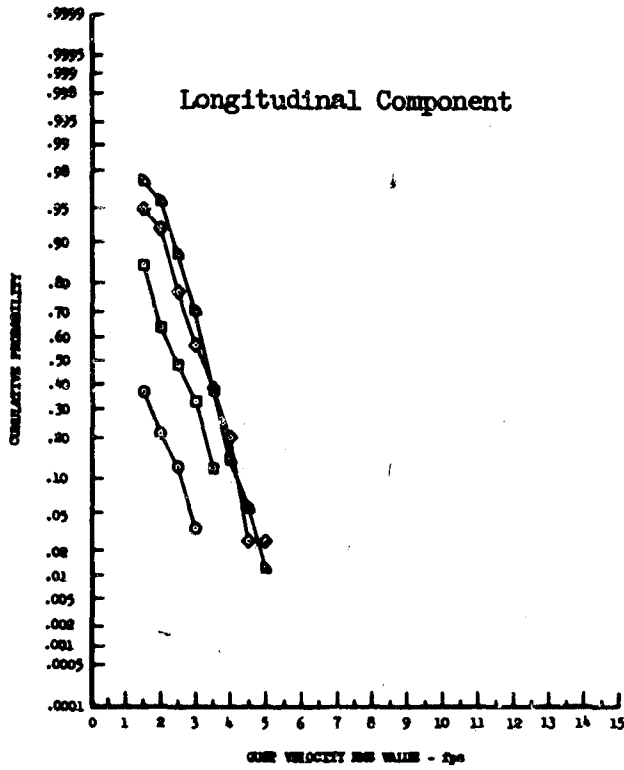
- Very Stable
- Stable
- ◆ Neutral
- ▲ Unstable

Figure 13.25 Atmospheric Stability Effects on Gust Velocity RMS Values - 750 Feet, High Mountains



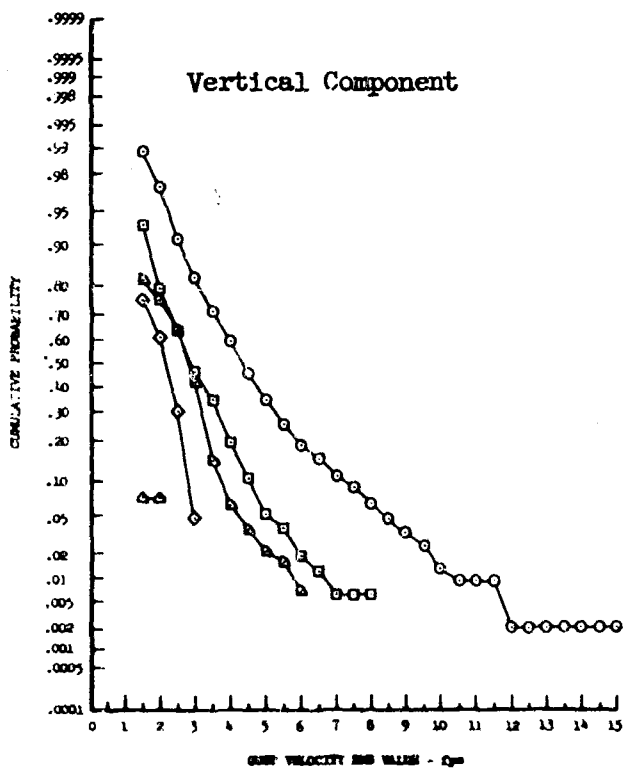
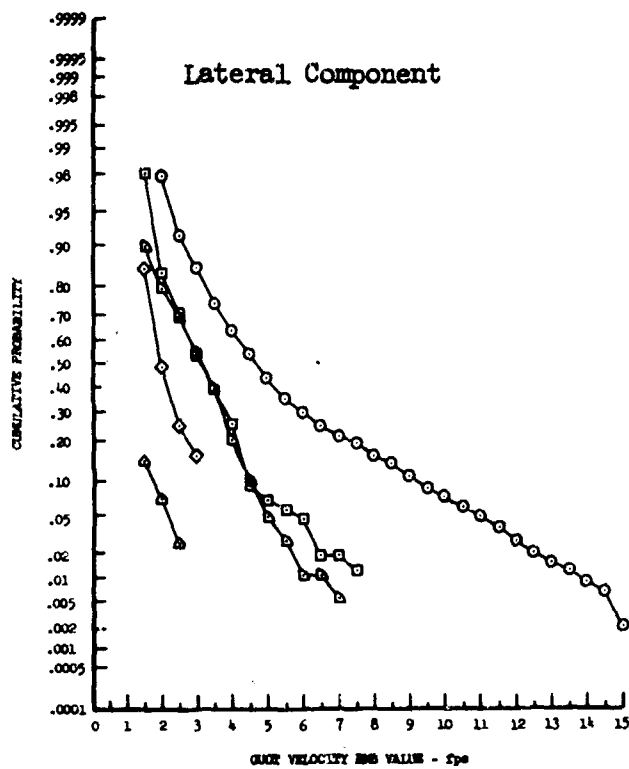
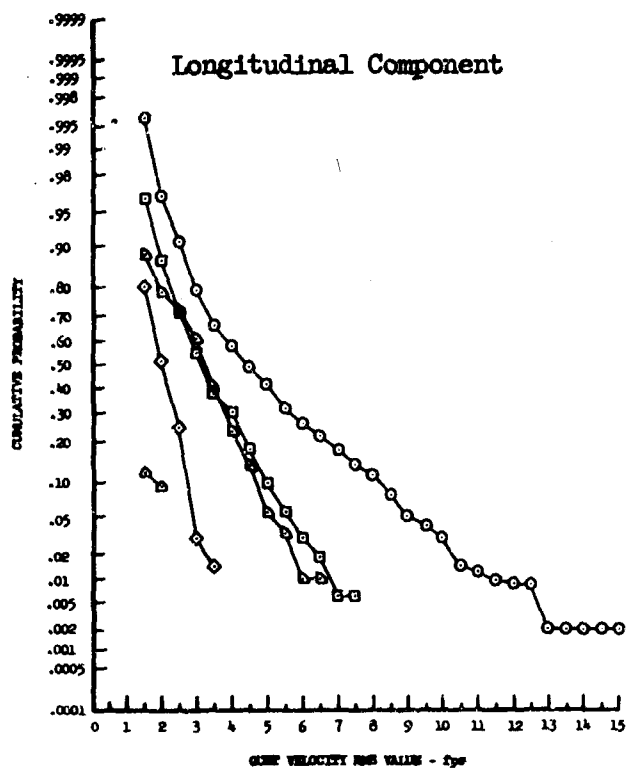
- Very Stable
- Stable
- ◇ Neutral
- △ Unstable

Figure 13.26 Atmospheric Stability Effects on Gust Velocity RMS Values - 250 Feet, Plains



- Very Stable
- Stable
- ◆ Neutral
- ▲ Unstable

Figure 13.27 Atmospheric Stability Effects on Gust Velocity RMS Values - 750 Feet, Plains



- High Mountains
- Low Mountains
- ◆ Desert
- ▲ Plains
- ▼ Water

Figure 13.28 Terrain Effects on Gust Velocity RMS Values - 250 Feet

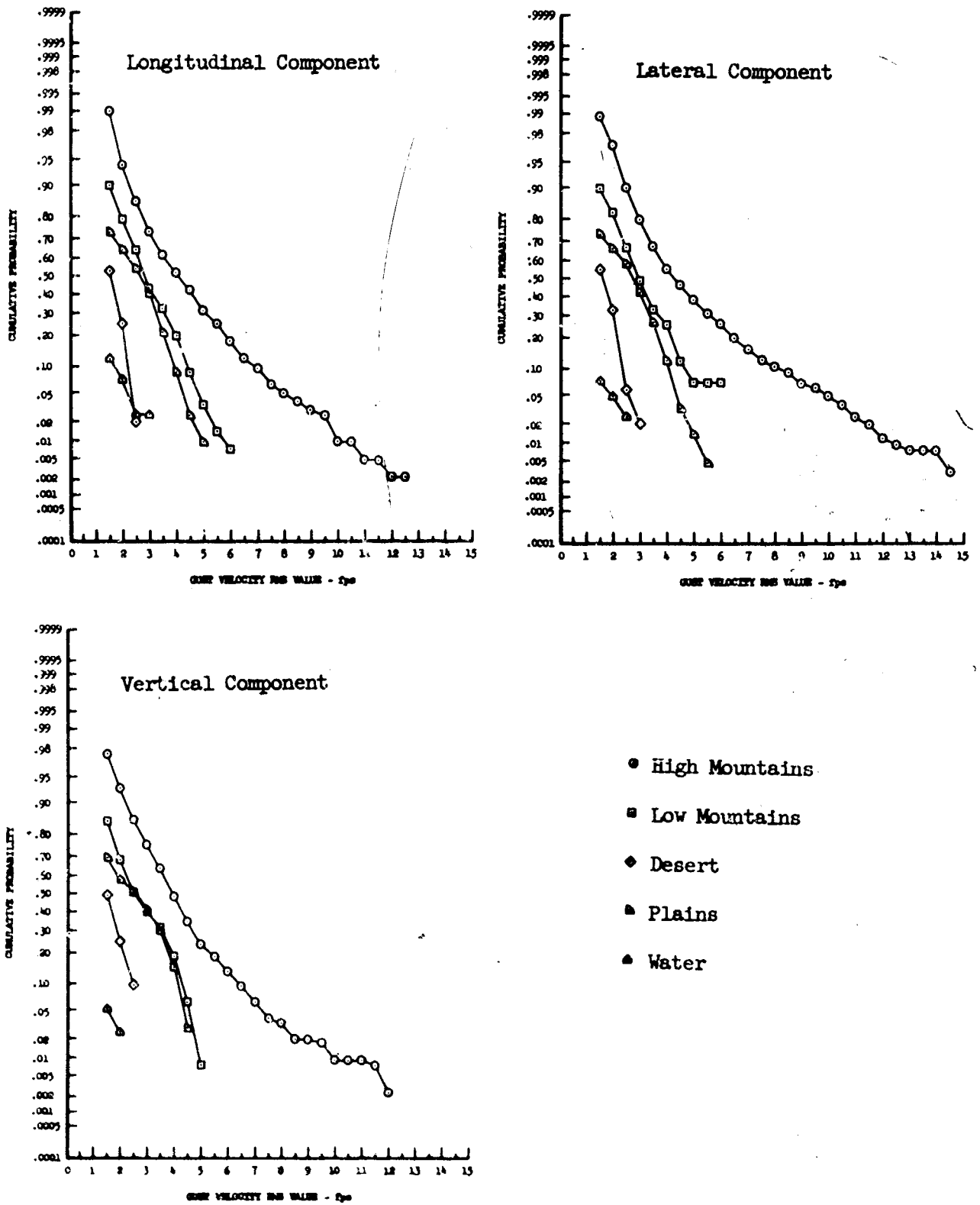
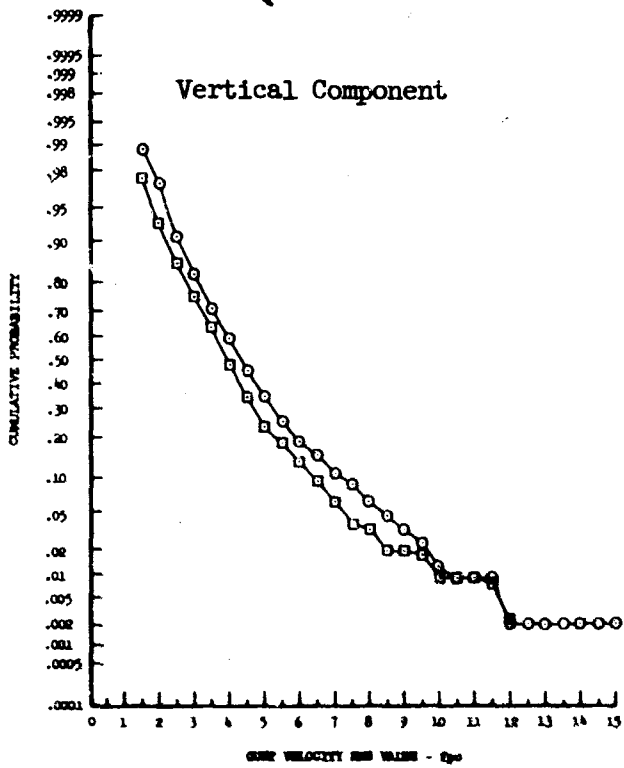
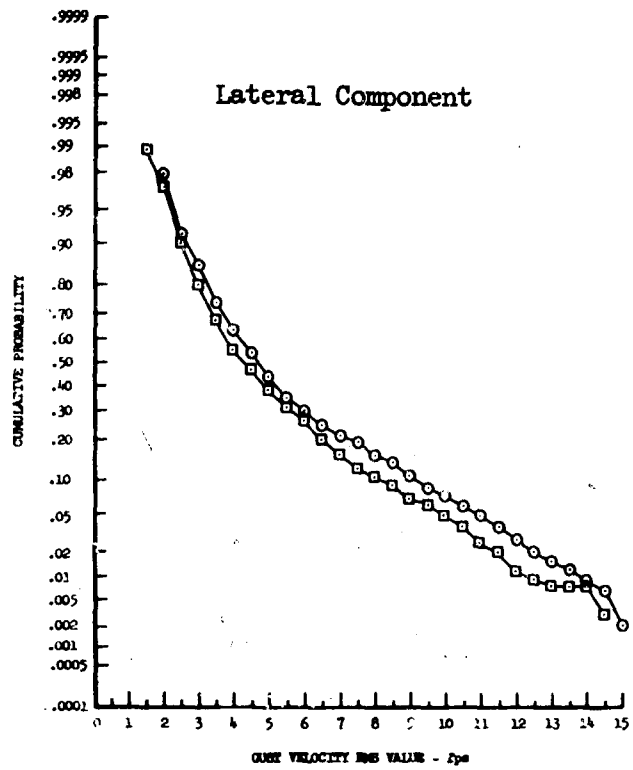
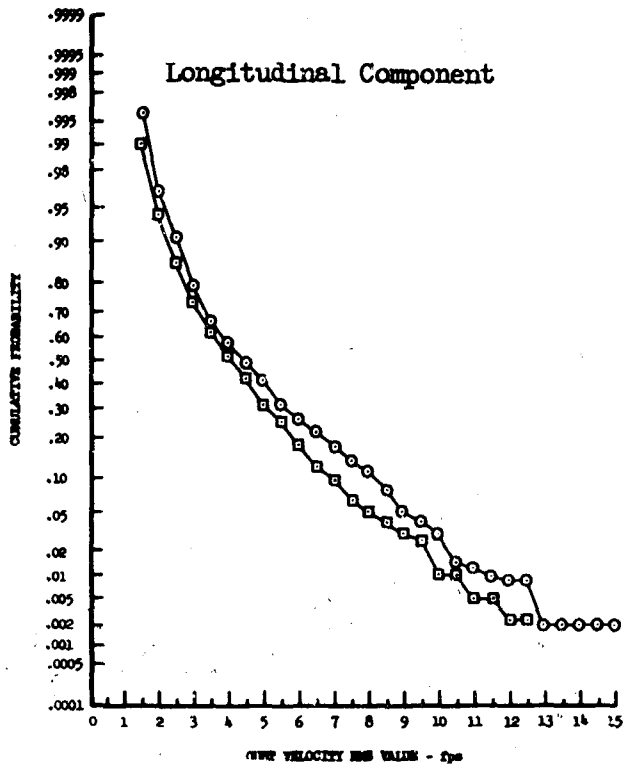


Figure 13.29 Terrain Effects on Gust Velocity RMS Values - 750 Feet



- 250 Feet
- 750 Feet

Figure 13.30 Altitude Effects on Gust Velocity RMS Values - High Mountains



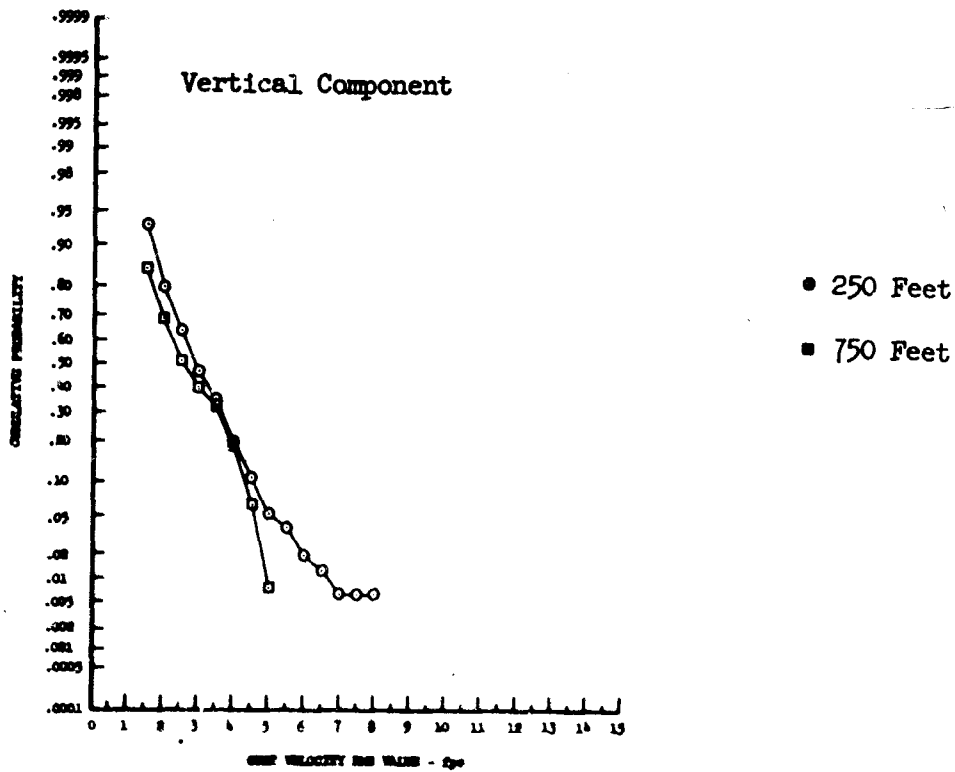
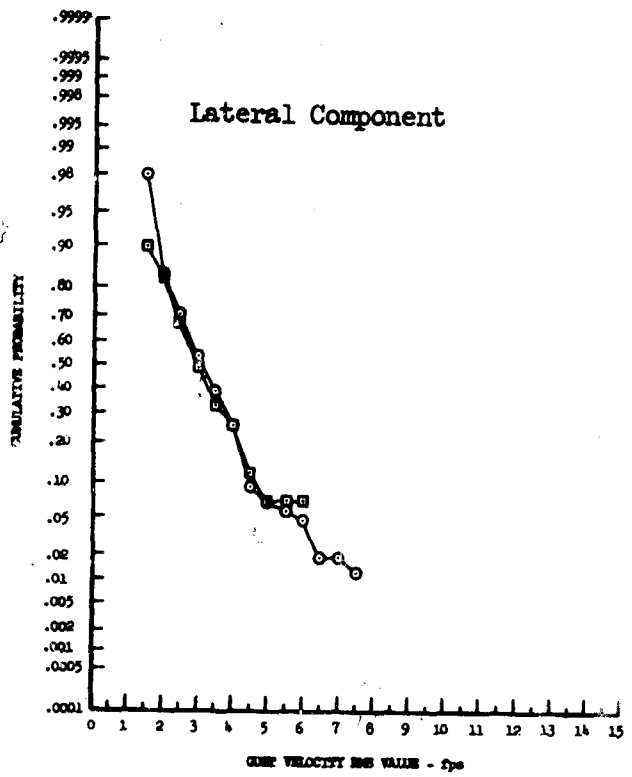
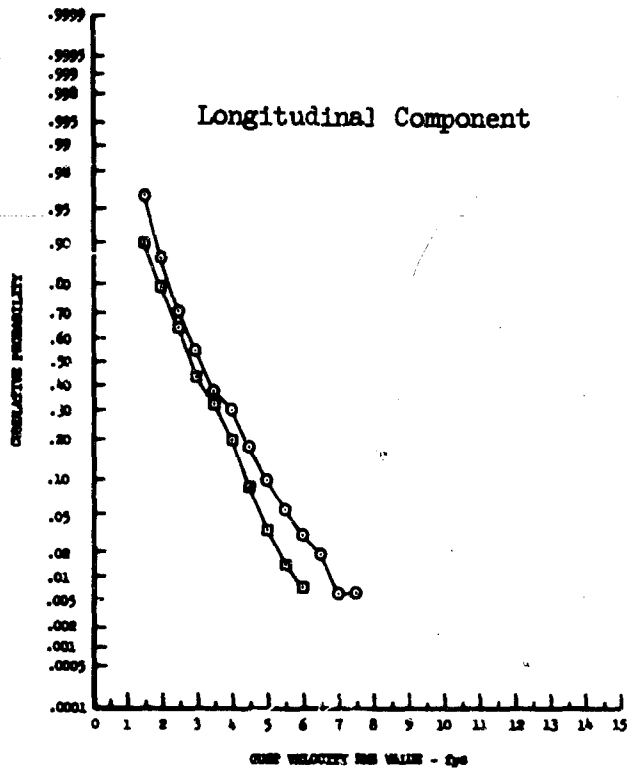
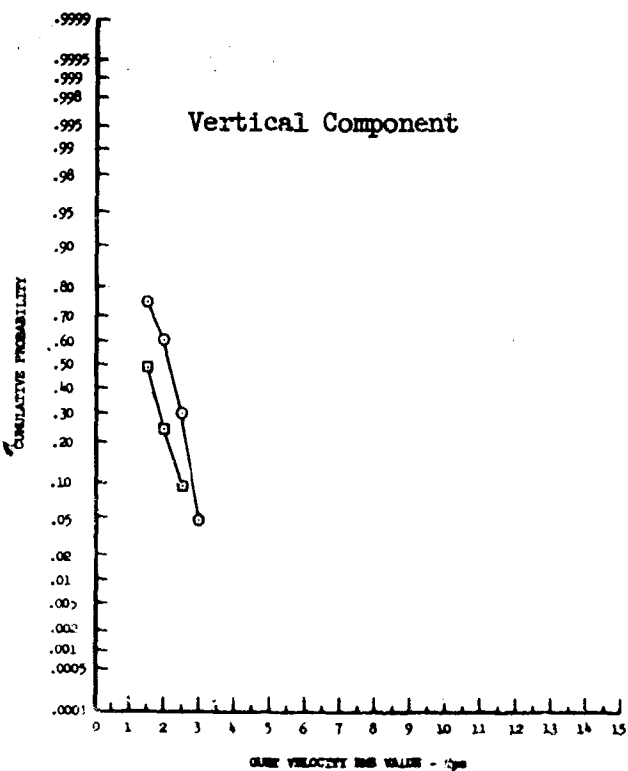
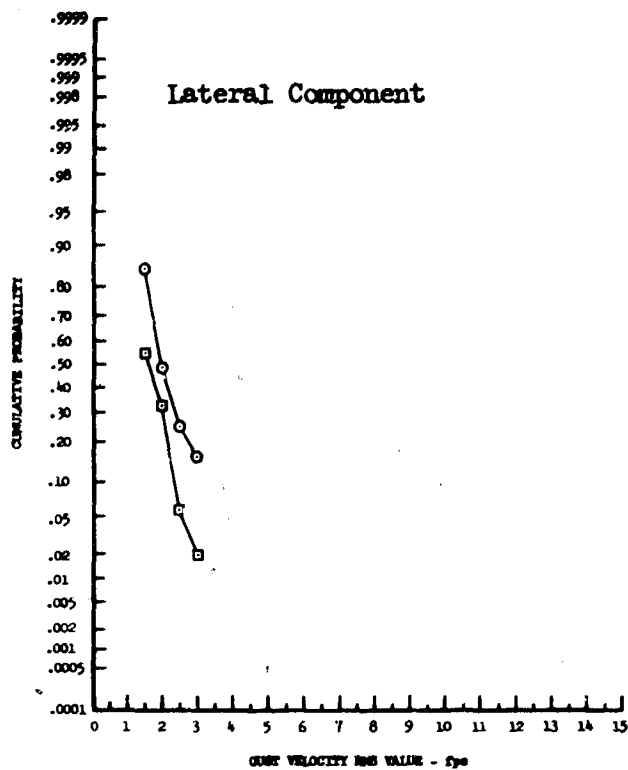
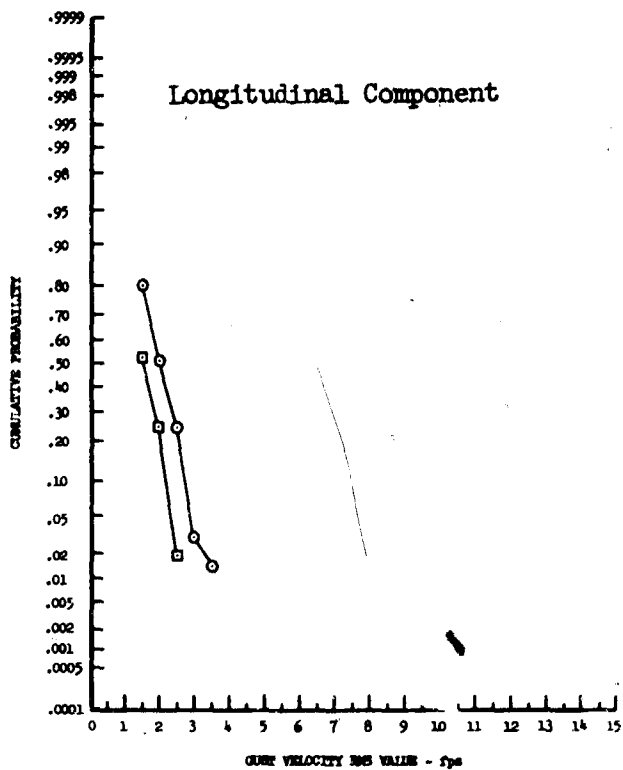
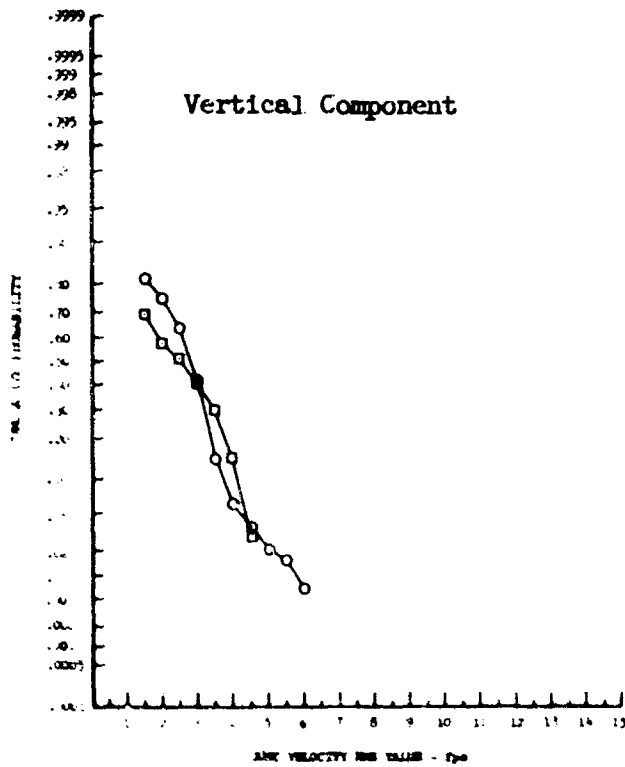
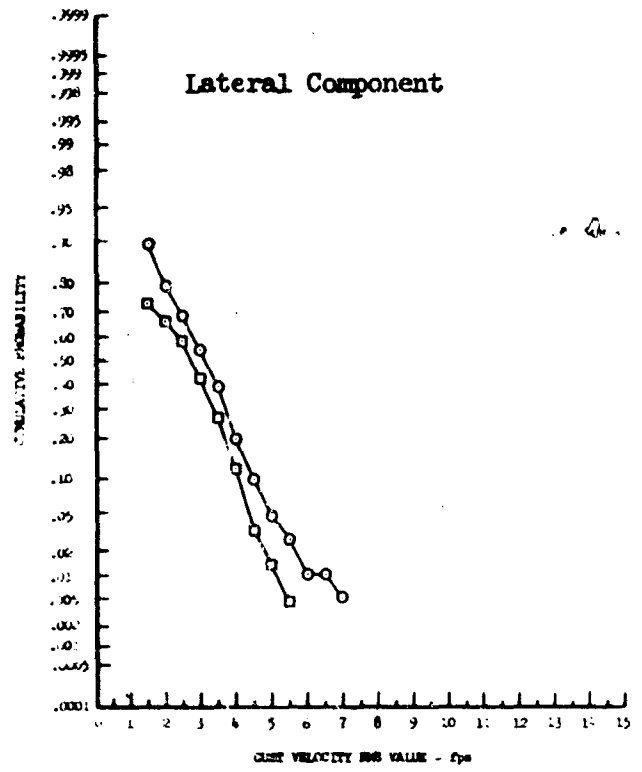
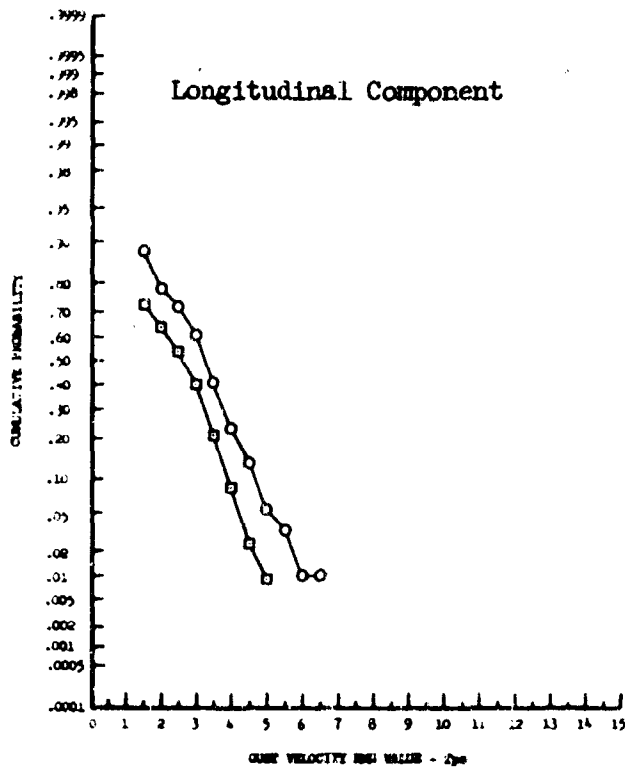


Figure 13.31 Altitude Effects on Gust Velocity RMS Values - Low Mountains



- 250 Feet
- 750 Feet

Figure 13.32 Altitude Effects on Gust Velocity RMS Values - Desert



- 250 Feet
- 750 Feet

Figure 13.33 Altitude Effects on Gust Velocity RMS Values - Plains

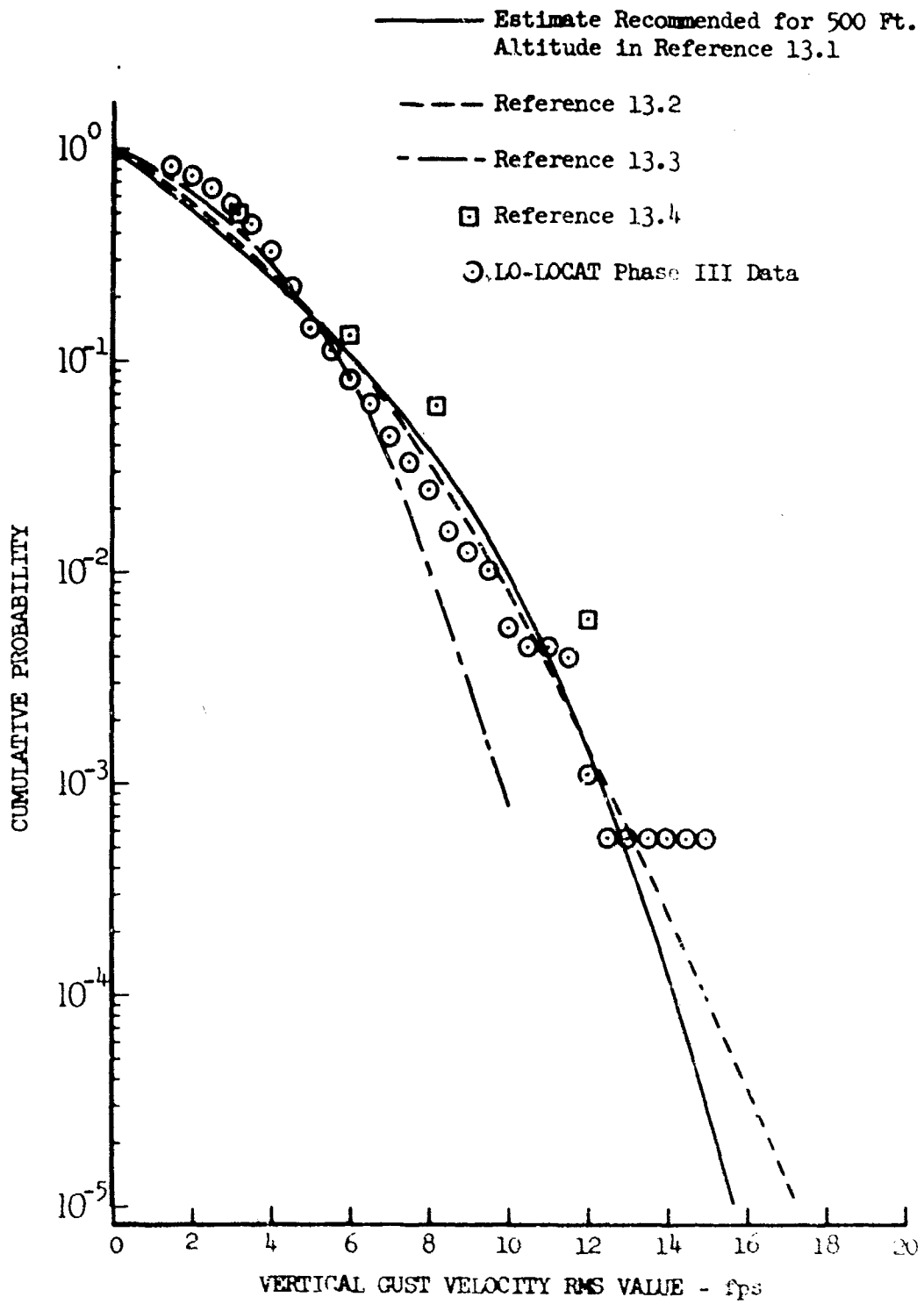


Figure 13.34 Comparison of Vertical Gust Velocity RMS Values from Various Research Programs

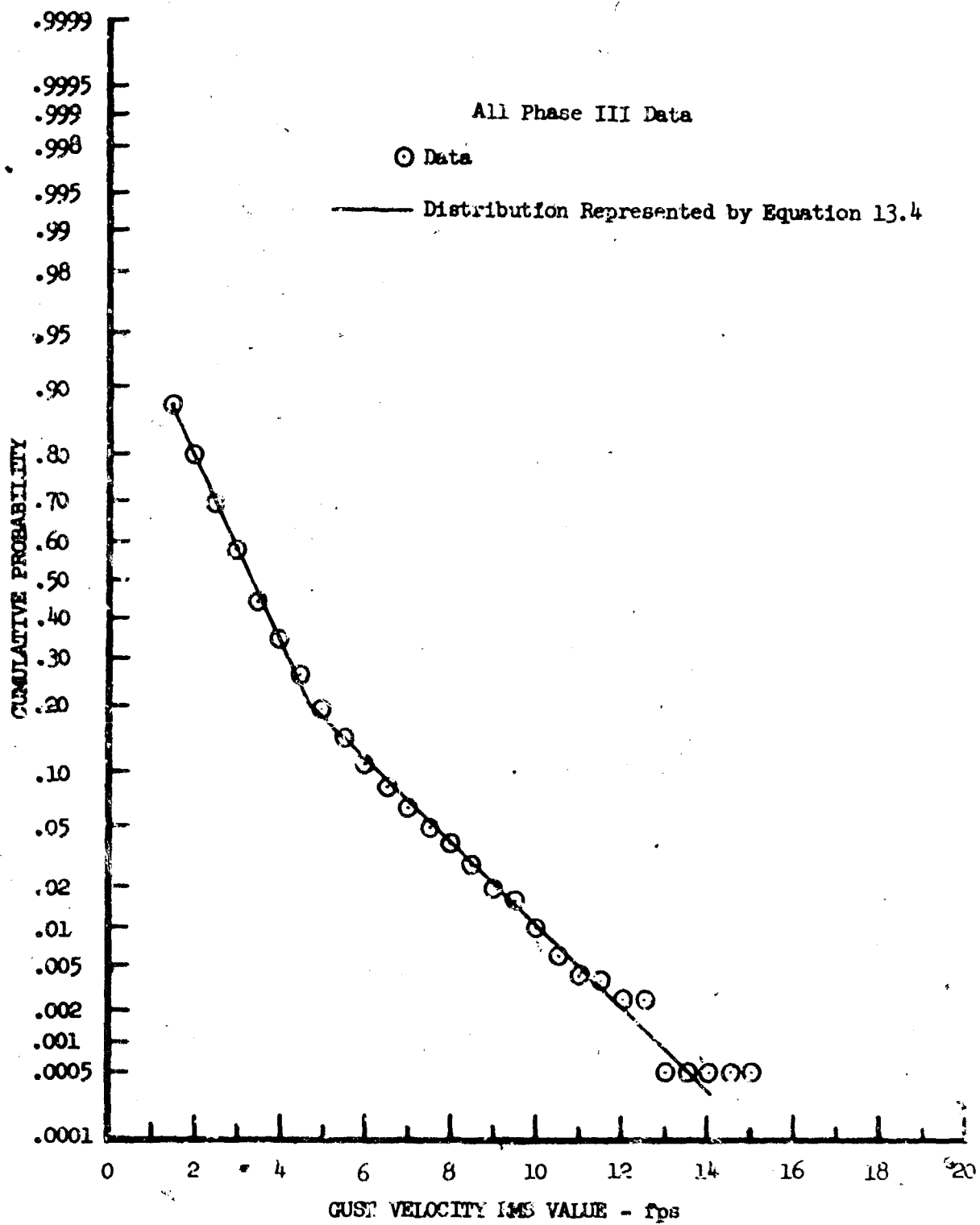


Figure 13.35 Longitudinal Gust Velocity RMS Cumulative Probability Distribution Shape

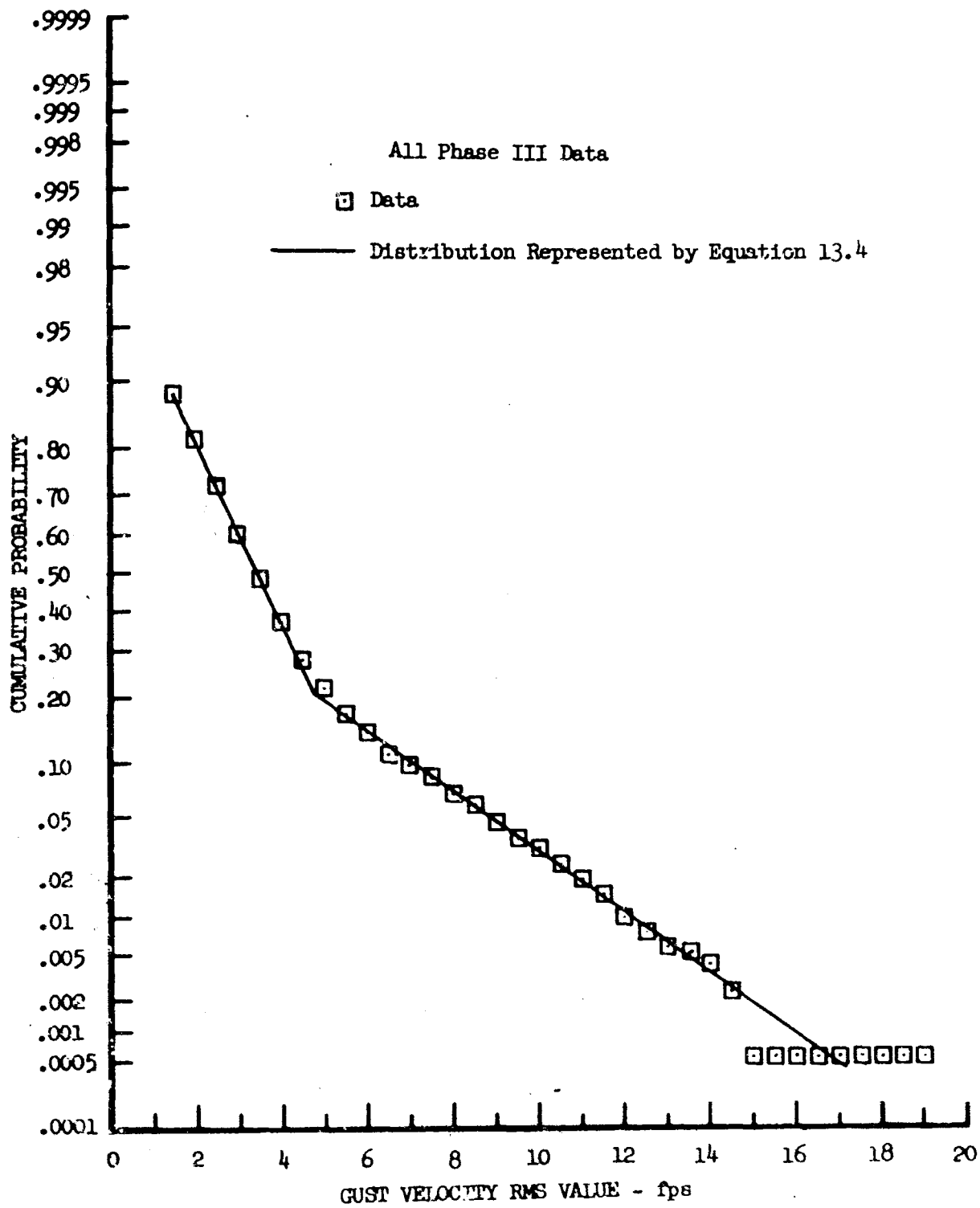


Figure 13.36 Lateral Gust Velocity RMS Cumulative Probability Distribution Shape

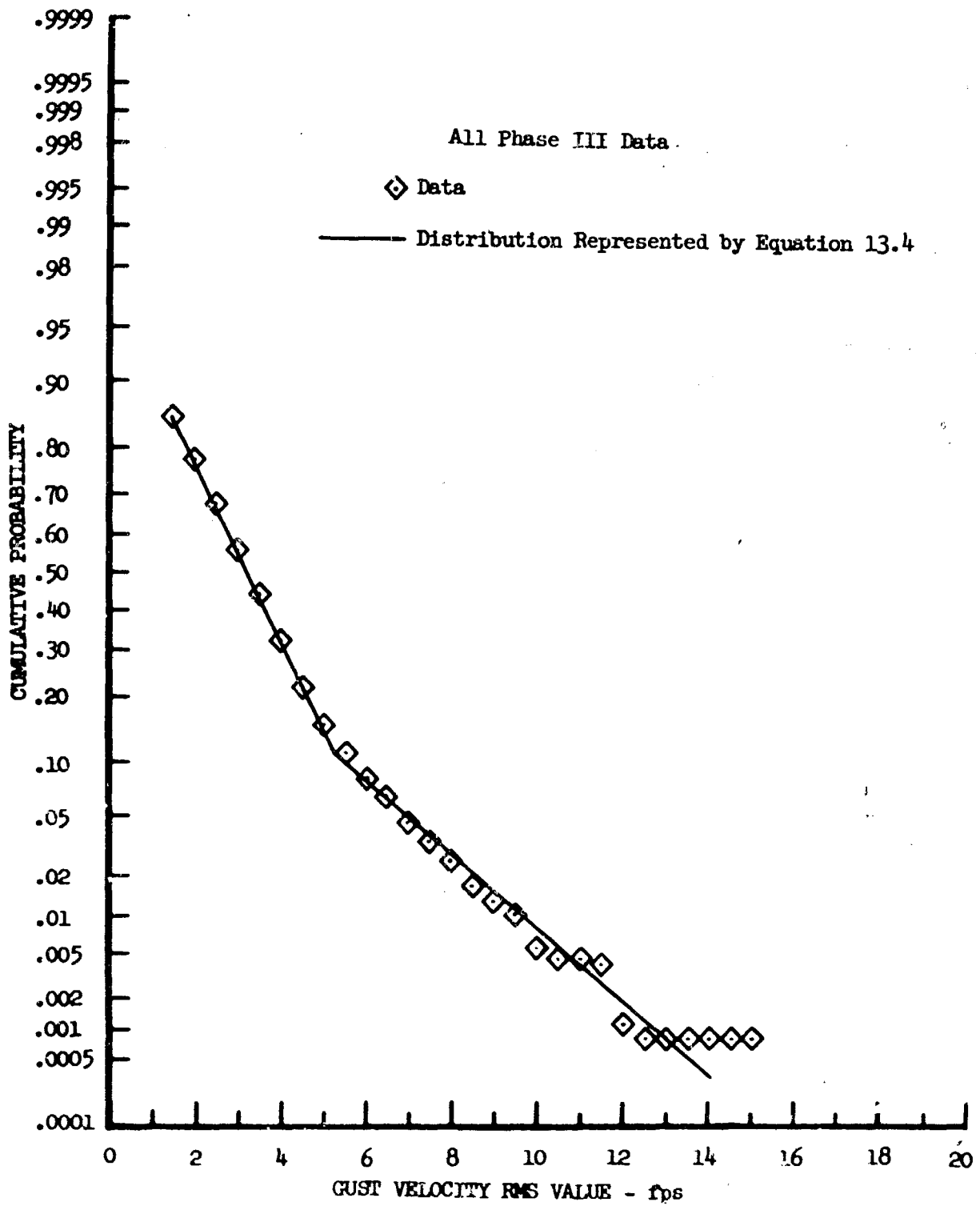


Figure 13.37 Vertical Gust Velocity RMS Cumulative Probability Distribution Shape

#### 14. GUST VELOCITY RMS VERSUS INFLIGHT MEASURED WIND VELOCITY

The relationship between gust velocity rms values and recorded inflight wind velocity was investigated with respect to type of terrain and altitude above the terrain. The terrain and wind involved during IO-LOCAT Phase III are discussed in Section VI.

An analysis of rms values as a function of wind speed was accomplished by two different methods. The first method involved plotting the gust velocity rms values versus wind speed. The slopes and intercepts of first-order least square lines (Equation 14.1) which best fit the data were computed:

$$\sigma_t = y_0 + mW \quad (14.1)$$

where:

$m$  = slope of line

$y_0$  =  $y$  intercept

The standard deviation of the data about the least-square line was calculated as follows:

$$\sigma_D = \left[ \frac{1}{N} \sum_{i=1}^N (x_i - R_i)^2 \right]^{1/2} \quad (14.2)$$

where:

$x_i$  = value of gust velocity rms at a given wind speed

$R_i$  = value of least square line at the given wind speed

The standard deviation of the data about the least square line indicates the degree of data scatter. The results of this method are shown in Figures 14.1 through 14.8. The applicable least square line and  $\pm$  one standard deviation lines for the data are shown on each plot.

The slope of the least-square line indicates the effect of wind speed on gust velocity rms values; the greater the slope, the greater the effect. The wind speed-turbulence relationships of Figures 14.1 through 14.8 are summarized in Figure 14.9 by showing the slopes of the least square lines plotted as a function of terrain and altitude.

For the second method of analysis, the gust velocity rms values were separated into several different groups. The particular group within which the rms value for a given data sample was placed was dependent upon the corresponding wind velocity for the sample. Each group covered a wind speed band of 10 fps. The cumulative probability of gust velocity rms was then calculated for each group. Probability plots were constructed and are shown in Figures 14.10 through 14.13. Not all bands contained enough data for statistical reliability (30 samples), therefore, all



combinations of terrain and altitude could not be statistically analyzed. A greater change in the wind versus gust rms relationship with terrain than with altitude was indicated (Figure 14.9). Therefore, the data were categorized on the basis of terrain type only. Figures 14.10 through 14.13 show the cumulative probability distributions of gust velocity rms values as a function of wind speed for given types of terrain. The vertical and longitudinal gust velocity rms values exhibit approximately the same relationship with respect to wind speed for both the high and low mountain data. The lateral component shows a greater relationship with wind speed over the high mountain terrain than either the longitudinal or vertical components, while over the low mountain terrain the opposite is true. This may be due, in part, to the wind direction effects discussed later.

The effect of altitude on the wind speed versus rms value relationship seems to be small. For all data, except those recorded over low mountain terrain, gust velocity rms values showed slightly more correlation with wind speed at the 250-foot altitude.

Gust velocity rms values from legs within the proximity of predominant mountain ridges were studied with respect to wind direction. In order to study the effects of being on the leeward or windward side of a ridge, only legs which were completely on one side or the other were chosen. Also considered was the wind direction with respect to the ridge (perpendicular, diagonal, or parallel) when the turbulence was being recorded on the leeward side. The data from legs 5, 6, 7, and 8 of the Peterson route are the most applicable to this type of analysis. The McConnell route, of course, consisted entirely of smooth terrain. Although the Edwards and Griffiss routes did include rough terrain there were no close predominant ridges completely on one side of a leg.

The layout of the Peterson legs is shown in Figure IV.3 of Appendix IV. The same ridge line was used for a wind direction reference on both legs 5 and 6 and was assumed to run in a north-south direction. The predominant ridge was assumed to run in a  $340^\circ$  direction for leg 7. For leg 8, the wind direction was referenced to the same ridge line as for leg 7, except that effects of wind blowing from the direction of the mountains near Colorado Springs were also taken into account. Therefore, the ridge line was assumed to curve and run from  $340^\circ$  to  $360^\circ$  for leg 8 data. The data were categorized by wind direction, as shown in Table 14.1.

The plotted data are shown in Figures 14.14 through 14.29. Gust velocity rms values were plotted versus wind speed for wind direction category. In Figures 14.14 through 14.25, the data for different categories were plotted separately and approximate mean lines were drawn through the data. These mean lines for each leg are shown in Figures 14.26 through 14.29. Certain trends can be seen although the data are widely scattered.

The most significant differences between the gust rms values recorded when wind direction was perpendicular to a mountain ridge and those recorded for a diagonal wind direction occur for the leg 7 data. The reason for this may be the fact that the first part of leg 7 does not run along any predominant mountain ridge. The airplane required only approximately 32 statute miles to record a 4.5 minute turbulence sample although the legs were laid out to be approximately 45 statute miles long. Therefore, approximately one-half of the data recorded on leg 7 were recorded prior to when the aircraft reached the beginning of the ridge. Some effects of the ridge would probably be included when the wind direction was perpendicular to the ridge or diagonal from 272.5° to 317.5° (see Table 14.1). Less effects should have been present when the wind blew diagonally from 182.5° to 227.5°. Only approximately 8 per cent of the wind directions that were classified as diagonal were between 182.5° and 227.5°. Thus, diagonally categorized data of leg 7 are probably more related to what could be expected from parallel or windward wind direction data.

TABLE 14.1

WIND DIRECTION CATEGORIZATION

Leg No.	Airplane on Leeward Side of Ridge			Airplane on Windward Side of Ridge
	Wind Direction When Categorized Parallel to Ridge	Wind Direction When Categorized Diagonal to Ridge	Wind Direction When Categorized Perpendicular to Ridge	Wind Direction
5 and 6	157.5° to 202.5° and 337.5° to 22.5°	202.5° to 247.5° and 292.5° to 337.7°	247.5° to 292.5°	0° to 180°
7	137.5° to 182.5° and 317.5° to 2.5°	182.5° to 227.5° and 272.5° to 317.5°	227.5° to 272.5°	0° to 180°
8	137.5° to 182.5° and 337.5° to 22.5°	182.5° to 227.5° and 272.5° to 337.5°	227.5° to 272.5°	0° to 160°

Unfortunately only a small amount of data were recorded when the wind direction was either parallel to the ridge or the airplane was on the windward side of the ridge. The prevailing wind direction over all legs was such that the airplane was usually on the leeward sides of the ridges. This is probably one reason for the higher gust velocity rms values recorded at Peterson than at the other three locations. Only approximately 17 per cent of the wind direction data recorded over legs 5, 6, 7, and 8 at Peterson were classified as parallel or windward. Although these data are few, there are enough to indicate that lower gust velocity rms values were recorded during these wind conditions on legs 5 and 7 than during conditions when the wind direction was categorized as perpendicular or diagonal. Also, the correlation between gust velocity rms values and wind

speed was less for data recorded on the windward sides of the mountain ridges. This agrees with the results shown in Figure 14.9 regarding the effects of terrain on the relationship between gust velocity rms and wind speed. The windward and parallel data recorded on leg 6 are mostly clustered at the low wind speeds and are inconclusive.

Leg 8 is classified as a plains leg but data were evaluated with respect to wind direction because of its proximity to a predominant mountain ridge and rough terrain. The gust velocity rms values show a different correlation with wind speed, depending upon how the wind direction was categorized. The gust rms values for the perpendicular and diagonal grouping generally increased slightly with increasing wind speed. An opposite trend is noted for the parallel and windward data, and these data contain greater gust velocity rms values at the lower wind speeds.

For data recorded on legs 5, 6, and 7, the gust velocity rms values, and their relationships to perpendicular and diagonal wind speeds, are significantly larger for the lateral component than for either the vertical or the longitudinal components of turbulence. This is probably because the airplane was flown parallel to the ridges on these legs and, therefore, the predominant winds blowing across these ridges were side winds with respect to the airplane. The peaks and openings along these ridges would cause an intermittent side wind, or lateral wind component, and increase the lateral gust velocity rms values.

Relationships between vertical gust velocity rms values and wind speed were investigated in Reference 14.1. This reference suggests that for flight over smooth terrain, the rms gust-wind speed relationship varies primarily as a function of atmospheric stability, while over mountainous terrain, the effects of stability do not appear to be significant. The LO-LOCAT Phase III data were also investigated with respect to terrain and stability. These data are shown in Figure 14.30 where the slope of the least-square lines of wind versus gust velocity rms data are plotted. The data were plotted for all three components of turbulence. The only significant variation with stability occurs for data obtained over the low mountains. For these data, the relationship between wind and rms gusts becomes less as the atmosphere becomes more unstable. The relationship over high mountains is slightly less during very stable conditions than during conditions of stable, neutral, and unstable atmospheric stability. Stability seems to have very little effect on the relationship of data obtained over the plains.

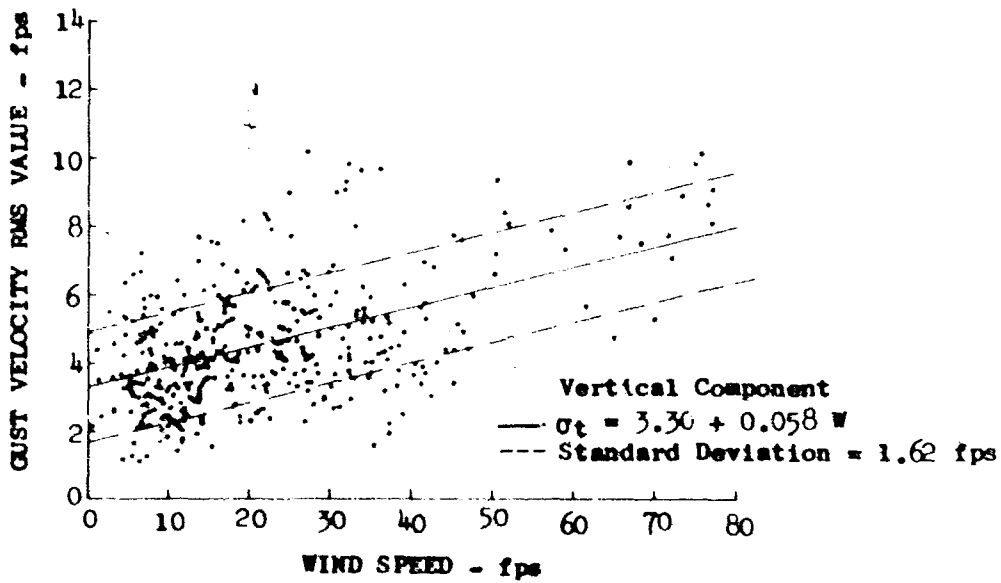
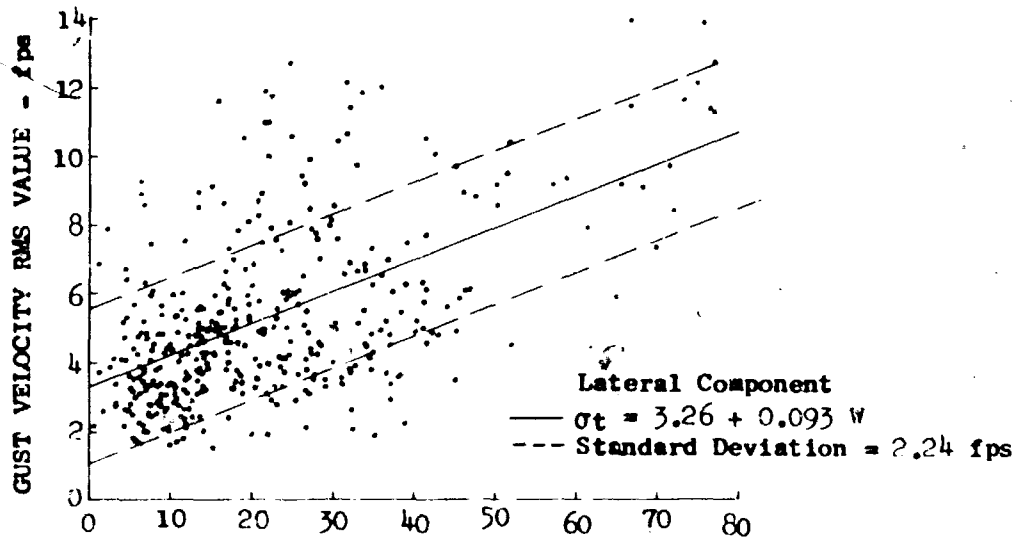
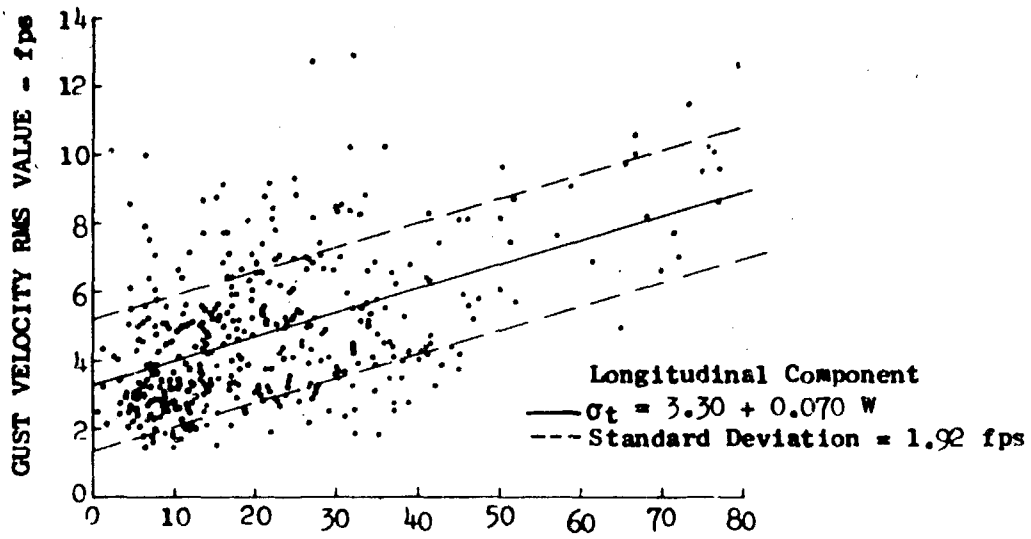


Figure 14.1 Gust Velocity RMS Values Versus Wind Speed at 250 Feet Over High Mountains

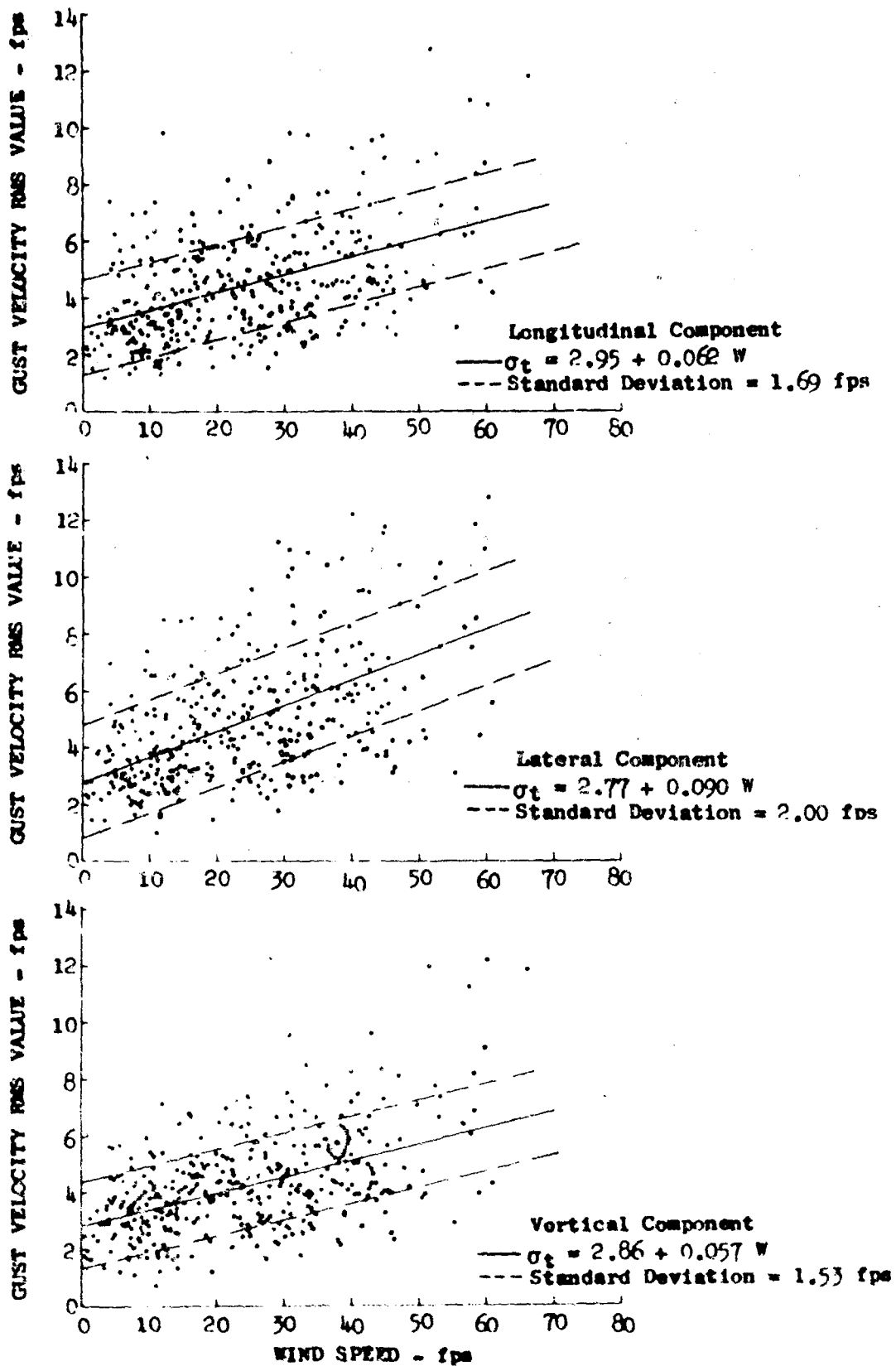


Figure 14.2 Gust Velocity RMS Values Versus Wind Speed at 750 Feet Over High Mountains

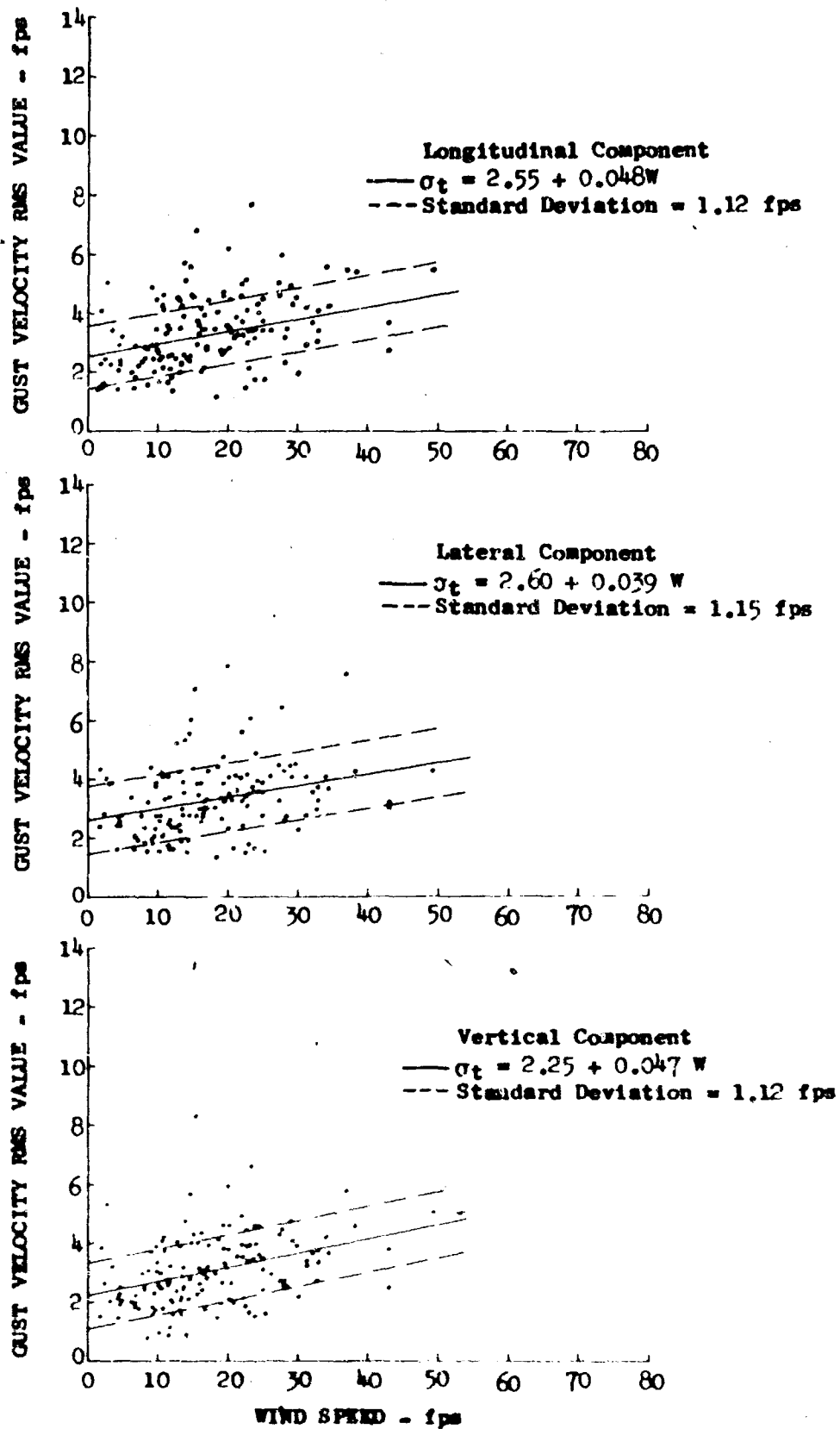


Figure 14.3 Gust Velocity RMS Values Versus Wind Speed at 250 Feet Over Low Mountains

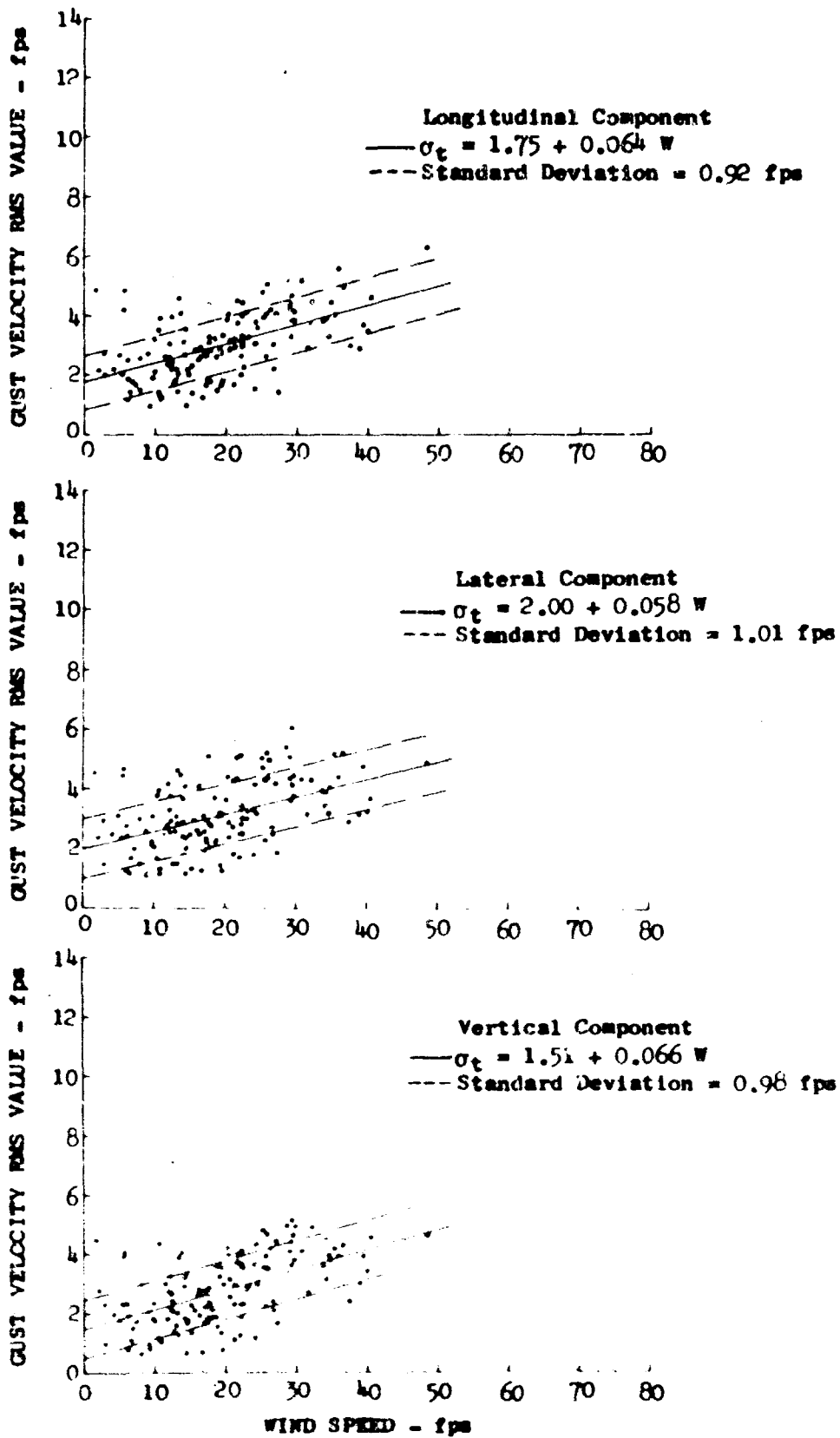


Figure 14.4 Gust Velocity RMS Values Versus Wind Speed at 750 Feet Over Low Mountains

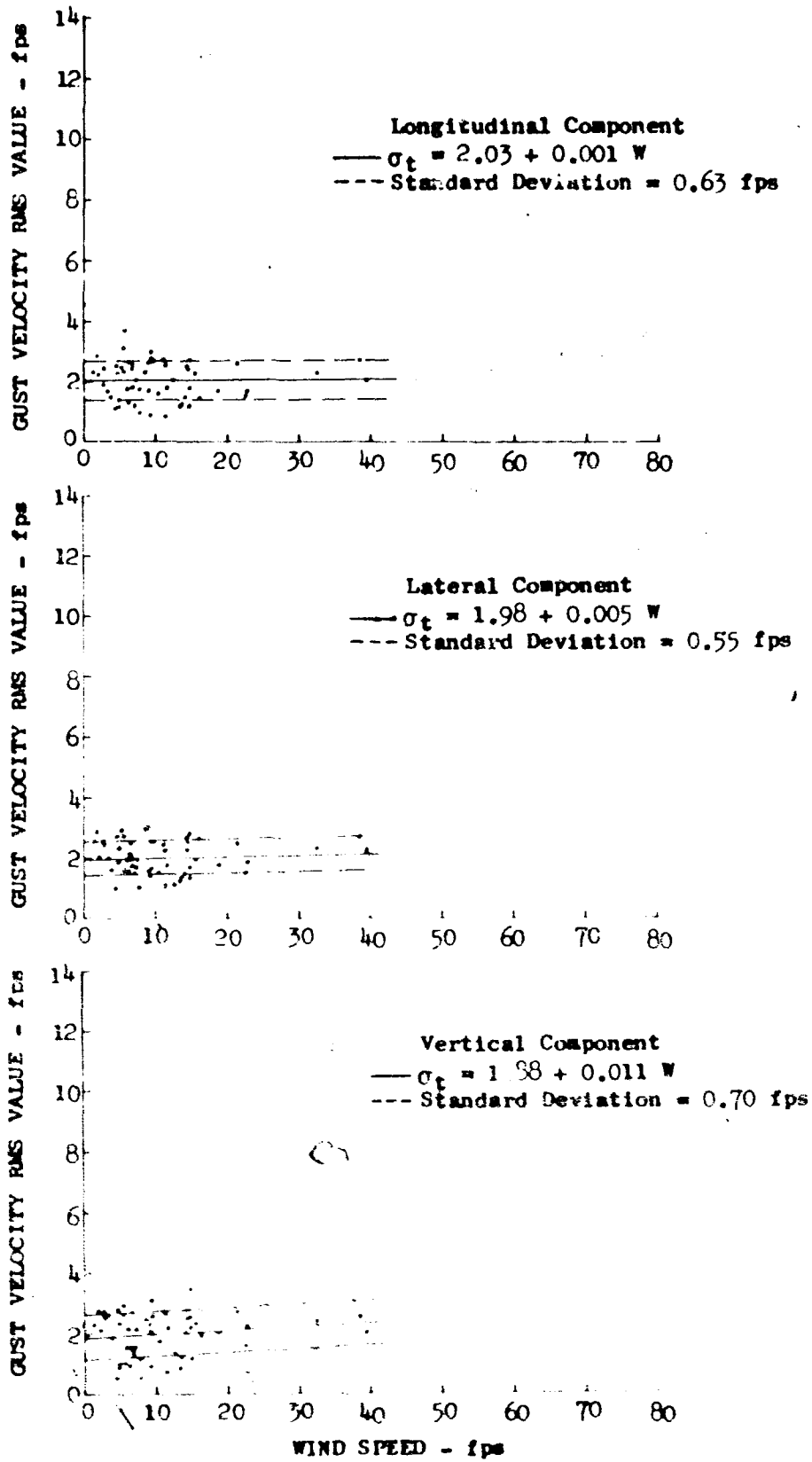


Figure 14.5 Gust Velocity RMS Values Versus Wind Speed at 250 Feet Over Desert



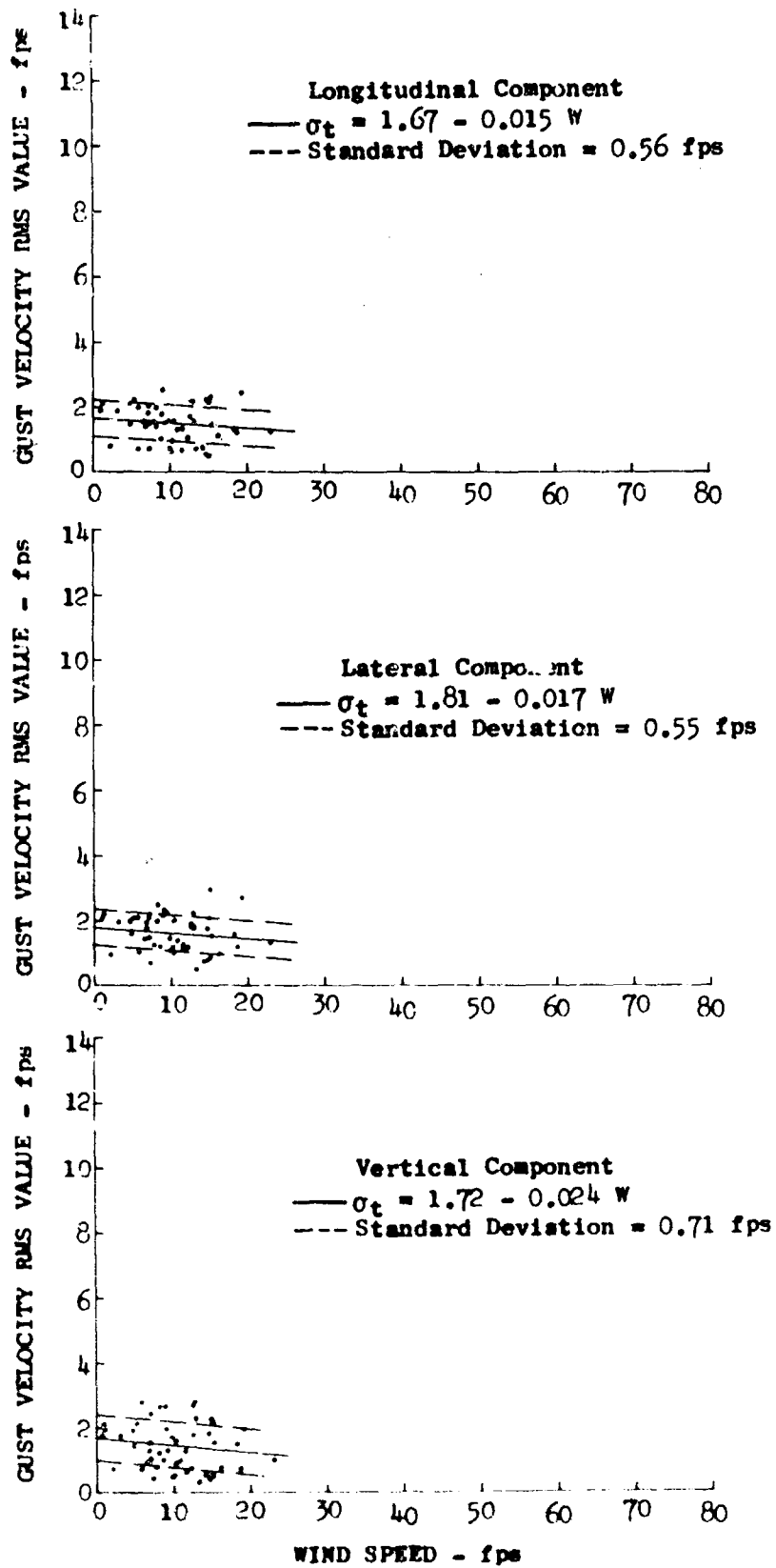


Figure 14.6 Gust Velocity RMS Values Versus Wind Speed at 750 Feet Over Desert

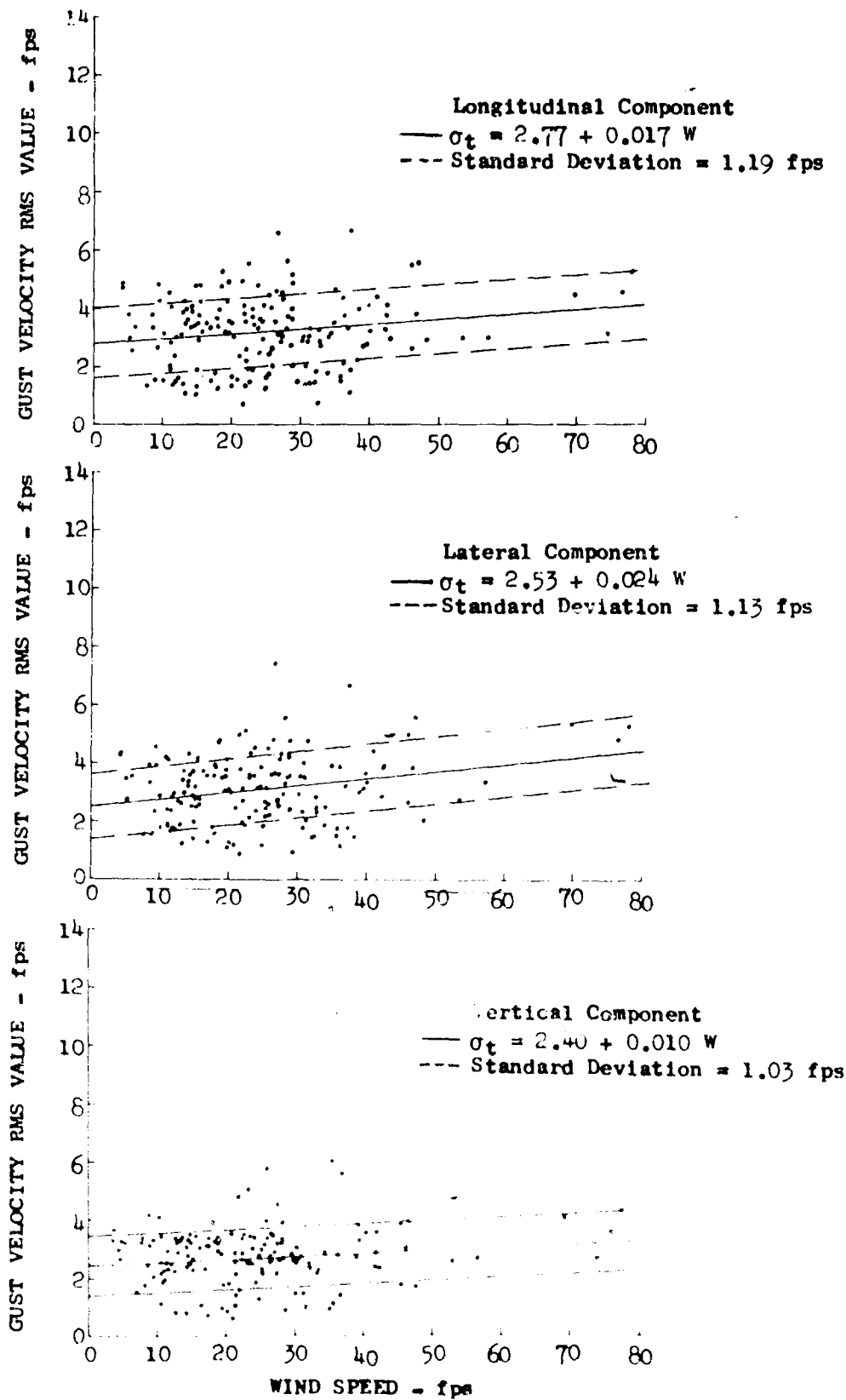


Figure 14.7 Gust Velocity RMS Values Versus Wind Speed at 250 Feet Over Plains

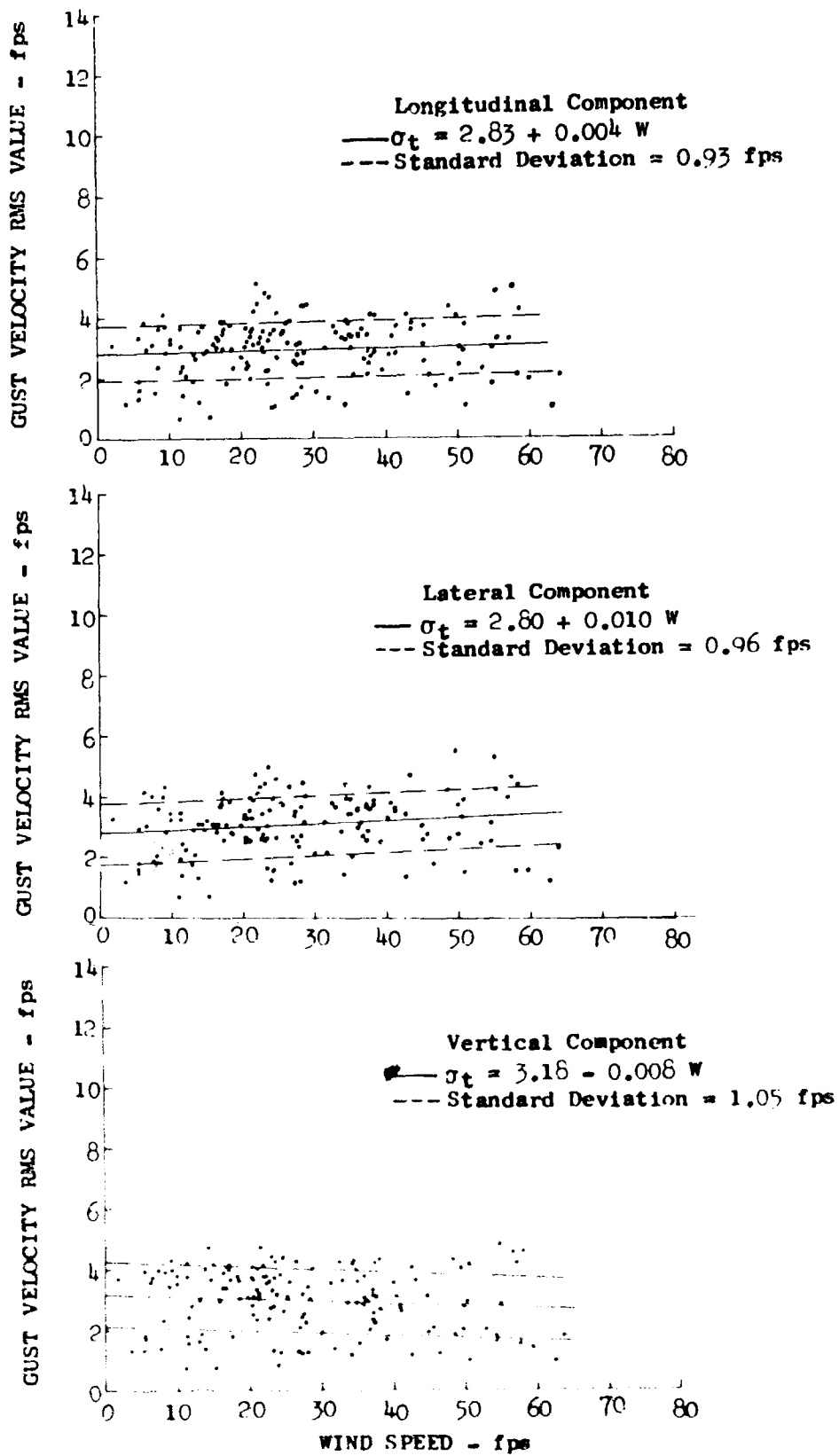


Figure 14.8 Gust Velocity RMS Values Versus Wind Speed at 750 Feet Over Plains

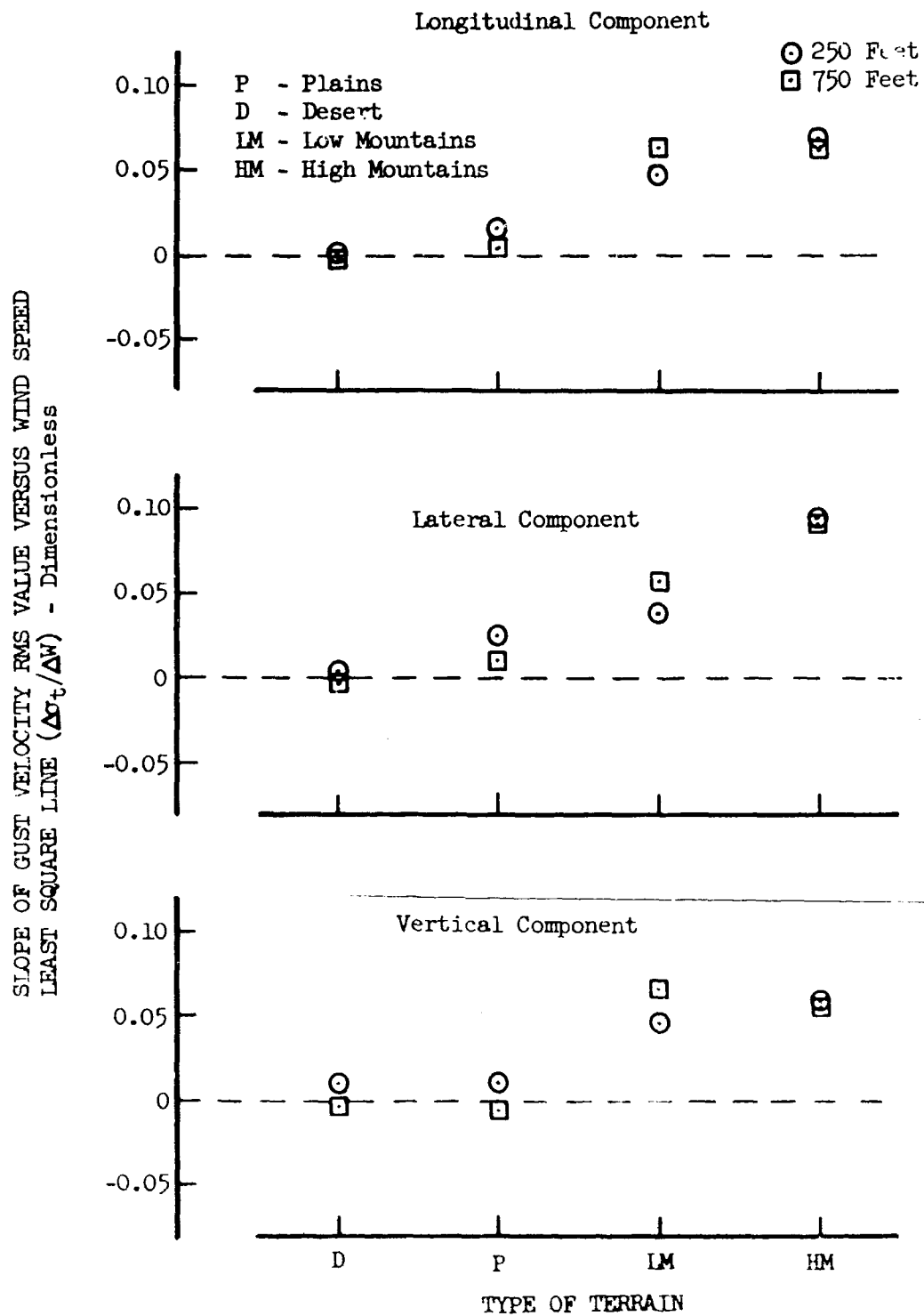
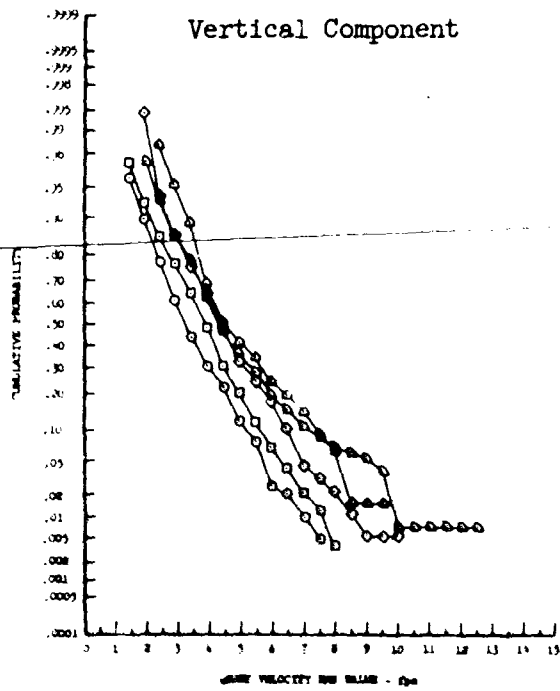
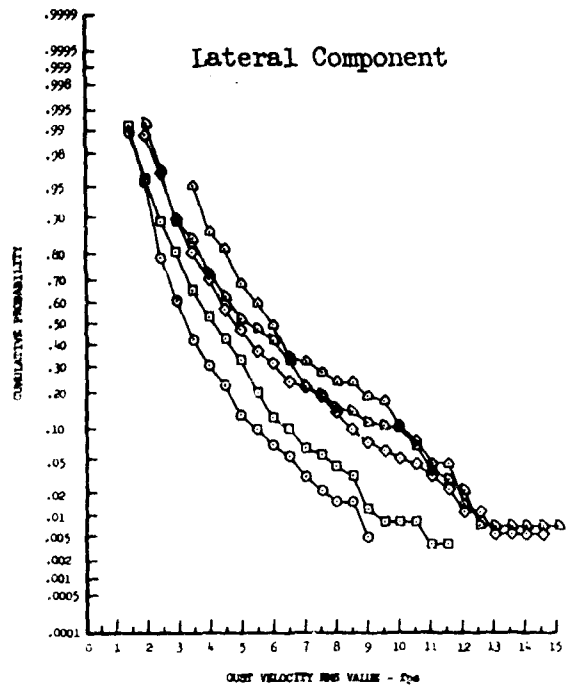
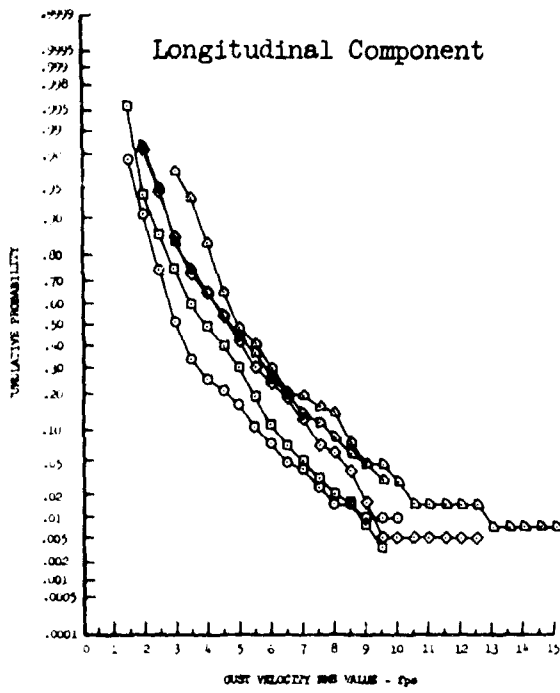
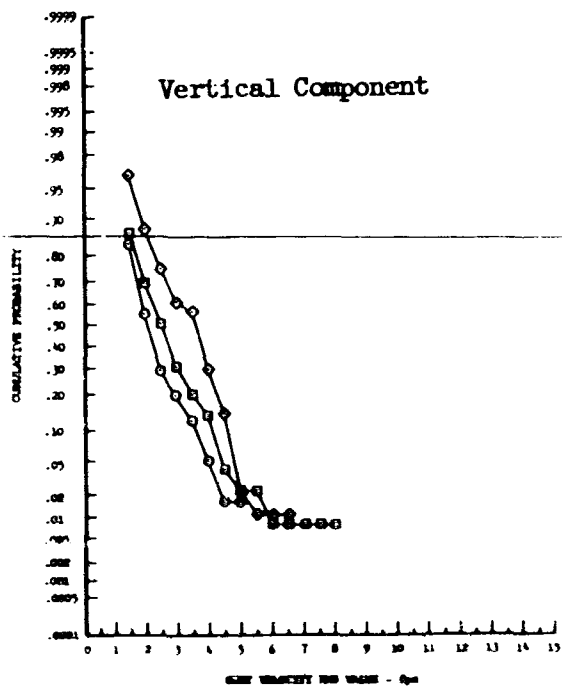
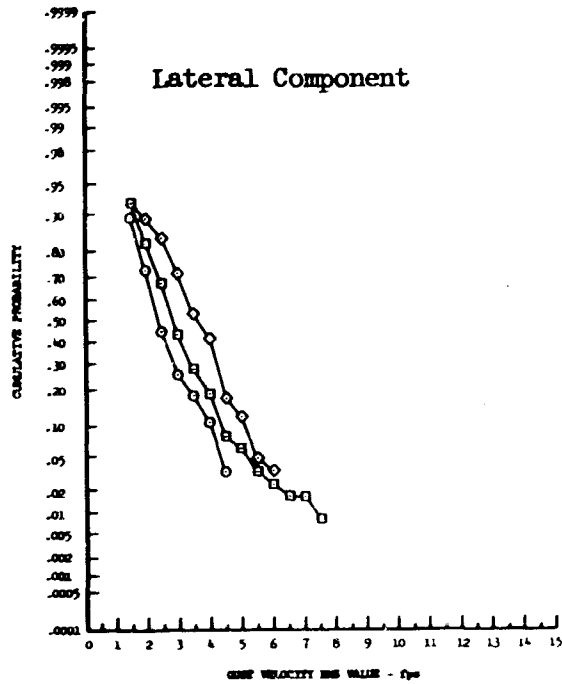
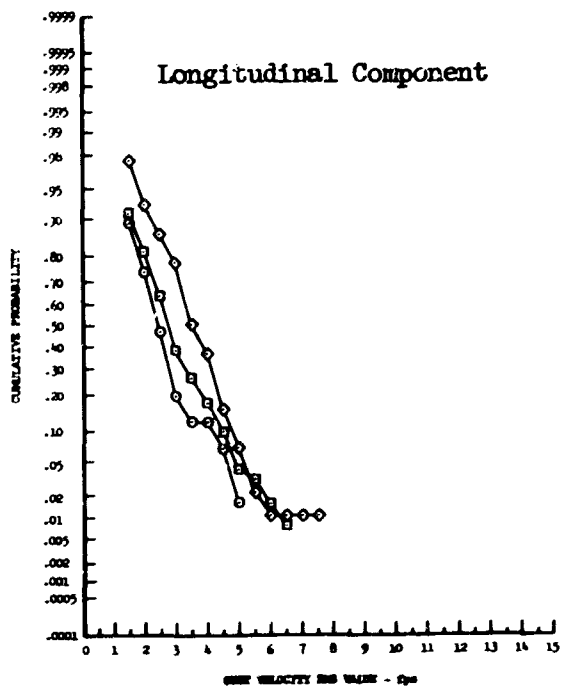


Figure 14.9 Correlation of Gust Velocity RMS Values with Wind Speed as a Function of Terrain and Altitude



- 0 < W < 10 fps
- 10 < W < 20 fps
- ◇ 20 < W < 30 fps
- ▷ 30 < W < 40 fps
- △ 40 < W < 50 fps

Figure 14.10 Effect of Wind Speed on Gust Velocity RMS Values - High Mountains



- 0 < W < 10 fpm
- 10 < W < 20 fpm
- ◇ 20 < W < 30 fpm

Figure 14.11 Effect of Wind Speed on Gust Velocity RMS Values - Low Mountains

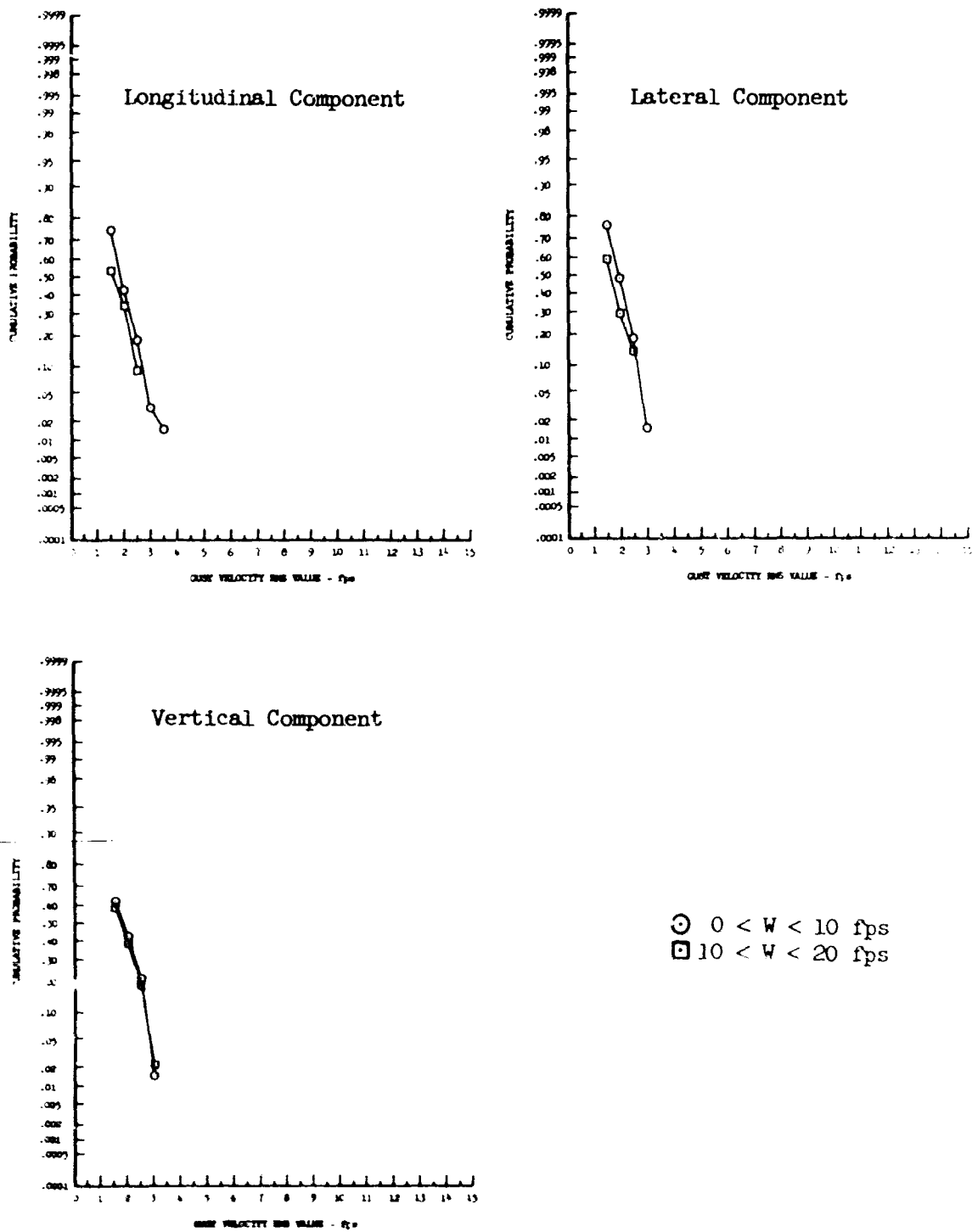
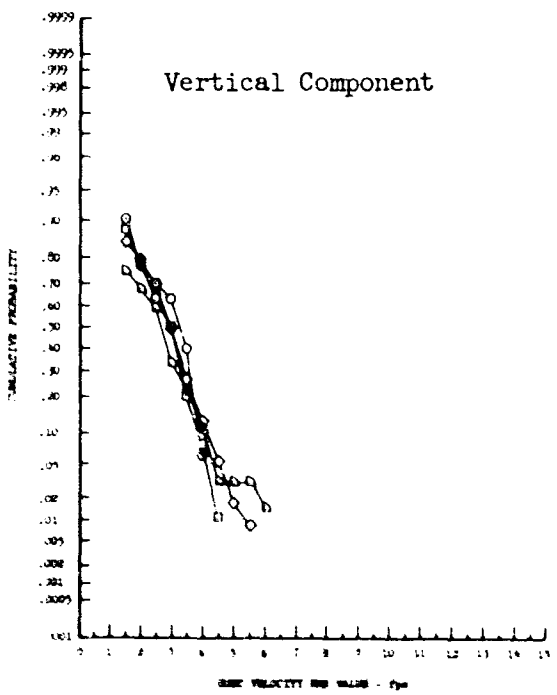
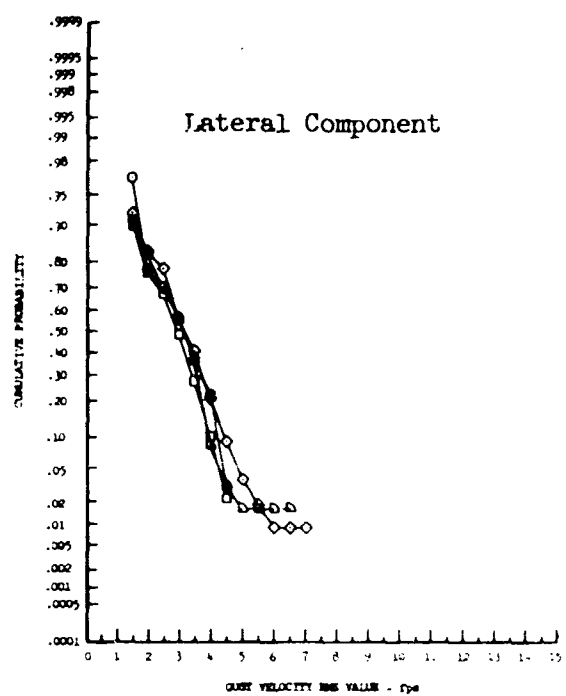
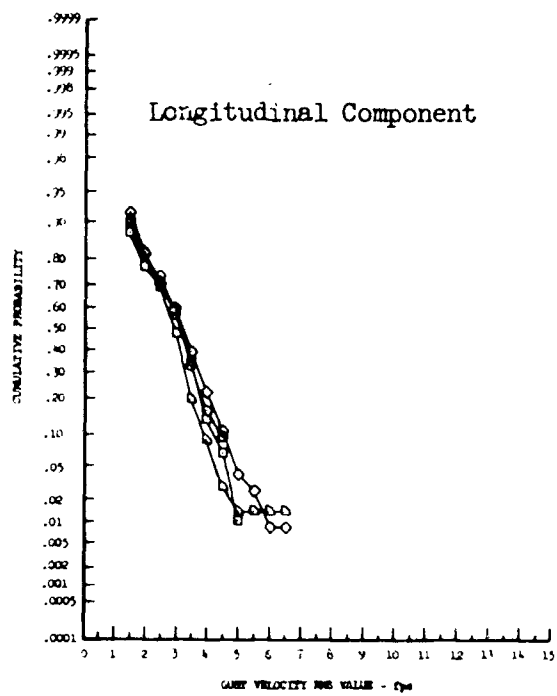


Figure 14.12 Effect of Wind Speed on Gust Velocity RMS Values - Desert

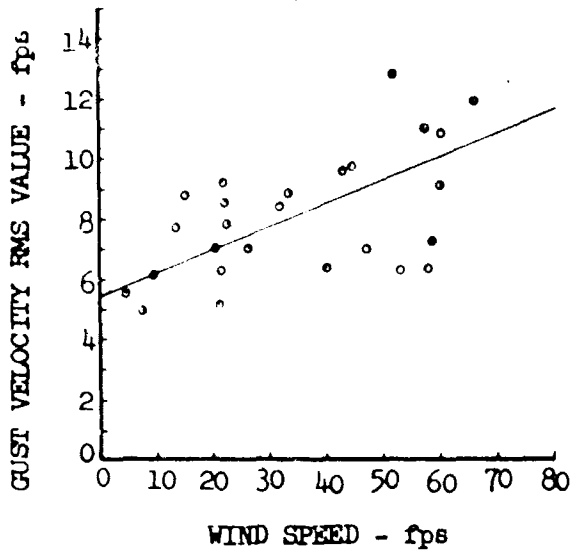


- 0 < W < 10 fps
- 10 < W < 20 fps
- ◇ 20 < W < 30 fps
- ▢ 30 < W < 40 fps

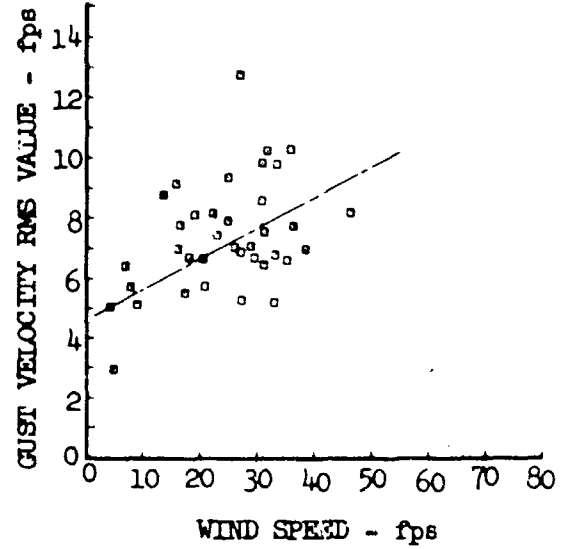
Figure 14.13 Effect of Wind Speed on Gust Velocity RMS Values - Plains



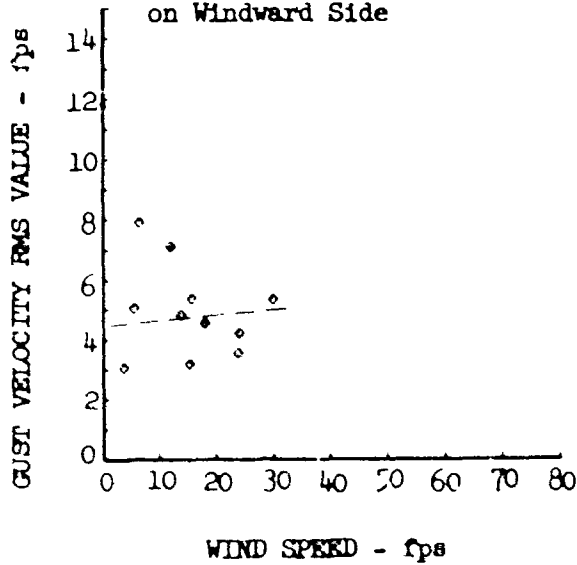
Wind Perpendicular to Ridge Line - Airplane on Leeward Side



Wind Diagonal to Ridge Line - Airplane on Leeward Side



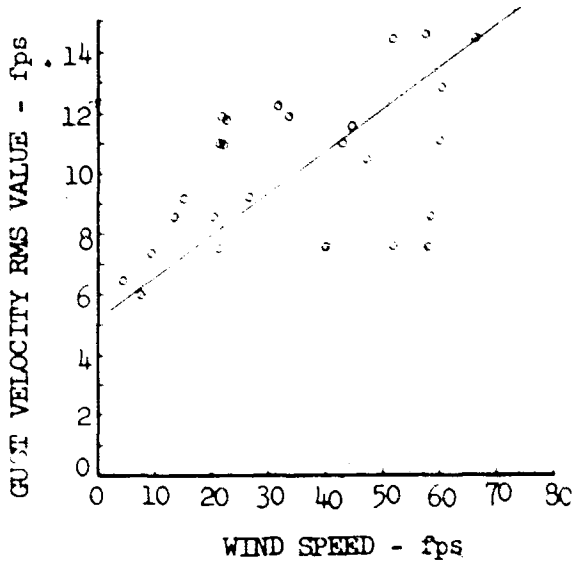
Wind Parallel to Ridge Line and/or Airplane on Windward Side



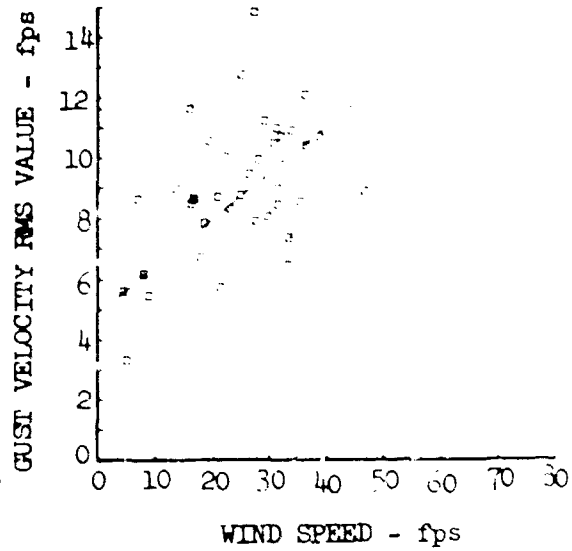
Approximate Mean Lines

Figure 14.14 Correlation Between Longitudinal Gust Velocity RMS Values and Wind Speed with Respect to Wind Direction - Leg 5 at Peterson

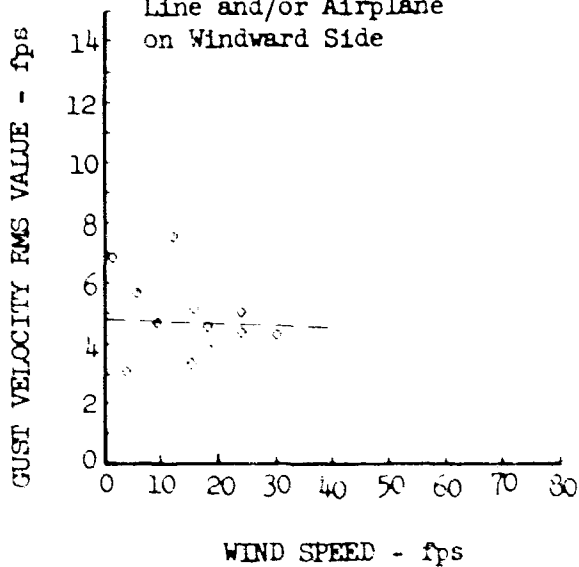
Wind Perpendicular to Ridge Line - Airplane on Leeward Side



Wind Diagonal to Ridge Line - Airplane on Leeward Side



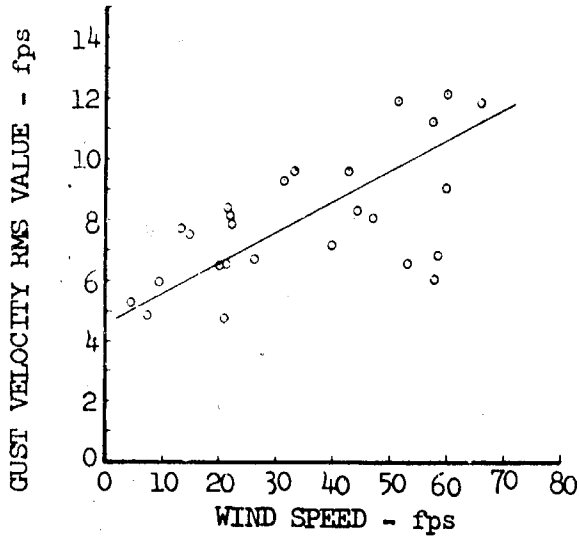
Wind Parallel to Ridge Line and/or Airplane on Windward Side



— Approximate Mean Lines

Figure 14.15 Correlation Between Lateral Gust Velocity RMS Values and Wind Speed with Respect to Wind Direction - Leg 5 at Peterson

Wind Perpendicular to  
Ridge Line - Airplane  
on Leeward Side



Wind Diagonal to Ridge  
Line - Airplane on  
Leeward Side

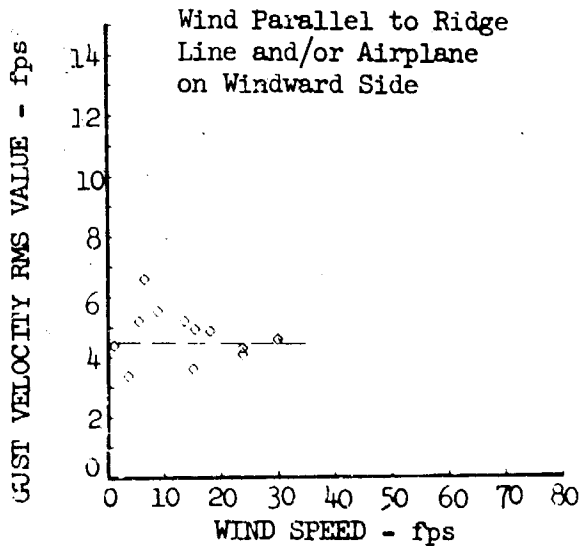
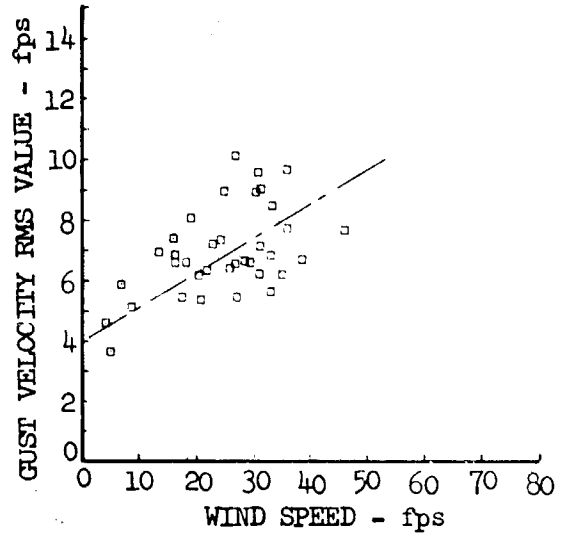


Figure 14.16 Correlation Between Vertical Gust Velocity RMS Values and Wind Speed with Respect to Wind Direction - Leg 5 at Peterson

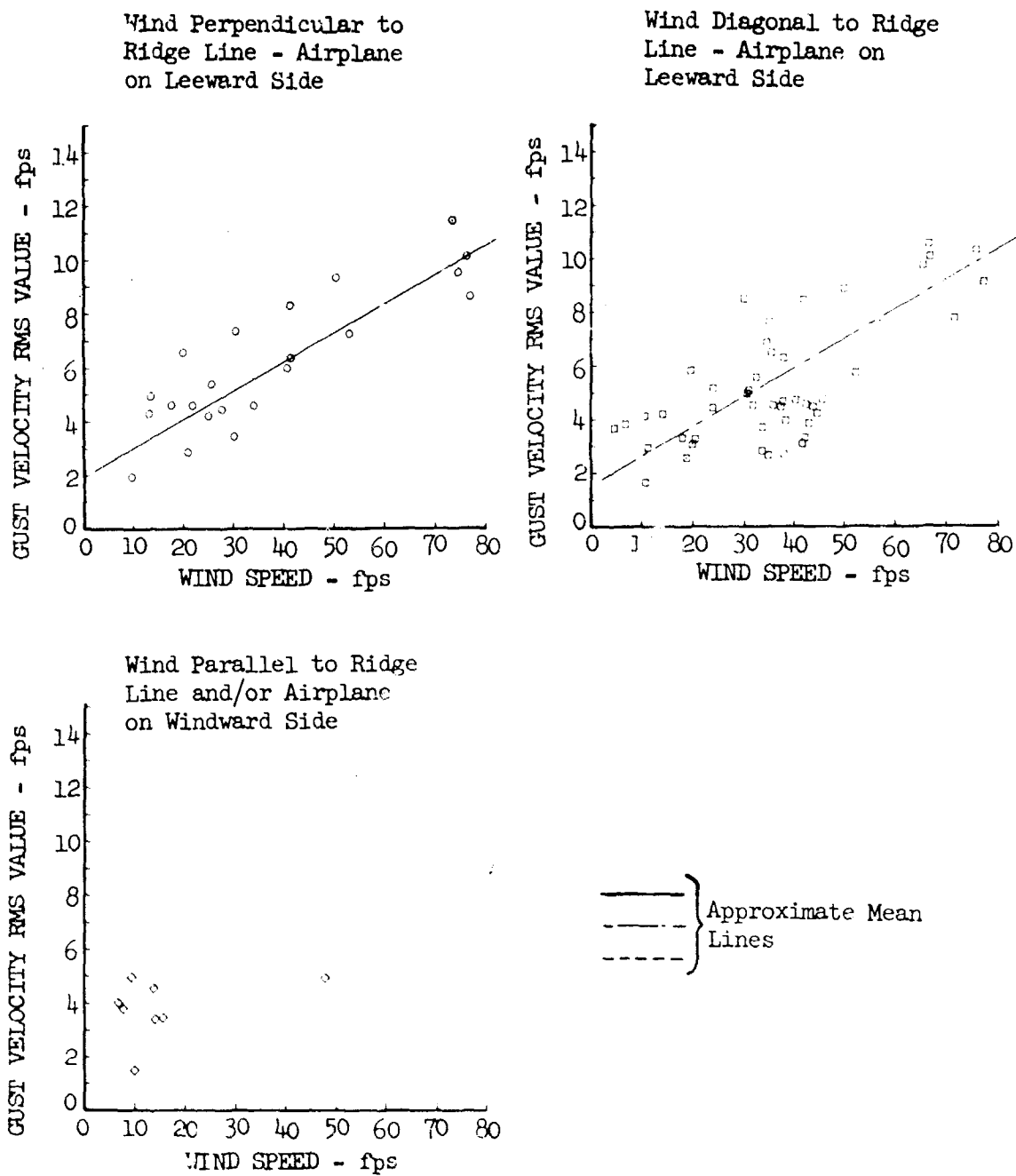
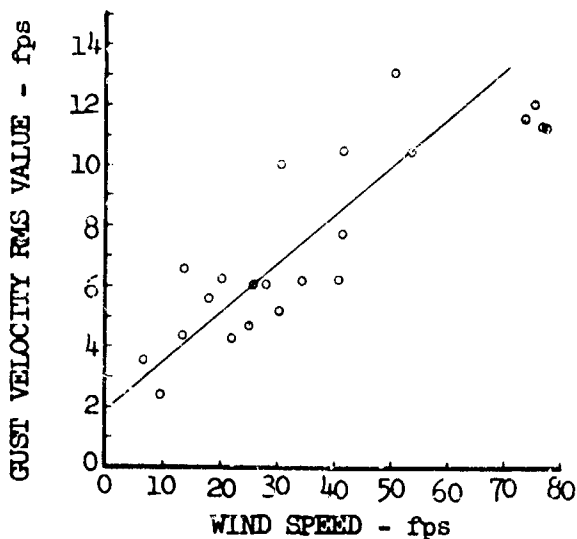
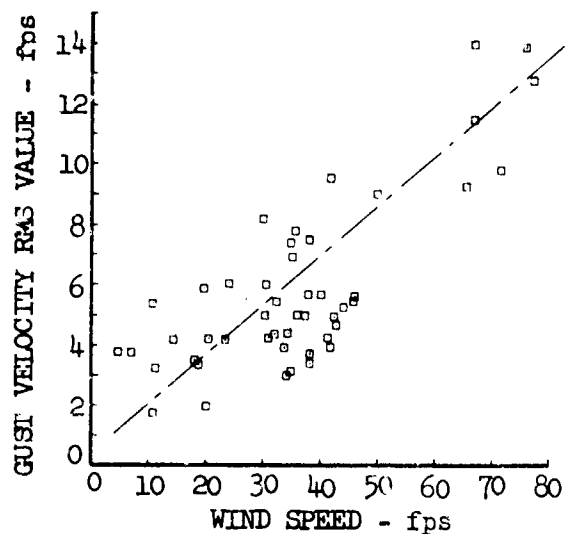


Figure 14.17 Correlation Between Longitudinal Gust Velocity RMS Values and Wind Speed with Respect to Wind Direction - Leg 6 at Peterson

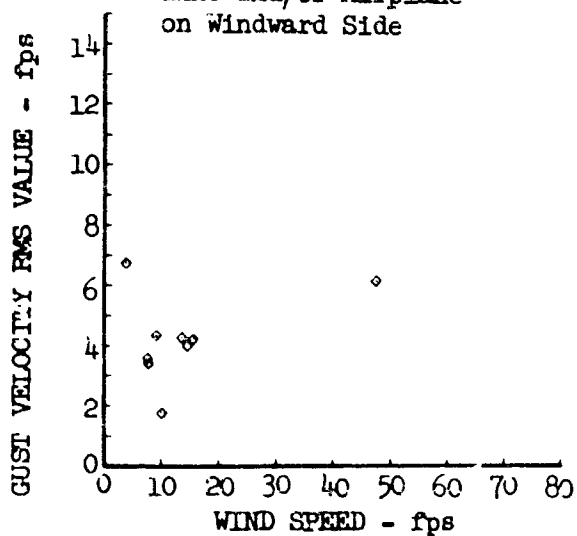
Wind Perpendicular to Ridge Line - Airplane on Leeward Side



Wind Diagonal to Ridge Line - Airplane on Leeward Side



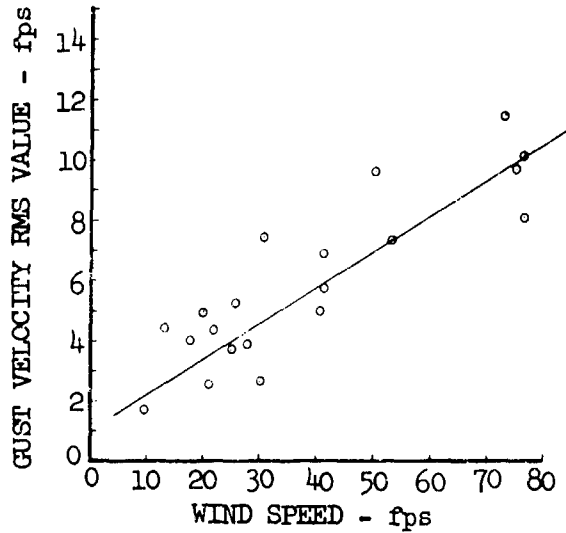
Wind Parallel to Ridge Line and/or Airplane on Windward Side



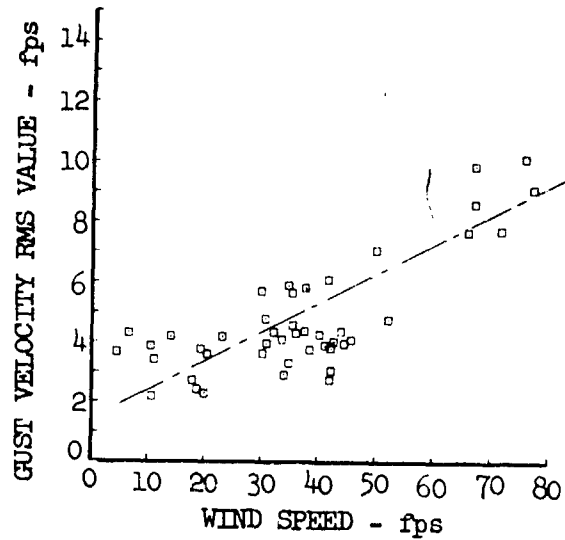
Approximate Mean Lines

Figure 14.18 Correlation Between Lateral Gust Velocity RMS Values and Wind Speed with Respect to Wind Direction - Leg 6 at Peterson

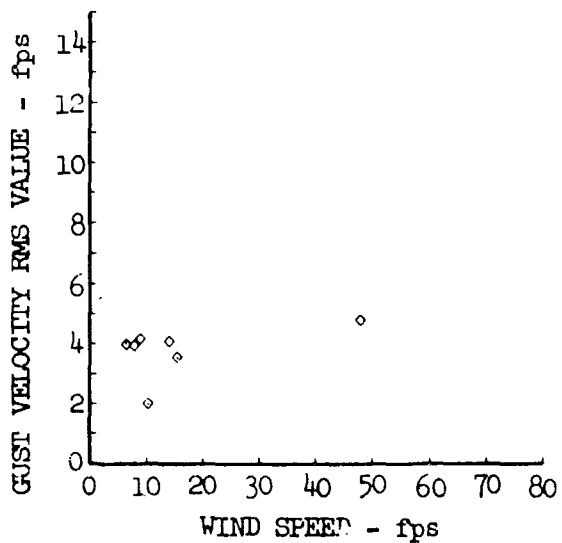
Wind Perpendicular to Ridge Line - Airplane on Leeward Side



Wind Diagonal to Ridge Line - Airplane on Leeward Side



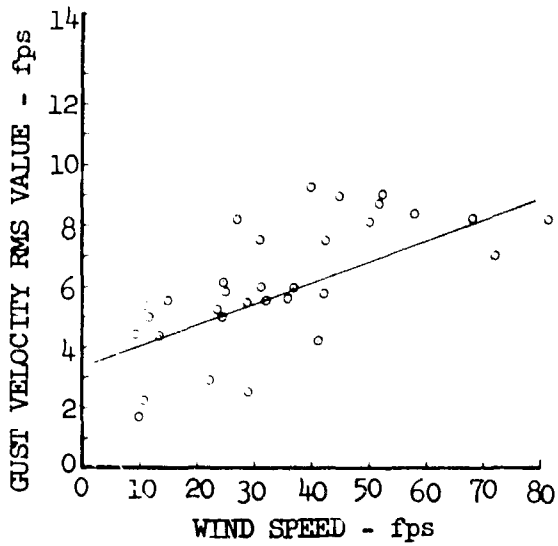
Wind Parallel to Ridge Line and/or Airplane on Windward Side



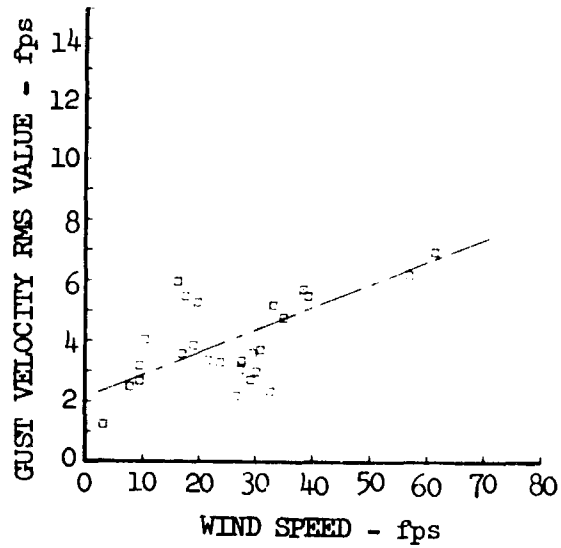
} Approximate Mean Lines

Figure 14.19 Correlation Between Vertical Gust Velocity RMS Values and Wind Speed with Respect to Wind Direction - Leg 6 at Peterson

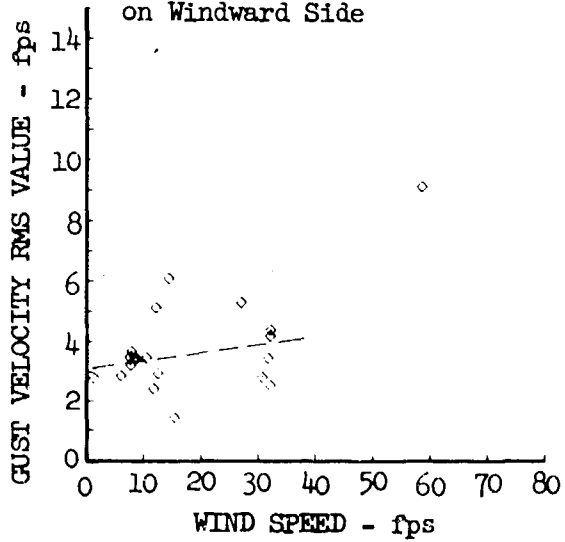
Wind Perpendicular to  
Ridge Line - Airplane  
on Leeward Side



Wind Diagonal to Ridge  
Line - Airplane on  
Leeward Side



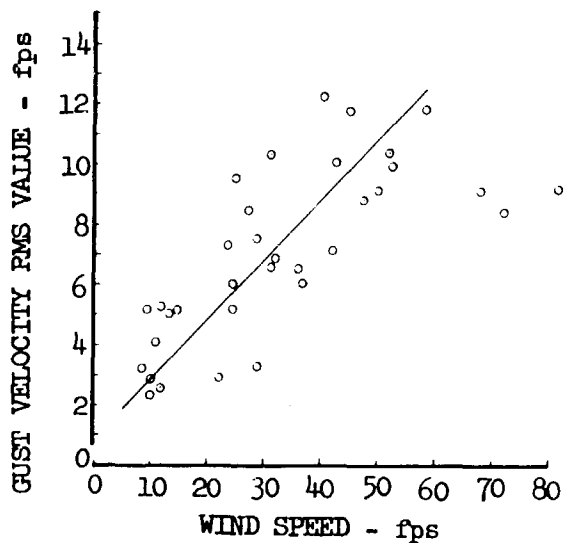
Wind Parallel to Ridge  
Line and/or Airplane  
on Windward Side



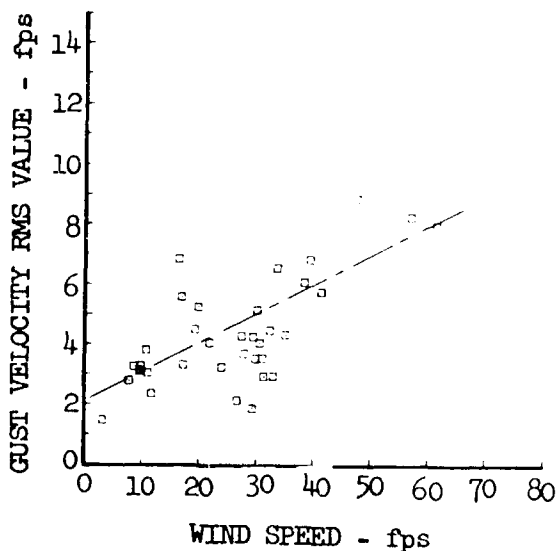
— } Approximate Mean  
- - - } Lines

Figure 14.20 Correlation Between Longitudinal Gust Velocity RMS Values and Wind Speed with Respect to Wind Direction - Leg 7 at Peterson

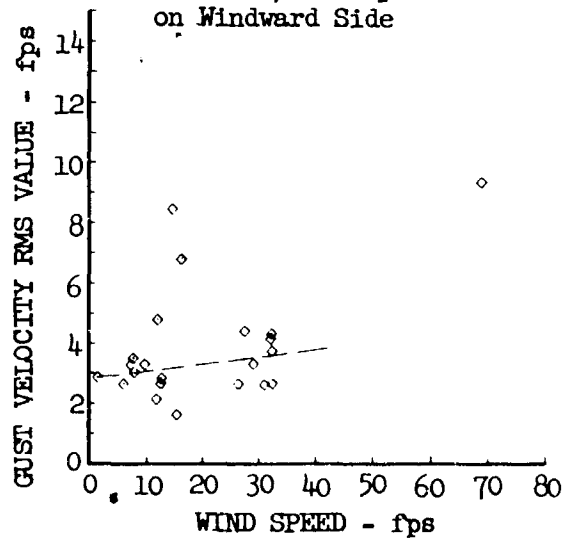
Wind Perpendicular to  
Ridge Line - Airplane  
on Leeward Side



Wind Diagonal to Ridge  
Line - Airplane on  
Leeward Side



Wind Parallel to Ridge  
Line and/or Airplane  
on Windward Side



— } Approximate Mean  
- - - } Lines

Figure 14.21 Correlation Between Lateral Gust Velocity RMS Values and Wind Speed with Respect to Wind Direction - Leg 7 at Peterson



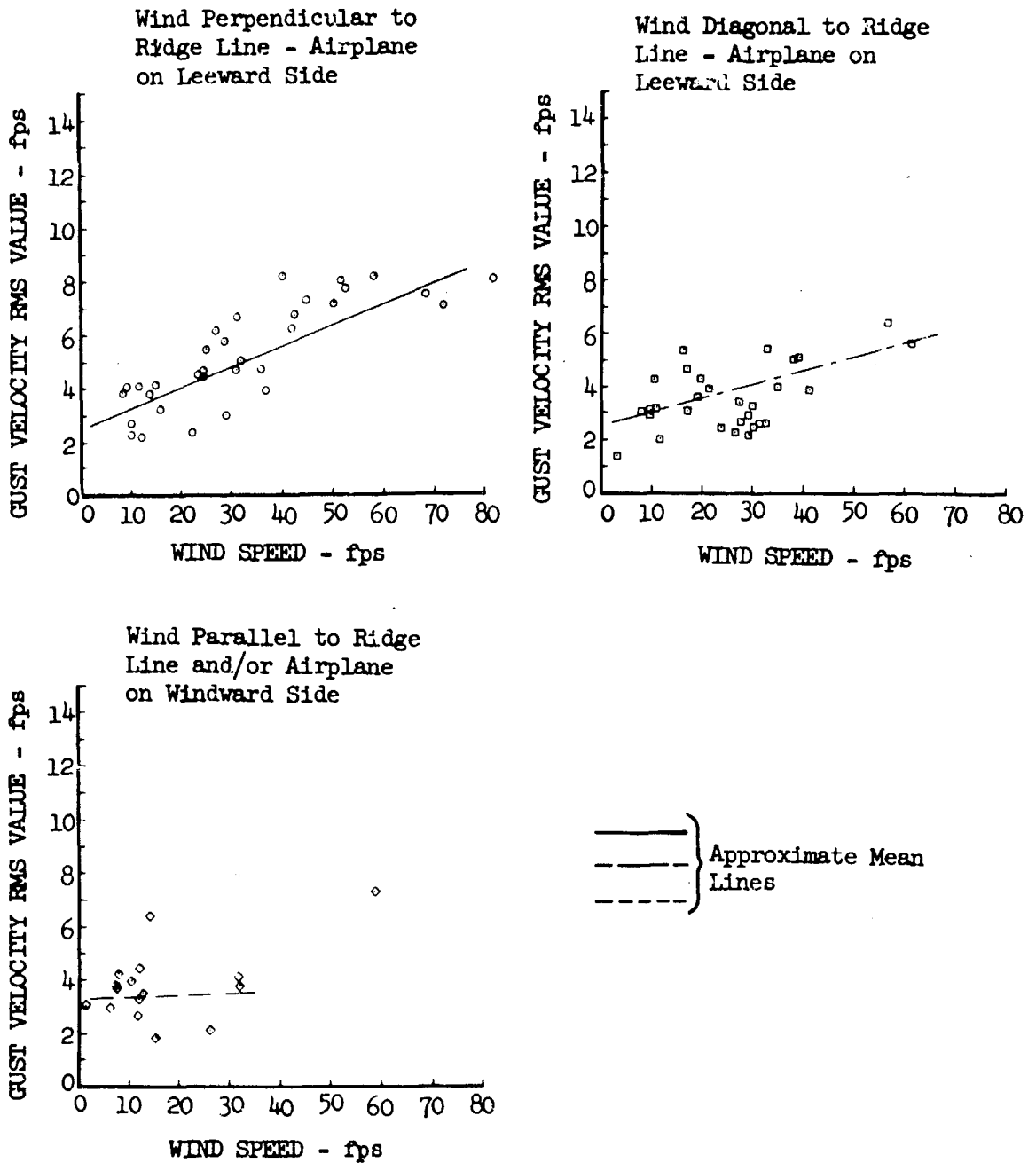


Figure 14.22 Correlation Between Vertical Gust Velocity RMS Values and Wind Speed with Respect to Wind Direction - Leg 7 at Peterson

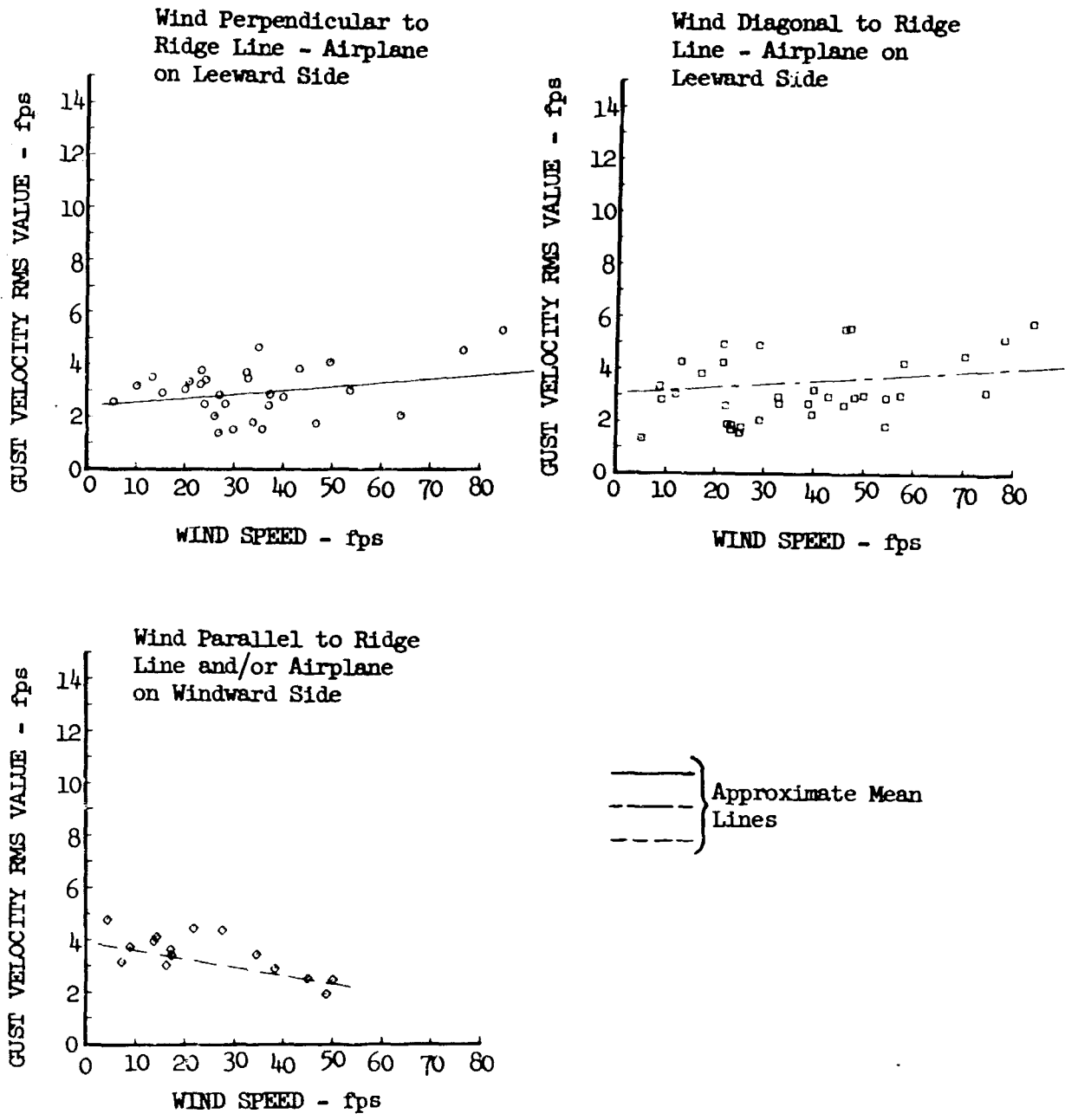


Figure 14.23 Correlation Between Longitudinal Gust Velocity RMS Values and Wind Speed with Respect to Wind Direction - Leg 8 at Peterson

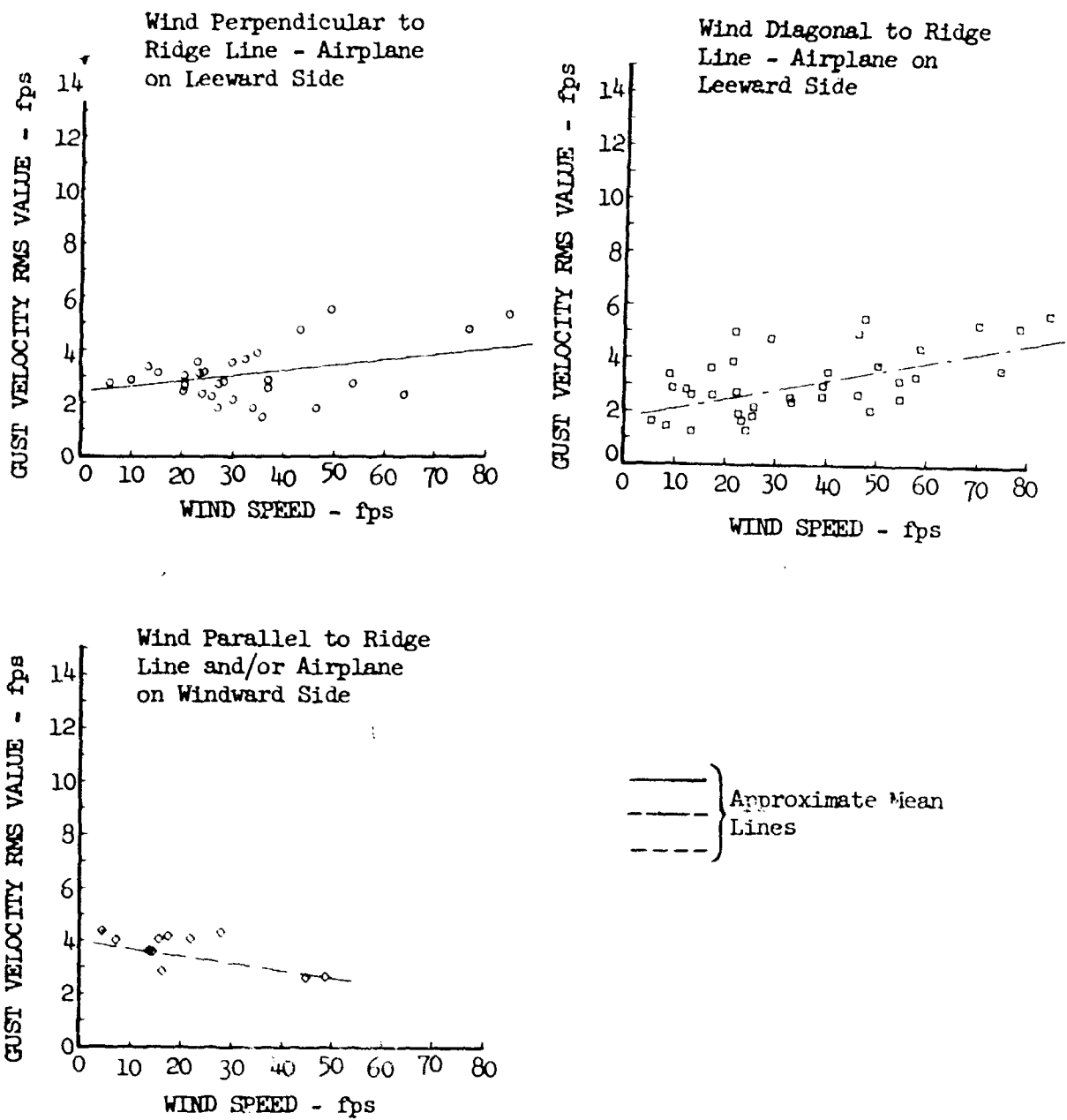
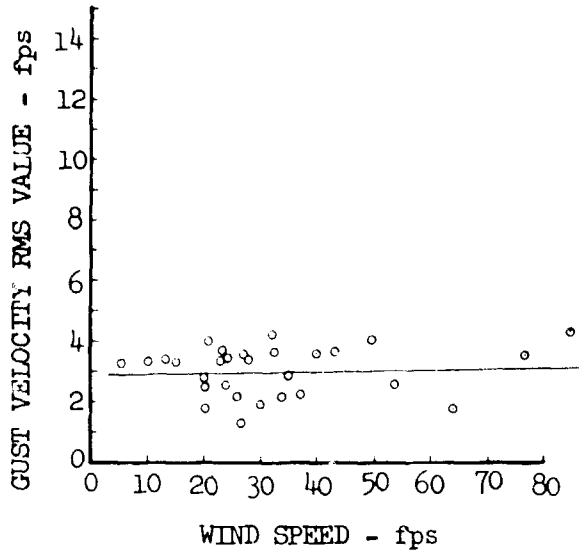
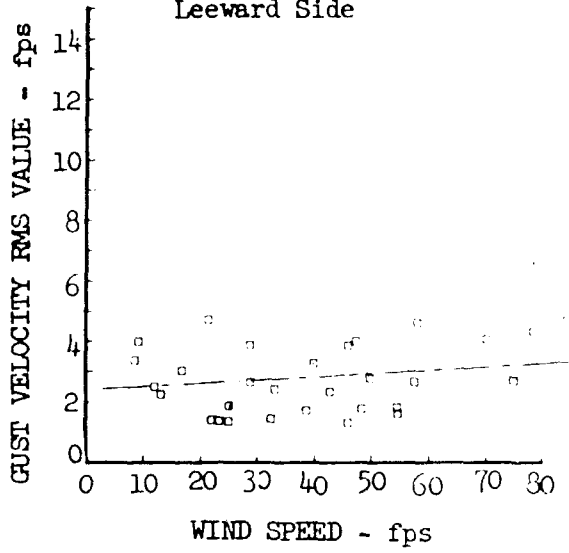


Figure 14.24 Correlation Between Lateral Gust Velocity RMS Values and Wind Speed with Respect to Wind Direction - Leg 8 at Peterson

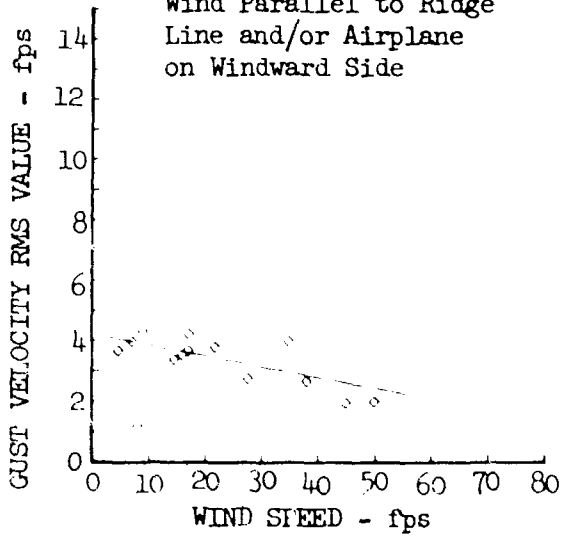
Wind Perpendicular to  
Ridge Line - Airplane  
on Leeward Side



Wind Diagonal to Ridge  
Line - Airplane on  
Leeward Side



Wind Parallel to Ridge  
Line and/or Airplane  
on Windward Side



— } Approximate Mean  
- - - } Lines  
- - - }

Figure 14.25 Correlation Between Vertical Gust Velocity RMS Values and Wind Speed with Respect to Wind Direction - Leg 8 at Peterson

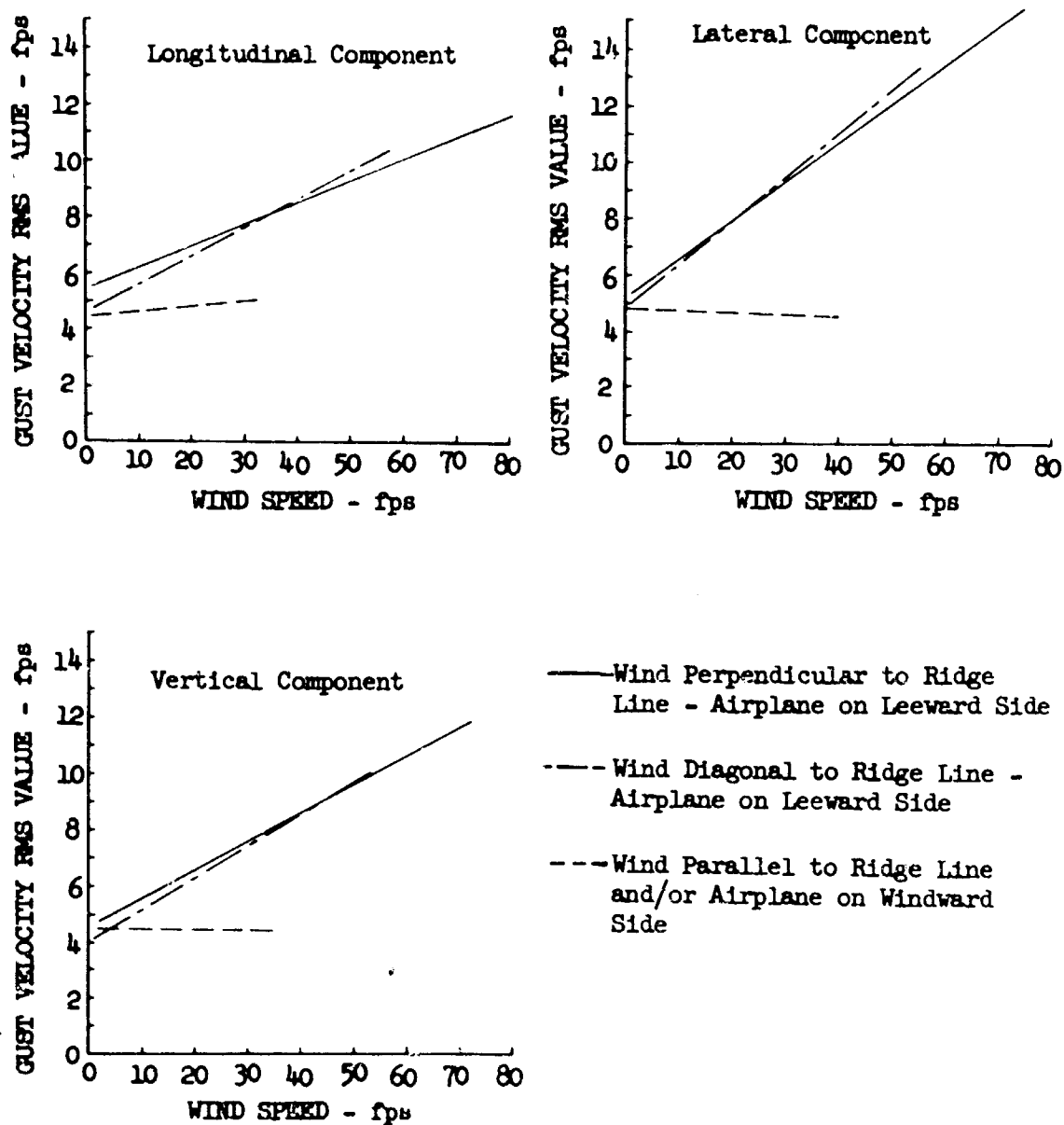


Figure 14.26 Effects of Wind Direction on the Correlation Between Gust Velocity RMS Values and Wind Speed - Leg 5 at Peterson

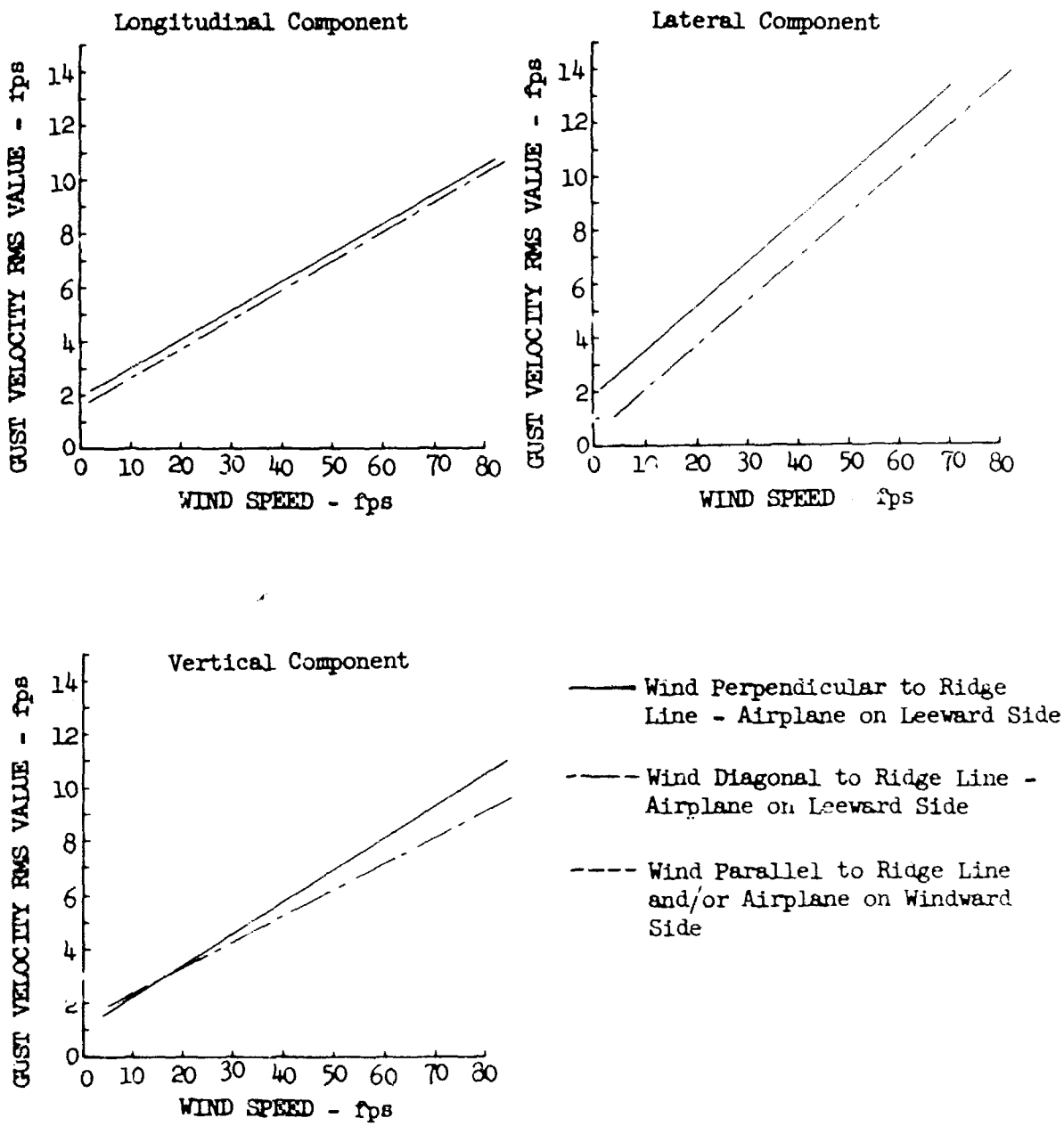


Figure 14.27 Effects of Wind Direction on the Correlation Between Gust Velocity RMS Values and Wind Speed - Leg 6 at Peterson

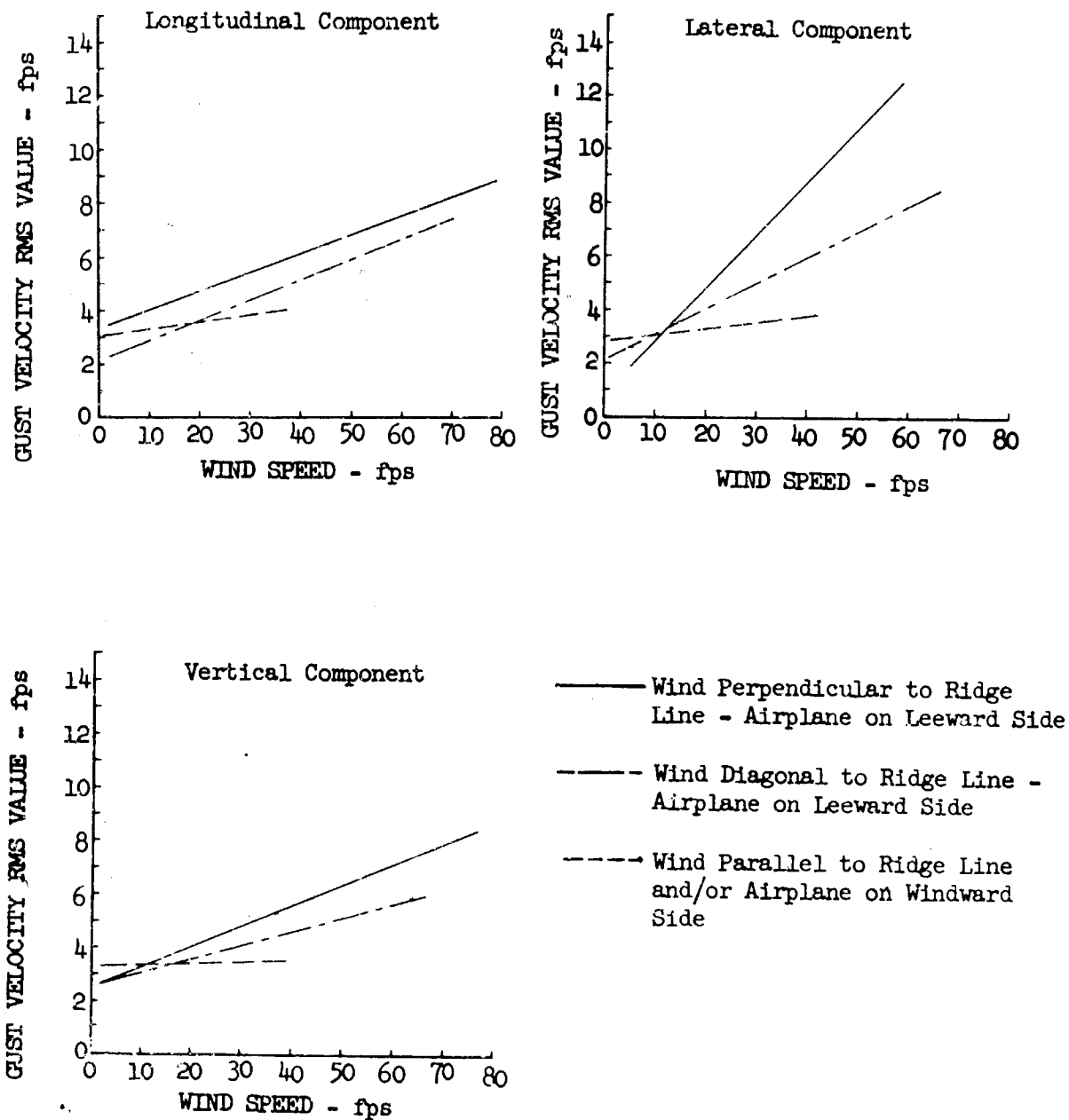


Figure 14.28 Effects of Wind Direction on the Correlation Between Gust Velocity RMS Values and Wind Speed - Leg 7 at Peterson

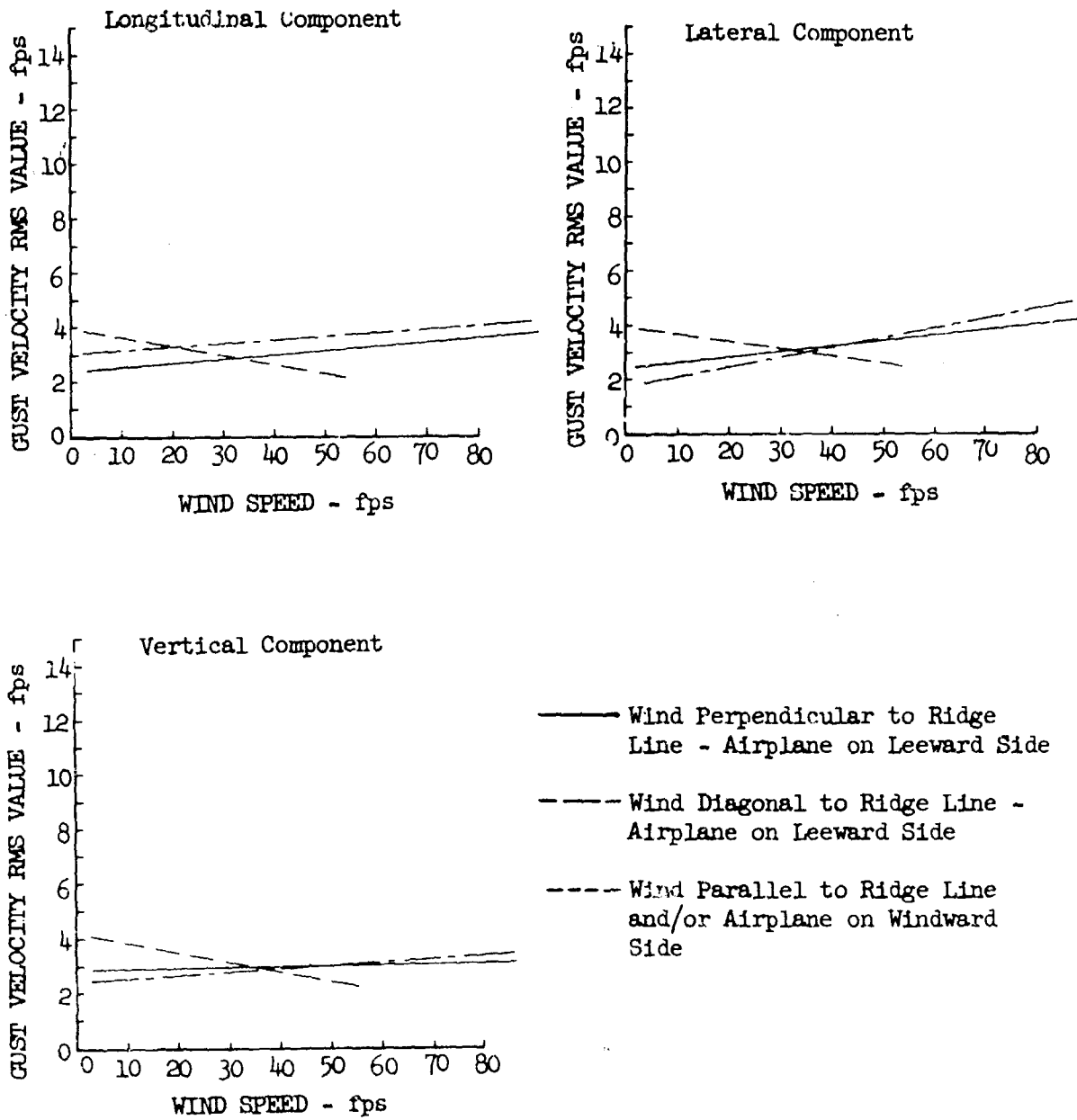


Figure 14.29 Effects of Wind Direction on the Correlation Between Gust Velocity RMS Values and Wind Speed - Leg 8 at Peterson



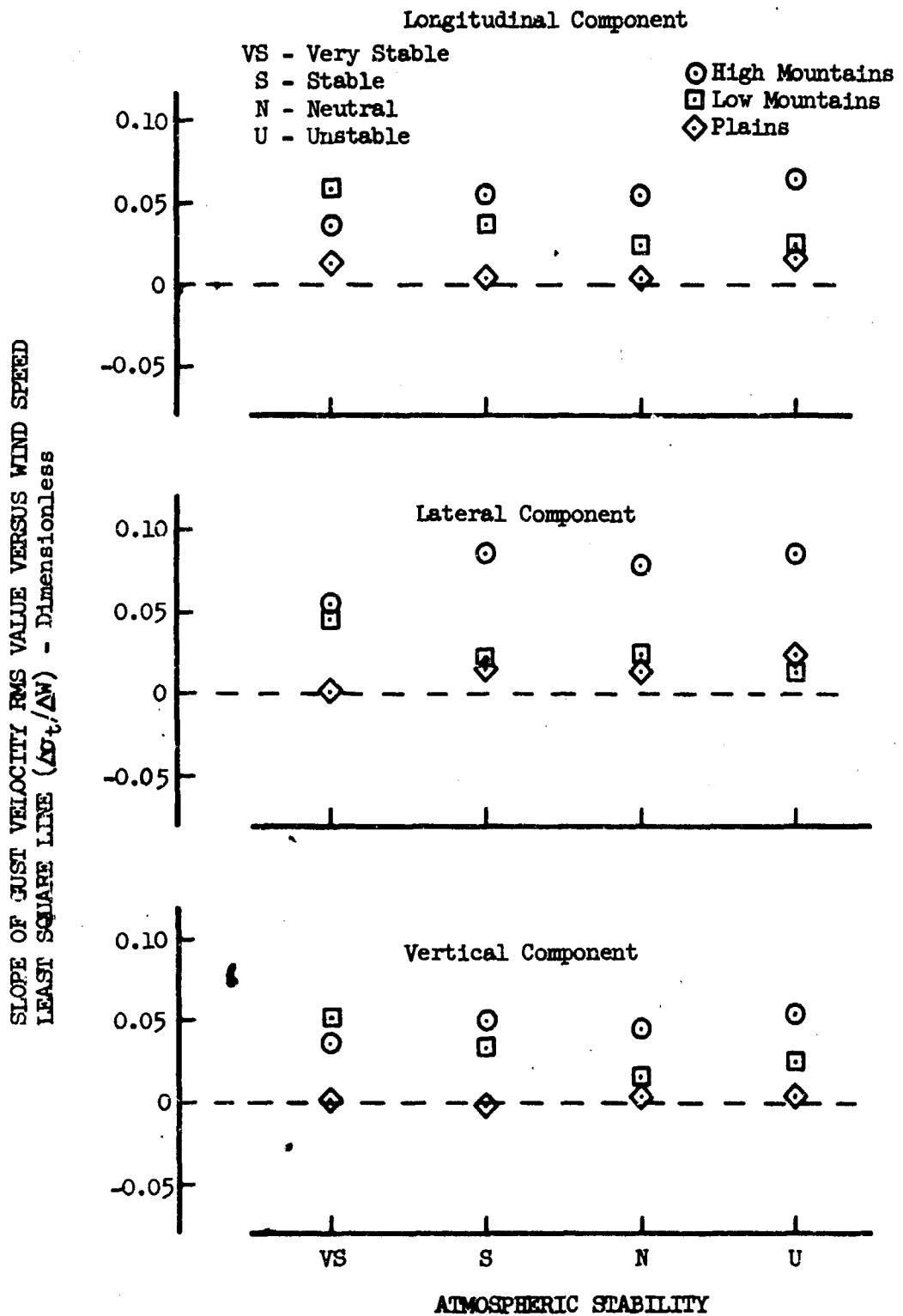


Figure 14.30 Correlation of Gust Velocity RMS Values with Wind Speed as a Function of Terrain and Atmospheric Stability

## 15. MAXIMUM DERIVED EQUIVALENT GUST VELOCITIES

An approximate maximum and/or minimum value of derived equivalent gust velocity was calculated for each turbulence sample. These values were used to establish the approximate turbulence level encountered and as an immediate guideline in determining if gust encounters were of a magnitude to warrant an airplane structural inspection. Maximum incremental acceleration from a one g mean was determined from "quick-look" strip charts of vertical acceleration at the airplane center of gravity. Computation of the derived equivalent gust velocity was accomplished using the equation:

$$U_{de} = \left[ \frac{2W}{C_{L_e} \rho_0 S V_e K_g} \right] \Delta N z c g \quad (15.1)$$

where  $K_g$ , the gust alleviation factor, is expressed as:

$$K_g = \frac{.88 \mu}{5.3 + \mu} \quad (15.2)$$

and  $\mu$ , the dimensionless airplane mass ratio, is defined by:

$$\mu = \frac{2W}{C_{L_e} \rho c g S} \quad (15.3)$$

Using the equation of state,  $\rho$  (air density) may be expressed as:

$$\rho = \frac{\rho_0 T_0}{P_c} \left( \frac{P_s}{T_s} \right) = .0412 \frac{P_s}{T_s} \quad (15.4)$$

The values of  $U_{de}$  equation constants for the T-33A airplane are defined below:

$c$  = mean aerodynamic chord = 6.72 feet

$g$  = gravitational constant = 32.2 feet/sec<sup>2</sup>

$\rho_0$  = standard day air density = .002378 slug/feet<sup>3</sup>

$S$  = wing area = 238 feet<sup>2</sup>

Constant values were determined for the equation variables to facilitate calculations in the field. This was accomplished by using an average gross weight for the airplane over the route (12,500 pounds), an equivalent airspeed approximated by target airspeed (591.15 feet per second), and the slope of the lift coefficient versus angle of attack curve at a Mach number equivalent to target airspeed and average altitude (5.91/radian). The ratio of static pressure to ambient temperature was estimated from data obtained during Phases I and II. This ratio was calculated by averaging

these data over a corresponding seasonal time period for each similar route leg. The values for this ratio and the simplified  $U_{de}$  equation derived by substitution of the assigned constants into Equation 15.1 are given in Table 15.1.

Cumulative probability distributions of  $U_{de}$  values calculated during Phase III are shown in Figures 15.1 through 15.4. A comparison of the  $U_{de}$  cumulative probability distributions to those of the maximum recorded gust velocities is discussed in the next section.

The absolute values of the maximum derived equivalent gust velocities are tabulated in Appendix VI for each turbulence sample.

TABLE 15.1

$U_{de}$  EQUATIONS AND EQUATION CONSTANTS

Route	Leg	$P_s/T_a$ (In Hg/°R)	$U_{de}$ (ft/sec)	Route	Leg	$P_s/T_a$ (In Hg/°R)	$U_{de}$ (ft/sec)
McConnell	1	.0534 ↓	$16.31\Delta N_{zCG}$ ↓	Peterson	1	.0439 ↓	$15.95\Delta N_{zCG}$ ↓
	2						
	3						
	4						
	5						
	6						
	7						
	8						
Edwards	1	.0500 ↓	$16.18\Delta N_{zCG}$ ↓	Griffiss	1	.0477 ↓	$16.09\Delta N_{zCG}$ ↓
	2						
	3						
	4						
	5						
	6						
	7						
	8						

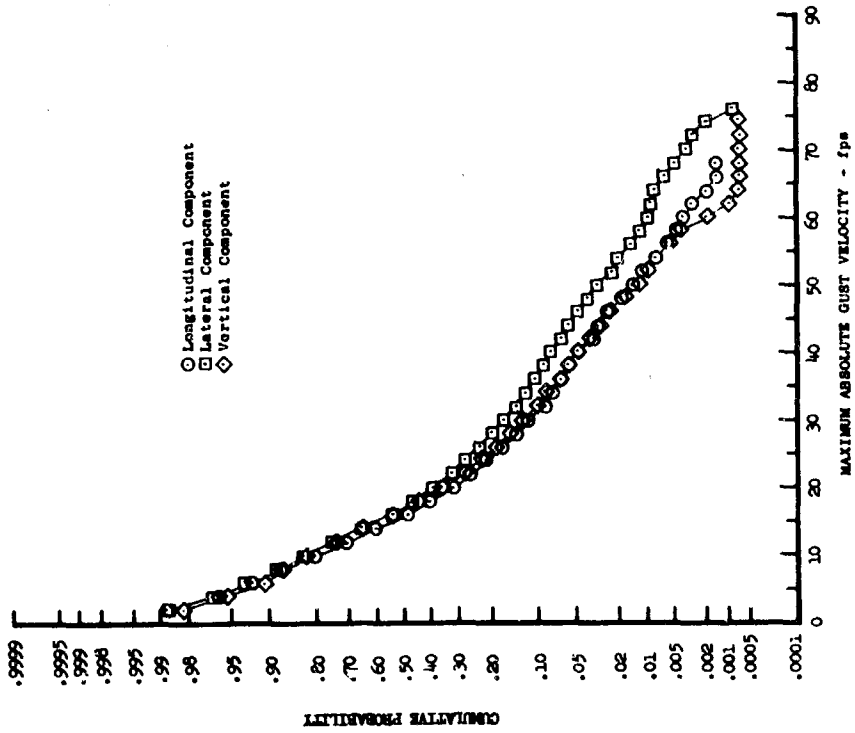
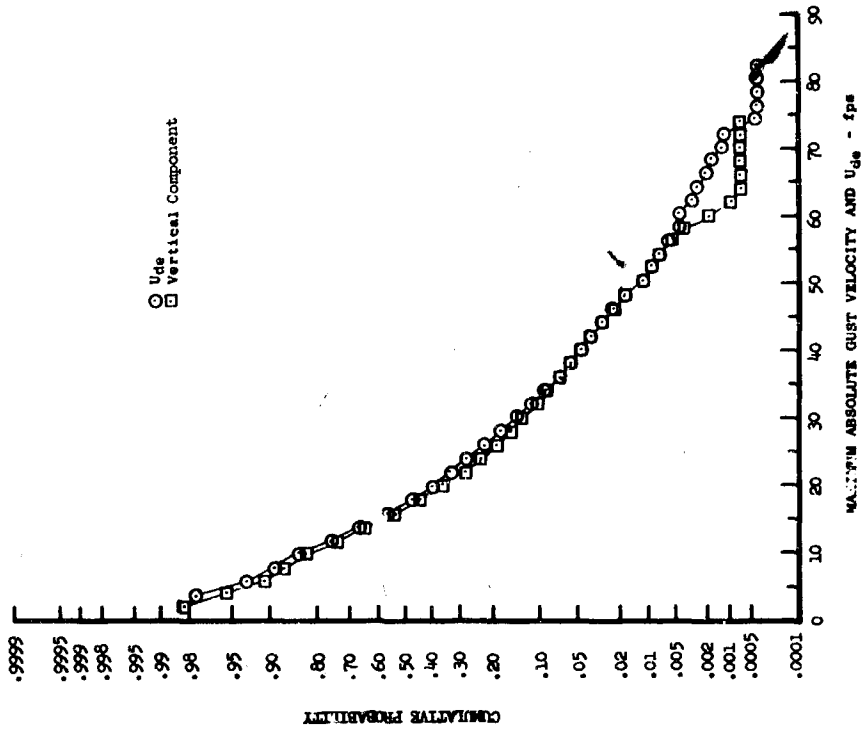


Figure 15.1 Cumulative Probability of Maximum Absolute Gust Velocity and U<sub>de</sub> - All Categories

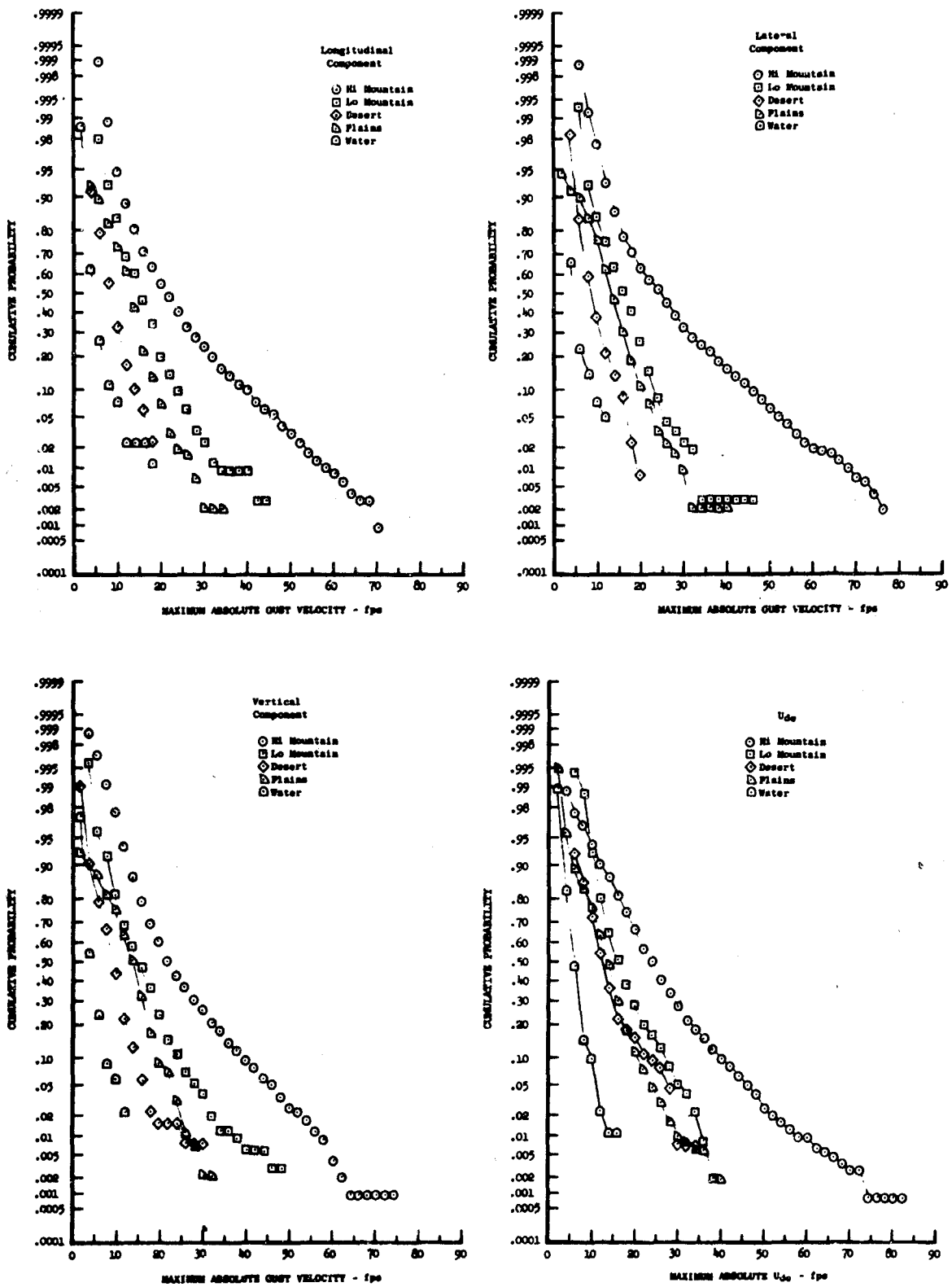


Figure 15.2 Cumulative Probability of Maximum Absolute Gust Velocity and  $U_{de}$  as a Function of Terrain

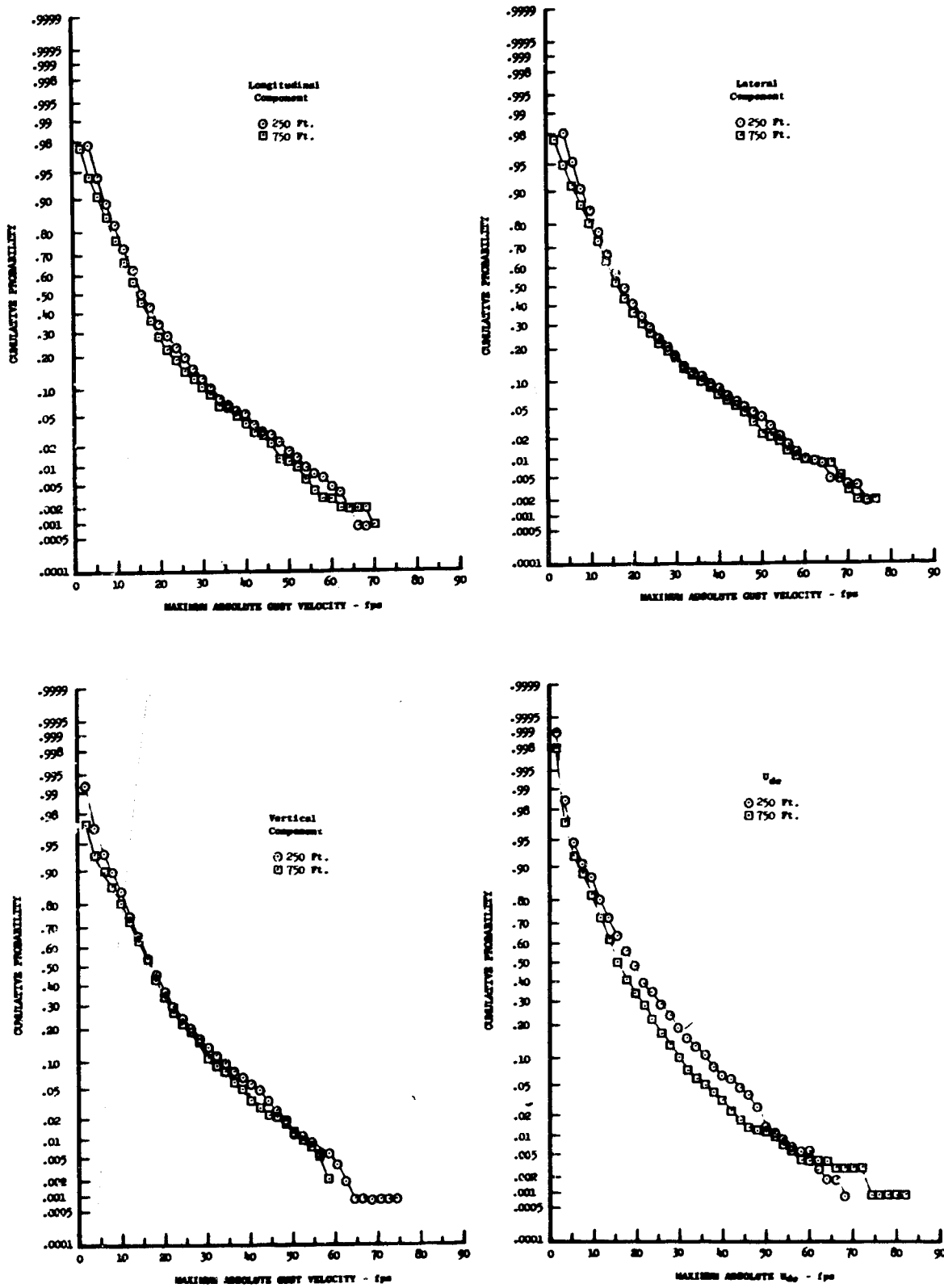


Figure 15.3 Cumulative Probability of Maximum Absolute Gust Velocity and  $U_{de}$  as a Function of Altitude

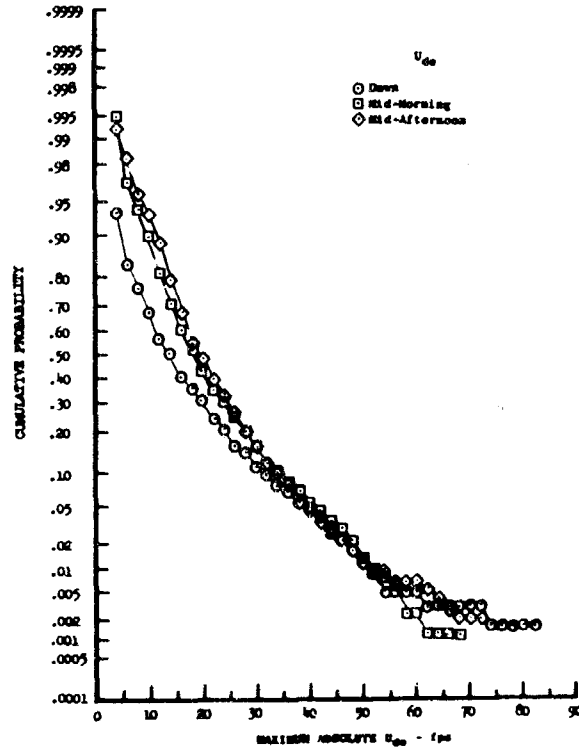
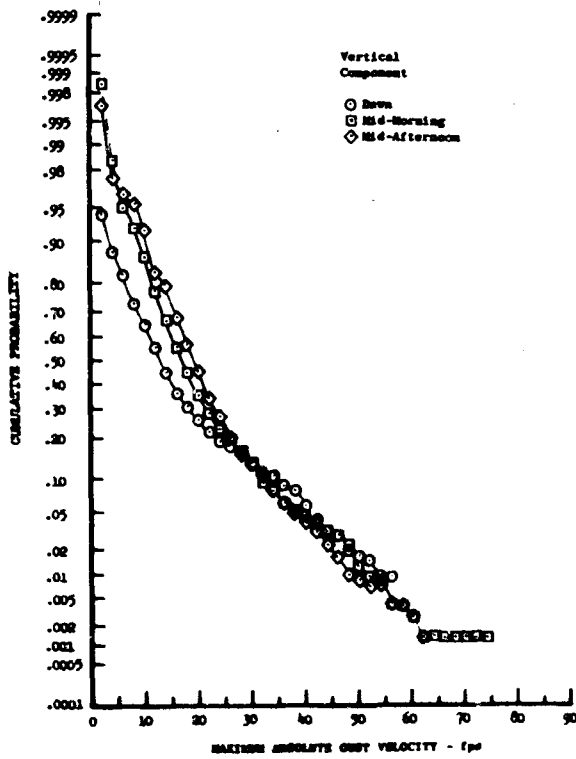
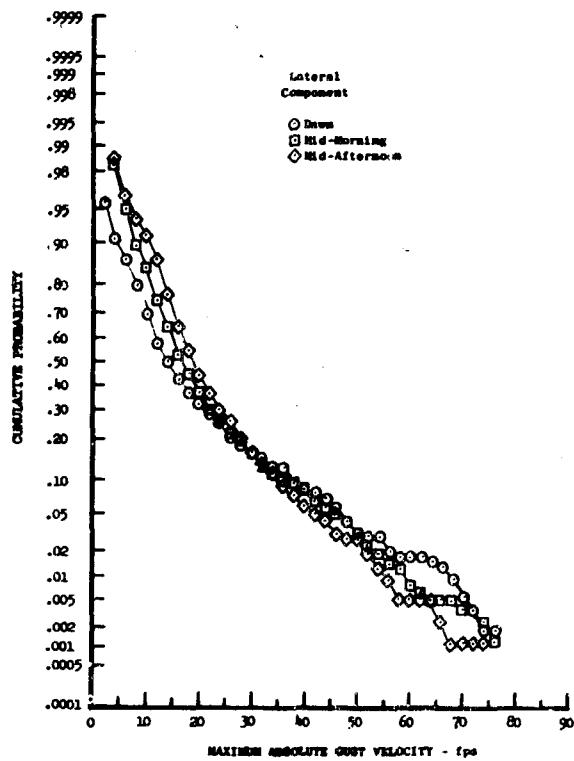
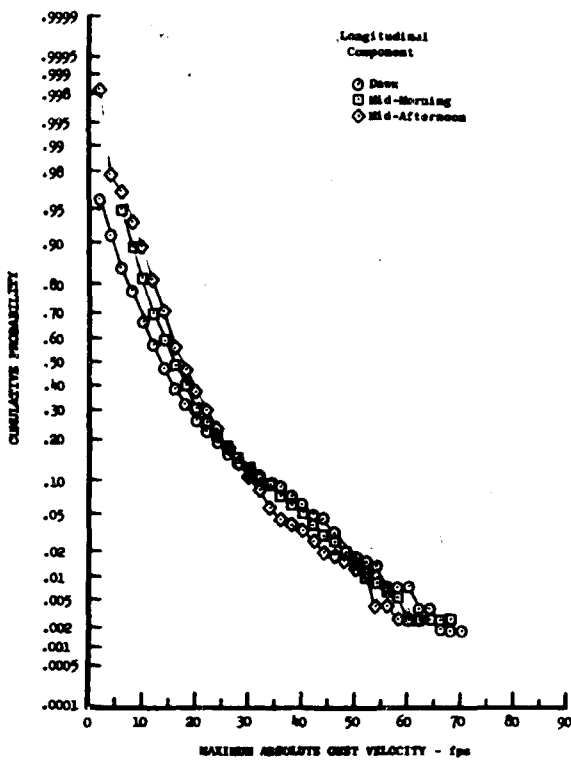


Figure 15.4 Cumulative Probability of Maximum Absolute Gust Velocity and  $U_{de}$  as a Function of Time of Day

## 16. MAXIMUM GUST VELOCITY DURING EACH SAMPLE

The maximum absolute values of each gust velocity component for each turbulence sample were obtained. Absolute values not calculated because of low signal-to-noise ratios were represented by average values estimated from typical low sigma turbulence samples. The cumulative probability distributions of these data, as well as of the maximum absolute derived equivalent gust velocities were calculated and are shown in Figures 15.1 through 15.4. Figure 15.1 shows the overall cumulative probability as obtained from all categories; Figure 15.2, the probability with respect to terrain; Figure 15.3, the probability with respect to altitude; and Figure 15.4, the probability with respect to time of day. Comparison of the vertical gust velocity component with the maximum derived equivalent gust velocity indicates fairly good agreement in practically all cases. Comparison of the three calculated gust velocity components shows that the cumulative probability distributions of the vertical and longitudinal components are very similar for all the categories presented. The lateral component, however, shows probabilities higher than the other components for the overall category, the high mountain category, the time of day category, and the altitude category. The high mountain data is included in these categories and it appears that the cumulative probability distribution of the lateral component is higher than that of the longitudinal or vertical because of flying parallel to the high mountain ridge lines.

Other factors to be considered when comparing gust velocity components are:

- High-pass filtering of the gust velocity components attenuates the magnitude of the long wavelength amplitudes of the longitudinal component slightly more than the vertical or lateral components because the amplitudes of the longitudinal component are higher at the long wavelengths, as discussed in Section V.
- The long wavelength amplitudes of the vertical component are smaller than those of the lateral or longitudinal components because of the airplane's close proximity to the ground, allowing measurement of the compressed wavelength vertical eddys.
- Incomplete removal of the effects of airplane motion from the gust velocity components tends to increase the level of the lateral component during flight over plains, water, and desert and would also tend to increase the level of both the vertical and lateral components during contour flight over the high and low mountain legs. This effect is believed to be the major source of error in true gust velocity calculations. The magnitudes of these errors are small and are discussed in Appendix III.



## 17. SEVERE AND EXTREME TURBULENCE SAMPLES

Time histories of the longitudinal, lateral, and vertical gust velocity components were plotted for turbulence samples during which the maximum value of one or more of the components equaled or exceeded  $\pm 50$  feet per second.

Samples meeting the above criteria were not encountered over the McConnell or Griffiss routes. One turbulence sample meeting these criteria was encountered over the Edwards route while seventy separate occurrences were encountered during flight over the Peterson route. The criteria were exceeded only on those samples flown over terrain classified as high mountain. Time histories of the gust velocity components for the single Edwards encounter are presented in Figure 17.1 and those for the Peterson occurrences are shown in Figures 17.2 through 17.71. A data block included on each figure identifies the test number and the leg over which these data were obtained. Also tabulated in the data block are the maximum and minimum gust velocities, turbulence time series standard deviation, and, if available, the average wind direction and velocity, average ambient air temperature, average true airspeed, average radar altitude, and category number.

The vertical gust velocity component in Figure 17.1 should be particularly noted. These data show a turbulence wavelength of approximately 14,300 feet with peak magnitudes of 74.5 and -65.0 feet per second. The long wavelength component appears at a frequency of approximately 0.04 cycles per second in the time history. This same turbulence, if encountered during Phases I and II testing, would have appeared as 0.02 cycles per second data due to the lower speed at which the C-131 aircraft were flown. Phases I and II gust velocity measurements in this frequency regime would have been attenuated approximately 80 per cent due to the low frequency data filtering techniques utilized to alleviate the effects of instrumentation drift. This is a cogent example of the fact that there is turbulence at low altitude containing wavelengths longer than 7,000 feet and is the reason why, in comparing Phase III results with Phases I and II for equivalent categories, that: (1) the probability distributions of gust velocity peaks are higher, (2) the probability distributions of gust velocity rms values are higher, (3) integral scale lengths are longer, (4) Taylor's microscales are longer, and (5) the viscous dissipation rates are less.

The number of Peterson turbulence samples and the number of samples during which a particular gust velocity component met the 50 feet per second criteria are tabulated, with respect to leg number, in Table 17.1. This tabulation shows that the total number of severe turbulence encounters over leg five exceeded that of the other legs by a factor greater than two. As shown in Appendix IV, leg five proceeds south along the eastern slope of the Sangre de Cristo Culebra Range. The wind direction at the time of these encounters varied from 254 to 319 degrees; therefore, the airplane was on the lee side of the range where the most severe turbulence would most likely occur. Also, on leg five, the lateral component exceeded 50 feet per second during more turbulence samples than did the longitudinal or vertical components.

TABLE 17.1

TABULATION OF SAMPLES AND COMPONENTS  
EQUAL TO OR EXCEEDING 50 FPS

Peterson Leg Number	Number of Turbulence Samples $\geq 50$ fps	Number of Gust Velocity Components $\geq 50$ fps		
		u	v	w
1	8	1	8	0
2	9	5	3	1
3	0	-	-	-
4	7	2	6	2
5	25	12	23	11
6	11	3	10	4
7	10	4	10	3
8	0	-	-	-
Total	70	27	60	21

The above set of conditions for leg 5 were analogous to those encountered on legs 1, 4, 6, and 7, viz; for turbulence samples gathered on the lee side of a mountain range, the lateral component exceeded 50 fps during more samples than did the vertical or longitudinal component. It should be noted that almost always the lateral component exhibited higher positive than negative excursions when the airplane was flying south (legs 4 and 5) and higher negative than positive excursions when the airplane was flying north (legs 1, 6, and 7). The lateral component is defined as positive for gusts from the left of the airplane.

The longitudinal component for leg 2, Figures 17.10 through 17.18, exceeded 50 feet per second during more severe turbulence samples than did either the lateral or vertical components. This again is probably due to the south-westerly direction of the leg with respect to the wind direction. The wind direction for the time histories shown varied from 241 to 306 degrees with one sample showing winds from 47 degrees.

The striking similarity of the gust velocity components depicted in Figures 17.11, 17.12, and 17.13 should also be noted. These turbulence samples were gathered over leg 2 of the Peterson route on three separate flights conducted on the same day. The elapsed time between the first turbulence sample gathered during the dawn flight and the last turbulence sample gathered during the mid-afternoon flight is approximately seven hours. Time histories having the severe turbulence characteristics similar to the three mentioned above were also obtained 19 and 23 days later as shown in Figures 17.14 and 17.18.

The most severe continuous turbulence encountered occurred over leg 5 and is shown in Figure 17.38. The time series standard deviations were 15.45 fps, 19.05 fps, and 15.04 fps for the longitudinal, lateral, and vertical gust velocity components, respectively. None of the maximum excursions occurred during this particular turbulence sample. These maximum values occurred as shown in Figures 17.1 for the vertical component, in Figure 17.33 longitudinal component, and in Figure 17.34 for the lateral component.

Test	87	Ambient Air Temp (°F)	38.8	u max (fps)	46.1
Date	11-13-68	True Airspeed (fps)	612.5	u min (fps)	-41.4
Leg No.	3	Radar Altitude (ft)	572	v max (fps)	34.0
Category No.	112231	$\sigma_{tu}$ (fps)	8.59	v min (fps)	-46.2
Wind Direction (deg)	No Data	$\sigma_{tv}$ (fps)	6.89	w max (fps)	74.5
Wind Velocity (fps)	No Data	$\sigma_{tw}$ (fps)	11.98	w min (fps)	-65.0

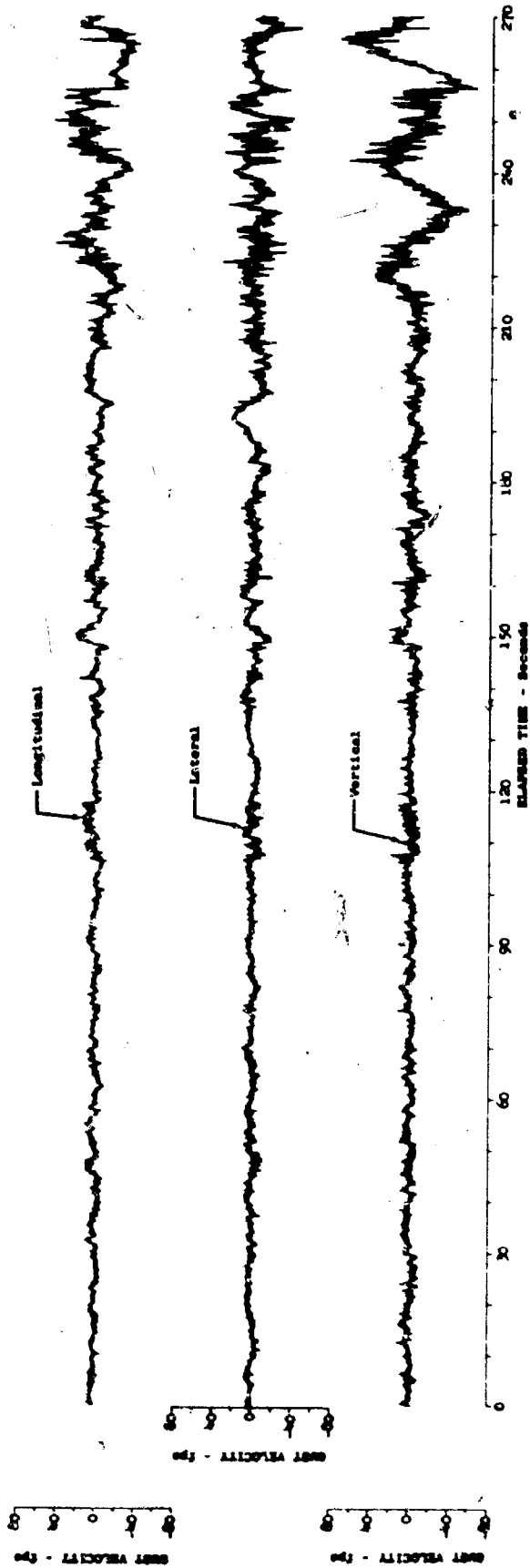


Figure 17.1 Time History of Severe Turbulence Encounter -  
Edwards

Test	154	Ambient Air Temp (°F)	36.7	u max (fps)	27.0
Date	1-21-69	True Airspeed (fps)	577.0	u min (fps)	-34.6
Leg No.	1	Radar Altitude (ft)	749	v max (fps)	32.8
Category No.	12143	$\sigma_{tu}$ (fps)	4.19	v min (fps)	-55.7
Wind Direction (deg)	222.7	$\sigma_{tv}$ (fps)	5.59	w max (fps)	34.5
Wind Velocity (fps)	60.9	$\sigma_{tw}$ (fps)	4.28	w min (fps)	-46.8

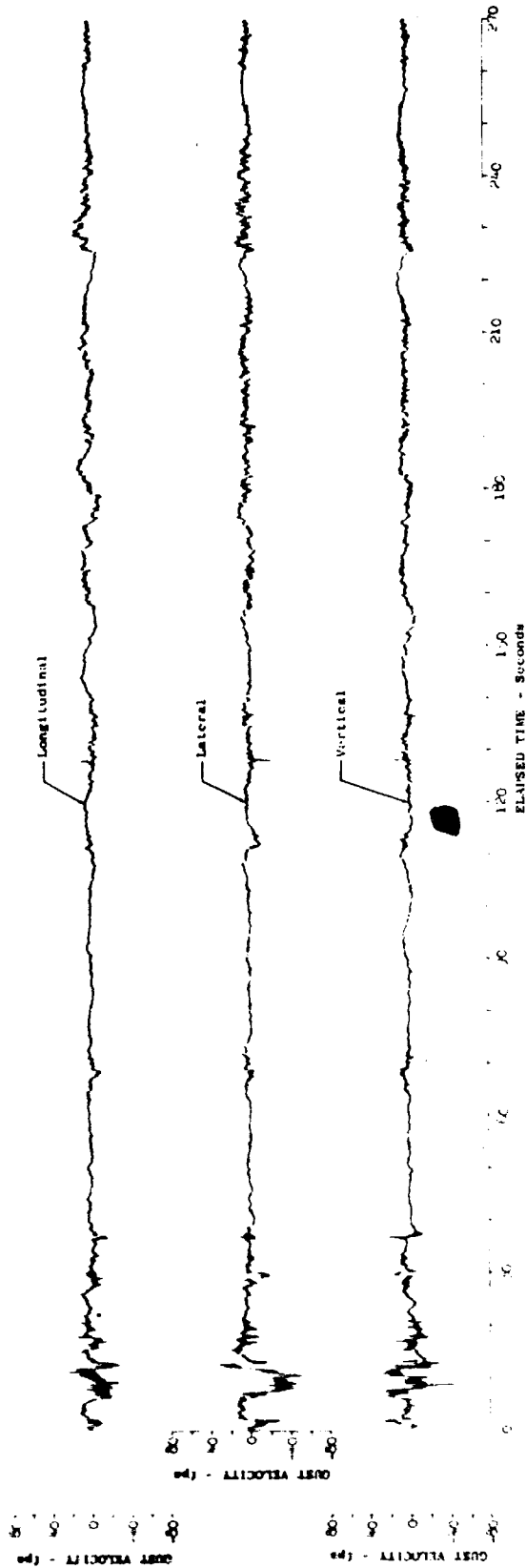


Figure 17.2 Time History of Severe Turbulence Encounter - Peterson

Test	164	Ambient Air Temp (°F)	25.5	u max (fps)	26.4
Date	1-30-69	True Airspeed (fps)	641.9	u min (fps)	-38.2
Leg No.	1	Radar Altitude (ft)	588	v max (fps)	28.6
Category	123343	$\sigma_{tu}$ (fps)	7.28	v min (fps)	-51.2
Wind Direction (deg)	202.8	$\sigma_{tv}$ (fps)	9.50	w max (fps)	33.2
Wind Velocity (fps)	42.7	$\sigma_{tw}$ (fps)	6.66	w min (fps)	-30.2

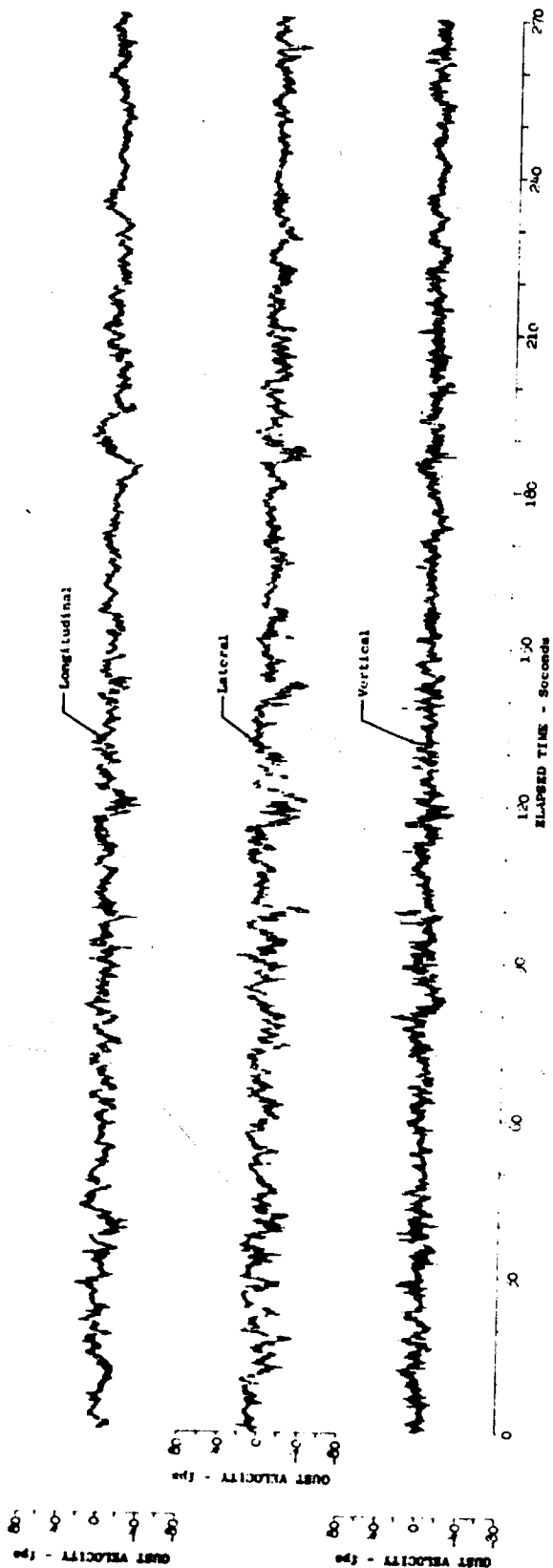


Figure 17.3 Time History of Severe Turbulence Encounter - Peterson

Test	170	Ambient Air Temp ( $^{\circ}$ F)	27.6	$u_{max}$ (fps)	28.4
Date	2-6-69	True Airspeed (fps)	609.4	$u_{min}$ (fps)	-38.4
Leg No.	1	Radar Altitude (ft)	401	$v_{max}$ (fps)	29.6
Category No.	113143	$\sigma_{tu}$ (fps)	6.08	$v_{min}$ (fps)	-56.8
Wind Direction (deg)	216.0	$\sigma_{tv}$ (fps)	8.60	$v_{max}$ (fps)	37.1
Wind Velocity (fps)	50.2	$\sigma_{tv}$ (fps)	6.59	$v_{min}$ (fps)	-45.8

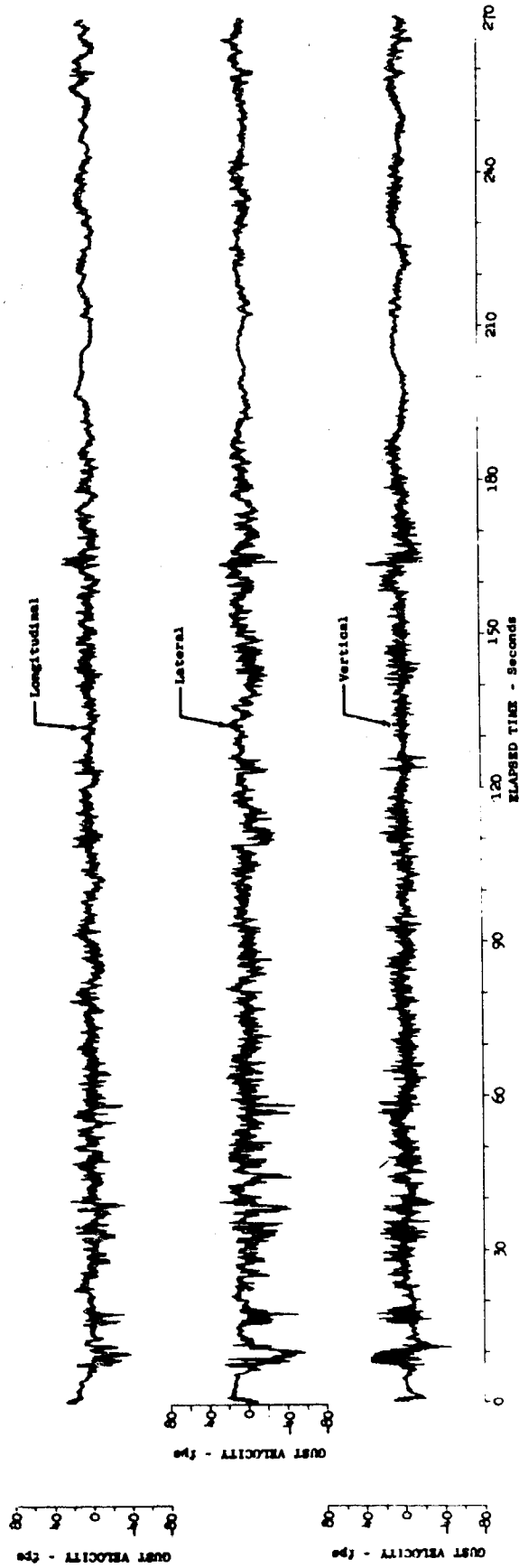


Figure 17.4 Time History of Severe Turbulence Encounter - Peterson

Test	171	Ambient Air Temp (°F)	32.4	$u_{max}$ (fps)	47.3
Date	2-6-69	True Airspeed (fps)	616.8	$u_{min}$ (fps)	-49.4
Leg No.	1	Padar Altitude (ft)	389	$v_{max}$ (fps)	32.6
Category No.	114243	$\sigma_{tu}$ (fps)	8.15	$v_{min}$ (fps)	-55.4
Wind Direction (deg)	213.6	$\sigma_{tv}$ (fps)	9.72	$v_{max}$ (fps)	45.1
Wind Velocity (fps)	45.0	$\sigma_{tv}$ (fps)	7.70	$v_{min}$ (fps)	-43.0

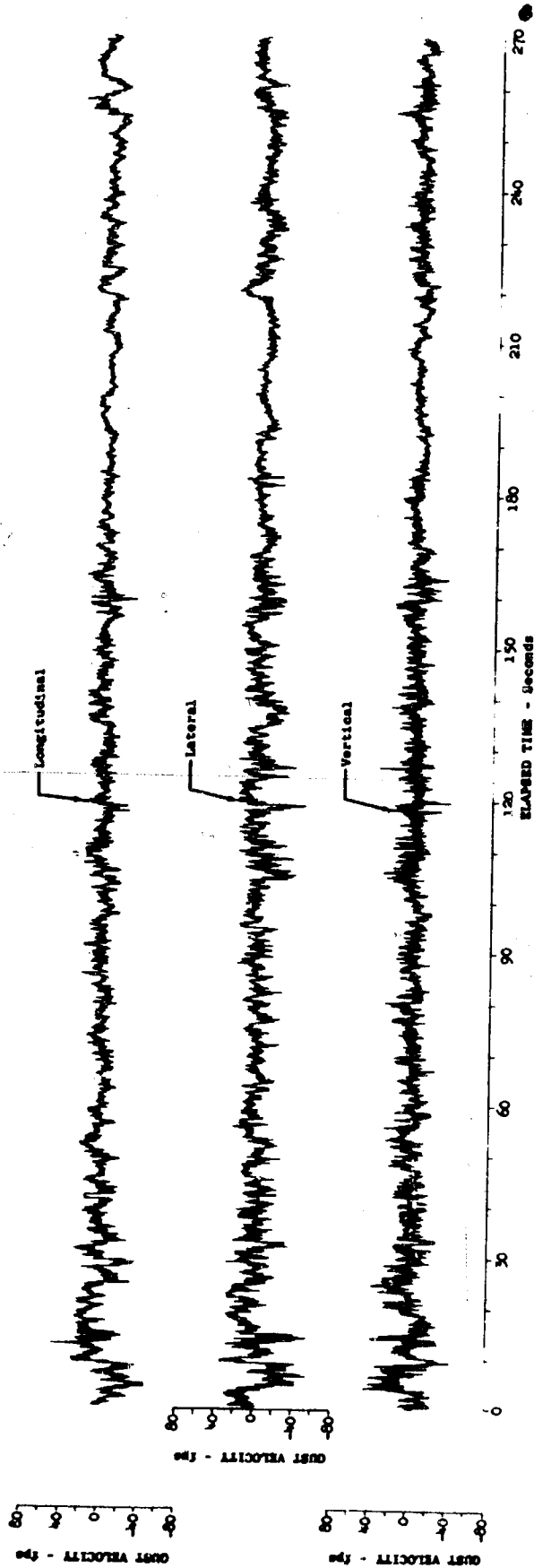


Figure 17.5 Time History of Severe Turbulence Encounter - Peterson

Test	172	Ambient Air Temp (°F)	39.2	u max (fps)	33.5
Date	2-6-69	True Airspeed (fps)	624.8	u min (fps)	-33.8
Leg No.	1	Radar Altitude (ft)	414	v max (fps)	32.5
Category No.	112343	$\sigma_{tu}$ (fps)	7.53	v min (fps)	-55.5
Wind Direction (deg)	No Data	$\sigma_{tv}$ (fps)	10.26	v max (fps)	45.1
Wind Velocity (fps)	No Data	$\sigma_{tv}$ (fps)	8.00	v min (fps)	-36.6

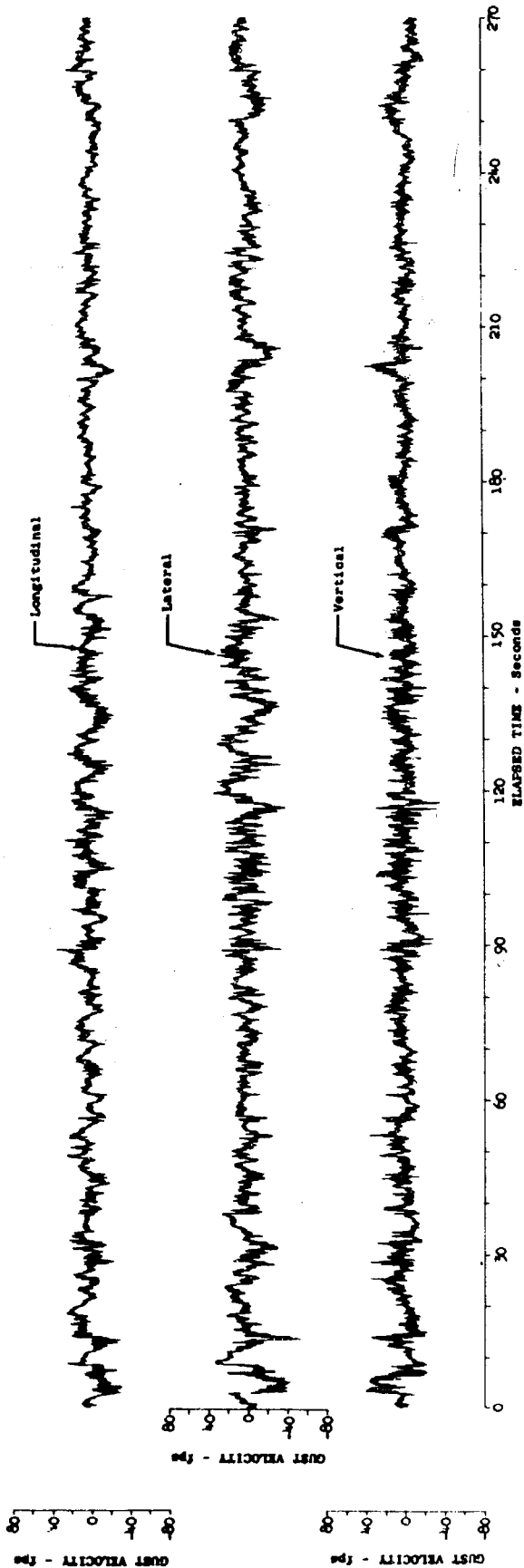


Figure 17.6 Time History of Severe Turbulence Encounter - Peterson



Test	187	Ambient Air Temp (°F)	26.6	u max (fps)	36.6
Date	2-22-69	True Airspeed (fps)	633.5	u min (fps)	-31.2
Leg No.	1	Radar Altitude (ft)	No Data	v max (fps)	24.9
Category No.	123243	$\sigma$ tu (fps)	6.03	v min (fps)	-50.8
Wind Direction (deg)	203.6	$\sigma$ tv (fps)	7.67	w max (fps)	34.6
Wind Velocity (fps)	41.2	$\sigma$ tw (fps)	6.17	w min (fps)	-30.8

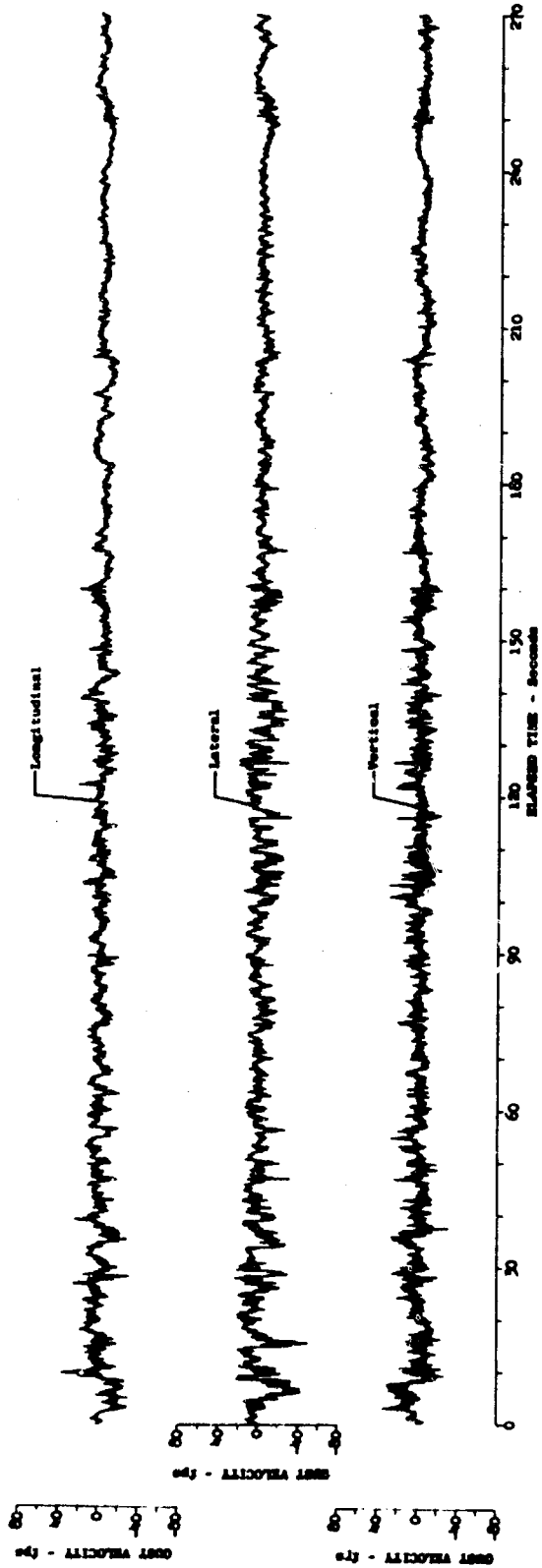


Figure 17.7 Time History of Severe Turbulence Encounter - Peterson

Test	212	Ambient Air Temp (°F)	28.9	u max (fps)	41.9
Date	3-19-69	True Airspeed (fps)	602.4	u min (fps)	-51.6
Leg No.	1	Radar Altitude (ft)	No Data	v max (fps)	35.9
Category	112243	$\sigma$ tu (fps)	12.93	v min (fps)	-50.5
Wind Direction (deg)	257.4	$\sigma$ tv (fps)	11.44	w max (fps)	38.8
Wind Velocity (fps)	32.0	$\sigma$ tw (fps)	9.80	w min (fps)	-43.6

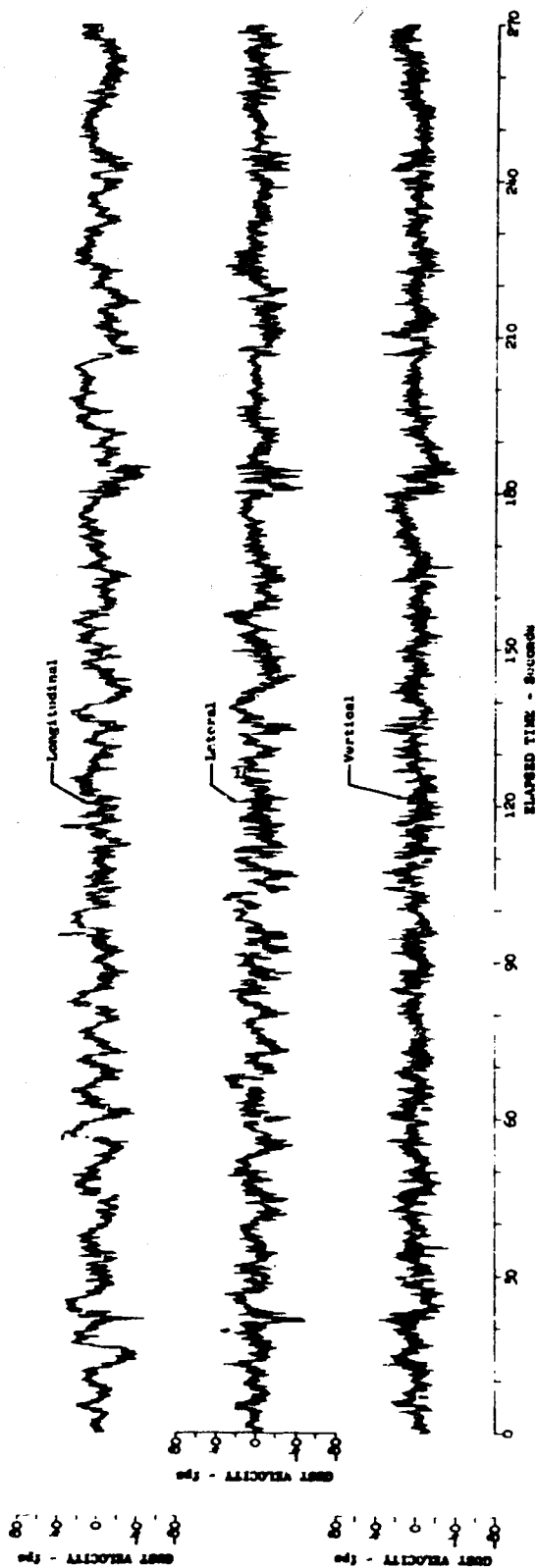


Figure 17.8 Time History of Severe Turbulence Encounter - Peterson

Test	213	Ambient Air Temp (°F)	33.4	u max (fps)	27.1
Date	3-19-69	True Airspeed (fps)	634.8	u min (fps)	-29.4
Leg No.	1	Radar Altitude (ft)	No Data	v max (fps)	50.8
Category No.	113343	$\sigma_{tu}$ (fps)	7.12	v min (fps)	-22.5
Wind Direction (deg)	72.9	$\sigma_{tv}$ (fps)	7.46	w max (fps)	30.2
Wind Velocity (fps)	7.6	$\sigma_{tw}$ (fps)	5.97	w min (fps)	-25.9

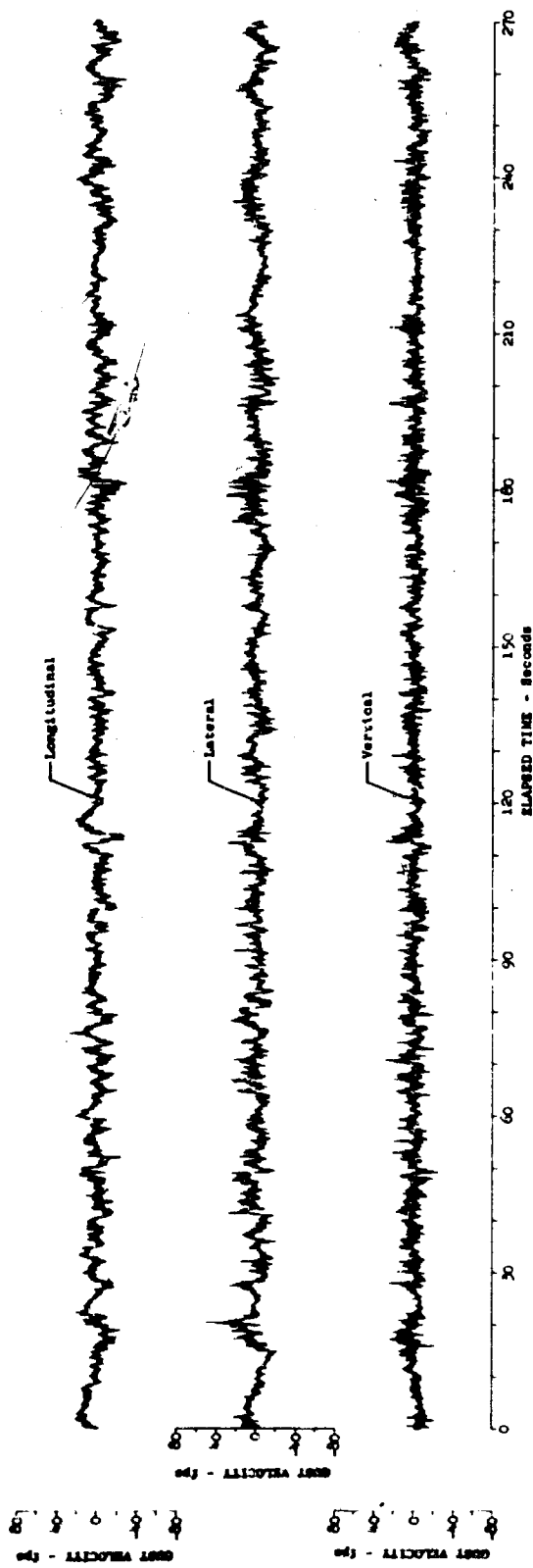


Figure 17.9 Time History of Severe Turbulence Encounter - Peterson

Test	159	Ambient Air Temp (°F)	26.8	u max (fps)	24.9
Date	1-27-69	True Airspeed (fps)	591.9	u min (fps)	-34.2
Leg No.	2	Radar Altitude (ft)	761	v max (fps)	33.5
Category No.	122143	$\sigma_{tu}$ (fps)	4.84	v min (fps)	-39.8
Wind Direction (deg)	155.5	$\sigma_{tv}$ (fps)	4.86	w max (fps)	44.9
Wind Velocity (fps)	27.3	$\sigma_{tw}$ (fps)	6.03	w min (fps)	-51.9

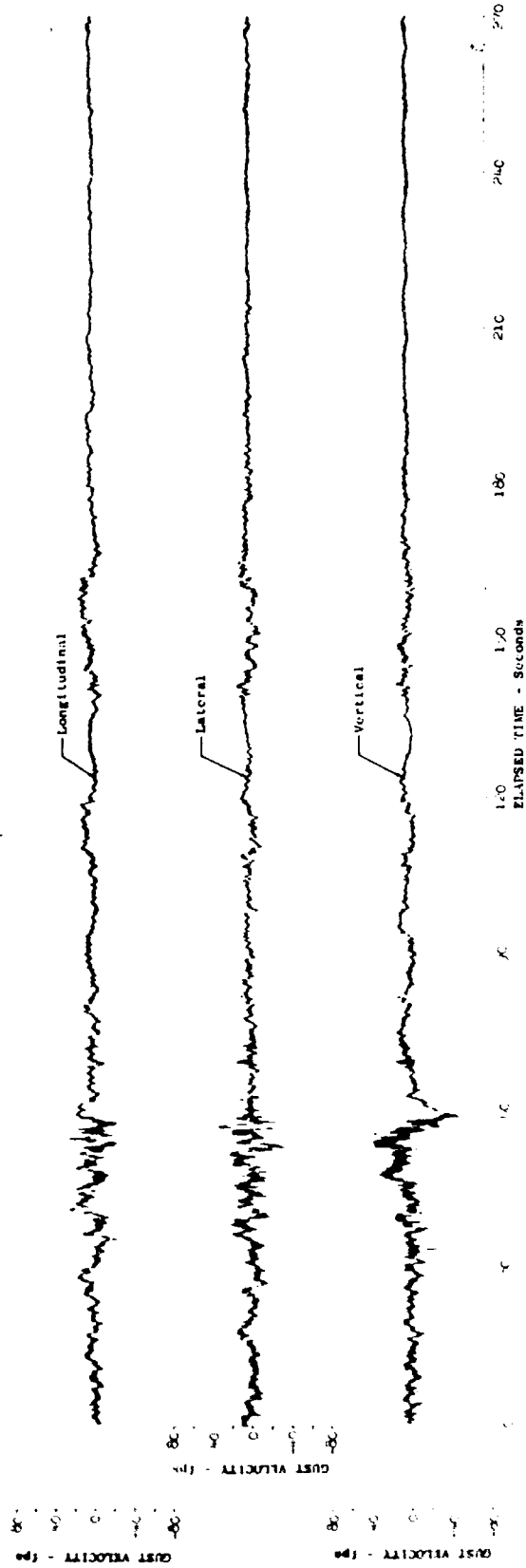


Figure 17.10 Time History of Severe Turbulence Encounter - Peterson

Test	170	Ambient Air Temp (°F)	18.6	$u_{max}$ (fps)	36.6
Date	2-6-69	True Airspeed (fps)	598.3	$u_{min}$ (fps)	-55.0
Leg No.	2	Barometric Altitude (ft)	389	$v_{max}$ (fps)	40.6
Category No.	112143	$\sigma_{tu}$ (fps)	9.52	$v_{min}$ (fps)	-33.9
Wind Direction (deg)	No Data	$\sigma_{tv}$ (fps)	7.28	$v_{max}$ (fps)	39.2
Wind Velocity (fps)	No Data	$\sigma_{tv}$ (fps)	5.57	$v_{min}$ (fps)	-38.7

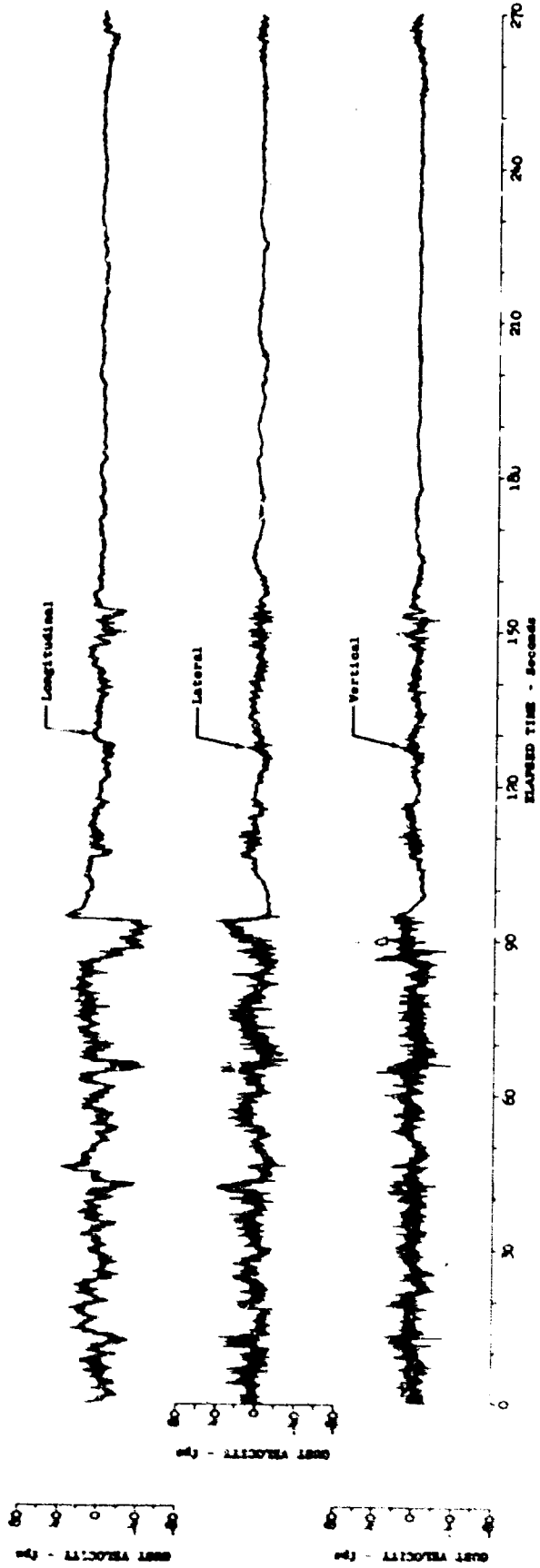


Figure 17.11 Time History of Severe Turbulence Encounter - Peterson

Test	171	Ambient Air Temp (°F)	23.5	u max (fps)	59.0
Date	2-6-69	True Airspeed (fps)	617.1	u min (fps)	-59.3
Log No.	2	Radar Altitude (ft)	No Data	v max (fps)	48.2
Category No.	112243	$\sigma_{tu}$ (fps)	10.14	v min (fps)	-40.1
Wind Direction (deg)	No Data	$\sigma_{tv}$ (fps)	7.88	v max (fps)	43.2
Wind Velocity (fps)	No Data	$\sigma_{tv}$ (fps)	7.77	v min (fps)	-45.0

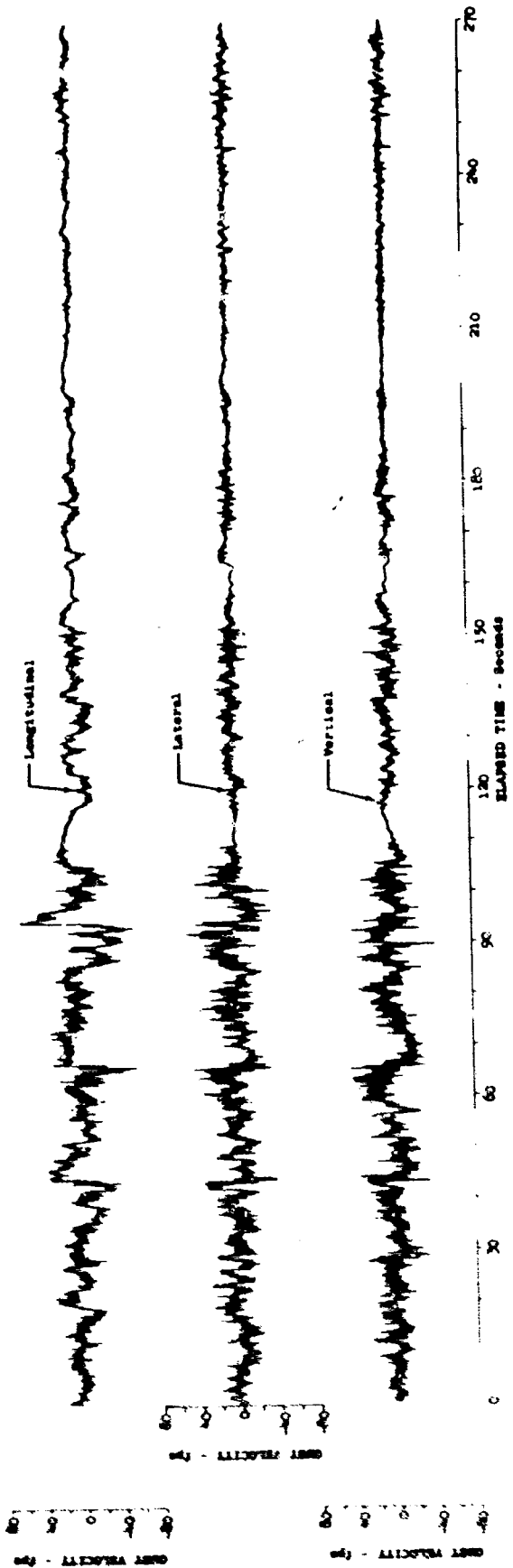


Figure 17.12 Time History of Severe Turbulence Encounter - Peterson

Test	172	Ambient Air Temp (°F)	29.8	$u_{max}$ (fps)	37.1
Date	2-6-69	True Airspeed (fps)	600.8	$u_{min}$ (fps)	-53.4
Leg No.	2	Pedar Altitude (ft)	405.0	$v_{max}$ (fps)	41.8
Category No.	114343	$\sigma_{tu}$ (fps)	8.58	$v_{min}$ (fps)	-34.1
Wind Direction (deg)	No Data	$\sigma_{tv}$ (fps)	6.74	$v_{max}$ (fps)	34.3
Wind Velocity (fps)	No Data	$\sigma_{tv}$ (fps)	6.34	$v_{min}$ (fps)	-40.2

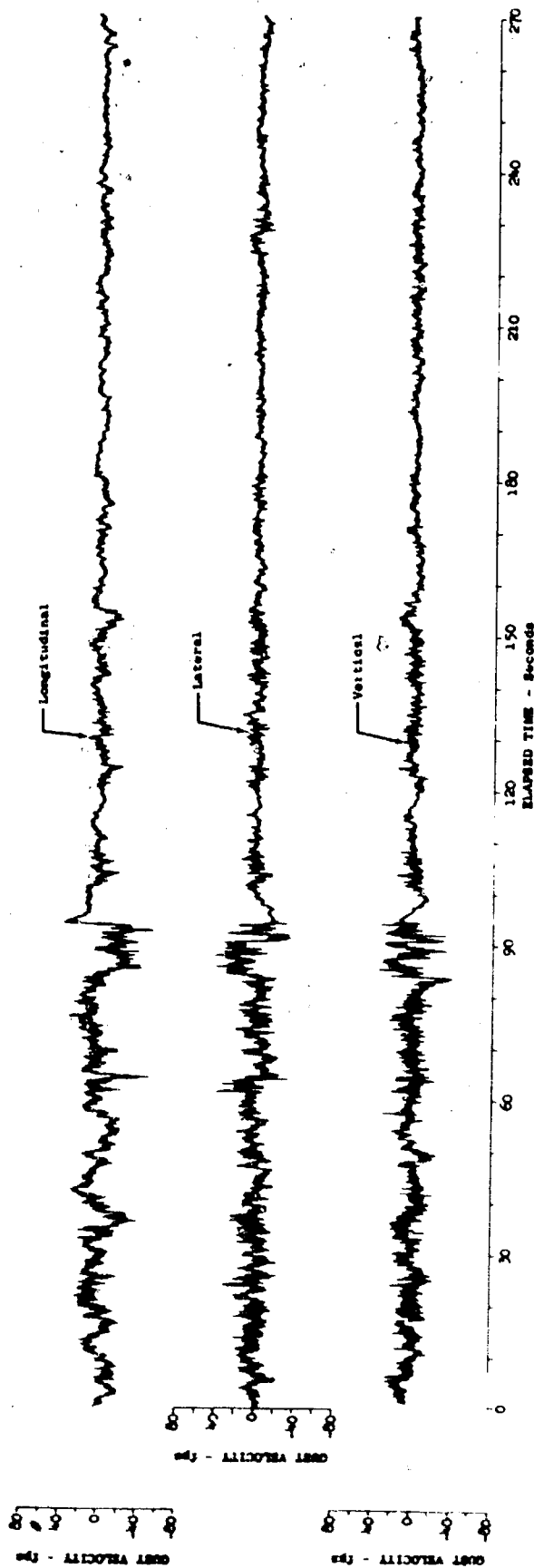


Figure 17.13 Time History of Severe Turbulence Encounter - Peterson

Test	191	Ambient Air Temp (°F)	28.9	u max (fps)	34.5
Date	2-25-69	True Airspeed (fps)	616.7	u min (fps)	-47.0
Leg No.	2	Radar Altitude (ft)	592	v max (fps)	67.9
Category	122143	$\sigma_{tu}$ (fps)	7.04	v min (fps)	-44.3
Wind Direction (deg)	47.3	$\sigma_{tv}$ (fps)	6.72	w max (fps)	40.1
Wind Velocity (fps)	9.3	$\sigma_{tw}$ (fps)	4.60	w min (fps)	-46.5

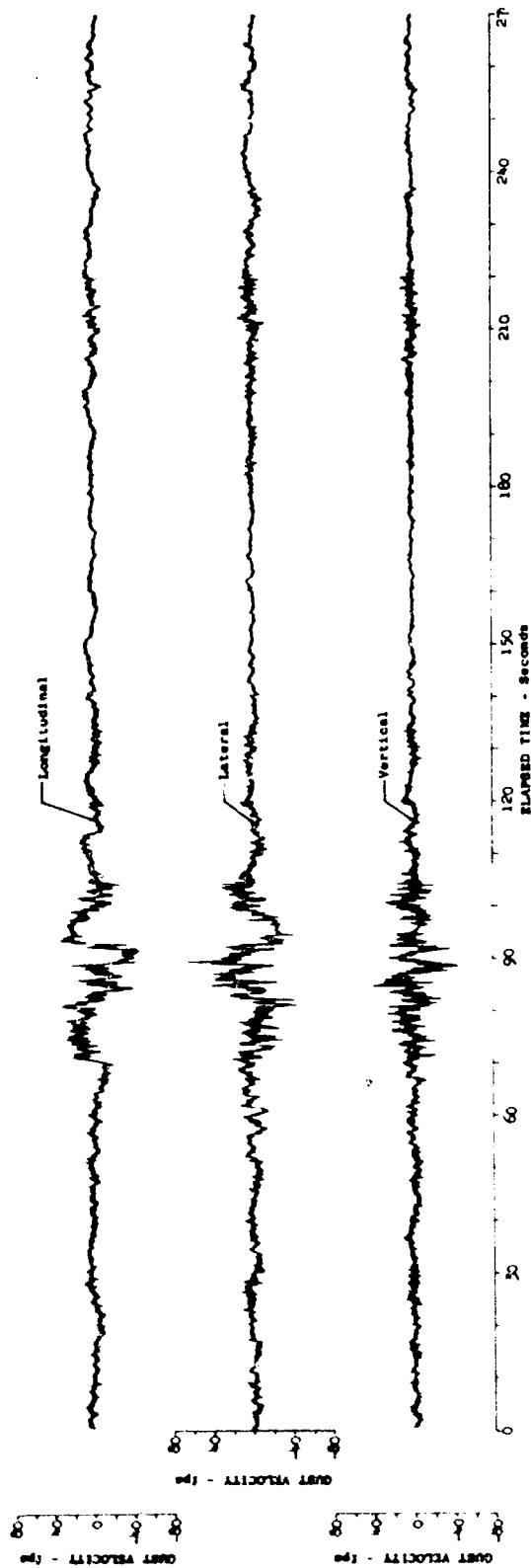


Figure 17.14 Time History of Severe Turbulence Encounter - Peterson



Test	193	Ambient Air Temp (°F)	39.7	u max (fps)	37.0
Date	2-25-69	True Airspeed (fps)	601.4	u min (fps)	-48.0
Leg No.	2	Radar Altitude (ft)	No Data	v max (fps)	41.7
Category	124343	$\sigma_{tu}$ (fps)	9.83	v min (fps)	-52.7
Wind Direction (deg)	241.1	$\sigma_{tv}$ (fps)	8.52	w max (fps)	30.4
Wind Velocity (fps)	12.0	$\sigma_{tw}$ (fps)	7.14	w min (fps)	-40.0

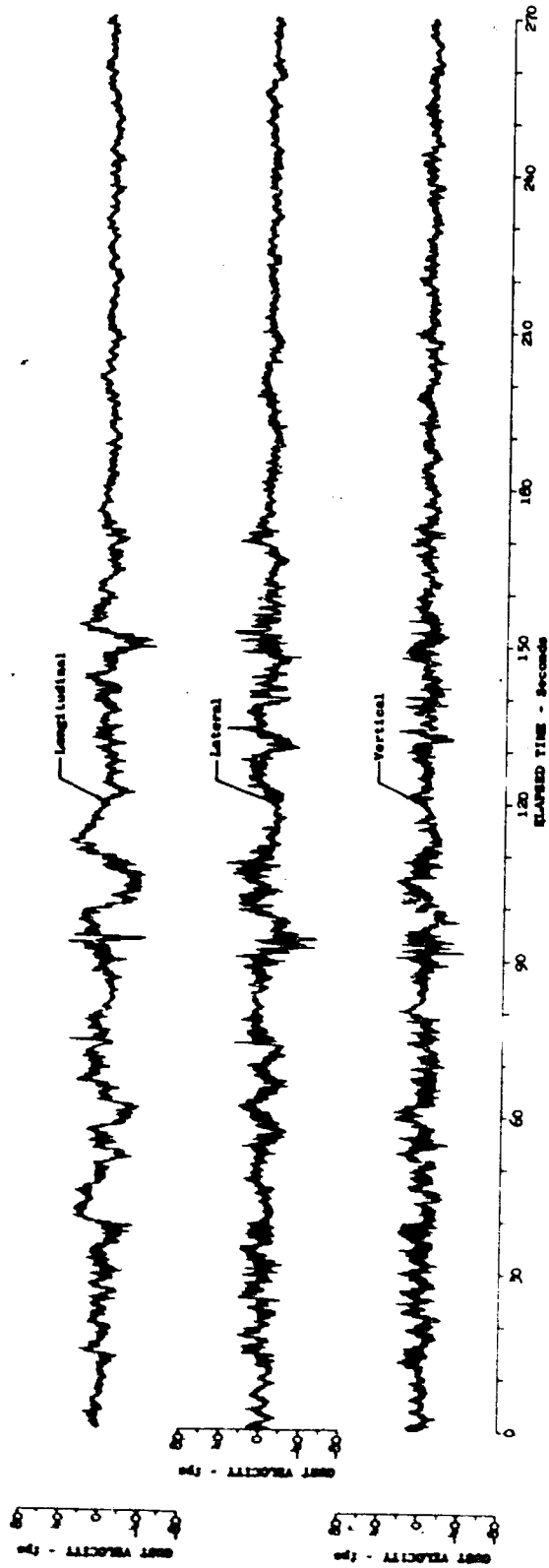


Figure 17.15 Time History of Severe Turbulence Encounter - Peterson

Test	196	Ambient Air Temp (°F)	37.4	u max (fps)	47.8
Date	2-26-69	True Airspeed (fps)	599.6	u min (fps)	-62.2
Log No.	2	Radar Altitude (ft)	No Data	v max (fps)	43.5
Category No.	114343	$\sigma_{tu}$ (fps)	10.02	v min (fps)	-39.8
Wind Direction (deg)	223.8	$\sigma_{tv}$ (fps)	8.94	w max (fps)	34.4
Wind Velocity (fps)	6.4	$\sigma_{tw}$ (fps)	7.22	w min (fps)	-34.4

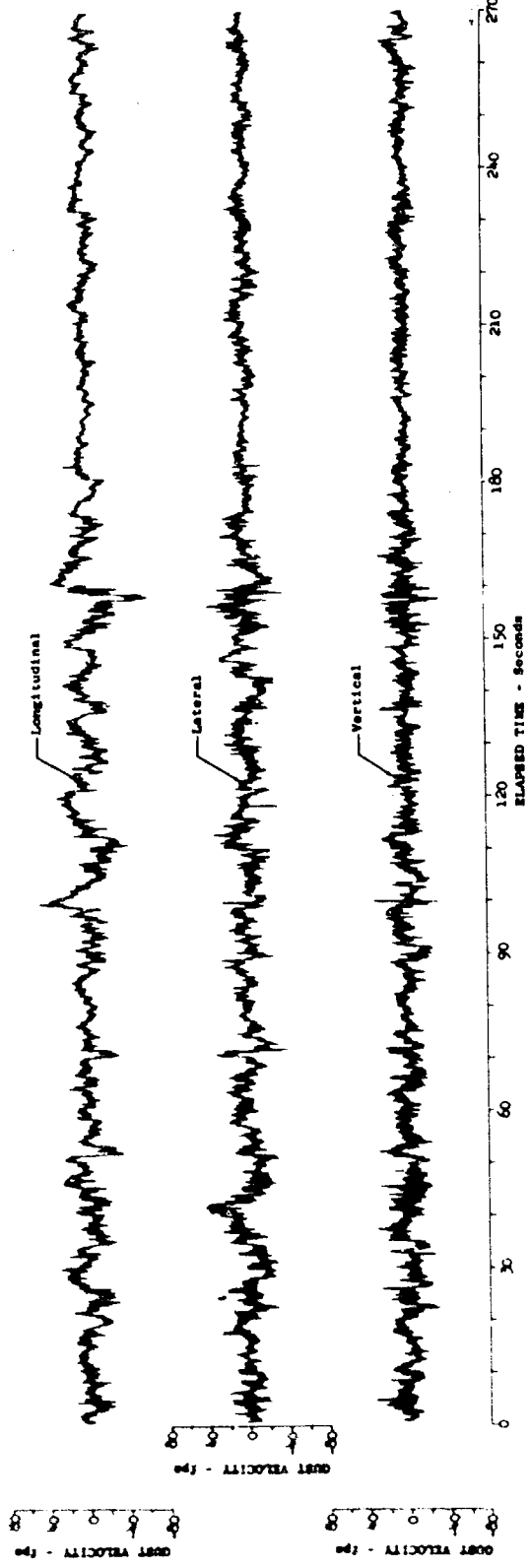


Figure 17.16 Time History of Severe Turbulence Encounter - Peterson

Test	225	Ambient Air Temp (°F)	39.3	u max (fps)	27.0
Date	3-27-69	True Airspeed (fps)	632.3	u min (fps)	-31.1
Leg No.	2	Radar Altitude (ft)	No Data	v max (fps)	52.2
Category No.	113313	$\sigma$ tu (fps)	6.99	v min (fps)	-31.1
Wind Direction (deg)	305.8	$\sigma$ tv (fps)	8.09	w max (fps)	26.7
Wind Velocity (fps)	24.7	$\sigma$ tw (fps)	5.76	w min (fps)	-24.1

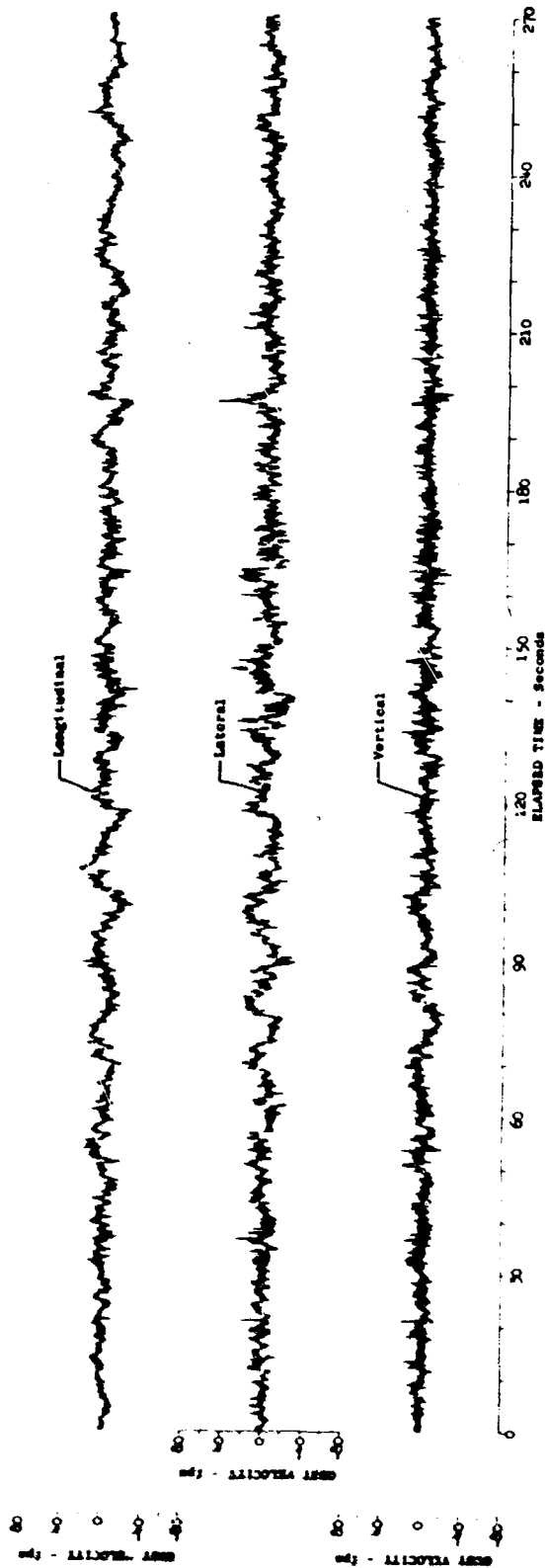


Figure 17.17 Time History of Severe Turbulence Encounter - Peterson

Test	232	Ambient Air Temp (°F)	36.8	u max (fps)	35.5
Date	4-1-69	True Airspeed (fps)	637.7	u min (fps)	-61.2
Leg No.	2	Radar Altitude (ft)	637	v max (fps)	29.6
Category	122113	$\sigma_{tu}$ (fps)	8.82	v min (fps)	-25.4
Wind Direction (deg)	254.0	$\sigma_{tv}$ (fps)	5.19	w max (fps)	31.4
Wind Velocity (fps)	27.8	$\sigma_{tw}$ (fps)	4.87	w min (fps)	-30.1

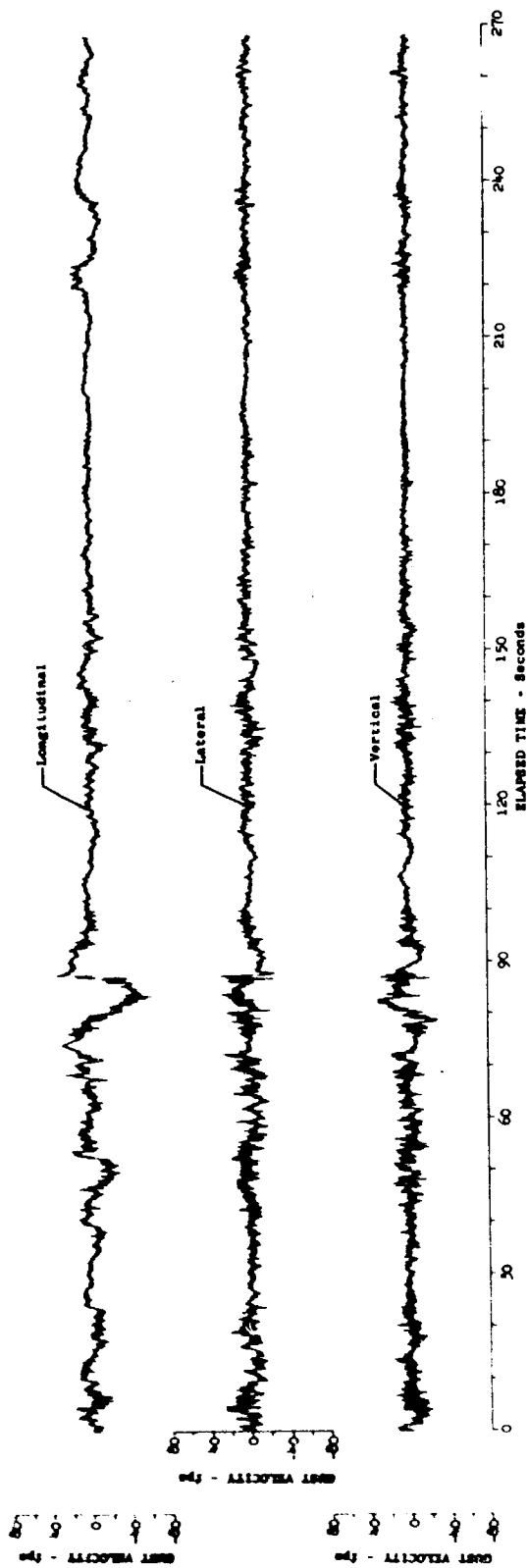


Figure 17.18 Time History of Severe Turbulence Encounter -  
Peterson

Test	190	Ambient Air Temp (°F)	35.4	u max (fps)	23.8
Date	2-24-69	True Airspeed (fps)	651.3	u min (fps)	-27.2
Log No.	4	Radar Altitude (ft)	339	v max (fps)	53.0
Category	114343	$\sigma_{tu}$ (fps)	6.57	v min (fps)	-25.3
Wind Direction (deg)	288.7	$\sigma_{tv}$ (fps)	6.98	w max (fps)	32.2
Wind Velocity (fps)	36.7	$\sigma_{tw}$ (fps)	5.32	w min (fps)	-24.2

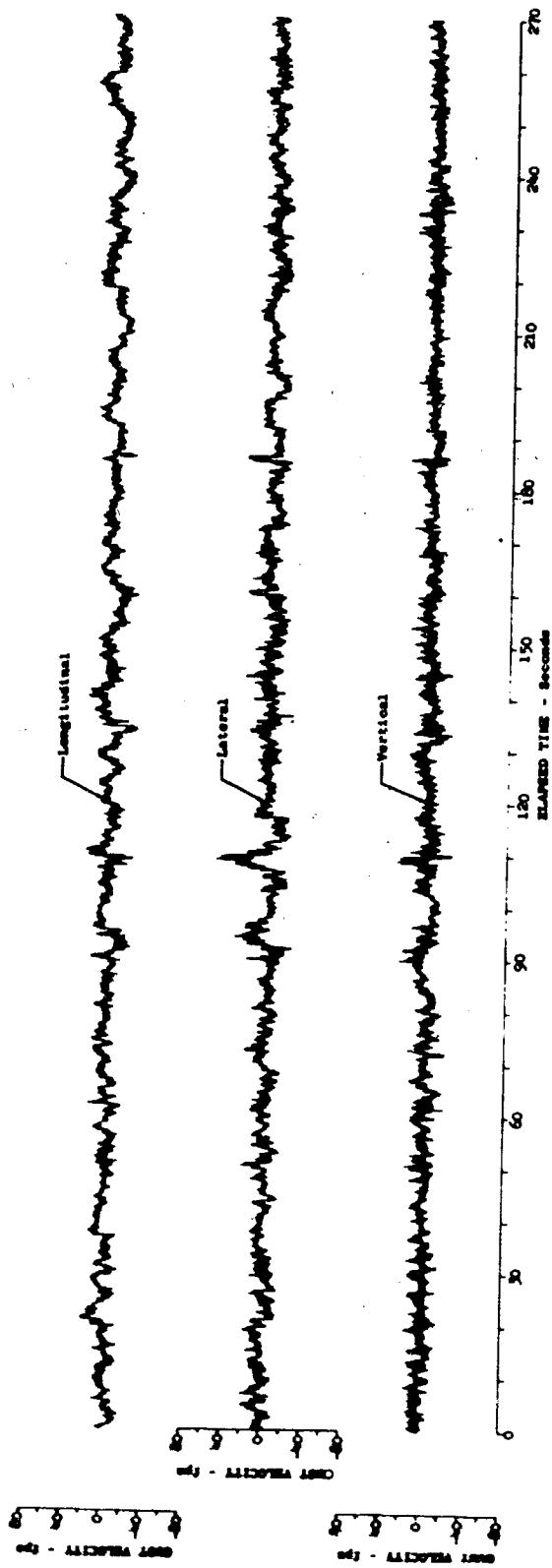


Figure 17.19 Time History of Severe Turbulence Encounter - Peterson

Test	191	Ambient Air Temp (°F)	34.0	u max (fps)	31.8
Date	2-25-69	True Airspeed (fps)	618.1	u min (fps)	-47.3
Leg No.	4	Radar Altitude (ft)	599	v max (fps)	76.8
Category No.	122143	$\sigma_{tu}$ (fps)	6.26	v min (fps)	-28.3
Wind Direction (deg)	277.2	$\sigma_{tv}$ (fps)	7.63	w max (fps)	53.8
Wind Velocity (fps)	24.7	$\sigma_{tw}$ (fps)	6.42	w min (fps)	-31.3

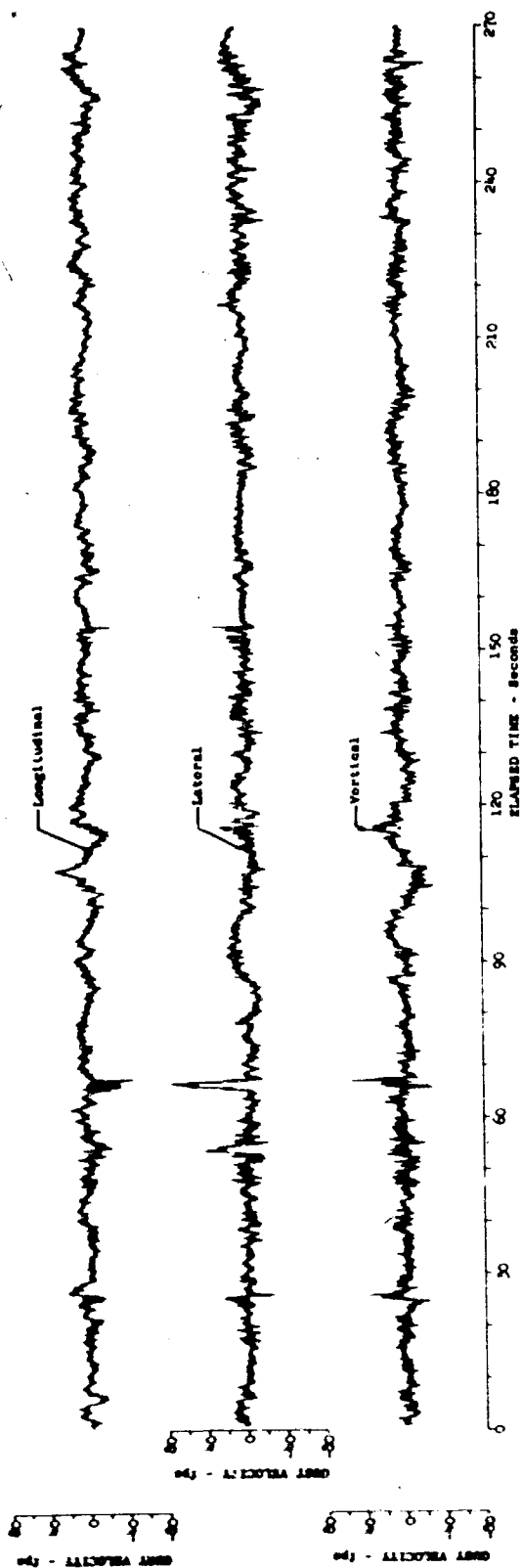


Figure 17.20 Time History of Severe Turbulence Encounter - Peterson

Test	194	Ambient Air Temp (°F)	33.8	u max (fps)	37.7
Date	2-26-69	True Airspeed (fps)	616.6	u min (fps)	-35.6
Leg No.	4	Radar Altitude (ft)	346	v max (fps)	50.8
Category No.	113143	$\sigma_{tu}$ (fps)	7.23	v min (fps)	-29.1
Wind Direction (deg)	No Data	$\sigma_{tv}$ (fps)	7.87	w max (fps)	35.7
Wind Velocity (fps)	No Data	$\sigma_{tw}$ (fps)	5.85	w min (fps)	-28.4

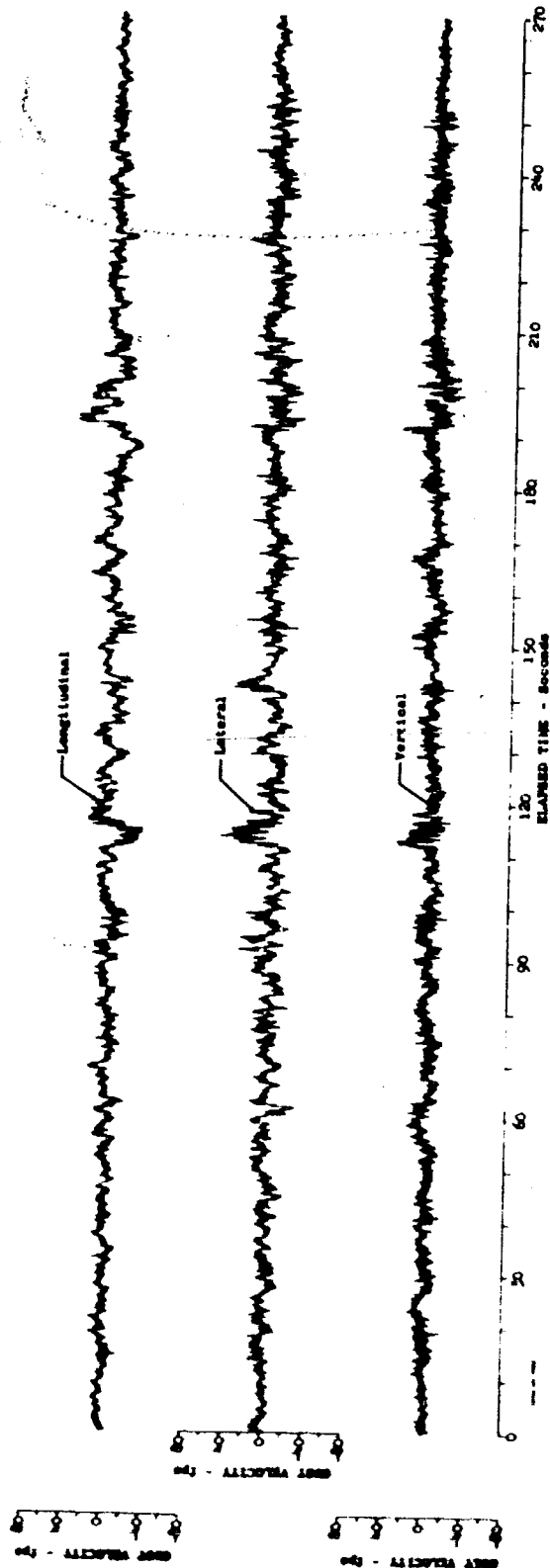


Figure 17.21 Time History of Severe Turbulence Encounter - Peterson

Test	196	Ambient Air Temp (°F)	37.4	u max (fps)	30.0
Date	2-26-69	True Airspeed (fps)	617.2	u min (fps)	-52.2
Leg No.	4	Radar Altitude (ft)	No Data	v max (fps)	64.6
Category	114343	$\sigma_{tu}$ (fps)	8.37	v min (fps)	-29.6
Wind Direction (deg)	269.9	$\sigma_{tv}$ (fps)	8.60	w max (fps)	42.0
Wind Velocity (fps)	30.1	$\sigma_{tw}$ (fps)	6.82	w min (fps)	-47.2

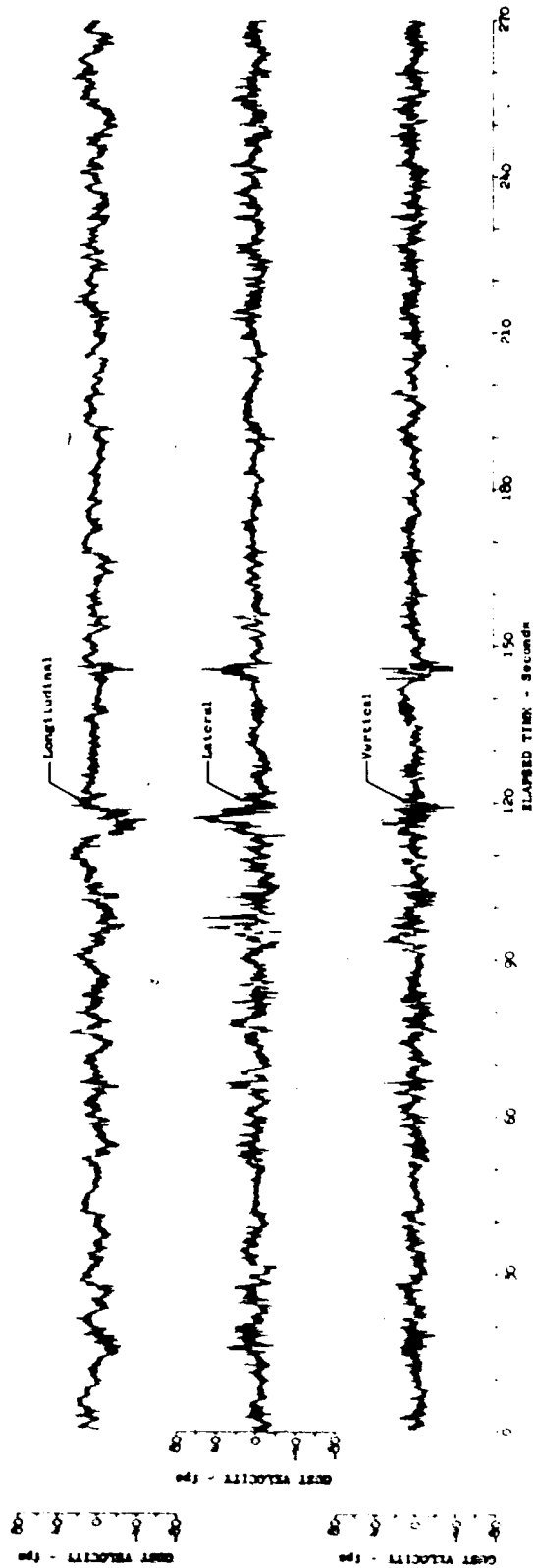


Figure 17.22 Time History of Severe Turbulence Encounter - Peterson



Test	212	Ambient Air Temp (°F)	27.1	u max (fps)	33.2
Date	3-19-69	True Airspeed (fps)	617.8	u min (fps)	-49.2
Leg No.	4	Radar Altitude (ft)	No Data	v max (fps)	53.1
Category No.	113243	$\sigma_{tu}$ (fps)	7.67	v min (fps)	-32.9
Wind Direction (deg)	323.3	$\sigma_{tv}$ (fps)	9.18	w max (fps)	51.3
Wind Velocity (fps)	57.1	$\sigma_{tw}$ (fps)	7.85	w min (fps)	-39.2

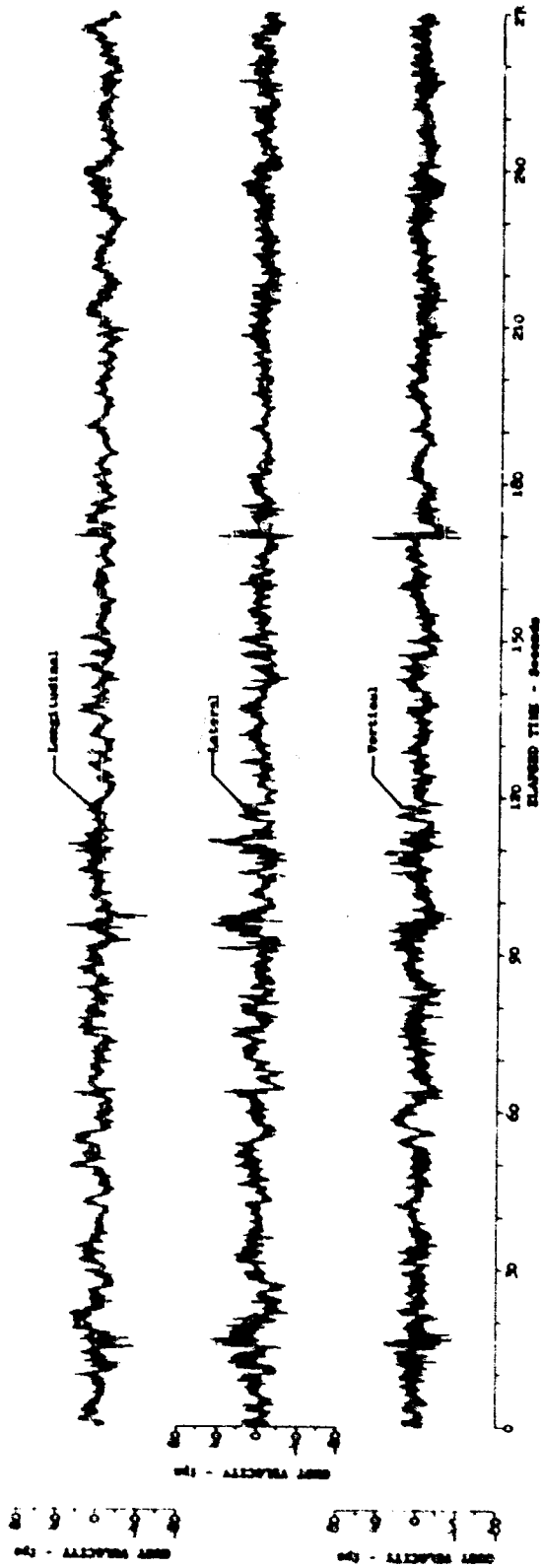


Figure 17.23 Time History of Severe Turbulence Encounter - Peterson

Test	249	Ambient Air Temp (°F)	43.8	u max (fps)	23.1
Date	4-15-69	True Airspeed (fps)	641.6	u min (fps)	-52.7
Log No.	4	Radar Altitude (ft)	643	v max (fps)	36.6
Category	122315	$\sigma_{tu}$ (fps)	6.57	v min (fps)	-21.4
Wind Direction (deg)	209.5	$\sigma_{tv}$ (fps)	5.95	w max (fps)	28.7
Wind Velocity (fps)	25.0	$\sigma_{tw}$ (fps)	5.22	w min (fps)	-23.7

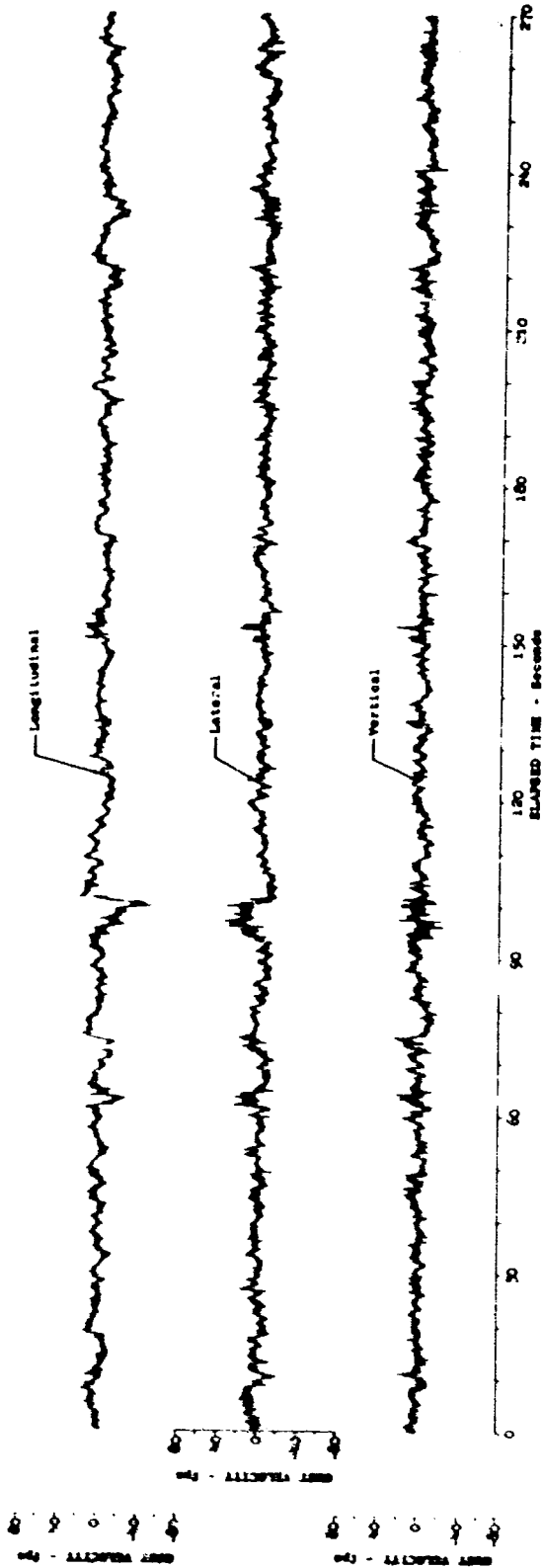


Figure 17.24 Time History of Severe Turbulence Encounter - Peterson

Test		262	Ambient Air Temp (°F)	51.4	u max (fps)	31.2
Date		4-22-69	True Airspeed (fps)	614.0	u min (fps)	-29.8
Leg No.		4	Radar Altitude (ft)	280	v max (fps)	28.2
Category No.		112313	$\sigma_{tu}$ (fps)	6.68	v min (fps)	-50.9
Wind Direction (deg)		98	$\sigma_{tv}$ (fps)	7.04	w max (fps)	42.3
Wind Velocity (fps)		28.4	$\sigma_{tw}$ (fps)	5.31	w min (fps)	-25.6

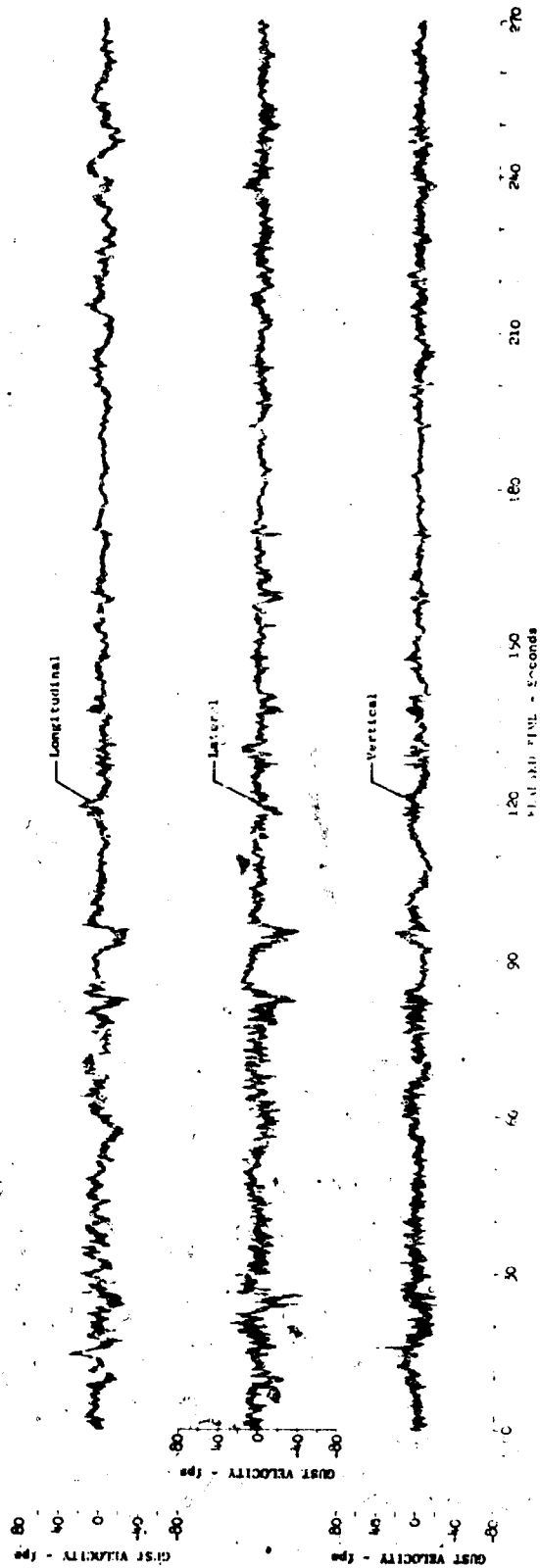


Figure 17.25 Time History of Severe Turbulence Encounter - Peterson

Test	155	Ambient Air Temp (°F)	33.1	u max (fps)	28.8
Date	1-21-69	True Airspeed (fps)	607.1	u min (fps)	-35.0
Leg No.	5	Radar Altitude (ft)	811	v max (fps)	52.6
Category	124243	$\sigma_{tu}$ (fps)	7.14	v min (fps)	-40.6
Wind Direction (deg)	261.7	$\sigma_{tv}$ (fps)	8.56	w max (fps)	40.6
Wind Velocity (fps)	58.4	$\sigma_{tw}$ (fps)	6.83	w min (fps)	-39.2

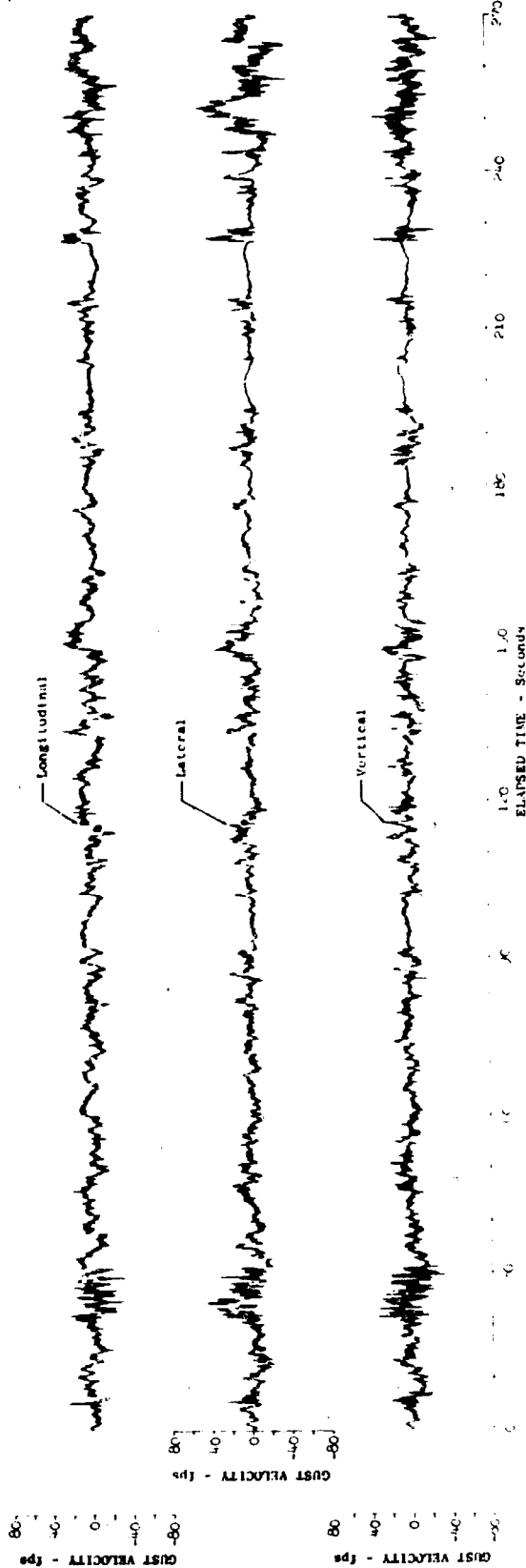


Figure 17.26 Time History of Severe Turbulence Encounter - Peterson

Test	156	Ambient Air Temp (°F)	34.4	u max (fps)	37.3
Date	1-21-69	True Airspeed (fps)	612.5	u min (fps)	-50.8
Leg No.	5	Radar Altitude (ft)	880	v max (fps)	57.6
Category No.	12343	$\sigma_{tu}$ (fps)	9.71	v min (fps)	-33.7
Wind Direction (deg)	260.9	$\sigma_{tv}$ (fps)	11.56	w max (fps)	34.6
Wind Velocity (fps)	44.5	$\sigma_{tw}$ (fps)	8.32	w min (fps)	-43.0

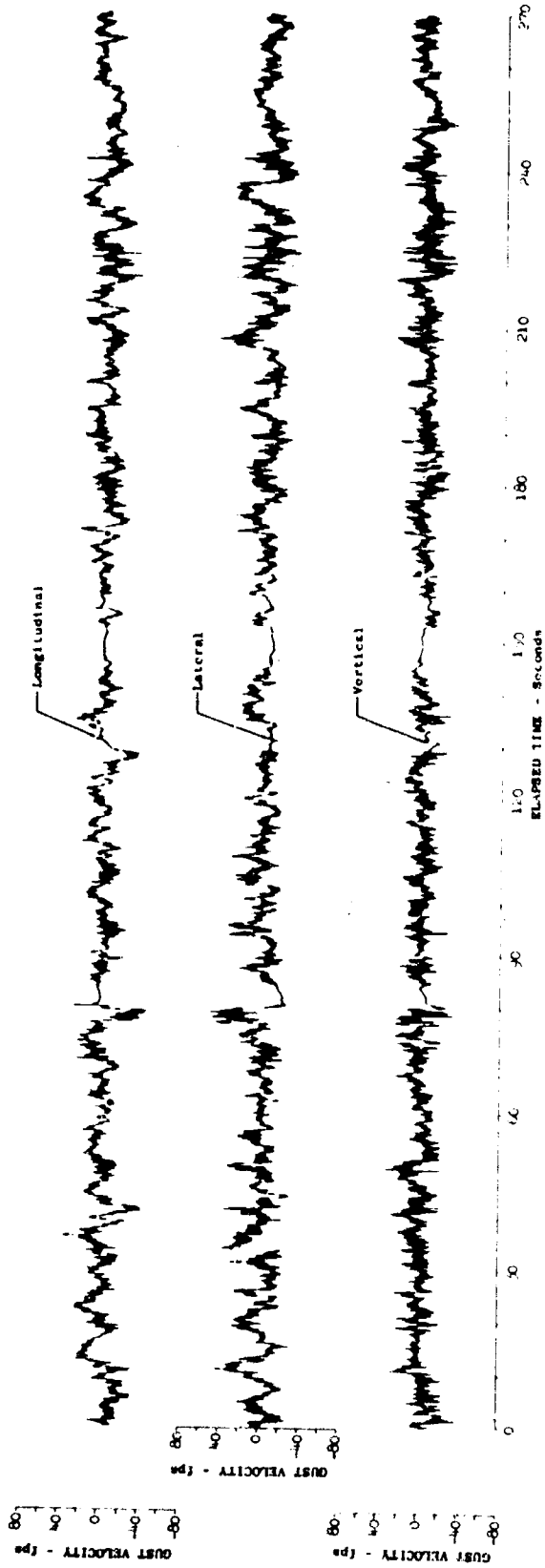


Figure 17.27 Time History of Severe Turbulence Encounter - Peterson

Test	168	Ambient Air Temp ( $^{\circ}$ F)	25.2	$u_{max}$ (fps)	43.0
Date	2-5-69	True Airspeed (fps)	565.3	$u_{min}$ (fps)	-55.1
Leg No.	5	Radar Altitude (ft)	No Data	$v_{max}$ (fps)	69.8
Category No.	121143	$\sigma_{tu}$ (fps)	6.77	$v_{min}$ (fps)	-34.6
Wind Direction (deg)	258.3	$\sigma_{tv}$ (fps)	11.01	$v_{max}$ (fps)	57.4
Wind Velocity (fps)	59.8	$\sigma_{tv}$ (fps)	9.06	$v_{min}$ (fps)	-37.0

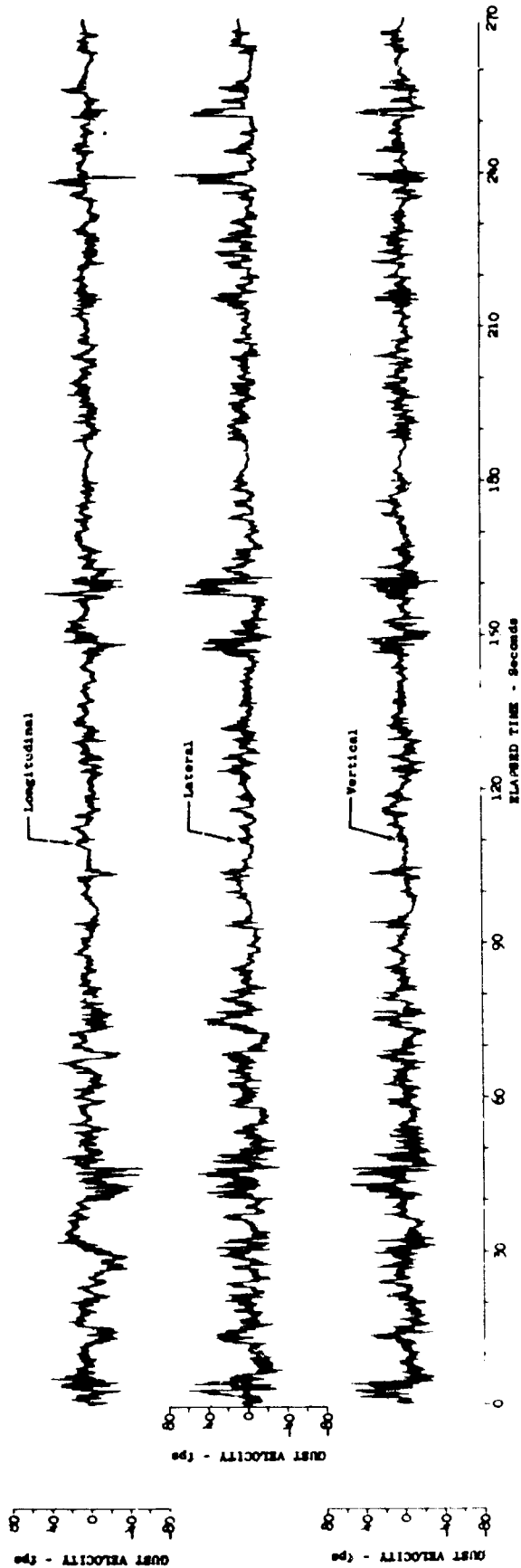


Figure 17.28 Time History of Severe Turbulence Encounter - Peterson

Test	181	Ambient Air Temp (°F)	34.5	$u_{max}$ (fps)	52.1
Date	2-13-69	True Airspeed (fps)	686.7	$u_{min}$ (fps)	-45.3
Leg No.	5	Padar Altitude (ft)	438	$v_{max}$ (fps)	48.1
Category No.	113343	$\sigma_{tu}$ (fps)	9.34	$v_{min}$ (fps)	-41.2
Wind Direction (deg)	307.6	$\sigma_{tv}$ (fps)	12.71	$v_{max}$ (fps)	61.9
Wind Velocity (fps)	24.8	$\sigma_{tv}$ (fps)	8.96	$v_{min}$ (fps)	-47.5

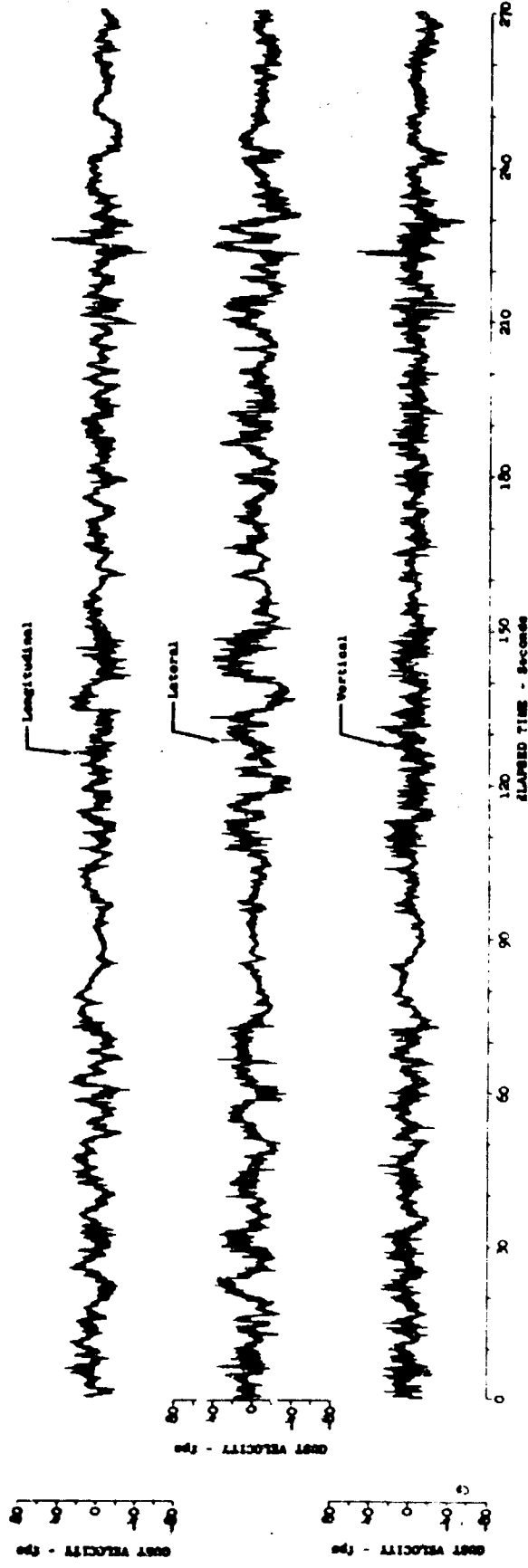


Figure 17.29 Time History of Severe Turbulence Encounter - Peterson

Test	187	Ambient Air Temp (°F)	19.6	u max (fps)	36.1
Date	2-22-69	True Airspeed (fps)	641.2	u min (fps)	-47.0
Leg No.	5	Radar Altitude (ft)	No Data	v max (fps)	48.8
Category	123243	$\sigma$ tu (fps)	6.34	v min (fps)	-25.3
Wind Direction (deg)	276.2	$\sigma$ tv (fps)	7.56	w max (fps)	50.5
Wind Velocity (fps)	40.0	$\sigma$ tw (fps)	7.19	w min (fps)	-34.2

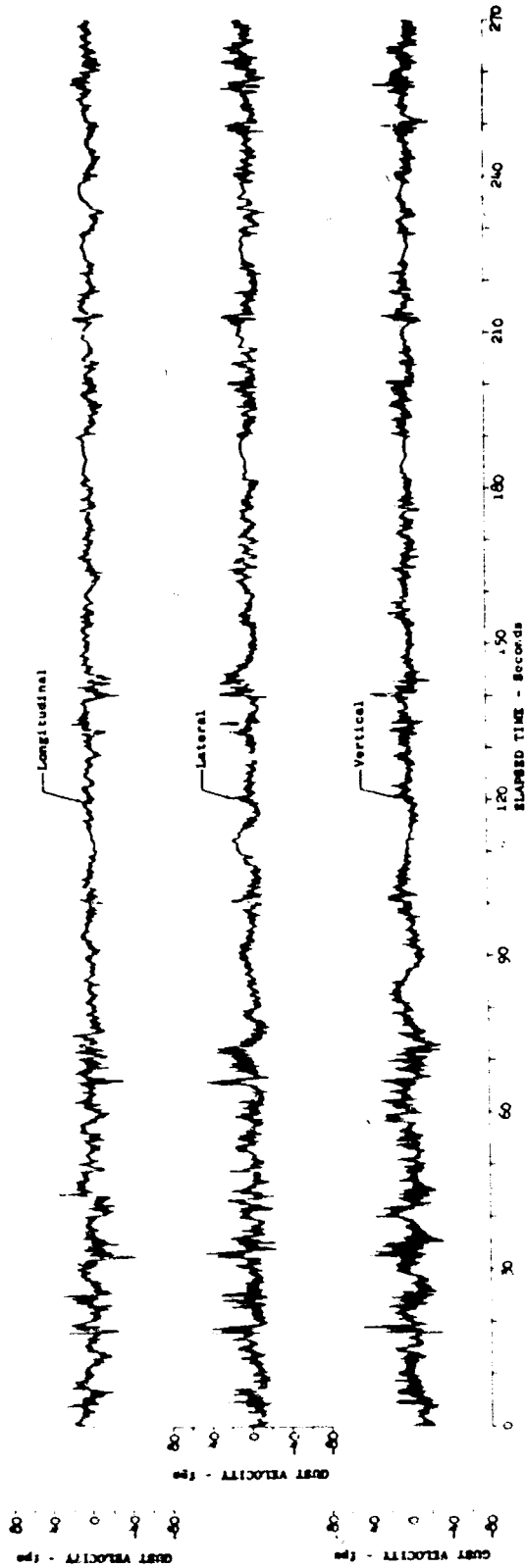


Figure 17.30 Time History of Severe Turbulence Encounter - Peterson



Test	189	Ambient Air Temp (°F)	25.0	u max (fps)	38.0
Date	2-24-69	True Airspeed (fps)	601.2	u min (fps)	-56.4
Leg No.	5	Radar Altitude (ft)	No Data	v max (fps)	58.2
Category No.	113243	$\sigma_{tu}$ (fps)	8.56	v min (fps)	-41.0
Wind Direction (deg)	294.6	$\sigma_{tv}$ (fps)	10.45	w max (fps)	46.4
Wind Velocity (fps)	30.6	$\sigma_{tw}$ (fps)	8.94	w min (fps)	-43.4

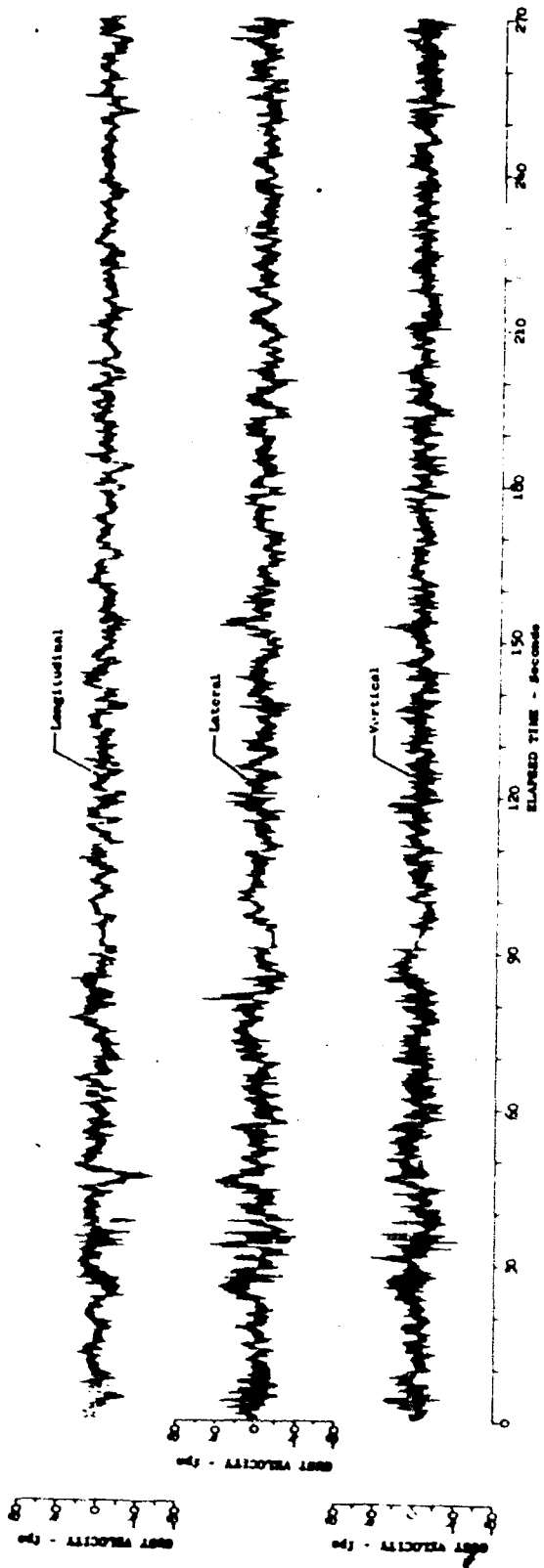


Figure 17.31 Time History of Severe Turbulence Encounter - Peterson

Test	190	Ambient Air Temp (°F)	29.3	u max (fps)	40.5
Date	2-24-69	True Airspeed (fps)	597.3	u min (fps)	-36.5
Leg No.	5	Radar Altitude (ft)	427	v max (fps)	57.2
Category No.	113343	$\sigma_{tu}$ (fps)	10.26	v min (fps)	-45.3
Wind Direction (deg)	295.0	$\sigma_{tv}$ (fps)	12.04	w max (fps)	38.5
Wind Velocity (fps)	35.9	$\sigma_{tw}$ (fps)	9.64	w min (fps)	-42.6

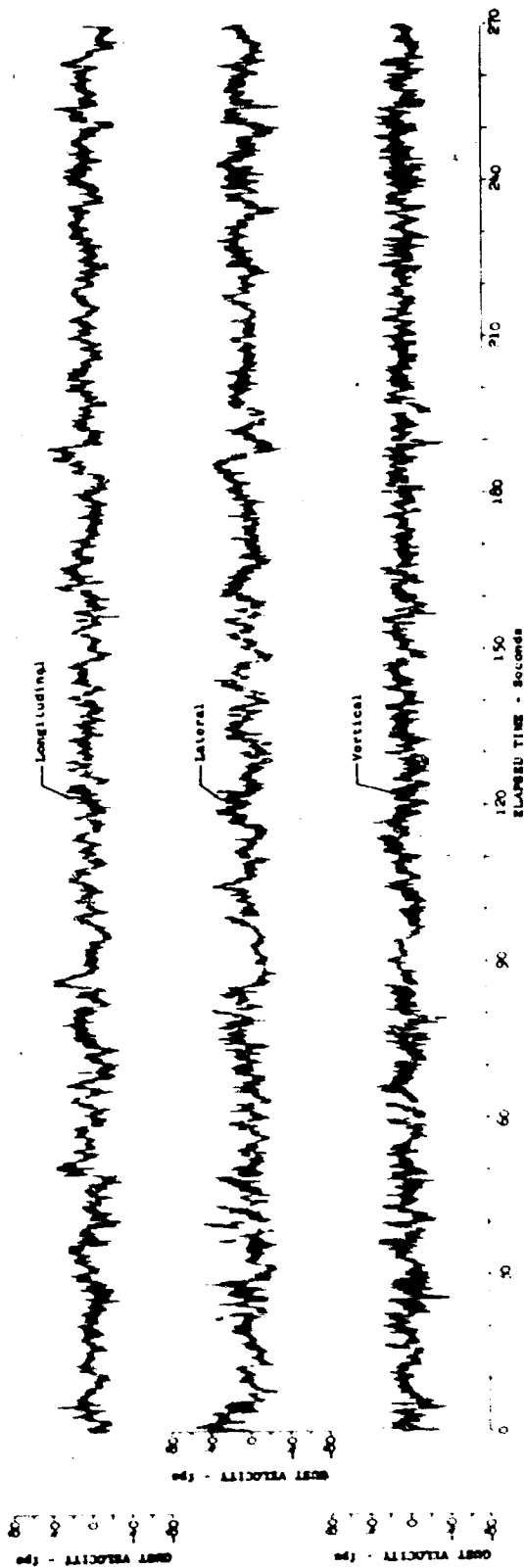


Figure 17.32 Time History of Severe Turbulence Encounter - Peterson

Test	191	Ambient Air Temp (°F)	27.5	u max (fps)	41.7
Date	2-25-69	True Airspeed (fps)	588.9	u min (fps)	-71.0
Leg No.	5	Radar Altitude (ft)	693	v max (fps)	-68.0
Category	122143	$\sigma_{tu}$ (fps)	10.81	v min (fps)	-55.6
Wind Direction (deg)	262.7	$\sigma_{tv}$ (fps)	12.81	w max (fps)	56.8
Wind Velocity (fps)	60.2	$\sigma_{tw}$ (fps)	12.16	w min (fps)	-58.1

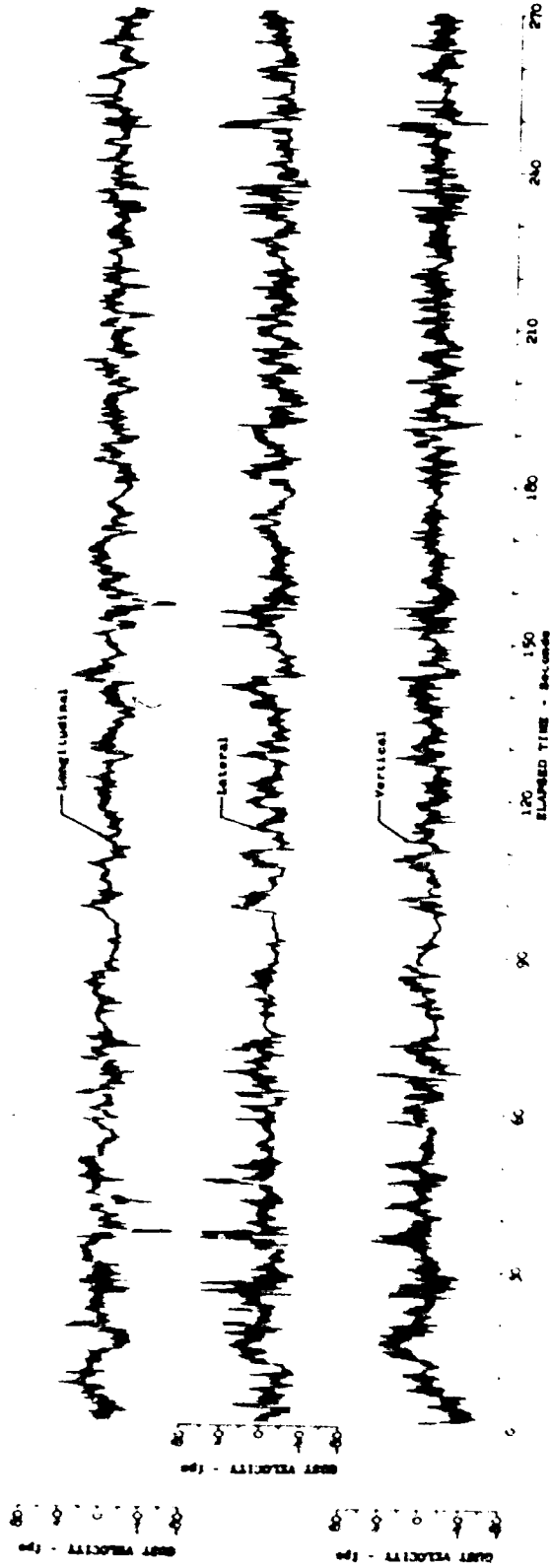


Figure 17.33 Time History of Severe Turbulence Encounter - Peterson

Test	192	Ambient Air Temp (°F)	31.9	u max (fps)	47.4
Date	2-25-69	True Airspeed (fps)	579.5	u min (fps)	-68.8
Leg No.	5	Radar Altitude (ft)	586	v max (fps)	76.9
Category No.	123243	σ tu (fps)	11.8	v min (fps)	-43.6
Wind Direction (deg)	265.0	σ ty (fps)	14.4	w max (fps)	59.4
Wind Velocity (fps)	66.2	σ tw (fps)	11.8	w min (fps)	-42.7

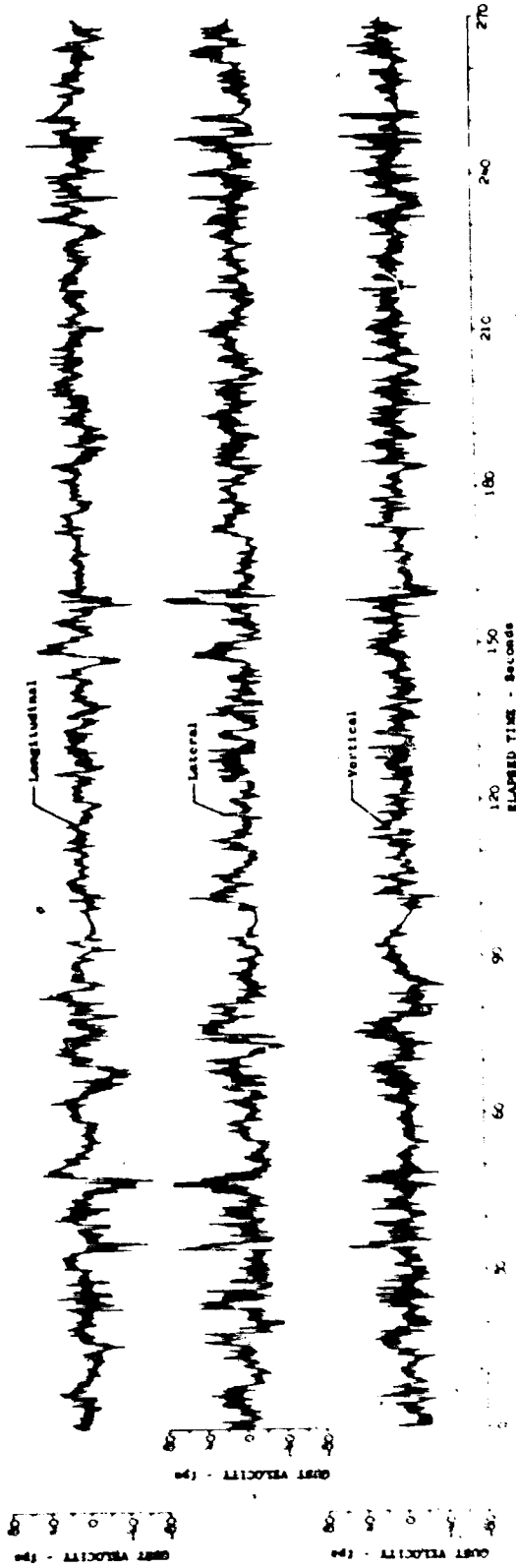


Figure 17.34 Time History of Severe Turbulence Encounter - Peterson

Test	175	Ambient Air Temp (°F)	54.9	u max (fps)	53.2
Date	2-25-69	True Airspeed (fps)	574.6	u min (fps)	-49.4
Log No.	7	Radar Altitude (ft)	497	v max (fps)	66.6
Category No.	124543	$\sigma_{tu}$ (fps)	12.79	v min (fps)	-45.9
Wind Direction (deg)	274.1	$\sigma_{tv}$ (fps)	14.45	w max (fps)	50.3
Wind Velocity (fps)	51.6	$\sigma_{tw}$ (fps)	11.95	w min (fps)	-51.5

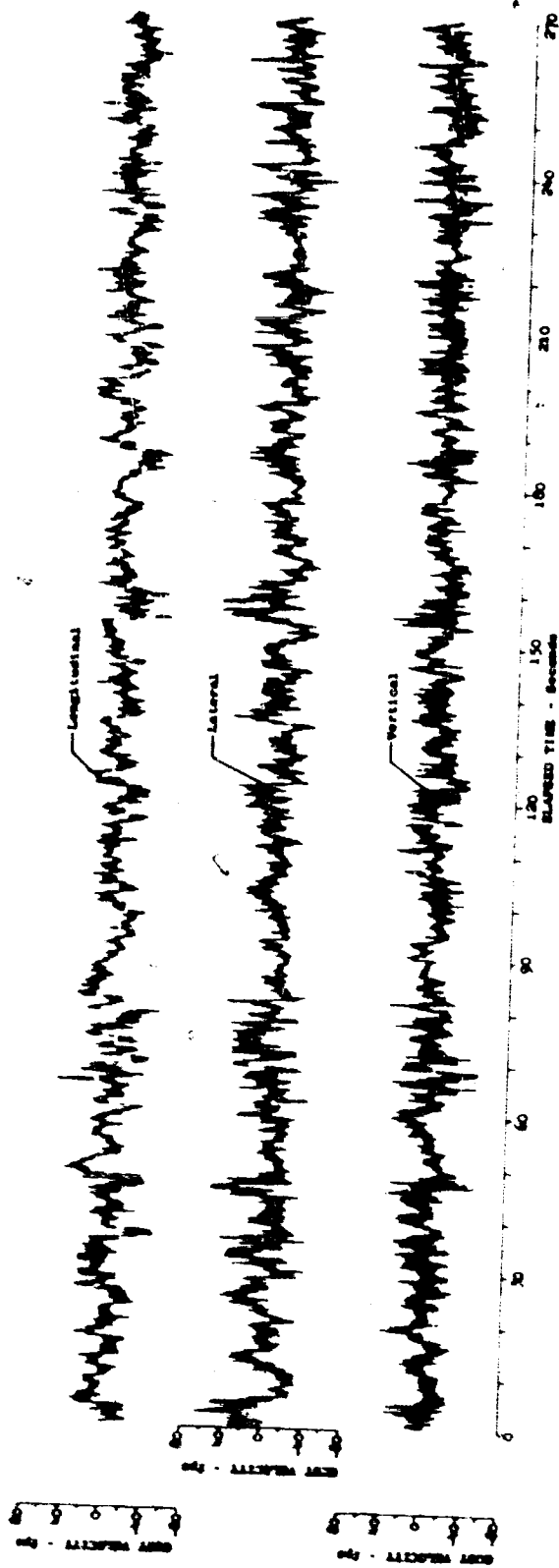


Figure 17.35 Time History of Severe Turbulence Encounter - Peterson

Test	194	Ambient Air Temp (°F)	27.3	u max (fps)	61.7
Date	2-26-68	True Airspeed (fps)	607.0	u min (fps)	-50.7
Leg No.	5	Radar Altitude (ft)	No Data	v max (fps)	58.6
Category	112143	$\sigma_{tu}$ (fps)	12.92	v min (fps)	-65.8
Wind Direction (deg)	No Data	$\sigma_{tv}$ (fps)	14.69	w max (fps)	52.0
Wind Velocity (fps)	No Data	$\sigma_{tw}$ (fps)	11.67	w min (fps)	-52.2

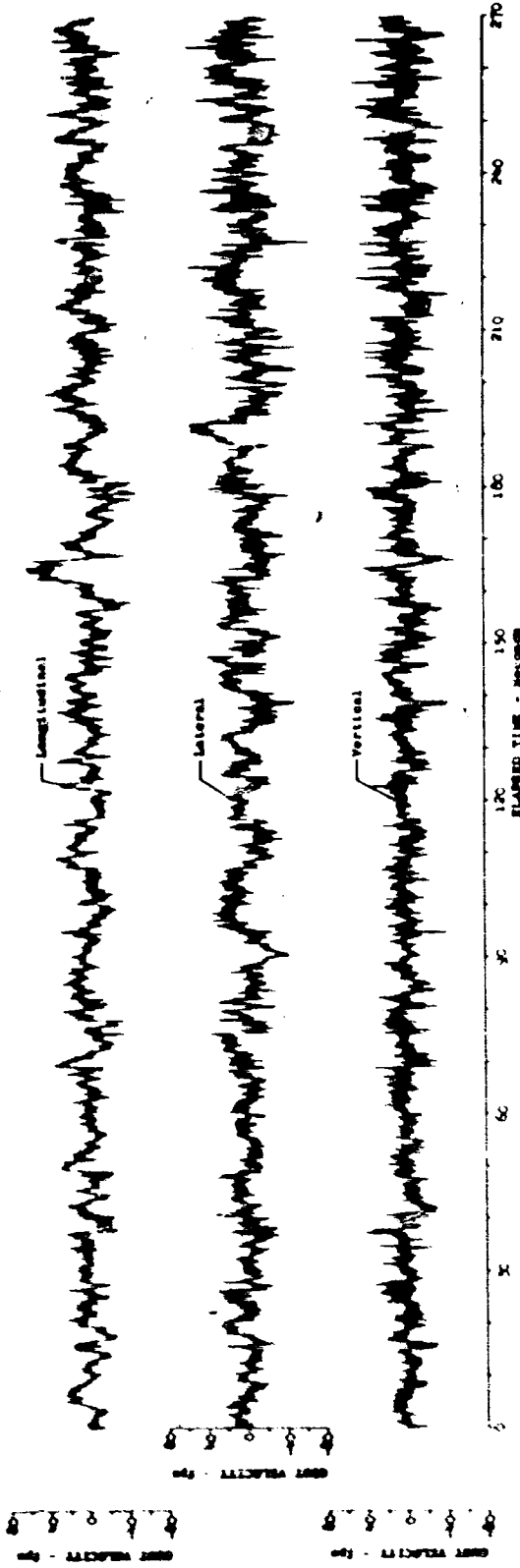


Figure 17.36 Time History of Severe Turbulence Encounter - Peterson

Test	195	Ambient Air Temp (°F)	29.6	u max (fps)	59.4
Date	2-26-69	True Airspeed (fps)	597.6	u min (fps)	-50.9
Leg No.	5	Radar Altitude (ft)	No Data	v max (fps)	75.6
Category No.	113213	$\sigma_{tu}$ (fps)	11.67	v min (fps)	-53.4
Wind Direction (deg)	No Data	$\sigma_{tv}$ (fps)	14.10	w max (fps)	45.0
Wind Velocity (fps)	No Data	$\sigma_{tw}$ (fps)	11.65	w min (fps)	-55.0

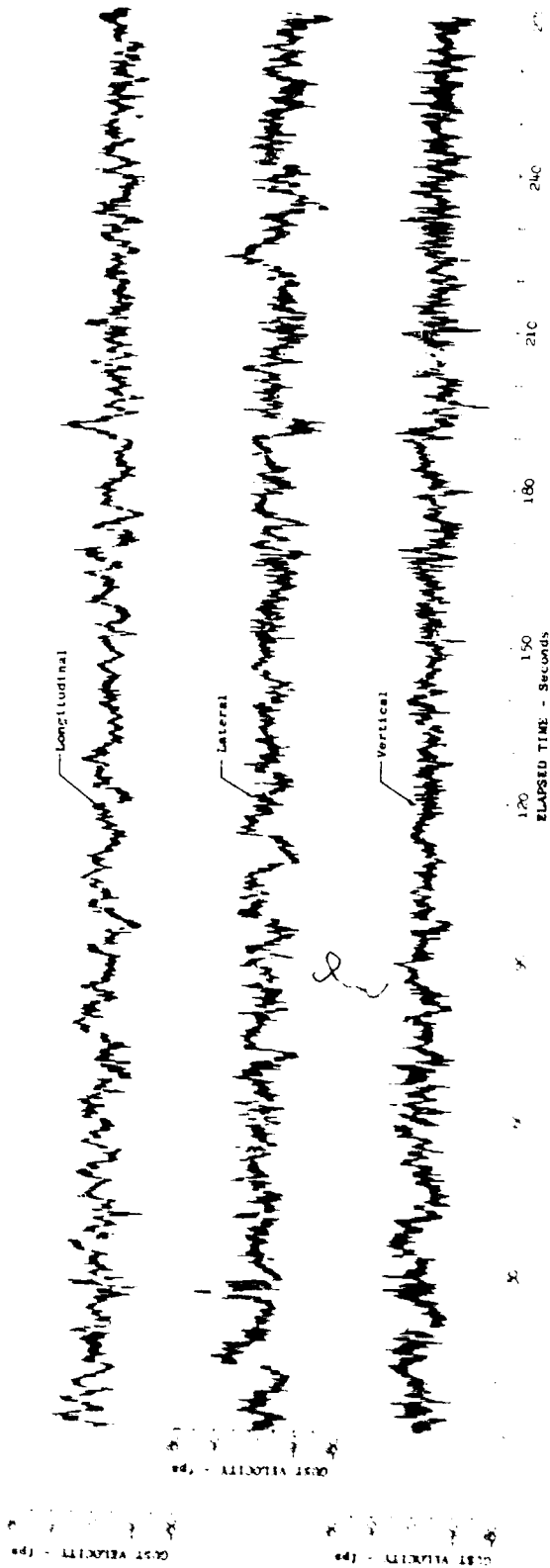


Figure 17.37 Time History of Severe Turbulence Encounter - Peterson

Test	196	Ambient Air Temp (°F)	31.8	u max (fps)	63.9
Date	2-26-69	True Airspeed (fps)	612.2	u min (fps)	-50.5
Leg No.	5	Radar Altitude (ft)	No Data	v max (fps)	69.9
Category No.	114343	$\sigma_{tu}$ (fps)	15.45	v min (fps)	-75.9
Wind Direction (deg)	281.4	$\sigma_{tv}$ (fps)	19.05	w max (fps)	58.1
Wind Velocity (fps)	35.2	$\sigma_{tw}$ (fps)	15.04	w min (fps)	-59.4

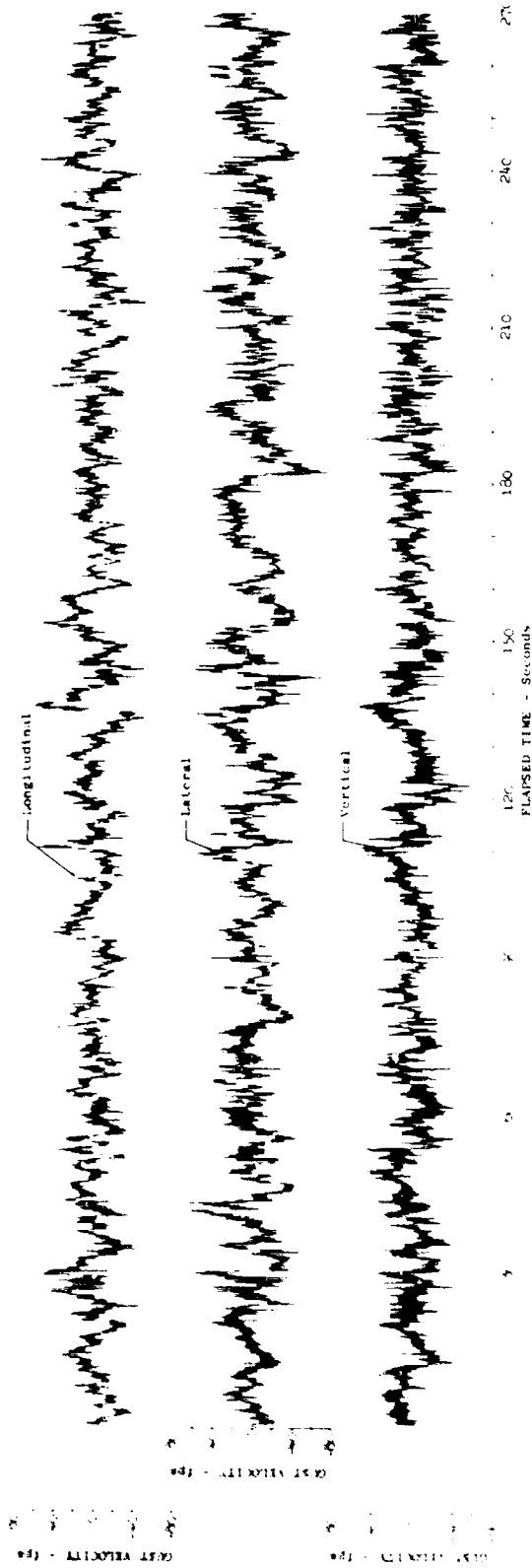


Figure 17.38 Time History of Severe Turbulence Encounter -  
Peterson



Test	199	Ambient Air Temp (°F)	18.8	u max (fps)	28.2
Date	3-6-69	True Airspeed (fps)	627.0	u min (fps)	-39.6
Leg No.	5	Radar Altitude (ft)	No Data	v max (fps)	70.1
Category	122143	$\sigma_{tu}$ (fps)	6.91	v min (fps)	-32.1
Wind Direction (deg)	304.1	$\sigma_{tv}$ (fps)	10.67	w max (fps)	40.0
Wind Velocity (fps)	38.5	$\sigma_{tw}$ (fps)	6.69	w min (fps)	-30.1

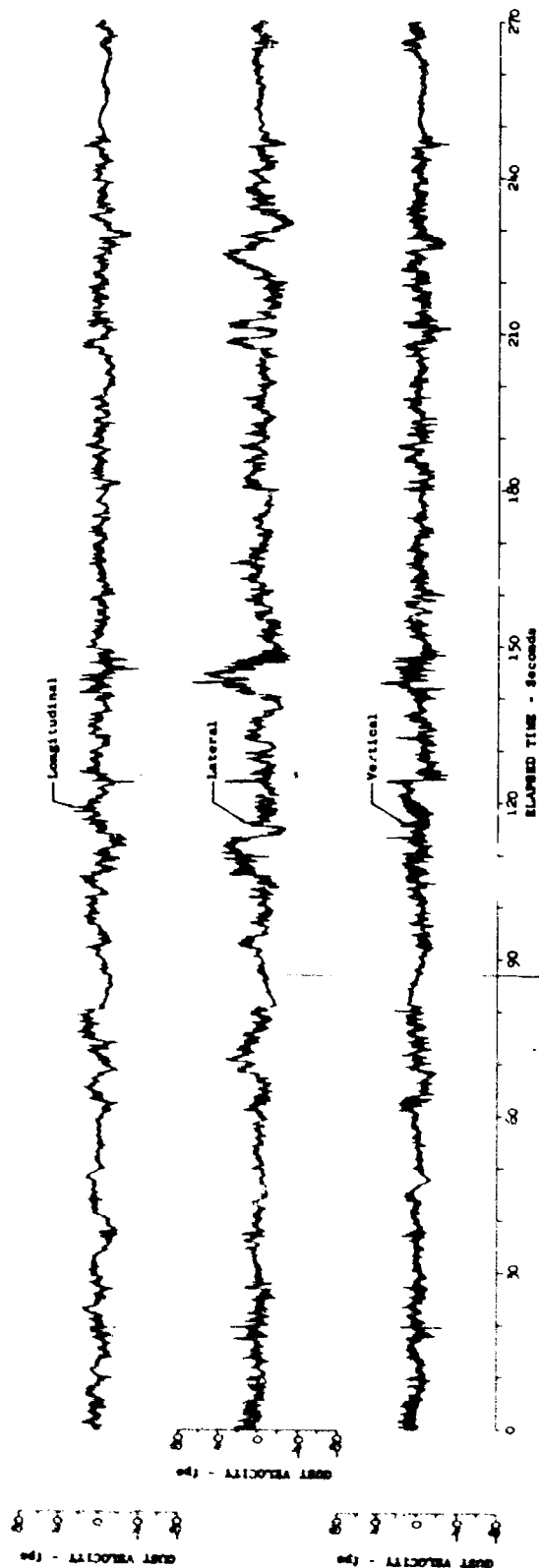


Figure 17.39 Time History of Severe Turbulence Encounter - Peterson

Test:	209	Ambient Air Temp (°F)	34.3	u max (fps)	39.0
Date	3-18-69	True Airspeed (fps)	632.9	u min (fps)	-34.2
Leg No.	5	Radar Altitude (ft)	No Data	v max (fps)	51.8
Category No.	122243	$\sigma$ tu (fps)	7.73	v min (fps)	-28.5
Wind Direction (deg)	305.0	$\sigma$ tv (fps)	10.44	w max (fps)	35.3
Wind Velocity (fps)	36.3	$\sigma$ tw (fps)	7.74	w min (fps)	-32.9

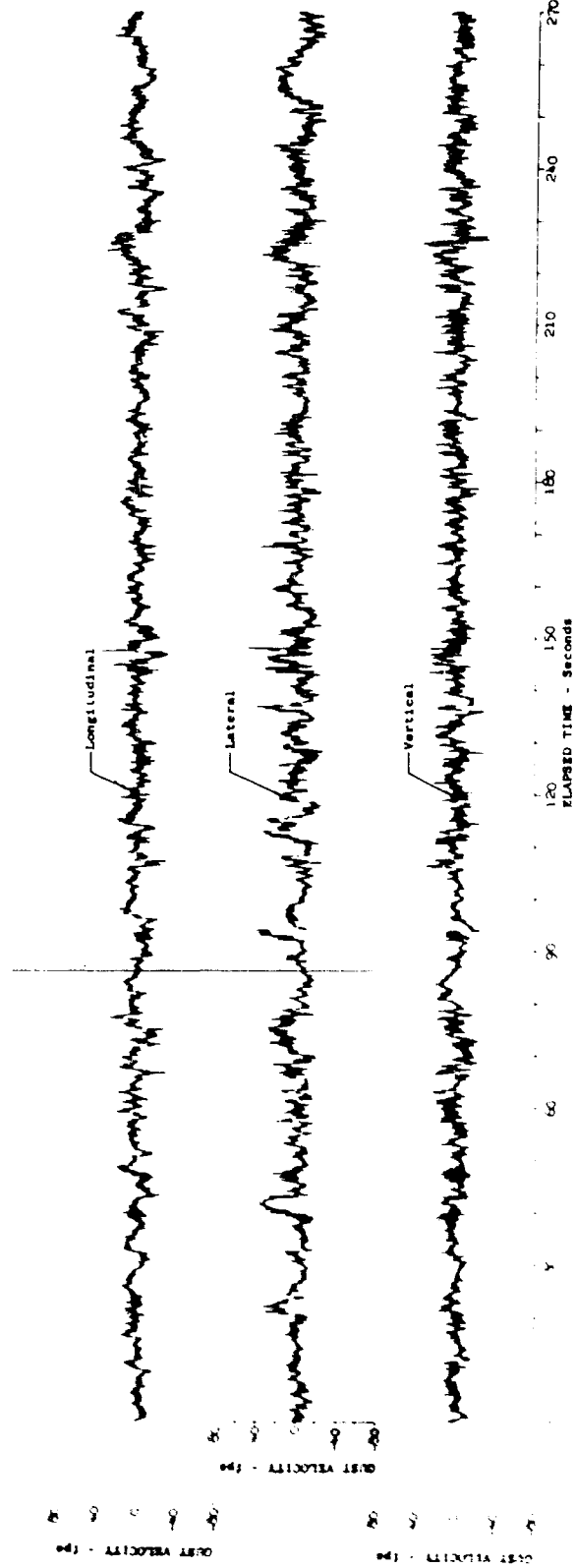


Figure 17.40 Time History of Severe Turbulence Encounter - Peterson

Test	212	Ambient Air Temp (°F)	27.9	u max (fps)	46.6
Date	3-19-69	True Airspeed (fps)	596.3	u min (fps)	-39.4
Leg No.	5	Radar Altitude (ft)	No Data	v max (fps)	49.7
Category	114243	$\sigma_{tu}$ (fps)	10.24	v min (fps)	-35.0
Wind Direction (deg)	318.6	$\sigma_{tv}$ (fps)	10.68	w max (fps)	40.9
Wind Velocity (fps)	31.7	$\sigma_{tw}$ (fps)	9.01	w min (fps)	-40.6

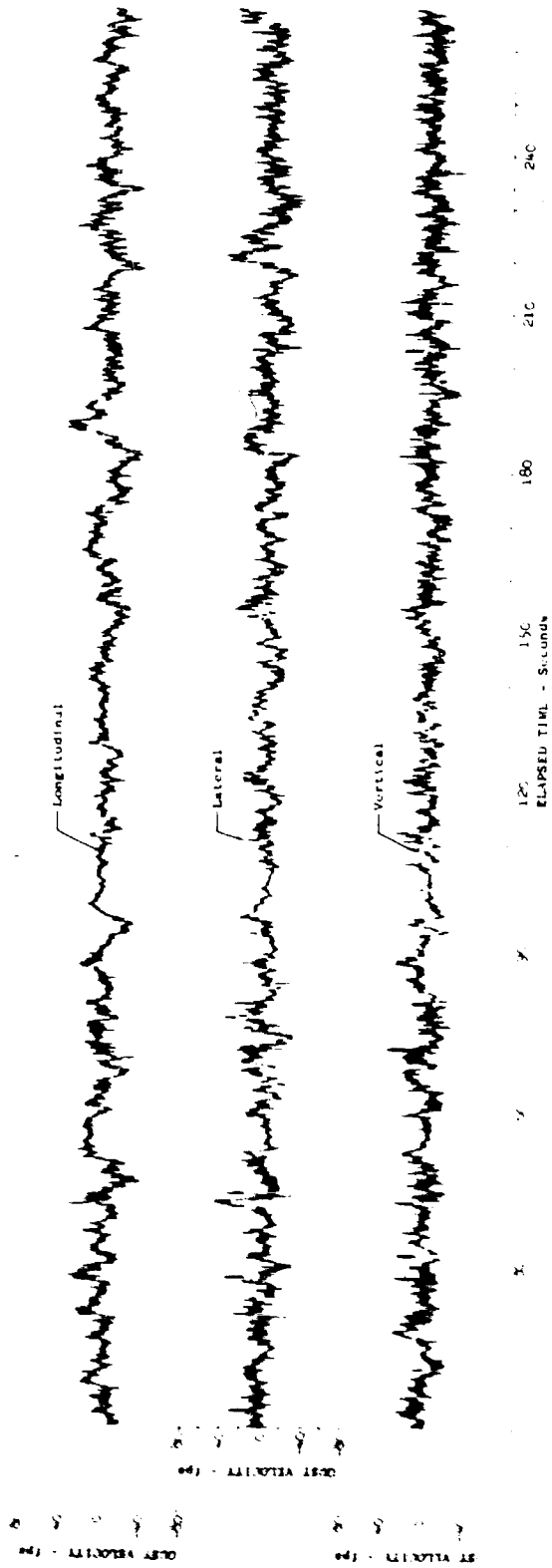


Figure 17.41 Time History of Severe Turbulence Encounter - Peterson

Test	219	Ambient Air Temp (°F)	13.0	u max (fps)	41.6
Date	3-25-69	True Airspeed (fps)	618.1	u min (fps)	-39.7
Leg No.	5	Radar Altitude (ft)	No Data	v max (fps)	58.8
Category	112213	$\sigma_{tu}$ (fps)	8.84	v min (fps)	-43.9
Wind Direction (deg)	291.4	$\sigma_{tv}$ (fps)	11.87	w max (fps)	48.9
Wind Velocity (fps)	33.6	$\sigma_{tw}$ (fps)	9.62	w min (fps)	-43.3

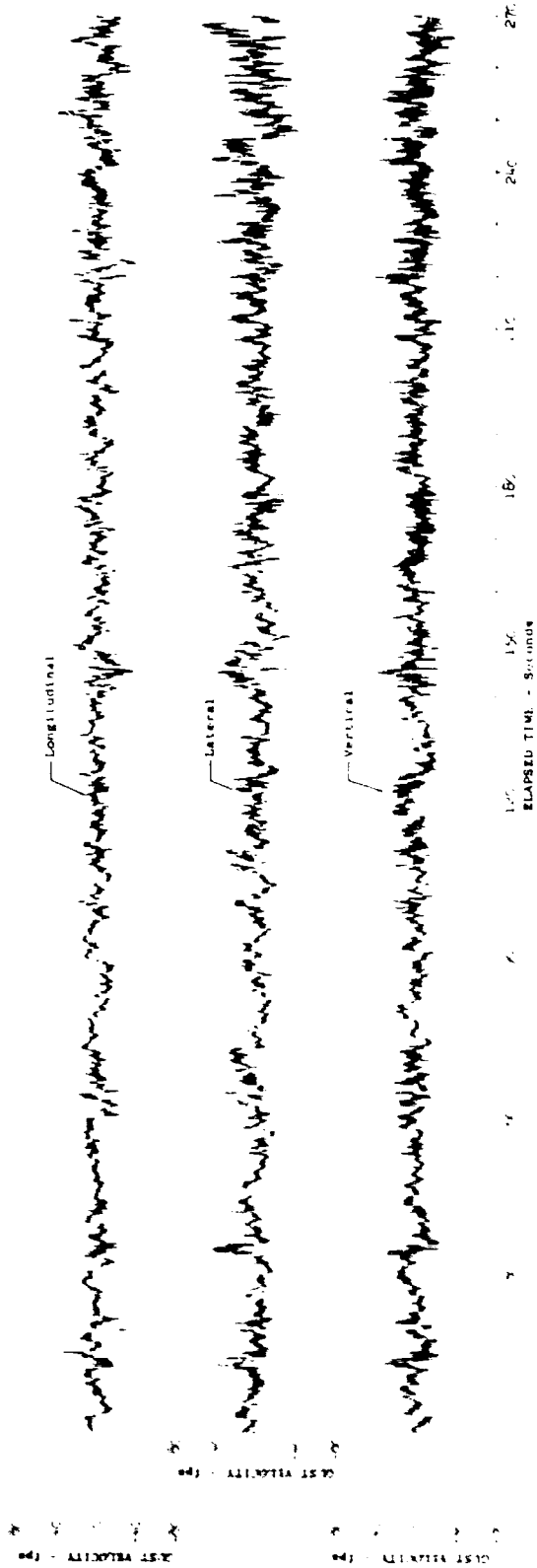


Figure 17.42 Time History of Severe Turbulence Encounter - Peterson

Test	220	Ambient Air Temp ( $^{\circ}F$ )	20.2	u max (fps)	37.4
Date	3-25-69	True Airspeed (fps)	609.2	u min (fps)	-40.6
Leg No.	5	Radar Altitude (ft)	No Data	v max (fps)	52.2
Category No.	112313	$\sigma_{tu}$ (fps)	8.11	v min (fps)	-34.2
Wind Direction (deg)	308.0	$\sigma_{tv}$ (fps)	10.55	w max (fps)	38.6
Wind Velocity (fps)	19.1	$\sigma_{tw}$ (fps)	8.14	w min (fps)	-44.8

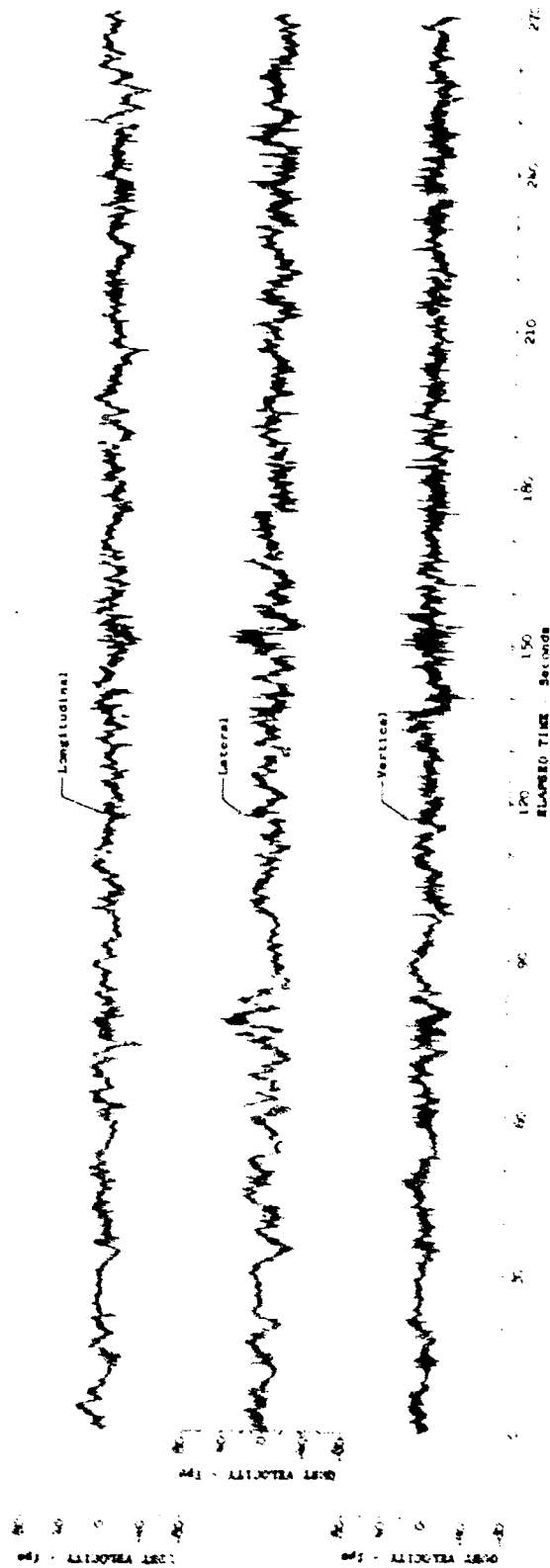


Figure 17.43 Time History of Severe Turbulence Encounter - Peterson

Test	224	Ambient Air Temp (°F)	30.2	u max (fps)	39.9
Date	3-27-69	True Airspeed (fps)	638.3	u min (fps)	-36.0
Leg No.	5	Radar Altitude (ft)	No Data	v max (fps)	54.3
Category	113213	$\sigma_{tu}$ (fps)	7.83	v min (fps)	-43.2
Wind Direction (deg)	274.3	$\sigma_{tv}$ (fps)	11.77	w max (fps)	33.4
Wind Velocity (fps)	22.5	$\sigma_{tw}$ (fps)	7.88	w min (fps)	-39.8

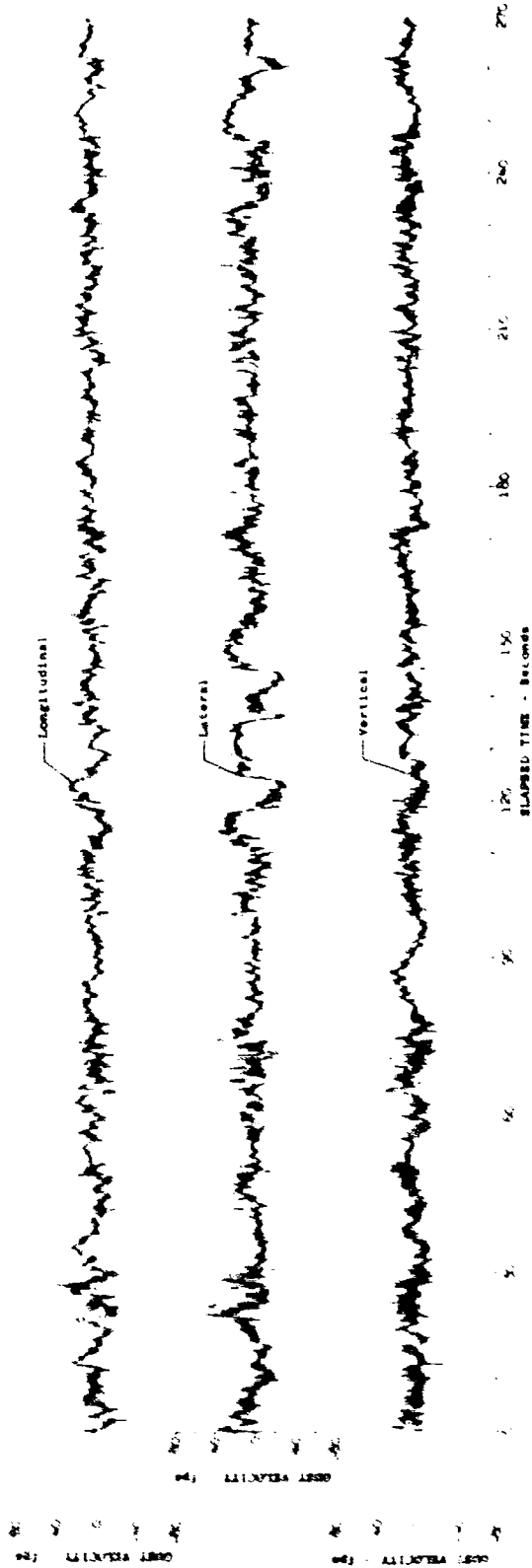


Figure 17.44 Time History of Severe Turbulence Encounter - Peterson

Test	225	Ambient Air Temp (°F)	35.7	u max (fps)	51.0
Date	3-27-59	True Airspeed (fps)	635.4	u min (fps)	-34.3
Leg No.	5	Radar Altitude (ft)	No Data	v max (fps)	52.2
Category	114313	$\sigma_{tu}$ (fps)	8.40	v min (fps)	-40.6
Wind Direction (deg)	285.2	$\sigma_{tv}$ (fps)	12.17	w max (fps)	47.5
Wind Velocity (fps)	31.7	$\sigma_{tw}$ (fps)	9.27	w min (fps)	-35.9

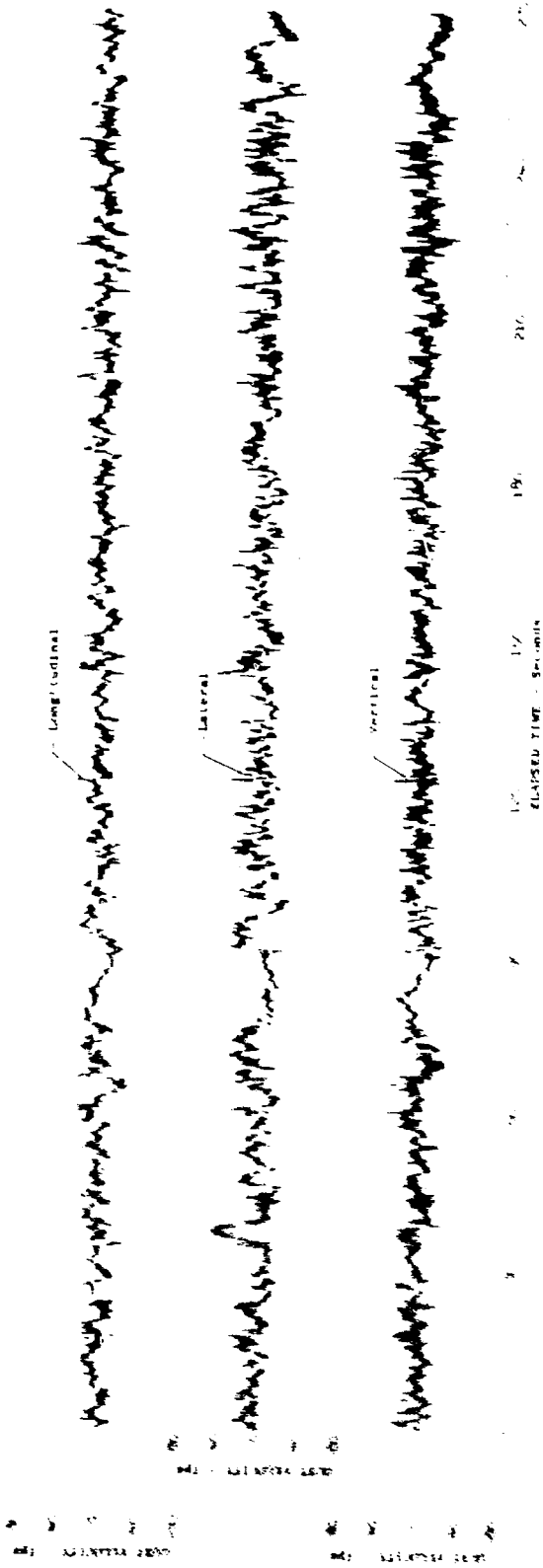


Figure 17.45 Time History of Severe Turbulence Encounter - Peterson

Test	226	Ambient Air Temp (°F)	29.1	u max (fps)	47.2
Date	3-28-69	True Airspeed (fps)	651.0	u min (fps)	-32.5
Leg No.	5	Radar Altitude (ft)	No Data	v max (fps)	67.7
Category No.	122115	$\sigma$ tu (fps)	6.98	v min (fps)	-6.4
Wind Direction (deg)	280.4	$\sigma$ tv (fps)	10.45	w max (fps)	37.7
Wind Velocity (fps)	47.1	$\sigma$ tw (fps)	8.10	w min (fps)	-41.6

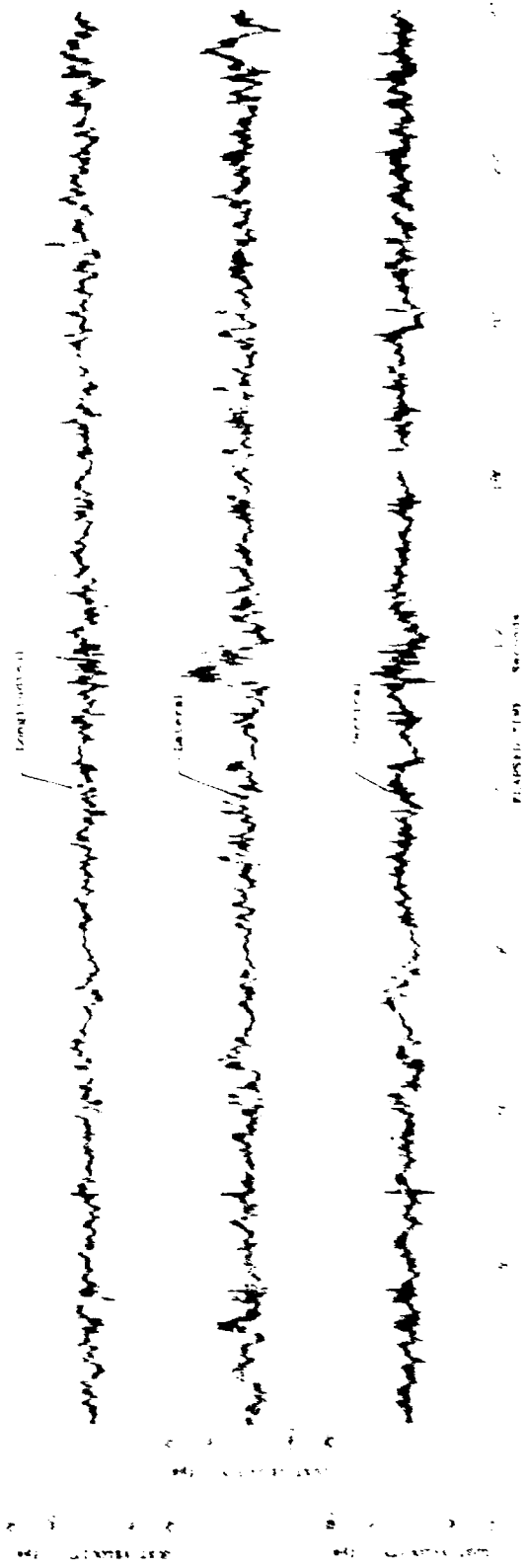


Figure 17.46 Time History of Severe Turbulence Encounter - Peterson



Test	232	Ambient Air Temp (°F)	37.2	u max (fps)	40.3
Date	4-1-69	True Airspeed (fps)	624.6	u min (fps)	-45.9
Leg No.	5	Radar Altitude (ft)	611	v max (fps)	55.1
Category No.	122113	$\sigma$ tu (fps)	9.65	v min (fps)	-32.2
Wind Direction (deg)	259.8	$\sigma$ tv (fps)	10.96	w max (fps)	56.7
Wind Velocity (fps)	57.5	$\sigma$ tw (fps)	9.74	w min (fps)	-41.4

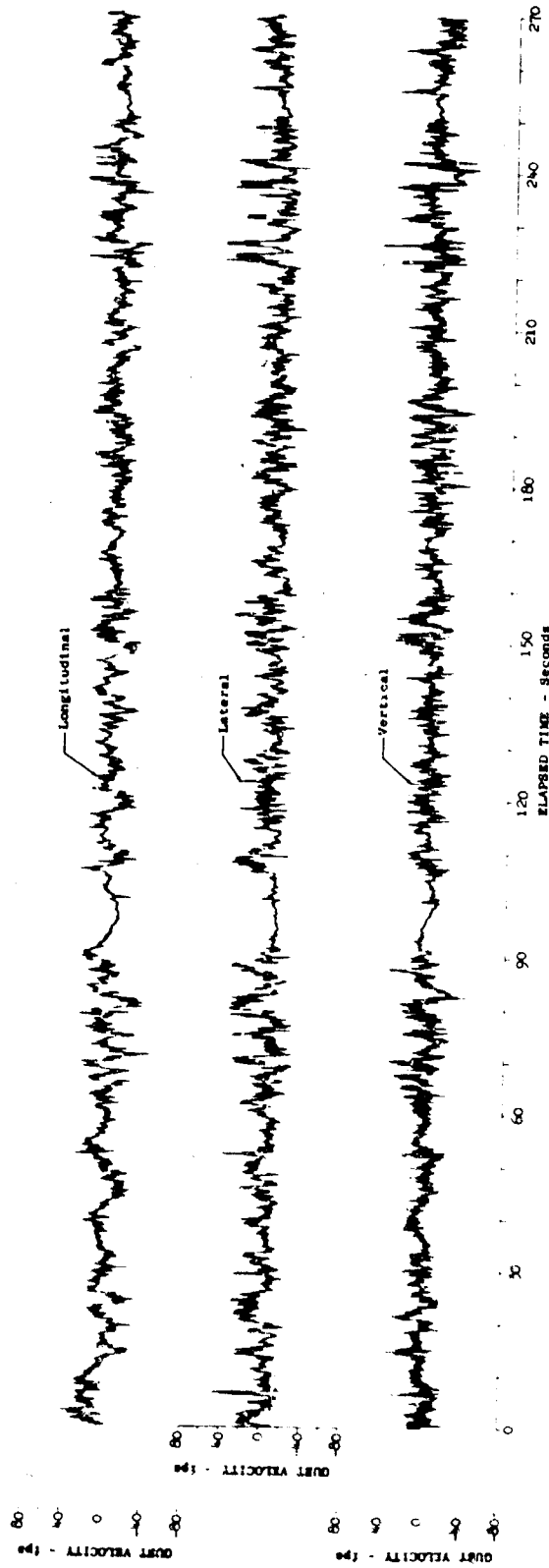


Figure 17.47 Time History of Severe Turbulence Encounter -  
Peterson

Test	233	Ambient Air Temp (°F)	40.1	u max (fps)	51.5
Date	4-1-69	True Airspeed (fps)	623.5	u min (fps)	-47.8
Leg No.	5	Radar Altitude (ft)	575	v max (fps)	63.8
Category	123213	$\sigma$ tu (fps)	9.56	v min (fps)	-30.4
Wind Direction (deg)	259.9	$\sigma$ tv (fps)	10.97	w max (fps)	52.1
Wind Velocity (fps)	42.9	$\sigma$ tw (fps)	9.59	w min (fps)	-38.9

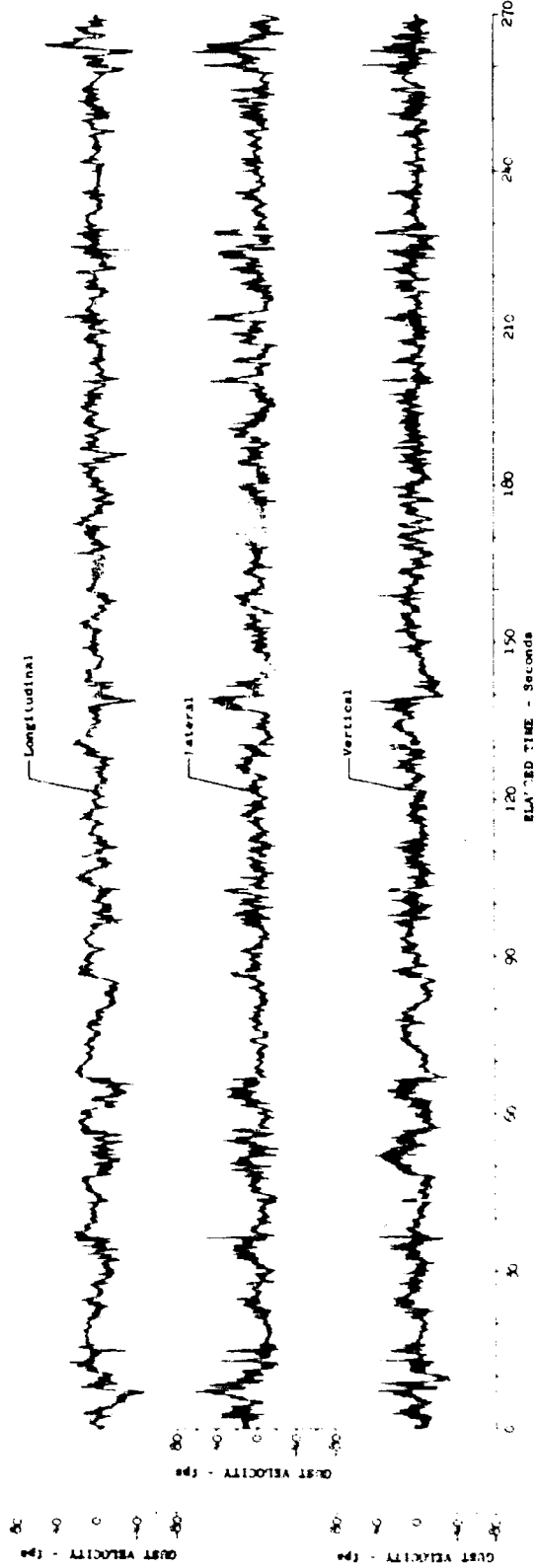


Figure 17.48 Time History of Severe Turbulence Encounter - Peterson

Test	236	Ambient Air Temp (°F)	36.9	u max (fps)	52.8
Date	4-3-69	True Airspeed (fps)	628.4	u min (fps)	-50.9
Leg No.	5	Radar Altitude (ft)	No Data	v max (fps)	68.5
Category	122113	$\sigma_{tu}$ (fps)	10.17	v min (fps)	-48.5
Wind Direction (deg)	254.3	$\sigma_{tv}$ (fps)	14.59	w max (fps)	48.5
Wind Velocity (fps)	57.5	$\sigma_{tw}$ (fps)	11.22	w min (fps)	-43.0

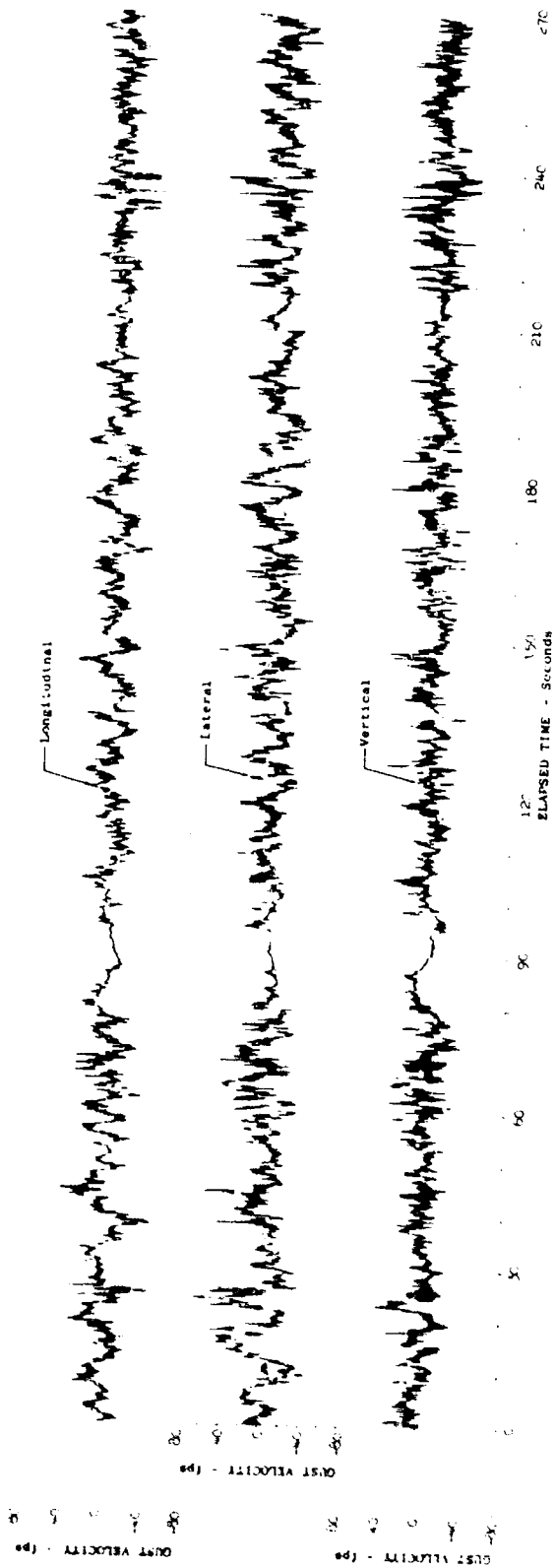


Figure 17.49 Time History of Severe Turbulence Encounter - Peterson

Test	265	Ambient Air Temp (°F)	50.3	u max (fps)	33.5
Date	5-1-69	True Airspeed (fps)	630.2	u min (fps)	-38.3
Leg No.	5	Radar Altitude (ft)	368	v max (fps)	51.6
Category	114313	$\sigma$ tu (fps)	9.20	v min (fps)	-33.6
Wind Direction (deg)	260.3	$\sigma$ tv (fps)	11.00	w max (fps)	38.6
Wind Velocity (fps)	21.7	$\sigma$ tw (fps)	8.35	w min (fps)	-32.9

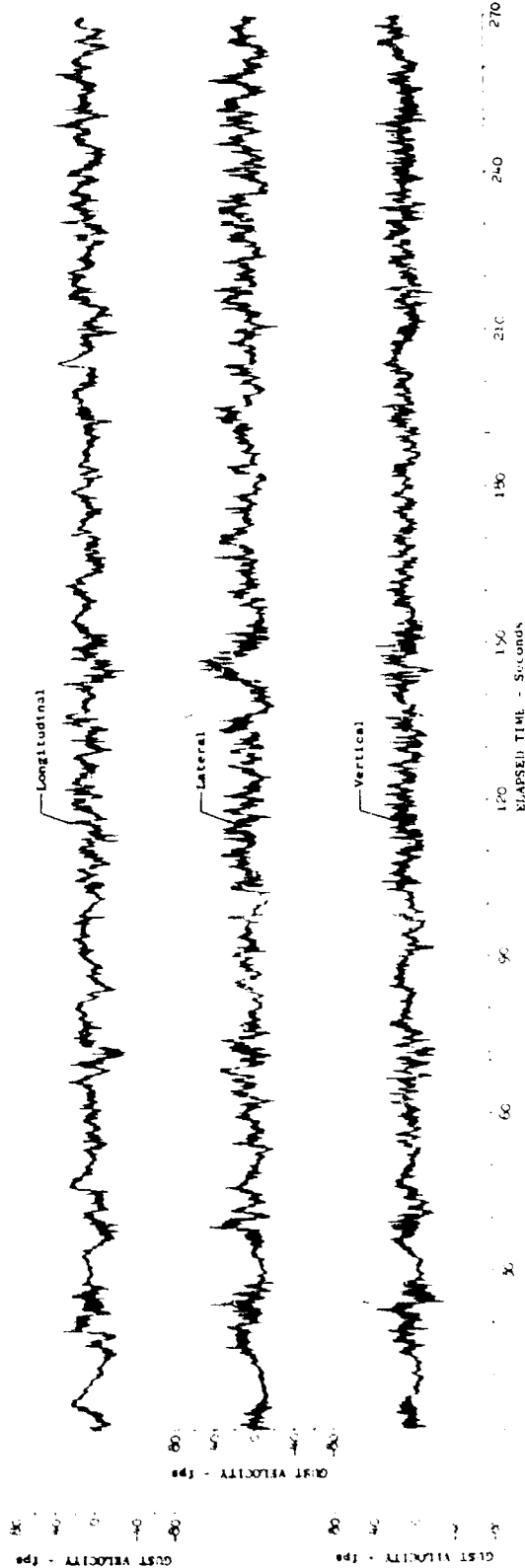


Figure 17.50 Time History of Severe Turbulence Encounter - Peterson

Test	157	Ambient Air Temp (°F)	35.0	$u_{max}$ (fps)	51.1
Date	1-22-69	True Airspeed (fps)	639.0	$u_{min}$ (fps)	-41.7
Log No.	6	Padar Altitude (ft)	421	$v_{max}$ (fps)	43.2
Category No.	113143	$\sigma_{tu}$ (fps)	9.55	$v_{min}$ (fps)	-55.0
Wind Direction (deg)	262.7	$\sigma_{tv}$ (fps)	12.14	$v_{max}$ (fps)	47.0
Wind Velocity (fps)	74.8	$\sigma_{tw}$ (fps)	9.79	$v_{min}$ (fps)	-42.4

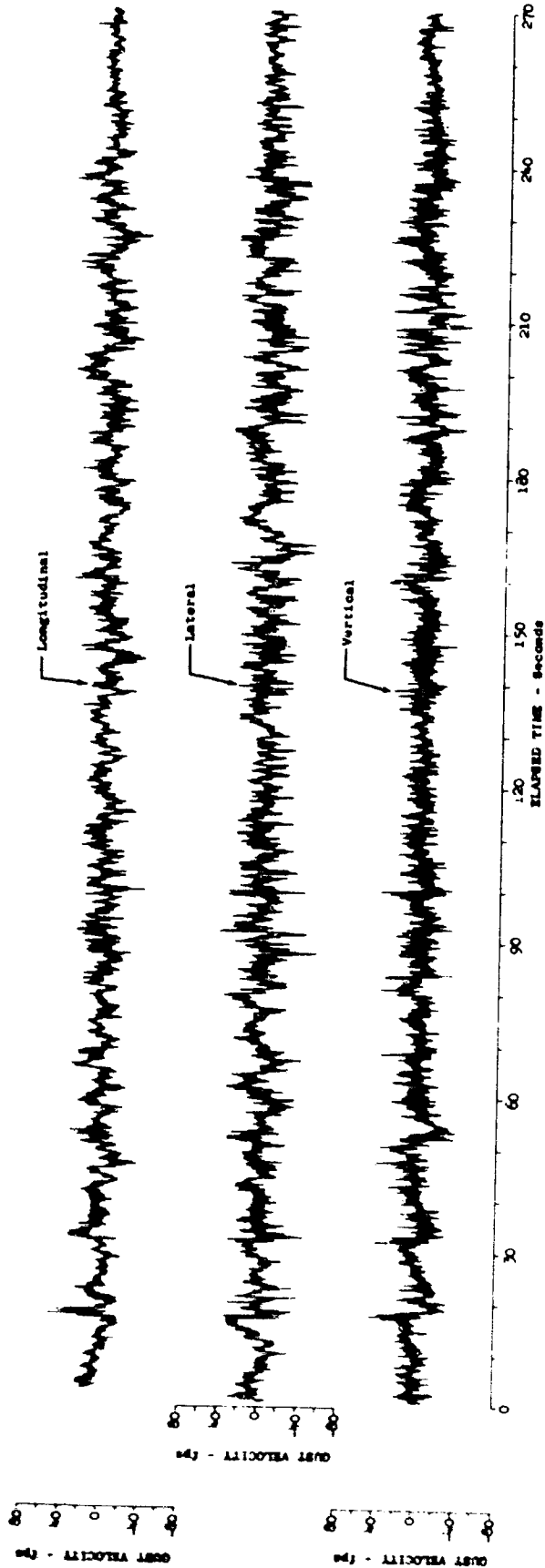


Figure 17.51 Time History of Severe Turbulence Encounter - Peterson

Test	158	Ambient Air Temp (°F)	37.3	u max (fps)	34.8
Date	1-22-69	True Airspeed (fps)	619.2	u min (fps)	-44.2
Leg No.	6	Padar Altitude (ft)	406	v max (fps)	51.0
Category No.	113243	$\sigma_{tu}$ (fps)	9.67	v min (fps)	-72.5
Wind Direction (deg)	269.8	$\sigma_{tv}$ (fps)	13.12	v max (fps)	49.3
Wind Velocity (fps)	50.4	$\sigma_{tw}$ (fps)	9.32	v min (fps)	-40.1

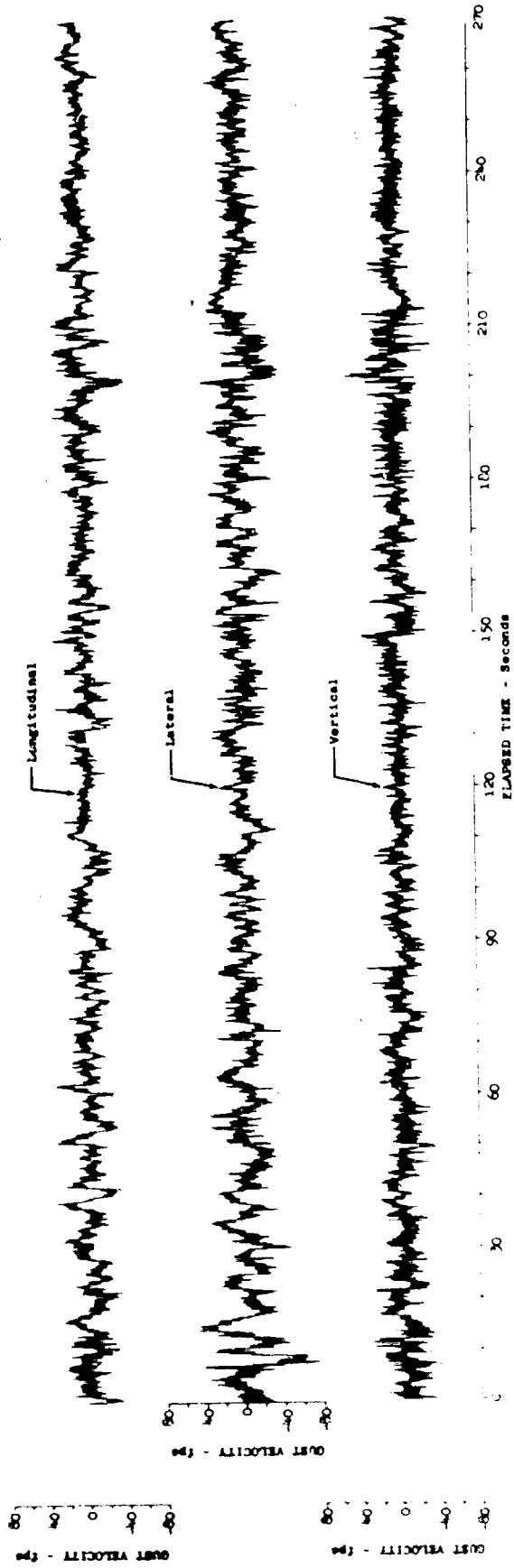


Figure 17.52 Time History of Severe Turbulence Encounter - Peterson

Test	170	Ambient Air Temp (°F)	31.8	u max (fps)	40.1
Date	2-6-69	True Airspeed (fps)	566.3	u min (fps)	-37.0
Leg No.	6	Padar Altitude (ft)	386	v max (fps)	49.6
Category No.	112143	$\sigma_{tu}$ (fps)	8.65	v min (fps)	-51.8
Wind Direction (deg)	260.9	$\sigma_{tv}$ (fps)	11.30	v max (fps)	37.9
Wind Velocity (fps)	76.8	$\sigma_{tw}$ (fps)	8.07	v min (fps)	-38.3

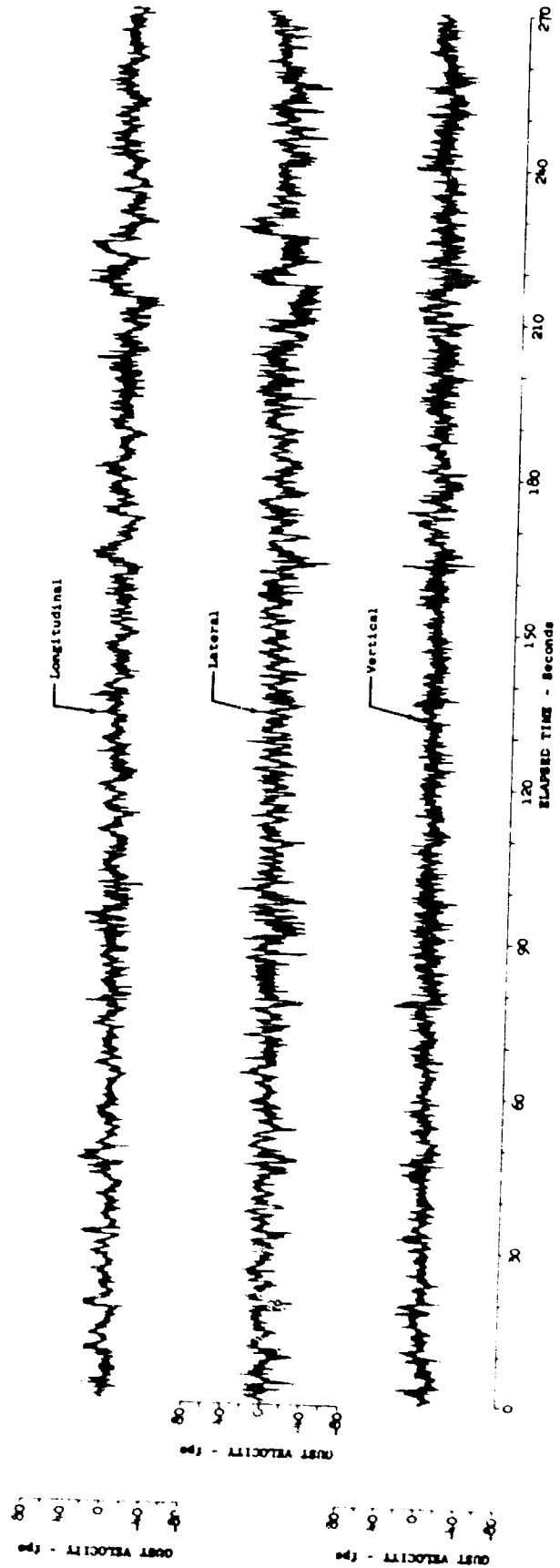


Figure 17.53 Time History of Severe Turbulence Encounter - Peterson

Test	171	Ambient Air Temp (°F)	33.9	u max (fps)	68.6
Date	2-6-69	True Airspeed (fps)	584.3	u min (fps)	-40.4
Leg No.	6	Padar Altitude (ft)	366	v max (fps)	57.2
Category No.	11243	$\sigma_{tu}$ (fps)	10.12	v min (fps)	-51.4
Wind Direction (deg)	258.7	$\sigma_{tv}$ (fps)	11.39	v max (fps)	48.2
Wind Velocity (fps)	76.4	$\sigma_{tw}$ (fps)	8.58	v min (fps)	-41.6

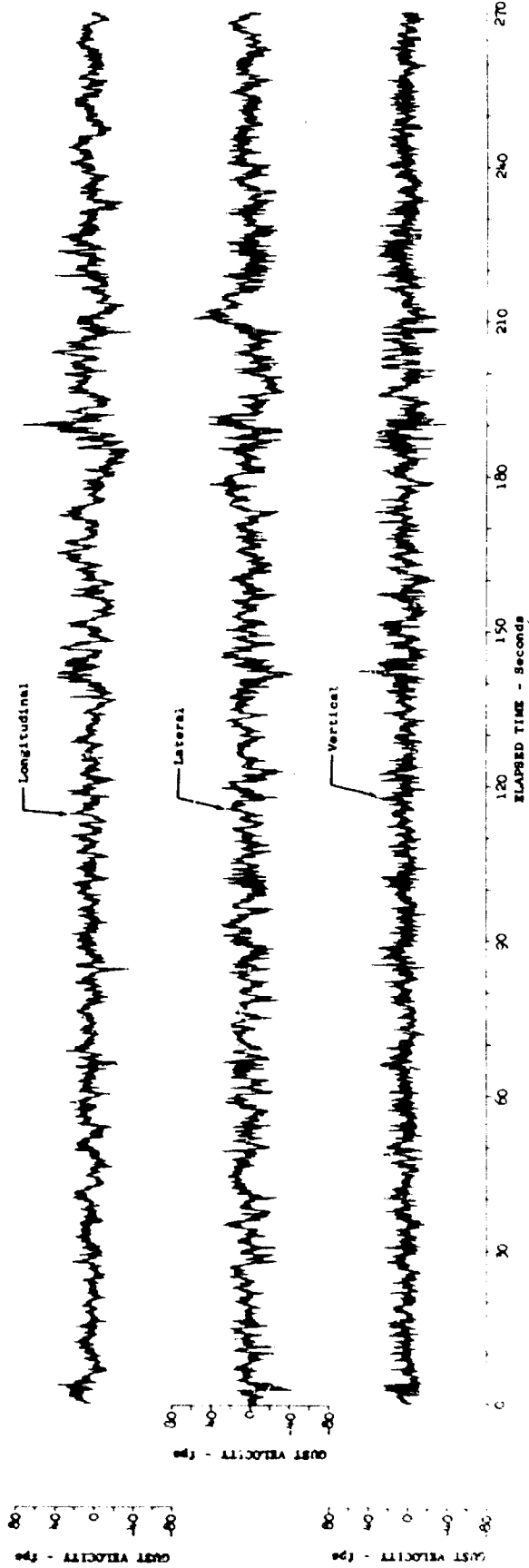


Figure 17.54 Time History of Severe Turbulence Encounter - Peterson



Test	172	Ambient Air Temp (°F)	36.9	$u_{max}$ (fps)	48.6
Date	2-6-69	True Airspeed (fps)	580.7	$u_{min}$ (fps)	-31.4
Leg No.	6	Podar Altitude (ft)	345.7	$v_{max}$ (fps)	38.0
Category No.	112343	$\sigma_{tu}$ (fps)	7.74	$v_{min}$ (fps)	-40.1
Wind Direction (deg)	239.9	$\sigma_{tv}$ (fps)	9.74	$w_{max}$ (fps)	36.9
Wind Velocity (fps)	71.5	$\sigma_{tw}$ (fps)	7.68	$w_{min}$ (fps)	-54.6

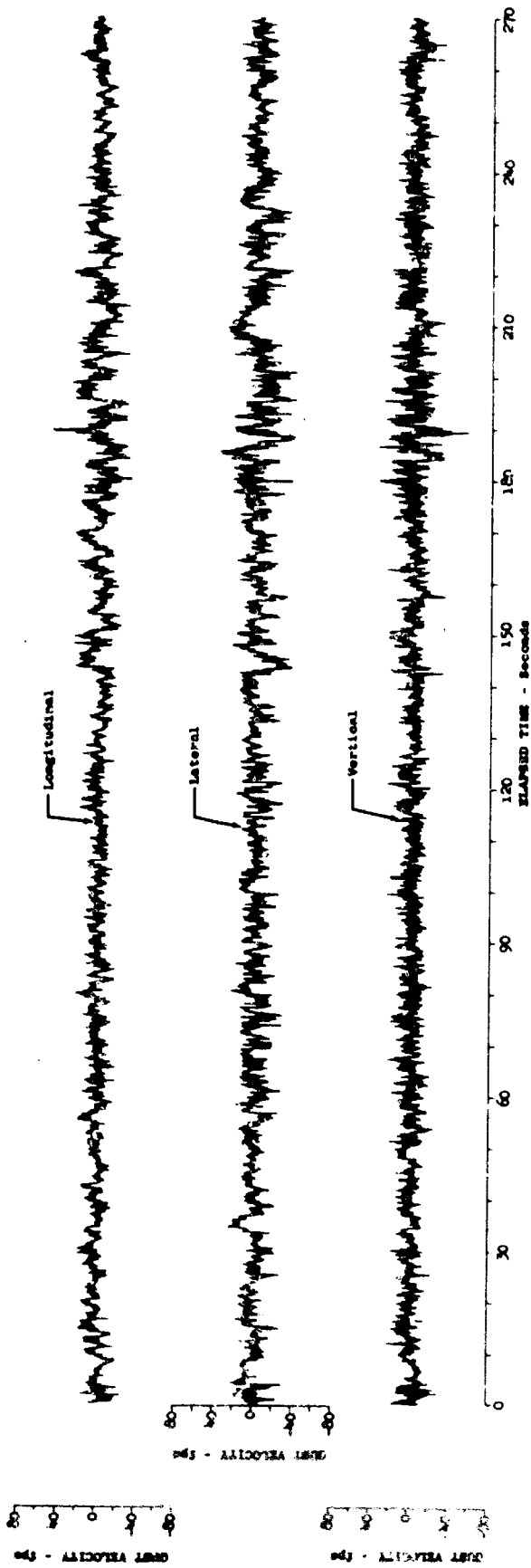


Figure 17.55 Time History of Severe Turbulence Encounter -  
Peterson

Test	189	Ambient Air Temp (°F)	38.5	u max (fps)	37.7
Date	2-24-69	True Airspeed (fps)	621.0	u min (fps)	-41.5
Leg No.	6	Radar Altitude (ft)	No Data	v max (fps)	39.2
Category	113243	$\sigma_{tu}$ (fps)	9.61	v min (fps)	-58.5
Wind Direction (deg)	260.6	$\sigma_{tv}$ (fps)	12.74	w max (fps)	47.5
Wind Velocity (fps)	77.0	$\sigma_{tw}$ (fps)	9.07	w min (fps)	-42.8

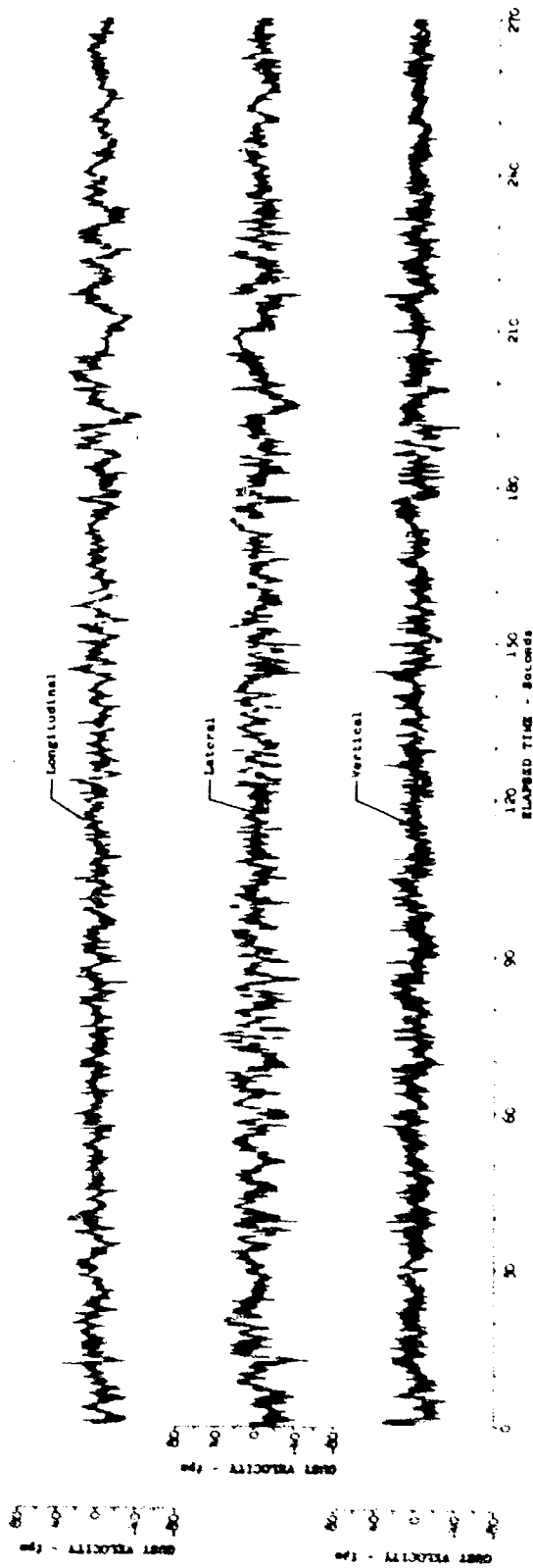


Figure 17.56 T18 - History of Severe Turbulence Encounter - Peterson

Test	190	Ambient Air Temp (°F)	42.1	u max (fps)	59.6
Date	2-24-69	True Airspeed (fps)	618.6	u min (fps)	-46.8
Leg No.	6	Radar Altitude (ft)	551	v max (fps)	52.8
Category	112343	$\sigma_{tu}$ (fps)	10.04	v min (fps)	-65.5
Wind Direction (deg)	263.0	$\sigma_{tv}$ (fps)	13.94	w max (fps)	43.9
Wind Velocity (fps)	66.7	$\sigma_{tw}$ (fps)	9.85	w min (fps)	-63.5

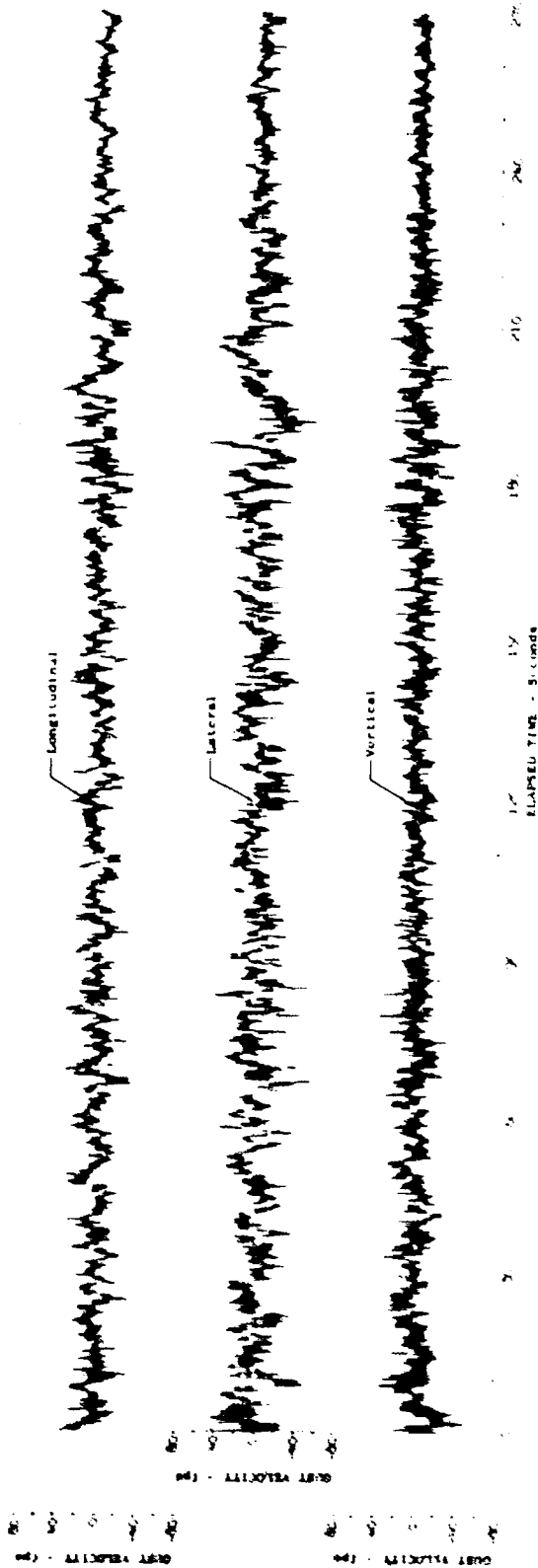


Figure 17.57 Time History of Severe Turbulence Encounter - Peterson

Test	195	Ambient Air Temp (°F)	43.0	u max (fps)	29.9
Date	2-26-69	True Airspeed (fps)	628.3	u min (fps)	-33.5
Leg No.	6	Radar Altitude (ft)	342	v max (fps)	43.8
Category	112243	$\sigma$ tu (fps)	8.97	v min (fps)	-54.0
Wind Direction (deg)	No Data	$\sigma$ tv (fps)	10.35	w max (fps)	38.0
Wind Velocity (fps)	No Data	$\sigma$ tw (fps)	7.80	w min (fps)	-40.8

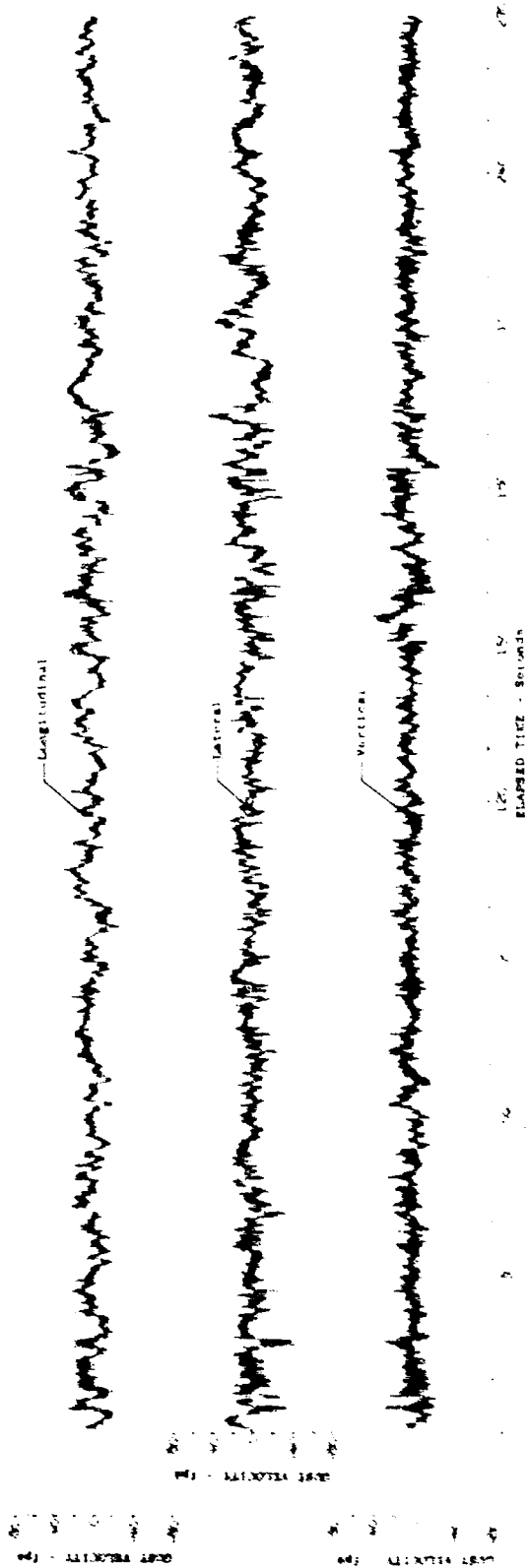


Figure 17.58 Time History of Severe Turbulence Encounter - Peterson

Test	211	Ambient Air Temp (°F)	40.2	u max (fps)	47.4
Date	3-19-69	True Airspeed (fps)	622.6	u min (fps)	-43.8
Leg No.	6	Radar Altitude (ft)	394	v max (fps)	60.1
Category No.	112143	$\sigma_{tu}$ (fps)	10.24	v min (fps)	-72.2
Wind Direction (deg)	246.6	$\sigma_{tv}$ (fps)	13.89	w max (fps)	59.6
Wind Velocity (fps)	75.6	$\sigma_{tw}$ (fps)	10.08	w min (fps)	-51.8

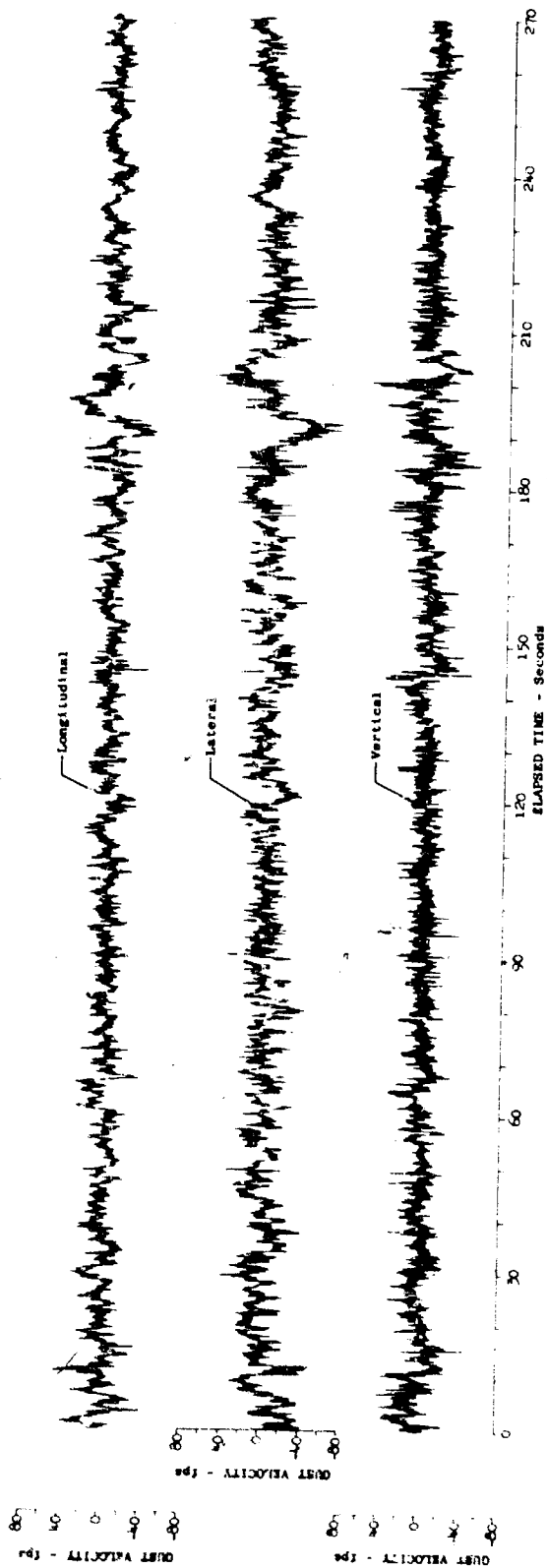


Figure 17.59 Time History of Severe Turbulence Encounter - Peterson

Test	212	Ambient Air Temp (°F)	40.2	u max (fps)	42.9
Date	3-19-69	True Airspeed (fps)	622.6	u min (fps)	-54.3
Leg No.	6	Radar Altitude (ft)	No Data	v max (fps)	45.1
Category No.	114243	$\sigma$ tu (fps)	11.49	v min (fps)	-53.8
Wind Direction (deg)	253.5	$\sigma$ tv (fps)	11.63	w max (fps)	54.2
Wind Velocity (fps)	73.2	$\sigma$ tw (fps)	8.84	w min (fps)	-53.8

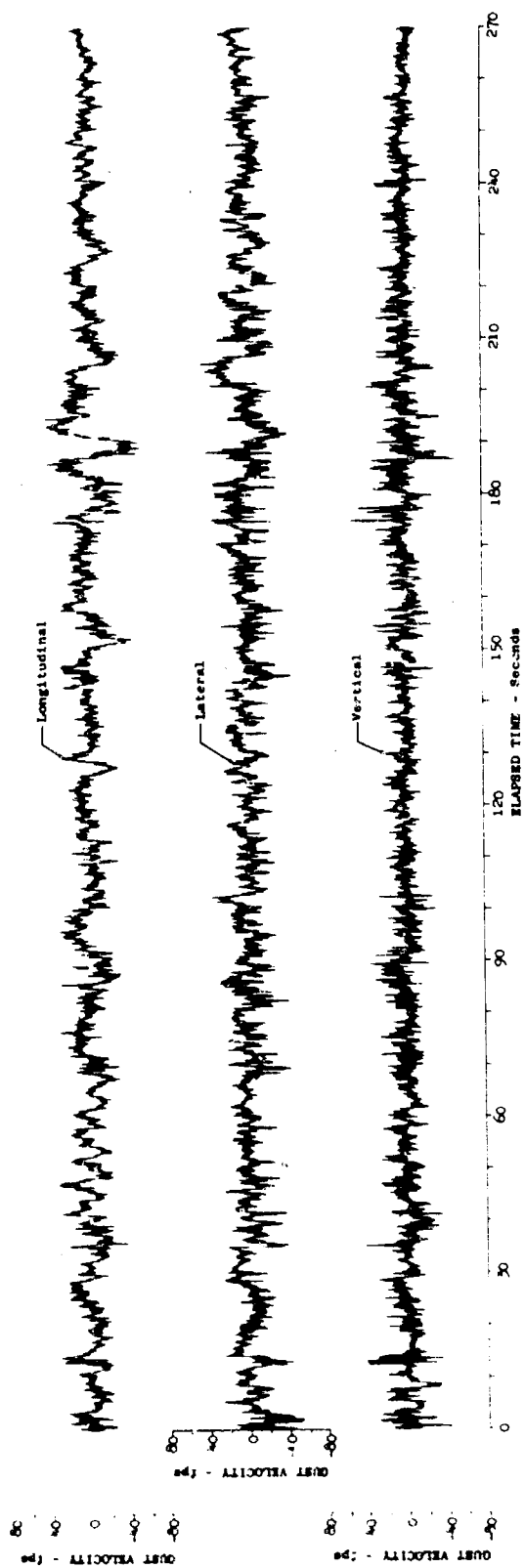


Figure 17.60 Time History of Severe Turbulence Encounter - Peterson

Test	233	Ambient Air Temp (°F)	52.9	u max (fps)	27.3
Date	4-1-69	True Airspeed (fps)	666.6	u min (fps)	-33.4
Leg No.	6	Radar Altitude (ft)	511	v max (fps)	59.1
Category No.	122213	$\sigma$ tu (fps)	7.33	v min (fps)	-53.9
Wind Direction (deg)	249.6	$\sigma$ tv (fps)	10.05	w max (fps)	46.9
Wind Velocity (fps)	30.5	$\sigma$ tw (fps)	7.48	w min (fps)	-35.5

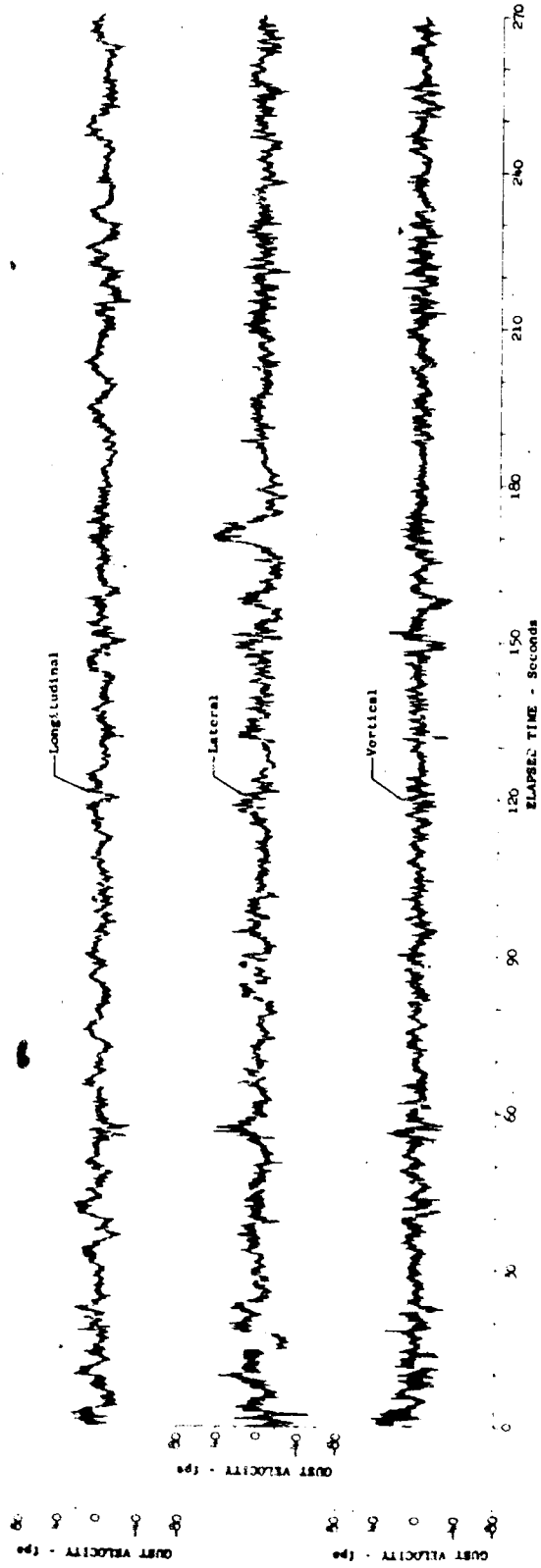


Figure 17.61 Time History of Severe Turbulence Encounter - Peterson

Test	155	Ambient Air Temp (°F)	47.0	u max (fps)	40.8
Date	1-21-69	True Airspeed (fps)	622.5	u min (fps)	-35.4
Leg No.	7	Pedar Altitude (ft)	801	v max (fps)	54.6
Category No.	122243	$\sigma_{t u}$ (fps)	7.58	v min (fps)	-42.8
Wind Direction (deg)	247.1	$\sigma_{t v}$ (fps)	10.35	w max (fps)	42.0
Wind Velocity (fps)	31.1	$\sigma_{t v}$ (fps)	6.68	w min (fps)	-42.2

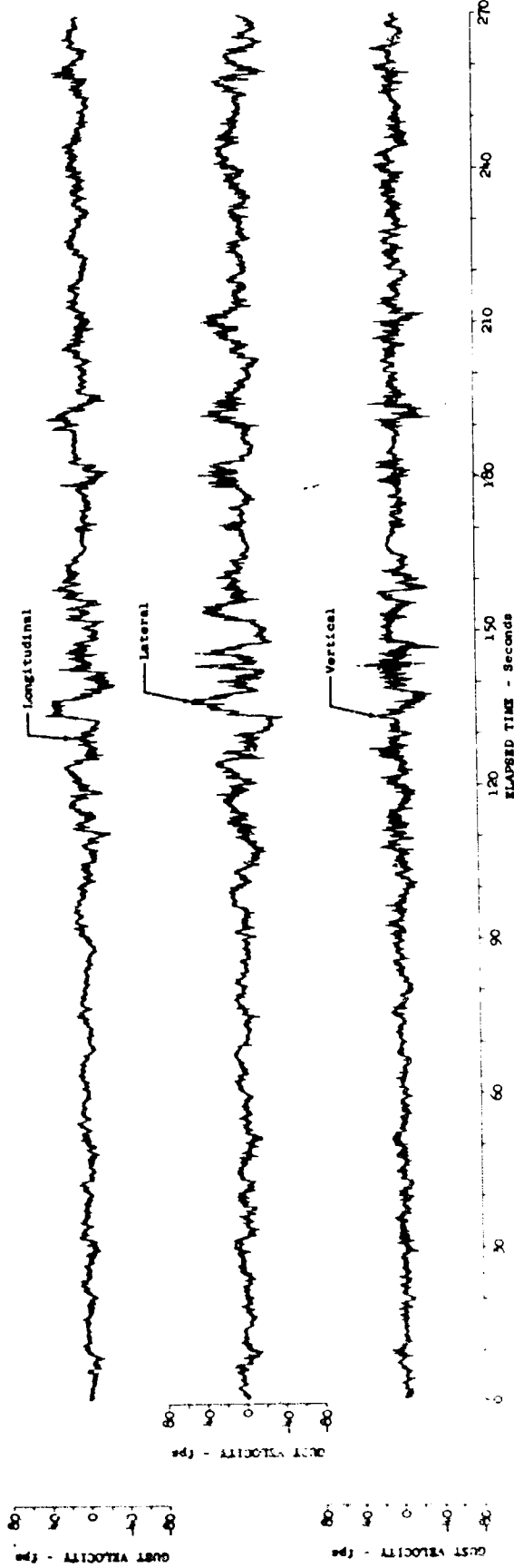


Figure 17.62 Time History of Severe Turbulence Encounter - Peterson



Test	156	Ambient Air Temp (°F)	47.8	u max (fps)	49.7
Date	1-21-69	True Airspeed (fps)	609.3	u min (fps)	-56.9
Log No.	7	Radar Altitude (ft)	708.9	v max (fps)	55.5
Category	124343	$\sigma_{tu}$ (fps)	9.28	v min (fps)	-56.9
Wind Direction (deg)	232.0	$\sigma_{tv}$ (fps)	12.21	w max (fps)	56.0
Wind Velocity (fps)	40.1	$\sigma_{tw}$ (fps)	8.21	w min (fps)	-43.1

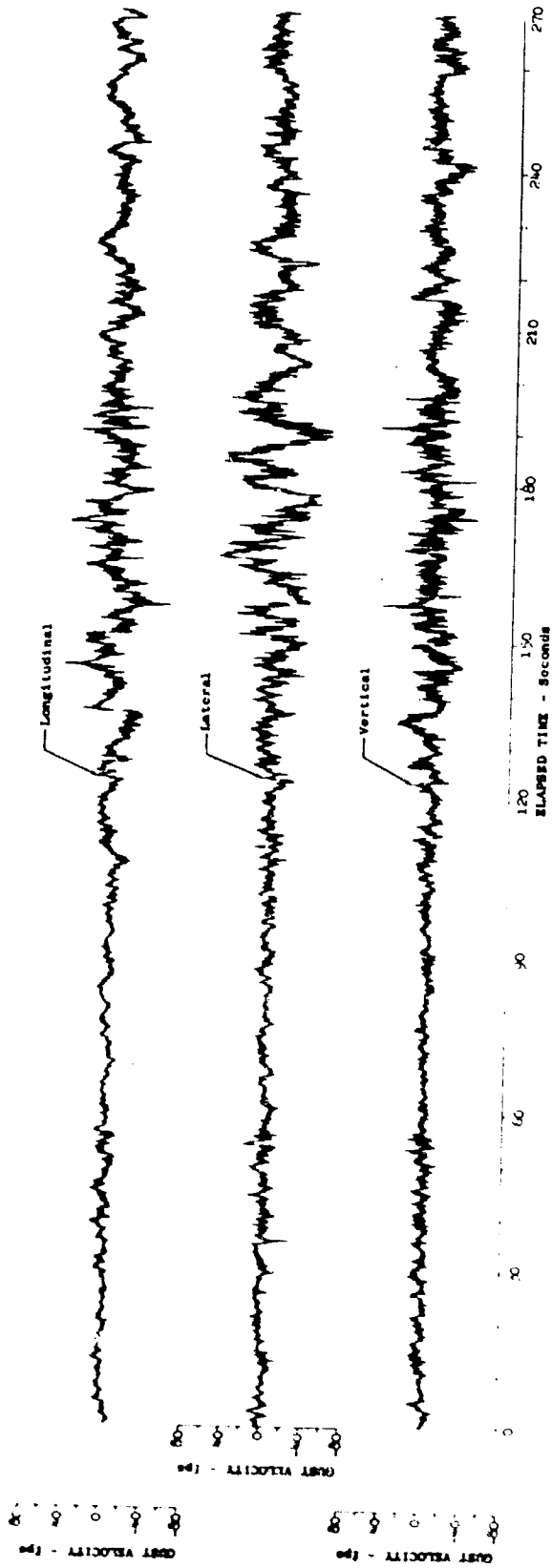


Figure 17.63 Time History of Severe Turbulence Encounter - Peterson

Test	157	Ambient Air Temp (°F)	40.1	$u_{max}$ (fps)	39.8
Date	1-22-69	True Airspeed (fps)	524.4	$u_{min}$ (fps)	-47.2
Leg No.	7	Padar Altitude (ft)	346	$v_{max}$ (fps)	51.0
Category No.	113143	$\sigma_{tu}$ (fps)	7.47	$v_{min}$ (fps)	-63.8
Wind Direction (deg)	251.4	$\sigma_{tv}$ (fps)	10.10	$v_{max}$ (fps)	37.3
Wind Velocity (fps)	42.5	$\sigma_{tv}$ (fps)	6.79	$v_{min}$ (fps)	-41.5

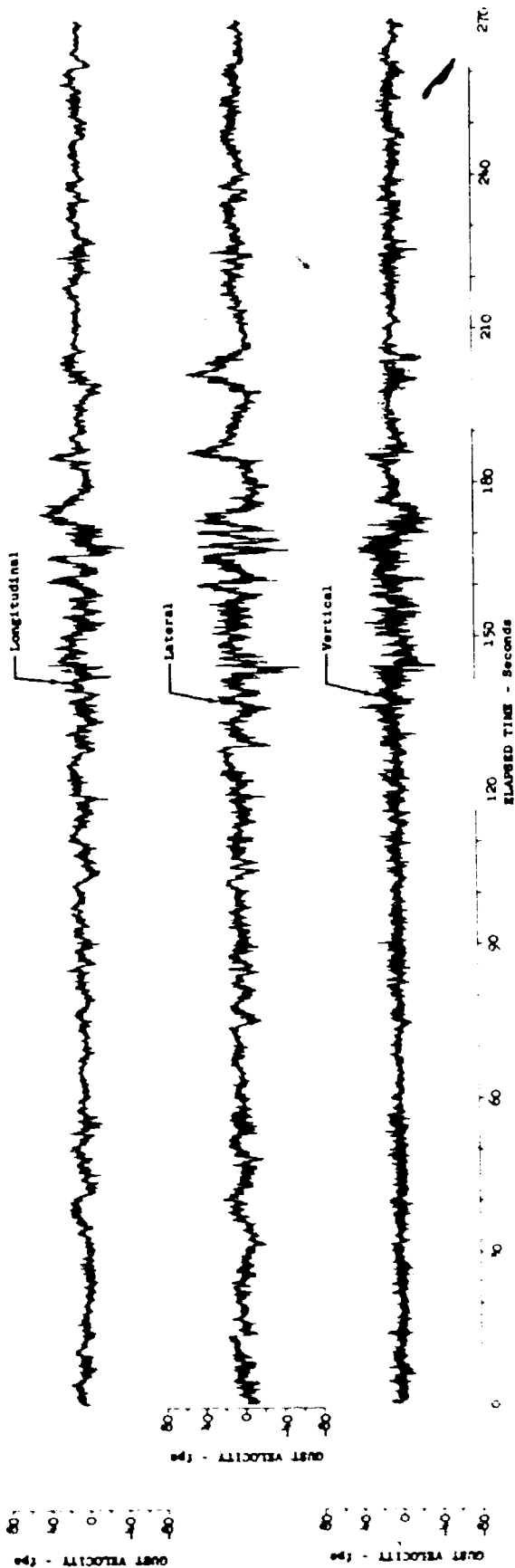


Figure 17.64 Time History of Severe Turbulence Encounter - Peterson

Test	168	Ambient Air Temp (°F)	37.5	$u_{max}$ (fps)	42.5
Date	2-5-69	True Airspeed (fps)	599.4	$u_{min}$ (fps)	-54.6
Leg No.	7	Radial Altitude (ft)	No Data	$v_{max}$ (fps)	54.9
Category No.	123143	$\sigma_{tu}$ (fps)	8.95	$v_{min}$ (fps)	-54.2
Wind Direction (deg)	240.5	$\sigma_{tv}$ (fps)	11.80	$w_{max}$ (fps)	36.1
Wind Velocity (fps)	44.9	$\sigma_{tw}$ (fps)	7.30	$w_{min}$ (fps)	-46.8

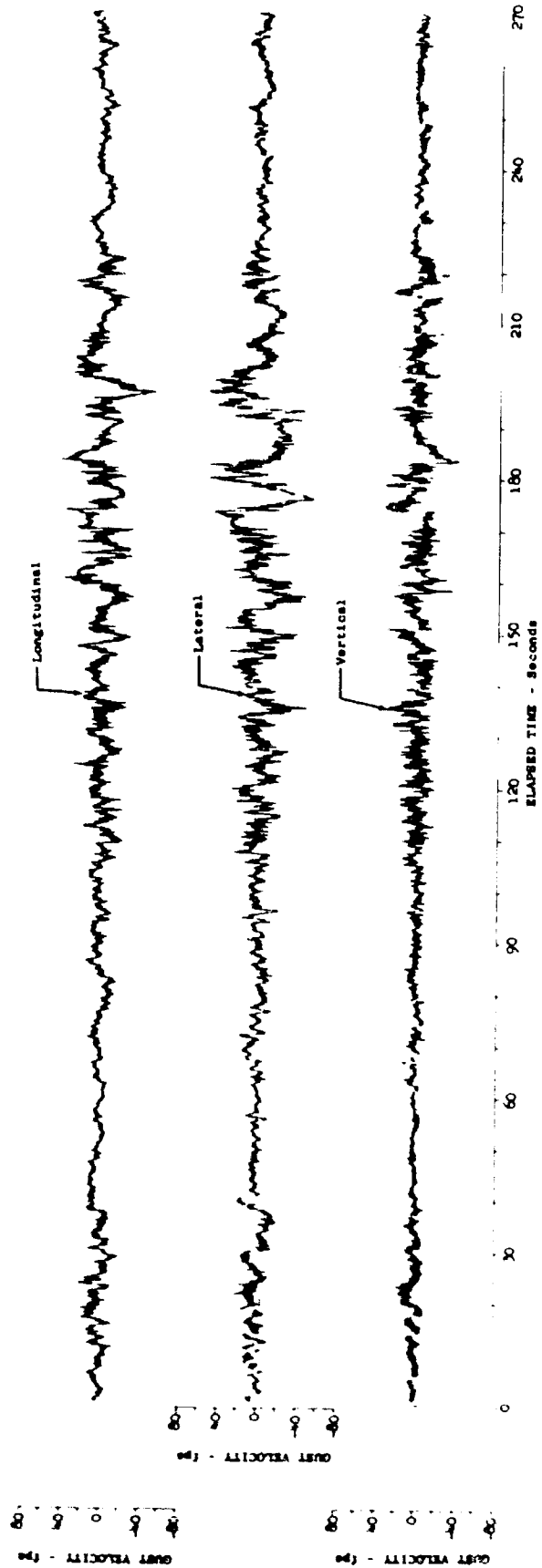


Figure 17.65 Time History of Severe Turbulence Encounter - Peterson

Test	170	Ambient Air Temp (°F)	34.0	u max (fps)	45.7
Date	2-6-69	True Airspeed (fps)	567.4	u min (fps)	-37.5
Leg No.	7	Radar Altitude (ft)	434	v max (fps)	32.5
Category No.	113143	$\sigma_{tu}$ (fps)	7.03	v min (fps)	-54.5
Wind Direction (deg)	250.4	$\sigma_{tv}$ (fps)	8.42	v max (fps)	52.8
Wind Velocity (fps)	72.0	$\sigma_{tw}$ (fps)	7.05	v min (fps)	-47.4

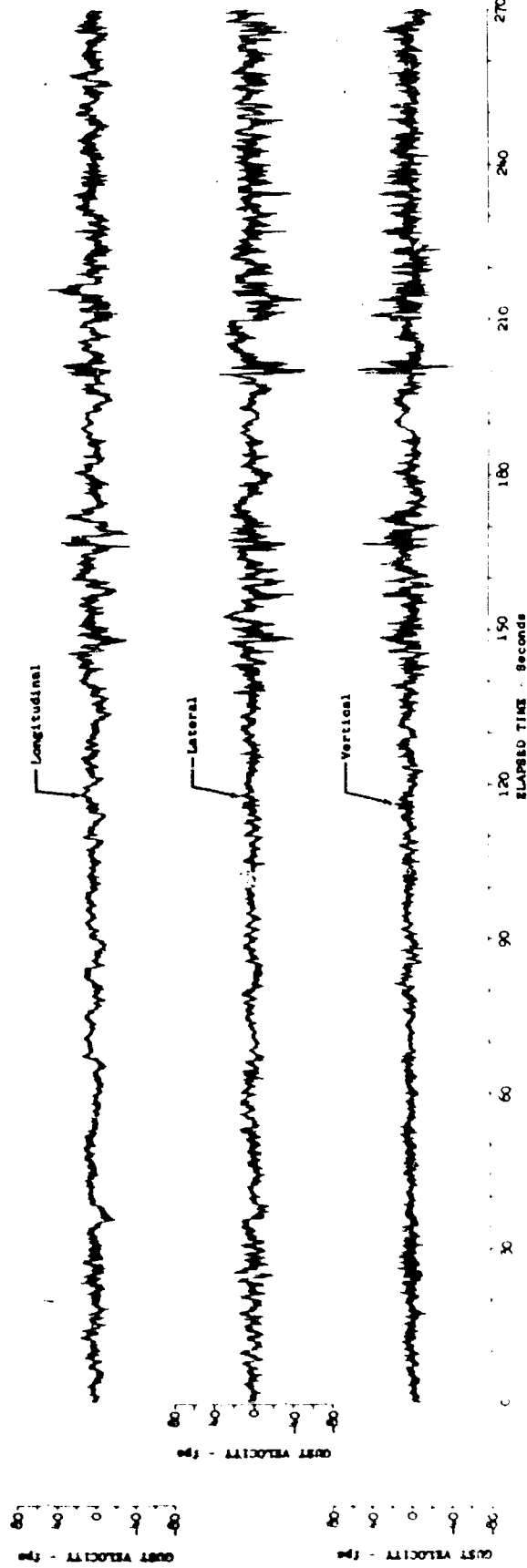


Figure 17.66 Time History of Severe Turbulence Encounter -  
Peterson

Test	171	Ambient Air Temp ( $^{\circ}F$ )	37.1	$u_{max}$ (fps)	34.8
Date	2-6-69	True Airspeed (fps)	583.9	$u_{min}$ (fps)	-40.8
Leg No.	7	Baro Altitude (ft)	422	$v_{max}$ (fps)	33.0
Category No.	113243	$\sigma_{tu}$ (fps)	8.20	$v_{min}$ (fps)	-60.8
Wind Direction (deg)	251.0	$\sigma_{tv}$ (fps)	9.20	$v_{max}$ (fps)	41.3
Wind Velocity (fps)	81.5	$\sigma_{tv}$ (fps)	8.07	$v_{min}$ (fps)	-37.5

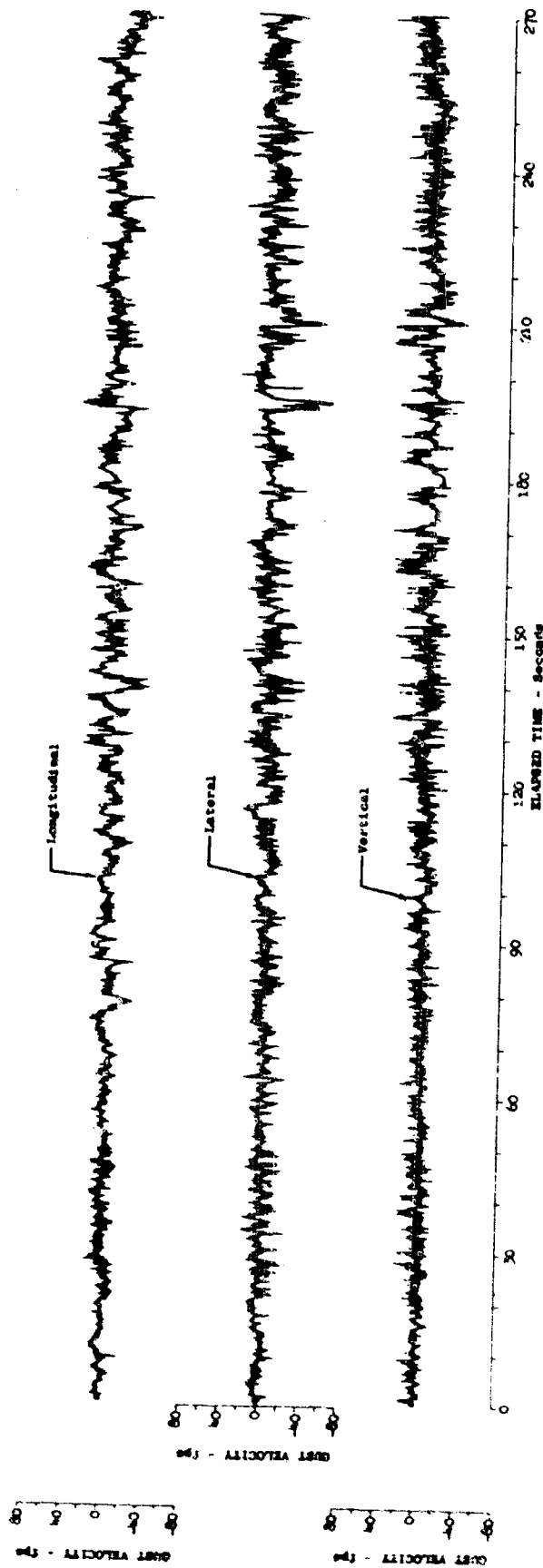


Figure 17.67 Time history of Severe Turbulence Encounter - Peterson

Test	189	Ambient Air Temp (°F)	39.6	u max (fps)	52.6
Date	2-24-69	True Airspeed (fps)	615.2	u min (fps)	-47.8
Log No.	7	Radar Altitude (ft)	No Data	v max (fps)	31.4
Category No.	113243	$\sigma_{tu}$ (fps)	8.21	v min (fps)	-69.2
Wind Direction (deg)	247.3	$\sigma_{tv}$ (fps)	9.12	w max (fps)	38.2
Wind Velocity (fps)	68.1	$\sigma_{tw}$ (fps)	7.48	w min (fps)	-46.4

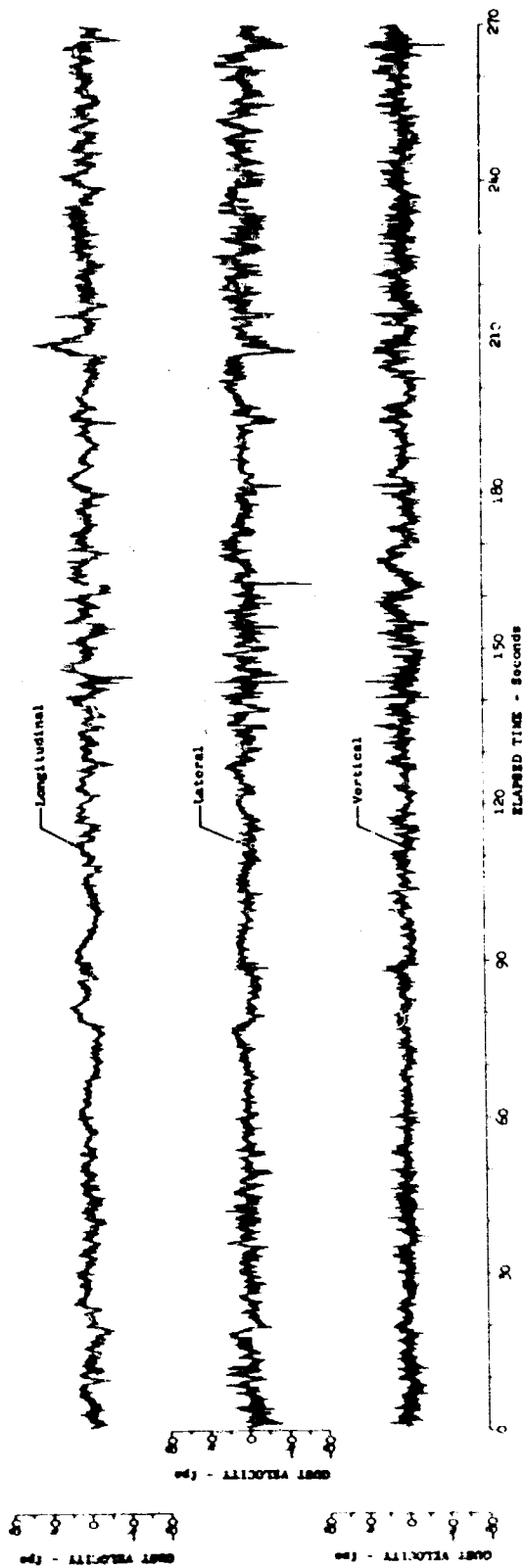


Figure 17.68 Time History of Severe Turbulence Encounter -  
Peterson

Test	190	Ambient Air Temp ( $^{\circ}$ F)	44.5	u max (fps)	32.5
Date	2-24-69	True Airspeed (fps)	607.8	u min (fps)	-31.8
Log No.	7	Radar Altitude (ft)	373	v max (fps)	30.6
Category No.	114343	$\sigma$ tu (fps)	8.17	v min (fps)	-50.1
Wind Direction (deg)	240.2	$\sigma$ tv (fps)	9.19	w max (fps)	43.6
Wind Velocity (fps)	50.2	$\sigma$ tw (fps)	7.18	w min (fps)	-32.6

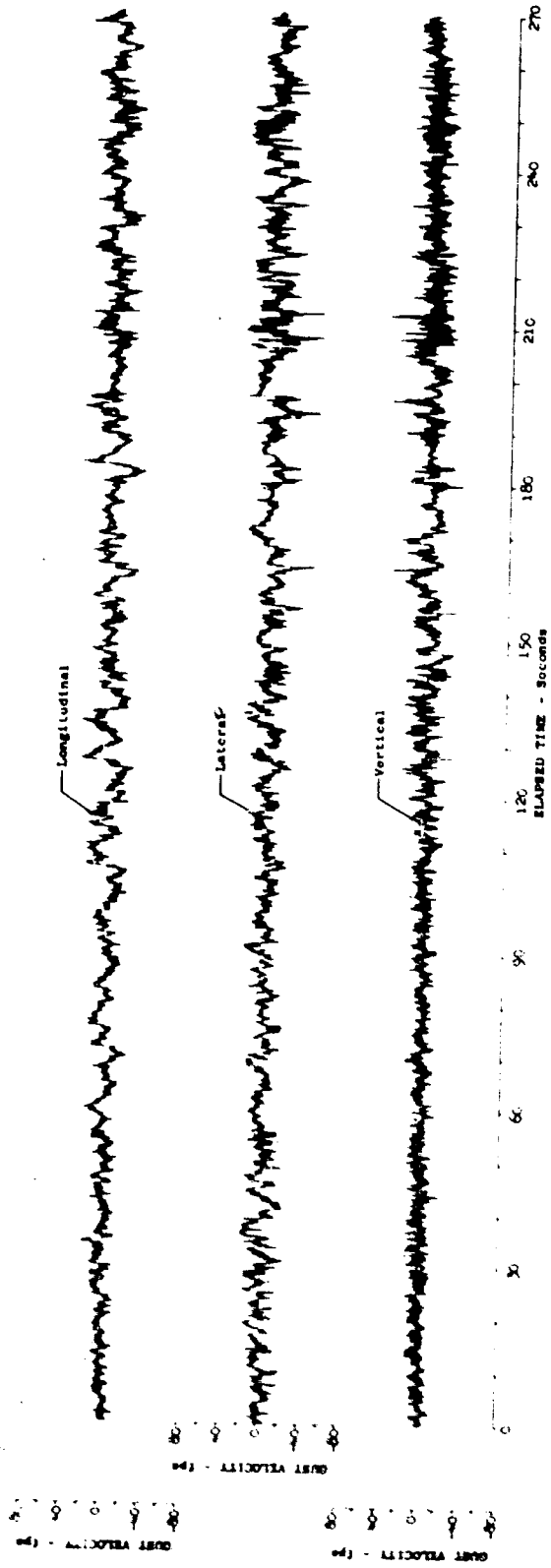


Figure 17.69 Time History of Severe Turbulence Encounter - Peterson

Test	193	Ambient Air Temp (°F)	50.8	u max (fps)	37.6
Date	2-25-69	True Airspeed (fps)	609.0	u min (fps)	-44.0
Leg No.	7	Radar Altitude (ft)	522	v max (fps)	50.4
Category	124343	$\sigma$ tu (fps)	8.36	v min (fps)	-54.6
Wind Direction (deg)	236.8	$\sigma$ tv (fps)	11.87	w max (fps)	39.4
Wind Velocity (fps)	57.8	$\sigma$ tw (fps)	8.13	w min (fps)	-48.6

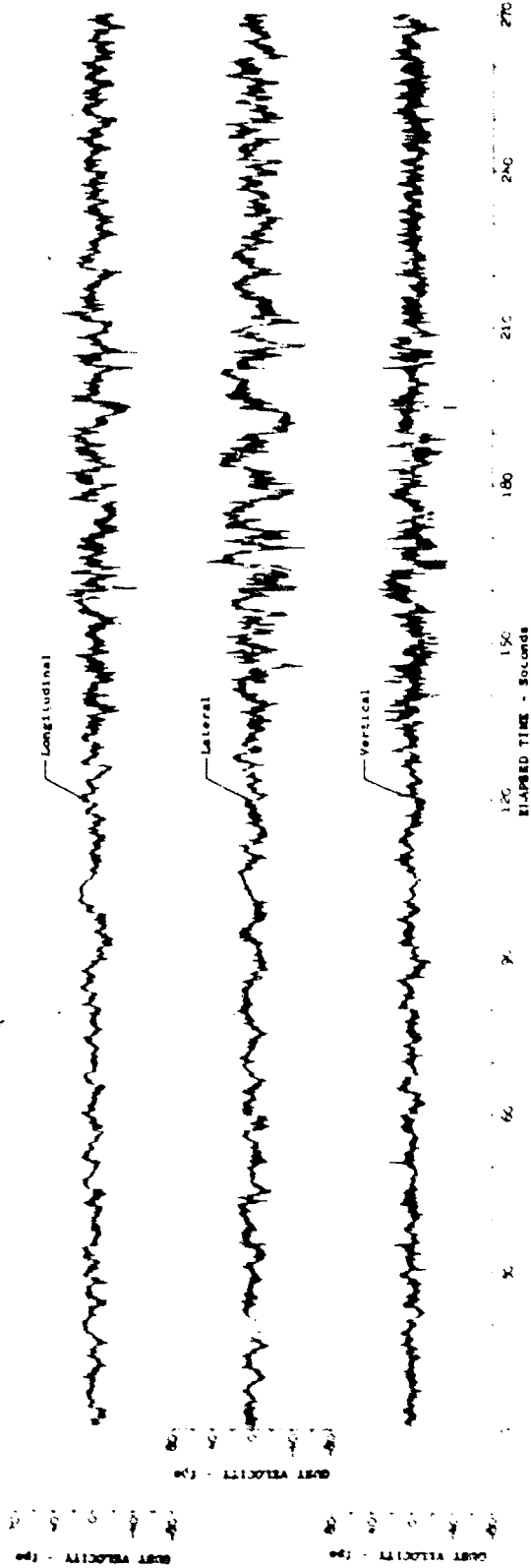


Figure 17.70 Time History of Severe Turbulence Encounter - Peterson



Test	212	Ambient Air Temp (°F)	39.4	u max (fps)	37.1
Date	3-19-69	True Airspeed (fps)	610.8	u min (fps)	-51.5
Leg No.	7	Radar Altitude (ft)	No Data	v max (fps)	50.3
Category	112243	$\sigma_{tu}$ (fps)	8.73	v min (fps)	-47.5
Wind Direction (deg)	246.9	$\sigma_{tv}$ (fps)	10.42	w max (fps)	60.3
Wind Velocity (fps)	51.8	$\sigma_{tw}$ (fps)	8.05	w min (fps)	-36.4

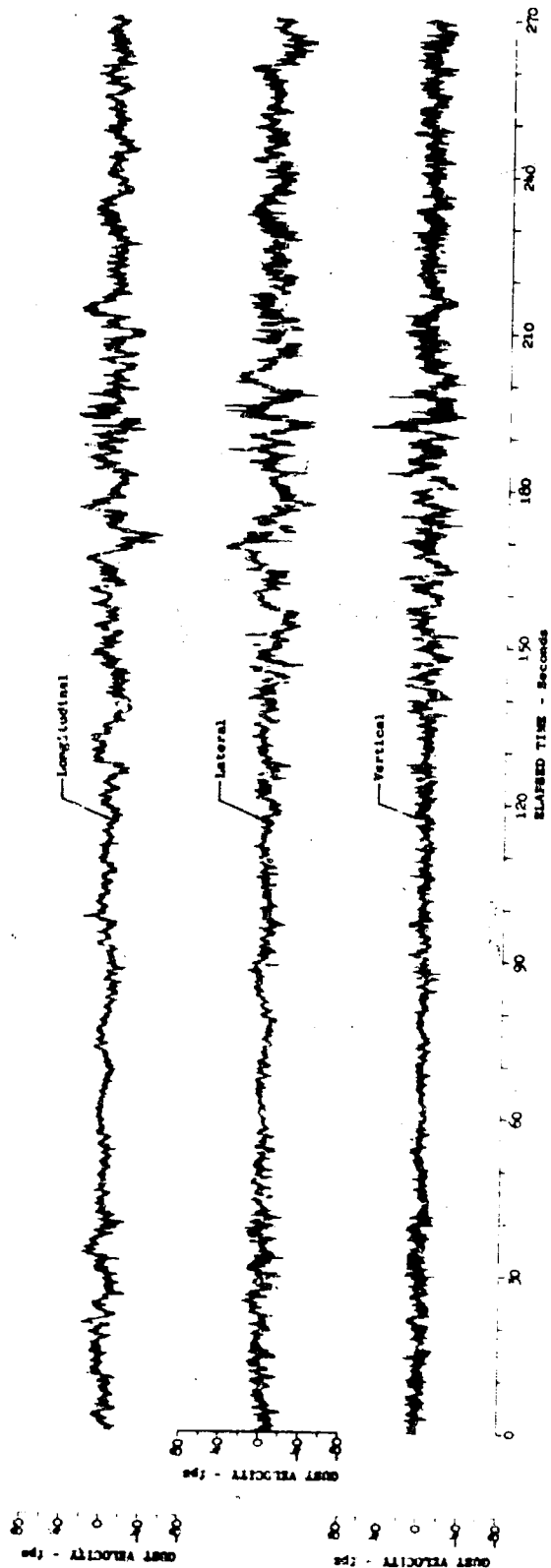


Figure 17.71 Time History of Severe Turbulence Encounter  
Peterson

## 18. GUST VELOCITY MAGNITUDE VERSUS TEMPERATURE CORRELATIONS

Since the advent of high altitude commercial and military flight activity, at least one program (Reference 18.1) has been accomplished to relate turbulence to air temperatures. The objective in determining this relationship was to predict the occurrence of CAT so that evasive action could be implemented. The feasibility of determining a correlation of turbulence with both air and ground surface temperatures was evaluated during the LO-LOCAT Program. Throughout the program, air and surface temperatures were recorded.

The coherency function between indicated OAT and vertical gust velocity and GST and vertical gust velocity was calculated as shown by Equation 18.1. This function indicates the degree of statistical correlation between two variables. A value of 1.0 would indicate perfect correlation and a value of zero would indicate no correlation.

$$\gamma_{xy}^2(k) = \frac{[\Phi_{xy}(k)]^2}{\Phi_x(k) \Phi_y(k)} \quad (18.1)$$

Four turbulence samples, one in each stability class recorded at 250 feet were chosen for this analysis. The coherency function for OAT and GST with respect to the vertical gust velocity component is shown in Figures 18.1 through 18.4. The degree of correlation is very low for GST and only slightly higher for OAT at frequencies between  $10^{-4}$  and  $10^{-3}$  cpf.

It is concluded that OAT and GST values recorded during this program are not correlated with gust velocity rms values. This may have been due to certain limitations in this data. Poor frequency response characteristics of the transducers would adversely effect any correlation of temperature with gust velocity.

The frequency input to the radiometer used to measure ground surface temperature could be altered by the speed of the airplane when flying above a terrain whose features vary significantly. If the radiometer has relatively slow response characteristics, the speed can have considerable effect on surface temperature measurements. Figure 18.5 shows the change of the PSD slope of GST with respect to ground speed for several data samples recorded over various "plains like" terrain segments. The slopes shown in this figure were obtained over that portion of the PSD frequency range where the power spectra decreased in an approximate logarithmic fashion. This terrain type was chosen because of the sharp contrasts in surface features which gave temperature changes. This figure shows that as the ground speed increases, the slope of the ground surface temperature PSD also increases. This indicates a frequency response problem since increasing speed and hence increasing frequency increases the amount of attenuation of the higher frequencies.

The PSD of indicated ambient air temperature out to 0.0065 cpf in Figure 18.6 shows that the response is near a  $-5/3$  logarithmic slope, which is what would be expected (Reference 18.2). The low frequency true airspeed

variations are evident in the higher power deviations above the  $-5/3$  slope since this parameter has the temperature effects due to ram rise included. Because of these variations due to airspeed, it is probable that true ambient temperature could provide a more meaningful correlation with gust velocity.

Standard deviations of ground surface temperature (GST) and vertical gust velocity for the plains leg at Peterson Field are compared in Figure 18.7. This figure indicates that there is no direct relationship between the standard deviations. It does show the increase in gust velocity rms with decreasing stability noted throughout the analysis of LO-LOCAT data. A similar comparison of OAT standard deviation versus gust velocity rms values showed a greater degree of scatter.

It is apparent that the radiometer and the OAT data should be corrected for frequency response before any valid correlation to gust velocities can be determined.

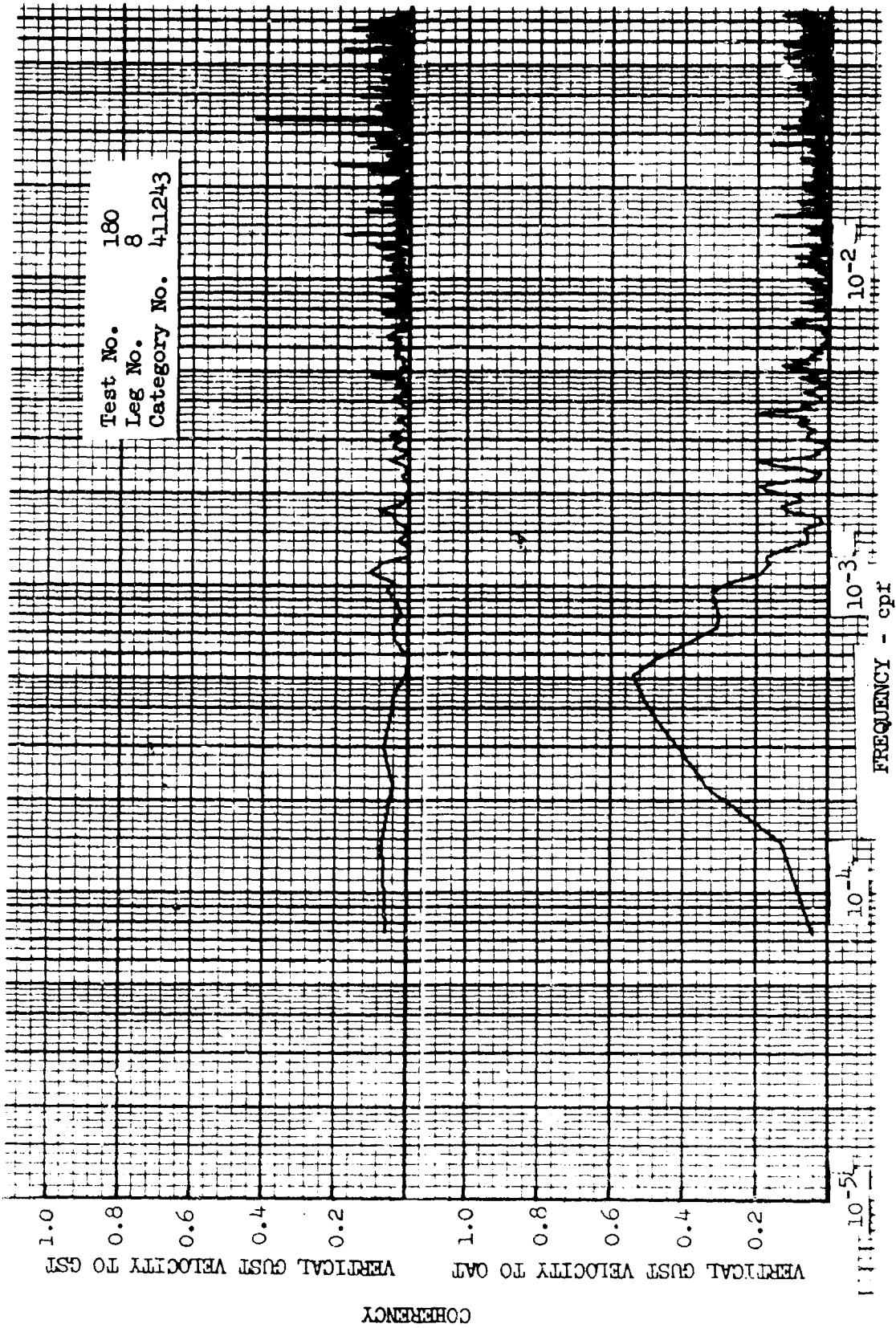


Figure 18.1 Coherency of Vertical Gust Velocity with Outside Air and Ground Surface Temperatures

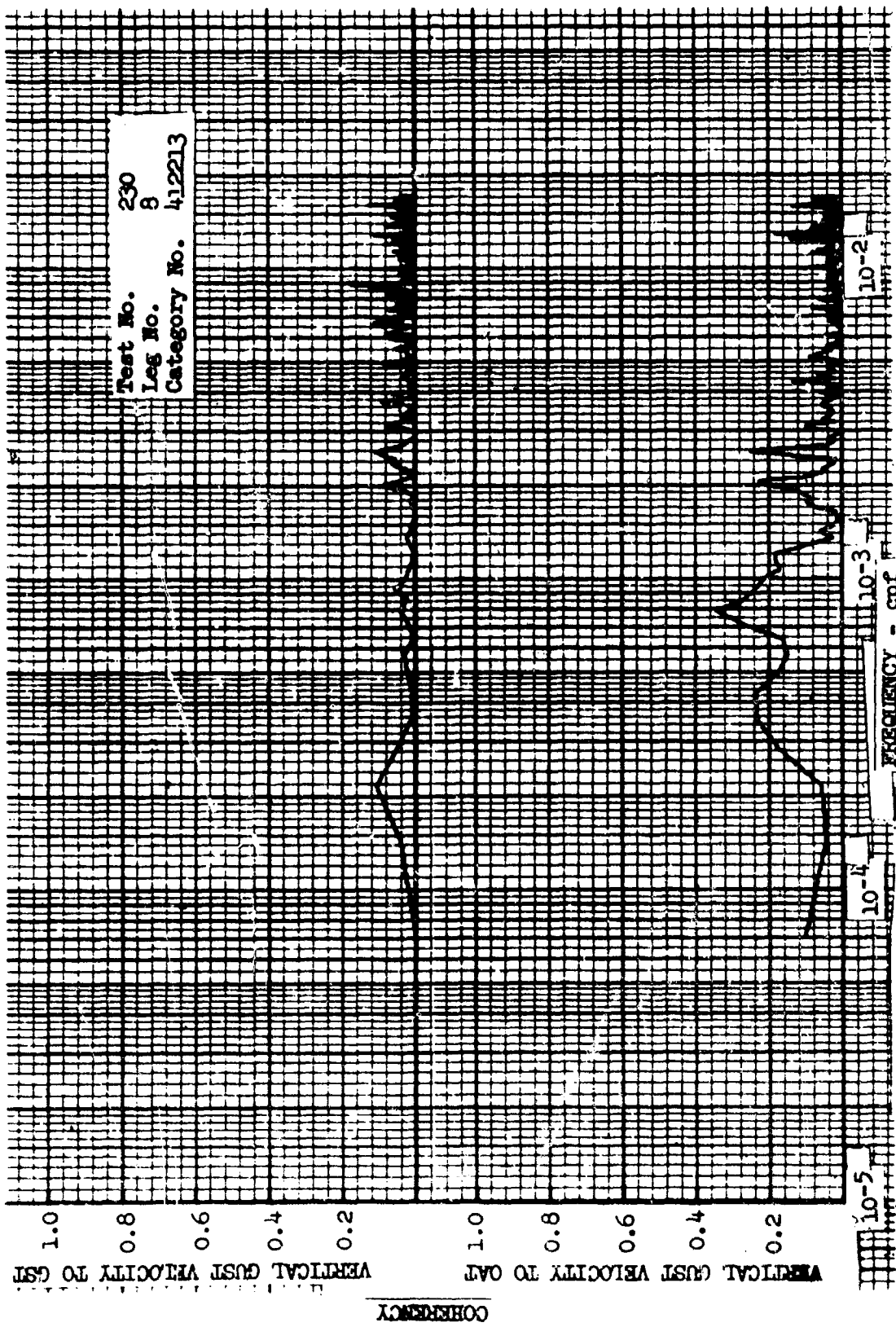


Figure 18.2 Coherency of Vertical Gust Velocity with Outside Air and Ground Surface Temperatures

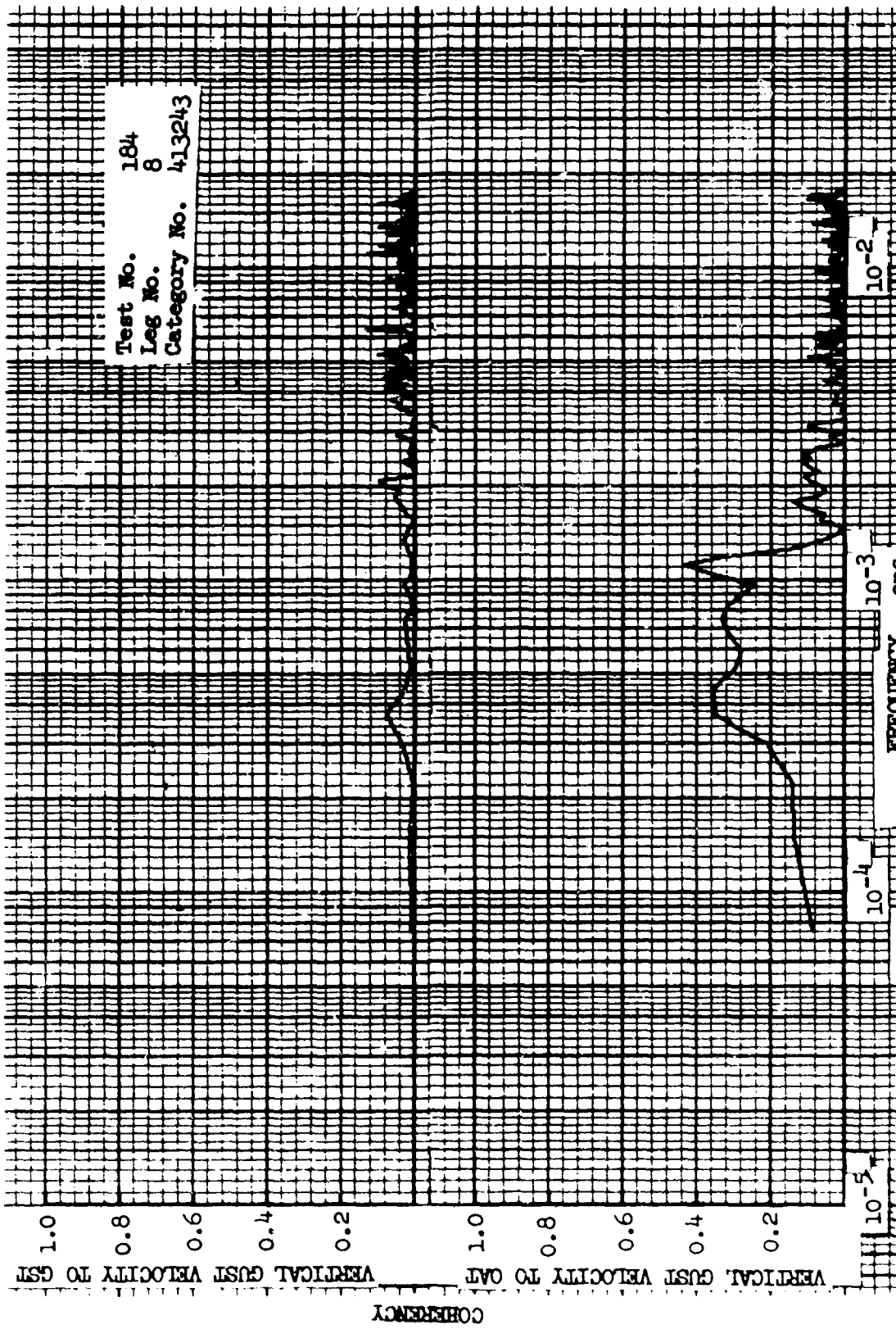


Figure 18.3 Coherency of Vertical Gust Velocity with Outside Air and Ground Surface Temperatures

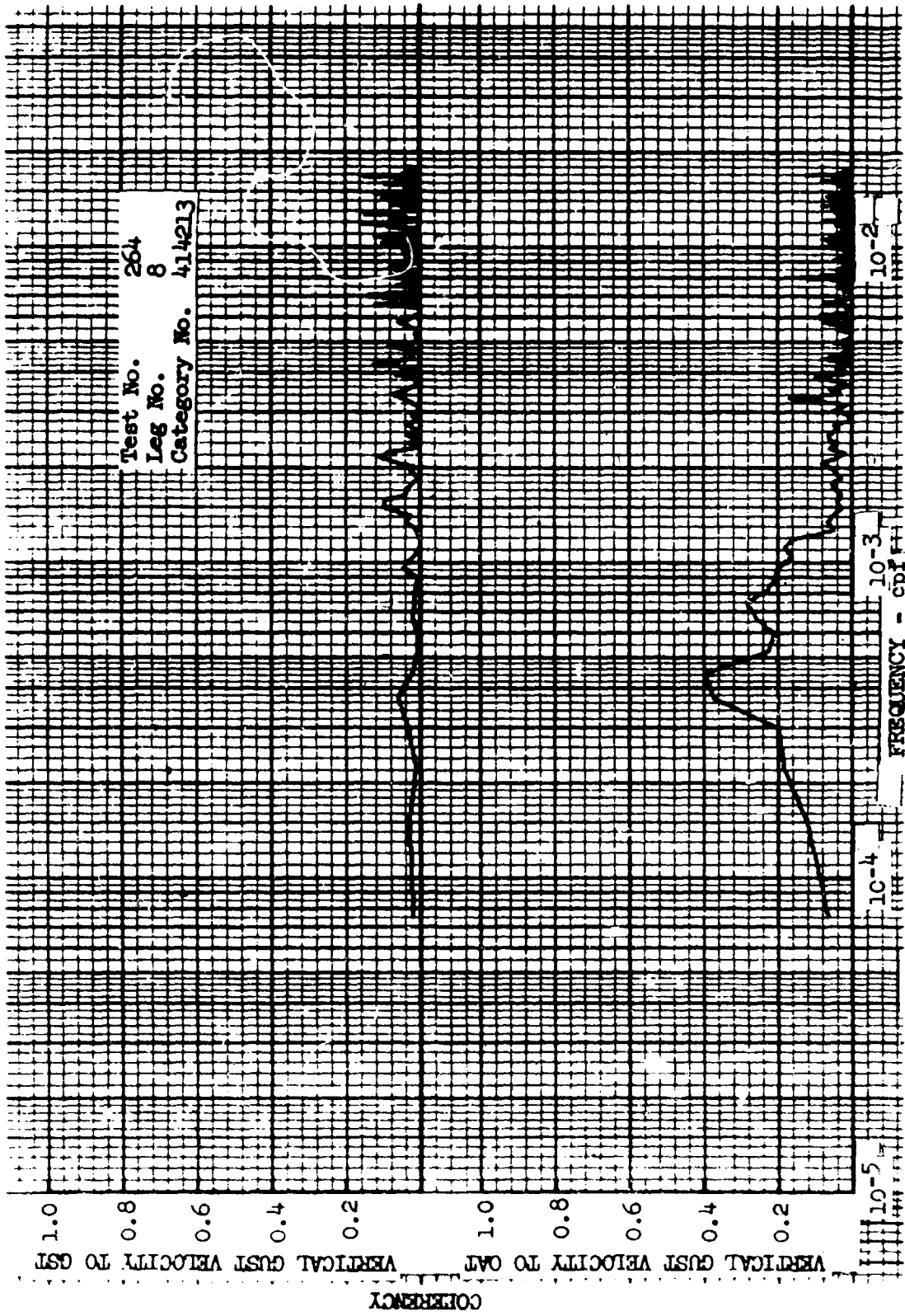


Figure 18.4 Coherency of Vertical Gust Velocity with Outside Air and Ground Surface Temperatures

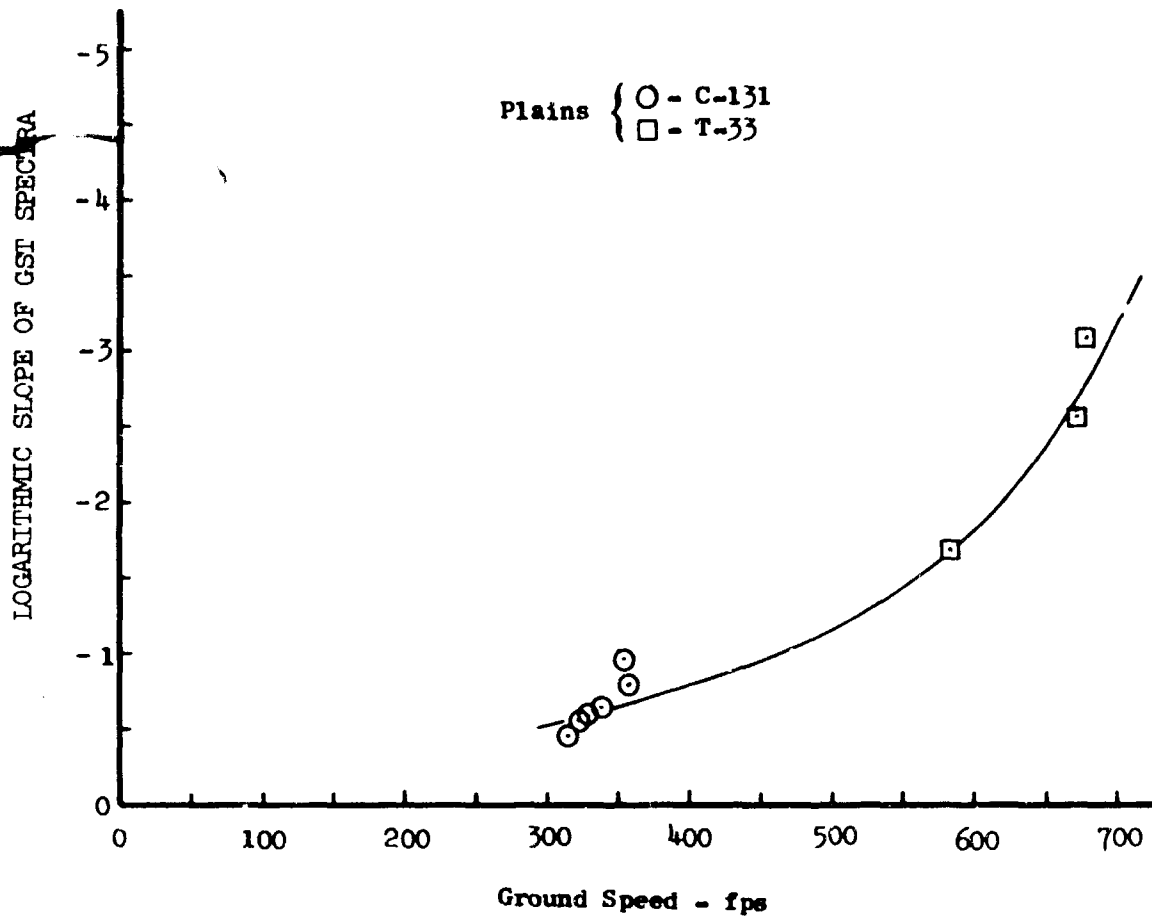


Figure 18.5 Slope of GST Spectra versus Ground Speed



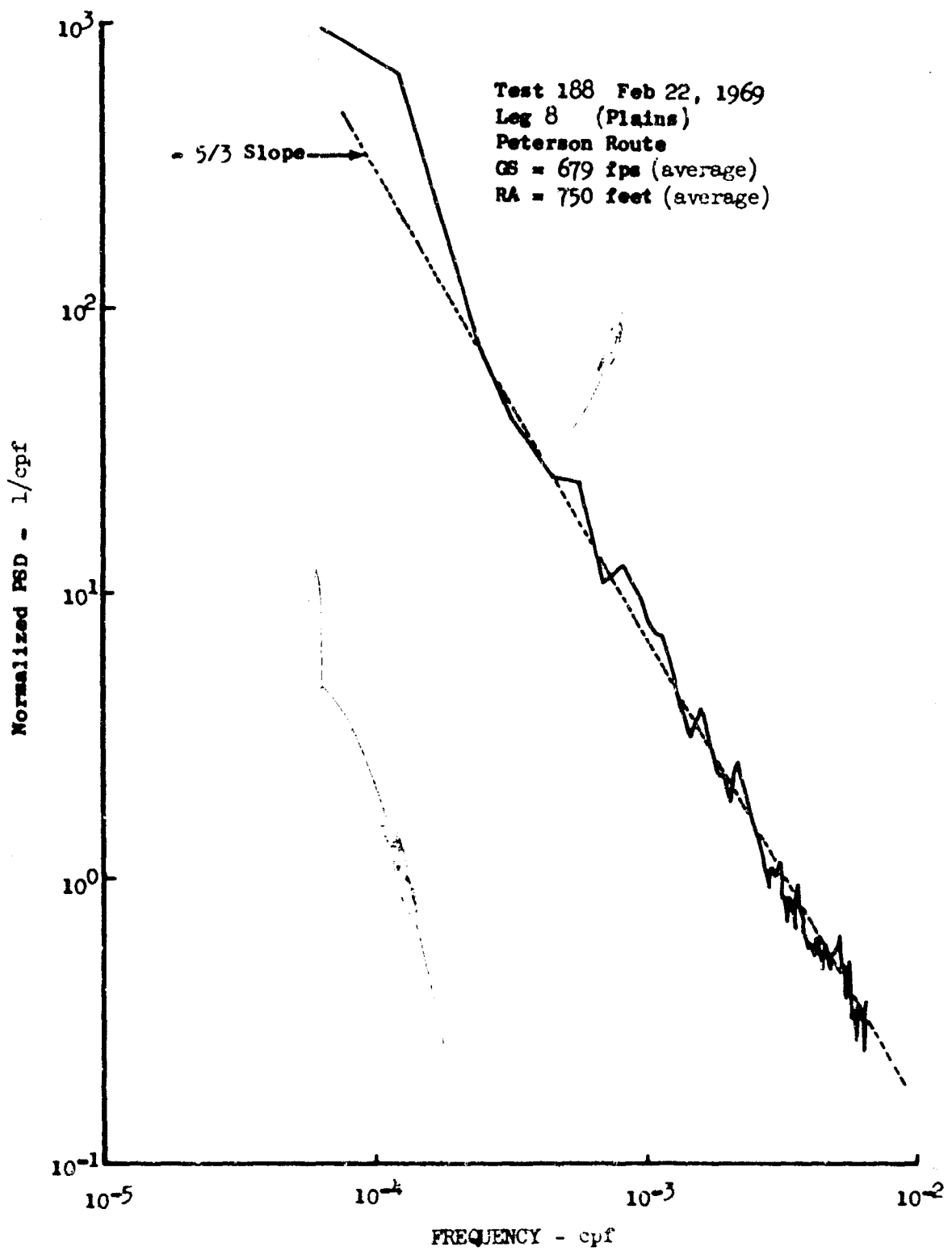


Figure 18.6 Power Spectrum of Total Air Temperature Measurement over Plains Leg

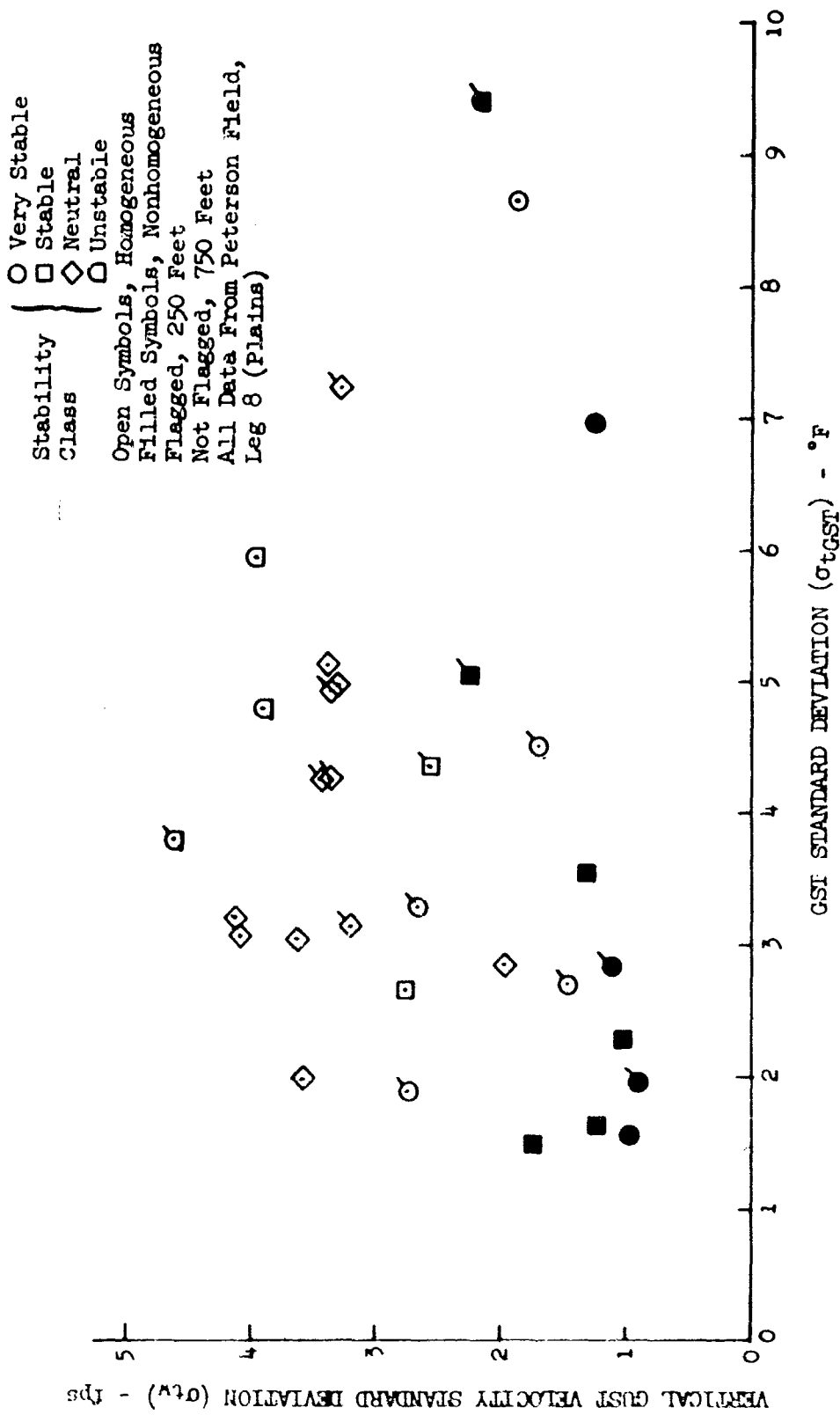


Figure 18.7 Ground Surface Temperature Standard Deviation Versus Gust Velocity Standard Deviation

## SECTION V

### GUST VELOCITY SPECTRA

Power spectra were calculated for 904 of the 1938 total four and one-half minute turbulence samples recorded during this program.

Of the 904 samples, 185 were discarded because the data from all three components exhibited low signal-to-noise ratios, instrumentation anomalies, or high coherency and an additional 98 were discarded because all three components showed non-homogeneity characteristics. This resulted in a total of 621 samples remaining for analysis of the above characteristics for each gust velocity component; 455 of these samples were considered to exhibit valid data for all components and 136, 69, and 41 additional samples were considered valid for the individual longitudinal, lateral, and vertical components, respectively. Thus, broken down into the individual components, the total number of samples considered valid with respect to the longitudinal, lateral, and vertical components were 591, 524, and 496, respectively. These latter numbers of samples were used to obtain normalized spectra, truncated standard deviations, comparison of experimental-mathematical spectra, and average turbulence scale lengths while the 455 number of samples were used in evaluating coherency and isotropy. Power spectral density data for these 455 conditions are presented in Appendix IX.

#### 19. INSTRUMENTATION ANOMALIES, LOW INTENSITY TURBULENCE

An example of power spectra, with suspected instrumentation problems, is presented in Figure 19.1. It is obvious that the spectra are suspect due to the large hump in the lateral spectrum, which occurs at the airplane short period mode. Experience has shown that when spectra such as that shown in Figure 19.1 are obtained, it can ultimately be proven to be caused by instrumentation problems.

An example power spectra plot of low intensity turbulence is presented in Figure 19.2. Turbulence data samples containing low signal-to-noise ratios typically had  $\sigma_v$  values less than 1.4 fps, irregularly shaped spectra (i.e., spectra which do not have a definite  $-5/3$  logarithmic slope and in which the power turns upward at the higher frequencies), and uncommonly large integral scale lengths.

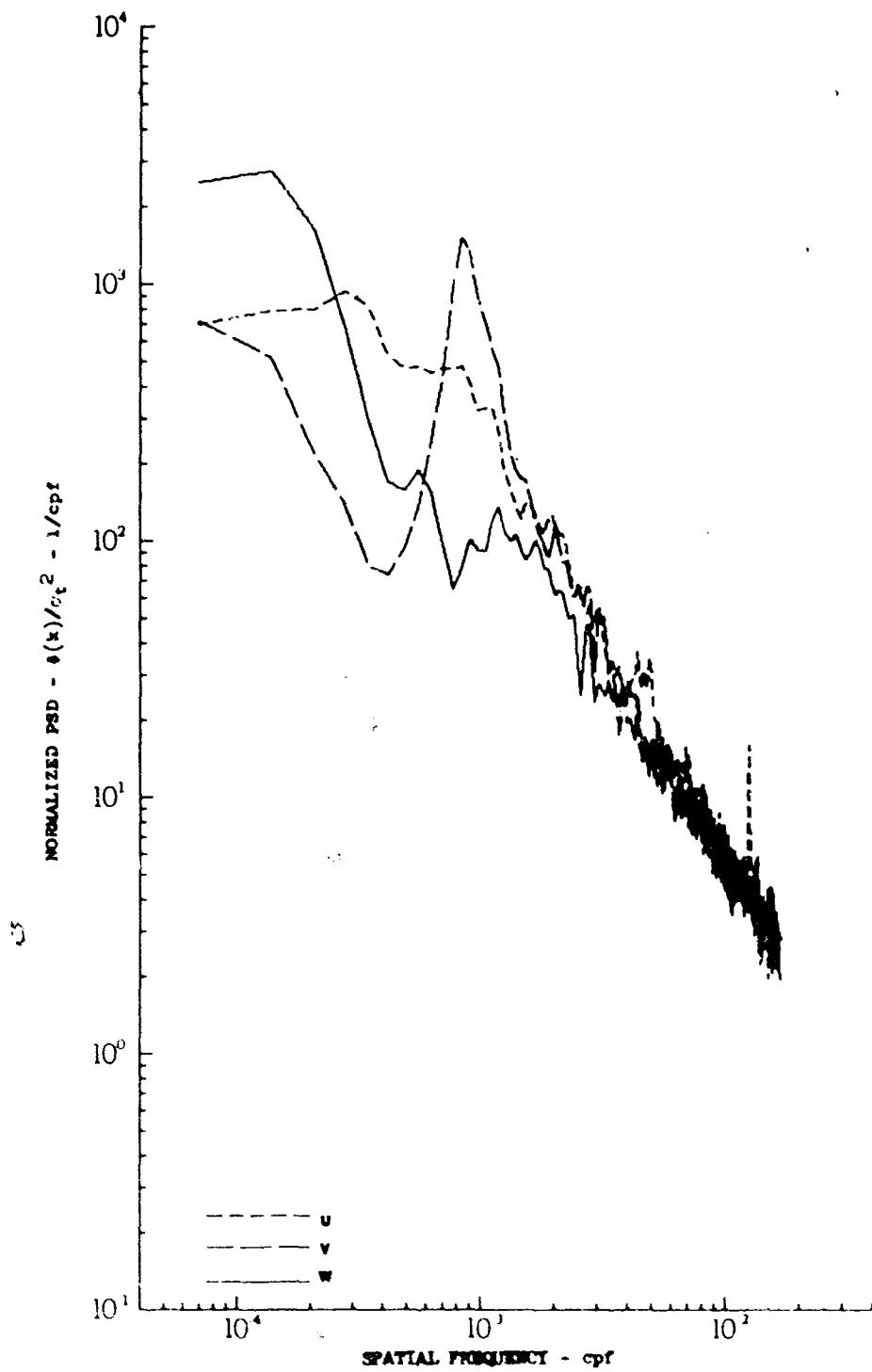


Figure 19.1 Gust Velocity Power Spectra of a Data Sample Containing Instrumentation Irregularities

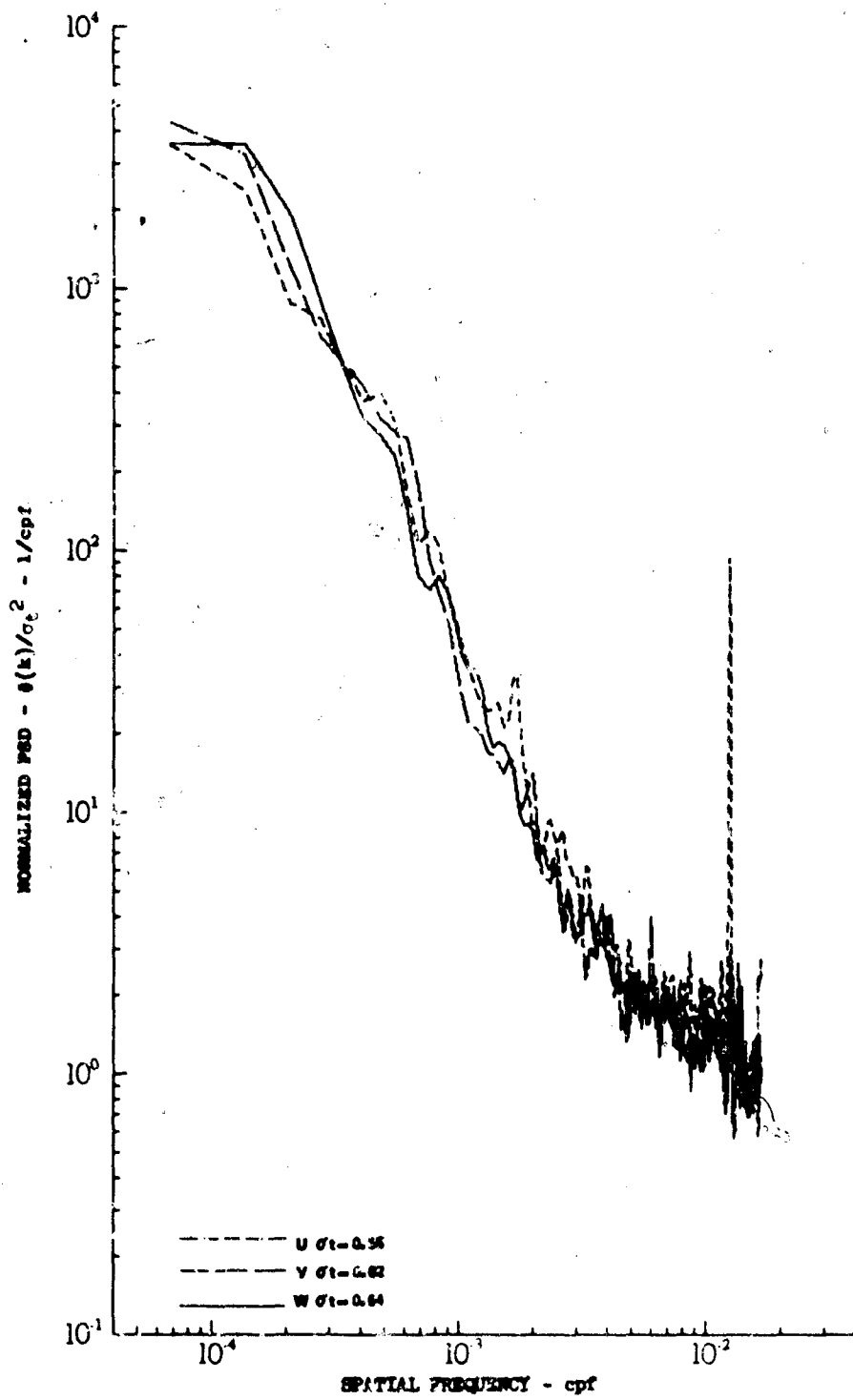


Figure 19.2 Gust Velocity Power Spectra of a Data Sample Having Low Signal-to-Noise Ratio

## 20. STATISTICAL CONFIDENCE AND INDEPENDENCY

### Confidence

Turbulence sample lengths were established to give a compromise between statistical confidence and turbulence stationarity considerations. Aliasing was prevented by the use of a high sampling rate to give a large frequency span between the break-point of the low-pass filter and the Nyquist frequency. Gust velocities were calculated using a sampling rate of 100 sps which results in a Nyquist frequency of 50 cps. PSD's were calculated by averaging adjacent points which resulted in a sampling rate of 50 sps for the PSD calculations. The break-point of low-pass filters used was 22 cps the Nyquist frequency for the PSD calculations was 25 cps.

With negligible aliasing, the stability of uniformly spaced power spectral density estimates may be judged by analogy with a chi-square variate with  $d$  degrees of freedom where:

$$d \approx \frac{2n\Delta f}{f_N} \quad (20.1)$$

With the number of data points  $n = 13,500$ ,  $\Delta f = 0.0416$  cps and  $f_N = 25$  cps, approximately 45 degrees of freedom were obtained for individual samples.

Statistical reliability was also evaluated by defining an interval of confidence on either side of the measured spectrum. The interval indicates the amount of variation that may be expected in the spectrum.

Based on 90 per cent confidence the equivalent degrees of freedom are defined in Reference 20.1 as:

$$k = 1 + \frac{400}{(20 \text{Log}_{10} \Phi_{90})^2} \quad (20.2)$$

and:

$$(10 \text{Log}_{10} \Phi_{90})^2 = \frac{100}{k - 1} \quad (20.3)$$

where:

$$k \approx \frac{2T_n'}{T_n} \quad (20.4)$$

$$\text{and: } T_n' = \text{effective record length} = T_n - \frac{p}{3}(T_m) \quad (20.5)$$

$$T_m = \text{total lag} = m\Delta t \quad (20.6)$$

$$T_n = \text{length of record} = n\Delta t \quad (20.7)$$

$$\Delta t = \text{time between data points} = 0.02 \text{ seconds}$$

$$p = \text{number of data pieces} = 1$$

$$m = \text{number of frequency estimates} = \frac{f_N}{\Delta f} = 601 \quad (20.8)$$

therefore:

$$\begin{aligned} \left(10 \text{Log}_{10} \Phi_{90}\right)^2 &= \frac{100 T_m}{2T_n - \frac{2}{3} p T_m - T_m} \\ &= \frac{100 m \Delta t}{2n\Delta t - \frac{2}{3} p m \Delta t - m \Delta t} = \frac{300 m}{6n - 5m} \end{aligned} \quad (20.9)$$

Converting to natural logs and solving for  $\Phi_{90}$ , the interval of confidence on either side of the measured spectrum is defined as:

$$\Phi_{90} = \exp \left[ \frac{1}{4.343} \left( \frac{300 m}{6n - 5m} \right)^{1/2} \right] \quad (20.10)$$

The 80 per cent confidence is determined in a similar manner except that the equivalent degrees of freedom are defined as:

$$k = 1 + \frac{250}{(20 \text{Log}_{10} \Phi_{80})^2} \quad (20.11)$$

and:

$$\Phi_{80} = \exp \left[ \frac{1}{4.343} \left( \frac{187.5 m}{6n - 5m} \right)^{1/2} \right] \quad (20.12)$$

The 90 and 80 per cent confidence intervals were approximately  $\pm 42$  per cent and  $\pm 32$  per cent, respectively, for the individual data samples.

If it is assumed that the pooling of turbulence samples in a category is equivalent to placing them end to end, then the statistical confidence for averaged spectra is quite high. Degrees of freedom are increased by a factor equal to the number of samples pooled. Confidence bands are reduced as shown in Figure 20.1. This occurs since  $m$  remains the same and  $n$  is increased by a factor equal to the number of samples pooled.

### Independency

The statistical independence of the gust components  $u$ ,  $v$ , and  $w$  was evaluated using the coherency function. The coherency function between  $u$  and  $v$ , and  $v$  and  $w$ , was calculated, e.g.:

$$\gamma_{uv}^2(k) = \frac{[\Phi_{uv}(k)]^2}{\Phi_u(k) \Phi_v(k)} \quad (20.13)$$

Two parameters are said to be completely dependent (coherent) if their coherency function is equal to 1.0 and completely independent (not coherent) if the coherency is equal to zero. Due to statistical variations in the recorded data, electronic noise, etc., a coherency of zero is impossible to achieve. The gust velocity components are therefore considered to be independent if the coherency function approaches zero.

The coherency function was evaluated by category. This was accomplished by comparing average data from different categories. The average coherency function was calculated by determining the value of the coherency function of each sample at spatial frequencies of  $5 \times 10^{-5}$ ,  $7 \times 10^{-5}$ ,  $1 \times 10^{-4}$ ,  $1.5 \times 10^{-4}$ ,  $2 \times 10^{-4}$ ,  $3 \times 10^{-4}$ ,  $4 \times 10^{-4}$ ,  $6 \times 10^{-4}$ ,  $1 \times 10^{-3}$ ,  $1.5 \times 10^{-3}$ ,  $2 \times 10^{-3}$ ,  $4 \times 10^{-3}$ ,  $7 \times 10^{-3}$ ,  $1 \times 10^{-2}$ , and  $1.5 \times 10^{-2}$  cpf. The values obtained at each of these frequencies were then averaged and the standard deviation calculated.

No significant or consistent difference in coherency was associated with different categories. The magnitude of the coherency function was reasonably small indicating statistical independency, especially at the shorter wavelengths. The maximum value of the average was less than 0.15 as can be seen in Figure 20.2. These data represent the average of coherency values for all categories. Statistical independency for individual turbulence samples is shown in Appendix IX.



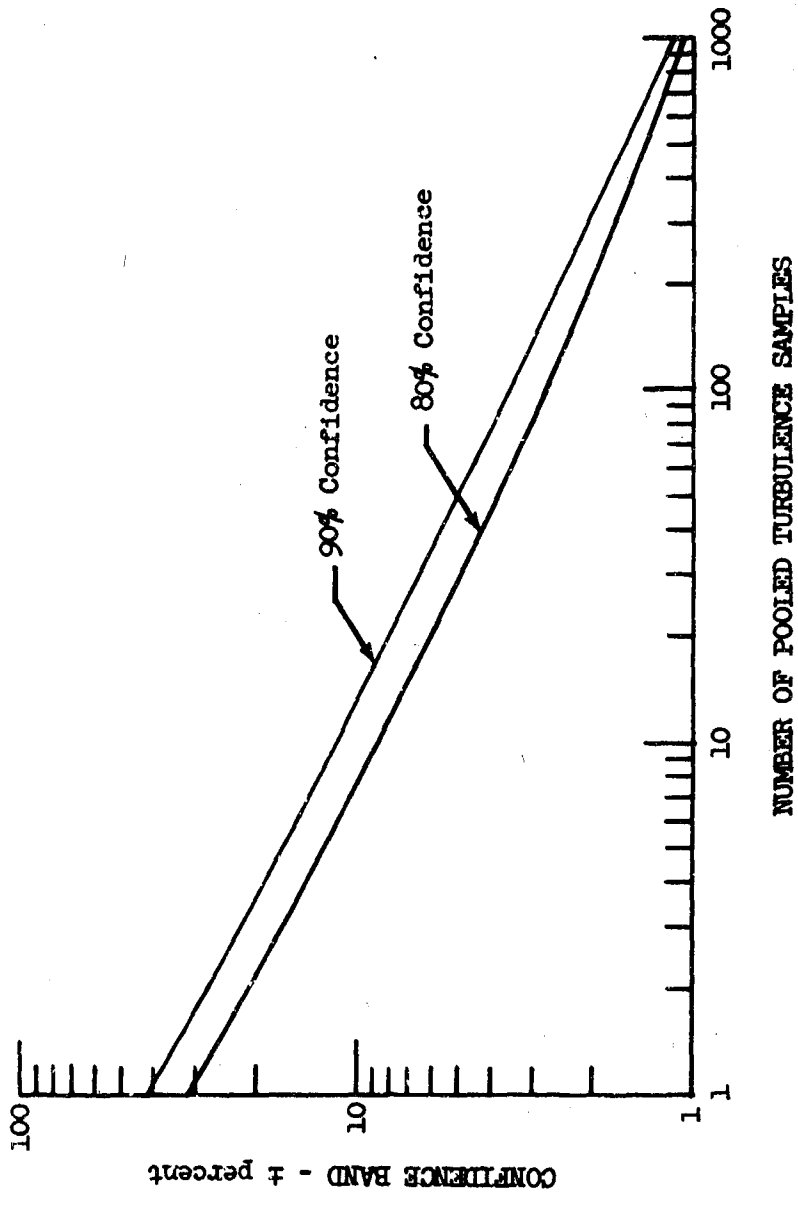


Figure 20.1 Confidence Bands Associated with Pooled Samples

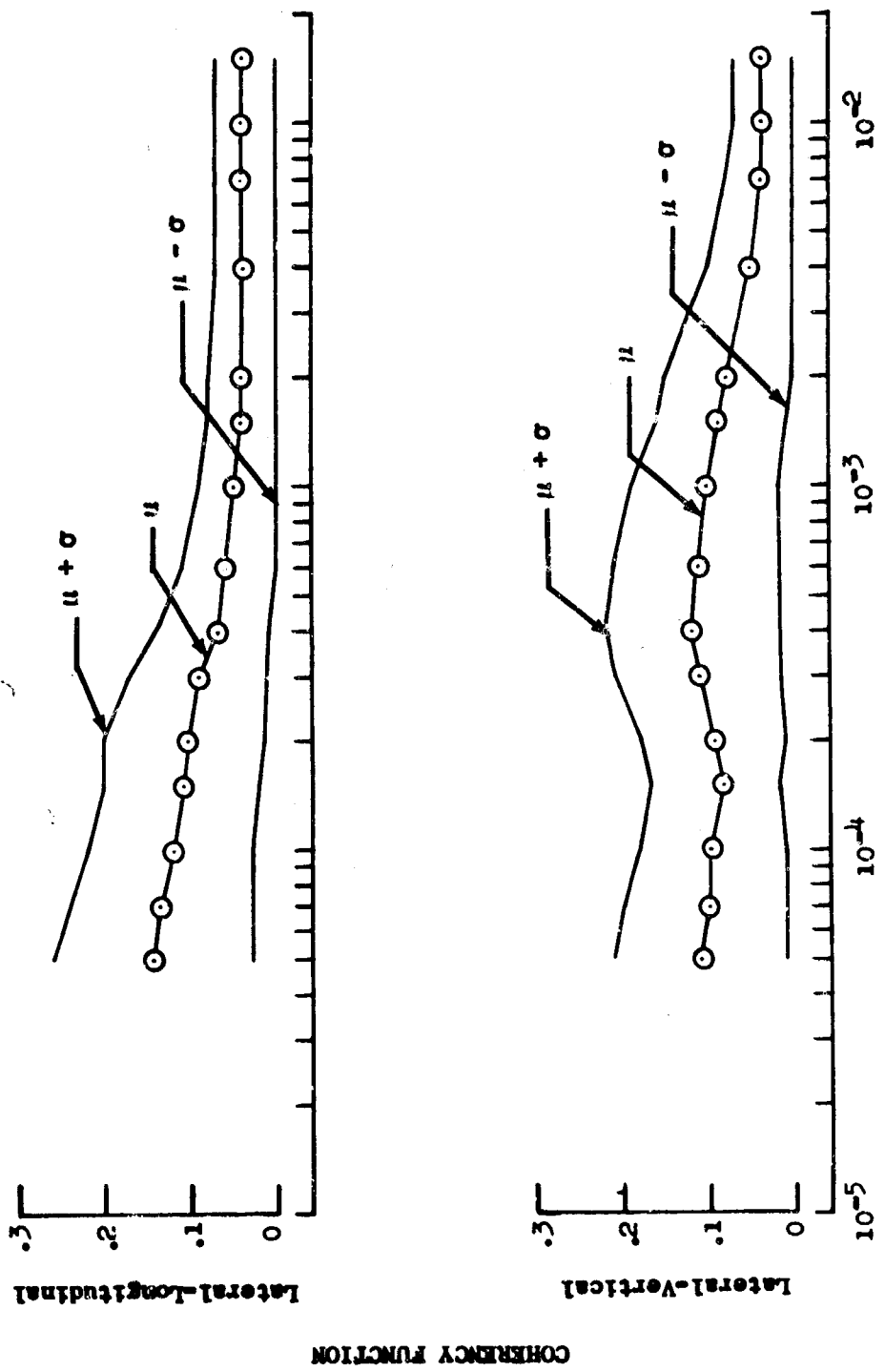


Figure 20.2 Average Coherency

## 21. HOMOGENEITY

Only turbulence samples considered to be homogeneous can be used to accurately define valid scale lengths and spectra shape. Those samples considered to be non-homogeneous were eliminated from the data being used to define scale lengths and spectra shape.

Homogeneity is the property which in space coordinates corresponds to the stationarity property in time coordinates. The entire analysis of gust velocity time histories as recorded by an airplane is based upon the validity of Taylor's hypothesis. Assuming Taylor's hypothesis to be valid, then spatial homogeneity of the turbulence sample is indicated by the stationarity of the time history. Detailed discussions of Taylor's hypothesis may be found in References 21.1 and 18.2. An indication of turbulence homogeneity was obtained by dividing the un-normalized spectrum of the middle third of a data sample by the un-normalized spectrum of the entire sample for each gust velocity component. Homogeneity is indicated when the spectrum ratios are 1.0. Each turbulence sample for which power spectra were calculated was individually evaluated for homogeneous characteristics. The method used for evaluating these characteristics involved plotting the spectrum ratios versus spatial frequency (see Appendix IX for example plots) and visually examining each plot. Those spectrum ratio values which did not approximate one throughout the frequency range were considered to be indicative of nonhomogeneous turbulence.

Homogeneity characteristics of the turbulence were studied by calculating the mean value of each spectrum ratio. Mean values which were less than one were replaced by their reciprocals. Cumulative probabilities of these mean values were then computed and plotted for evaluation.

Note that, if the shapes of the spectra are the same, the mean of the ratio of two un-normalized spectra is equal to the ratio of the variances from each spectrum. That is:

$$\frac{\Phi(k)_1}{\Phi(k)_2} = \frac{\sigma_{t_1}^2}{\sigma_{t_2}^2} \quad (21.1)$$

where: subscripts 1 and 2 refer to the middle third of the data sample and the entire data sample, respectively.

Since essentially all the homogeneity characteristic plots (Appendix IX) have a zero slope, the two spectra are either coincident or parallel. Therefore, it is concluded that the ratio of the variance of the middle third of the data sample to the variance of the entire sample could be employed as an indicator of homogeneity and would give results similar to the results from the spectrum ratio method which was used throughout the LO-LOCAT program.

The cumulative probabilities of the spectrum ratio mean values are shown for all three components in Figure 21.1. These data include the turbulence samples which were considered to be both homogeneous and nonhomogeneous. It was determined from the stationarity run test, Section 5, that an average of 77 per cent of the data may be considered to be stationary. Based on this percentage, it can be seen from Figure 21.1 that the data may be considered to be homogeneous when the spectra ratio mean is between 1.0 and approximately 1.4. When the ratio is greater than 1.4, the data are non-homogeneous according to the run test criteria.

As discussed above, the homogeneity characteristics of the IO-LOCAT data were evaluated visually from the spectrum ratio plots. Only the data for the samples considered to be homogeneous are plotted in Figure 21.2. Approximately 93 per cent of these data are between the values of 1.0 and 1.4. Thus, the visual method of homogeneity determination and the stationarity run test give approximately the same homogeneity characteristic results.

Figures 21.3 through 21.6 show variations of homogeneity as functions of the categories of terrain, absolute altitude, atmospheric stability, and time of day. The data contained in these figures are those from both the homogeneous and nonhomogeneous turbulence samples. All of these figures are comprised of the same data and vary only by which a particular category component is held constant. The data in these figures show that the turbulence became more homogeneous as: (1) terrain roughness decreased; (2) atmospheric stability decreased; and (3) time of day progressed from dawn to mid-afternoon. Altitude appears to have very little effect on the homogeneity characteristics of the data.

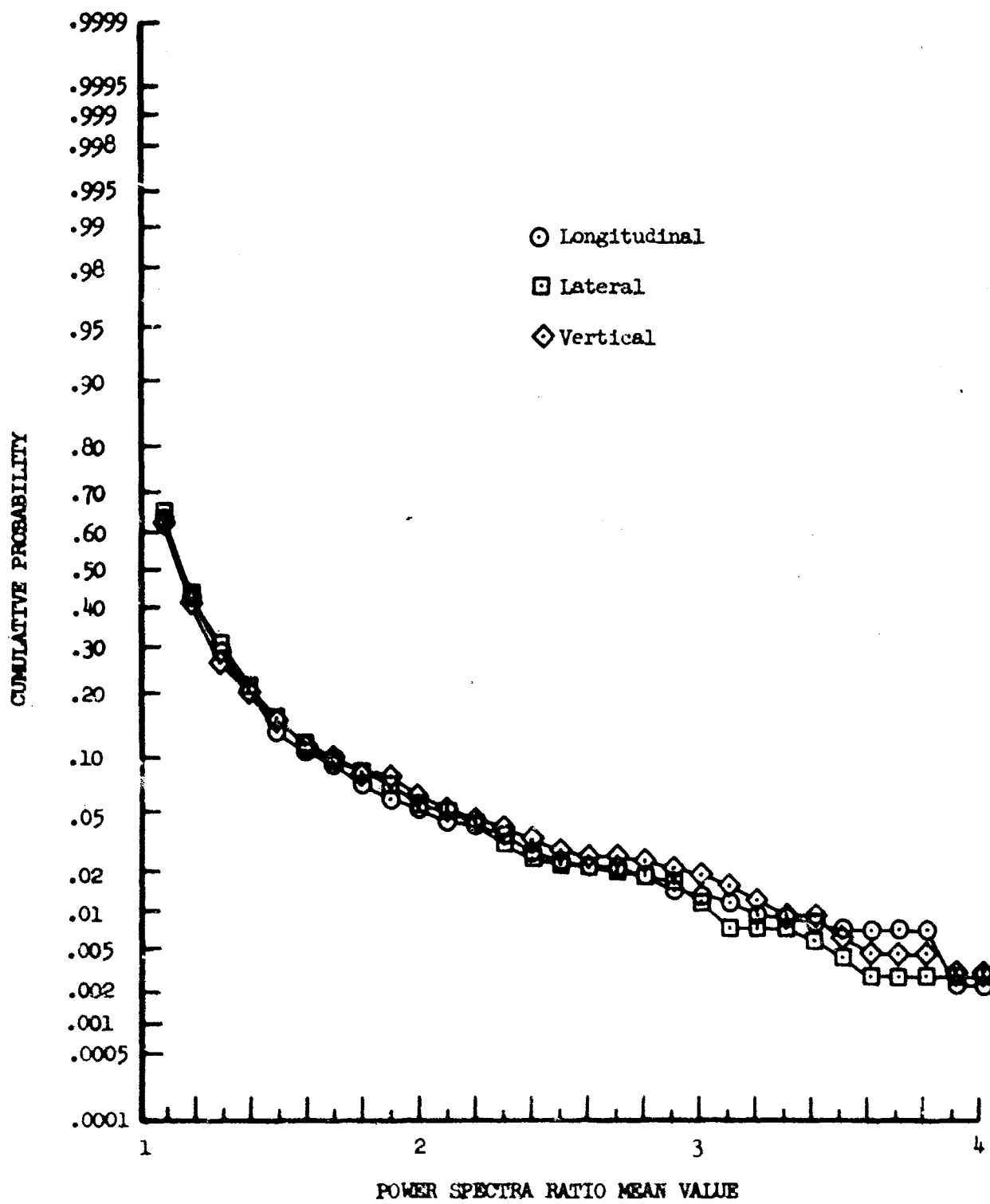


Figure 21.1 Homogeneity Characteristics for LO-LOCAT Phase III

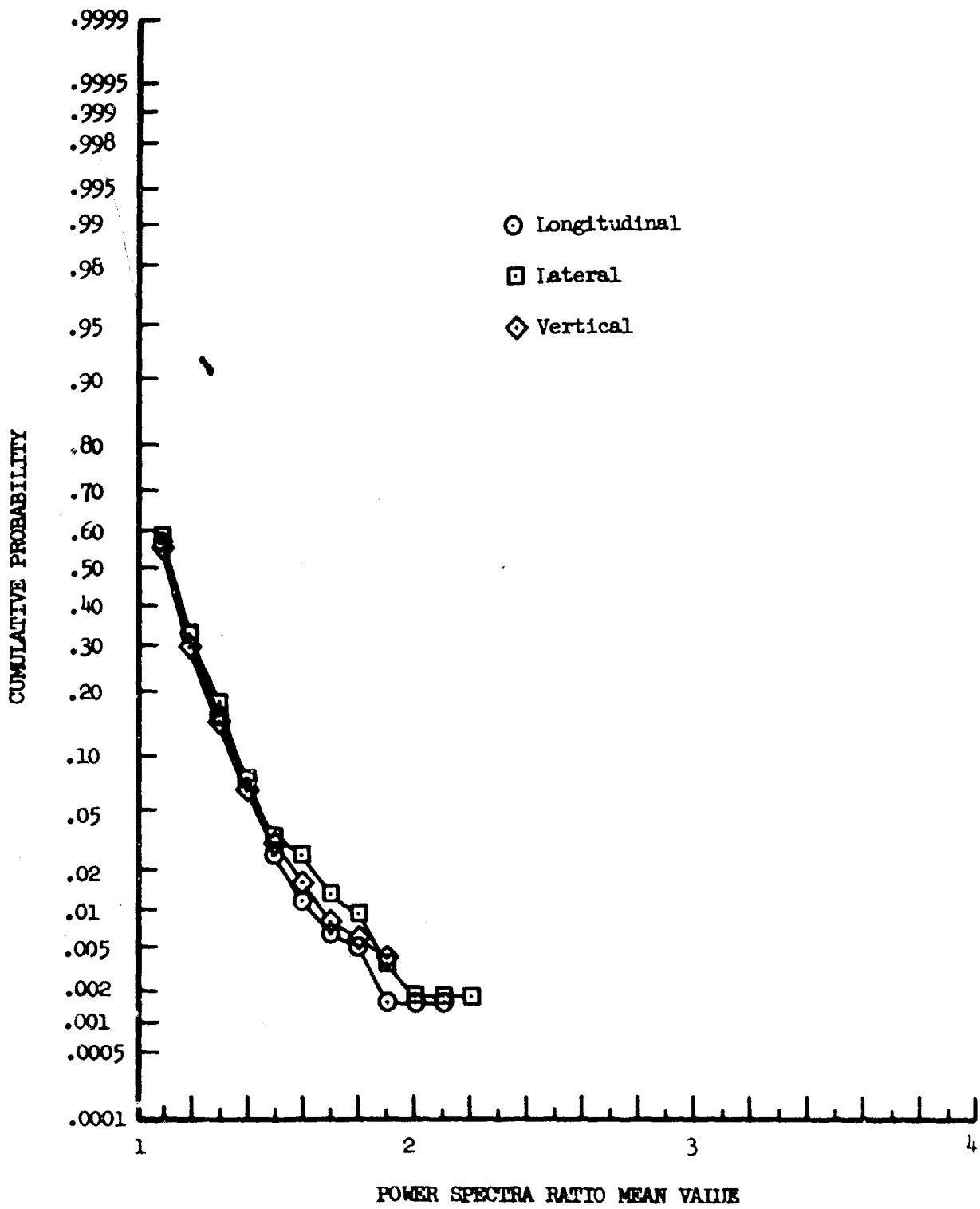


Figure 21.2 Cumulative Probability Distribution of Power Spectra Ratio Mean Values - Homogeneous Samples Only

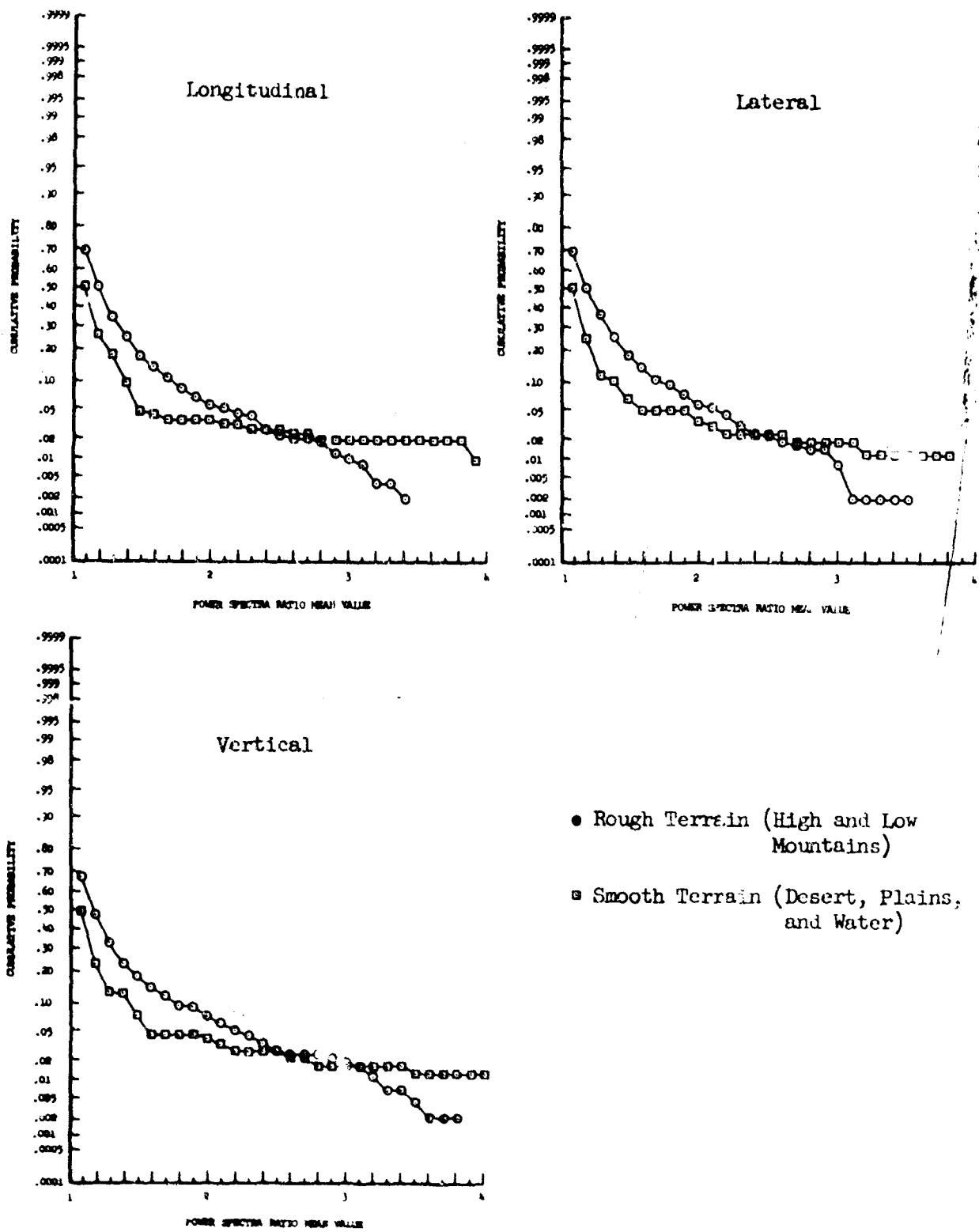


Figure 21.3 Variation of Homogeneity Characteristics with Terrain

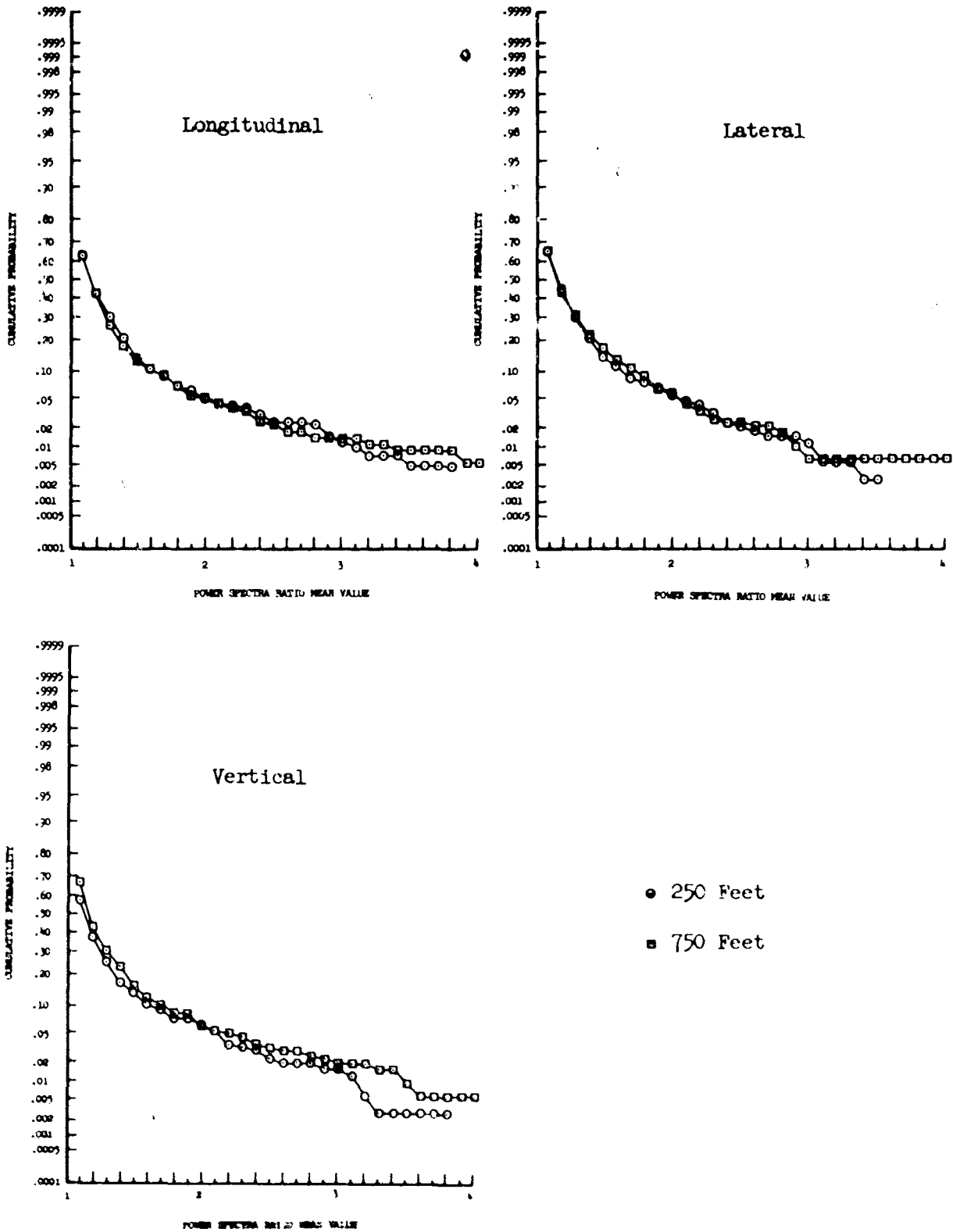


Figure 21.4 Variation of Homogeneity Characteristics with Absolute Altitude



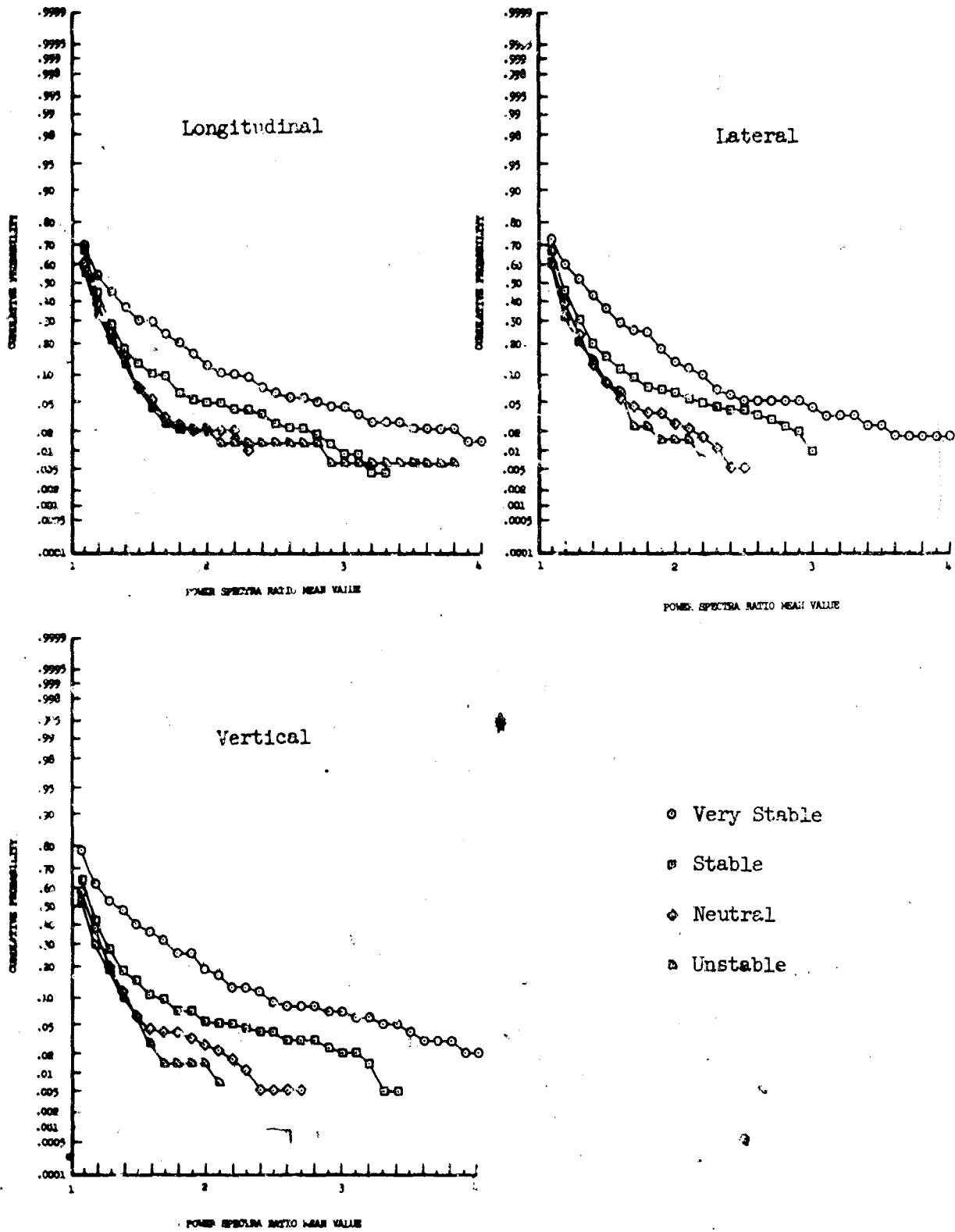
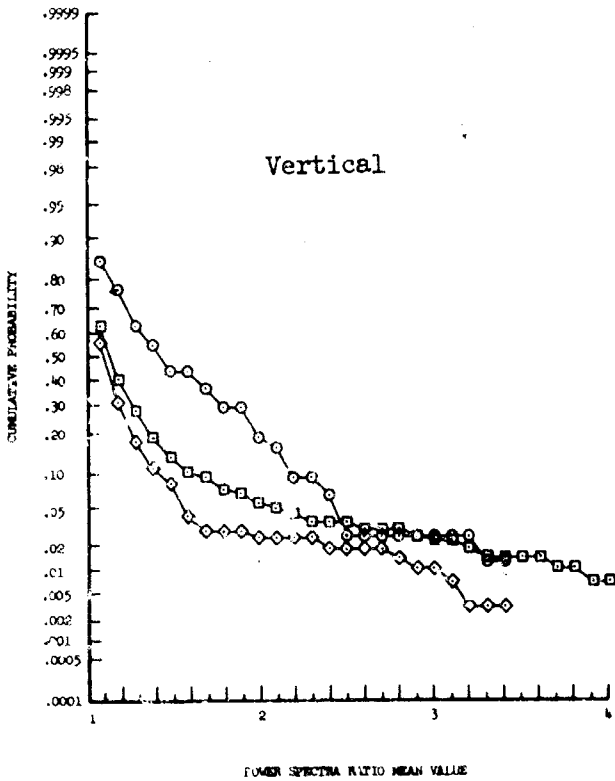
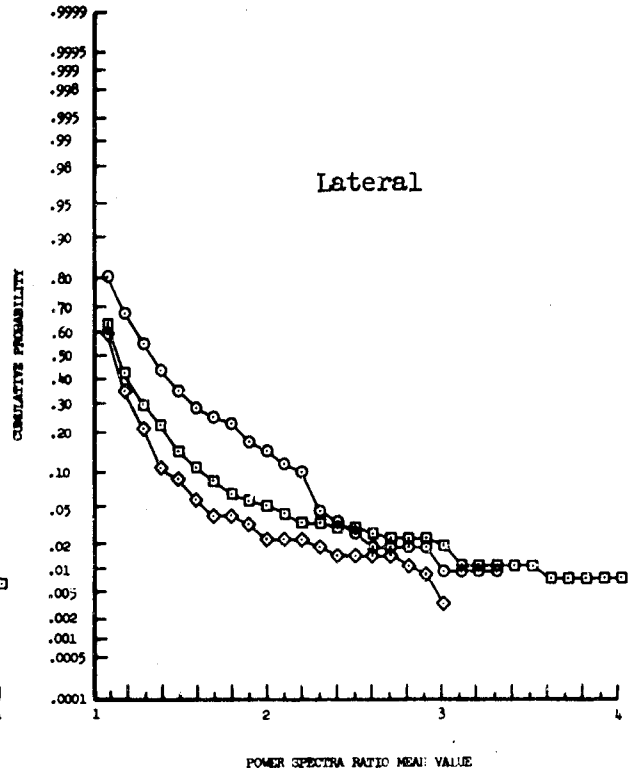
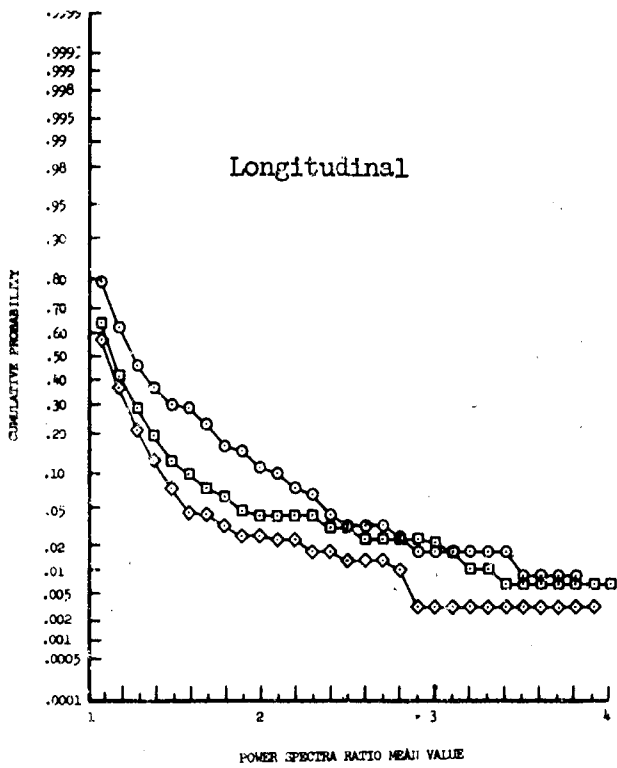


Figure 21.5 Variation of Homogeneity Characteristics with Atmospheric Stability



- Dawn
- Mid-Morning
- ◇ Mid-Afternoon

Figure 21.6 Variation of Homogeneity Characteristics with Time of Day

## 22. ISOTROPY

A turbulent field which is isotropic is one in which there is no preferred direction and therefore all average functions describing this field must remain unchanged regardless of a rotation or reflection of the coordinate system. Experimental evidence has shown that most localized turbulence is nearly isotropic (local isotropy).

According to References 21.1, 18.2, and 22.1, the isotropic characteristics will follow  $\Phi_w(k)/\Phi_v(k) = 1$  and  $\Phi_u(k)/\Phi_v(k)$  will vary from 1.0 to 0.75 with frequency and scale length. The characteristics of the experimental data were established by dividing the unnormalized power spectra of  $u$  and  $w$  by the unnormalized power spectrum of  $v$ . In this manner, if the turbulence is isotropic, the  $w/v$  spectra ratio will be equal to 1.0 and the  $u/v$  ratio will approach a form similar to that in Figure 22.1. Figure 22.1 illustrates how the  $u/v$  ratio varies with the scale length and was calculated using the von Karman equations for turbulence spectra.

Unnormalized spectra ratios were determined at selected spatial frequency values for each homogeneous turbulence sample. The selected frequencies were the same as those used in the coherency analysis (Section 20). The mean value of the spectra ratios at each frequency was calculated and plotted versus frequency for selected categories. Isotropy characteristics for the combined categories and with respect to terrain, altitude, stability, and time of day are shown in Figures 22.2 through 22.6. Isotropy characteristics for the individual turbulence samples are presented in Appendix IX.

Theoretical longitudinal to lateral spectra ratio values indicative of isotropic turbulence were determined from the von Karman expressions (see Section 28) and are shown in Figures 22.2 through 22.6 for comparison purposes. The von Karman spectra ratios shown in Figures 22.2 through 22.6 were determined from Figure 22.1 by using the average of the longitudinal and lateral scale lengths applicable to the set of categorized data analyzed. As stated previously, if the turbulence is isotropic, then the vertical to lateral spectra ratios should be equal to 1.0 throughout the frequency range regardless of scale length.

Standard deviations of the ratios from the mean at each frequency were calculated. These values based on all of the vertical to lateral ratios are shown in Figure 22.2. Standard deviations of the longitudinal to lateral ratios are not shown. This ratio varies as a function of scale length. Therefore, standard deviations in the lower frequency range are increased due to the scale length variations (see Figure 22.1) and do not give a true indication of variations in isotropic characteristics.

There is a trend for the turbulence to be slightly more isotropic over rough terrain than over smooth terrain and at 750 feet compared to 250 feet. There is very little difference in the isotropy characteristics of the data recorded during the different atmospheric stability conditions. The turbulence data recorded at dawn show much less isotropy than the data recorded at either mid-morning or mid-afternoon. It should

be noted, however, that 85 per cent of the dawn data analyzed for isotropic characteristics were obtained over the Peterson route. This is because the majority of turbulence samples gathered at dawn over the McConnell route had low signal-to-noise ratios and were, therefore, not included in the analysis. Also, the number of dawn flights over the Edwards route was limited due to inclement weather. The discussion in Section 17 points out that lateral gust velocities at Peterson were larger than the other two components of turbulence. Thus, the vertical to lateral and longitudinal to lateral unnormalized spectra ratios from the Peterson data and, consequently, the dawn data are less than required for isotropic conditions.

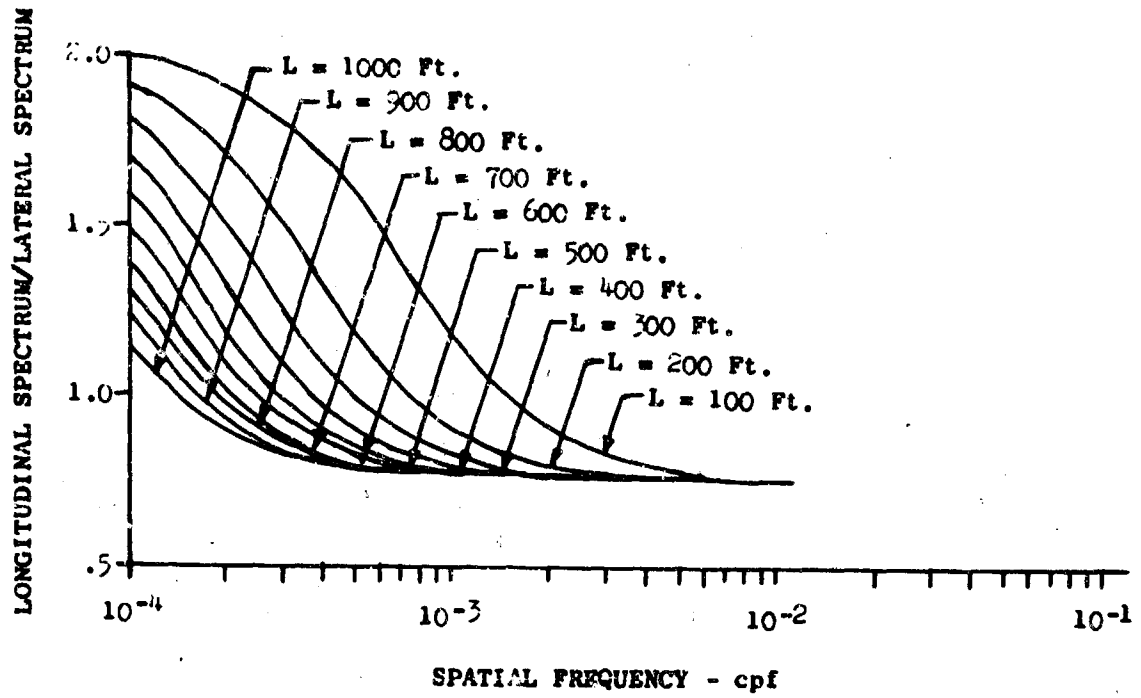


Figure 22.1 Isotropy Based on von Karman Expressions

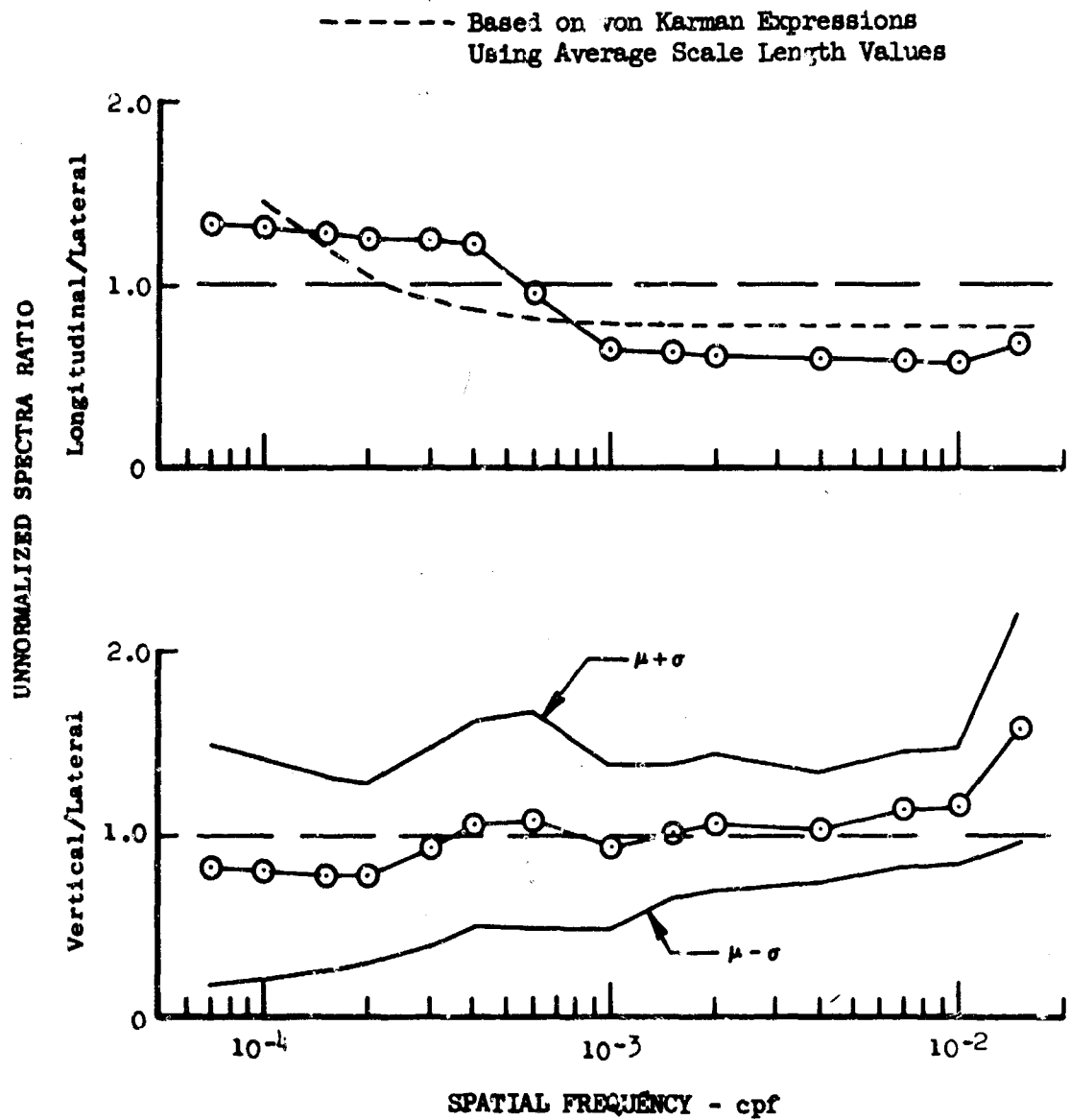


Figure 22.2 Isotropy Characteristics - All Categories

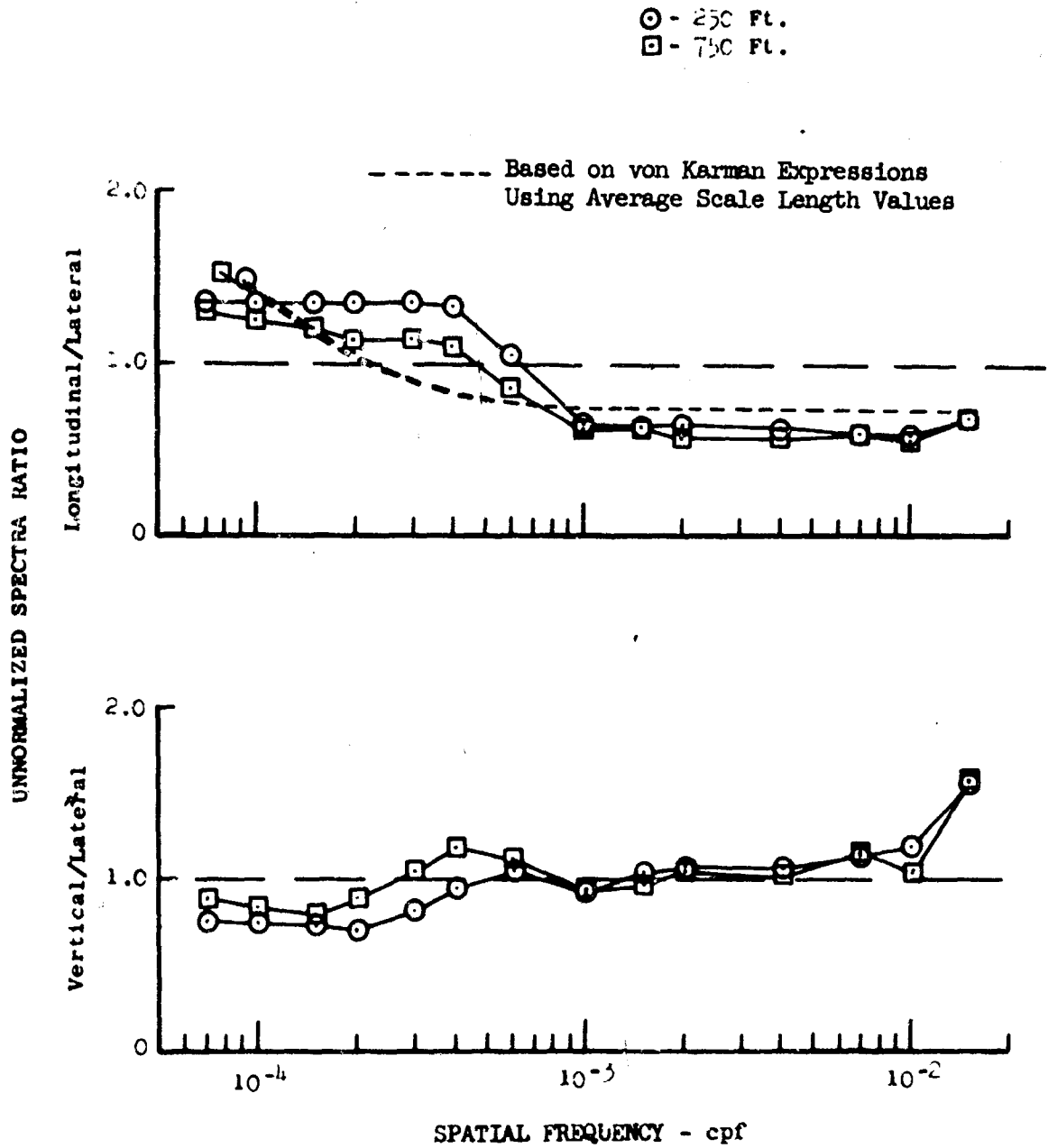


Figure 22.3 Isotropy Characteristics for Different Altitudes

- Rough Terrain (High and Low Mountains)
- Smooth Terrain (Desert, Plains, and Water)

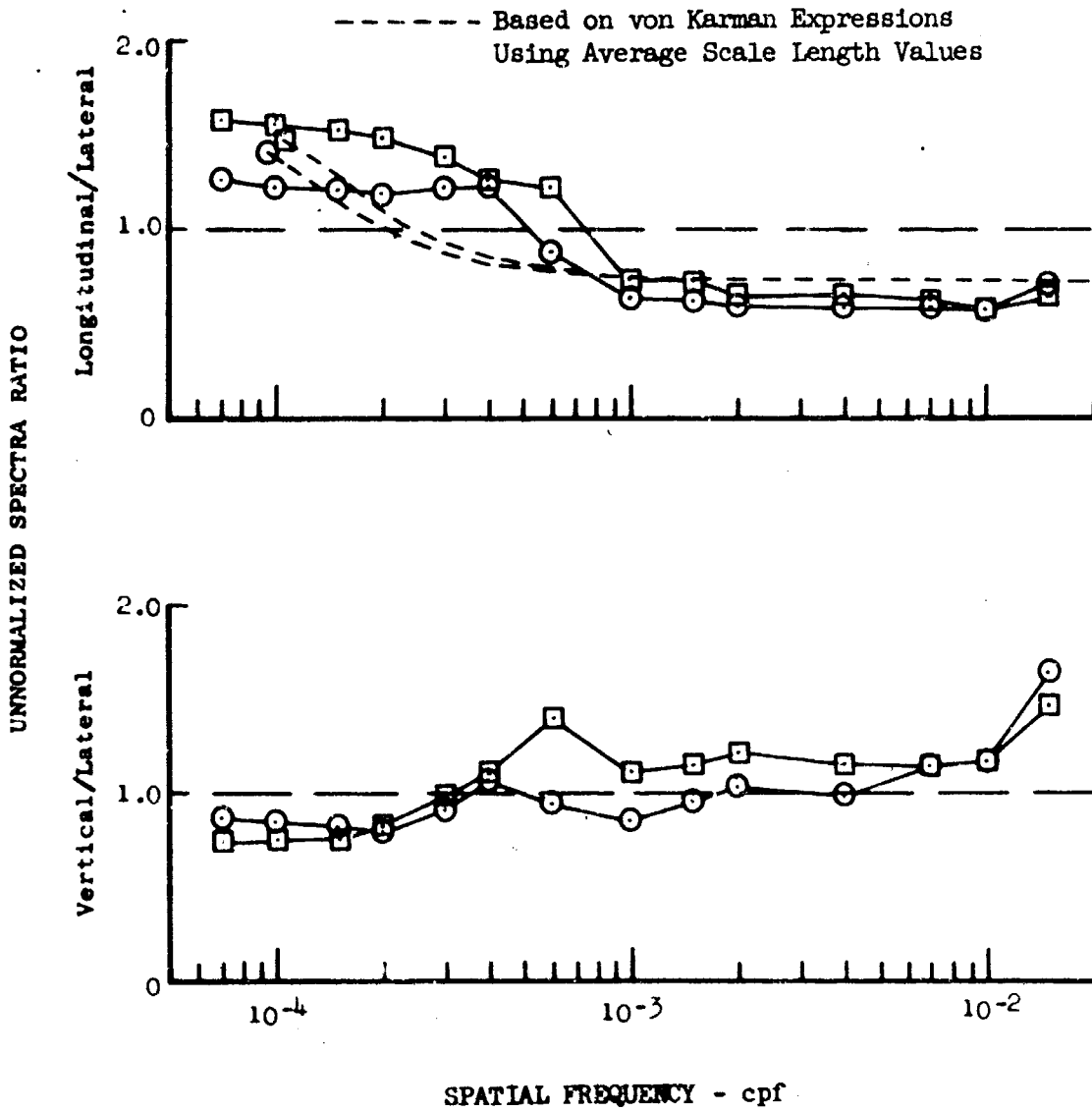


Figure 22.4 Isotropy Characteristics for Different Terrain



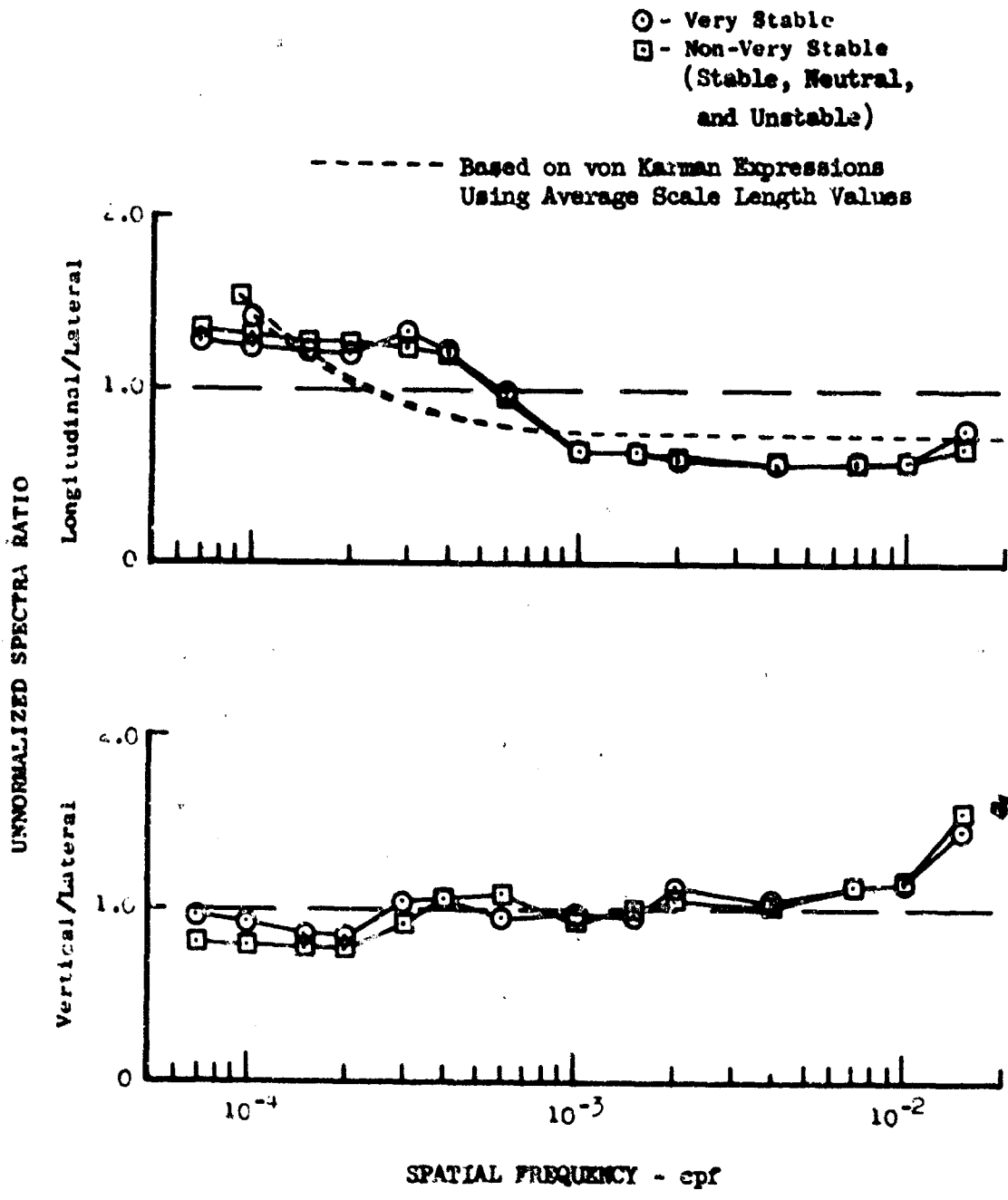


Figure 4.2 Isotropy Characteristics for Different Atmospheric Stabilities

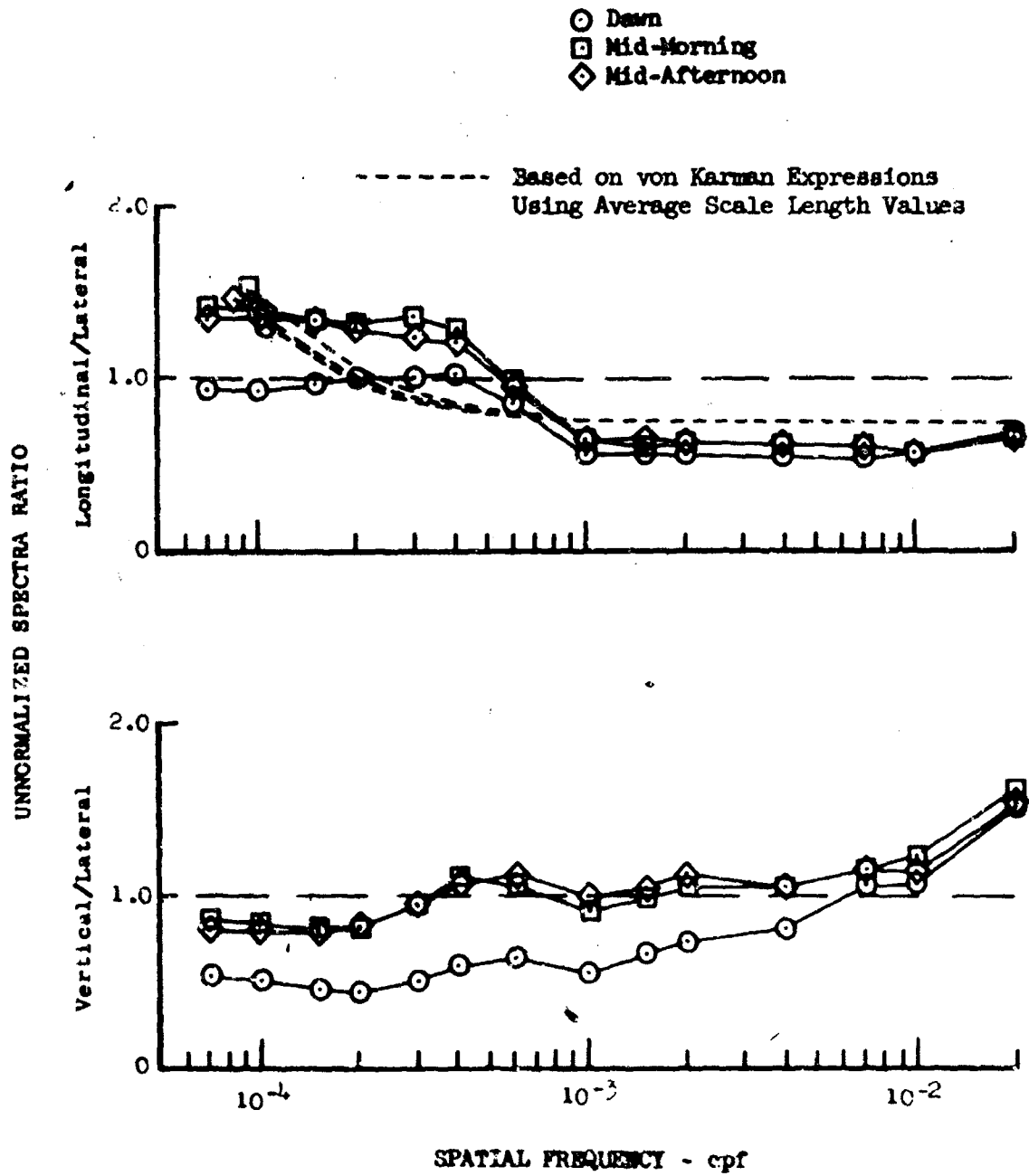


Figure 22.6 Isotropy Characteristics for Different Times of Day

### 23. NORMALIZED SPECTRA

The power spectra were normalized by dividing the power magnitude by  $\sigma_t^2 L$  and plotting versus  $kL$ . Spectra shift up and down in power with a respective increase or decrease in  $\sigma_t^2$ , and change shape with a change in  $L$ . Therefore, normalizing in this manner permitted comparison of the spectra for different categories without having to account for the influence of  $\sigma_t^2$  and  $L$ .

Change in the shape of the normalized spectra with category variation was evaluated by comparing the average normalized spectra for the different category classifications. The average spectrum for a category was determined in the same way that average coherency functions were determined in Section 20.

Spectra, normalized by  $\sigma_t^2 L$ , obtained over different types of terrain were compared for high and low mountains, and rough and smooth terrain. Rough terrain refers to the combination of high and low mountain data and smooth terrain refers to the combination of plains, desert, and water data. No consistent or significant difference in spectra shape resulted because of terrain. Figures 23.1 through 23.3 show comparisons of those categories which exhibited the maximum differences.

The lateral gust velocity spectra in Figure 23.2 exhibit a peculiarity that is also present to a lesser degree in the vertical gust velocity spectra. This appears as a dip at a  $kL$  of 0.25 and is believed to be caused in part by incomplete removal of probe motion which occurs at approximately 0.3 cps. This 0.3 cps probe motion, accounting for variations in ground speed and scale length, falls in the  $kL$  range from approximately 0.14 to 0.46  $kL$ . An example plot of sideslip differential pressure illustrating the probe motion is presented in Figure 23.4.

The removal of probe motion is more difficult in lateral gust velocity than in vertical or longitudinal because of the greater amount of motion in the lateral direction in this particular frequency range.

It has been found in the past, Reference I.2, that certain errors generated in calculated gust velocities are a function of the amount of airplane motion. Since airplane motion and hence, probe motion, is inherently larger laterally than vertically or longitudinally, lateral gust velocity is inherently more inaccurate.

Further indication that airplane motion contributes to the dip in the spectra was obtained by comparing the normalized spectra of low intensity turbulence samples to those of high intensity turbulence level. The assumption here is that the lower the intensity of turbulence the less error is induced by airplane motion.

Figure 23.5 illustrates this comparison. The data represented by squares were obtained from 10 samples exhibiting a relatively low intensity of turbulence ( $\bar{\sigma}_t = 1.78$  fps) but still sufficiently high so as not to be adversely affected by noise. The solid line connecting the circles represents the average of over 100 high intensity turbulence samples,  $\bar{\sigma}_t = 5.13$  fps.

This comparison indicates the samples representing the low turbulence intensities are in better agreement with the results from Phases I and II and with the von Karman spectra. In particular, the lower intensity turbulence data are in better agreement with the von Karman mathematical expressions at  $kL$  values below 0.1 than with the average of the high turbulence data.

An example plot showing the dip in the spectra for an individual sample is presented in Figure 23.6. Numerous samples containing this type spectra shape produced the effect seen in Figure 23.2. The location of the dip in each sample shifts due to different ground speeds and scale lengths and the averaging effect which produces a smoother function over a broad range of  $kL$  values.

Comparison of average spectra, normalized by  $\sigma^2 L$ , to determine effects caused by altitude are presented in Figures 23.7 through 23.9. Figure 23.7 contains a comparison for longitudinal gust velocity. No significant or consistent change in longitudinal gust velocity can be attributed to the effect of altitude. The maximum change due to altitude was noted for the lateral gust velocity component as shown in Figure 23.8. Here, however, the difference is again influenced by increased airplane motion effects while contour flying at 250 feet as compared to 750 feet.

The difference obtained in the vertical spectra for the two different altitudes is presented in Figure 23.9. The vertical gust spectra for the 250-foot data are consistently lower in power in the  $kL$  range of 0.1 to 0.4 and are consistently higher at  $kL$  values less than 0.06. The difference in the spectra in the  $kL$  range from 0.1 to 0.4 is similar to the characteristic previously discussed for lateral spectra. The existence of airplane motion in the 250-foot altitude data is the result of a generally higher level of turbulence at 250 feet than at 750 feet. A comparison of low intensity turbulence to high intensity turbulence data, both obtained at 250 feet, did produce indications of increased probe motion in the  $kL$  range of 0.06 and less. This is shown in Figure 23.10. The conclusion is that there is no effect due to altitude and the differences seen are due mostly to probe motion. This seems valid since low frequency power in vertical gust spectra would not be expected to increase with decreasing frequency.

As in the case of altitude, no consistent or significant changes in the shape of the spectra were found to be caused by atmospheric stability variations. The spectra comparison for the different stabilities is presented in Figures 23.11 through 23.13. The maximum difference obtained in the comparison for time of day effects on the spectra shape are presented in Figures 23.14 through 23.16.

Plots showing the scatter bands for a selected category combination are presented in Figures 23.17 through 23.19. These data show the mean,  $\mu$ , and  $(\mu \pm \sigma)$  obtained by the averaging process previously discussed. The scatter bands for all other categories analyzed were in good agreement. The irregularity in lateral gust spectra is shown in Figure 23.18.

Plots of normalized PSD's for the turbulence samples exhibiting valid data for all three gust velocity components are presented in Appendix IX.

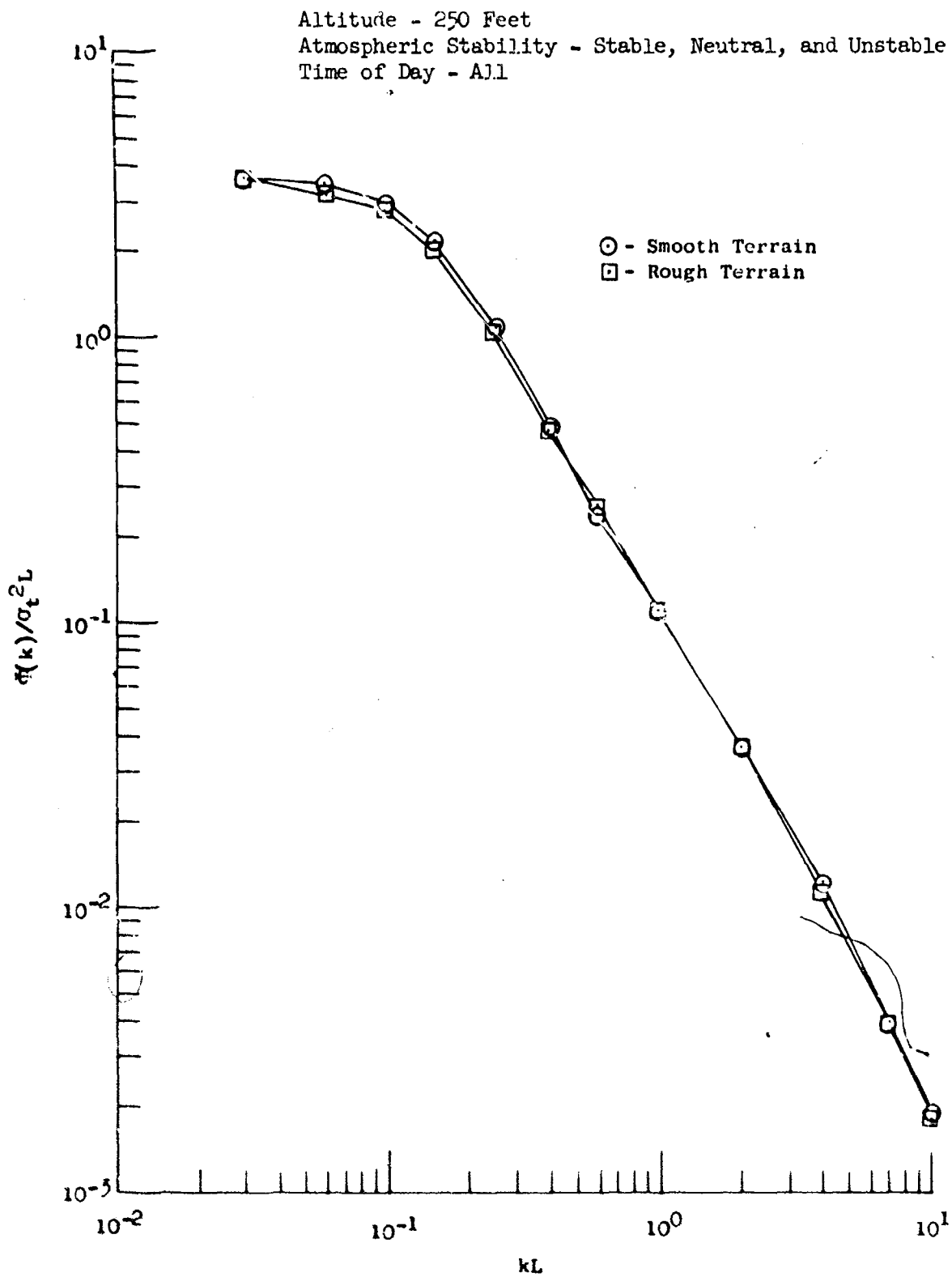


Figure 23.1 Longitudinal Power Spectrum Variation with Terrain

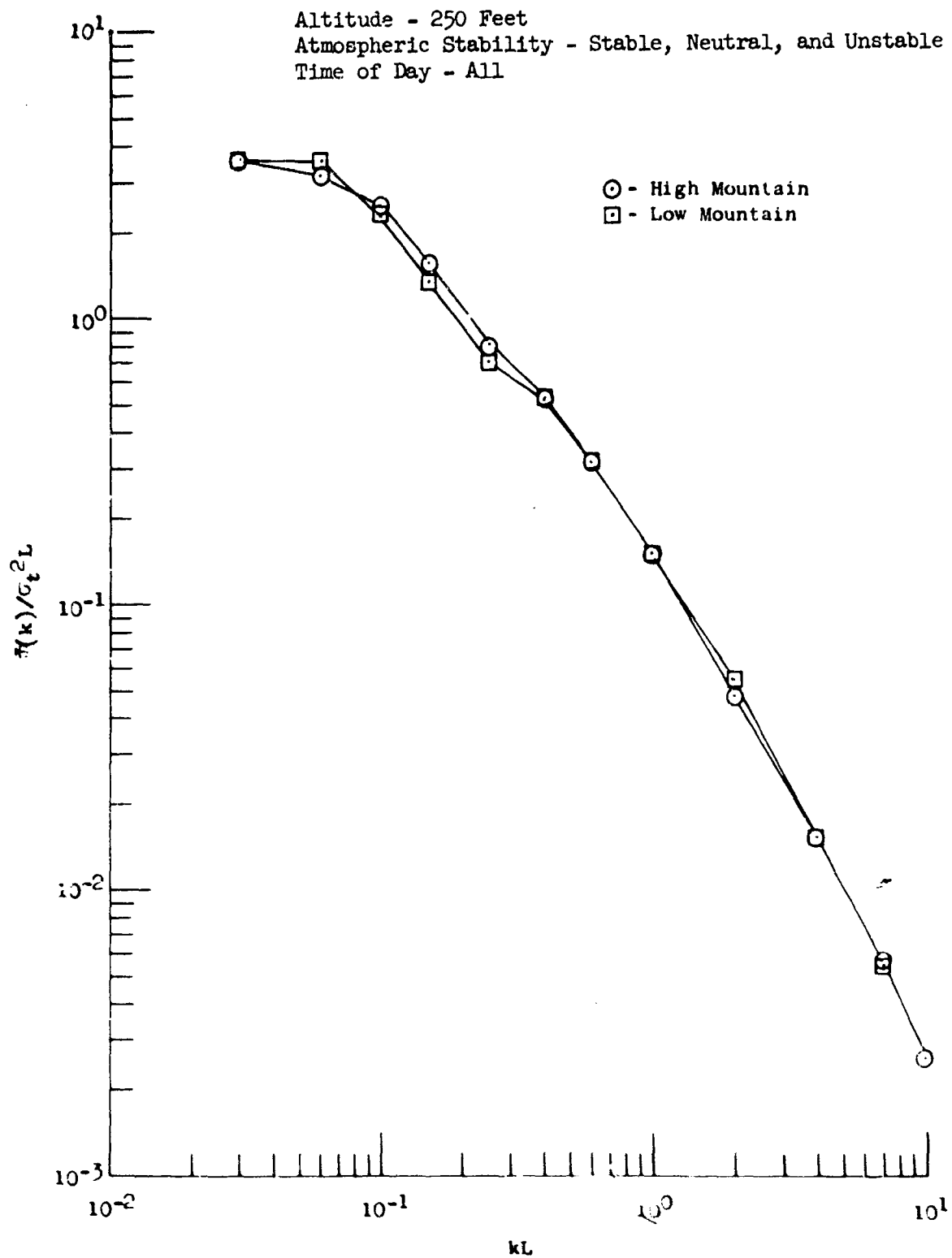


Figure 23.2 Lateral Power Spectrum Variation with Terrain

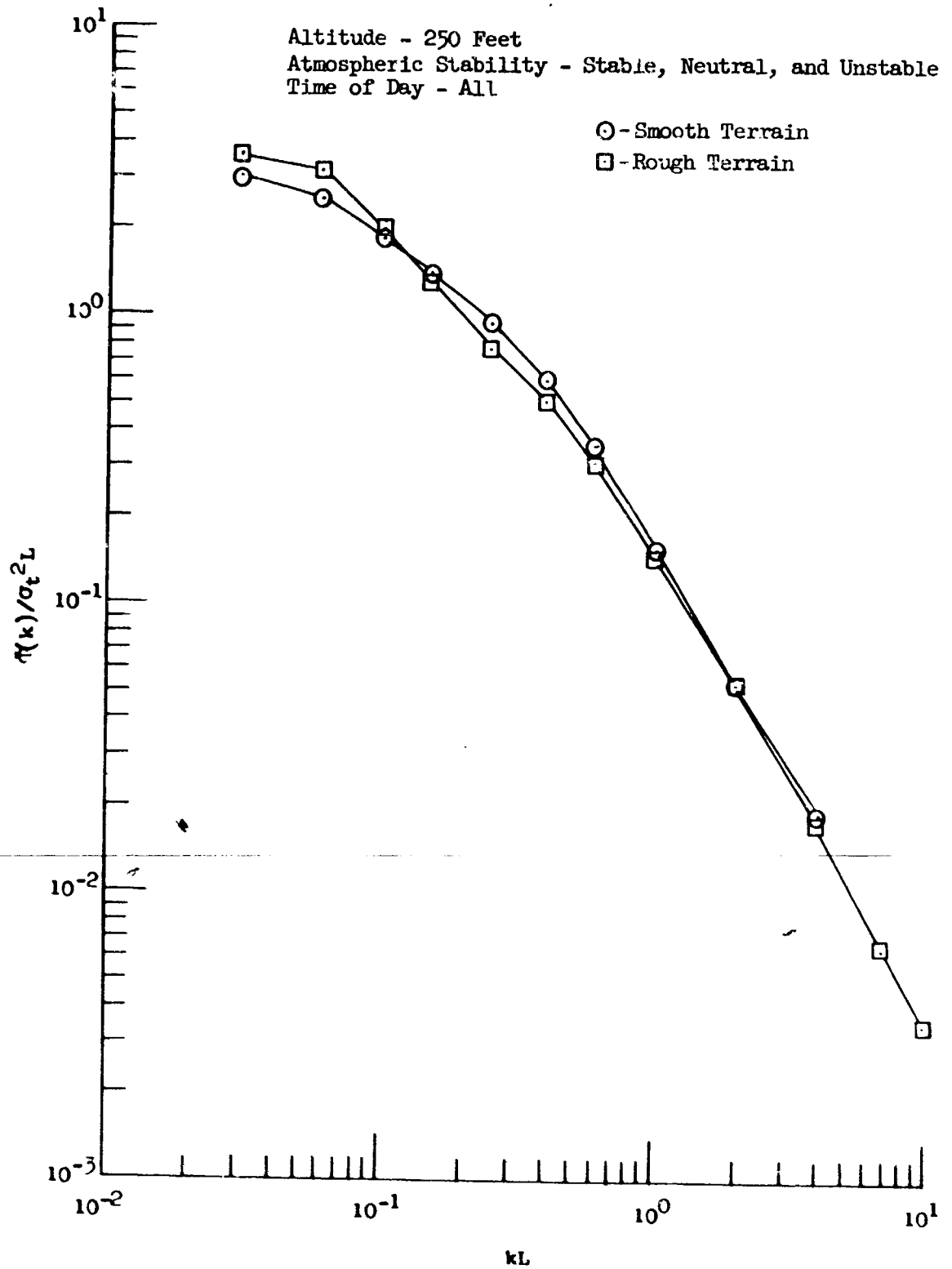


Figure 23.3 Vertical Power Spectrum Variation with Terrain

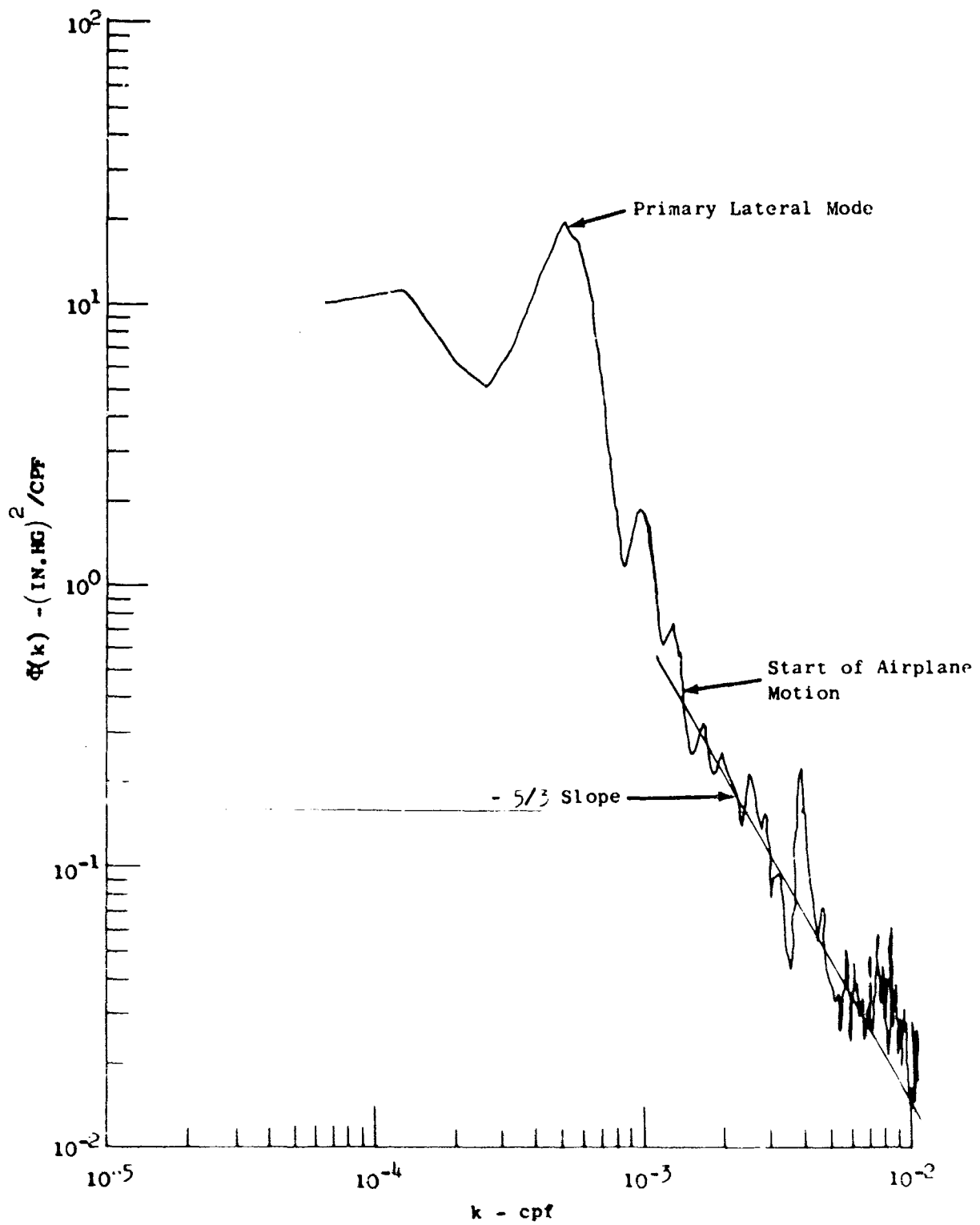


Figure 23.4 Power Spectrum of Differential Sideslip Pressure



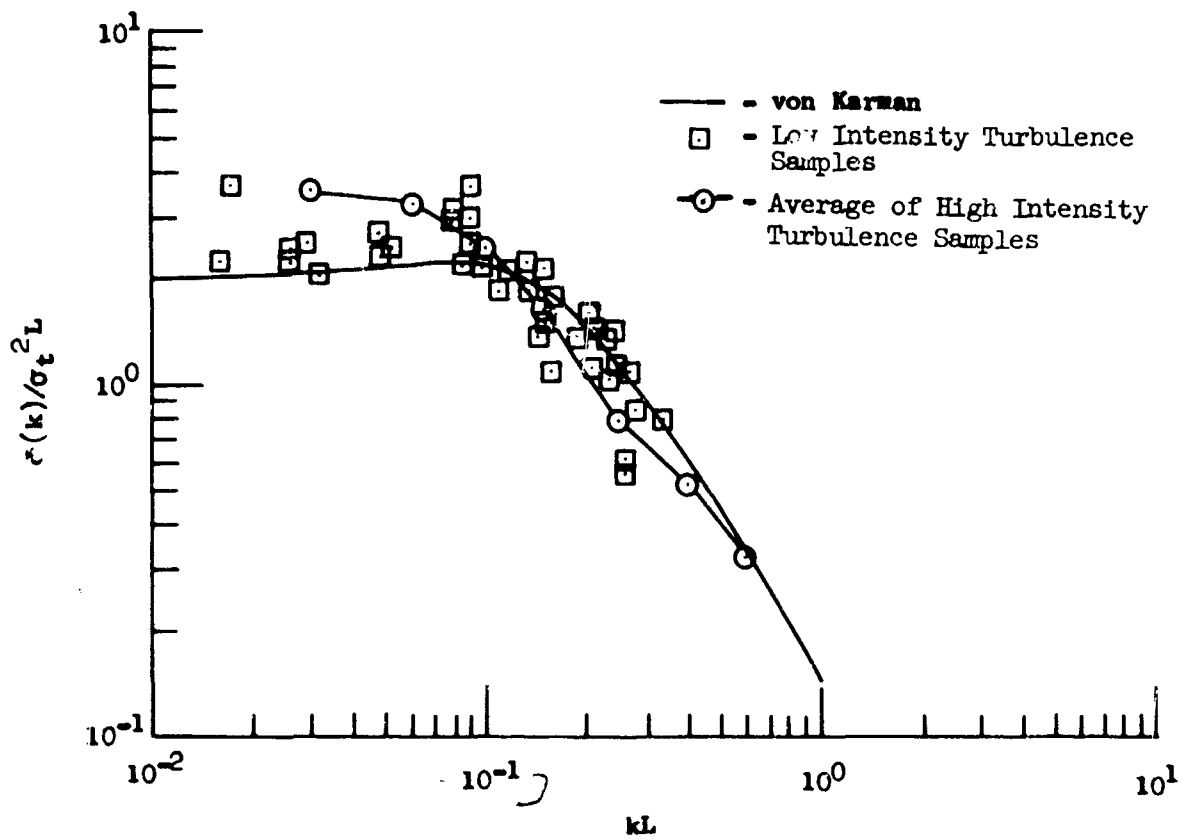


Figure 23.5 Lateral Power Spectrum

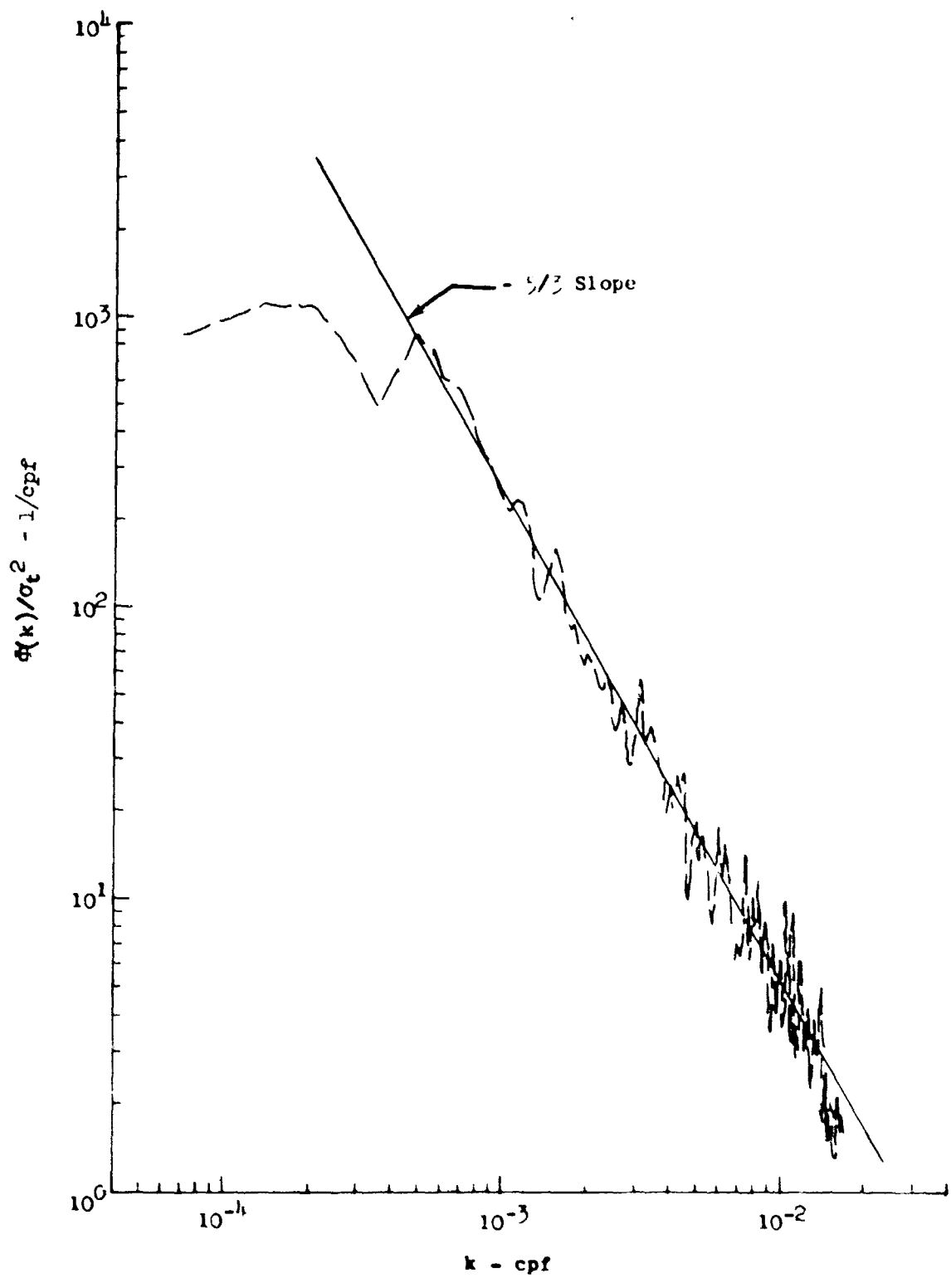


Figure 23.6 Lateral Power Spectrum

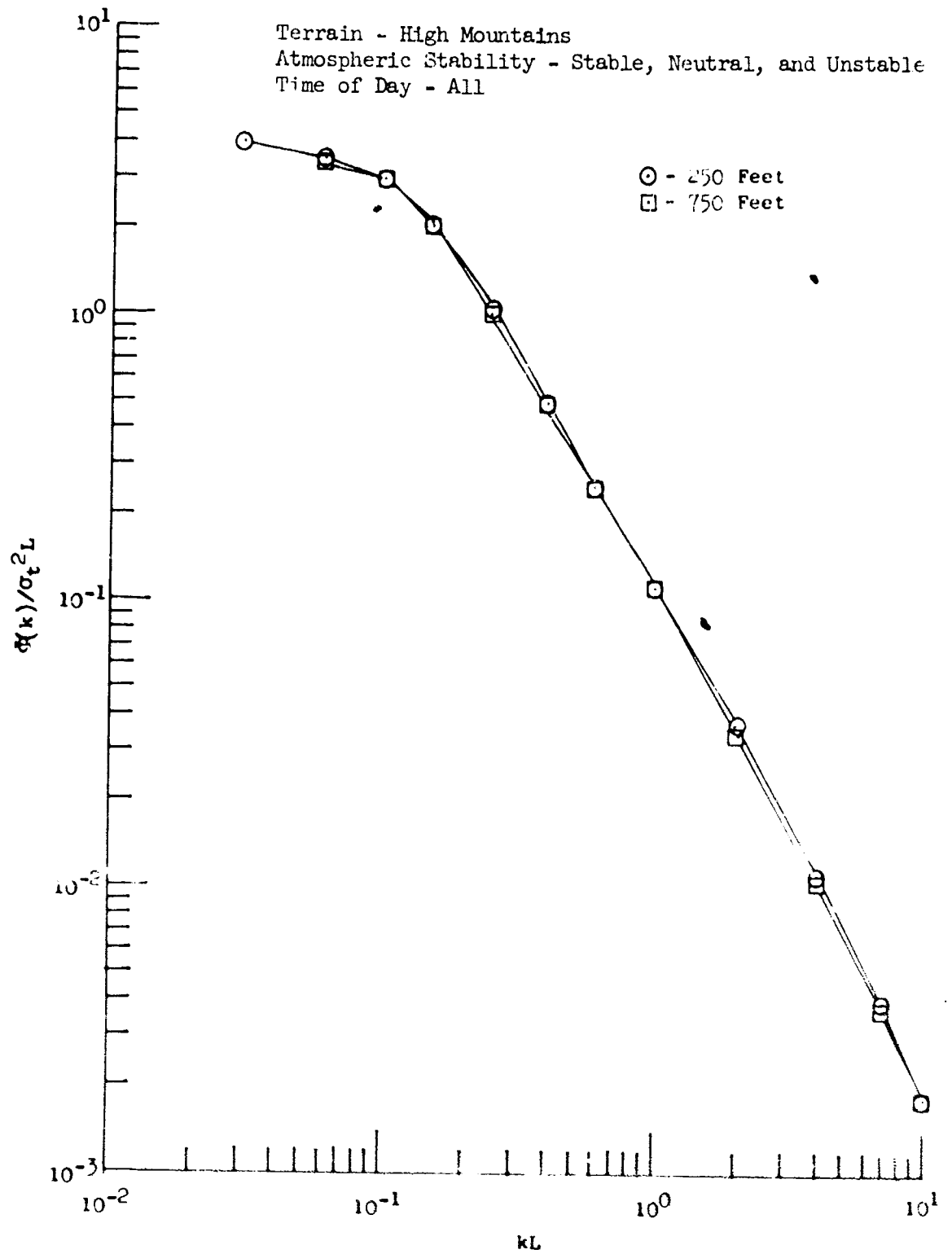


Figure 23.7 Longitudinal Power Spectrum Variation with Altitude

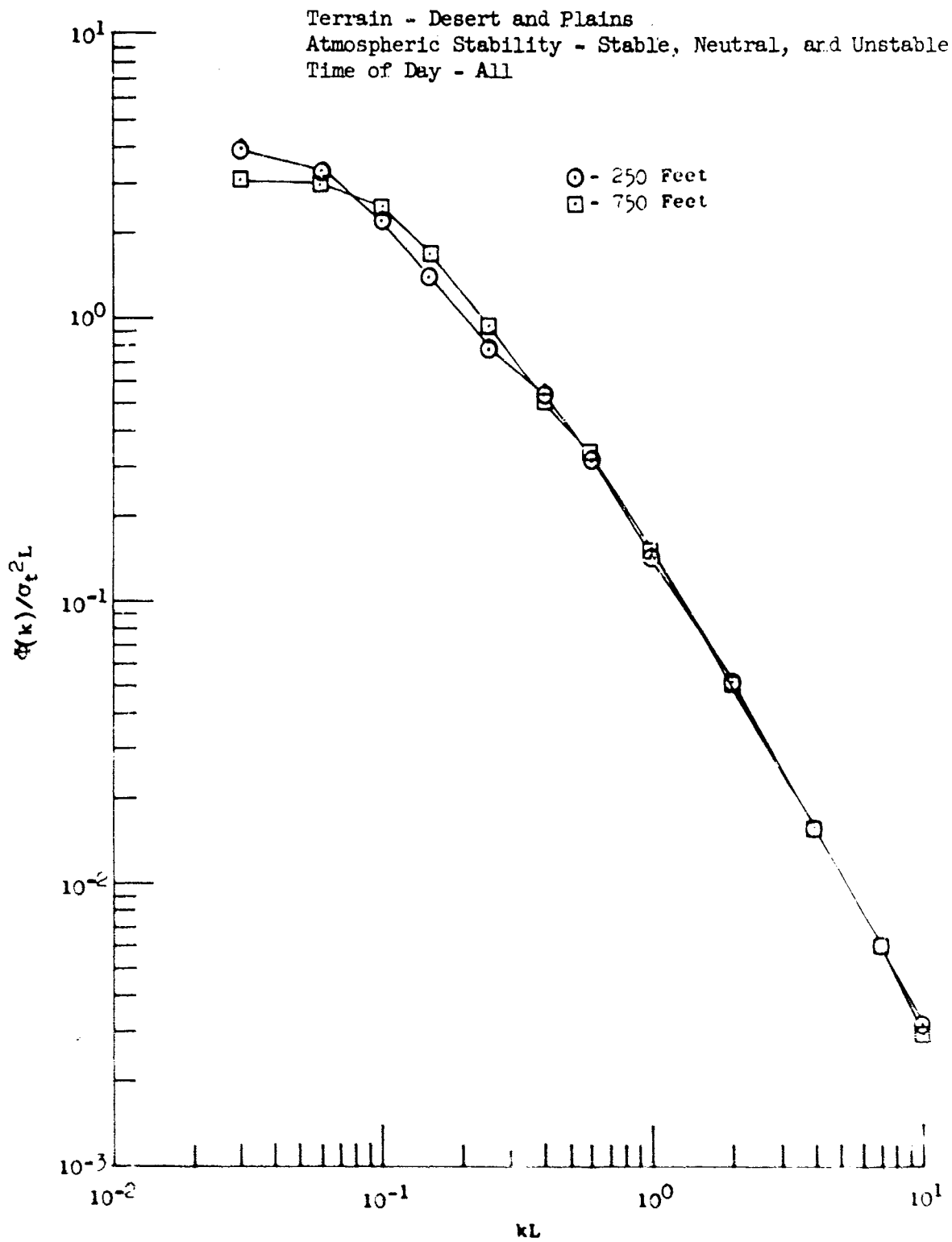


Figure 23.8 Lateral Power Spectrum Variation with Altitude

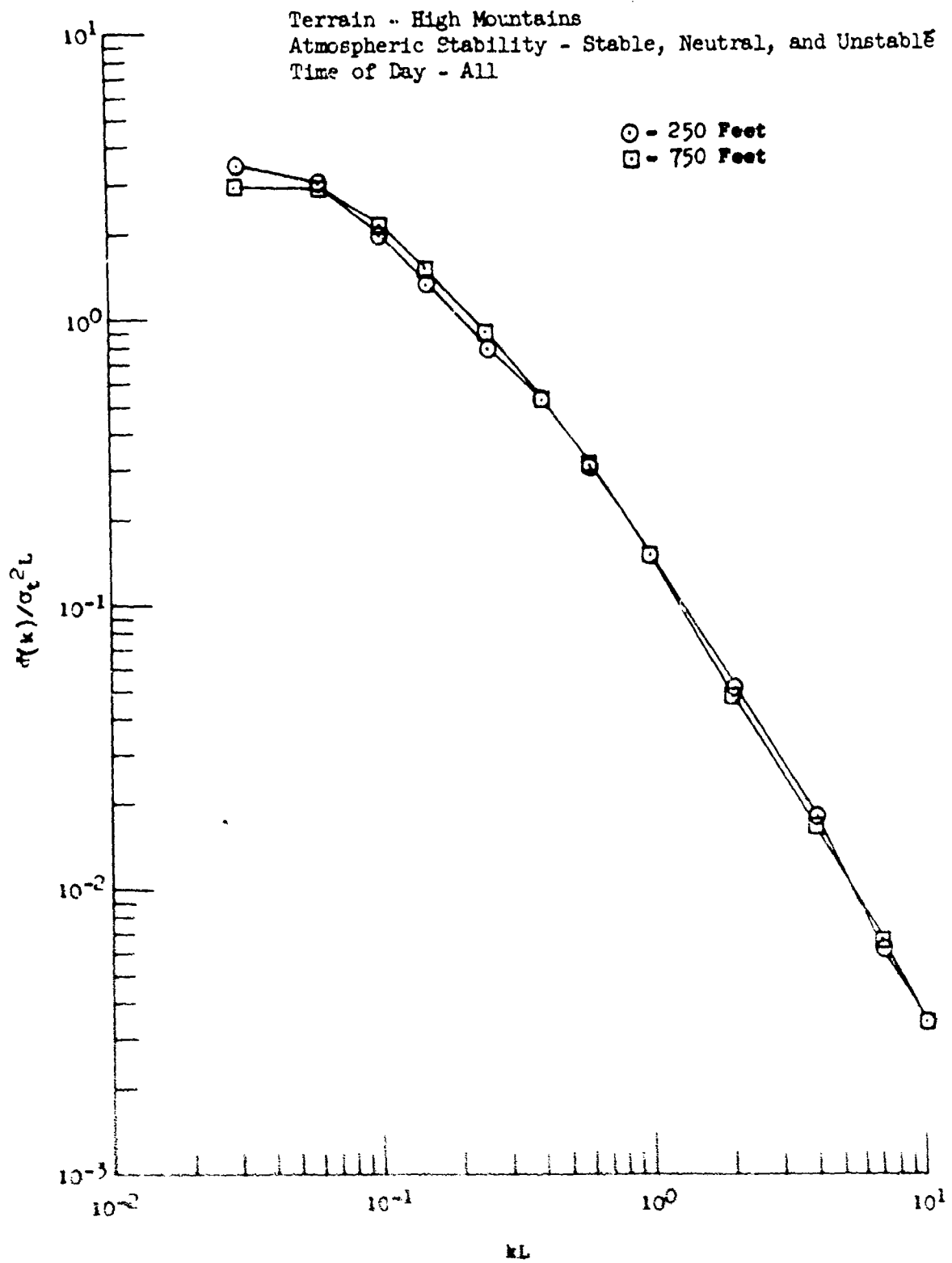


Figure 23.9 Vertical Power Spectrum Variation with Altitude

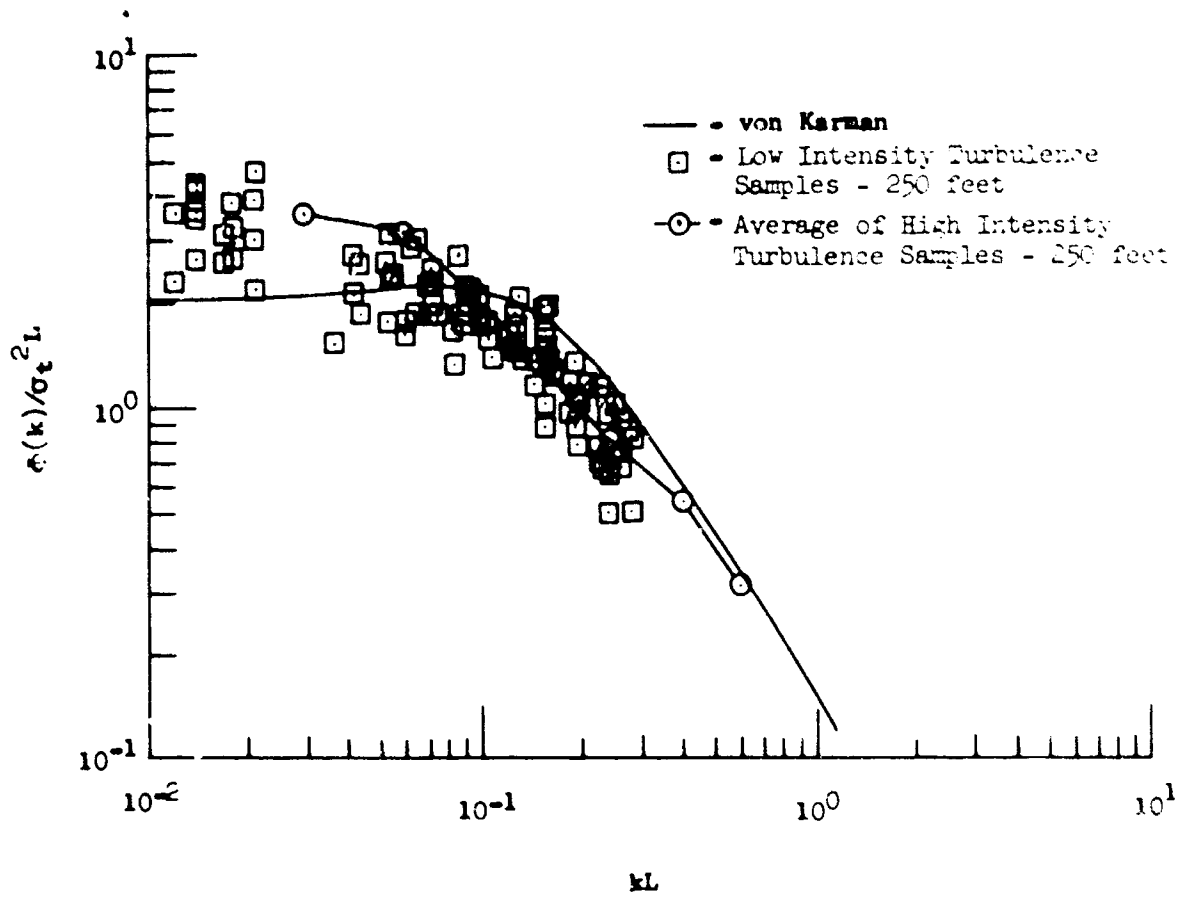


Figure 23.10 Vertical Power Spectrum

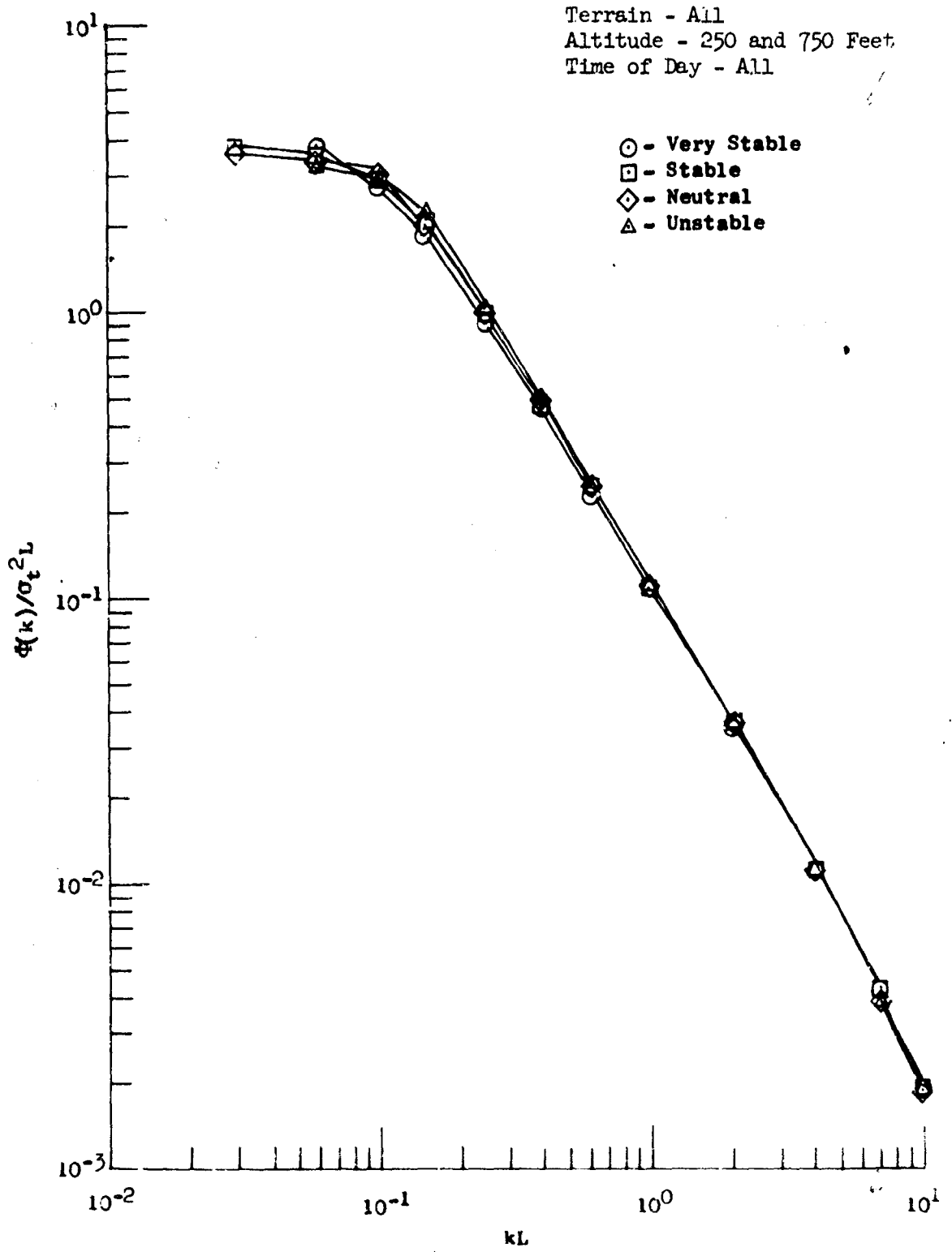


Figure 23.11 Longitudinal Power Spectrum Variation with Stability

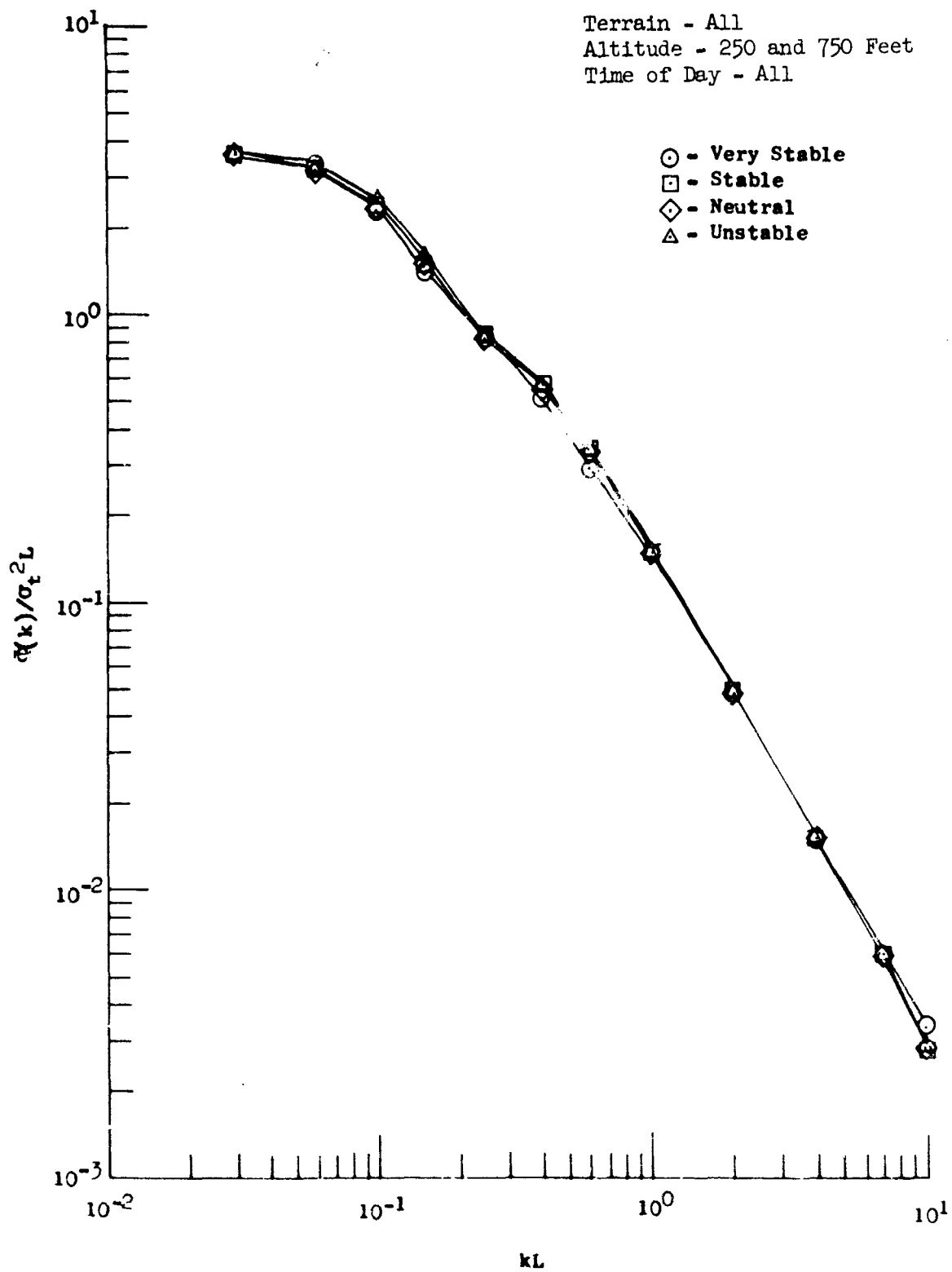


Figure 23.12 Lateral Power Spectrum Variation with Stability



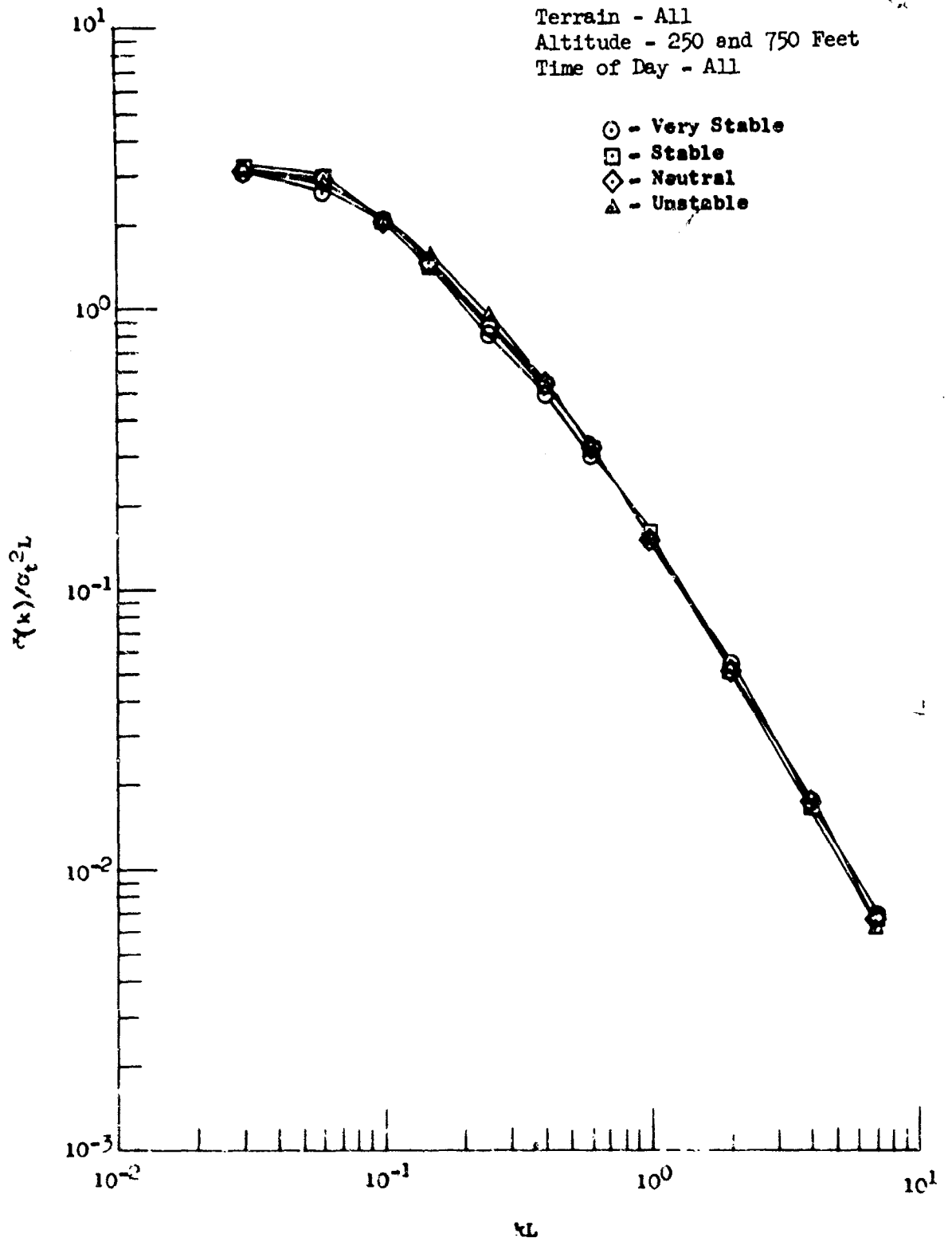


Figure 23.13 Vertical Power Spectrum Variation with Stability

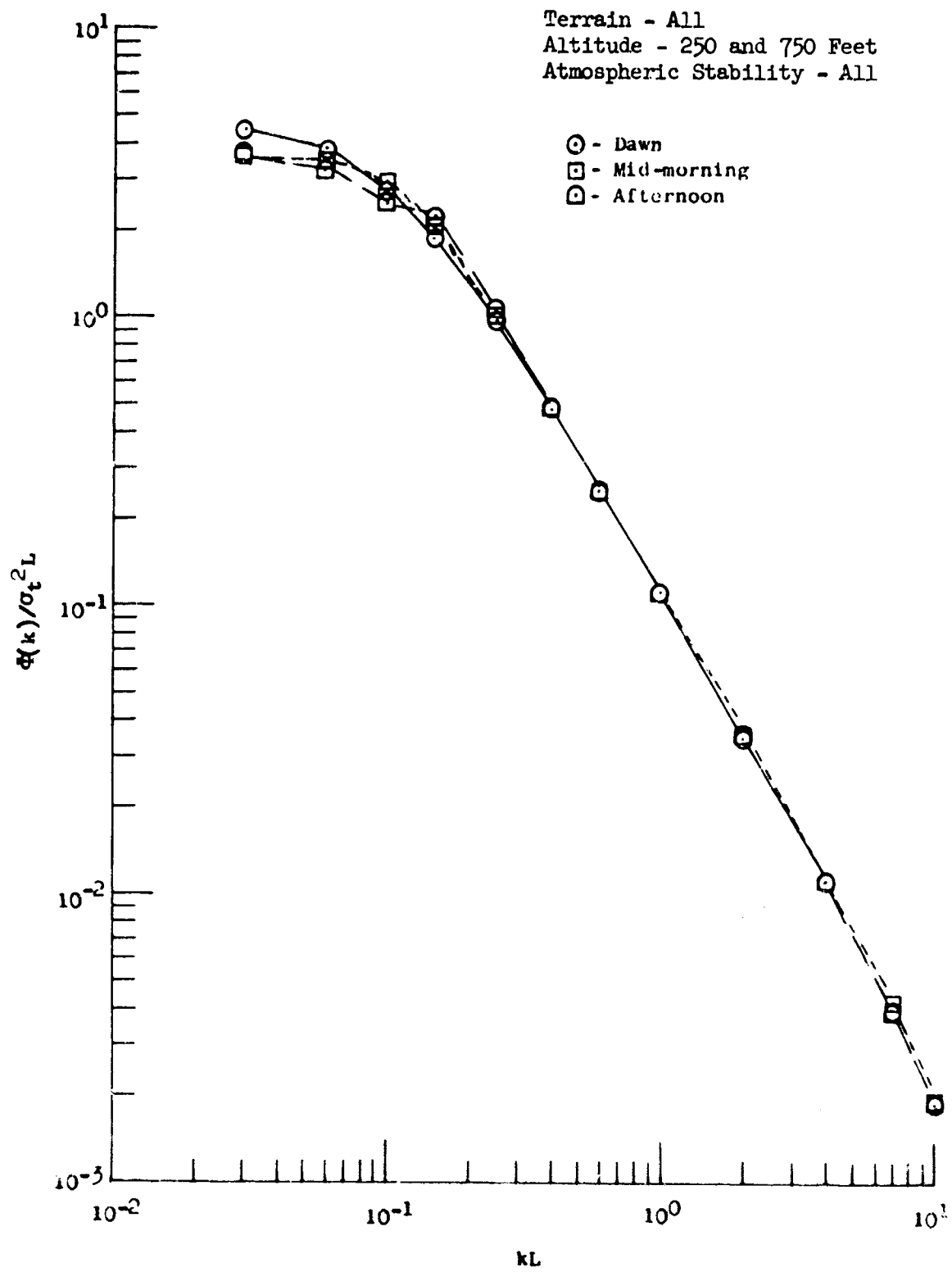


Figure 23.14 Longitudinal Power Spectrum Variation with Time of Day

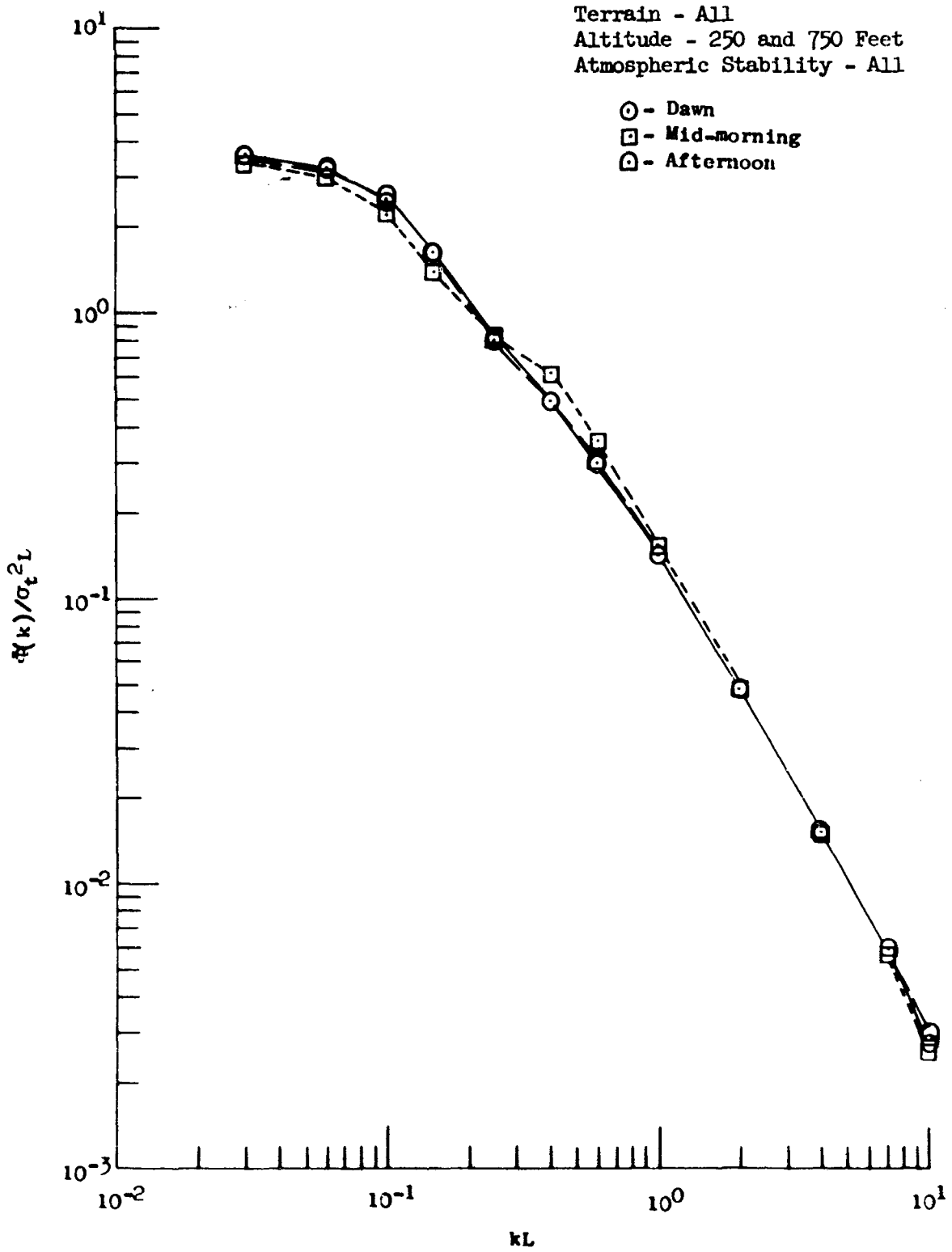


Figure 23.15 Lateral Power Spectrum Variation with Time of Day

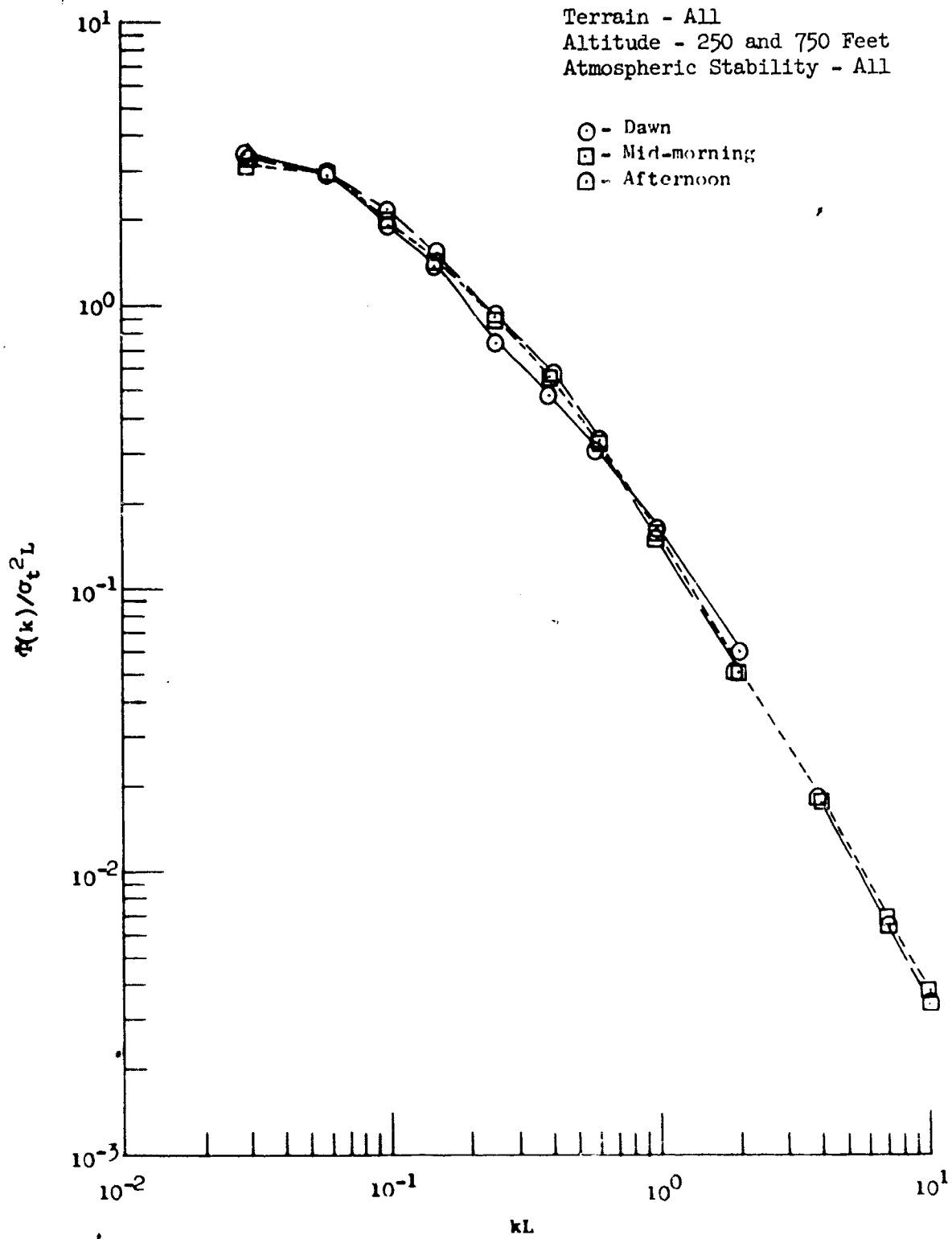


Figure 23.16 Vertical Power Spectrum Variation with Time of Day

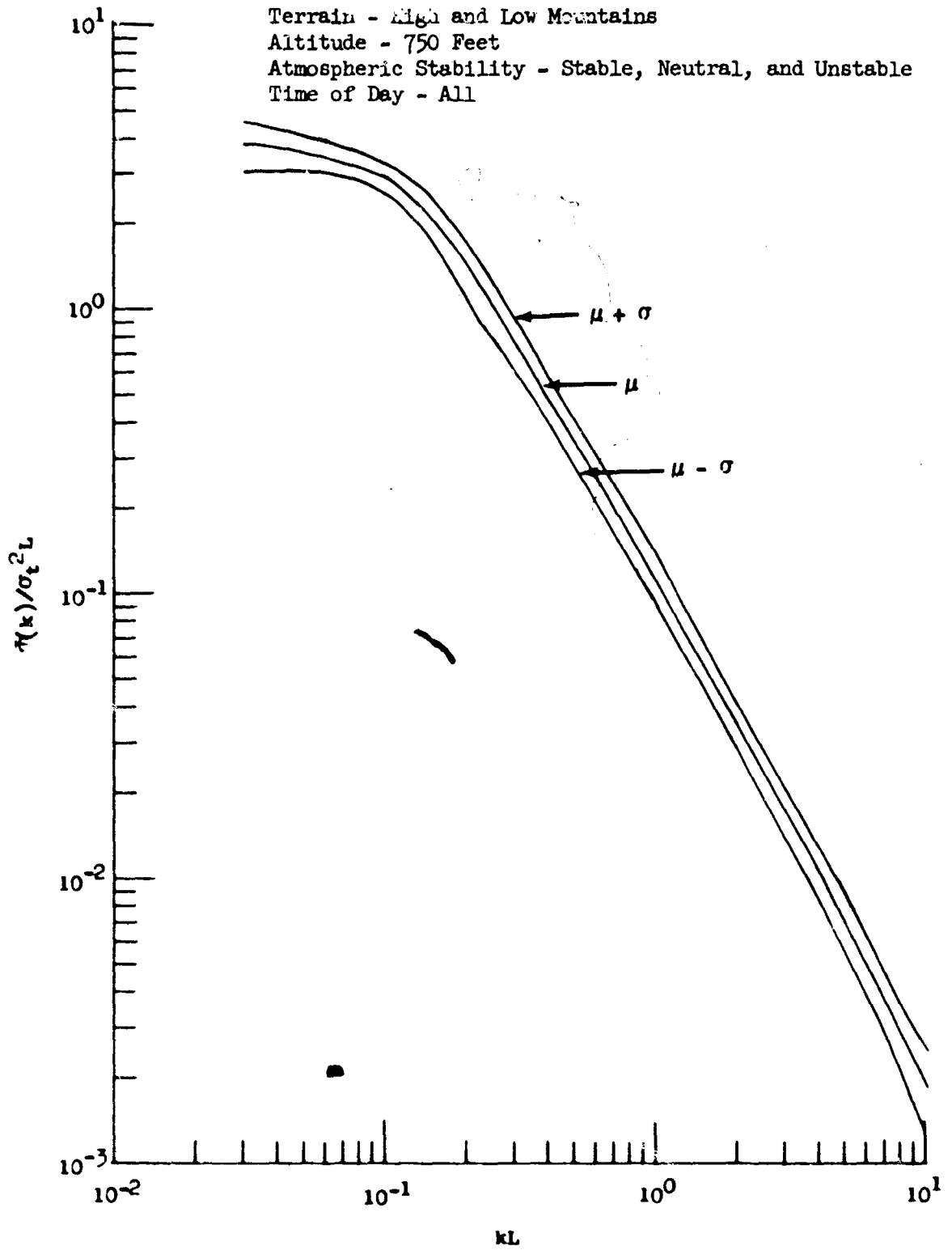


Figure 23.17 Representative Scatter Bands for Categorized Longitudinal Power Spectra

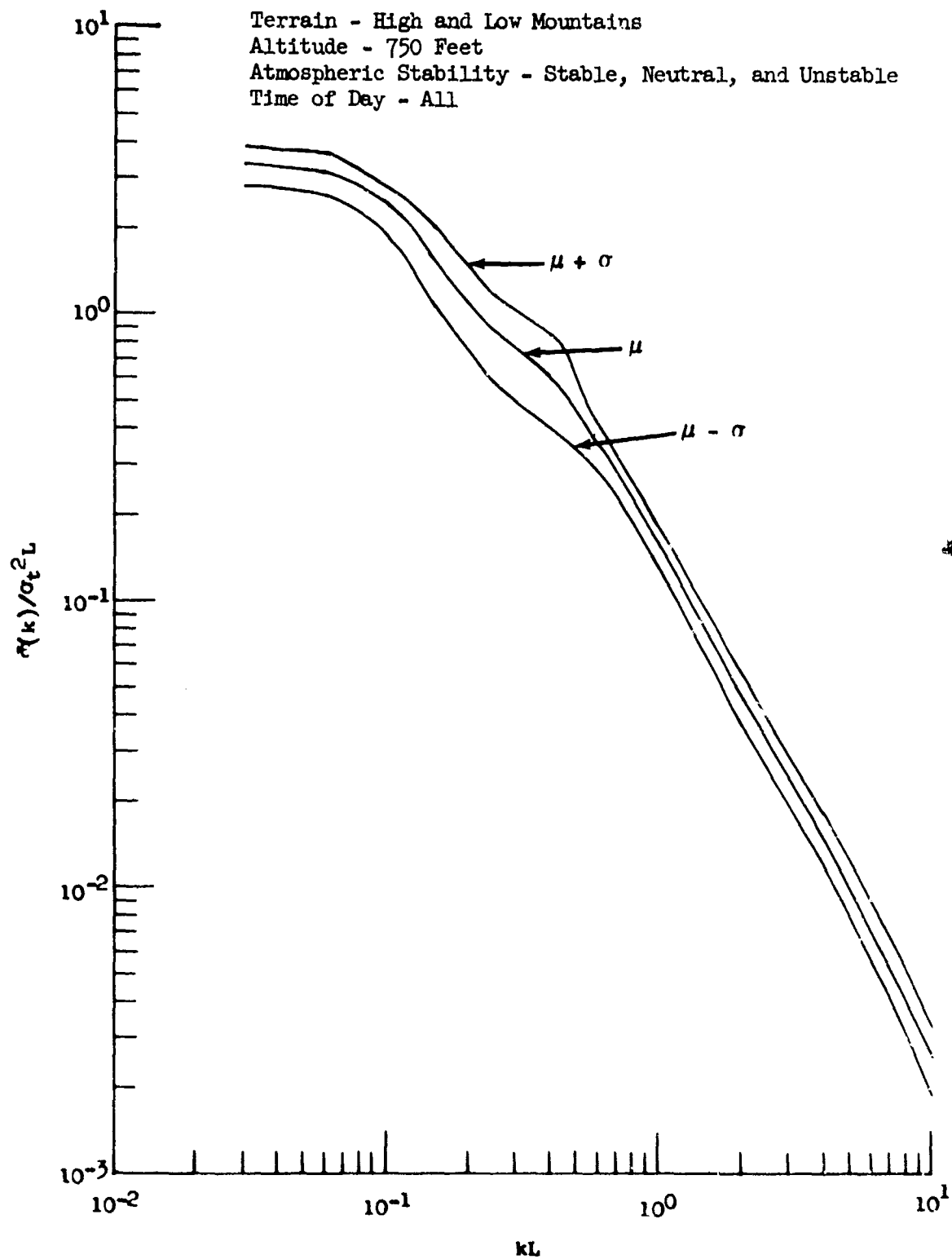


Figure 23.18 Representative Scatter Bands for Categorized Lateral Power Spectra

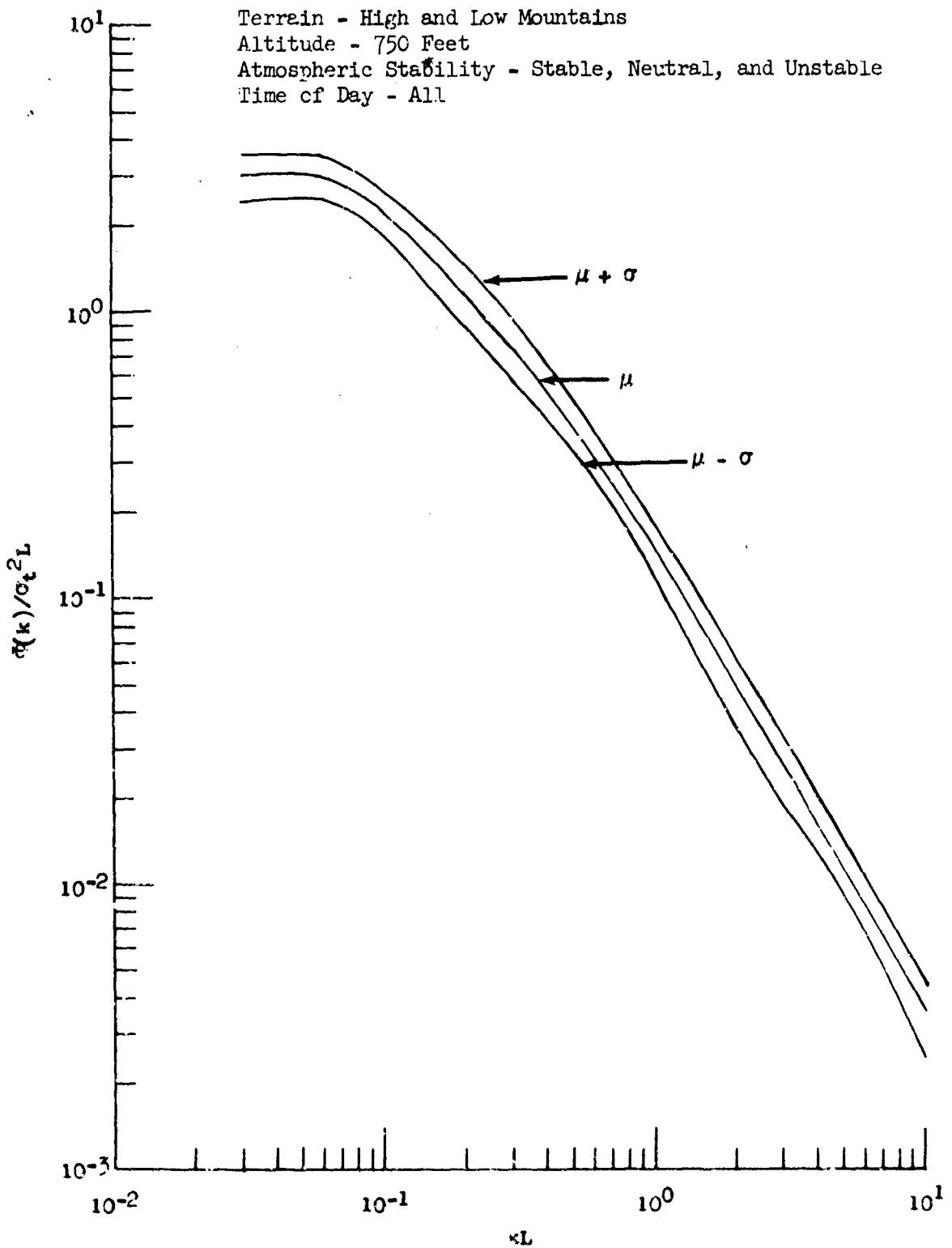


Figure 23.19 Representative Scatter Bands for Categorized Vertical Power Spectra

## 24. CROSS SPECTRA

The cross spectra of longitudinal with vertical gust velocity and longitudinal with lateral gust velocity were calculated primarily for use in the computation of coherency functions associated with the turbulence samples for which power spectra were to be calculated. A limited number of the turbulence samples were plotted in the forms of cross-spectra, cospectra and quadrature spectra in an attempt to investigate the contribution of energy from each component to the correlation between the components being analyzed and to possibly define an "isotropic limit" representing the wave number beyond which there is no significant contribution to the Reynolds stress. It is suggested in Reference 18.2 that both the energy contribution and the isotropic limit may be obtained from cross-spectrum information.

According to Reference 18.2, the longitudinal-vertical quadrature spectrum (imaginary part of the cross spectrum) will give an indication as to what part of the turbulence eddies are being passed through when gust velocities are measured. This is visualized by assuming eddies of equal wavelength arranged as shown in Figure 24.1. If these eddies are penetrated below center, the gust velocity time histories of Figure 24.2 will result. If they are penetrated above center, the time histories of Figure 24.3 result.

In direct frequency terms, the quad-spectrum can be thought of as the average product of  $u$  and  $w'$  within a narrow frequency interval divided by the interval.  $w'$  is  $w$  displaced to the left 90 degrees. Note that when  $w$  is displaced 90 degrees to the left, passing through the bottom of the eddy gives a negative quadrature power value ( $u$  and  $w'$  are out of phase), and passing through the top gives a positive value ( $u$  and  $w'$  are in phase).

Representative plots of the cross-spectra, cospectra, and quad-spectra obtained during MO-LOCAT Phase III are presented in Figures 24.4 through 24.15. Trends of the quad-spectra are shown in Figure 24.16. The trends were obtained by smoothing each longitudinal-vertical quadrature spectra (Figures 24.6, 24.9, 24.12, and 24.15). These curves were then averaged for the categories noted. All curves show the bottom of the largest eddies being sensed, on the average, as would be expected since the eddy radius is much larger than the measuring height.

More isotropy is shown at 750 feet than at 250 feet, as was found by the analysis of isotropy in Section 22. Reference 18.2 suggests an isotropic limit of 1.7 times the height. These values, 1270 and 425 feet, are shown in Figure 24.16. The curves indicate that eddies smaller than 1270 and 425 feet were sensed both above and below their centers, giving center indications on the average. The fact that the quadrature power of 750-foot data reaches the center indication at the longer wavelength and stays there with decreasing wavelength indicates that these data are more isotropic than the 250-foot data.

More isotropy is indicated over high mountains than over the plains. The quadrature spectra for plains deviates from a center indication at a shorter wavelength than the quadrature spectra for high mountains. The plains curve has a top indication, on the average, for wavelengths between 1700 and 500 feet. This indicates that wavelengths from 500 feet to at least 1700 feet were compressed in the vertical direction. Wavelengths larger than 1700 feet for all the curves were probably compressed; however, this can not be concluded from the data since 750 feet was the maximum measuring height. These results agree with those obtained during the general analysis of isotropy in Section 22.



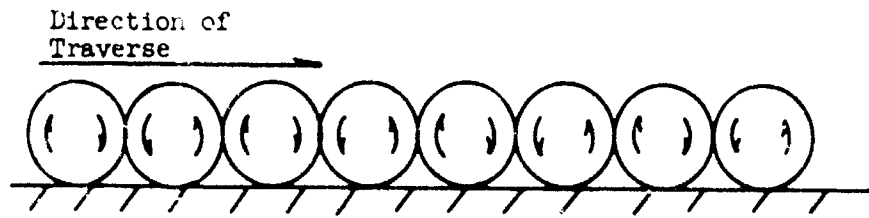


Figure 24.1 Schematic of Eddies Arranged Contiguously Next to the Ground

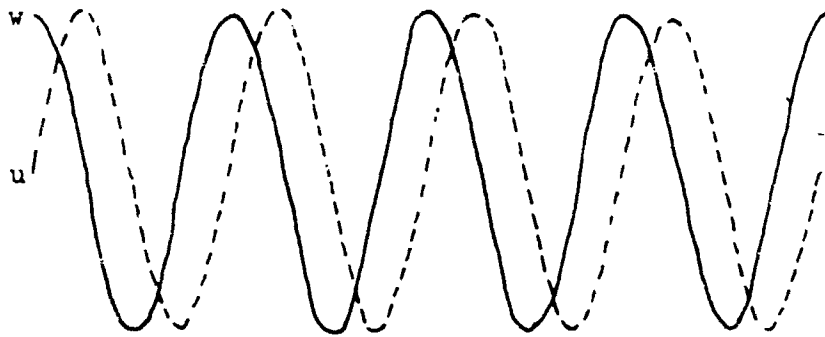


Figure 24.2 Gust Velocities Encountered when Passing Through Contiguous Eddies Below Center

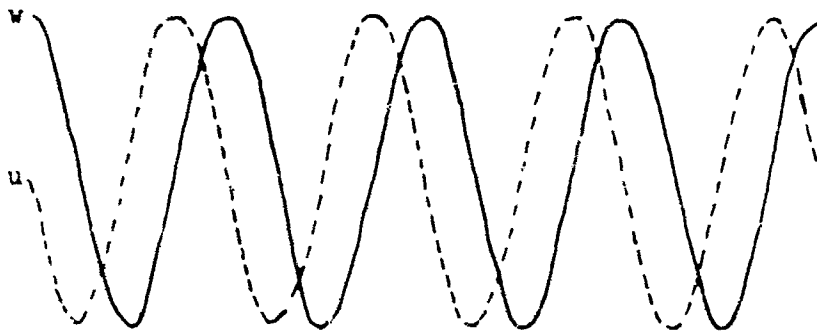


Figure 24.3 Gust Velocities Encountered when Passing Through Contiguous Eddies Above Center

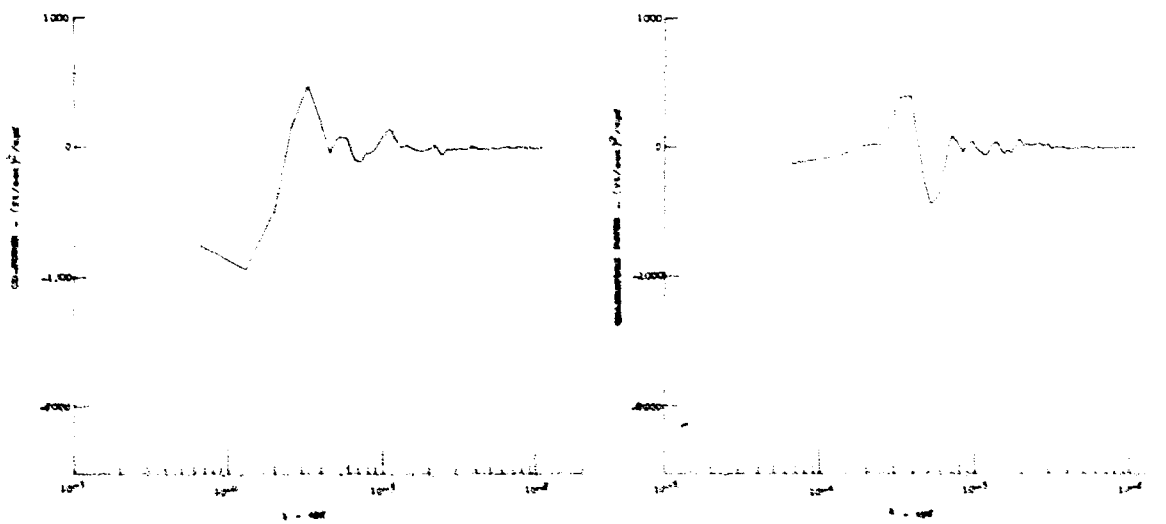
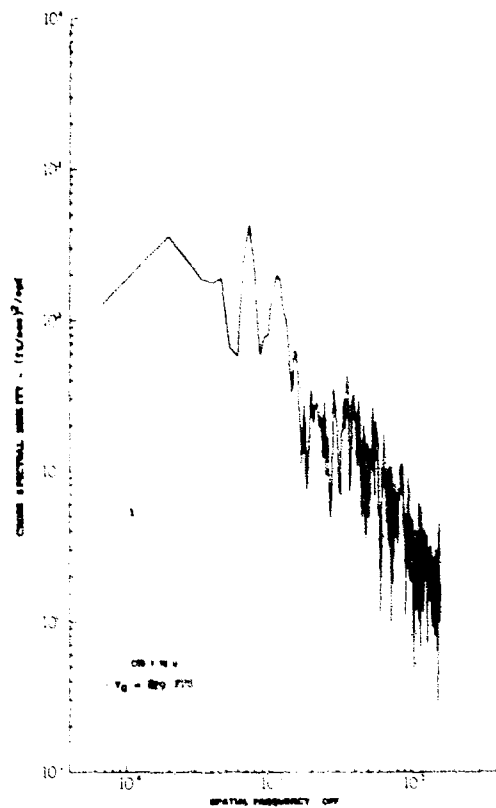


Figure 24.4 Cross, Co, and Quadrature Power Relationship  
for Lateral - Longitudinal Gust Velocity  
Test 28, Leg 6, Category 412224

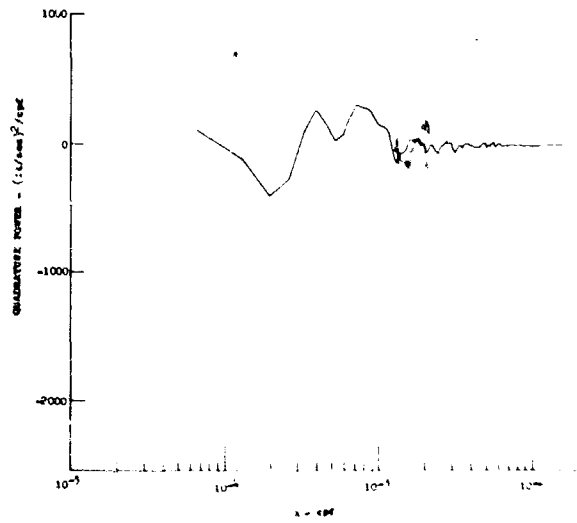
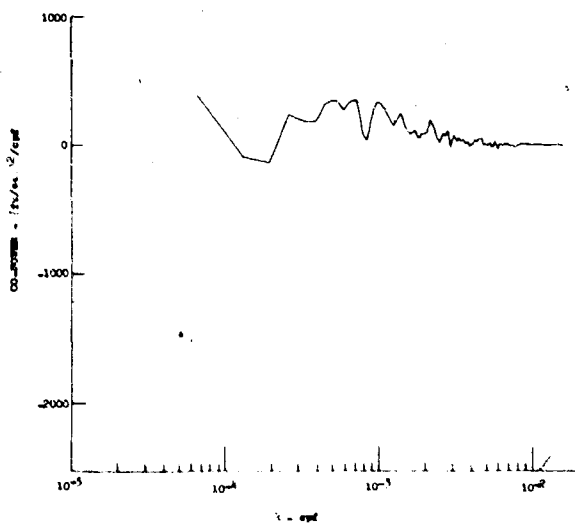
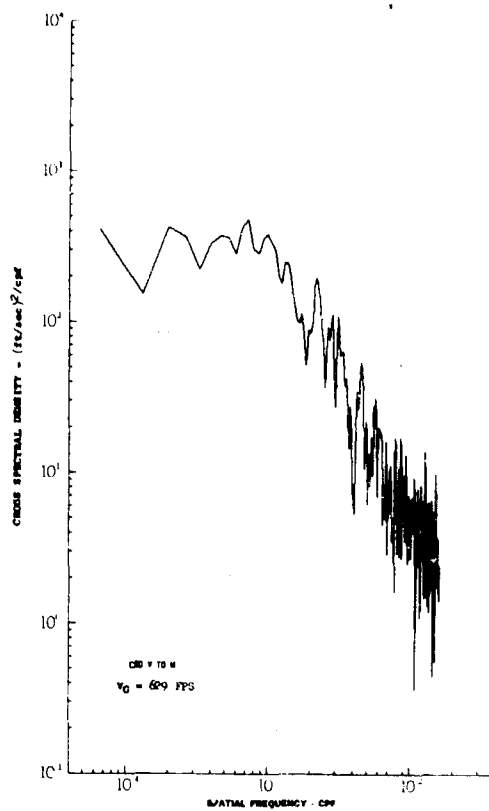


Figure 24.5 Cross, Co, and Quadrature Power Relationship for Lateral - Vertical Gust Velocity Test 28, Leg 6, Category 412224

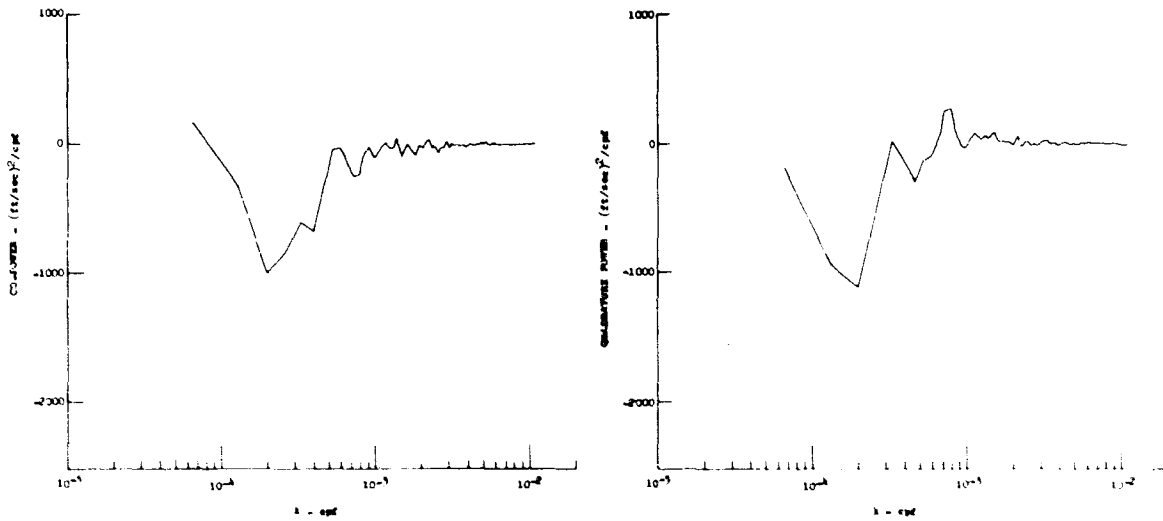
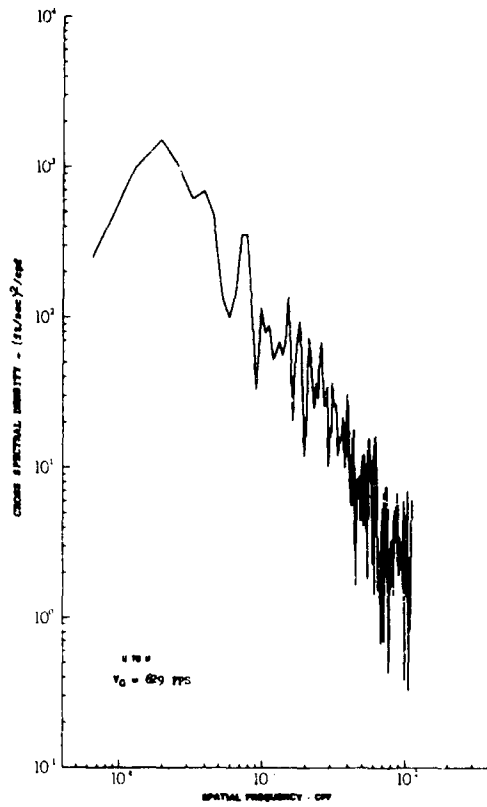


Figure 24.6 Cross, Co, and Quadrature Power Relationship for Longitudinal - Vertical Gust Velocity Test 28, Leg 6, Category 412224

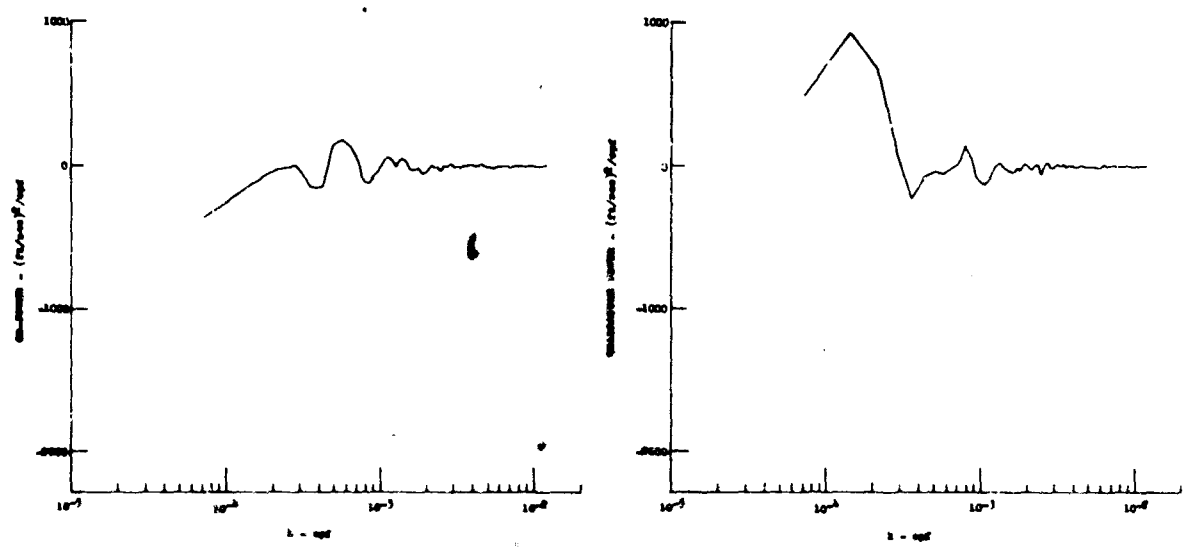
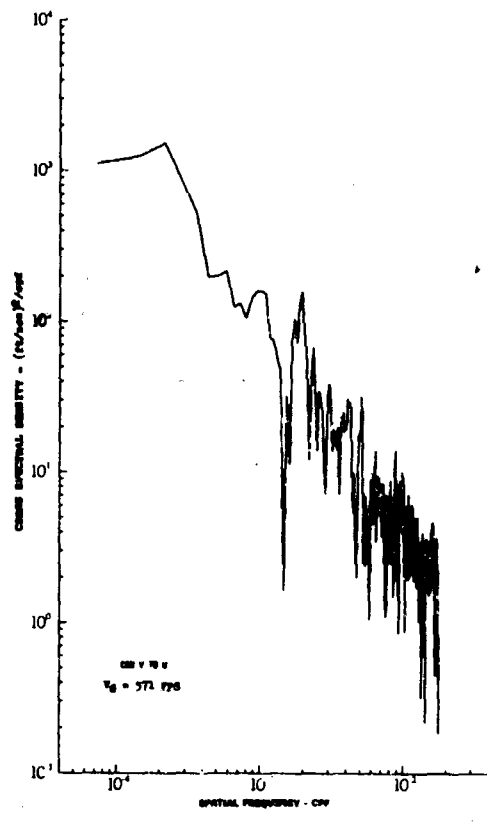


Figure 24.7 Cross, Co, and Quadrature Power Relationship for Lateral - Longitudinal Gust Velocity Test 51, Leg 3, Category 2231

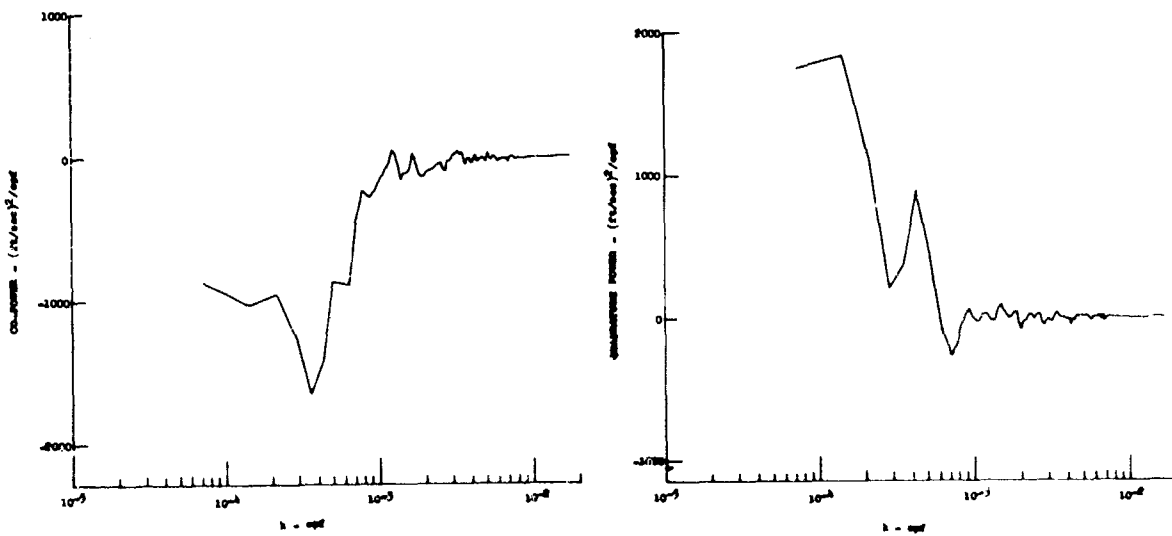
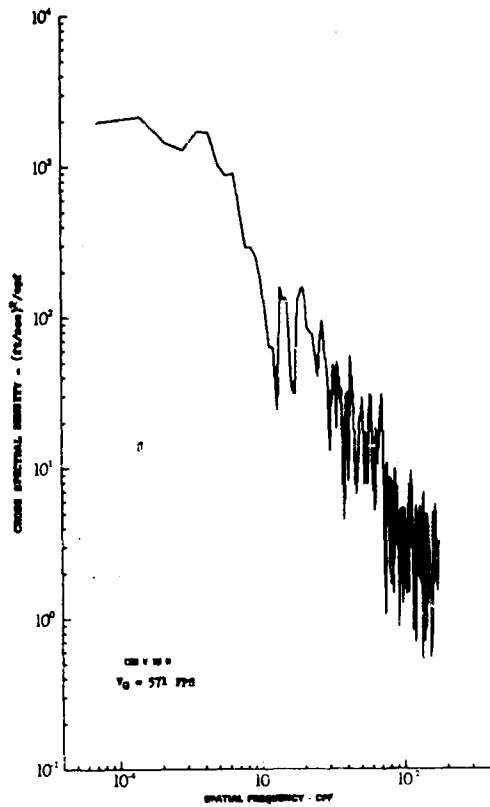


Figure 24.8 Cross, Co, and Quadrature Power Relationship for Lateral - Vertical Gust Velocity Test 51, Leg 3, Category 2231

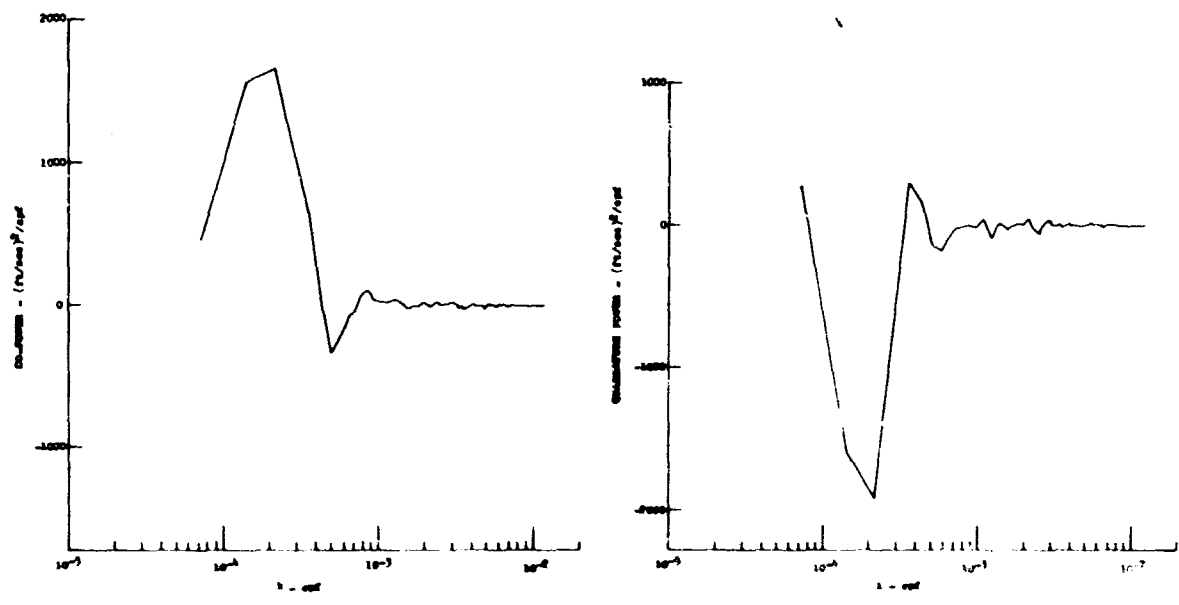
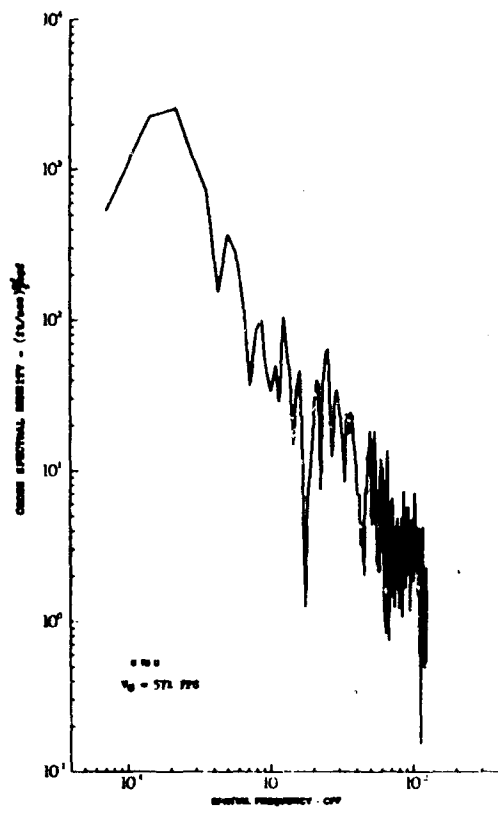


Figure 24.9 Cross, Co, and Quadrature Power Relationship for Longitudinal - Vertical Gust Velocity Test 51, Leg 3, Category 3331

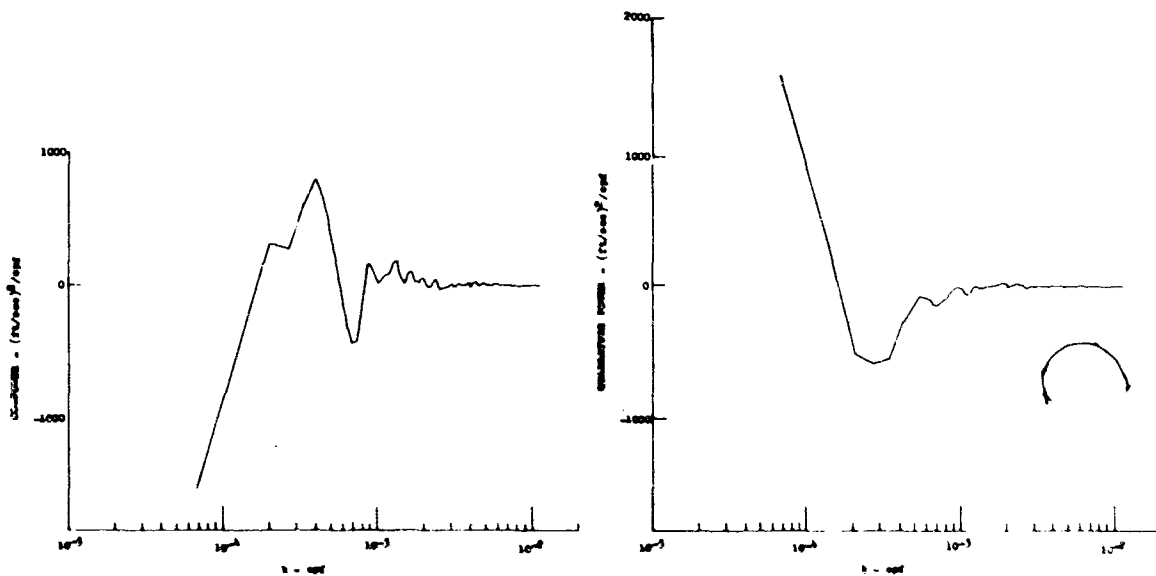
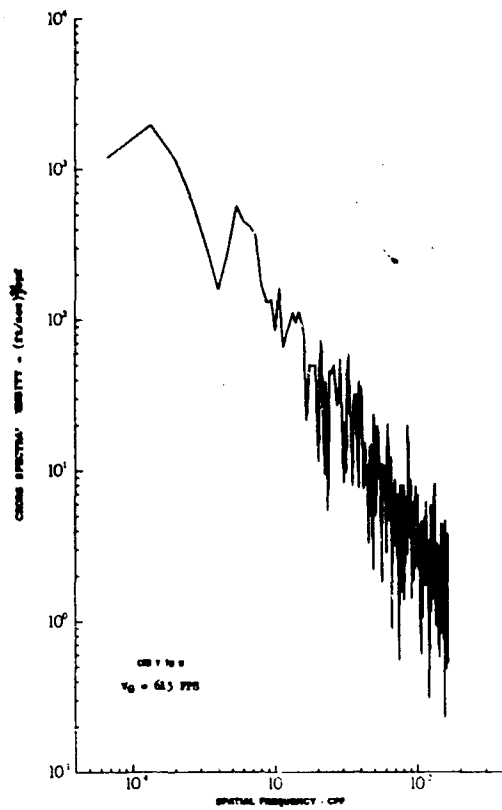


Figure 24.10 Cross, Co, and Quadrature Power Relationship  
for Lateral - Longitudinal Gust Velocity  
Test 66, Leg 2, Category 312331



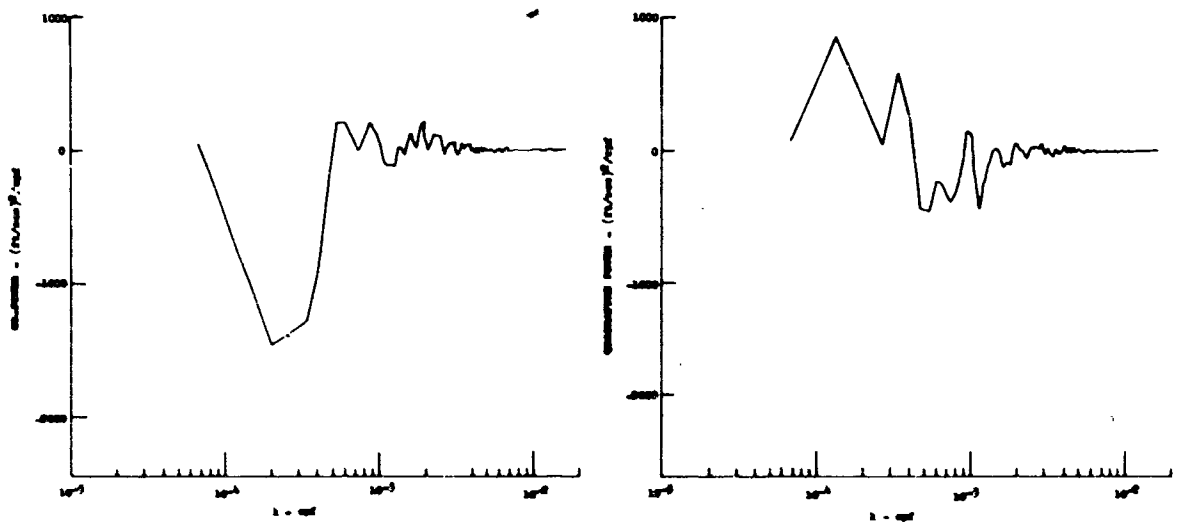
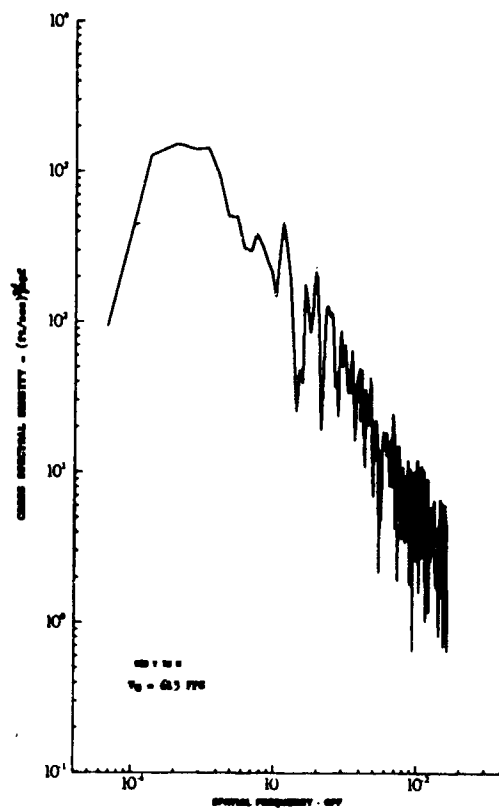


Figure 24.11 Cross, Co, and Quadrature Power Relationship for Lateral - Vertical Gust Velocity Test 66, Leg 2, Category 312331

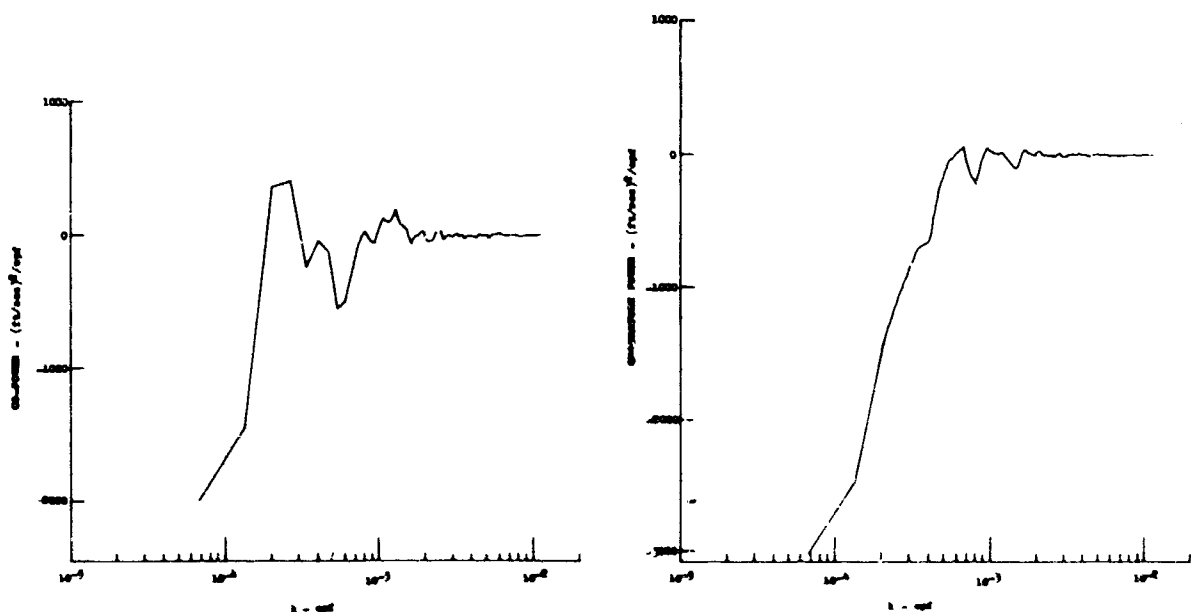
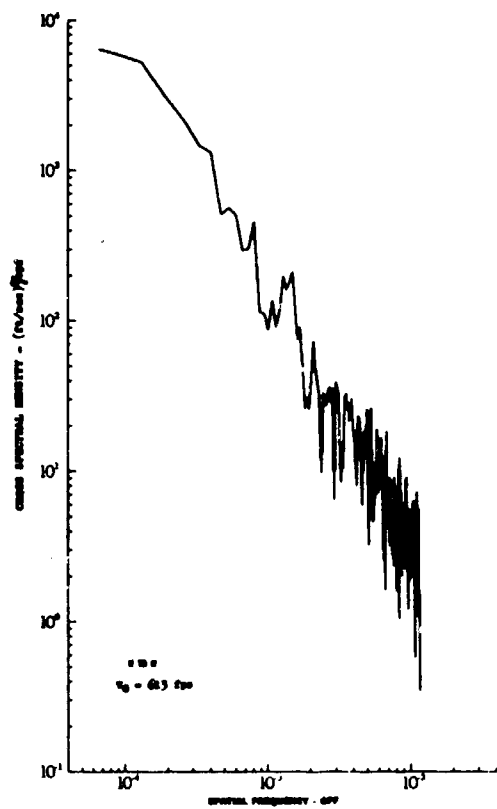


Figure 24.12 Cross, Co, and Quadrature Power Relationship for Longitudinal - Vertical Gust Velocity Test 66, Leg 2, Category 312331

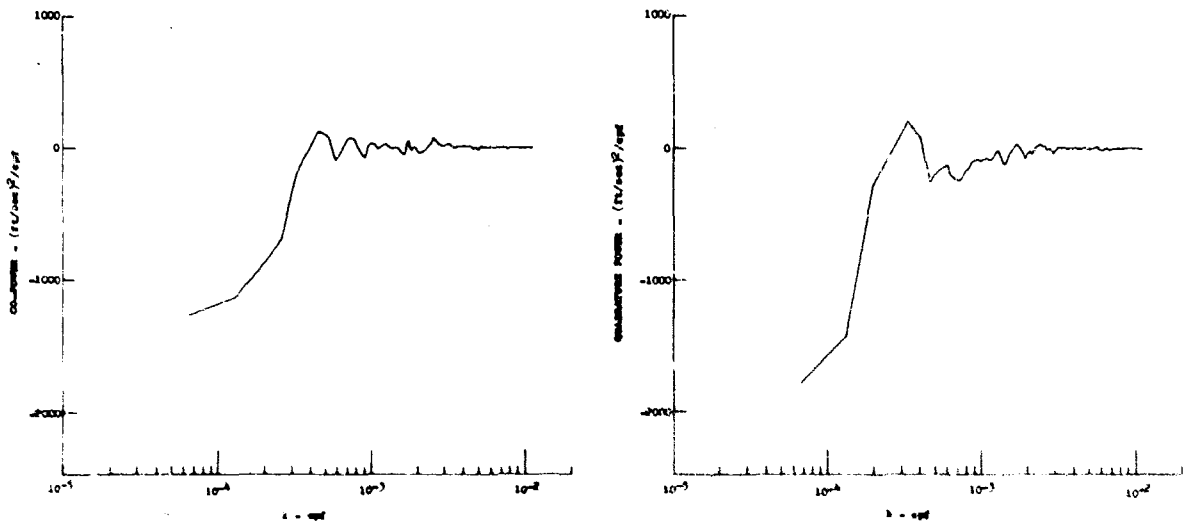
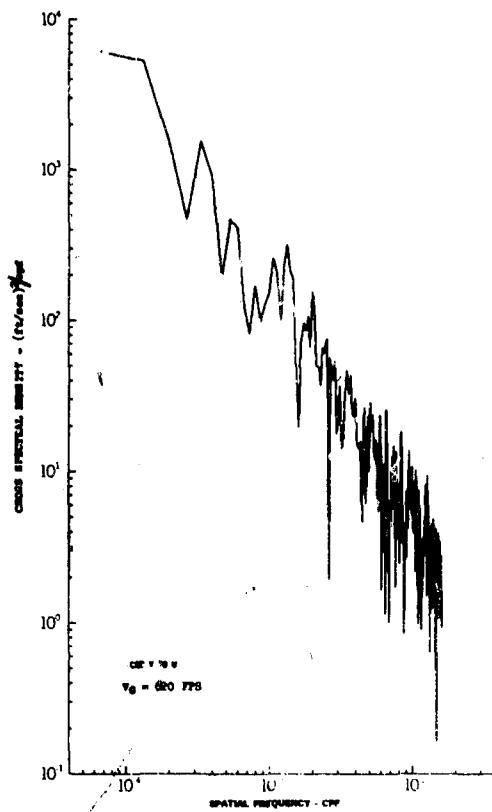


Figure 24.13 Cross, Co, and Quadrature Power Relationship  
for Lateral - Longitudinal Gust Velocity  
Test 66, Leg 6, Category 113331

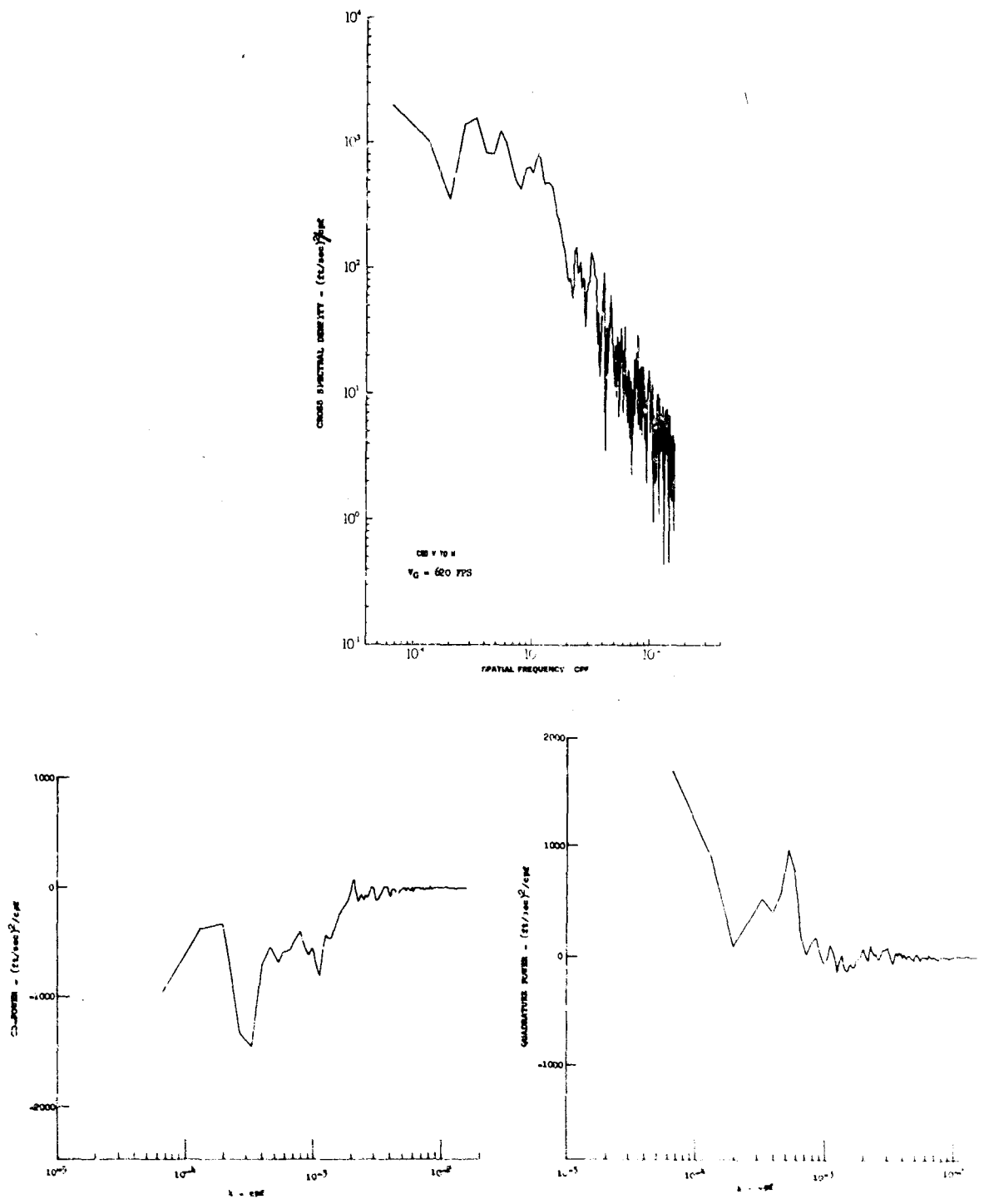


Figure 24.14 Cross, Co, and Quadrature Power Relationship for Lateral - Vertical Gust Velocity Test 66, Leg 6, Category 113331

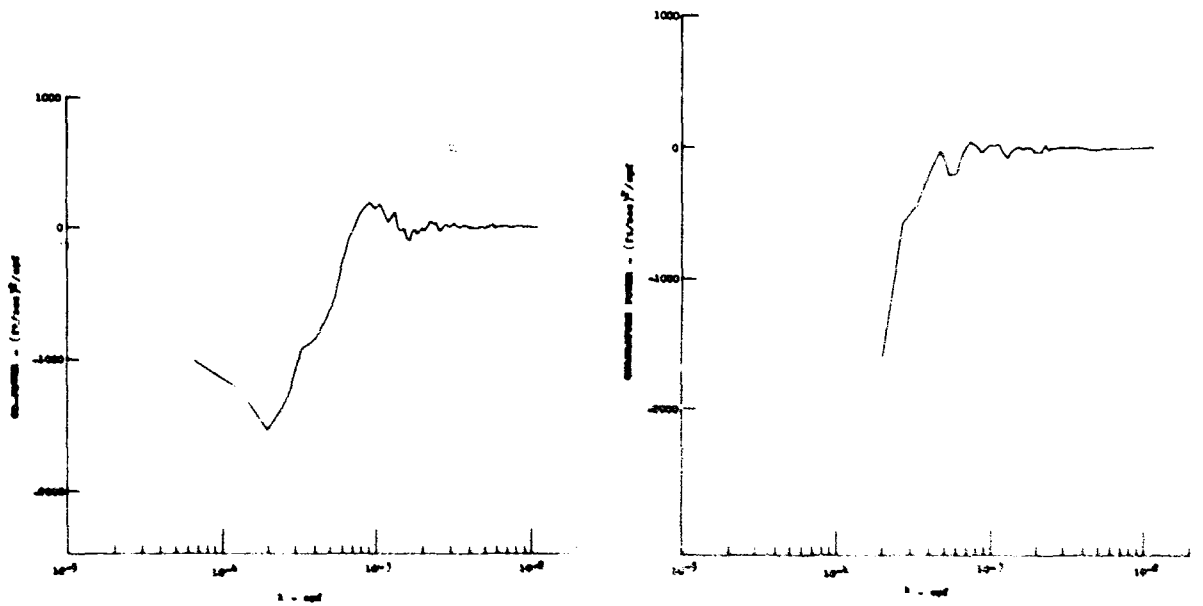
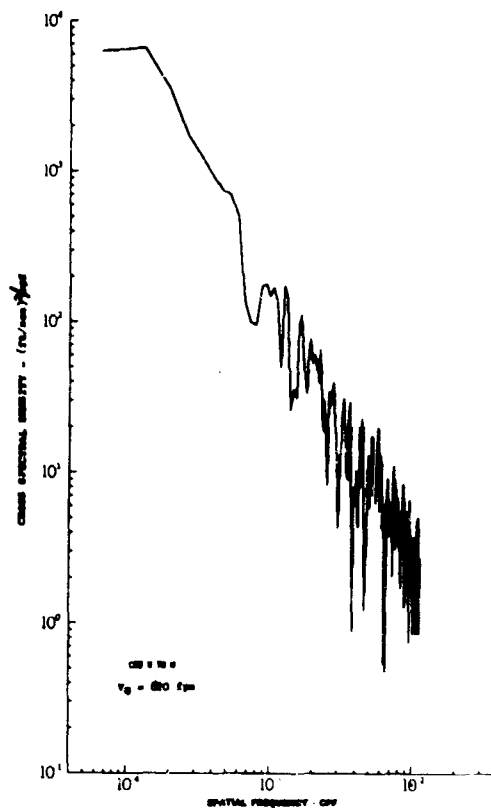


Figure 24.15 Cross, Co, and Quadrature Power Relationship for Longitudinal - Vertical Gust Velocity Test 66, Leg 6, Category 312331

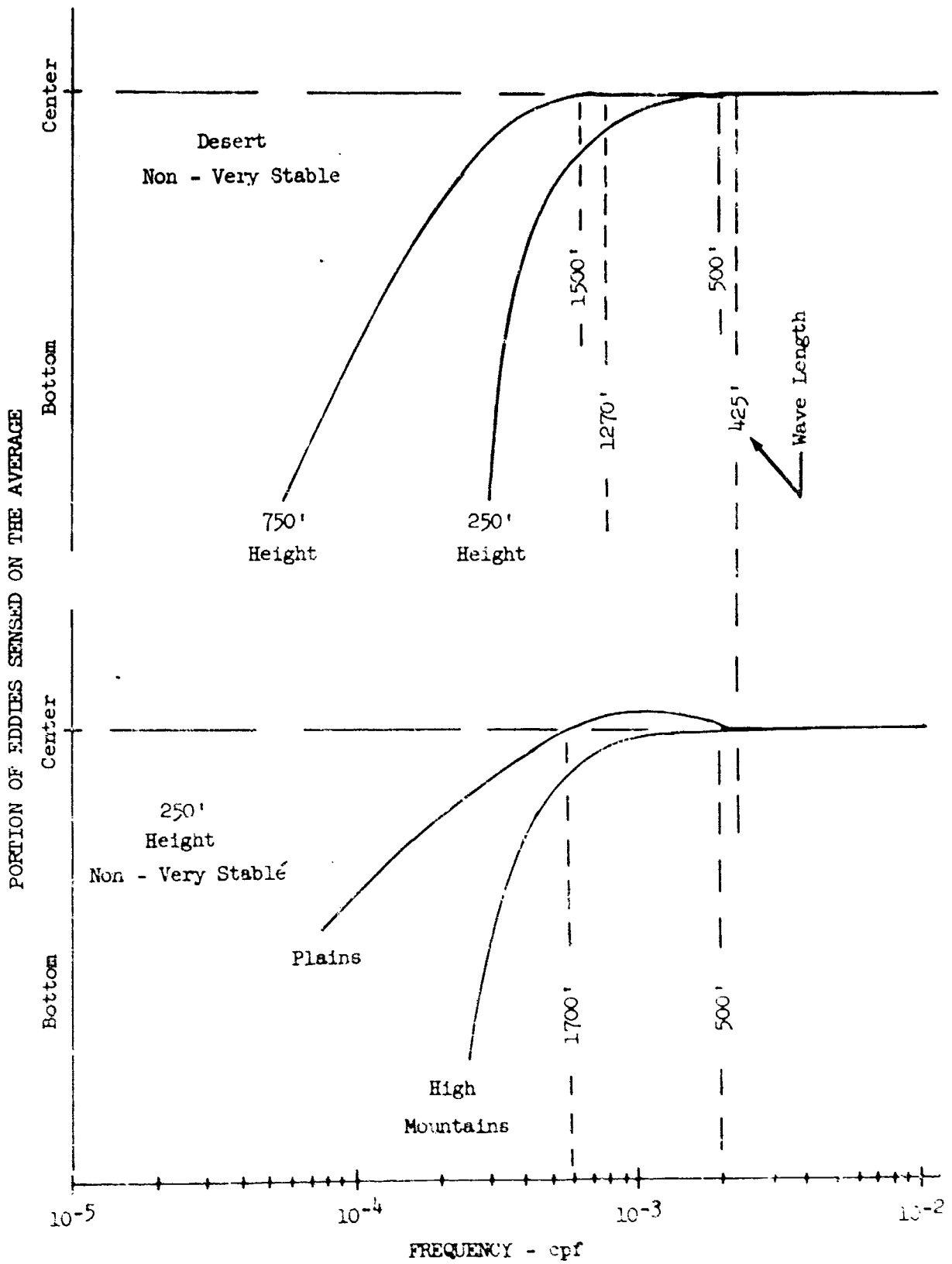


Figure 24.10 u to w Quad - Spectra Trends

## 25. TRUNCATED STANDARD DEVIATIONS

The truncated standard deviation is the square root of the area under the truncated spectrum. The lower truncation limit of the Phase III spectra in cps was increased by a factor of two over that of Phases I and II. This was done to make the lower limit in terms of spatial frequency essentially the same despite the approximate factor of two difference in speed between the Phases I and II aircraft and the Phase III aircraft.

The truncated standard deviation was calculated as follows:

Phases I and II

$$\sigma_{T_I}^2 = \int_{\frac{.33}{V_I}}^{\frac{10}{V_I}} \Phi(k) dk \quad (25.1)$$

Phase III

$$\sigma_{T_{III}}^2 = \int_{\frac{.667}{V_{III}}}^{\frac{10}{V_{III}}} \Phi(k) dk \quad (25.2)$$

where:  $V_I$  and  $V_{III}$  are the ground speeds flown during Phases I and II and during Phase III, respectively.

It should be noted that the upper limit of integration was held constant. This was not changed because the area under the truncated spectrum at the higher spatial frequencies contributes only a small amount to the total area under the spectrum. However, because of this, the truncated standard deviations obtained from samples of like categories would be expected to be slightly higher for Phases I and II than for Phase III if the speed for the Phase III category is exactly double that for the Phases I and II category.

Since the truncated standard deviation is calculated from that portion of the spectrum in the inertial subrange defined by  $\Phi(k) = Ak^{-5/3}$  and since  $V_{III} = 2V_I$ , the relationship between equation 25.1 and 25.2 can be expressed as:

$$\sigma_{T_{III}} = 0.965 \sigma_{T_I} \quad (25.3)$$

Cumulative probabilities of the truncated standard deviations from Phases I and II spectra are compared in Figures 25.1 and 25.2 to those obtained from the Phase III spectra. The low mountain and plains category data were utilized for this comparison because these data were considered to be comparable with respect to the geophysical categories for the different phases and consisted of enough samples to be considered statistically reliable. The comparisons show that, for like geophysical categories, the truncated standard deviation values obtained from Phases I and II spectra are, in most instances, equal to or slightly greater than those obtained from Phase III spectra.



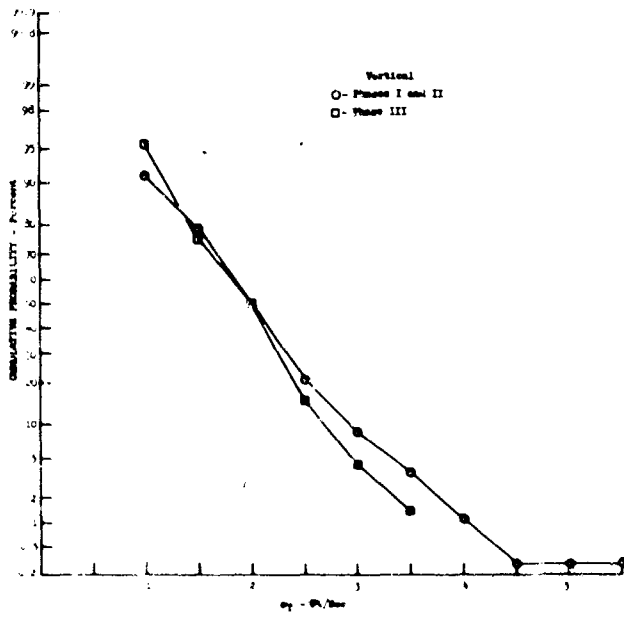
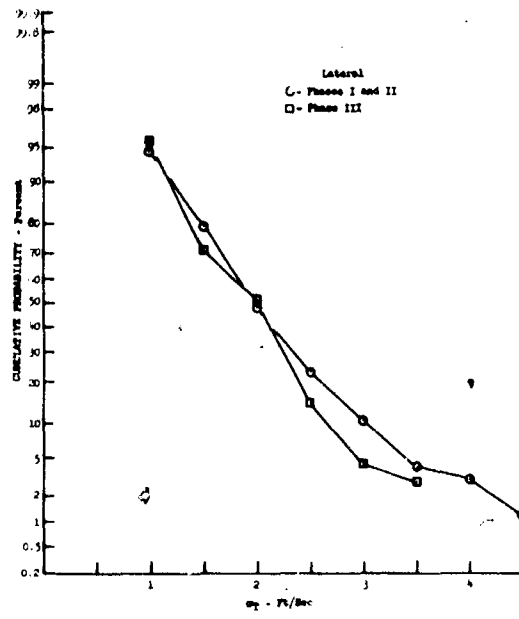
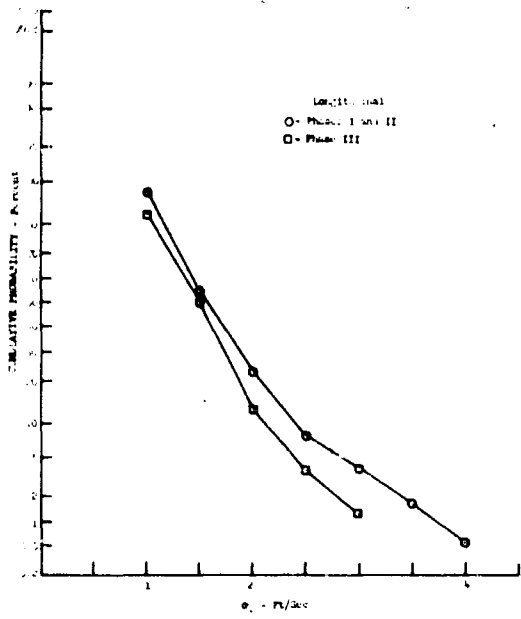


Figure 25.1 Truncated Standard Deviation Variation with Phase - Low Mountains

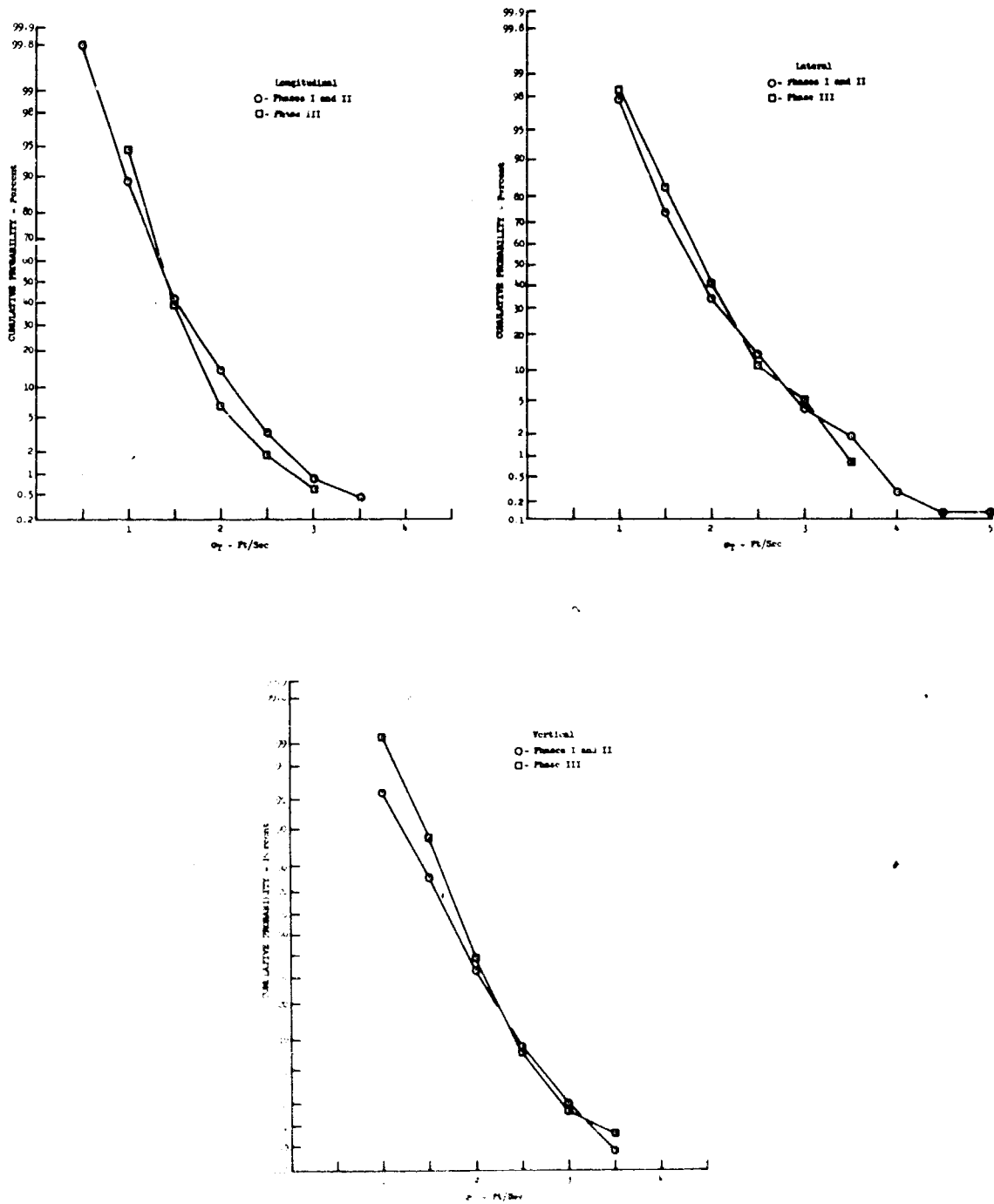


Figure 25.2 Truncated Standard Deviation Variation with Phase - Plains

## 26. GUST VELOCITY DISTANCE HISTORY POWER SPECTRA

The power spectral density of clear air turbulence defines the energy content of the turbulence at given wavelengths ( $1/k$ ). The wavelength being in terms of distance traversed over the ground per cycle of turbulence.

In relating the wavelength of the turbulence to distance traversed over the ground rather than through the air mass, a more accurate definition of the turbulence is obtained. The assumption is made, of course, that the turbulence is relatively stationary with respect to the ground and does not move with the air mass. This assumption seems valid since the type of turbulence being measured is either of a mechanical or convective nature and the turbulence generated in either case would be more stationary in relation to the ground than to the air mass.

If the turbulence is generated by wind flow over a mountain or some similar object (mechanical), the turbulence will persist until the protuberance in the wind flow corridor is eliminated or a predominant change in the prevailing wind flow occurs. In this case, the turbulence in the general vicinity of the mountain will not move with the air mass. If the turbulence is generated by convection, the turbulence will remain as long as a temperature gradient remains. Since the gradient exists due to the difference in ground and air temperature, then the turbulence must remain relatively stationary with respect to the ground.

This leads to the conclusion that turbulence properties may be defined more accurately if studied in terms of distance rather than time. Some investigators contend that if the airplane speed over the ground does not vary significantly throughout the data collection interval that one may work with the time function and subsequently convert the spectra to a function of spatial (distance) frequency. This hypothesis was proven to be true. Power spectra of each of the three components of gust velocity were calculated for four samples with the gust velocity being in terms of both time and distance. These samples were selected on the basis of having large variations in ground speed, being homogeneous, and having an adequate signal-to-noise ratio.

The power spectrum as a function of spatial frequency,  $k$ , was obtained by using the time function and calculating each spectrum in terms of frequency,  $f$ , in cps and then converting to  $k$  by dividing  $f$  by the average ground speed for the 4-1/2-minute sample. The power spectrum was also calculated on gust velocity distance history data. The gust velocity time history was converted to distance history using instantaneous ground speed values prior to spectrum calculations. The resulting spectra were in terms of spatial frequency  $k$ .

These normalized spectra for gust velocity distance history and time history data are compared in Figures 26.1 through 26.4. The turbulence samples cover a gust velocity rms range from 2.64 to 3.55 fps with scale lengths varying from 199 to 659 feet. The pertinent data, along with the maximum speed change during each sample, ( $\Delta V$ ), is presented in Table 26.1.

As can be seen from the spectra comparisons in Figures 26.1 through 26.4, there is essentially no difference in the spectra even for a sample having a  $\Delta V = 106$  fps. It should be noted, however, that this is the maximum change and for this particular case was encountered over a 90-second time interval while contour flying over the mountains.

Although scale lengths were not calculated using the distance histories, the normalized spectra practically overlay, and therefore, the scale lengths would not differ. This good agreement indicates that the use of average speeds for the calculations of  $k$  is justified.

TABLE 26.1

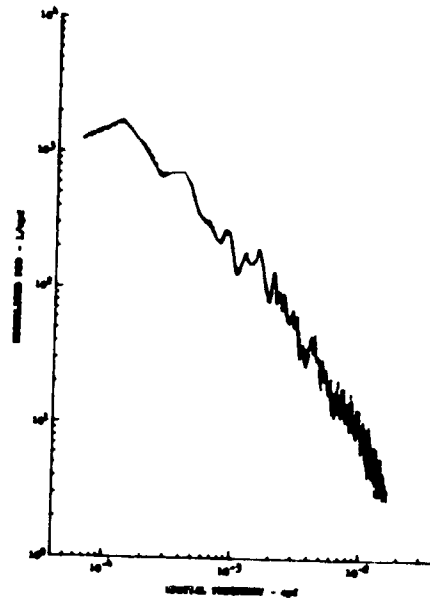
COMPARISON OF DISTANCE HISTORY AND  
TIME HISTORY STANDARD DEVIATIONS

Test	Leg	$\bar{G}_s$ (fps)	$\Delta V$ (max) (fps)	Standard Deviation - fps			Scale Length $L_k$ (ft)
				Variable	Time History	Distance History	
40	4	643	32.1	u	3.18	3.17	644
				v	2.74	2.72	342
				w	2.76	2.74	262
46	4	597	57.6	u	3.56	3.55	658
				v	3.21	3.19	359
				w	3.01	2.99	263
46	6	589	61.7	u	3.24	3.21	442
				v	2.76	2.74	239
				w	2.67	2.64	199
87	7	616	106.1	u	2.72	2.72	614
				v	2.78	2.78	602
				w	3.44	3.44	659

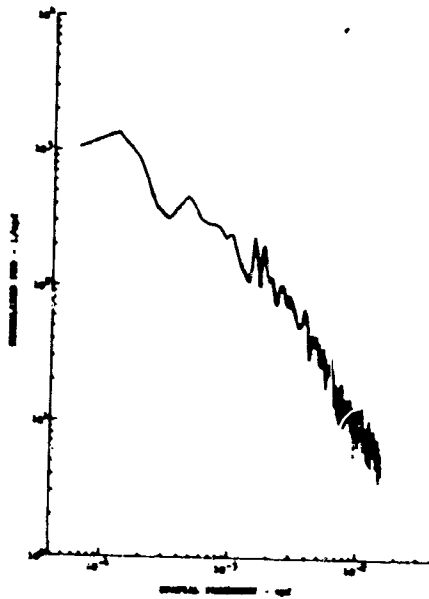
Longitudinal



Lateral



Vertical



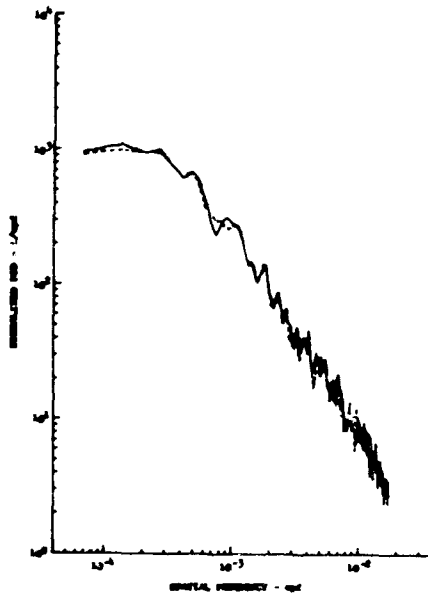
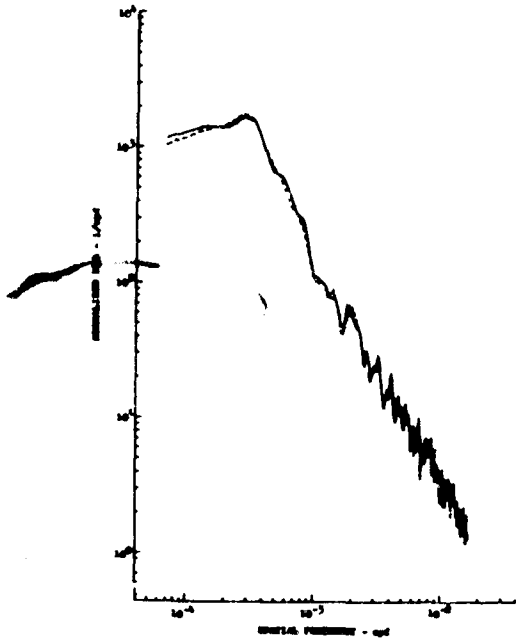
Var	Standard Deviation - fps		L <sub>k</sub> (ft)
	Time History	Distance History	
u	3.18	3.17	644
v	2.74	2.72	342
w	2.76	2.74	262

- - - Distance History  
 — Time History

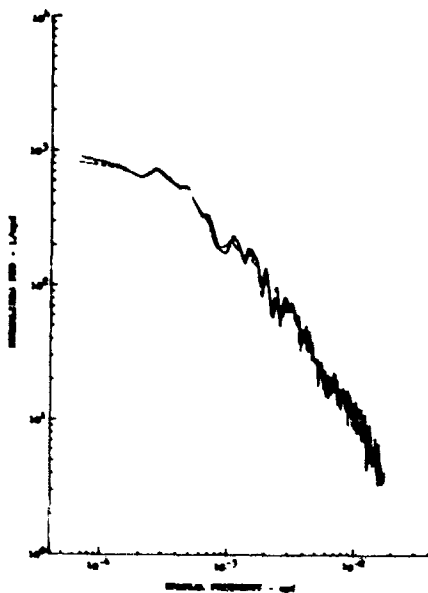
Figure 26.1 Time History-Distance History Power Spectra Comparison  
Test 40 Leg 4

Longitudinal

Lateral



Vertical



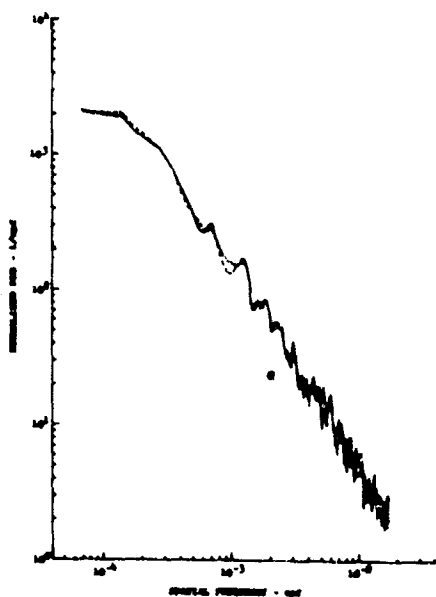
Var	Standard Deviation - fps		Lk (ft)
	Time History	Distance History	
u	3.56	3.55	658
v	3.21	3.19	359
w	3.01	2.99	263

--- Distance History

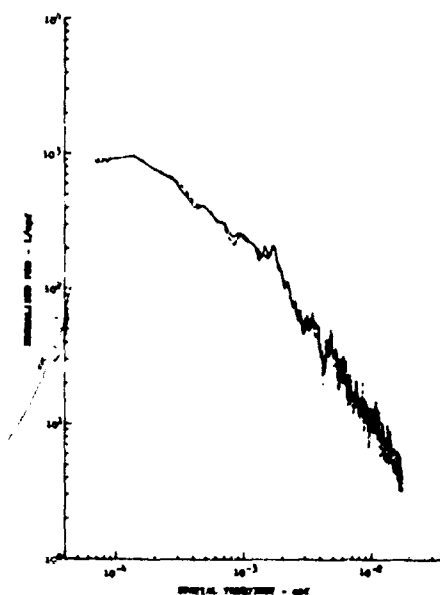
— Time History

Figure 26.2 Time History-Distance History Power Spectra Comparison  
Test 46 Leg 4

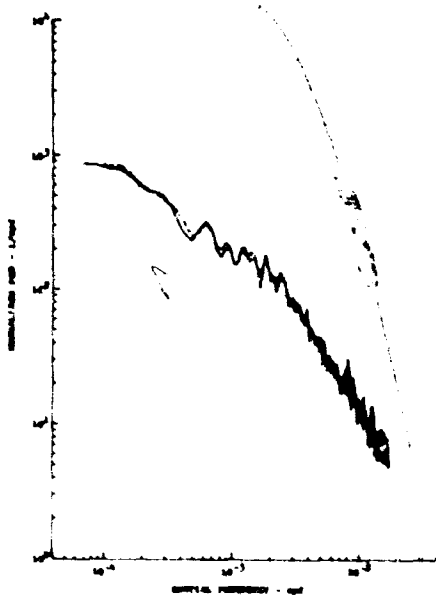
Longitudinal



Lateral



Vertical



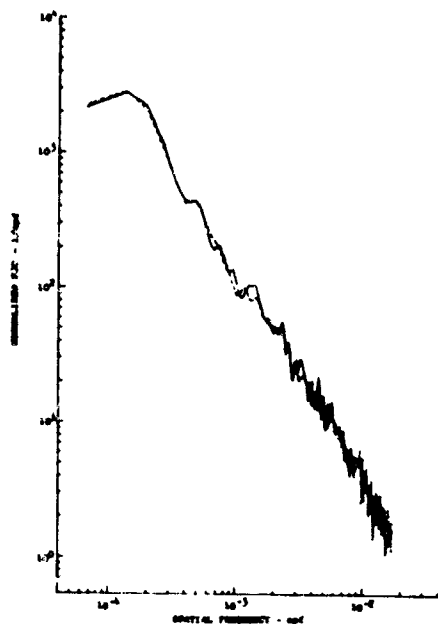
Var	Standard Deviation - fps		Lx (ft)
	Time History	Distance History	
u	3.24	3.21	442
v	2.76	2.74	239
w	2.67	2.64	199

--- Distance History

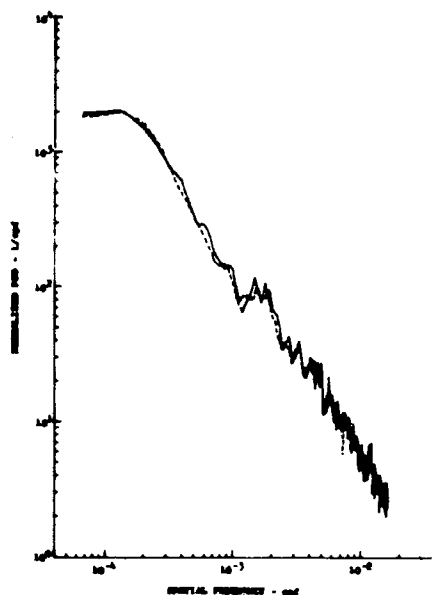
— Time History

Figure 26.3 Time History-Distance History Power Spectra Comparison  
Test 46 Leg 6

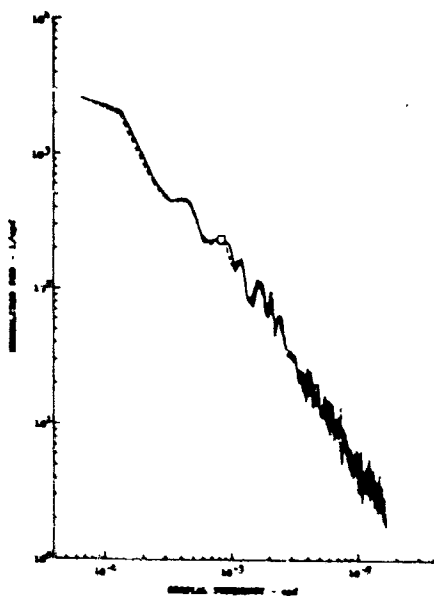
Longitudinal



Lateral



Vertical



Var	Standard Deviation - fps		Lk (ft)
	Time History	Distance History	
u	2.72	2.72	614
v	2.78	2.78	602
w	3.44	3.44	659

--- Distance History  
 — Time History

Figure 26.4 Time History-Distance History Power Spectra Comparison  
Test 87 Leg 7



## 27. SPECTRA DURING HIGH SPEED FLIGHT

One objective of the Phase III Program was to define low altitude turbulence to wavelengths in excess of 21,500 feet for a limited number of turbulence samples recorded while flying at the maximum speed. The airplane maximum speed, however, was lower than originally expected and the maximum wavelength measured was therefore only 18,000 feet. The maximum average wavelength for Phase III is approximately 15,000 feet, whereas it is 16,700 feet for the turbulence samples recorded at high speed. The lower maximum speed is attributed to an increase in the airplane drag characteristics caused by the installation of externally mounted instrumentation.

A total of 54 turbulence samples, during which the ground speed was equal to or greater than 675 fps, were selected for analysis. These samples were obtained over Leg 8 at both the McConnell and Peterson routes using maximum engine thrust. These legs were selected to give maximum flight safety.

Twenty-nine of the 54 selected samples exhibited the necessary homogeneity characteristics required for a valid analysis. The time series rms values and scale lengths for these data are presented in Table 27.1. The average rms values are 3.69, 3.75, and 3.30 fps for u, v, and w, respectively. The corresponding average scale lengths are 782, 502, and 362 feet. These values are in general agreement with the rest of the Phase III data recorded over the plains.

The resulting normalized spectra and isotropy and coherency characteristics are presented in Figures 27.1 through 27.3. These data agree in general with the rest of the Phase III data. Lateral gust velocity spectrum values obtained at high speed are compared in Figure 27.1 to the normalized spectrum obtained at 250 feet above the plains and desert terrain. The spectrum for 250 feet was used since a high percentage (76%) of the high speed samples were obtained at 250 feet.

These high speed samples were included with the lower speed samples for statistical analyses discussed elsewhere in this report.

TABLE 27.1

TURBULENCE SAMPLES RECORDED AT HIGH SPEED

Test No.	Leg No.	Category No.	Maximum Wavelength $\lambda$ (feet)	$\sigma_x$ (fus)			$L_k$ (feet)		
				u	v	w	u	v	w
24	8	414324	16200	3.99	4.22	3.19	695	636	239
32	8	424324	16400	3.29	3.08	3.38	1118	531	718
40	8	412234	17100	2.07	2.31	2.50	308	335	353
46	8	412234	16800	2.46	3.14	2.68	480	400	294
161	8	414343	16900	3.00	2.76	2.59	640	435	285
162	8	422143	16600	2.98	3.18	--	767	750	--
163	8	424243	16500	4.07	5.53	4.02	546	895	375
166	8	411243	16300	2.94	2.04	--	1191	321	--
170	8	411143	16900	3.15	--	--	267	--	--
171	8	414243	17000	5.35	5.37	4.33	850	467	336
172	8	413343	17300	4.55	4.80	--	722	701	--
185	8	414343	16200	3.72	3.51	3.36	796	419	269
187	8	423243	16500	2.47	2.85	2.20	777	673	452
188	8	423343	16300	3.49	3.65	3.61	964	687	547
190	8	413343	16600	4.51	5.37	--	649	768	--
209	8	424243	16500	2.87	2.58	2.54	1078	483	469
211	8	412143	16900	3.02	3.37	2.67	251	216	231
212	8	414243	17100	5.80	5.71	4.64	838	470	318
213	8	413343	16500	5.51	4.99	3.85	861	338	244
220	8	413313	16500	4.09	3.59	3.41	1180	382	381
224	8	413213	16600	3.23	3.34	3.29	489	356	300
225	8	414313	16700	5.53	5.58	3.93	1218	766	331
230	8	412213	16600	2.85	2.69	2.55	592	328	238
231	8	414313	16500	4.65	3.92	2.88	1547	612	327
233	8	423213	16800	4.26	4.47	4.57	968	639	664
236	8	413213	16300	3.15	2.86	3.31	664	257	346
241	8	413213	17500	3.35	3.31	3.36	693	374	300
246	8	414213	17400	3.35	3.57	3.03	797	473	316
255	8	413213	16500	3.48	3.38	3.35	729	351	362

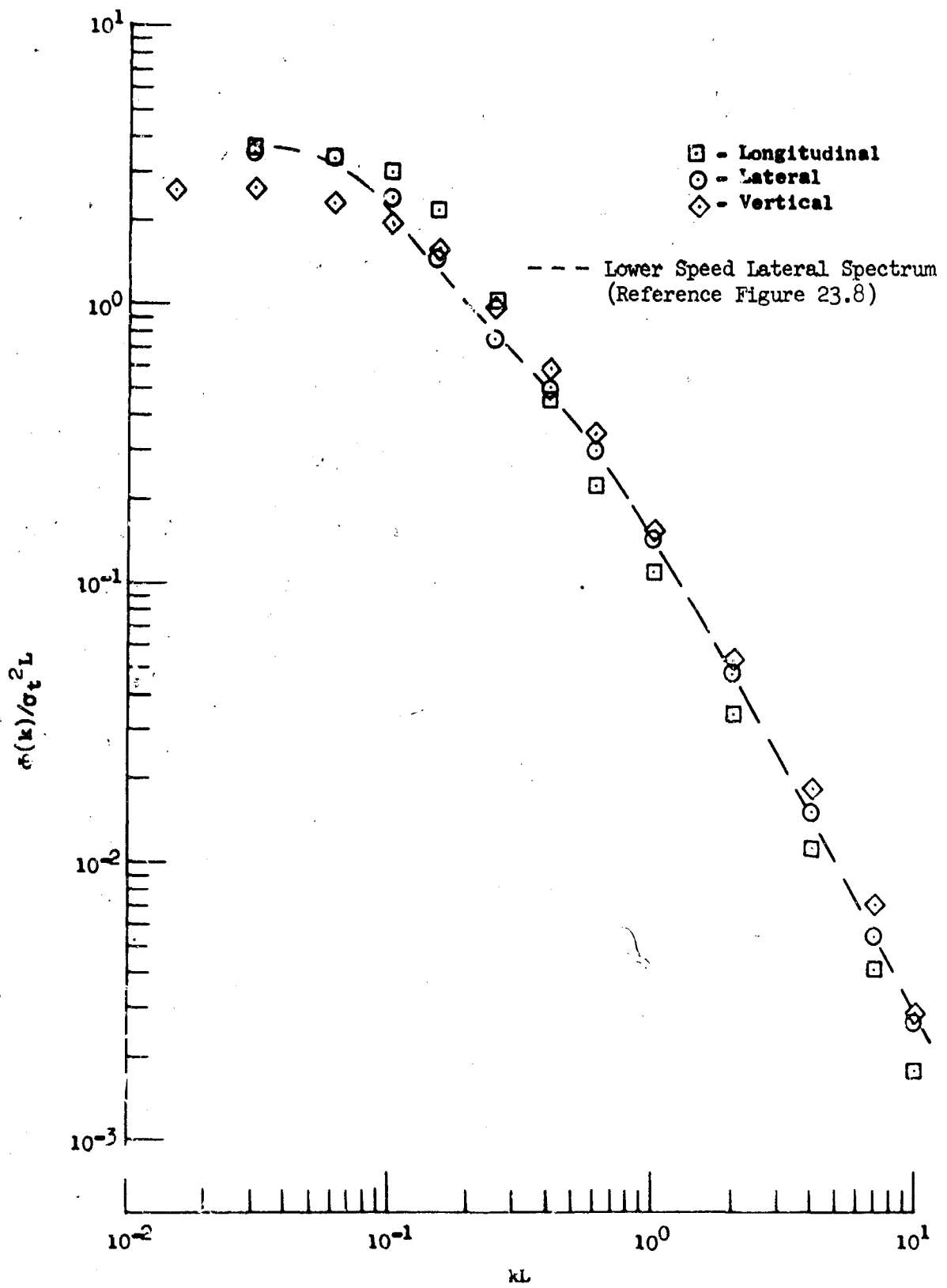


Figure 27.1 High Speed Flight Gust Velocity Power Spectra

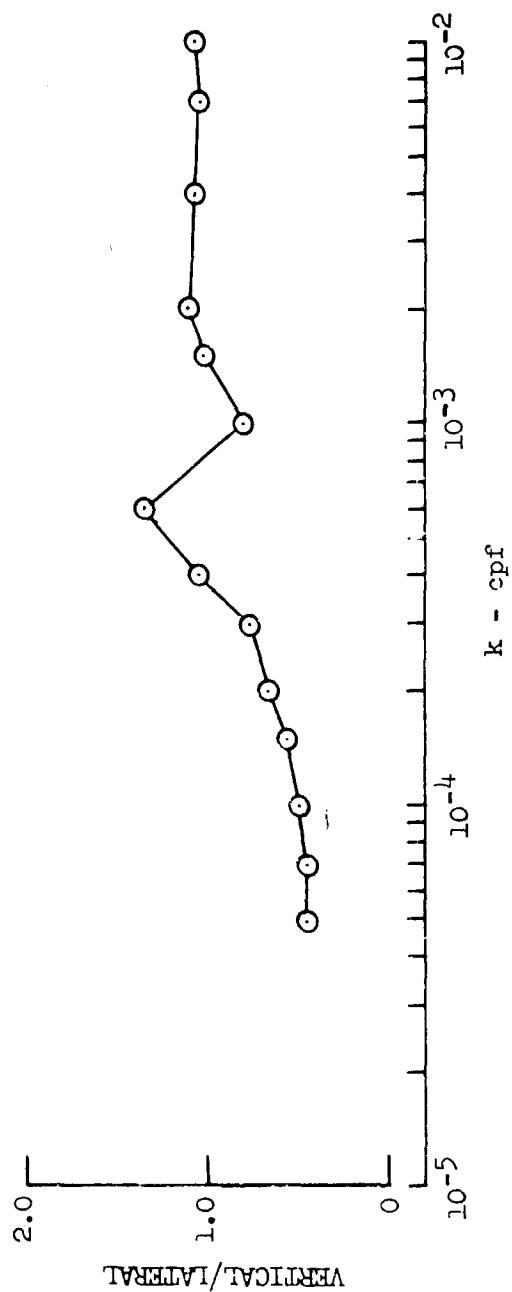
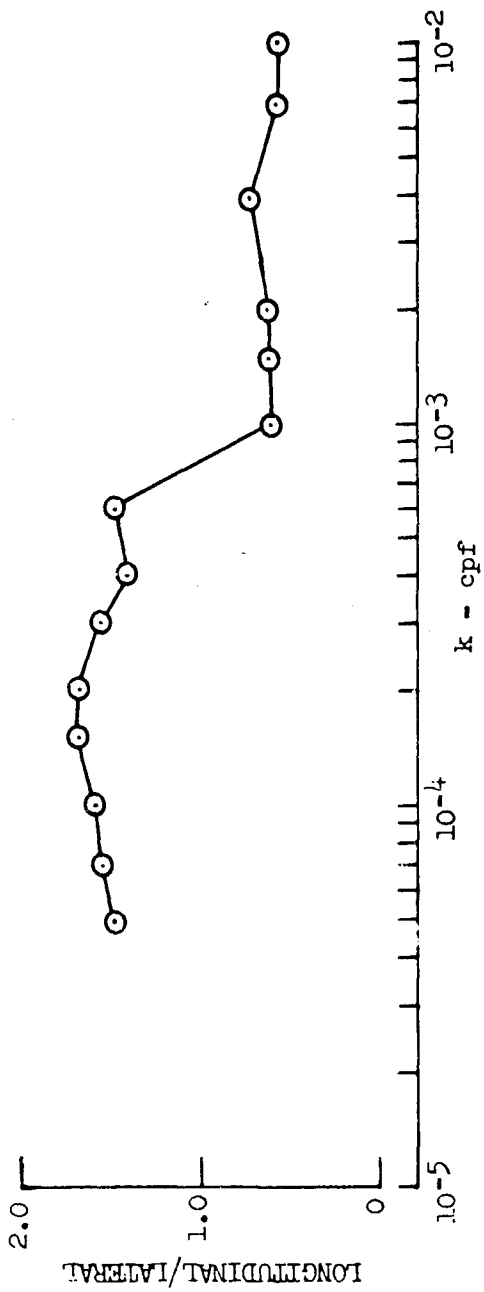


Figure 27.2 Average Isotropy for High Speed Flight Samples

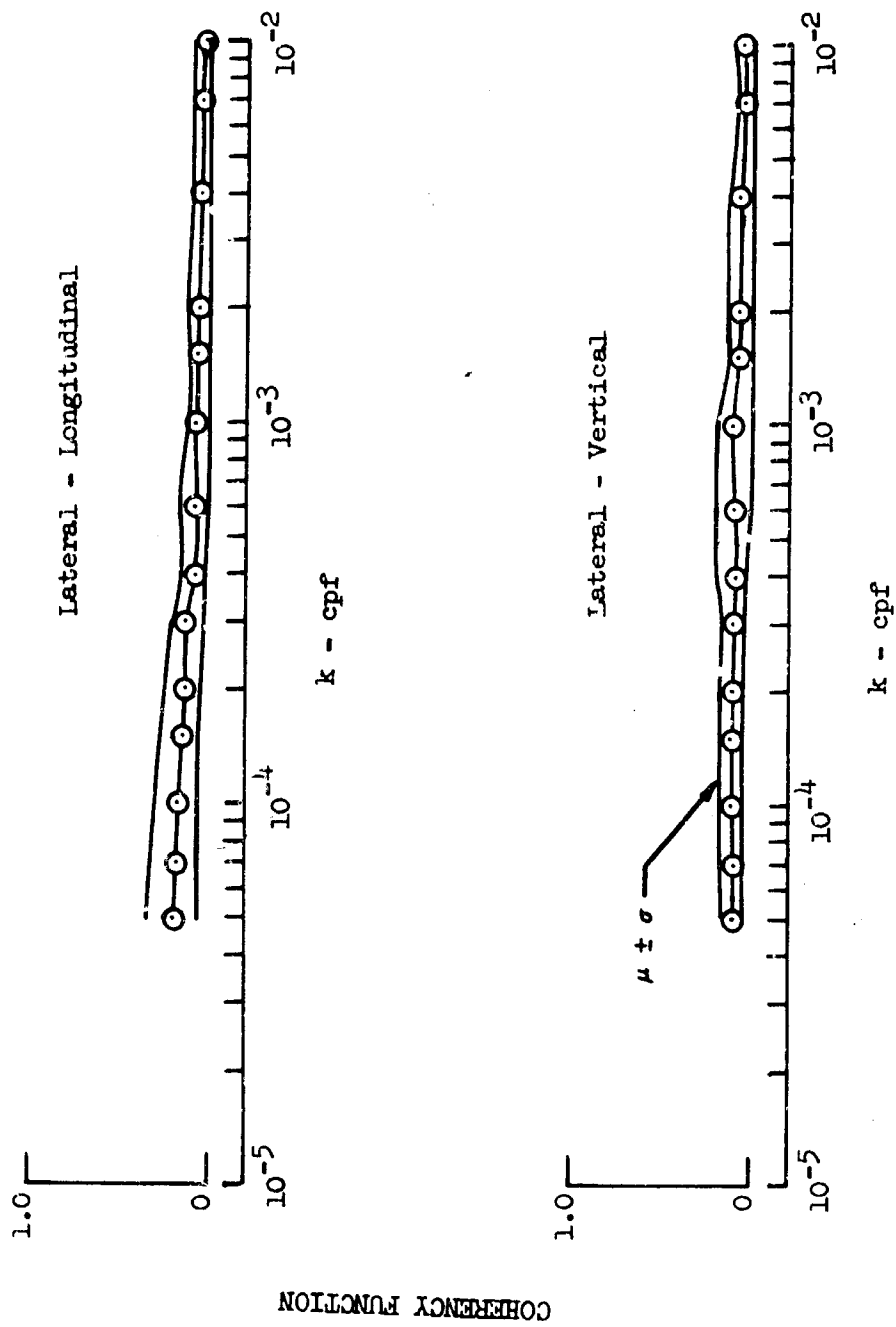


Figure 27.3 Average Coherency for High Speed Flight Samples

## 28. EXPERIMENTAL/MATHEMATICAL SPECTRA COMPARISON

Use of the power spectral density approach in aircraft design predicates the need for a mathematical model of the PSD curve. Many mathematical expressions have been proposed to represent the atmospheric turbulence spectra. The expressions most widely used in the aircraft industry at the present time include expressions suggested by Theodore von Karman (Reference 28.1) and H. L. Dryden (Reference 28.2). These expressions, as shown below, vary according to the gust velocity component being represented.

von Karman Vertical and Lateral -

$$\left[ \frac{\Phi_v(k)}{\sigma_{t_v}^2} \right]_K = \frac{L_{Kv} [2 + 377.5 (L_{Kv} k)^2]}{[1 + 70.78 (L_{Kv} k)^2]^{11/6}} \quad (28.1)$$

von Karman Longitudinal

$$\left[ \frac{\Phi_u(k)}{\sigma_{t_u}^2} \right]_K = \frac{4 L_{Ku}}{[1 + 70.78 (L_{Ku} k)^2]^{5/6}} \quad (28.2)$$

Dryden Vertical and Lateral -

$$\left[ \frac{\Phi_v(k)}{\sigma_{t_v}^2} \right]_D = \frac{L_{Dv} [2 + 6 (2\pi L_{Dv} k)^2]}{[1 + (2\pi L_{Dv} k)^2]^2} \quad (28.3)$$

Dryden Longitudinal -

$$\left[ \frac{\Phi_u(k)}{\sigma_{t_u}^2} \right]_D = \frac{4 L_{Du}}{1 + (2\pi L_{Du} k)^2} \quad (28.4)$$

As suggested in Reference 28.3, the equations may be represented by the following general forms:

Vertical and Lateral -

$$\frac{\Phi_v(k)}{\sigma_{t_v}^2} = \frac{2L [1 + 8\pi^2 a^2 k^2 (n+1)]}{(1 + 4\pi^2 a^2 k^2)^{n+3/2}} \quad (28.5)$$

Longitudinal -

$$\frac{\Phi_u(k)}{\sigma_{t_v}^2} = \frac{4L}{(1 + 4\pi^2 a^2 k^2)^{n+1/2}} \quad (28.6)$$

where  $a$  is related to the scale of turbulence,  $L$ , as follows:

$$a = \frac{L[(n-1)!]}{[\sqrt{\pi}(n-\frac{1}{2})!]}$$

Thus, depending upon the value of  $n$  chosen, various expressions for the power spectral density may be derived. If  $n = 1/2$  these general equations produce the Dryden expressions. The von Karman equations are the special form of the general equations when  $n = 1/3$ .

Mathematical expressions suggested by N. E. Busch and H. A. Panofsky (Reference 28.4) and by J. J. Lumley and H. A. Panofsky (Reference 18.2) to describe the turbulence power spectra were also evaluated.

Busch-Panofsky Vertical and Lateral -

$$\left[ \frac{\Phi_v(k)}{\sigma_{t_v}^2} \right]_{BP} = \frac{0.644 C_v}{1 + 1.5 C_v^{5/3} k^{5/3}} \quad (28.7)$$

Lumley-Panofsky Longitudinal -

$$\left[ \frac{\Phi_u(k)}{\sigma_{t_v}^2} \right]_{LP} = \frac{11800}{C^2 [1 + (2950 k)^{5/3}]} \quad (28.8)$$

Theoretical spectra defined by Equations 28.1 through 28.8 were compared to the experimentally determined spectra from the Phase III program. These comparisons were made by dividing each experimental spectrum by the mathematical expression and plotting this ratio versus spatial frequency. A ratio of 1.0 indicates perfect agreement between the experimental and the mathematically defined spectra. These plots are shown in Appendix IX.

The von Karman expressions were analyzed throughout the entire Phase III program. The Dryden expressions were analyzed for data obtained at the McConnell, Edwards, and Peterson routes. The Lumley-Panofsky and Busch-Panofsky expressions were evaluated for data obtained at the Griffiss location.

Average values of these experimental to mathematical ratios were computed and plotted. This was done by determining the value of the ratios for each turbulence sample at certain values of spatial frequency. These ratios were then averaged at each of the chosen frequencies. The results are shown in Figures 28.1 through 28.3. These figures show the mean values and the standard deviation of the ratios about these mean values. All of the mean values shown in Figures 28.1 through 28.3 are plotted in Figure 28.4 for purposes of comparison.





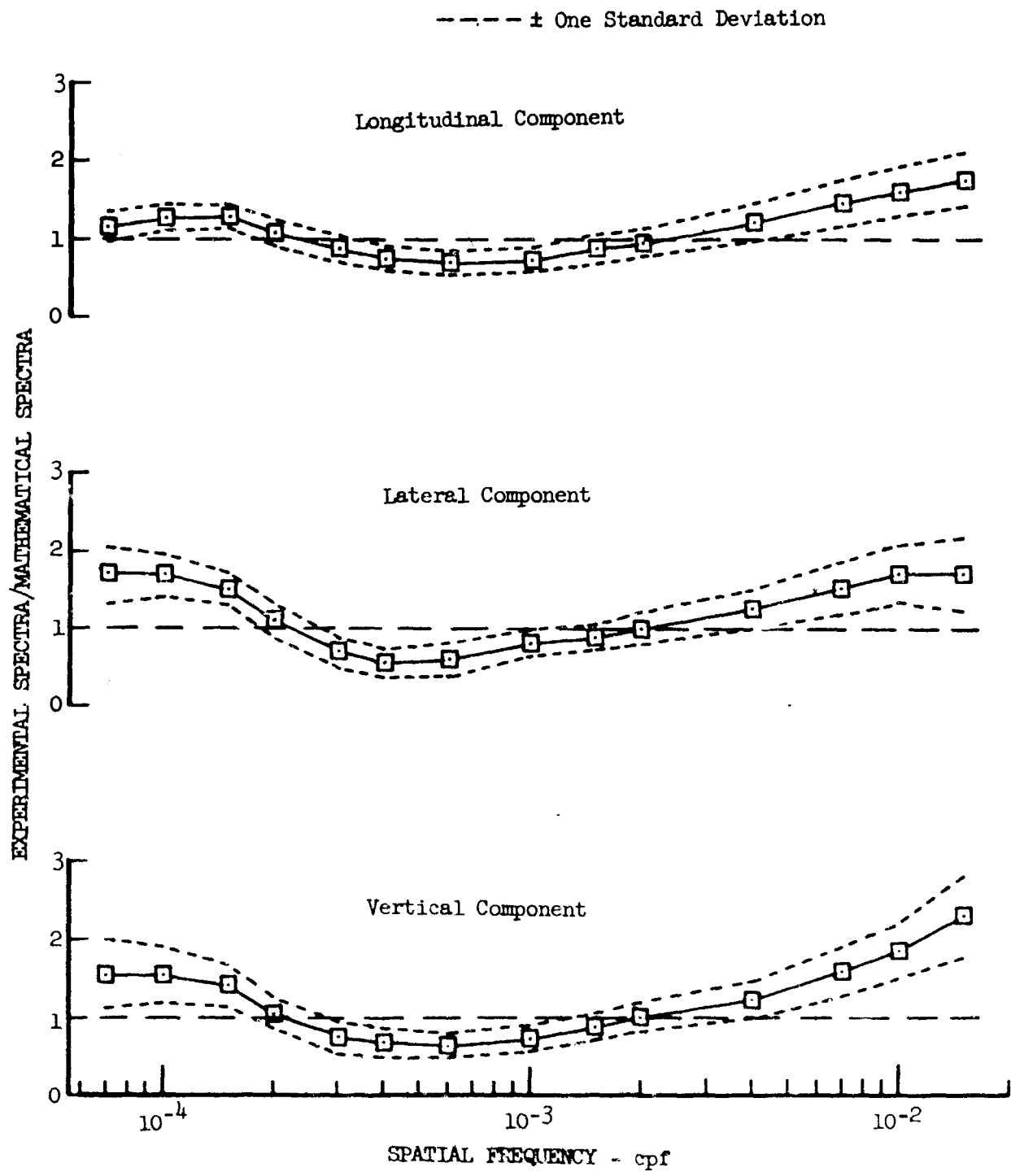


Figure 28.2 Comparison of Experimental and Dryden Power Spectra

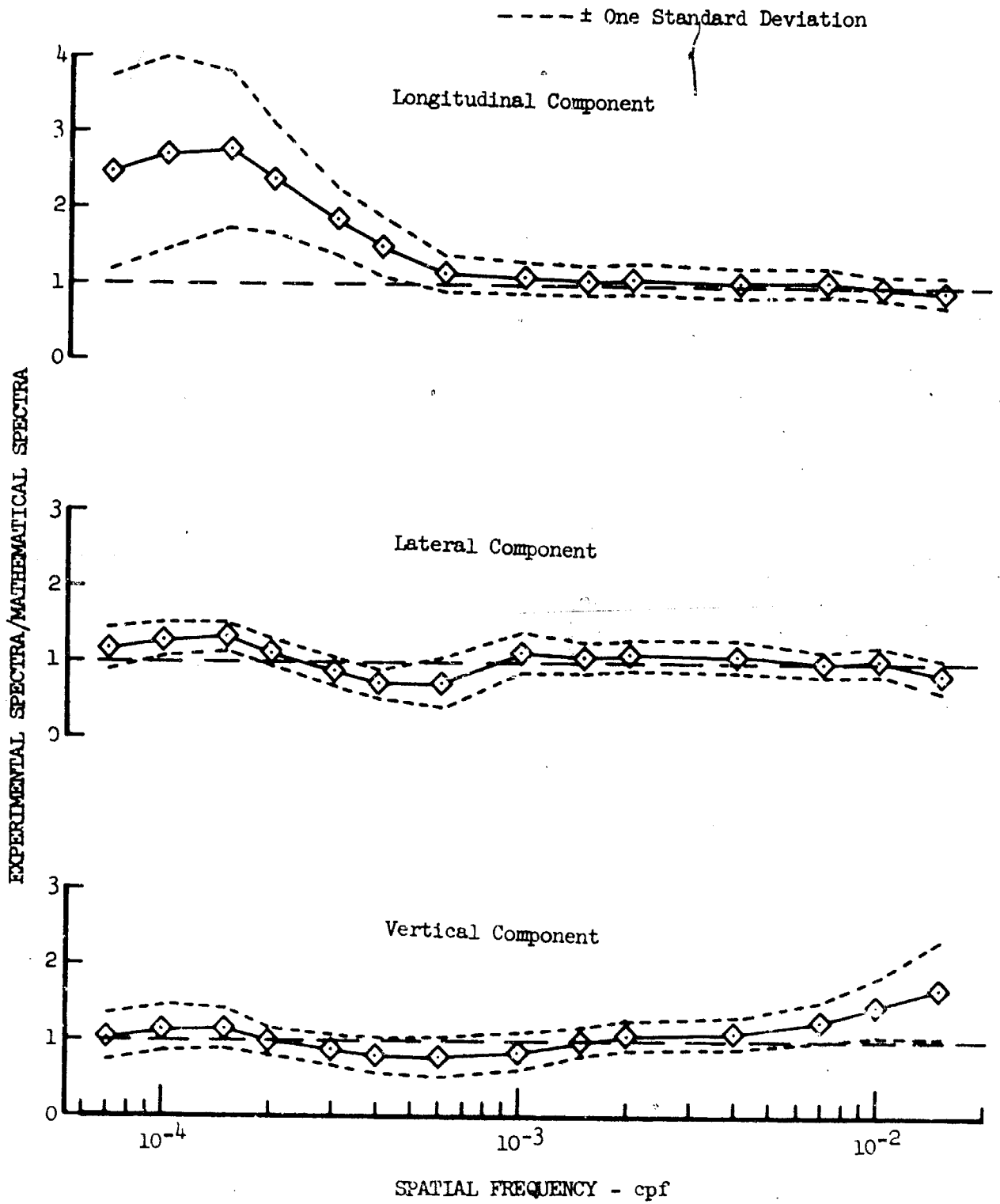


Figure 28.3 Comparison of Experimental Power Spectra with Lumley-Panofsky and Busch-Panofsky Power Spectra

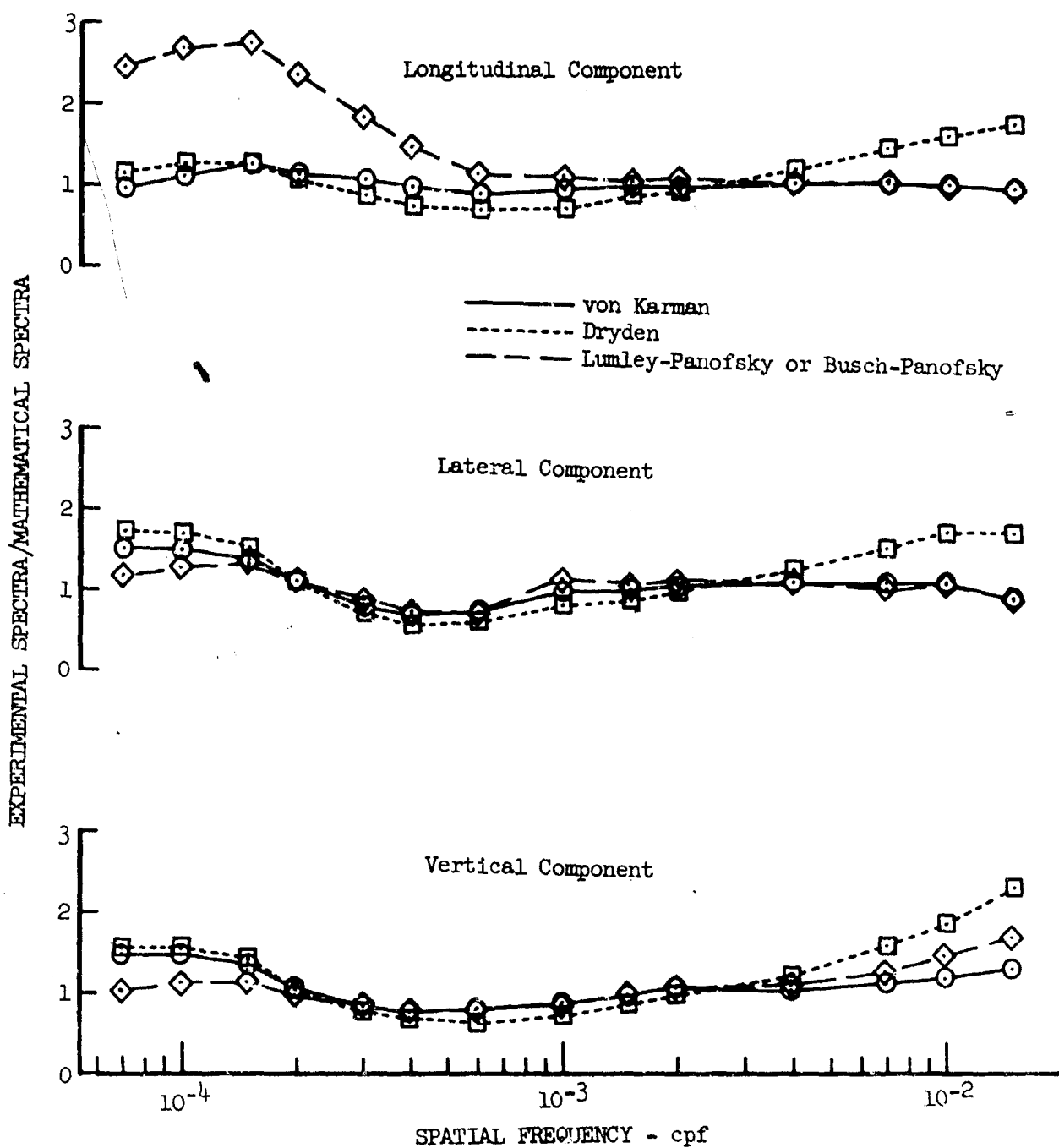


Figure 28.4 Comparison of Agreement Between Mathematical and Experimental Power Spectra

## 29. REPRESENTATIVE SPECTRA SHAPE

The power spectral density of turbulence has been found to be a function of spatial frequency to the  $-5/3$  power in the inertial subrange. This is illustrated in the Phases I and II data and by the Phase III data. Because of this, the von Karman mathematical expressions give a good representation of all components of the turbulence spectra within this frequency range. In the low frequency, long wavelength portion of the spectra, the vertical and lateral expressions show some deviation from the measured data. It appears this is due in part to difficulties encountered in accounting for all the vertical and lateral motion of the airplane at low frequency. Longitudinal spectra agree well with the von Karman mathematical expression.

The correlation between von Karman and experimental spectra is shown in Figure 28.1. The disagreement in the low frequency portion of the lateral and vertical spectra where the von Karman expression underestimates the spectra power is discussed further in Sections 46 and 47.

The Dryden expressions show a greater amount of disagreement with the experimentally determined data, especially at the higher frequencies (Figure 28.2) where the Dryden expressions have a  $-2$  logarithmic slope rather than the  $-5/3$  slope of the data. At the lower frequencies, the Dryden expressions show the same type of disagreement as those suggested by von Karman in that they underestimate the power of the spectra. This underestimation is slightly more for the Dryden expressions, however.

The Lumley-Panofsky expression for the longitudinal component of turbulence shows good agreement with the experimentally determined data at the higher frequencies (Figure 28.3). However, at the lower frequency values this expression deviates from the data significantly. In this area the mathematical expression underestimates the experimentally determined spectra by a factor of approximately 2.5.

The Busch-Panofsky mathematical expressions for vertical and lateral spectra are in good agreement with the experimental data (Figure 28.3). This agreement extends throughout the frequency range investigated except for the vertical component at the highest end of the frequency range. At the high frequencies the experimentally determined vertical spectra showed some deviation from the theoretical  $-5/3$  slope (see Sections 46 and 47). At the low frequency end of the spectra these expressions show the best agreement of those studied.

The results discussed here for the von Karman and Dryden expressions are similar to those obtained during LO-LOCAT Phases I and II (Reference I.2). The Lumley-Panofsky expression, which was also evaluated during Phases I and II, shows more disagreement with the experimentally determined spectra at the lower frequencies for the Phase III data. The Phase III data extend to lower frequency values than the Phases I and II data because of the higher speed aircraft used as the instrumentation platform. The Phases I and II data extended to a low spatial frequency of approximately  $1.5 \times 10^{-4}$  cpf, whereas the Phase III data in Figures 28.1 through 28.4 are plotted to a low frequency value of  $7 \times 10^{-5}$  cpf. The Busch-Panofsky

expressions were not analyzed during Phases I and II. Instead, an expression suggested by U. O. Lappe (Reference 14.1) was investigated and the results showed the same type of disagreement as that discussed above for the Dryden expressions.

It is felt that the low frequency portion of the spectrum should be studied further through the use of higher speed aircraft. This would provide a more accurate record of the long wavelength data. Spectra models based on the data from all three phases are shown and compared to the von Karman spectra in Section 46.

### 30. TURBULENCE SCALE LENGTH

In order to use either the von Karman or Dryden mathematical expressions (Equations 28.1 through 28.4), a value for the integral scale of turbulence,  $L$ , must be known.  $L$  is defined as the area under the autocorrelation curve:

$$L_x = \int_0^{\infty} f(r) dr \quad (30.1)$$

and,

$$L_y = L_z = \int_0^{\infty} g(r) dr \quad (30.2)$$

where:

$f(r)$  = longitudinal autocorrelation function

$g(r)$  = lateral or vertical autocorrelation function

The magnitude of the integral scale, or scale length, is an indication of the average eddy size. It can be shown that these scale lengths in the three orthogonal directions are related by  $L_x = 2L_y = 2L_z$  for isotropic turbulence and that  $L_u = L_x$ ,  $L_v = 2L_y$ , and  $L_w = 2L_z$ . It should be pointed out that Equations 28.1 through 28.4 are written in terms of longitudinal scale length. Thus  $L_u$ ,  $L_v$ , and  $L_w$  are longitudinal scale lengths calculated from the longitudinal, lateral, and vertical gust velocity components, respectively.

Scale lengths may be computed from the autocorrelation function if Taylor's hypothesis is valid (Reference 22.1). They may also be computed from the spectrum in the following manner: Standard deviation has been defined as the square root of the area under the spectrum. For the computation of scale length, a truncated standard deviation,  $\sigma_T$ , covering only the inertial subrange of the spectrum is defined in Section 25 as:

$$\sigma_T = \left[ \int_{k_2}^{k_3} \Phi(k) dk \right]^{1/2} \quad (30.3)$$

where:

$$k_2 = 0.667/V$$

$$k_3 = 10/V$$

For calculations of  $L$  using the von Karman expressions, Equations 28.1 and 28.2 were simplified by noting that, in the inertial subrange,  $377.5 (L_K)^2$  and  $70.78 (L_K)^2 \gg 1$ . Thus, the only terms remaining in the numerators

and denominators of these expressions were those terms containing L and/or k. The resulting expressions for  $\Phi(k)$ , from either Equation 28.1 or 28.2 were substituted in Equation 30.3. The resulting expression was integrated and solved for scale length, yielding Equations 30.4 and 30.5, respectively.

Longitudinal Scale Length - Vertical or Lateral Component

$$L_{Kv} = 0.110 \left( \frac{\sigma_t}{\sigma_T} \right)_v^3 \left( \frac{1}{k_2^{2/3}} - \frac{1}{k_3^{2/3}} \right)^{3/2} \quad (30.4)$$

Longitudinal Scale Length - Longitudinal Component

$$L_{Ku} = 0.0717 \left( \frac{\sigma_t}{\sigma_T} \right)_u^3 \left( \frac{1}{k_2^{2/3}} - \frac{1}{k_3^{2/3}} \right)^{3/2} \quad (30.5)$$

Scale lengths used in the Dryden expressions were determined in the same manner. Equations 28.3 and 28.4 were simplified by noting that  $(2\pi L_K)^2 \gg 1$  in the inertial subrange. The resulting equations obtained by inserting these simplified equations into Equation 30.3 and integrating were:

Longitudinal Scale Length - Vertical or Lateral Component

$$L_{Dv} = 0.152 \left( \frac{\sigma_t}{\sigma_T} \right)_v^2 \left( \frac{1}{k_2} - \frac{1}{k_3} \right) \quad (30.6)$$

Longitudinal Scale Length - Longitudinal Component

$$L_{Du} = 0.101 \left( \frac{\sigma_t}{\sigma_T} \right)_u^2 \left( \frac{1}{k_2} - \frac{1}{k_3} \right) \quad (30.7)$$

Equations 30.4 and 30.6 are expressions for the longitudinal scale length as computed from the vertical or lateral gust velocity components while Equations 30.5 and 30.7 representative longitudinal scale length as computed from the longitudinal component of gust velocity.

As mentioned previously, scale lengths could also be calculated from the area under the gust velocity autocorrelation function. Basically, the autocovariance function  $R(\tau)$  was normalized by dividing it by  $R(0)$  where:



$$R(0) = \int_0^{\infty} \phi(k) dk = \sigma_t^2 \quad (30.8)$$

thus yielding the autocorrelation function  $R(\tau)/R(0)$ . The longitudinal scale length could then be computed from the longitudinal component:

$$L = G_s \int_0^{\infty} [R(\tau)/R(0)] d\tau \quad (30.9)$$

The area was multiplied by ground speed to convert from units of time to units of distance. Equation 30.9 is for the calculation of longitudinal scale length from the longitudinal component. If calculated from either of the transverse components, the scale length obtained from Equation 30.9 must be multiplied by two to get longitudinal scale length.

During the LO-LOCAT Program, scale lengths were computed from the power spectrum, as shown by Equations 30.4 through 30.7. However, autocorrelation functions were calculated for a few randomly selected turbulence samples, and scale lengths were computed using Equation 30.9. The scale lengths calculated by the two different methods were compared.

The autocorrelation functions from one of the samples used for these scale length calculations are shown in Figures 30.1 through 30.3. The areas under the curves were manually computed to the point where the function crosses zero. This assumes that the function oscillates about zero from that point to infinity with positive and negative areas tending to cancel each other. The functions obviously cannot be calculated out to infinity. Likewise, calculating them out to greater and greater lag times means decreasing the value of  $\Delta f$ , the distance between frequency samples, and thus, decreasing the confidence level of the data. Therefore, it is not known whether these particular functions do, in fact, oscillate about zero.

Comparisons of scale lengths calculated by the two methods are shown in Figures 30.4 through 30.6. Scale length values agree well when calculated from the longitudinal component of turbulence. However, scale lengths computed from the lateral and vertical components differ according to the method used. As can be seen in Figures 30.5 and 30.6, the values obtained from the autocorrelation functions are somewhat larger in magnitude than those obtained from the power spectra.

Both of these methods are based on the assumption that the von Karman expressions describe gust velocity spectra shapes. Since the autocorrelation function is the Fourier transform of the power spectrum, it would seem that the differences in scale lengths from the two methods of

calculation occur because the area under the autocorrelation function beyond where the function crosses zero could not be considered.

Reference 22.1 suggests another method for calculating scale length from the autocorrelation function. This method considers only the point at which the autocorrelation function crosses zero, i.e.:

$$L = 0.402 r_c \quad (30.10)$$

where:

$$r_c = \tau_c V$$

and  $\tau_c$  = value of  $\tau$  at which autocorrelation function crosses zero

Comparisons of scale lengths calculated using this method and using the power spectra method are shown in Figures 30.7 through 30.9. It should be noted that when Equation 30.10 was used for calculation of scale length from the vertical and lateral autocorrelation functions, the results were multiplied by two to correspond to the longitudinal scale length.

Compared to scale lengths calculated from the area under the autocorrelation function, Equation 30.10 showed less agreement with the power spectra method for the scale length from the vertical and lateral components and about the same agreement for scale length from the longitudinal component.

Still another method for calculating scale length was suggested in Reference 28.4. This method also involved use of the power spectra. Scale length was calculated by multiplying the power density of the spectra by spatial frequency,  $k$ , and plotting this product versus  $1/k$ . The scale length was defined as being proportional to the value of  $1/k$  at which  $k\phi(k)$  is a maximum.

$$L = A \frac{1}{k_m} \quad (30.11)$$

where:

$A$  = constant of proportionality

$k_m$  = value of  $k$  where  $k\phi(k)/\sigma_t^2$  is a maximum

The von Karman spectra expressions were used to determine  $A$ . Equations 28.1 and 28.2 were multiplied by  $k$ , differentiated, set equal to zero, and solved for  $L$ . The resulting expressions for scale length were:

$$L_{Kv} = 0.1456 \frac{1}{k_m} \text{ (from longitudinal component)} \quad (30.12)$$

$$L_{Kv} = 0.2119 \frac{1}{k_m} \text{ (from lateral and vertical components)} \quad (30.13)$$

Scale lengths calculated by this method are compared to those calculated from Equations 30.4 and 30.5 in Figures 30.10 through 30.12. The agreement for scale length from the longitudinal component is good. Values do not agree well for scale lengths computed from the vertical and lateral components, however. This may be due to excessive airplane motion included in the vertical and lateral gust velocities (See Section 23). The method of Equations 30.12 and 30.13 involved use of spectra values at the relatively low frequencies while the scale lengths calculated by the method of Equations 30.4 and 30.5 were a function of the spectra in the inertial sub-range where the data were considered to be more accurate.

Another problem that arose concerning the use of Equations 30.12 and 30.13 was the difficulty in determining a value for  $1/k_m$ . The turbulence samples chosen for making these comparisons were the same as those used for the comparisons in Figures 30.4 through 30.9. However, not all of these samples could be used. For some of these samples, there was no distinct peak in the value of  $k\Phi(k)/\sigma_t^2$ , so that an accurate value of  $1/k_m$  could not be determined. The values of the spectra were such that the maximum value of  $k\Phi(k)/\sigma_t^2$  in this frequency range extended over a large range of  $1/k_m$  values. This occurred in over half of the turbulence samples selected and these samples were not included in the analysis.

Since the von Karman expressions gave a good representation of the experimentally determined spectra for all three components, the scale lengths from these expressions were analyzed statistically by category. The cumulative probability distributions of these scale lengths for all the Phase III data, regardless of category, are shown in Figure 30.13.

The von Karman scale lengths are shown as functions of terrain, absolute altitude, atmospheric stability, and time of day in Figures 30.14 through 30.17. The general trend of the data in these figures indicates that scale length tends to increase with increasing terrain roughness, increasing absolute altitude, and decreasing atmospheric stability.

Scale lengths recorded at dawn are greater than those recorded during the other two times of day when calculated from the lateral component. When calculated from the longitudinal and vertical components, the probabilities at dawn are less for the smaller values of scale length, but tend to become greater than at mid-morning or mid-afternoon at the larger scale length values. This seems somewhat inconsistent with  $\sigma_t$  statistics. For a given airspeed (therefore, given values of  $k_2$  and  $k_3$ ), scale length is a function of  $(\sigma_v/\sigma_T)^3$  (see Equations 30.4 and 30.5). As shown in Section 13,  $\sigma_t$  increases from dawn to mid-morning to mid-afternoon. Thus, it would seem that the smallest values of scale length would occur at dawn. The reason why this is not so requires consideration of how the turbulence samples were chosen for the scale length calculations. As previously discussed in Section 19, the power spectra were edited and analyzed according to the attributes of the data. Low intensity turbulence samples were generally nonhomogeneous and exhibited high coherence characteristics which resulted in turbulence spectra of generally poor quality. Therefore, these data were not considered valid for spectral analysis. Many of these low intensity turbulence samples were obtained at dawn since, as previously mentioned, the intensity of turbulence at this time of day was

generally less than at the other times of day. However, the turbulence samples obtained at Peterson over the high mountains have been shown to consist of gust velocities greater than at the other locations. Many of the dawn turbulence samples obtained at Peterson were of great enough magnitude to be used for spectral analysis. Thus, approximately 85 per cent of the dawn turbulence samples chosen for spectral analysis, and consequently, scale length calculation, were obtained at Peterson. The data obtained at mid-morning and mid-afternoon were more evenly distributed among the four locations. This caused the gust velocities in the dawn category to be higher than at the other times of day for the power spectra turbulence samples. The values of  $\sigma_t$  used for scale length calculations are shown as functions of time of day in Figure 30.18.

The conclusions concerning variation of scale length with time of day should be made with respect to the considerations discussed above. The distributions of  $\sigma_t$  and  $\sigma_T$  for all PSD samples (not only those chosen for analysis) tend to indicate that scale length values increase from dawn to mid-morning to mid-afternoon.

During Phases I and II of the IO-LOCAT Program, (Reference I.2), scale lengths at the 250-foot altitude were found to be primarily a function of terrain, increasing with greater terrain roughness. At the 750-foot altitude, atmospheric stability appeared to have the greatest effect on scale lengths. As the atmosphere became more unstable the scale lengths showed a tendency to increase in magnitude.

The Phase III data were investigated for the same trends. Figures 30.19 and 30.20 show the variations of scale length with terrain for data obtained at each altitude. Scale lengths at the 250-foot altitude tend to increase with increasing terrain roughness. Those recorded at 750 feet show the same tendency, but to a somewhat lesser degree. Scale lengths are shown as a function of absolute altitude and atmospheric stability in Figures 30.21 and 30.22. The only distinct variation that occurs is for scale lengths calculated from the longitudinal component at the 250-foot altitude. The reason for the very stable data showing higher probabilities at the larger values of scale length is analogous to the situation existing in the scale length analysis with respect to time of day. Otherwise, no consistent or predominant trends are noted in these data. Thus it would seem that, of the categories investigated, the primary variations in scale length are a result of changes in type of terrain and the altitude above the terrain. The effects of terrain at each altitude, discussed above, are shown in Figures 30.19 and 30.20. The effect of altitude over each type of terrain is shown in Figures 30.23 through 30.25. Scale lengths from the vertical component seem to be affected by altitude slightly more than those calculated from the other two components. Larger scale length values were recorded at the higher altitude. The results are summarized in Figure 30.26 where mean scale length values are shown. A summary of the altitude-stability analysis is shown in Figure 30.27. There were not enough scale length data obtained over the desert or water to permit a statistical analysis.

The following conclusions are included in Reference 30.1 for the behavior of longitudinal scale length from the vertical component as a function of altitude and stability:

- Scale length increases with altitude for atmospheric stability conditions other than very stable.
- Under very stable conditions, scale length is nearly constant with altitude.

With respect to these conclusions, the scale length from the vertical component does show a substantial increase with increase in altitude for the stability conditions other than very stable (Figure 30.27). However, a similar relationship is seen for the very stable conditions, although the effects of altitude appear to be less.

The scale lengths from the longitudinal and lateral components do not show these same variations with altitude for the various stability conditions. These scale lengths show the greatest increases with increased altitude for a stable atmosphere. Altitude change has no effect on these values for neutral stability. Scale lengths from the longitudinal component had greater mean values for the data at 250 feet than for the data at 750 feet for the very stable and unstable atmospheric conditions.

According to Reference 30.2, the scale lengths for clear air turbulence below an altitude of 2,500 feet for use in von Karman equations are to be calculated as:

Vertical Component

$$L_{Kv} = H \quad (30.14)$$

Longitudinal and Lateral Components

$$L_{Ku} = L_{Kv} = 184 H^{1/3} \quad (30.15)$$

It should be noted that different equations are used for the w and v components. Therefore, in the following discussion, the subscript v is used to signify the lateral component and w the vertical component.

A comparison between the scale lengths recommended by these equations and those obtained during the LO-LOCAT Phase III Program are shown in Table 30.1.

TABLE 30.1

LO-LOCAT PHASE III. SCALE LENGTHS FOR VON KARMAN EXPRESSIONS  
 COMPARED TO THOSE RECOMMENDED BY MIL-F-008785A (USAF)

Absolute Altitude(H) ~ Ft.	Reference 30.2 Recommended Scale Length ~ Ft.			Average LO-LOCAT Phase III Scale Length ~ Ft.		
	L <sub>Ku</sub>	L <sub>Kv</sub>	L <sub>Kw</sub>	L <sub>Ku</sub>	L <sub>Kv</sub>	L <sub>Kw</sub>
250	1159	1159	250	715	569	394
750	1670	1670	750	714	632	508

With the exception of scale length computed from the vertical component, scale lengths calculated from Equations 30.14 and 30.15 over estimate the LO-LOCAT Phase III experimentally determined data.

Although the Dryden expressions do not fit the LO-LOCAT data as well as the von Karman expressions, the Dryden expressions are used in aircraft design. Reference 30.2 states that the use of the Dryden expressions is permissible when it is not feasible to use the von Karman forms. According to this reference, the scales of turbulence to be used in the Dryden equations for flight below 1,000 feet are:

$$L_{Dv} = H \quad (30.16)$$

$$L_{Du} = L_{Dv} = 100H^{1/3} \quad (30.17)$$

Table 30.2 shows how the Phase III data compare with values calculated from Equations 30.16 and 30.17.

TABLE 30.2

LO-LOCAT PHASE III SCALE LENGTHS FOR DRYDEN EXPRESSIONS  
 COMPARED TO THOSE RECOMMENDED BY MIL-F-008785A (USAF)

Absolute Altitude(H) ~ Ft.	Reference 30.2 - Recommended Scale Length ~ Ft.			Average LO-LOCAT Phase III Scale Length ~ Ft.		
	L <sub>Du</sub>	L <sub>Dv</sub>	L <sub>Dw</sub>	L <sub>Du</sub>	L <sub>Dv</sub>	L <sub>Dw</sub>
250	630	630	250	509	502	389
750	909	909	750	512	538	465

The Dryden scale lengths, with the exception of those calculated from the vertical component, are over estimated by the Reference 30.2 equations, as was the case with the von Karman scale lengths. Equations 30.14 through 30.17 do indicate an increase in scale length for a corresponding increase in altitude. This trend was also noticed in the LO-LOCAT data. Likewise, the Reference 30.2 equations agree with the LO-LOCAT data in that the scale length from the vertical component is more dependent on altitude than are the scale lengths determined from either the longitudinal or lateral components.

The cumulative probability distributions of the Dryden scale lengths are shown in Figure 30.28.

Under isotropic conditions:

$$L_u = L_v = L_w \quad (30.18)$$

However, Reference 13.1 also states that as the ground level is approached, the scale length, as computed from the vertical component, decreases. Reference 13.1 suggests the following expressions as the approximate relationships between scale lengths calculated from the different components of turbulence:

For  $50 \leq H \leq 500$  feet:

$$\frac{L_u}{L_v} = \frac{L_v}{L_w} = 1.30 - 0.0006H \quad (30.19)$$

For  $H > 500$  feet:

$$\frac{L_u}{L_v} = \frac{L_v}{L_w} = 1 \quad (30.20)$$

For absolute altitude levels of 250 feet and 750 feet, these expressions yield ratios of 1.15 and 1.00, respectively. The values are compared to values from the LO-LOCAT Phase III experimentally determined data in Table 30.3.

TABLE 30.3

LO-LOCAT PHASE III SCALE LENGTH RATIOS COMPARED TO  
THOSE RECOMMENDED BY REFERENCE 13.1

Absolute Altitude(H) ~ Ft.	Values Predicted By Equations 30.19 and 30.20	LO-LOCAT Phase III Data			
		$\frac{L_{Ku}}{L_{Kw}}$	$\frac{L_{Kv}}{L_{Kw}}$	$\frac{L_{Du}}{L_{Dw}}$	$\frac{L_{Dv}}{L_{Dw}}$
250	1.15	1.82	1.44	1.31	1.29
750	1.00	1.40	1.25	1.10	1.16

Although the ratios computed from the LO-LOCAT Phase III data are somewhat larger than those predicted by Equations 30.19 and 30.20, the fact that the ratios are reduced in magnitude with increasing altitude above the terrain is apparent. The ratios computed for the Dryden scale lengths show better agreement with the values predicted by Equations 30.19 and 30.20 than do the von Karman ratios. If the same form as Equations 30.19 and 30.20 is used, approximations for the Phase III relationships would be as follows:

$$\frac{L_{Ku}}{L_{Kw}} = \frac{L_{Kv}}{L_{Kw}} = 1.73 - 0.0005H \quad (30.21)$$

$$\frac{L_{Du}}{L_{Dw}} = \frac{L_{Dv}}{L_{Dw}} = 1.39 - .00034H \quad (30.22)$$

These are only approximations. Equations 30.21 and 30.22 assume a linear relationship between the scale lengths at 250 and 750 feet and were derived by assuming the following average values:

$$\frac{L_{Ku}}{L_{Kw}} = \frac{L_{Kv}}{L_{Kw}} = 1.63 \text{ at } 250 \text{ feet} \quad (30.23)$$

$$\frac{L_{Ku}}{L_{Kw}} = \frac{L_{Kv}}{L_{Kw}} = 1.32 \text{ at } 750 \text{ feet} \quad (30.24)$$

$$\frac{L_{Du}}{L_{Dw}} = \frac{L_{Dv}}{L_{Dw}} = 1.30 \text{ at } 250 \text{ feet} \quad (30.25)$$

$$\frac{L_{Du}}{L_{Dw}} = \frac{L_{Dv}}{L_{Dw}} = 1.13 \text{ at } 750 \text{ feet} \quad (30.26)$$

The values were obtained by averaging the appropriate values in Table 30.3.

According to Lappe in Reference 30.3 the type of terrain may be taken into consideration by using the following formula for calculating L:

$$L = h_0 + H L_h \quad (30.27)$$

where  $L_h$  and  $h_0$  are defined as follows:



<u>Terrain Class</u>	<u>L<sub>s</sub></u>	<u>L<sub>0</sub></u>
Smooth	2/3	135
Low Mountains	1/2	300
High Mountains	1/8	675

Values from Equation 30.27 are compared to Phase III von Karman scale lengths in Table 30.4.

Scale lengths obtained over the plains legs were used for the smooth terrain classification in Table 30.4.

TABLE 30.4

LO-LOCAT PHASE III SCALE LENGTHS COMPARED TO THOSE  
RECOMMENDED BY AFFDL-TR-67-122

Absolute Altitude(H) ~ Ft.	Type of Terrain	L From Equation 30.27 ~ Ft.	Average LO-LOCAT Phase III Scale Length ~ Ft.		
			L <sub>Ku</sub>	L <sub>Kv</sub>	L <sub>Kw</sub>
250	Smooth	402	655	456	291
250	Lo. Mount.	425	671	518	420
250	Hi. Mount.	706	775	636	452
750	Smooth	635	640	572	503
750	Lo. Mount.	675	697	608	476
750	Hi. Mount.	769	765	663	520

It should be pointed out that L, as calculated in Reference 30.3 was designed for use in the mathematical spectra expression suggested therein, and not for use in the von Karman equations. The Reference 30.3 mathematical expression was evaluated during Phases I and II and it was found that experimental data did not correlate well with that expression. However, the fact that terrain is considered in the calculation of L is in harmony with the results obtained during the LO-LOCAT Program. The results from Equation 30.27 agree better with the experimentally determined data than did results from Equations 30.14 and 30.15, where only altitude is considered.

The average values of the von Karman and Dryden scale lengths, regardless of geophysical category, are shown in Table 30.5. It should be kept in mind that these mean values are biased due to the uneven distribution of data in the different categories.

TABLE 30.5

LO-LOCAT PHASE III AVERAGE SCALE LENGTHS

Scale Length ~ Ft.					
$I_{Ku}$	$L_{Kv}$	$L_{Kv}$	$I_{Du}$	$I_{Dv}$	$L_{Dv}$
715	598	450	511	519	427

In Section 28, mathematical expressions (Equations 28.7 and 28.8) for the PSD suggested by Busch and Panofsky and by Lumley and Panofsky were analyzed. Scale length, as such, is not contained in these expressions. Instead,  $C_v$  is used in the Busch-Panofsky expression and  $C$  is used in the Lumley-Panofsky expression. These parameters were calculated in a manner similar to the von Karman and Dryden scale lengths. Equations 28.7 and 28.8 were simplified by noting that in the inertial subrange  $1.5(C_v k)^{5/3} \gg 1$ , and  $(2950 k)^{5/3} \gg 1$ , respectively. If these expressions are substituted into the truncated standard deviation expression (Equation 30.3) and integrated, the following result is obtained:

$$C_v = 0.517 \left( \frac{\sigma_t}{\sigma_T} \right)_v^3 \left( \frac{1}{k_2^{2/3}} - \frac{1}{k_3^{2/3}} \right)^{3/2} \quad (30.28)$$

$$C = 0.172 \left( \frac{\sigma_t}{\sigma_T} \right)_u \left( \frac{1}{k_2^{2/3}} - \frac{1}{k_3^{2/3}} \right)^{1/2} \quad (30.29)$$

Thus,  $C$  and  $C_v$  are related to scale length and, from the preceding equations (30.28 and 30.29) and Equations 30.4 and 30.5, the following relationships were derived:

$$C_v = 4.70 I_{Kv} \quad (30.30)$$

$$C = 0.415 (I_{Ku})^{1/3}$$

The cumulative probability distributions of these parameters are presented in Figures 30.29 through 30.31. In Reference 18.2, a value of 2.45 is suggested for  $C$ . For the LO-LOCAT Phase III Program, a mean value of 3.54 was determined. The mean values of  $C_v$  calculated from the vertical and lateral components are 1805 and 2243, respectively.

It should be pointed out that all data analyzed within this discussion were derived from only homogeneous turbulence samples (see Section 19). Scale lengths for low frequency data are discussed in Section 52.

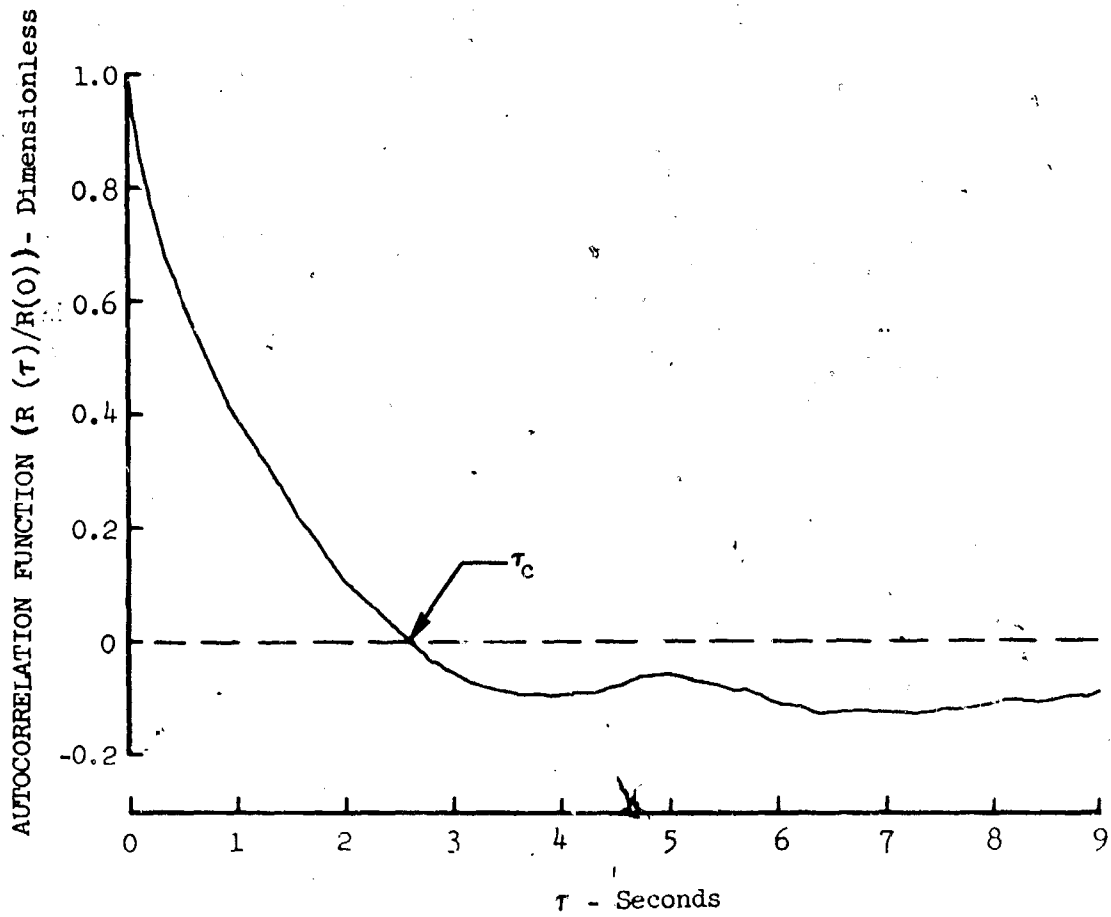


Figure 30.1 Example Longitudinal Gust Velocity Autocorrelation Function Plot

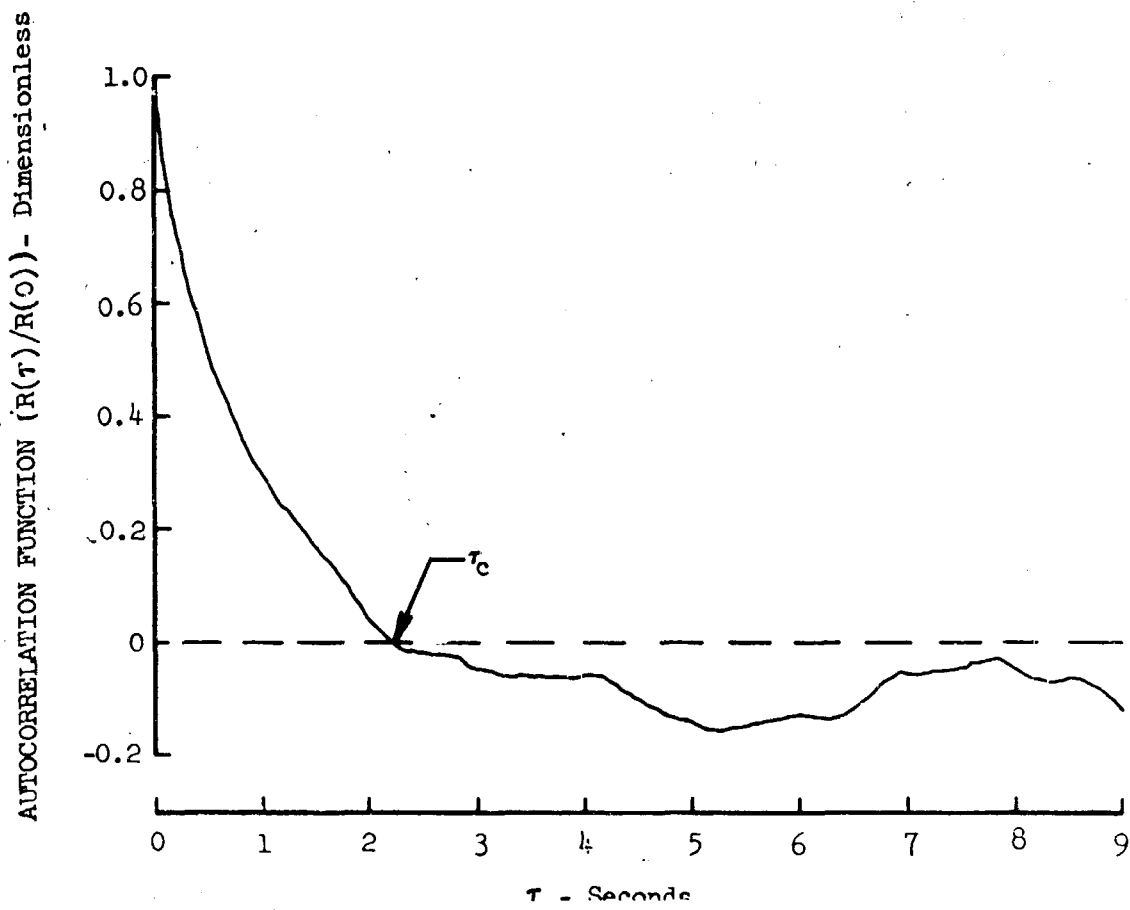


Figure 30.2 Example Lateral Gust Velocity Autocorrelation Function Plot

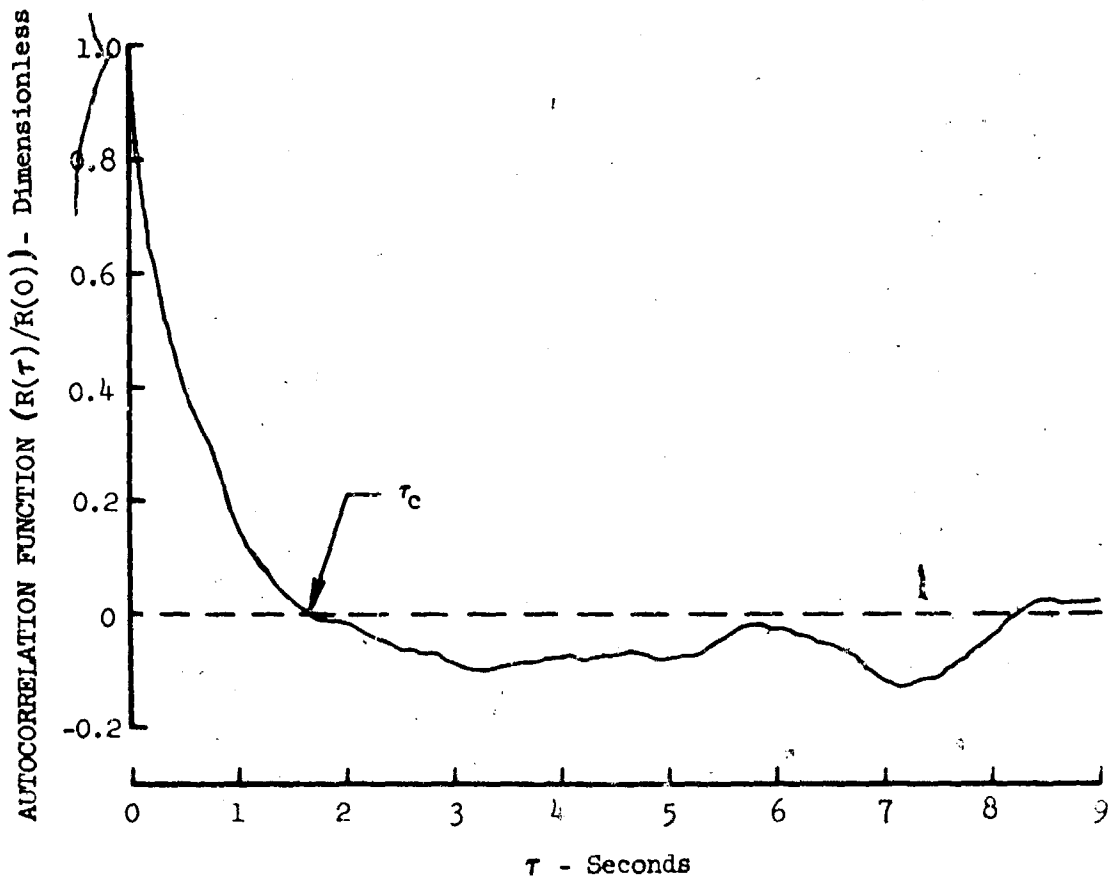


Figure 30.3 Example Vertical Gust Velocity Autocorrelation Function Plot

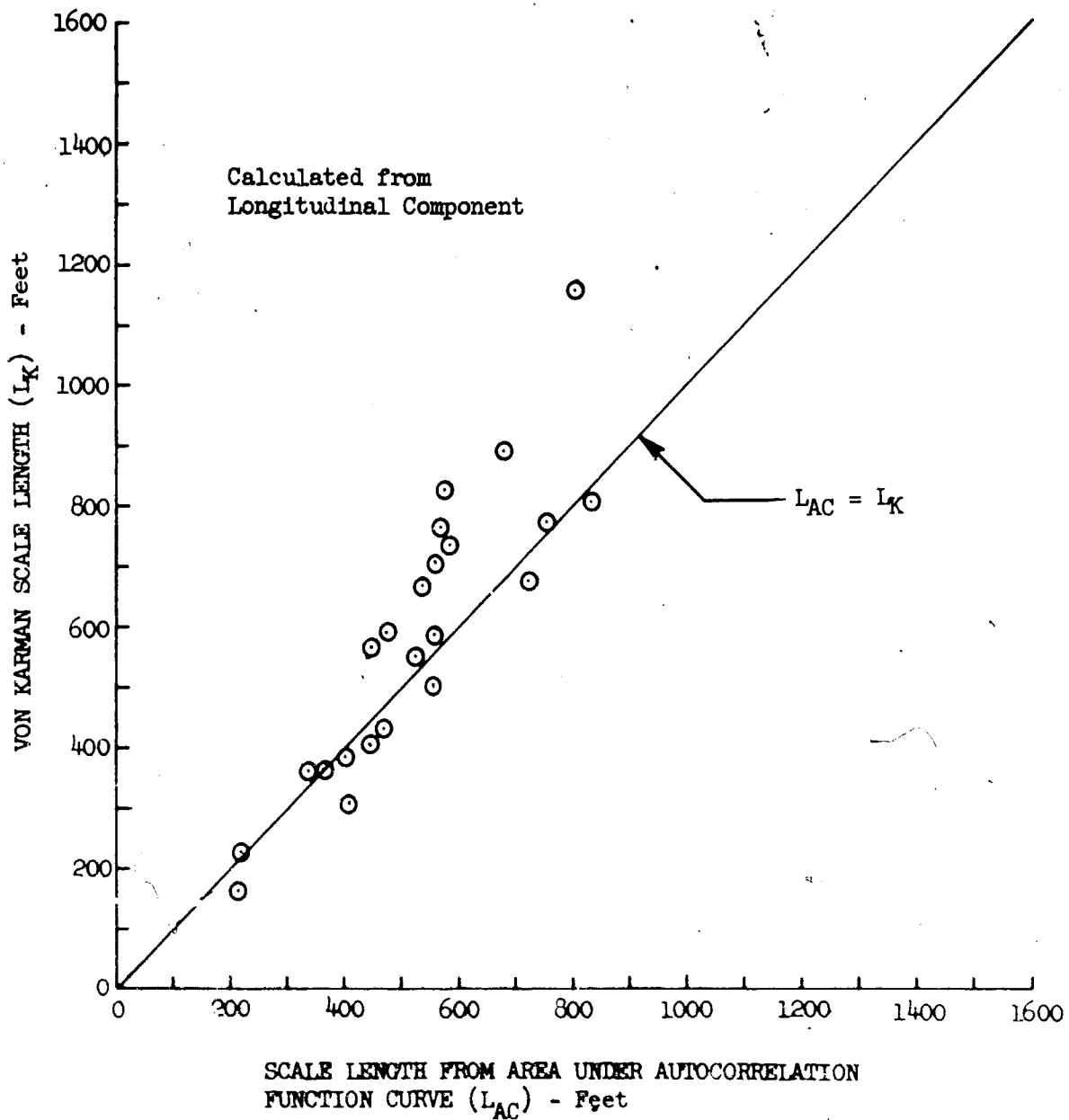


Figure 30.4 Comparison of von Karman and Autocorrelation Function Derived Longitudinal Scale Lengths

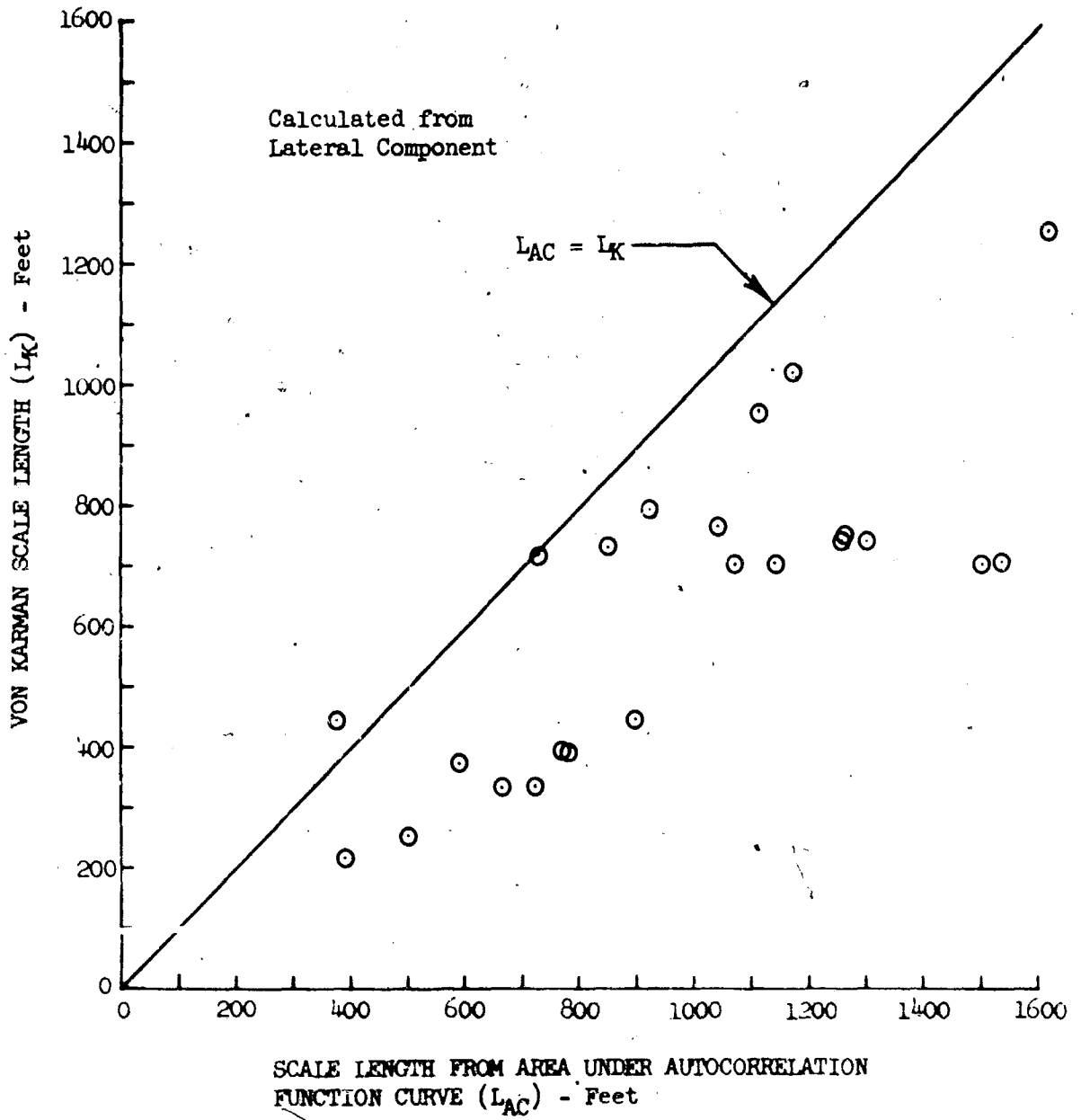


Figure 30.5 Comparison of von Karman and Autocorrelation Function Derived Longitudinal Scale Lengths

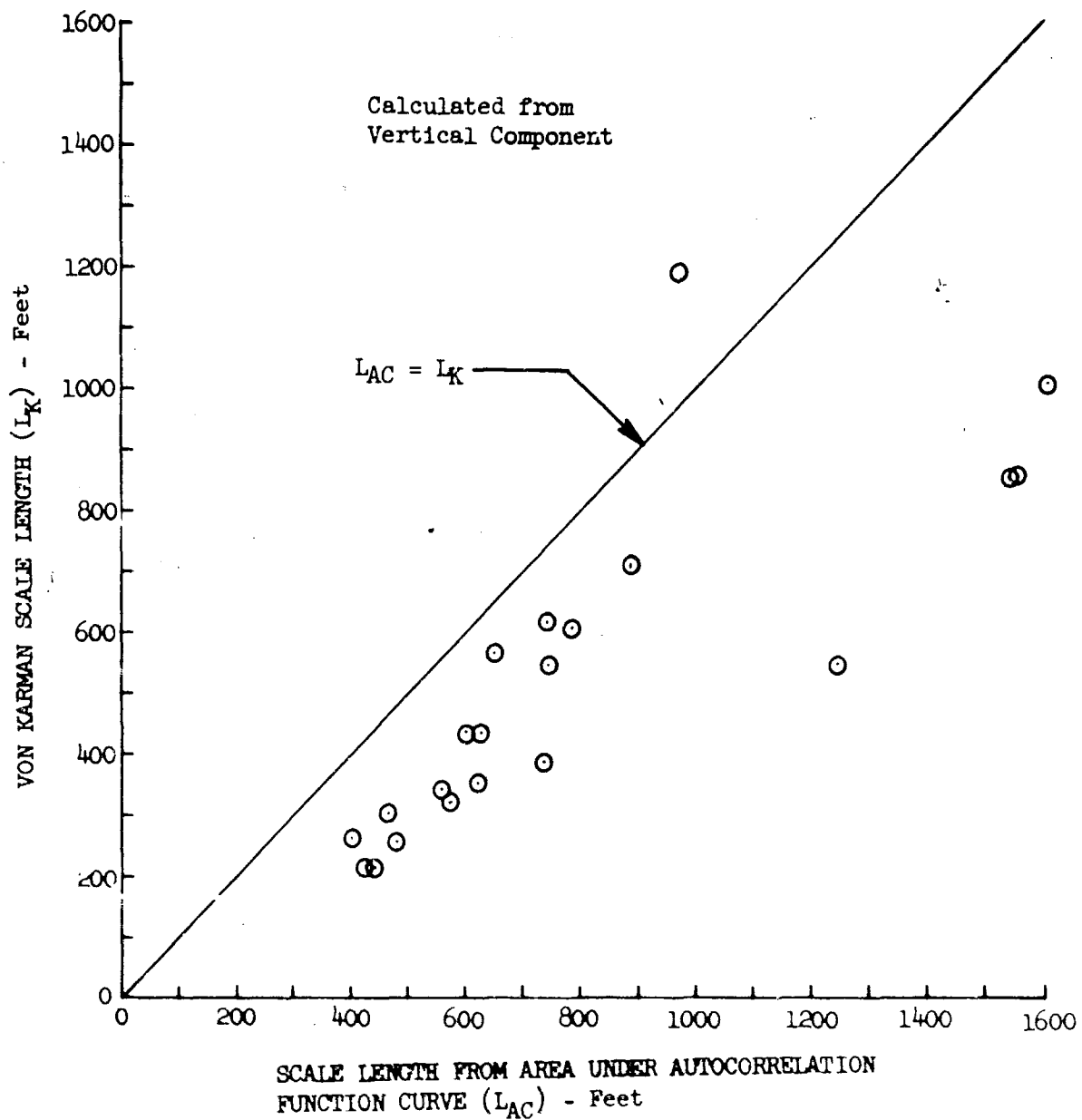


Figure 30.6 Comparison of von Karman and Autocorrelation Function Derived Longitudinal Scale Lengths



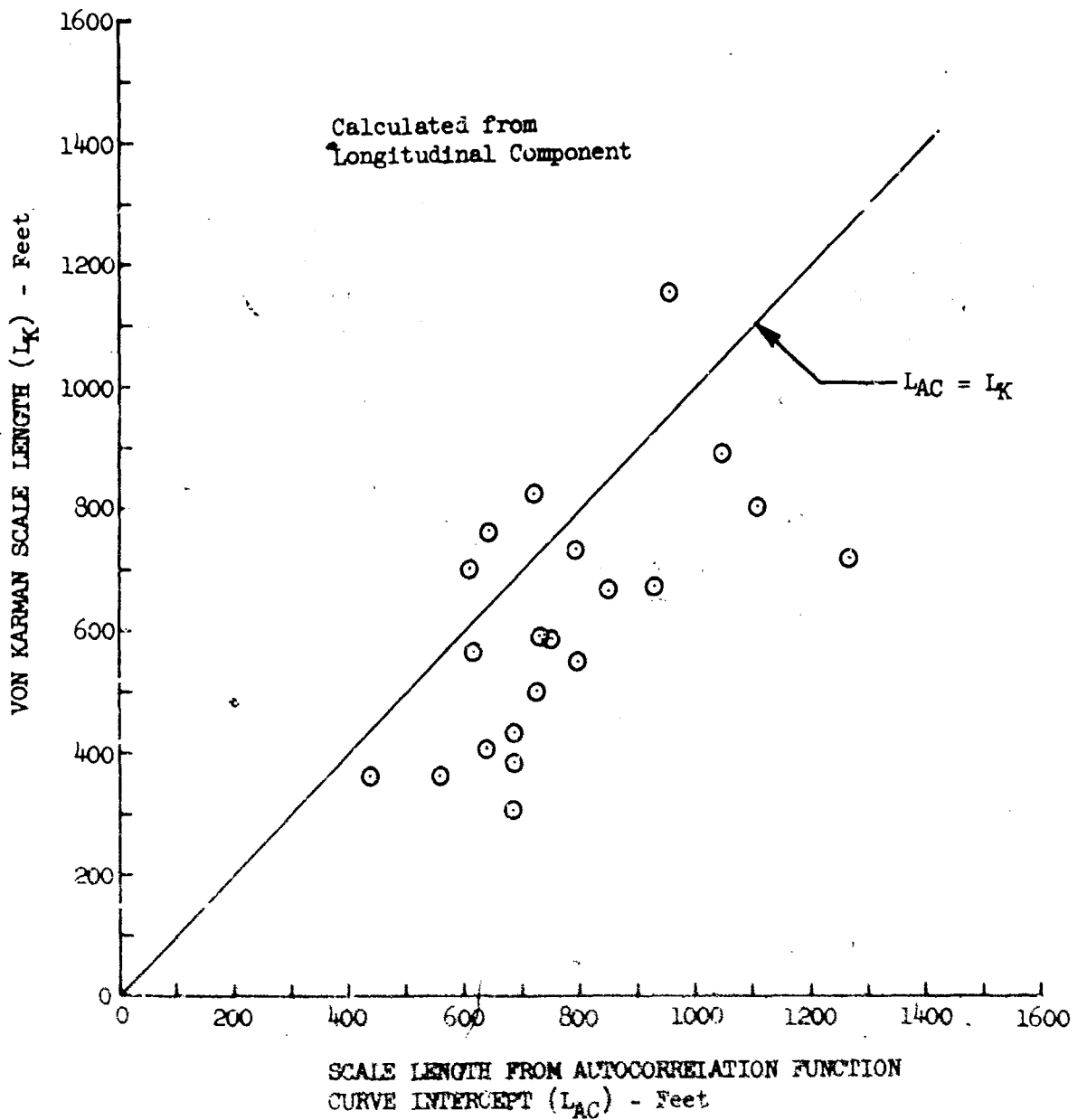


Figure 30.7 Comparison of von Karman and Autocorrelation Function Derived Longitudinal Scale Lengths

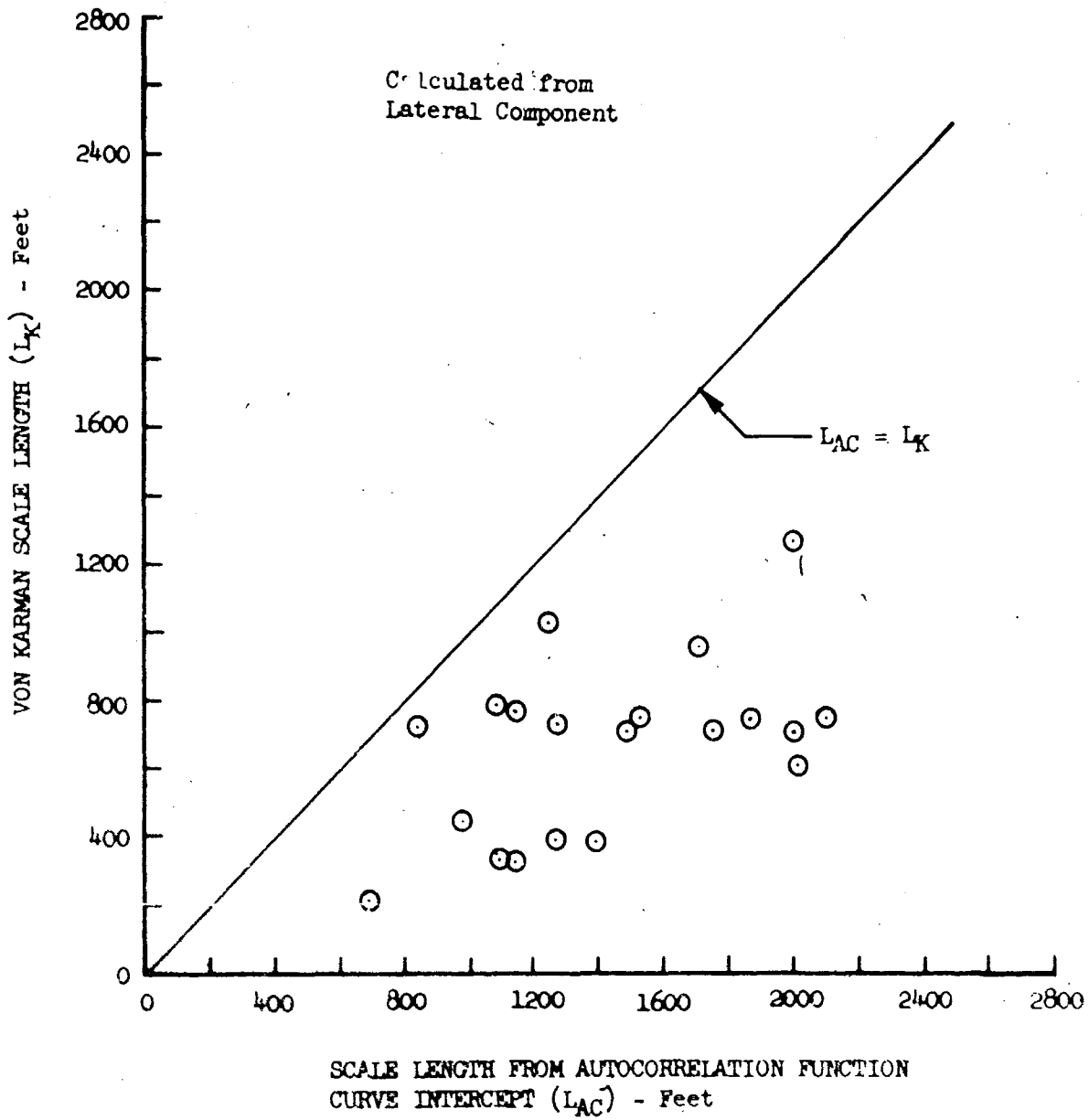


Figure 30.8 Comparison of von Karman and Autocorrelation Function Derived Longitudinal Scale Lengths

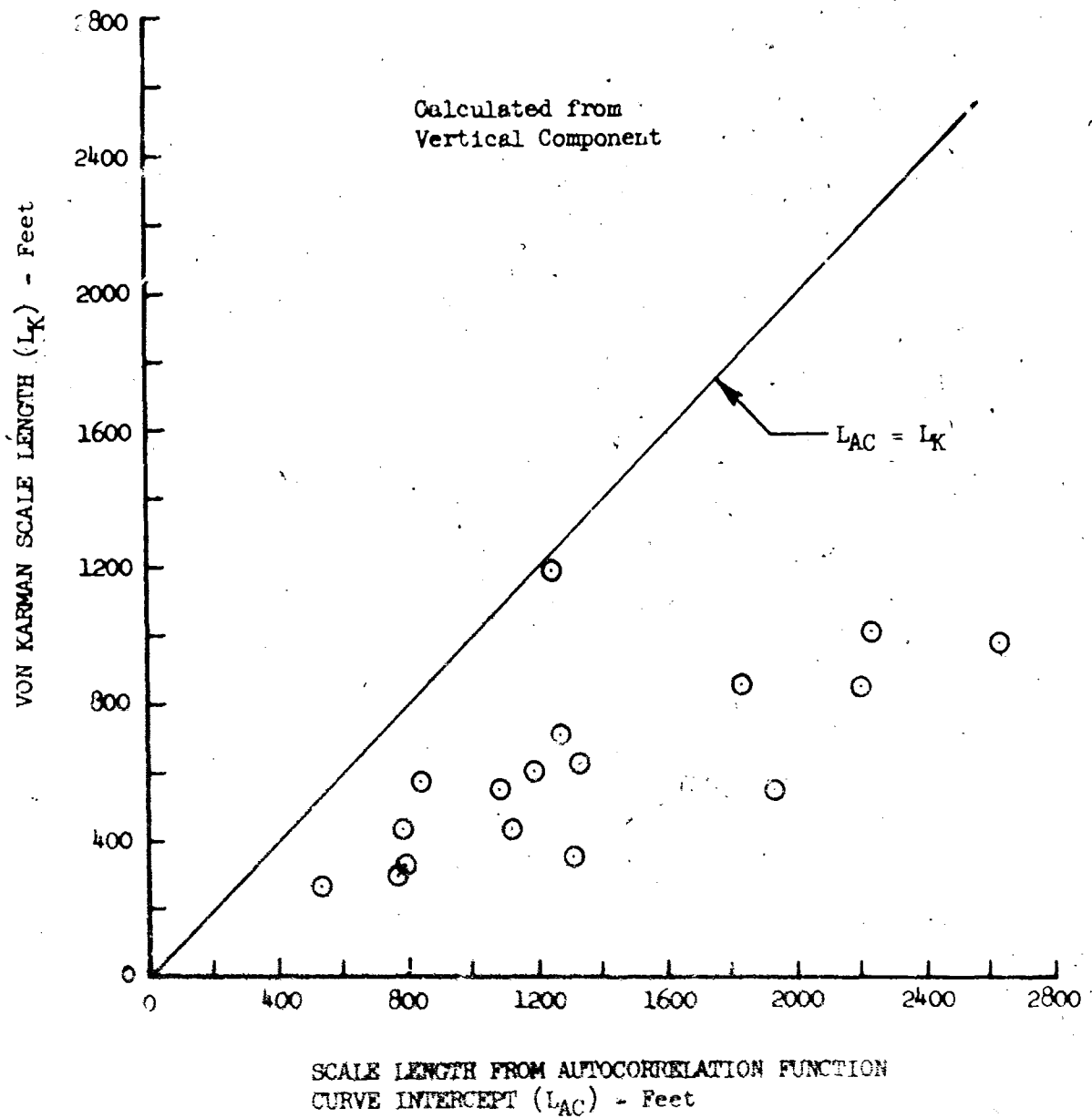


Figure 30.9 Comparison of von Karman and Autocorrelation Function Derived Longitudinal Scale Lengths

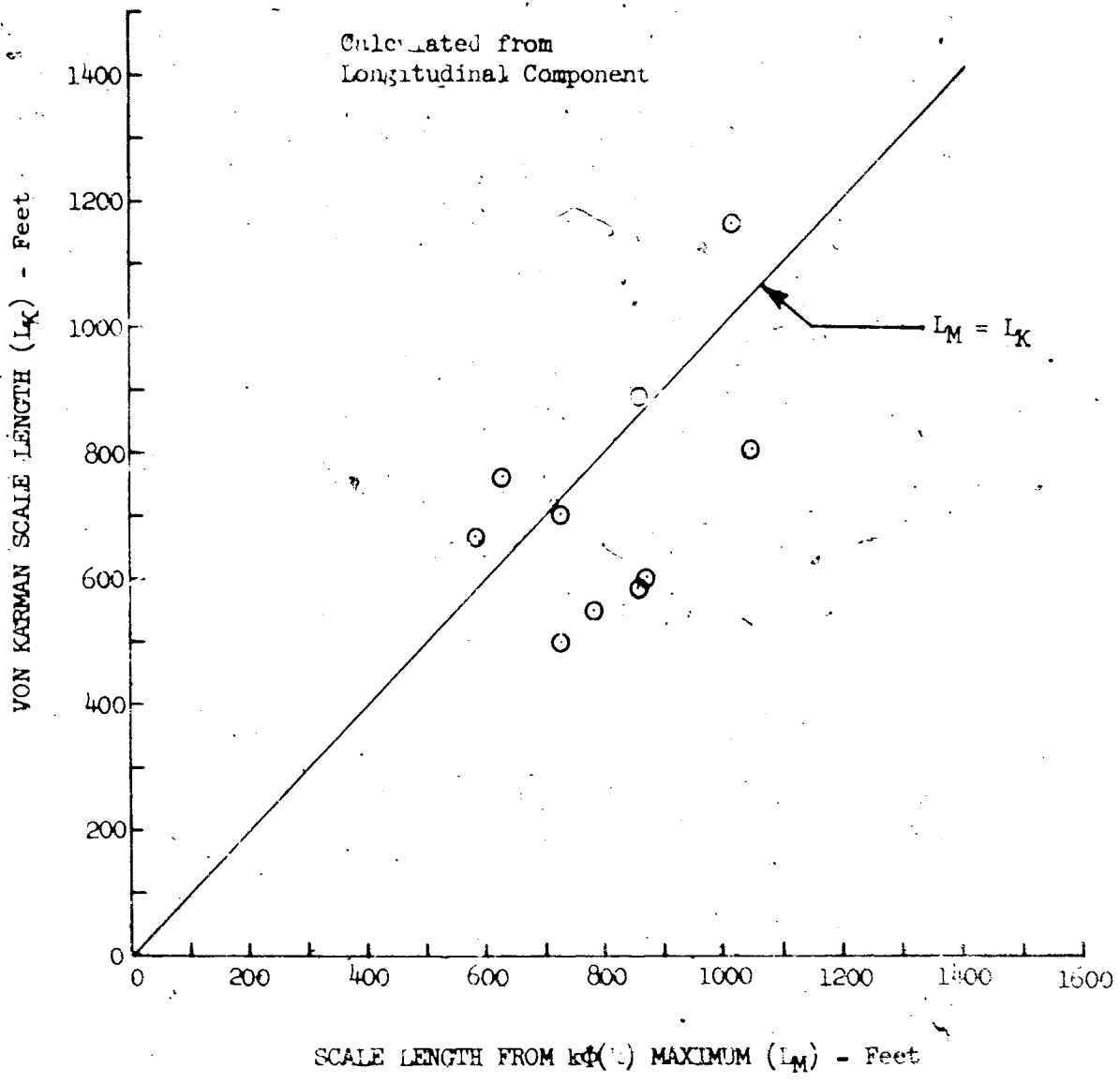


Figure 30.10 Comparison of von Karman and  $1/k$  Derived Longitudinal Scale Lengths

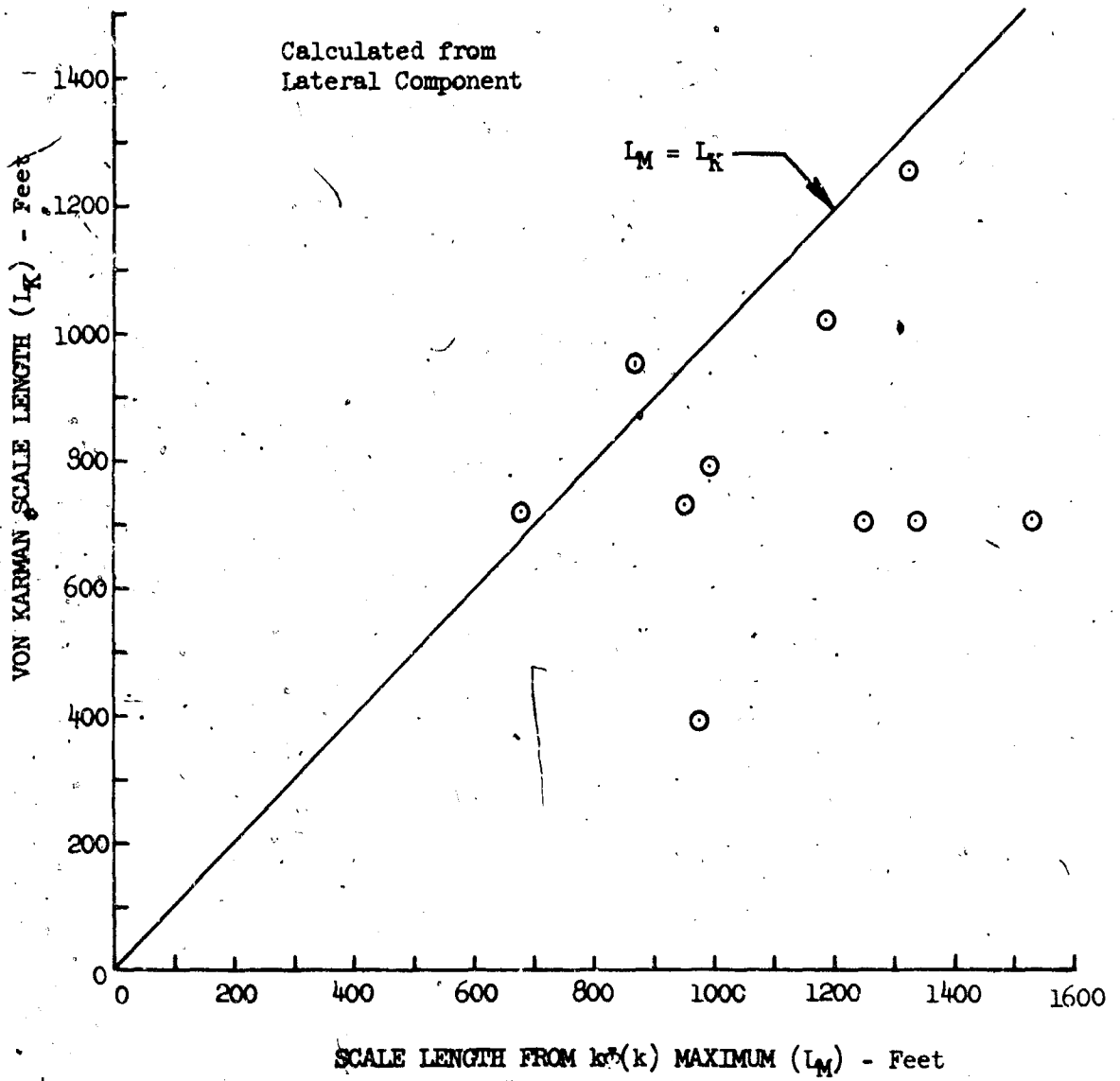


Figure 30.11. Comparison of von Karman and  $1/k$  Derived Longitudinal Scale Lengths.

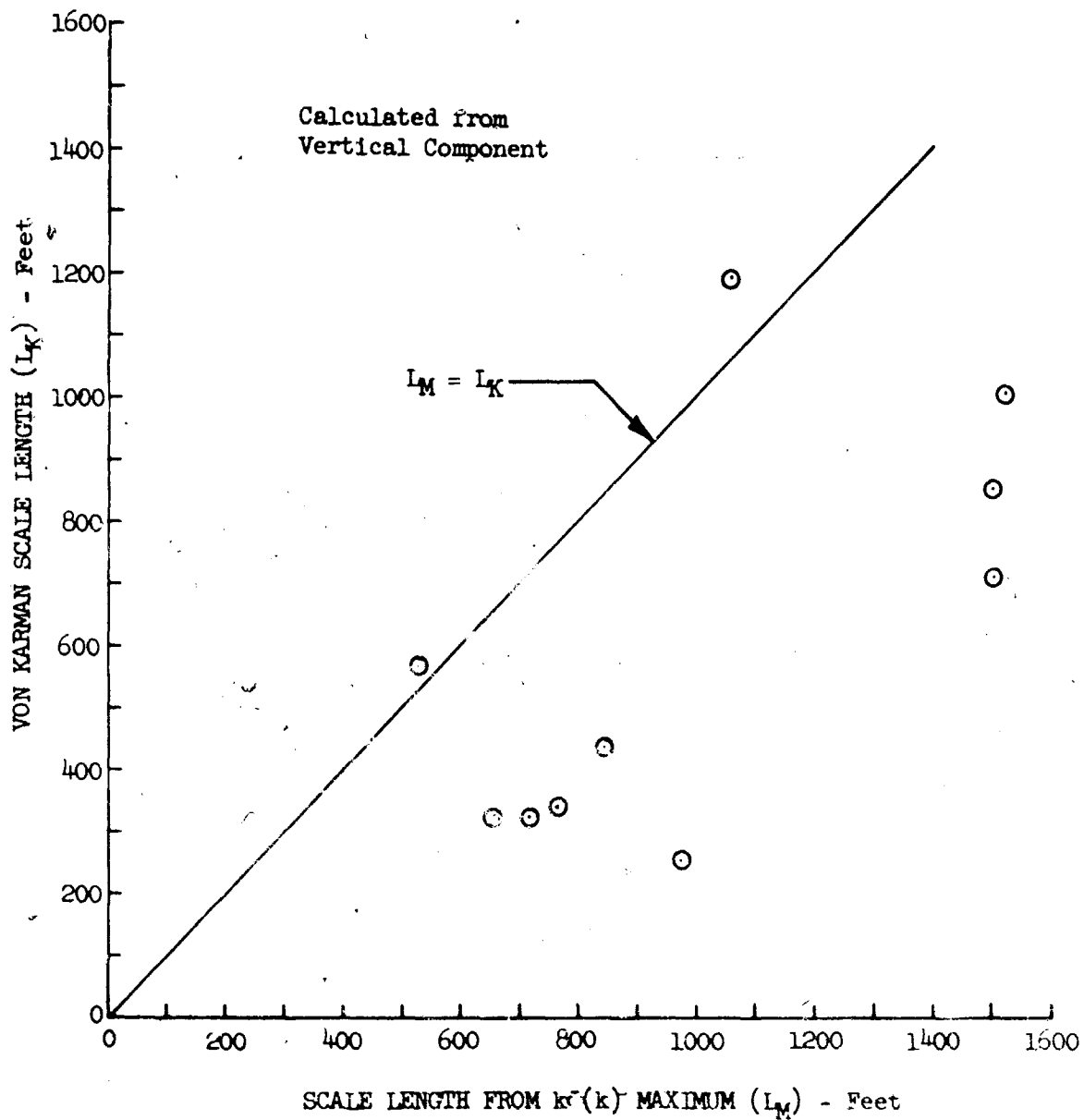


Figure 30.12 Comparison of von Karman and  $1/k$  Derived Longitudinal Scale Lengths

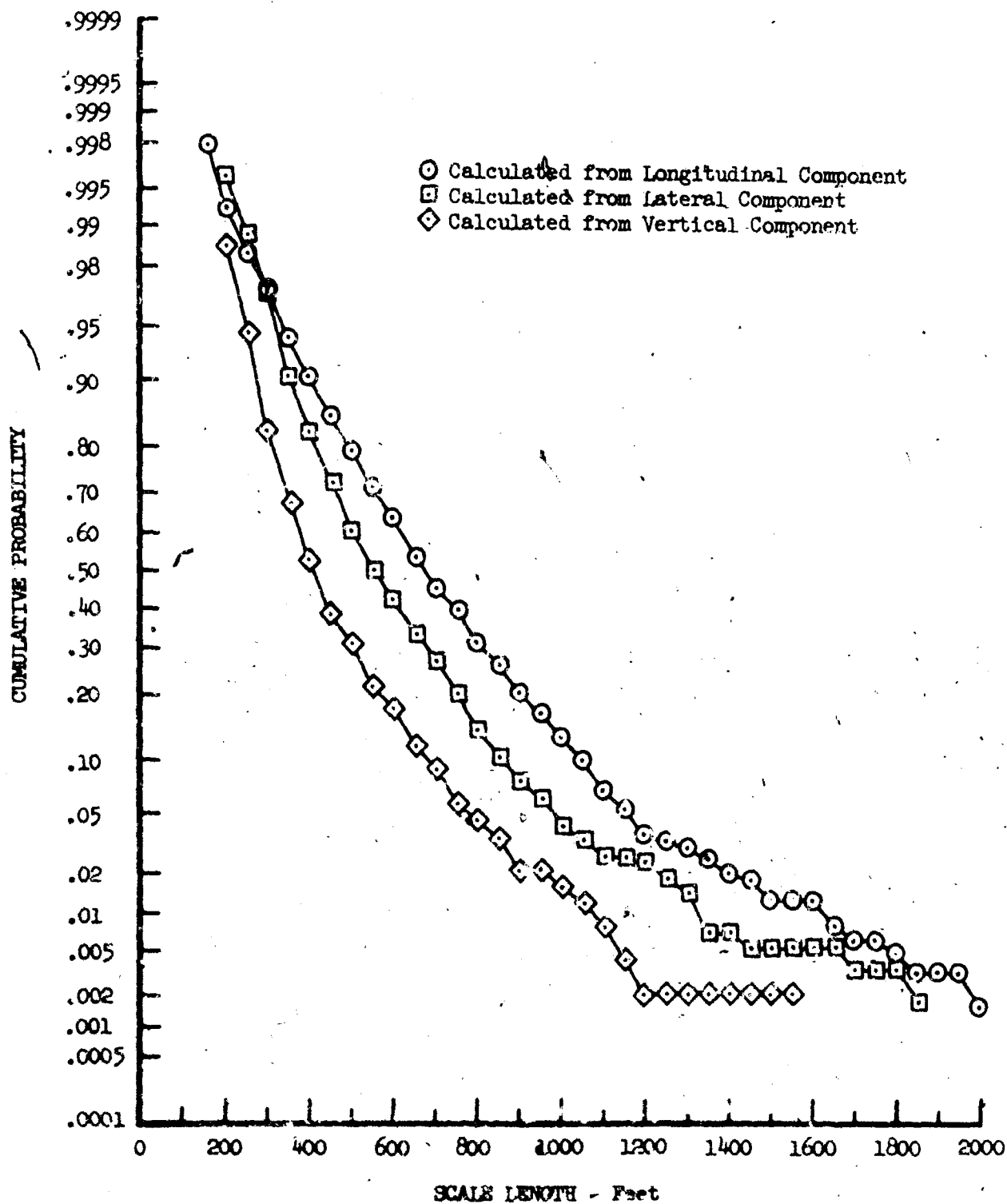


Figure 30.13 von Karman Longitudinal Scale Length Cumulative Probability

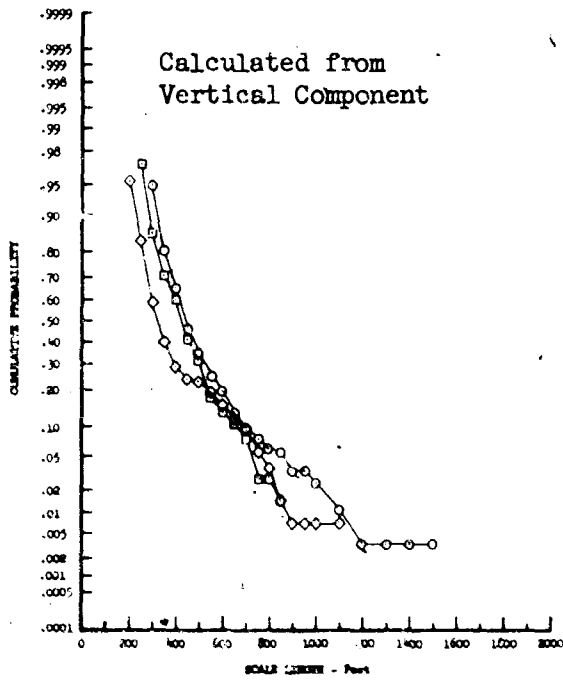
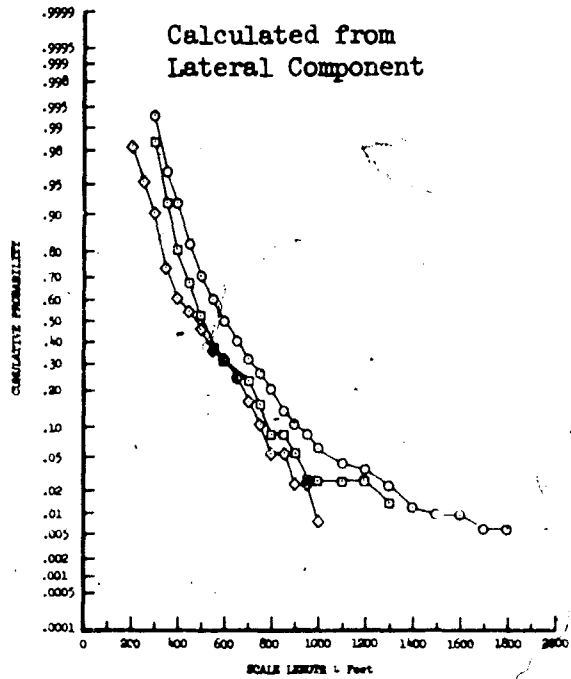
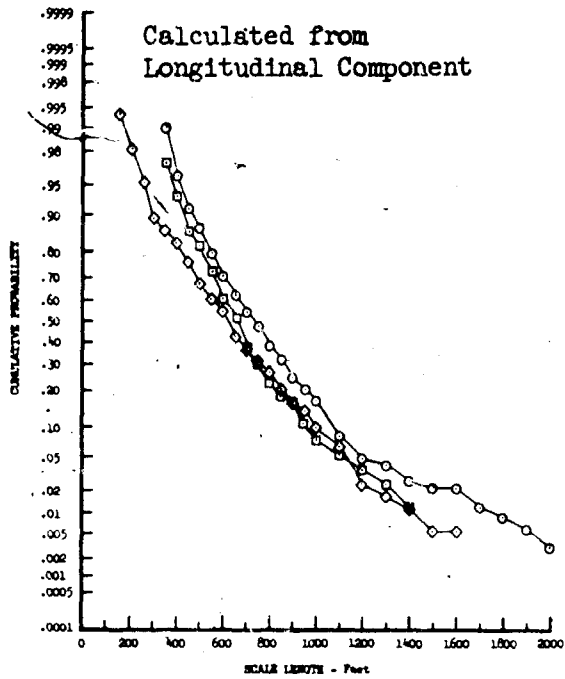
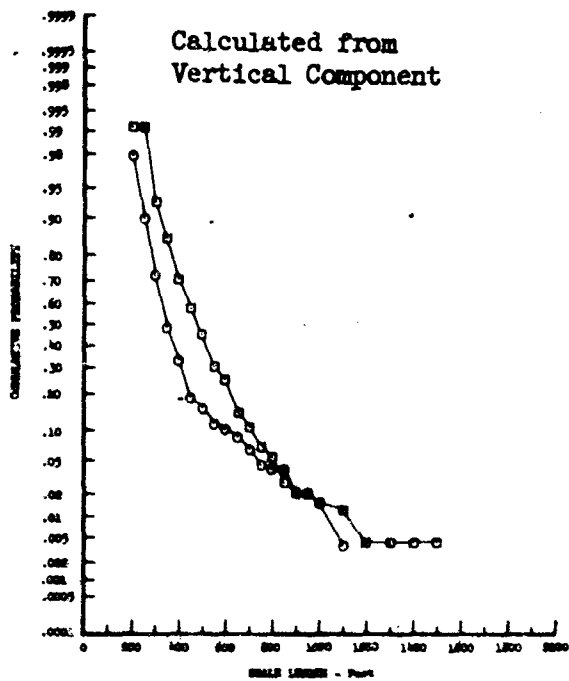
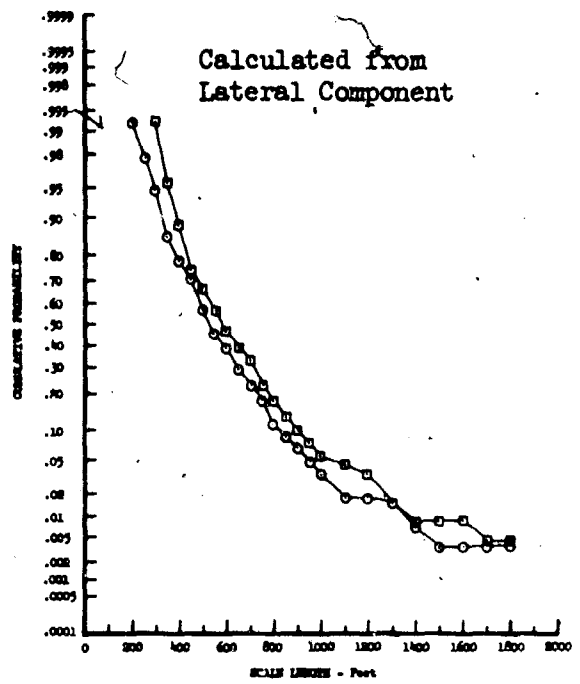
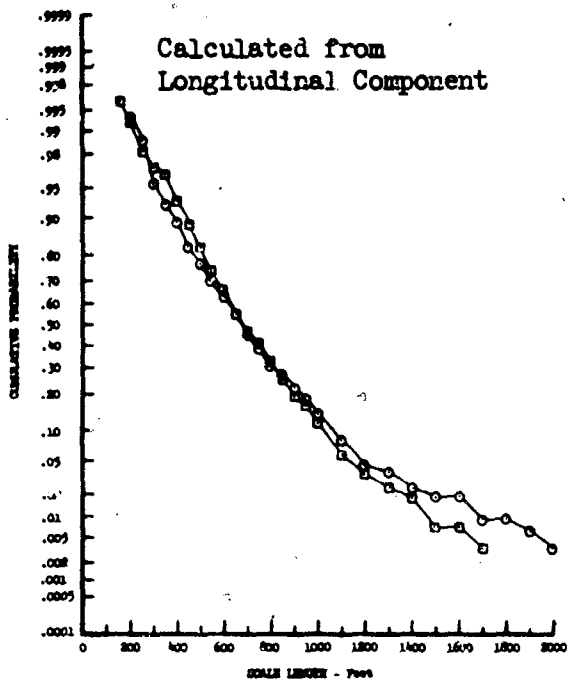


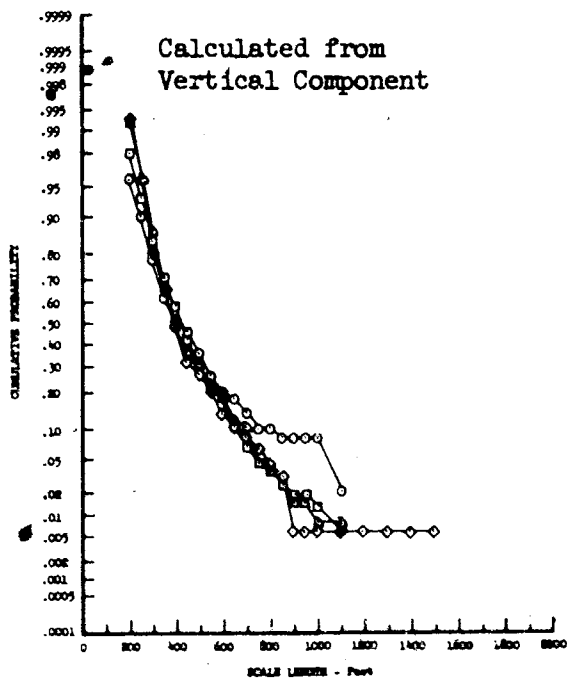
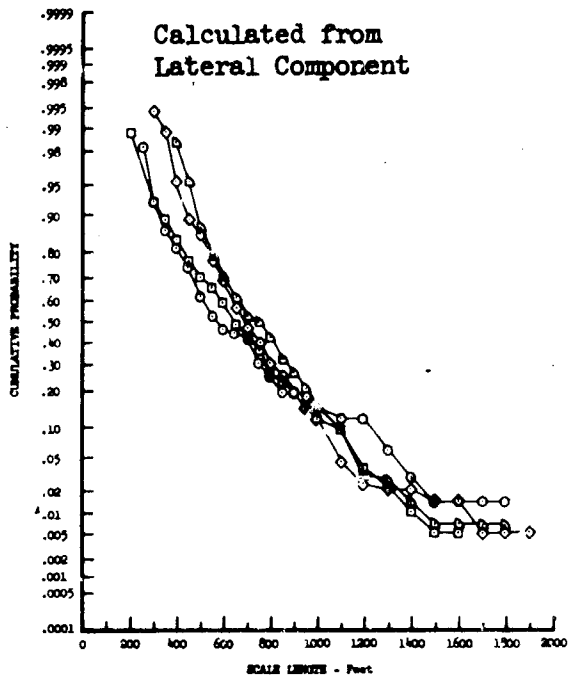
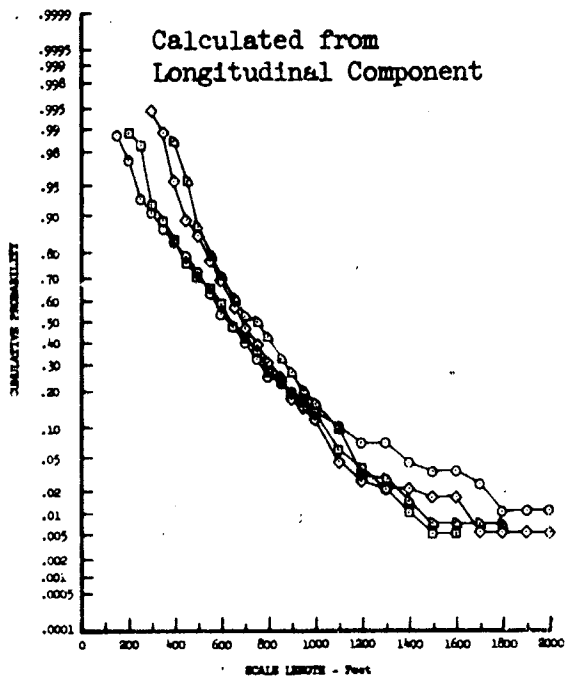
Figure 30.14 von Karman Longitudinal Scale Length  
Cumulative Probability Associated with  
Terrain Type





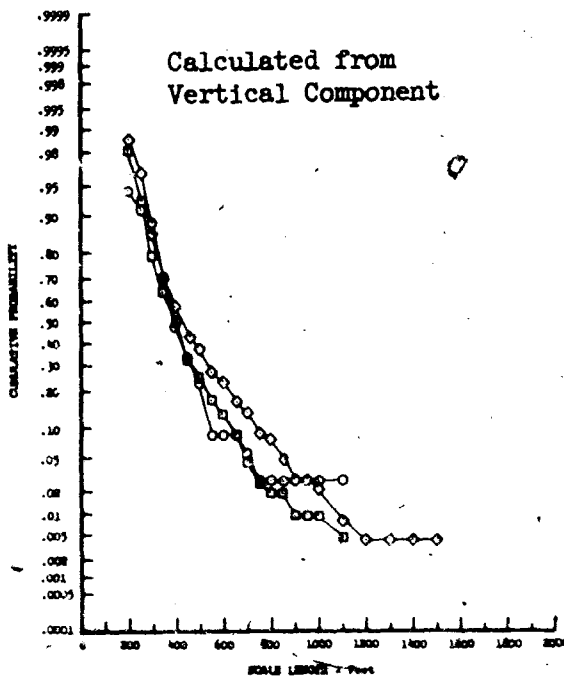
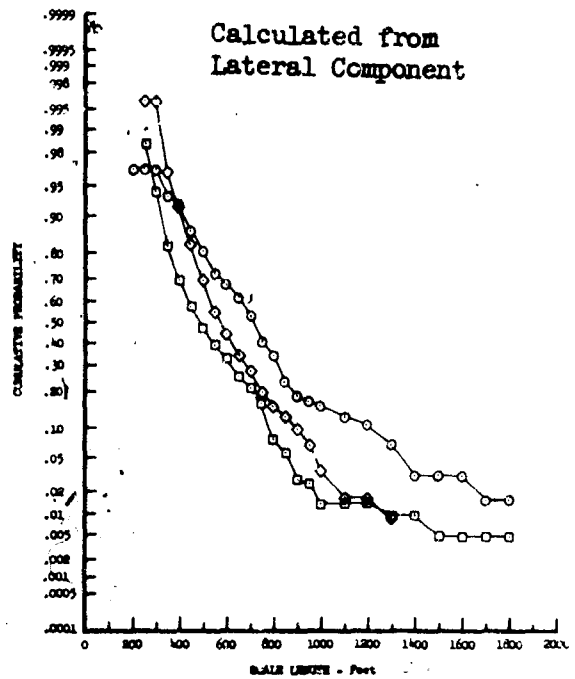
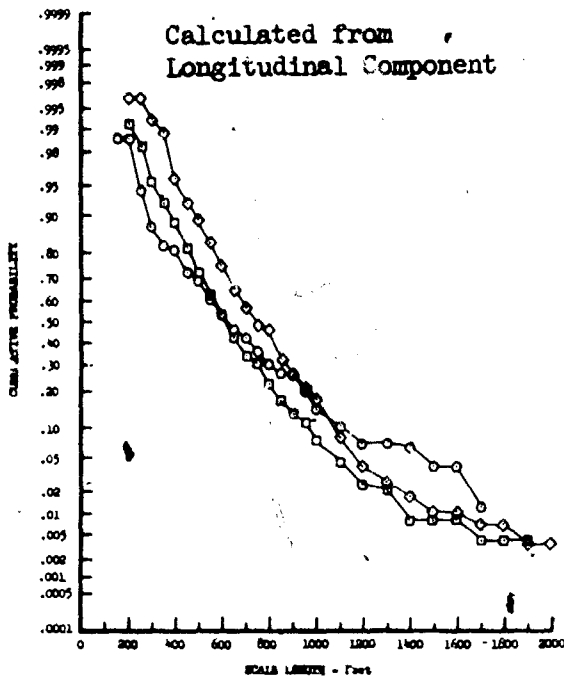
- 250 Feet
- 750 Feet

Figure 30.15 von Karman Longitudinal Scale Length  
Cumulative Probability Associated with  
Absolute Altitude



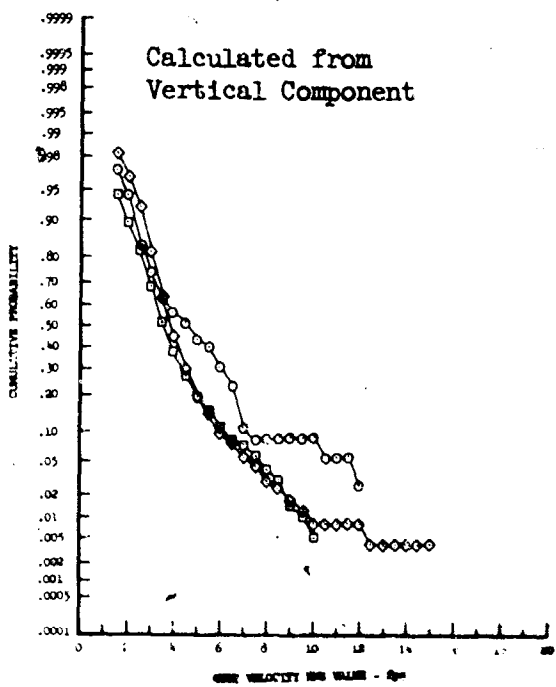
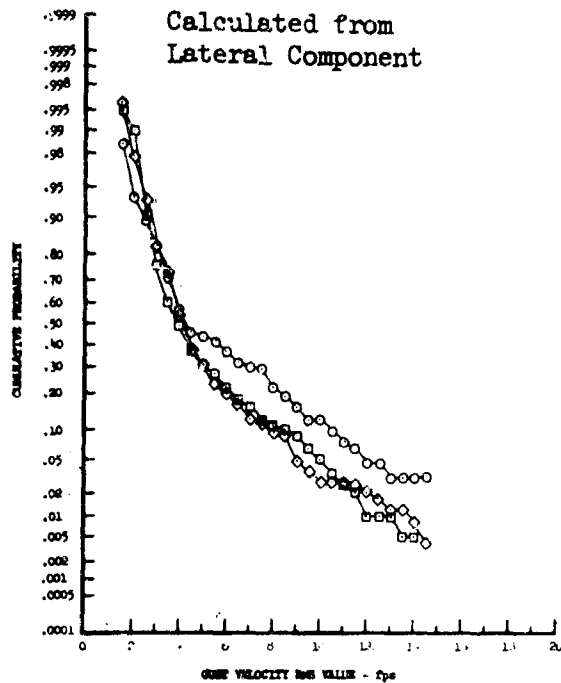
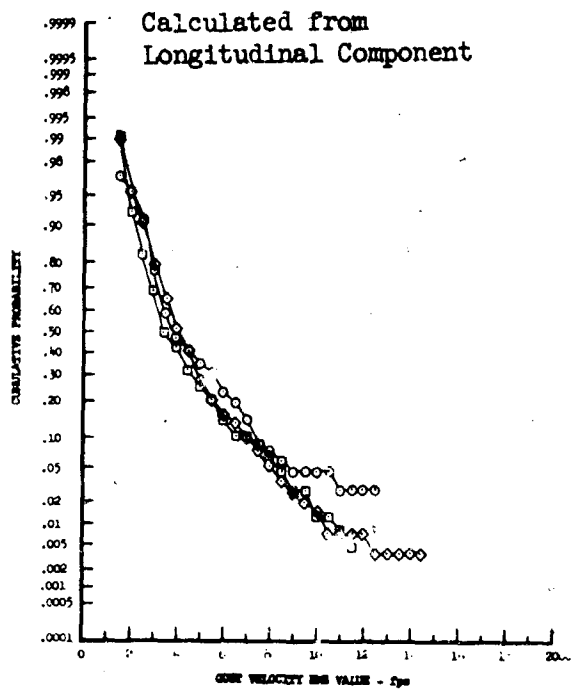
- Very Stable
- Stable
- ◇ Neutral
- ▲ Unstable

Figure 30.16 von Karman Longitudinal Scale Length Cumulative Probability Associated with Atmospheric Stability



- Dawn
- Mid-Morning
- ◇ Mid-Afternoon

Figure 30.17 von Karman Longitudinal Scale Length Cumulative Probability Associated with Time of Day



- Dawn
- Mid-Morning
- ◇ Mid-Afternoon

Figure 30.18 Effects of Time of Day on Cumulative Probability of Gust Velocity RMS Values Used in Scale Length Calculations

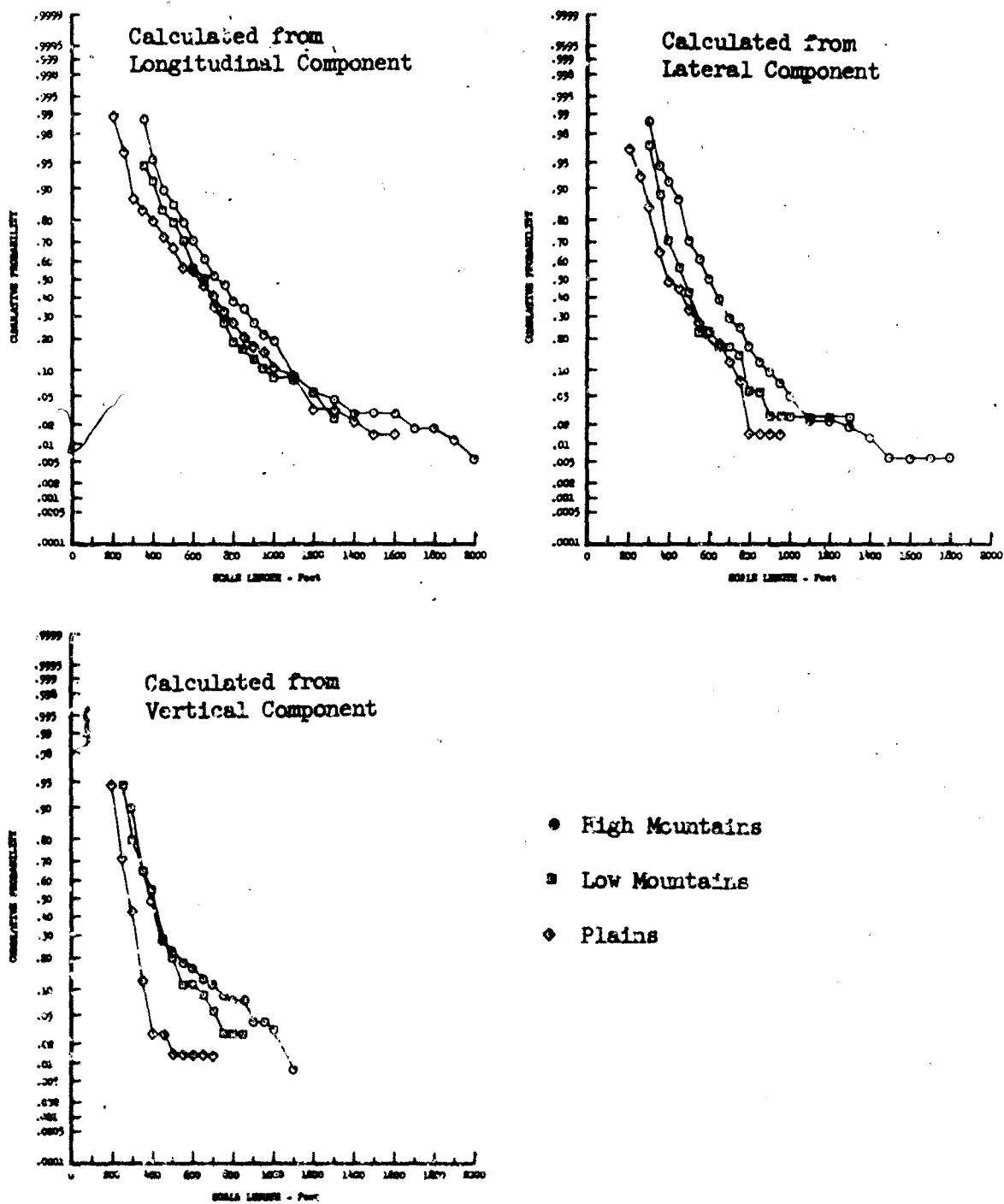
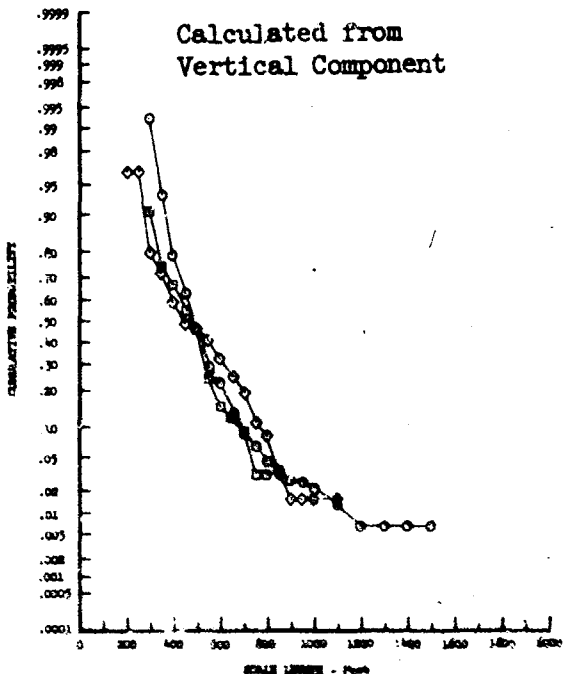
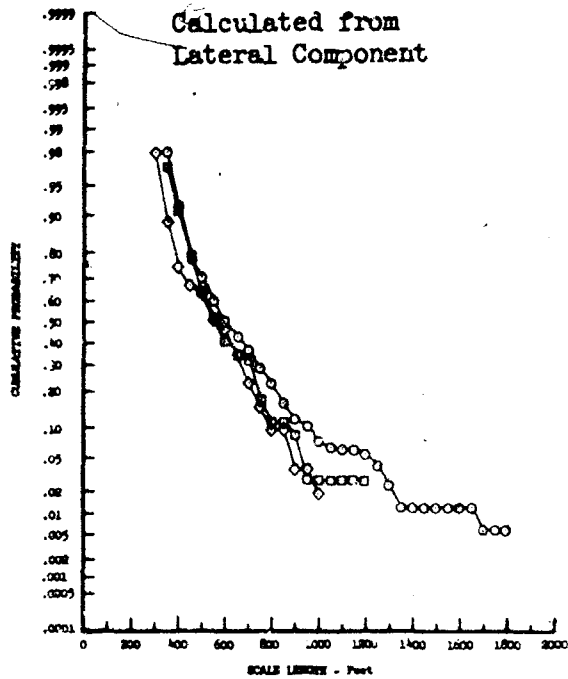
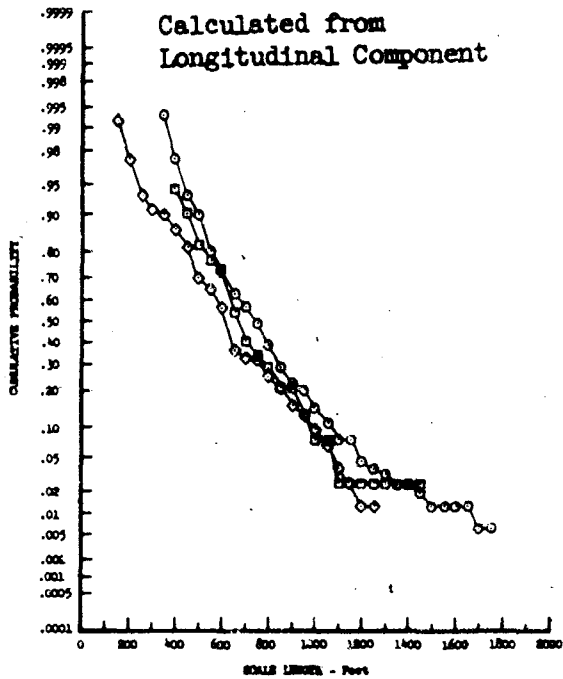


Figure 30.19 Effects of Terrain Type on Cumulative Probability of von Karman Longitudinal Scale Lengths from Data Recorded at 250 Feet



- High Mountains
- Low Mountains
- ◇ Plains

Figure 30.20 Effects of Terrain Type on Cumulative Probability of von Karman Longitudinal Scale Lengths from Data Recorded at 750 Feet

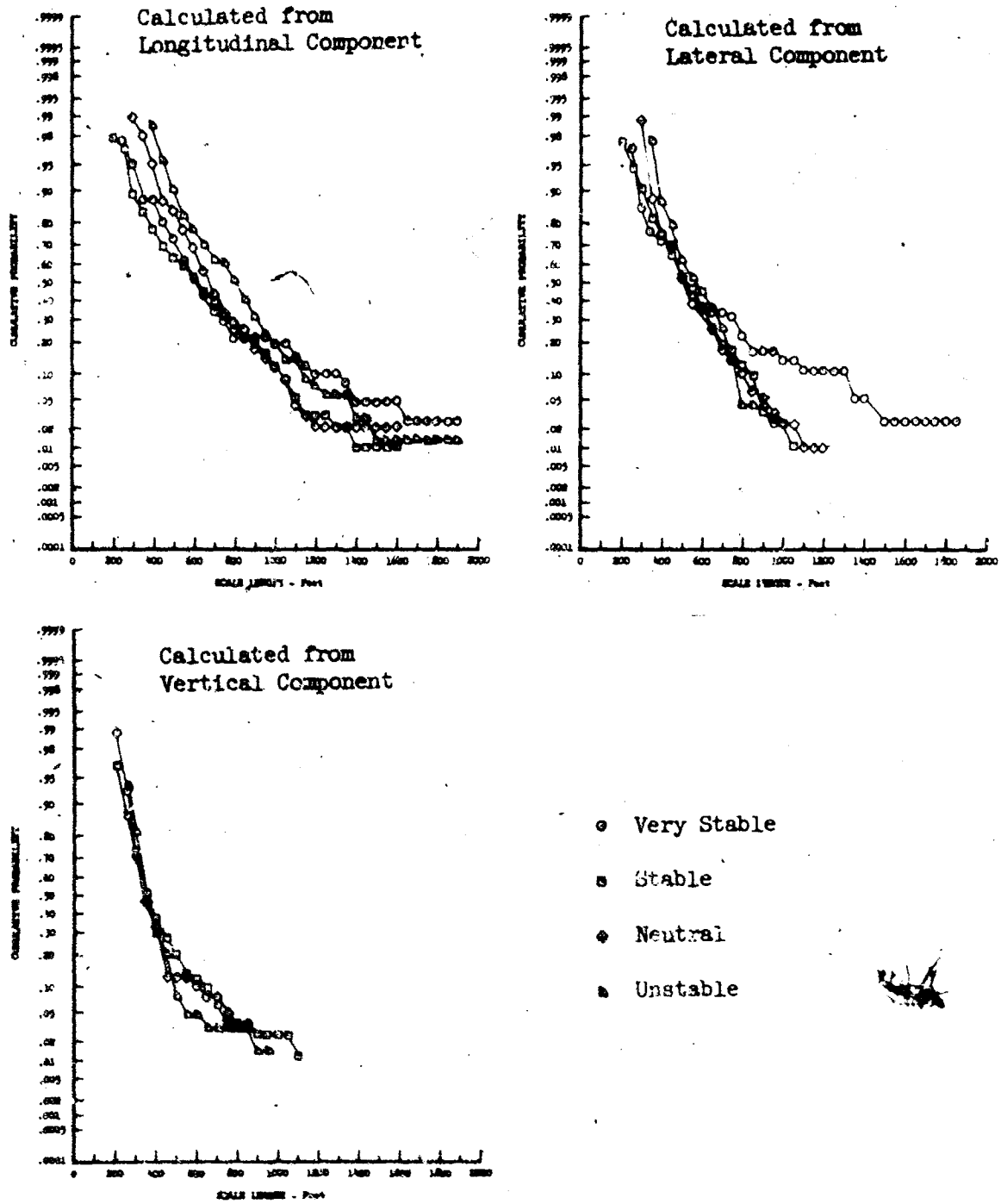
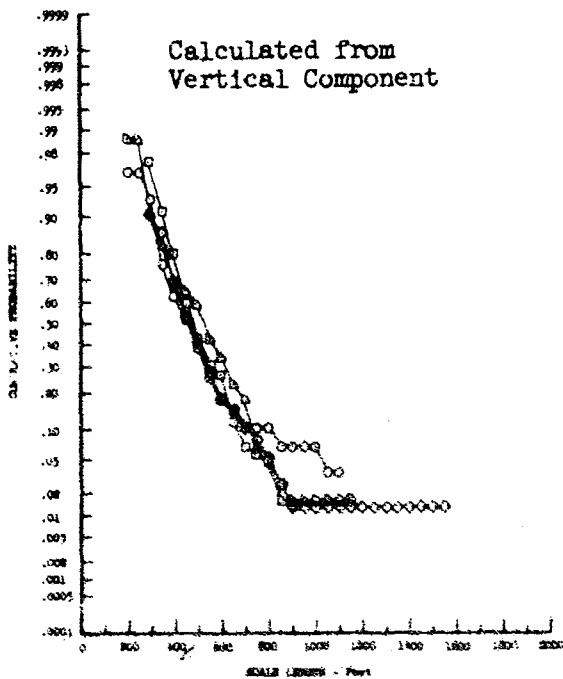
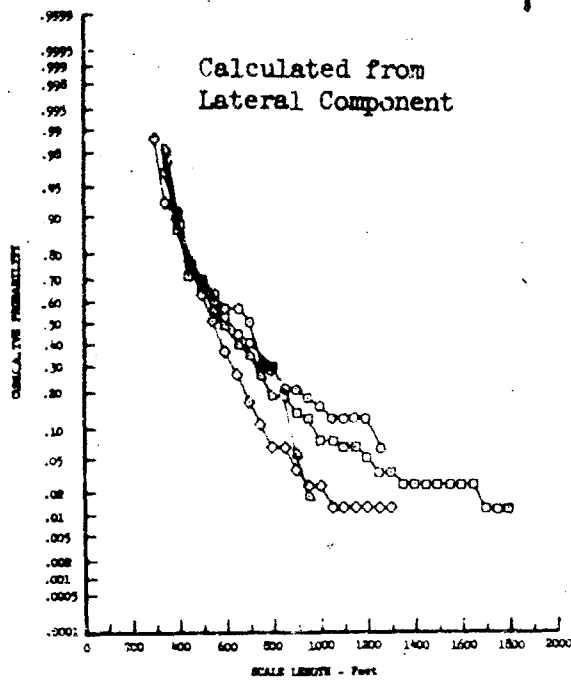
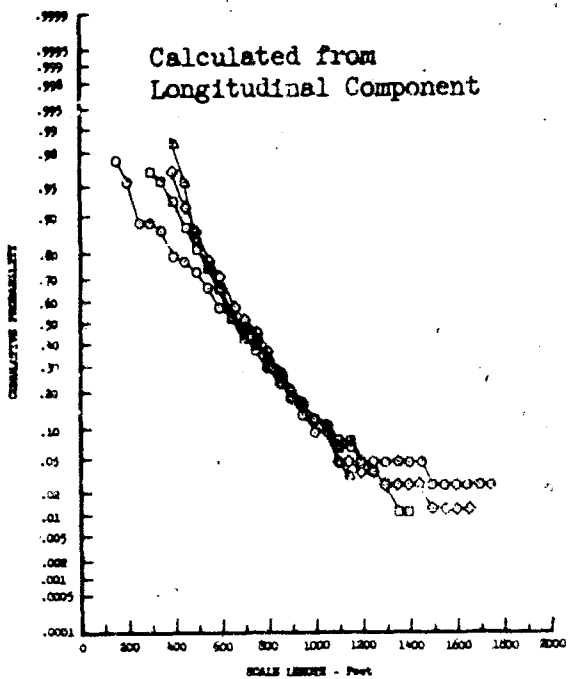


Figure 30.21 Effects of Atmospheric Stability on Cumulative Probability of von Karman Longitudinal Scale Lengths from Data Recorded at 250 Feet



- Very Stable
- Stable
- ◇ Neutral
- ▲ Unstable

Figure 30.22 Effects of Atmospheric Stability on Cumulative Probability of von Karman Longitudinal Scale Lengths from Data Recorded at 750 Feet



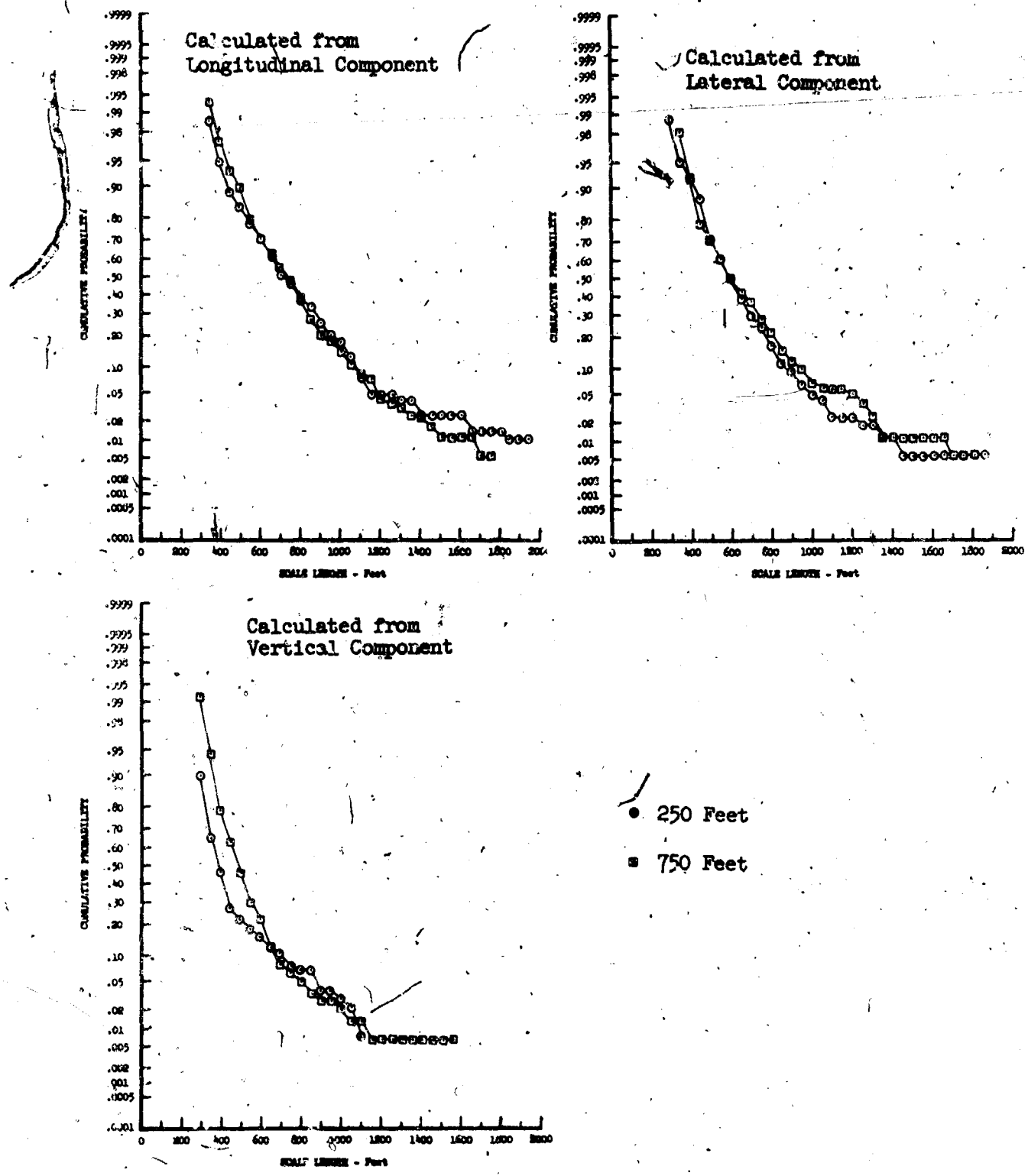
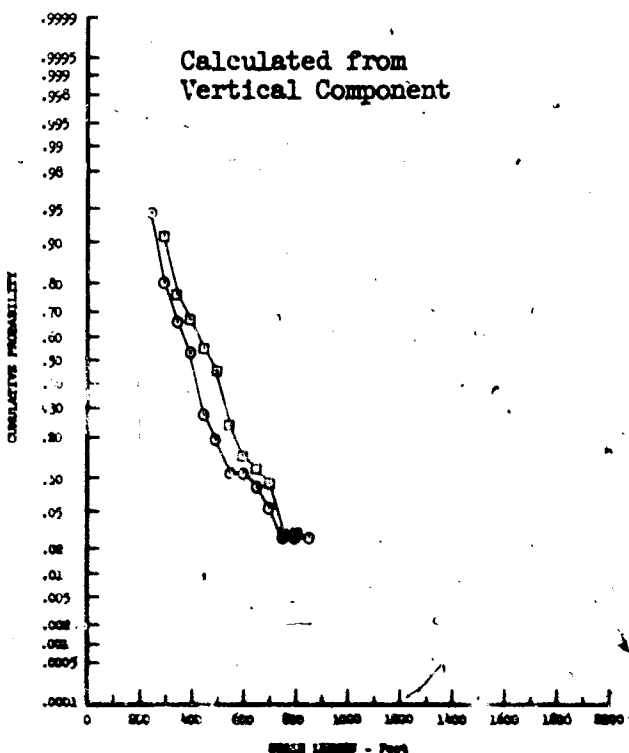
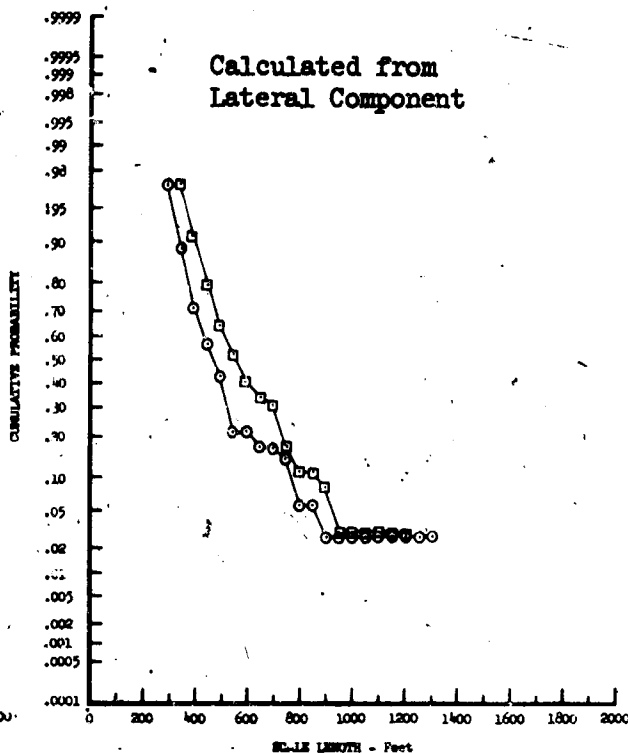
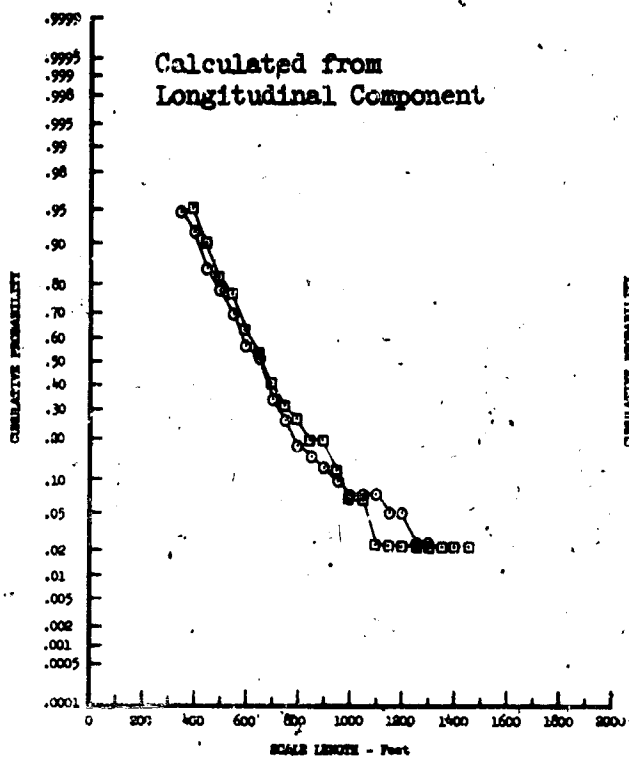
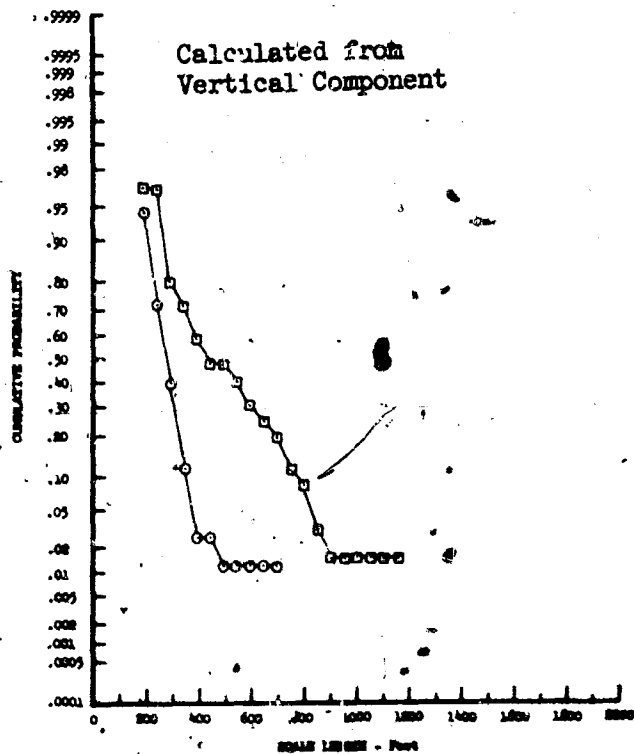
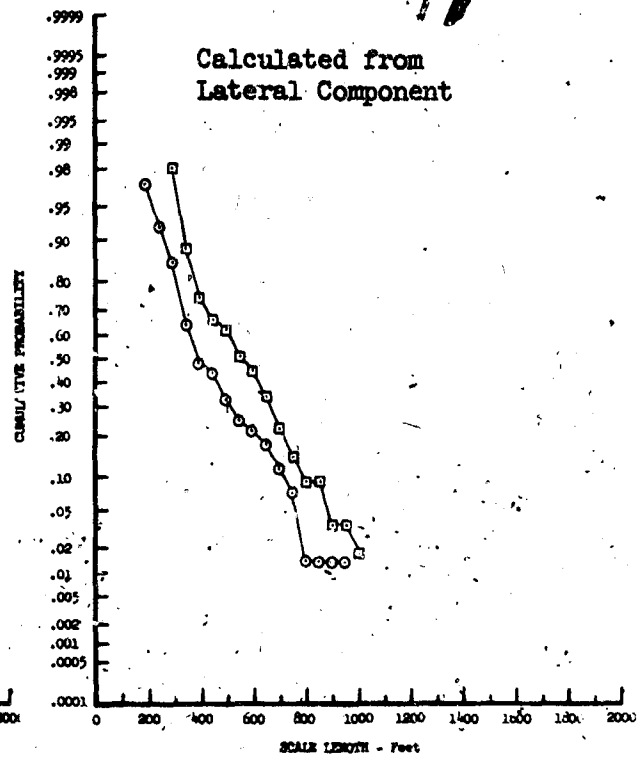
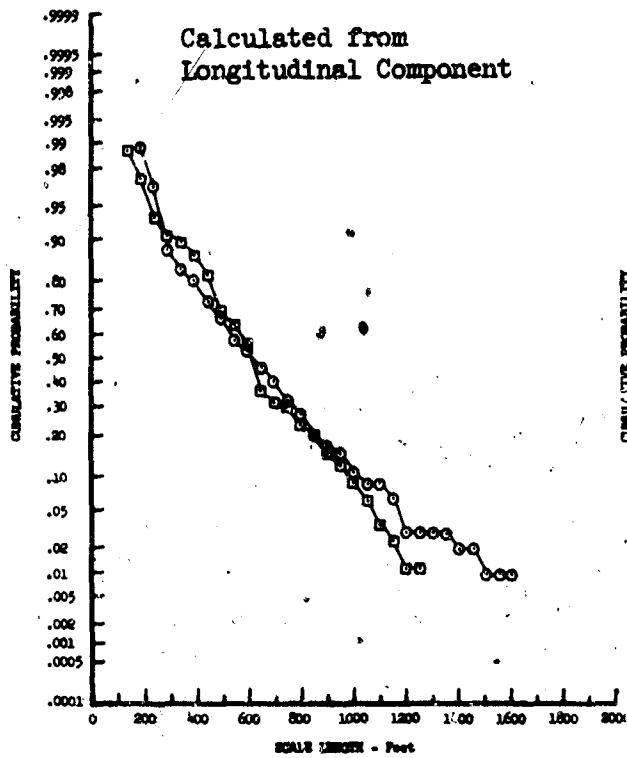


Figure 30.23 Effects of Absolute Altitude on Cumulative Probability of von Karman Longitudinal Scale Lengths from Data Recorded Over High Mountains



- 250 Feet
- 750 Feet

Figure 30.24 Effects of Absolute Altitude on Cumulative Probability of von Karman Longitudinal Scale Lengths from Data Recorded Over Low Mountains



○ 250 Feet

■ 750 Feet

Figure 30.25 Effects of Absolute Altitude on Cumulative Probability of von Karman Longitudinal Scale Lengths from Data Recorded Over Plains

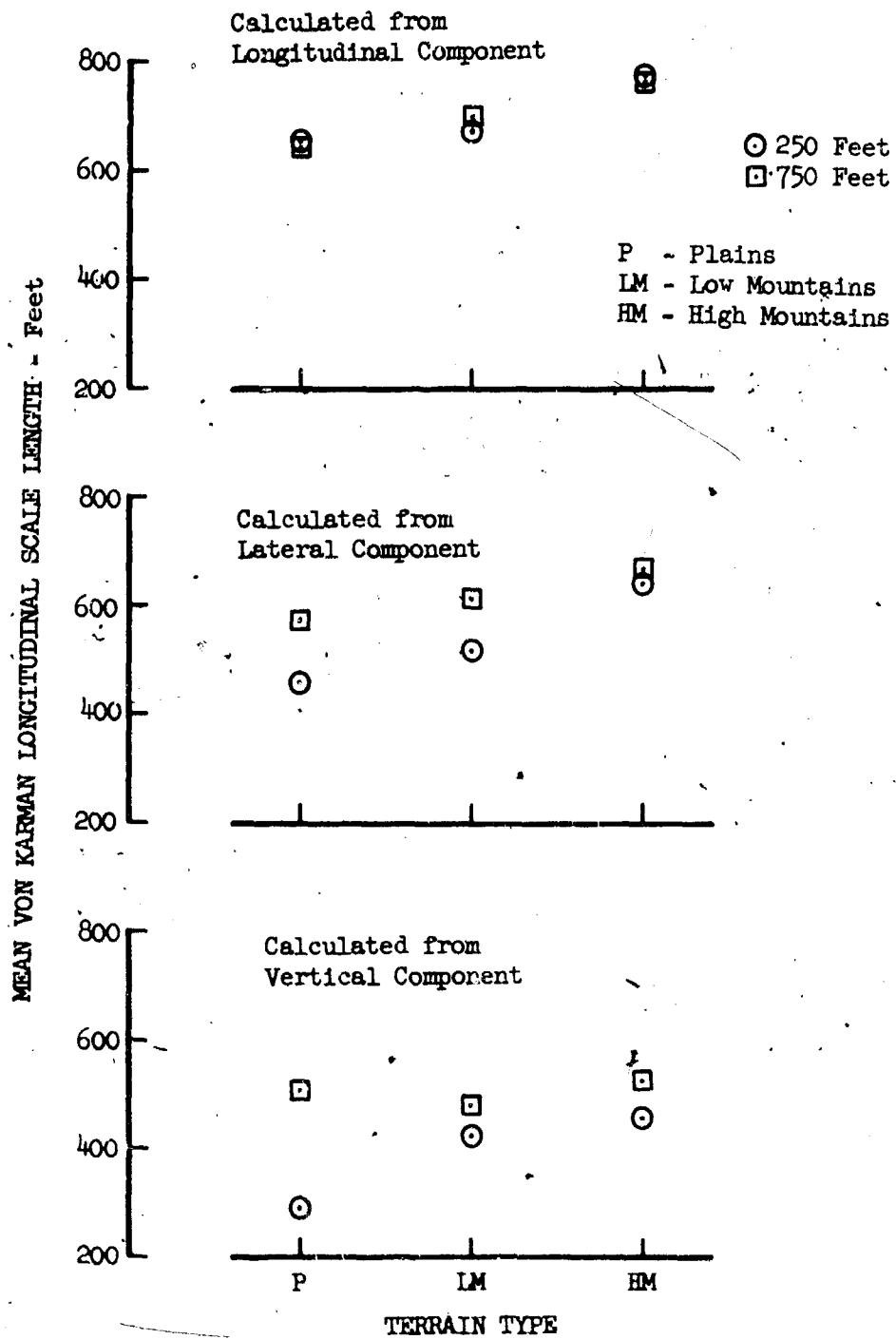


Figure 30.26 Variations of Mean von Karman Longitudinal Scale Length with Absolute Altitude and Terrain Type

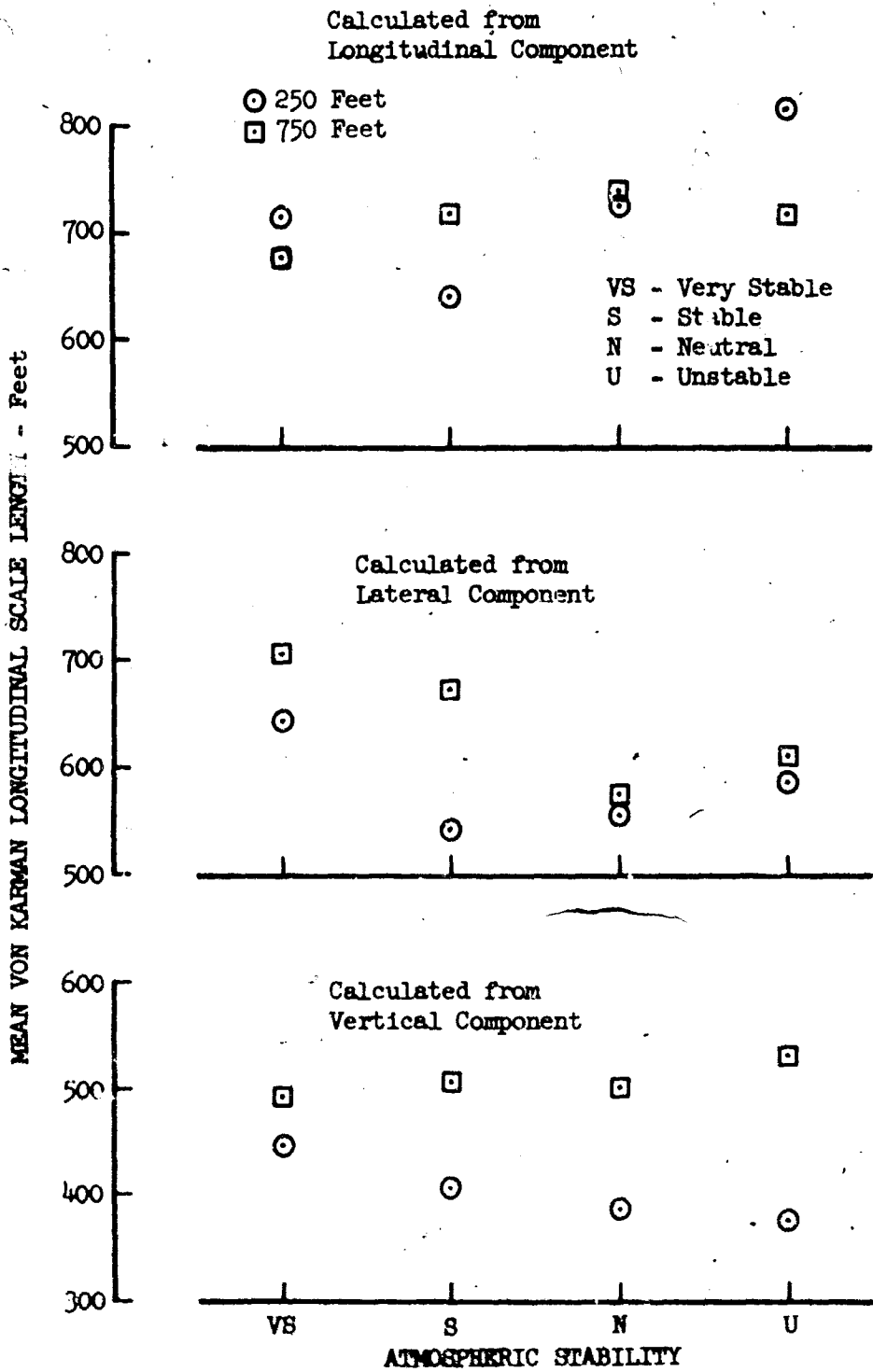


Figure 30.27 Variations of Mean von Karman Longitudinal Scale Length with Absolute Altitude and Atmospheric Stability

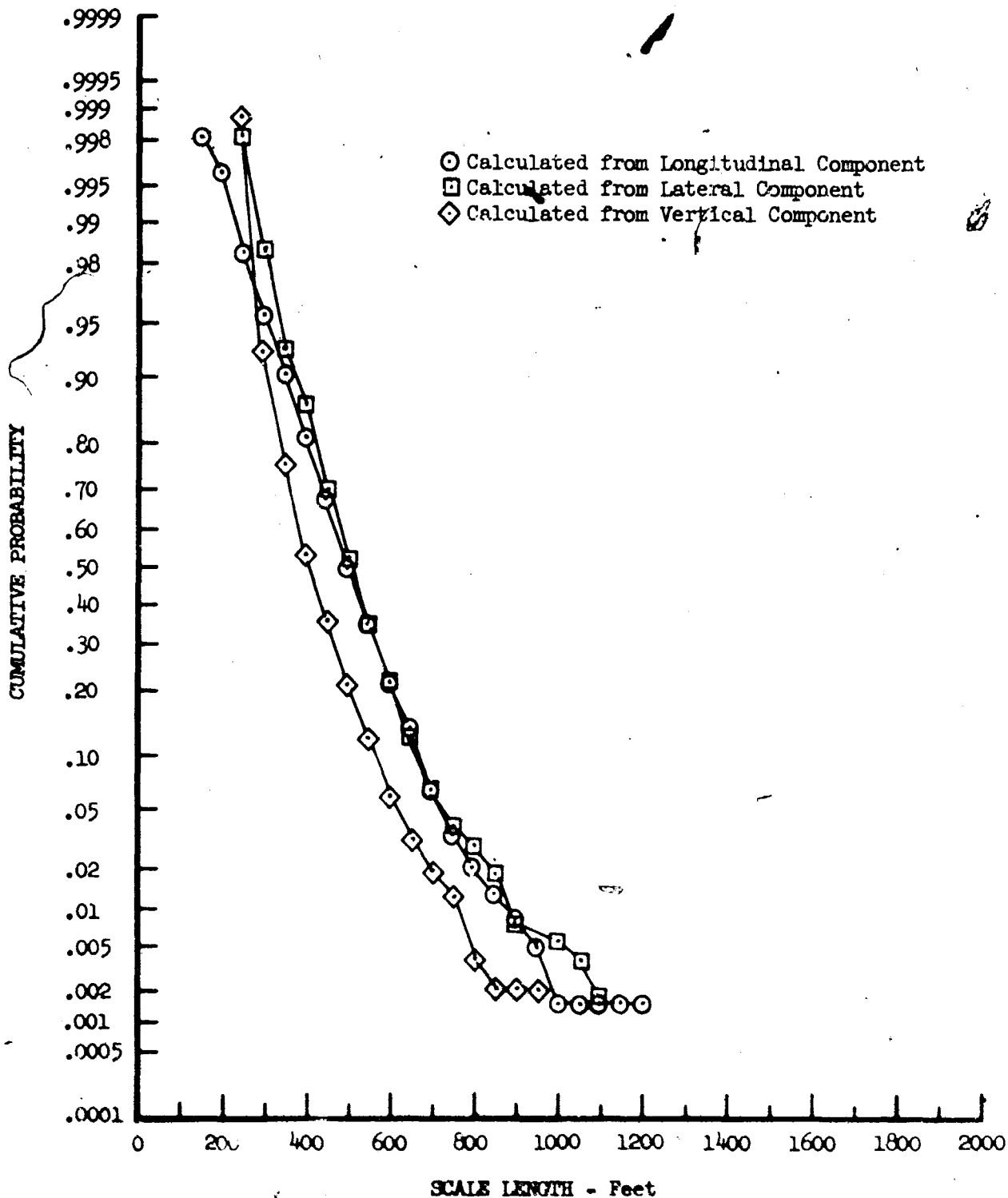


Figure 30.28 Dryden Longitudinal Scale Length Cumulative Probability

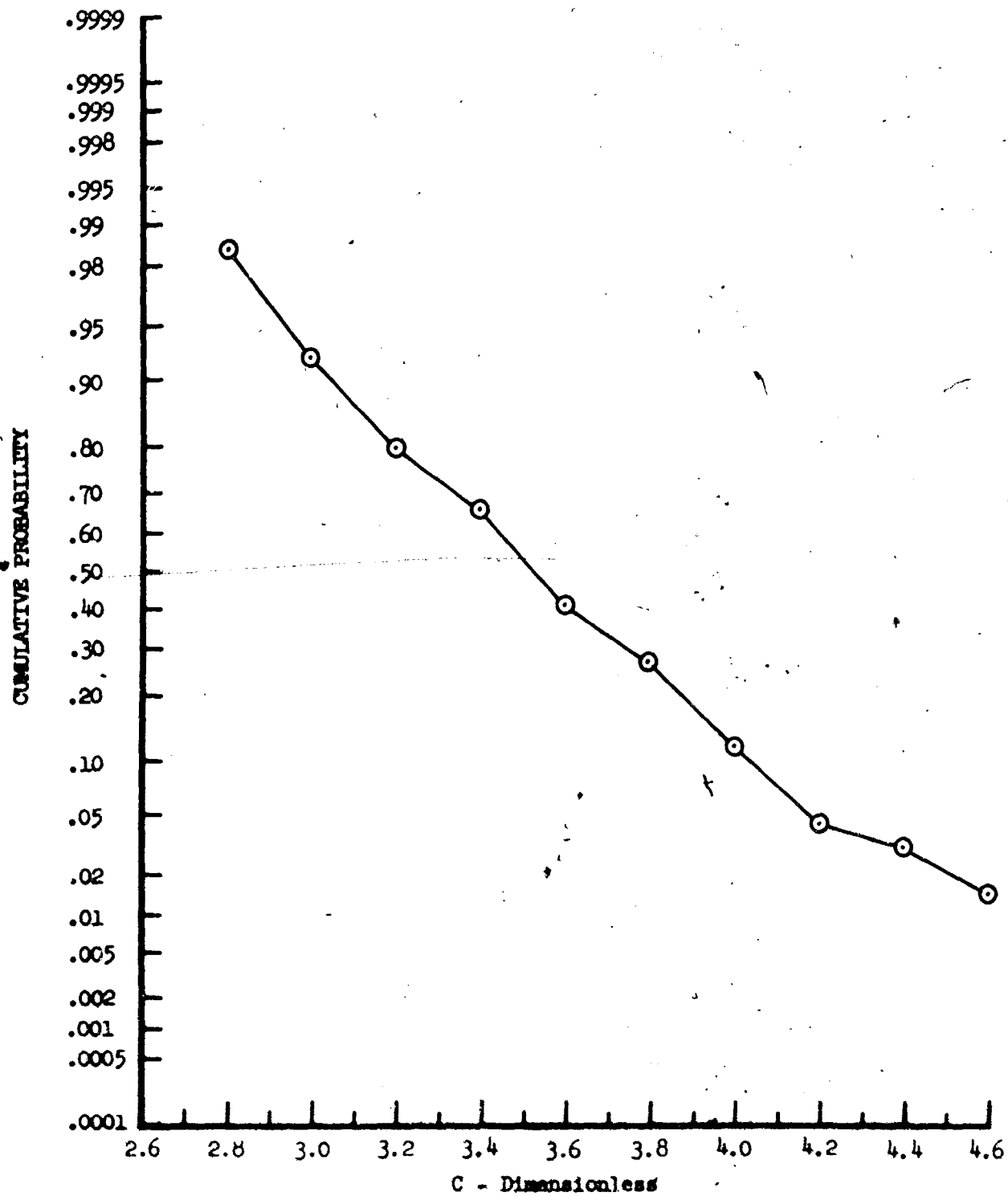


Figure 30.29 Cumulative Probability of Lamley-Panofsky Scale Parameter, C, as Calculated from the Longitudinal Component

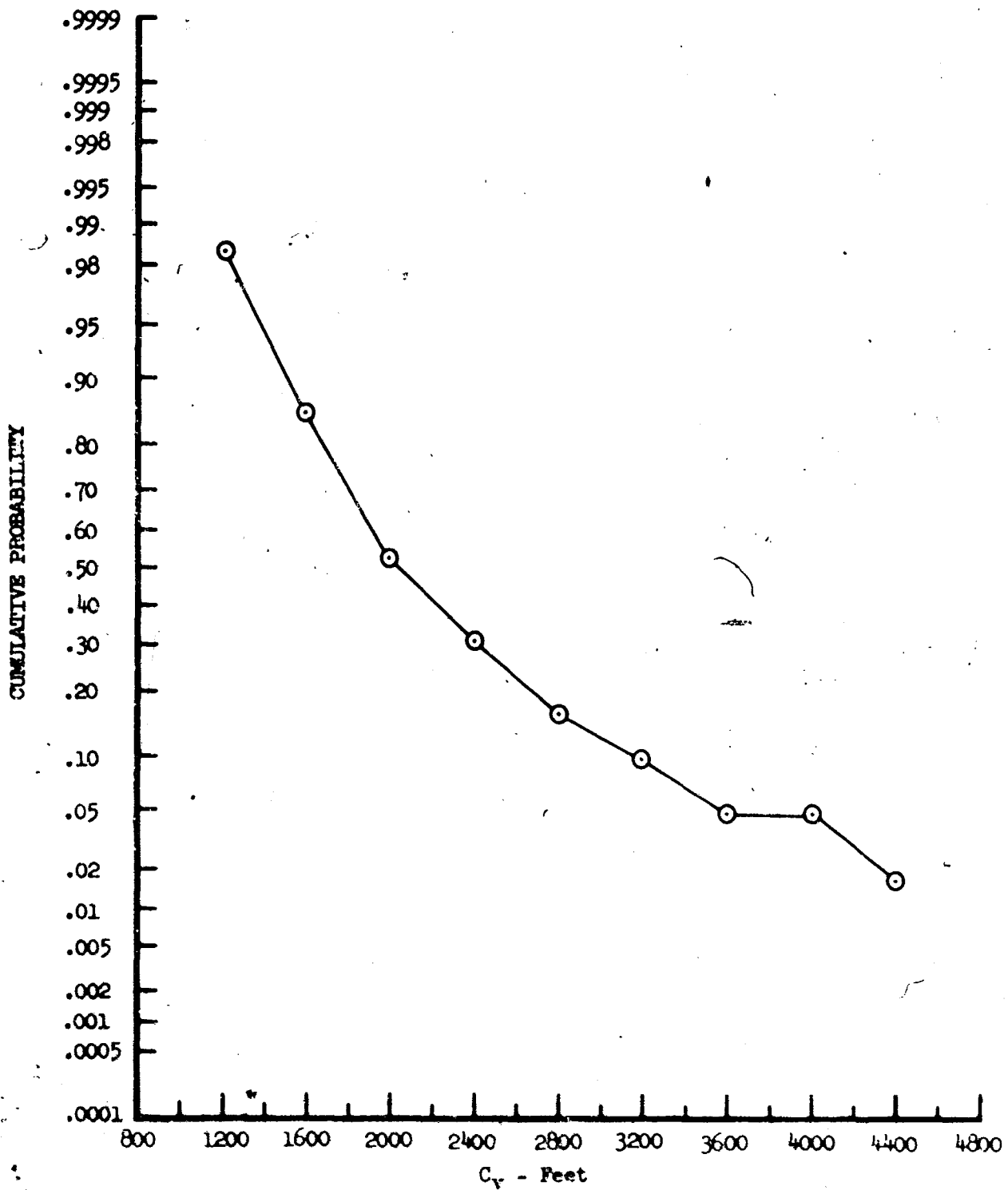


Figure 30.30 Cumulative Probability of Busch-Panofsky Scale Parameter,  $C_v$ , as Calculated from the Lateral Component



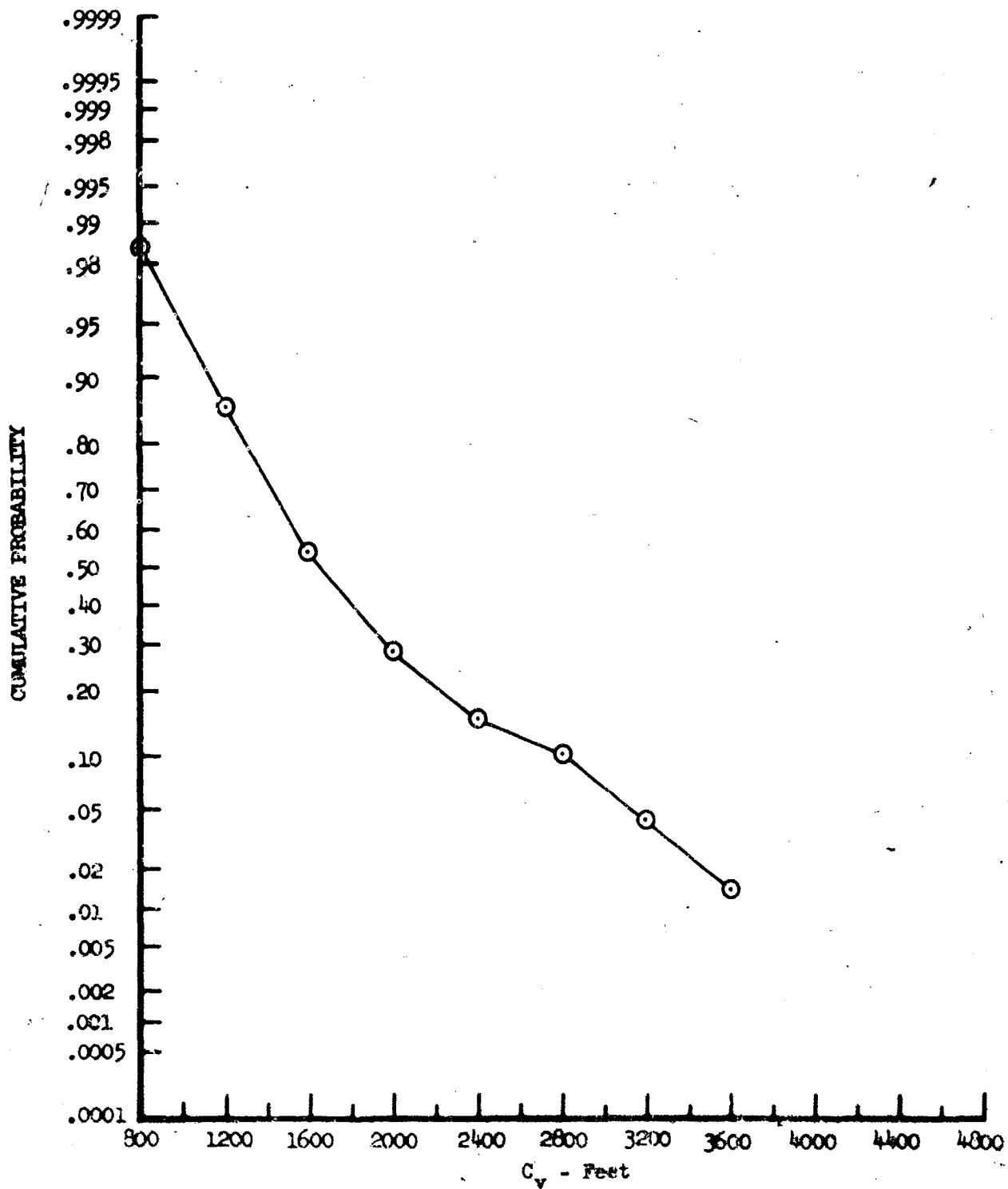


Figure 30.31 Cumulative Probability of Busch-Panofsky Scale Parameter,  $C_v$ , as Calculated from the Vertical Component

### 31. TURBULENCE MICROSCALES

The integral scale length is defined as being equal to the area under the gust velocity autocorrelation curve. The Taylor microscale can also be defined from the autocorrelation curve as the intercept on the y axis of a parabola fitted to the vertex of the curve. The Taylor microscale represents the average eddy size where viscous forces dissipate turbulent energy.

Taylor microscales were calculated using the following equation (Reference 18.2):

$$\lambda^2 = 15 \nu \sigma_{t_n}^2 / \epsilon \quad (31.1)$$

where  $\nu$  is the kinematic viscosity and  $\epsilon$  is the viscous dissipation rate. Viscous dissipation rates pertaining to Phase III data are discussed in Section 34.

The cumulative probability distributions of Taylor's microscale for the time of day categories are shown in Figure 31.1. As has been the case in the past (Reference 31.1), the distribution is shown to be very close to a log-normal. There is a slight difference in the distribution for dawn than for other times of day. The distributions by altitude and stability in Figure 31.2 show a definite difference between very stable and the other stabilities. It appears that the microscale in the dissipation range increases as altitude increases and as the atmosphere becomes more stable. High mountains and plains distributions shown in Figure 31.3 indicate that the microscale does not vary significantly between smooth and rough terrain.

Reference 31.1 suggests that the turbulence spectra should be a function of the kinematic viscosity and the rate at which the energy is dissipated. A scale length formulated in the form of:

$$\eta = \left( \frac{\nu^3}{\epsilon} \right)^{1/4} \quad (31.2)$$

is referred to as the Kolmogorov microscale. This length is much smaller than Taylor's microscale and represents an eddy size where viscous forces predominate, dissipating turbulence fluctuations into heat. Figure 31.4 shows the cumulative probability of the Kolmogorov microscale for the time of day categories indicating slight changes with time of day. Figure 31.5 gives the probability as a function of altitude and stability, showing that the values increase slightly as altitude increases and stability decreases. Terrain effects shown in Figure 31.6 indicate a trend toward longer microscales for plains type terrain.

Reference 18.2 indicates that values on the order of 10 cm (0.328 feet) and approximately 1 mm (0.00328 feet) for Taylor and Kolmogorov microscales, respectively, are to be expected in the atmosphere "near the surface." Table 31.1 summarizes the average values as determined during Phase III.

TABLE 31.1

AVERAGE TAYLOR AND KOLMOGOROV MICROSCALES

Altitude (Feet)	Taylor (Feet)	Kolmogorov (Feet)
250	0.84	0.0033
750	0.90	0.0036

Comparison of Phase III data with Phases I and II data reveals that there is a 20 per cent increase in the average Taylor microscale for data recorded at 250 feet during Phase III. This can be primarily attributed to the higher gust velocity standard deviations recorded during Phase III.

The average Taylor microscales obtained during Phase III are compared in Figure 31.7 with those presented by Taylor in Reference 31.2 and by MacCready in Reference 31.3 as well as with those obtained during Phases I and II (Reference I-2), the BREN Tower fly-bys (Reference Section 41), and the flights supporting the Operation Rough Rider Project (NSSL).

The average Kolmogorov microscales obtained during Phase III are compared in Figure 31.8 with those presented in Reference 18.2 by Lumley-Panofsky as well as with those obtained during Phases I and II, the BREN Tower fly-bys, and the flights supporting the Operation Rough Rider Project (NSSL).

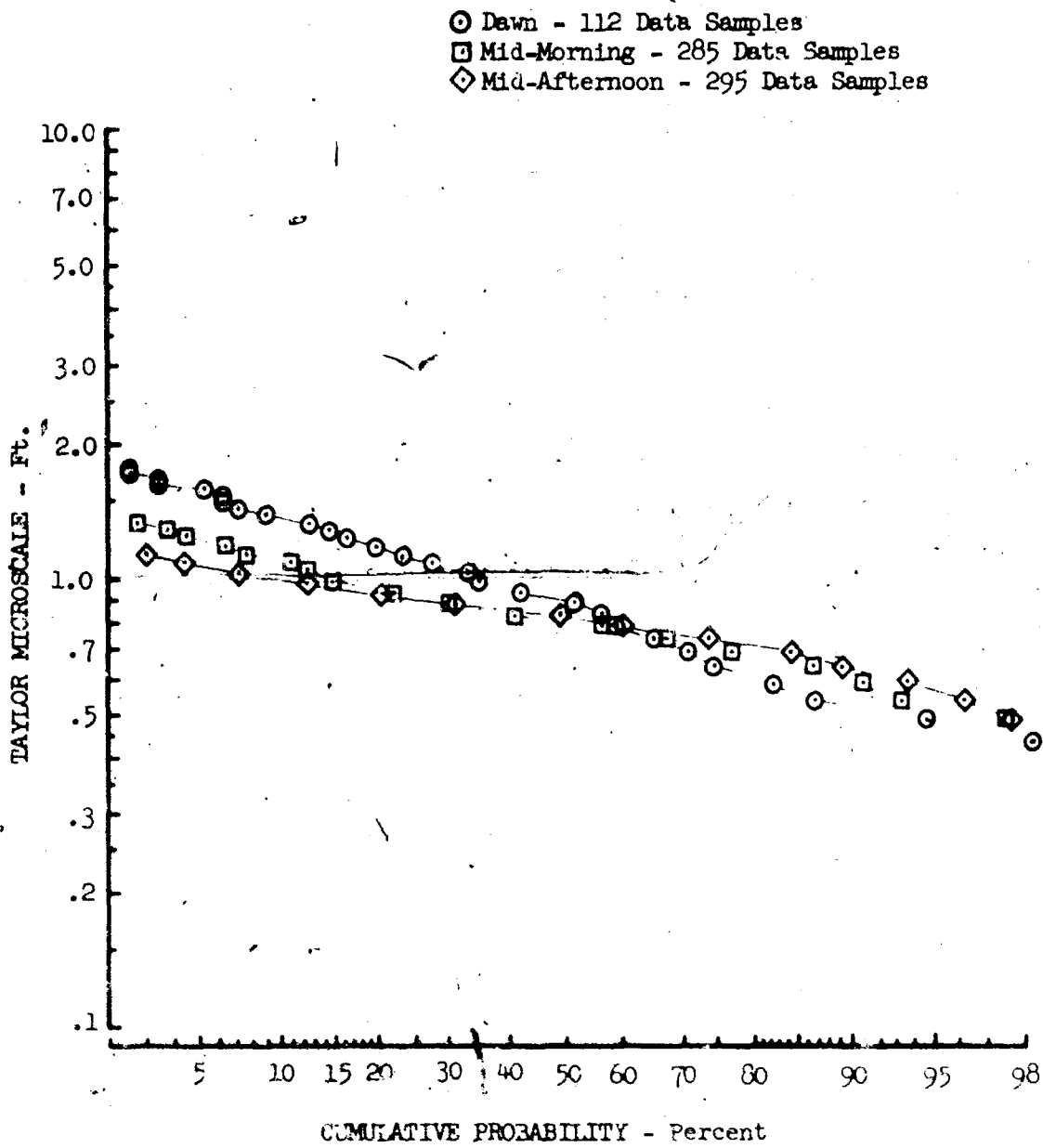


Figure 31.1 Variation of Taylor Microscale for Time of Day

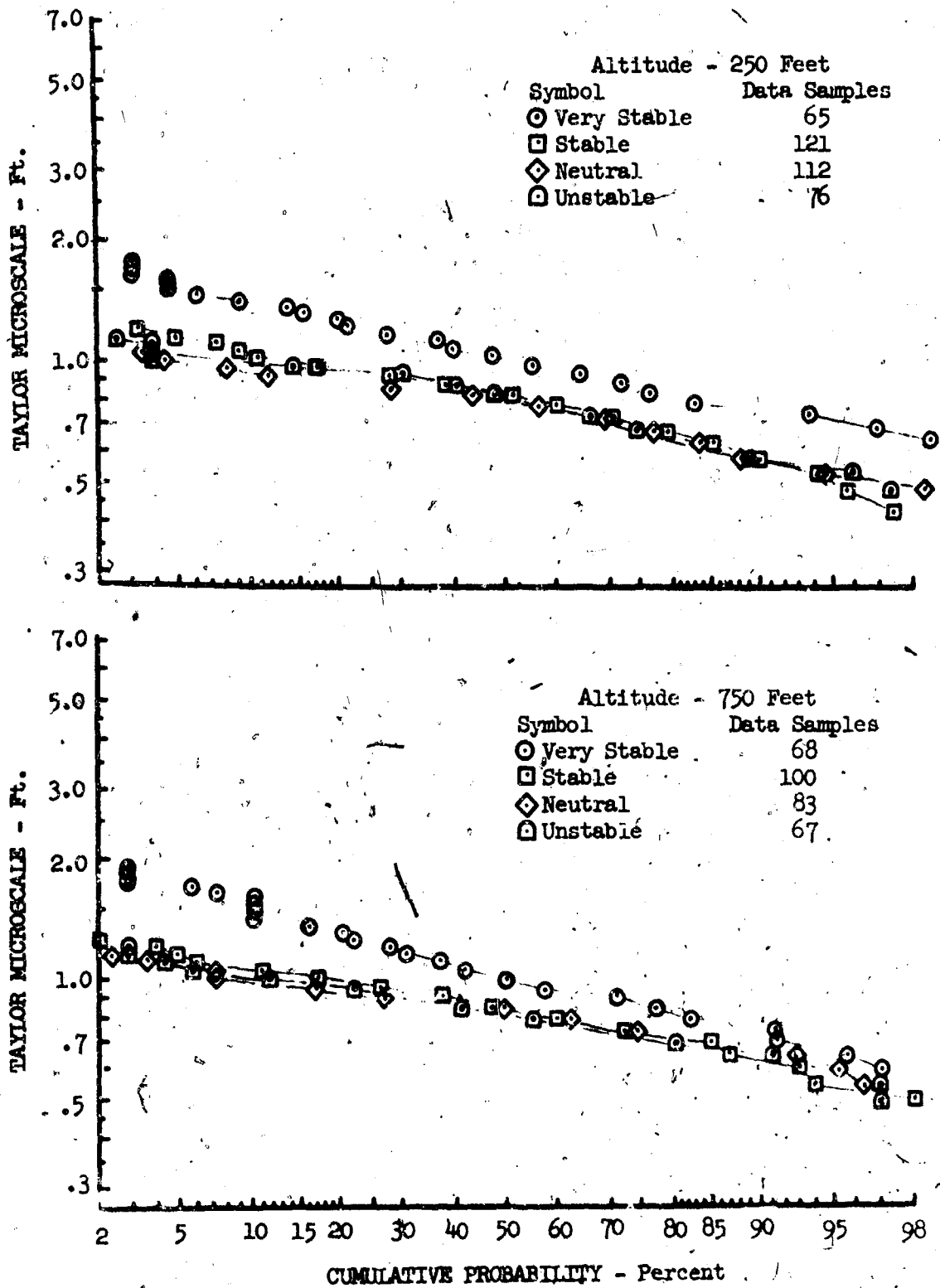


Figure 31.2 Variation of Taylor Microscale for Altitude and Atmospheric Stability

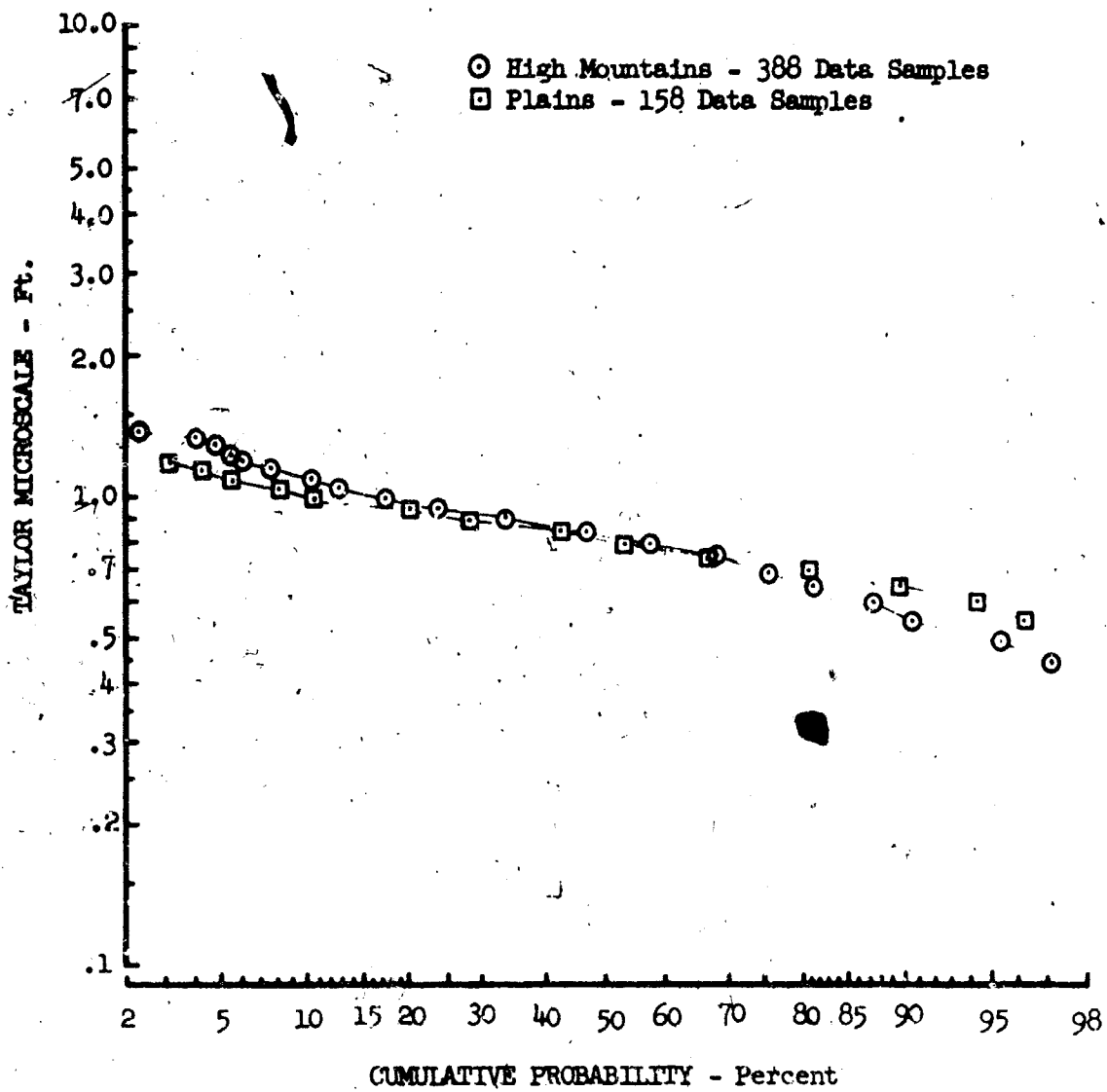


Figure 31.3 Variation of Taylor Microscale for Plains and Mountain Terrain

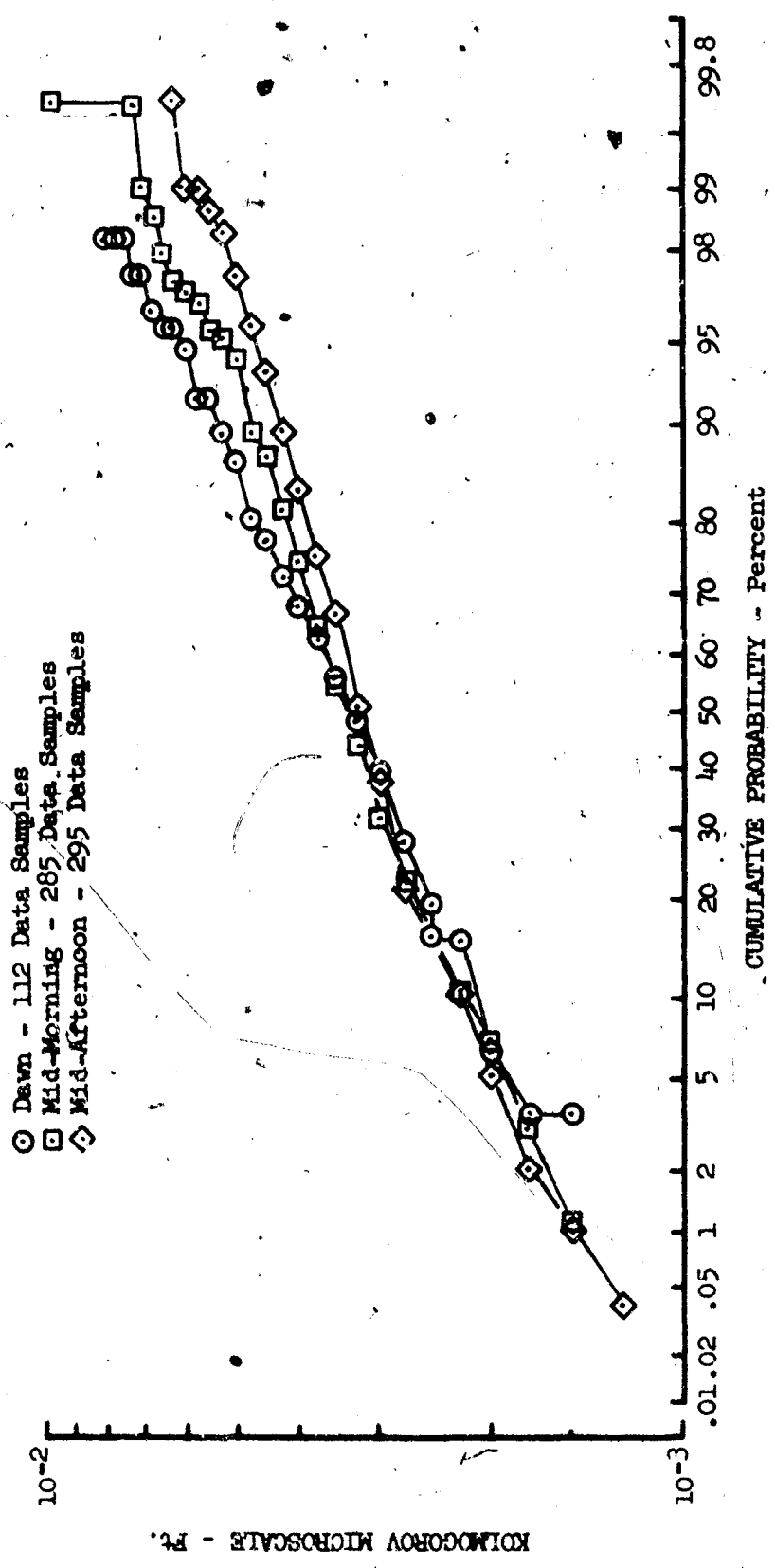


Figure 31.4 Variation of Kolmogorov Microscale for Time of Day

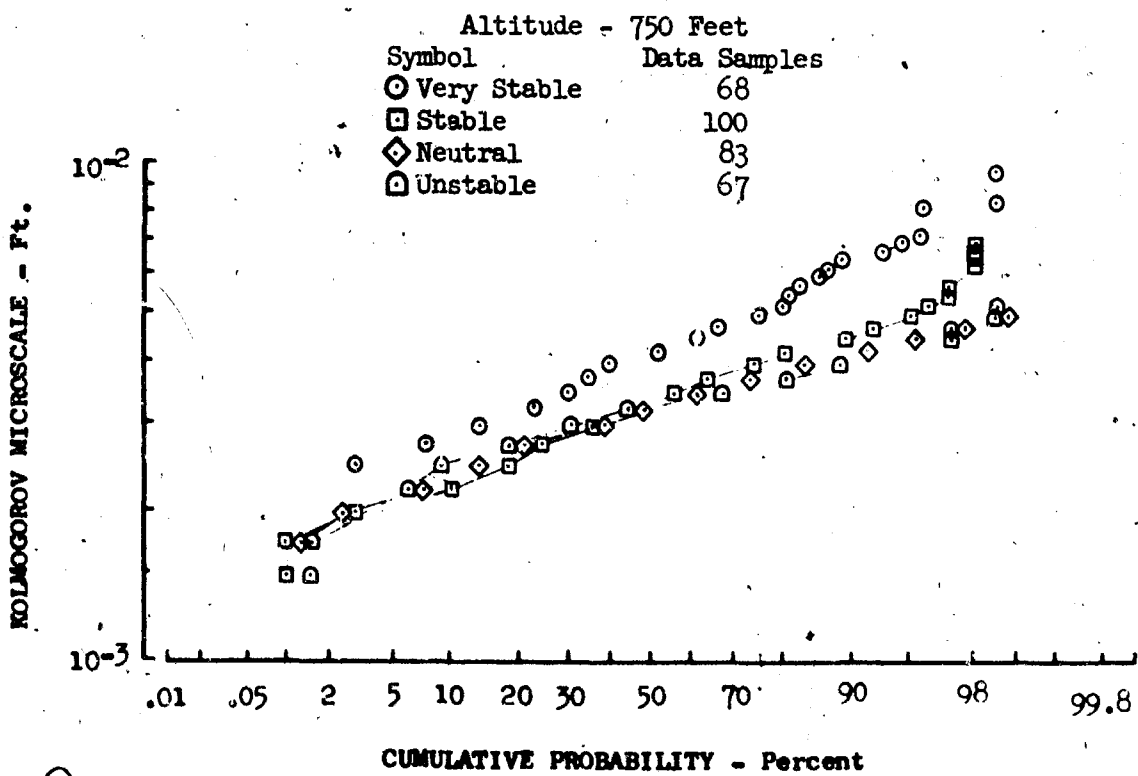
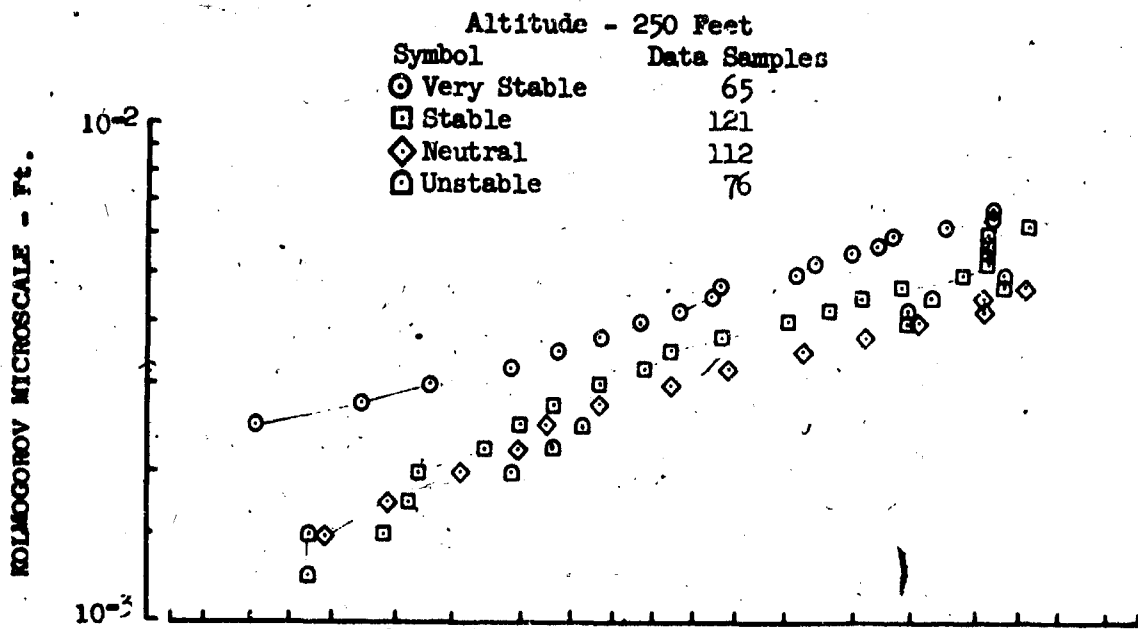


Figure 51.5 Variation of Kolmogorov Microscale for Altitude and Stability



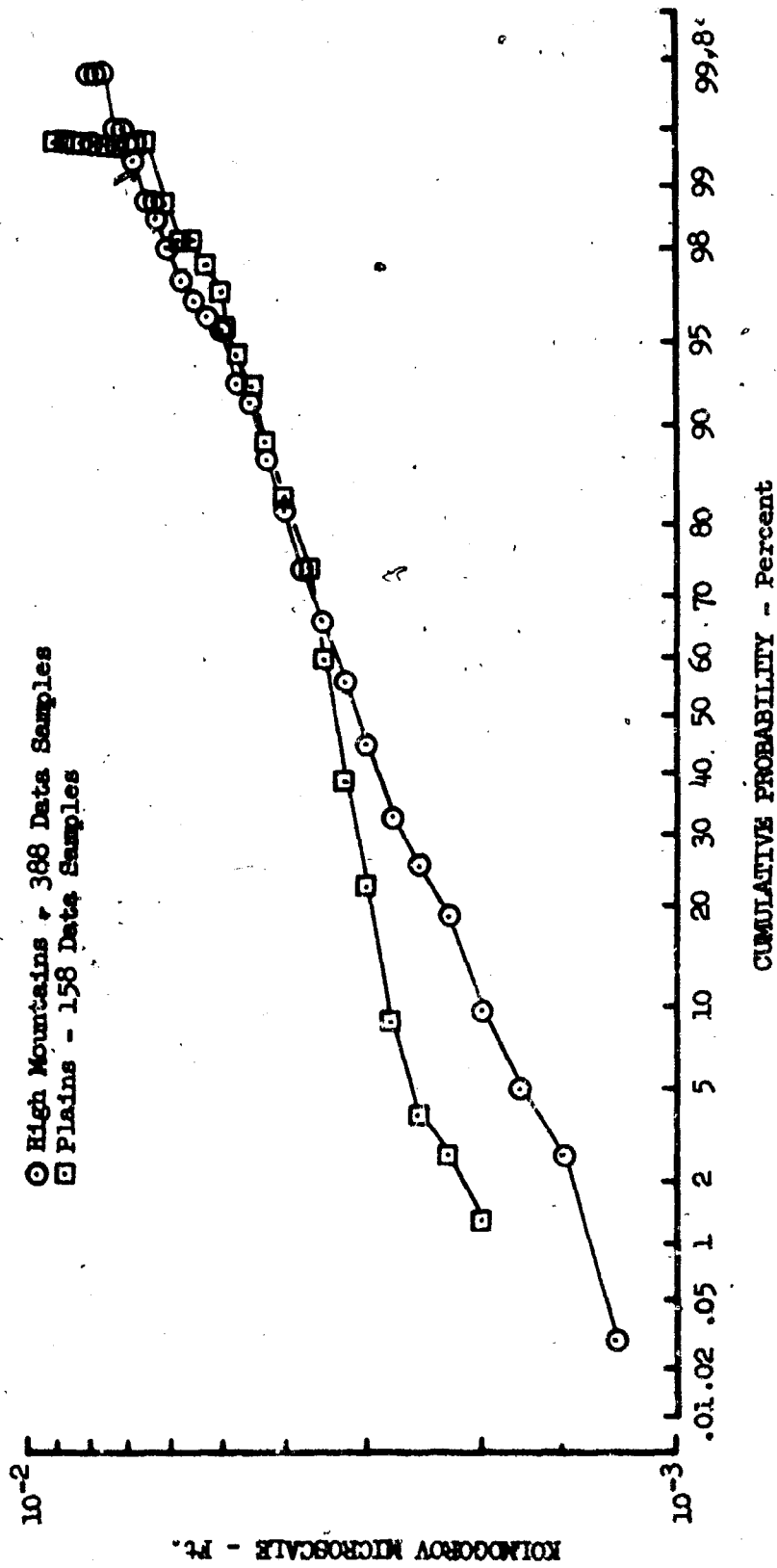


Figure 31.6 Variation of Kolmogorov Microscale for Plains and Mountain Terrain

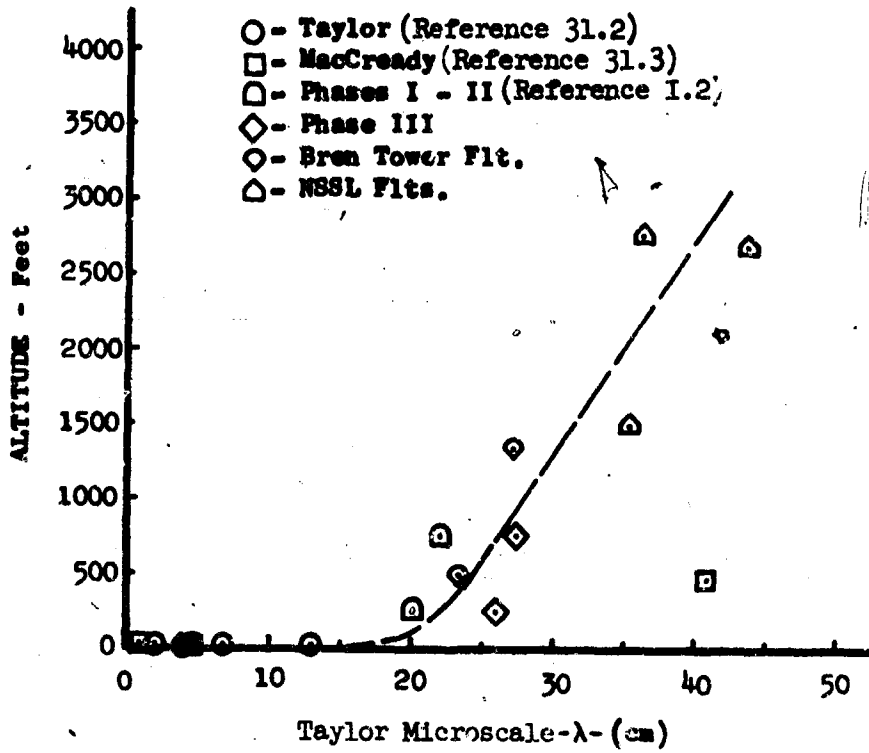


Figure 31.7 Variation of Taylor Microscale with Altitude

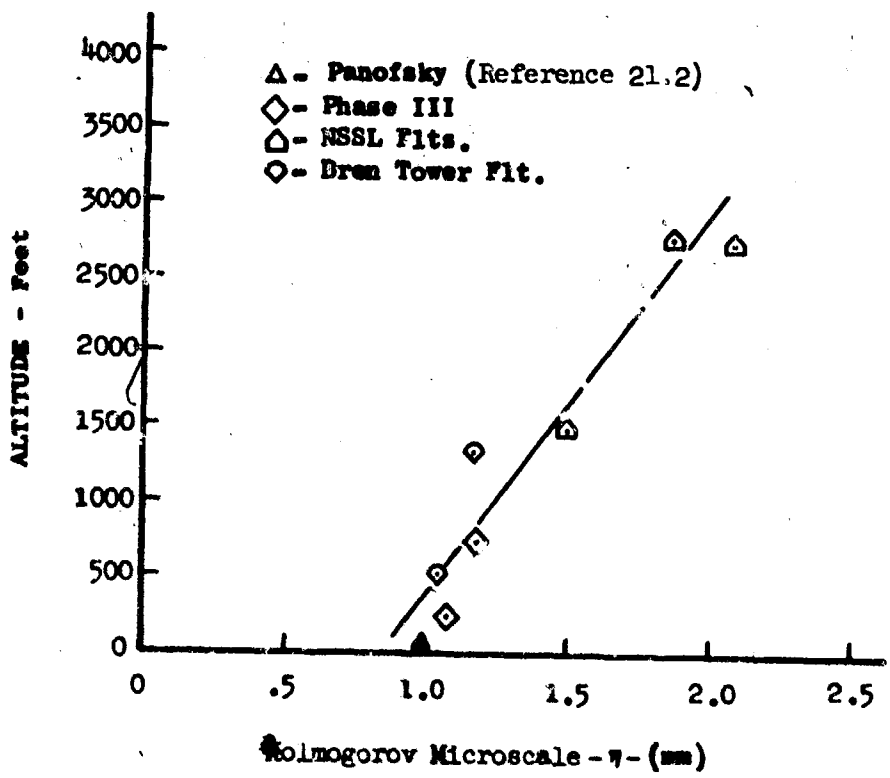


Figure 31.8 Variation of Kolmogorov Microscale with Altitude

REFERENCES

VOLUME I

- I.1 Neal V. Loving, Clear Air Turbulence (CAT) Measurement for Structural Design Criteria, AIAA Paper No. 65-510, American Institute of Aeronautics and Astronautics, Easton, Pa., July, 1965.
- I.2 D. E. Gunter, et al., Low Altitude Atmospheric Turbulence LO-LOCAT Phases I and II, ASD-TR-69-12, ASD-AFSC, Wright-Patterson Air Force Base, Ohio, February, 1969.
- 3.1 S. O. Rice, "Mathematical Analysis of Random Noise," Bell System Technical Journal, Vol. 23 (1944), pp 282-332, Vol. 24 (1945), pp 46-156.
- 4.1 Aviation Weather for Pilots and Flight Operations Personnel, AC 006, FAA and DOC, Washington, D.C., 1965.
- 4.2 Richard E. Rhyne and Roy Steiner, Power Spectral Measurement of Atmospheric Turbulence in Severe Storms and Cumulus Clouds, TN D-2469, National Aeronautics and Space Administration, Washington, D.C., October, 1964.
- 4.3 J. T. Lee, "Thunderstorm Turbulence and Radar Echoes, 1964 Data Studies, TN-3-NSRL-24," Papers on Weather Radar, Atmospheric Turbulence, Sferics, and Data Processing, U.S. Department Comm., ESSA, August, 1965.
- 5.1 W. J. Dixon and F. J. Massey, Jr., Introduction to Statistical Analysis, McGraw-Hill Book Co., Inc., 1957.
- 5.2 Neal Warner, The Run Test Criteria for Random Data Stationarity, ECOM-2840, United States Army Electronics Command, Fort Monmouth, N.J., 1967.
- 6.1 Julius S. Bendat and Allan G. Piersol, Measurement and Analysis of Random Data, John Wiley and Sons, Inc., New York, 1966.
- 8.1 Frenz E. Hohn, Elementary Matrix Algebra, The MacMillan Company, New York, 1965, pp 101-103.
- 8.2 J. F. Price, R. H. Simonsen, Various Methods and Computer Routines for Approximation, Curve Fitting and Interpolation, Mathematical Note No. 249, Mathematics Research Laboratory, Boeing Scientific Research Laboratories, July, 1963, pp 32-54.
- 8.3 Hilbert Schenck, Jr., Theories of Engineering Experimentation, McGraw-Hill Book Company, Inc., New York, 1961, pp 170-180.
- 8.4 R. S. Burrington, C. M. May, Jr., Handbook of Probability and Statistics with Tables, Handbook Publishers, Inc., Sandusky, Ohio, 1958.

- 8.5 Harry Press, May T. Meadows, and Ivan Hadlock, A Re-Evaluation of Data on Atmospheric Turbulence and Airplane Gust Loads for Application in Spectral Calculations, NACA Report 1272, Langley Research Center, Langley Air Force Base, Virginia, 1956.
- 8.6 W. H. Austin, Jr., Environmental Conditions to be Considered in the Structural Design of Aircraft Required to Operate at Low Levels, SEG-TR-65-4, Research and Technology Division, Wright-Patterson Air Force Base, Ohio, January 1965.
- 10.1 Julius S. Bendat, Probability Functions for Random Responses: Prediction of Peaks, Fatigue Damage, and Catastrophic Failures, NASA CR-33, April, 1964.
- 10.2 J. Burnham, An Experimental Check on the Theoretical Relationship Between the Spectral Density and the Probability Distribution of Crossings for a Stationary Random Process with Gaussian Distribution, Using Data Obtained in Measurements of Aircraft Response to Turbulent Air, Ministry of Aviation C. P. No. 834, Her Majesty's Stationary Office, London, 1965.
- 12.1 K. R. Monson, et al., Low Altitude Atmospheric Turbulence LO-LOCAT Phase III Interim Report, Aeronautical Systems Division Technical Report, AFFDL-TR-69-63, Wright-Patterson Air Force Base, Ohio, February, 1969.
- 13.1 Francis E. Pritchard, The Turbulence and Terrain Environments Affecting Low-Altitude, High-Speed Flight, FDM No. 393, Cornell Aeronautical Laboratory, Inc., Buffalo, New York, July, 1966.
- 13.2 J. B. Dempster and C. A. Bell, "Summary of Flight Load Environmental Data Taken on B-52 Fleet Aircraft," Journal of Aircraft, Vol. 2, No. 5, September-October, 1965.
- 13.3 C. B. Notess, The Effects of Atmospheric Turbulence Upon Flight at Low Altitude and High Speed, FDM No. 325, Cornell Aeronautical Laboratory, Buffalo, New York, 31 October 1961.
- 13.4 J. K. Zbrozek, The Relationship Between the Discrete Gust and Power Spectra Presentations of Atmospheric Turbulence, With a Suggested Model of Low-Altitude Turbulence, Aeronautical Research Council (England), R and M No. 3216, 1961.
- 14.1 U. O. Lappe, Design of a Low Altitude Turbulence Model for Estimating Gust Loads on Aircraft, AFFDL-TR-64-170, Wright-Patterson Air Force Base, Ohio, March, 1965.
- 18.1 Paul W. Kadlec, Flight Data Analysis of the Relationship Between Atmospheric Temperature Change and Clear Air Turbulence, AD 620 989, Dept. of Commerce, Weather Bureau, June, 1965.
- 18.2 J. L. Lumley and H. A. Panofsky, "The Structure of Atmospheric Turbulence," Inter-science Monographs and Texts in Physics and Astronomy, Vol. XII, John Wiley and Sons, 1964.

- 20.1. A. B. Blackman and J. W. Tukey, The Measurement of Power Spectra, Dover Publications, Inc., 1958.
- 21.1 J. O. Hinze, Turbulence, An Introduction to its Mechanism and Theory, McGraw-Hill Book Co., Inc., 1959.
- 22.1 John C. Houbolt, et al., Dynamic Response of Airplanes to Atmospheric Turbulence Including Flight Data on Input and Response, NACA Report TR R-199, Langley Research Center, Langley Station, Va., June, 1964.
- 28.1 T. von Karman, "Progress in the Statistical Theory of Turbulence," Turbulence Classic Papers on Statistical Theory, Edited by S. K. Friedlander and Leonard Topper, Interstate Publishers, Inc., 1961, pp 162-173.
- 28.2 H. L. Dryden, "A Review of the Statistical Theory of Turbulence," Turbulence Classic Papers on Statistical Theory, Edited by S. K. Friedlander and Leonard Topper, Interstate Publishers, Inc., 1961, pp 115-150.
- 28.3 J. Taylor, Manual on Aircraft Loads, AGARDograph 83, Pergamon Press Ltd., New York, N.Y., 1965.
- 28.4 N. E. Busch and H. A. Panofsky, "Recent Spectra of Atmospheric Turbulence," Quarterly Journal of the Royal Meteorological Society, Volume 94, 1968.
- 30.1 Francis E. Prichard, et al., Spectral and Exceedance Probability Models of Atmospheric Turbulence for Use in Aircraft Design and Operation, AFFDL-TR-65-122, Wright-Patterson Air Force Base, Ohio, 1965.
- 30.2 Flying Qualities of Piloted Airplanes, MIL-F-008785A, (MSC Project 345-10), October, 1966.
- 30.3 U. O. Lappe, A Climatological-Wind Turbulence Model for Estimating Low Altitude Gust Loads, AFFDL-TR-67-122, Wright-Patterson Air Force Base, Ohio, January, 1968.
- 31.1 O. G. Sutton, Micrometeorology, McGraw-Hill Book Co., Inc., 1952.
- 31.2 R. J. Taylor, "The Dissipation of Kinetic Energy in the Lowest Layers of the Atmosphere," Quarterly Journal of the Royal Meteorological Society, 78, 179-185, 1952.
- 31.3 Paul B. MacCready, Jr., "Structure of Atmospheric Turbulence," Journal of Meteorology, 10, 434-449, 1953.
- 34.1 F. K. Ball, "Viscous Dissipation in the Atmosphere," Journal of Meteorology, No. 18, pg 553, 1961.

- 39.1 Atrip, F. K., "Turbulence at Low Altitudes, Summary of the Results of Phases I and II," Clear Air Turbulence and Its Detection, Plenum Press, 1969.
- 39.2 Taylor, G. I., "Effect of Variation in Density on the Stability of Superposed Streams of Fluid," Proc. Roy. Soc. A 132, pp 499-523, 1931.
- 39.3 Businger, Joost A., On the Energy Supply of Clear Air Turbulence, Clear Air Turbulence and Its Detection, Plenum Press, 1969.
- 40.1 J. C. Kaimal and D. A. Haugen, "Characteristics of Vertical Velocity Fluctuations Observed on a 430-M Tower," Quart. J. R. Met. Soc., Vol. 93, No. 397, July, 1967.
- 40.2 Panofsky and Prasad, International Journal of Air Water Pollution, Pergamon Press, 1965, Vol. 9, pp 419-430.
- 41.1 J. W. Cooley and J. W. Tukey, "An Algorithm for the Machine Calculation of Complex Fourier Series," Math. of Computation, Vol. 19, pp 297-301, April, 1965.
- 41.2 M. J. Hinich and C. S. Clay, "The Application of the Discrete Fourier Transform in the Estimation of Power Spectra, Coherence, and Bispectra of Geophysical Data," Reviews of Geophysics, Vol. 6, No. 3, pp 347-363, August, 1968.
- 41.3 P. J. Daniell, "Discussion of Symposium on Autocorrelation in Time Series," J. Roy. Statist. Soc. (suppl.), pp 8, 88-90, 1946.
- 41.4 S. Pond, S. D. Smith, P. F. Hamblin, and R. W. Burling, "Spectra of Velocity and Temperature Fluctuations in the Atmospheric Boundary Layer Over the Sea." Journal of the Atmospheric Sciences, Vol. 23, No. 4, pp 376-386, July, 1966.
- 41.5 Climatic Changes, Technical Note No. 79, World Meteorological Organization, Commission for Climatology, p 36, 1966.
- 41.6 U. O. Lappe, B. Davidson, and C. B. Notess, Analysis of Atmospheric Turbulence Spectra Obtained from Concurrent Airplane and Tower Measurements, Institute of the Aeronautical Sciences Report No. 59-44, January, 1959.
- 41.7 J. Chandran Kaimal, An Analysis of Sonic Anemometer Measurements from the Cedar Hill Tower, Environmental Research Papers, No. 215, Bedford, Mass. Air Force Cambridge Research Laboratories, August, 1966.
- 43.1 Q-141 Aircrew Operational Procedures (Tactical Airlift), Military Airlift Command Manual MM55-141, United States Air Force, 31 July 1968.
- 43.2 Combat Airlift Test 4-69, Final Report, Department of the Air Force.

- X.1 J. Jones, Gust Environment Investigation (WFT 1254) - Formal Summary (using an F-106 airplane), B-52 Flight Test Activities Report, Boeing Document D-13273-361A, The Boeing Co., Wichita, Kansas, May, 1964.
- X.2 J. W. Jones, High Intensity Gust Investigation (WFT 1217 R3), B-52 Flight Test Activities Report, Boeing Document B-13273-333A, The Boeing Co., Wichita, Kansas, October, 1964.
- X.3 A. K. Cross, T-38 Dynamic Response Gust Loads Comparison Between Flight Test and Analytical Results, Northrop Corporation, NORAIR Division, Document NOR-60-306, March, 1964.
- X.4 Test Operations Unit, Dynamic Response and Loads Survey - B-52C through B-52F (WFT 1293), B-52 Flight Test Activities Report, Boeing Document D-13273-362A, The Boeing Co., Wichita, Kansas, July, 1966.
- X.5 Test Operations Unit, High Speed Low Level Investigation - B-52G and H (WFT 1286), B-52 Flight Test Activities Report, Boeing Document D-13273-365A, The Boeing Co., Wichita, Kansas, September, 1966.
- X.6 K. D. Saunders, B-66B Low-Level Gust Study, Wright Air Development Division, Wright-Patterson Air Force Base, Ohio, March, 1961.
- X.7 R. E. Peloubet and R. L. Haller, Application of a Power Spectral Gust Design Procedure to Bomber Aircraft, AFFDL-TR-66-35, Air Force Flight Dynamics Laboratory, Wright-Patterson Air Force Base, Ohio, June, 1966.
- 51.1 Ralph H. Pennington, Introductory Computer Methods and Numerical Analysis, The MacMillan Co., New York, New York.
- 51.2 Emanuel Parzen, Stochastic Processes, Holden-Day, Inc., San Francisco, California.
- 51.1 Ralph H. Pennington, Introductory Computer Methods and Numerical Analysis, The MacMillan Co., New York, New York
- 51.2 Emanuel Parzen, Stochastic Processes, Holden-Day, Inc., San Francisco, California

UNCLASSIFIED

Security Classification

## DOCUMENT CONTROL DATA - R&amp;D

(Security class/level of title, body of abstract and indexing annotation must be entered when the overall report is classified)

1. ORIGINATING ACTIVITY (Corporate method)		23. REPORT SECURITY CLASSIFICATION	
The Boeing Company Wichita Division Wichita, Kansas 67210		UNCLASSIFIED	
3. REPORT TITLE		25. GROUP	
Low Altitude Atmospheric Turbulence LO-LO CAT Phase III Volume I, Part I			
4. DESCRIPTIVE NOTES (Type of report and technical data)			
R&D Final Technical Report - 17 April 1968 to 17 August 1970			
5. AUTHOR(S) (Last name, first name, initial)			
Jones, J. W.; Mielke, R. H.; Jones, G. W.			
6. REPORT DATE	7a. TOTAL NO. OF PAGES	7b. NO. OF REFS	
October 1970	412	64	
8a. CONTRACT OR GRANT NO.	9a. ORIGINATOR'S REPORT NUMBER(S)		
PR3615-68-C-1468 ✓	None		
8b. PROJECT NO. ADF682E	9b. OTHER REPORT NO(S) (Any other numbers that may be assigned this report)		
	AFFDL-TR-70-10 Volume I, Part I		
10. AVAILABILITY/LIMITATION NOTICES This document is subject to special export controls and each transmittal to foreign governments or foreign nationals may be made only with prior approval of the Air Force Flight Dynamics Laboratory (FBE), Wright-Patterson AFB, Ohio 45433			
11. SUPPLEMENTARY NOTES		12. SPONSORING MILITARY ACTIVITY	
		Air Force Flight Dynamics Laboratory (FBE) Wright-Patterson AFB, Ohio 45433	
13. ABSTRACT This report presents procedures, analysis methods, and final results pertaining to the LO-LOCAT Phase III program. Approximately 150 hours of low altitude (100 - 1000 feet) turbulence and associated meteorological data were recorded from 16 August 1968 through 30 June 1969. A model of the turbulence environment at low-level is presented in terms of gust velocity primary peaks, level crossings, amplitude samples, rms values, and gust maxima, as well as derived equivalent gusts, turbulence scale lengths, and power spectra. Mathematical expressions for turbulence spectra, scale length, and primary peak statistics are shown. Correlations between atmospheric gust velocities and meteorological and geophysical phenomena are evaluated. It was found that gust velocity magnitude at low altitude is most affected by atmospheric stability and terrain. Gust velocity rms values above 1.5 fps may be approximated by truncated Gaussian distributions. For wavelengths less than 15,000 feet, turbulence spectra are best represented by the von Karman mathematical expressions. The turbulence, sampled for 4-1/2 minute intervals over a distance of approximately 32 miles at absolute altitudes below 1,000 feet, was found to be basically stationary, isotropic, and homogeneous. A high percentage of Phase III data were recorded over high mountains since very little high mountain data were recorded under contour flight conditions at low level during Phases I and II. Phase III data are compared with data from Phases I and II and with data from other low altitude programs.			
(Distribution of this Abstract is Unlimited)			

DD FORM 1 JAN 64 1473

UNCLASSIFIED

Security Classification



## Security Classification

14. KEY WORDS	LINK A		LINK B		LINK C	
	ROLE	WT	ROLE	WT	ROLE	WT
LO-LOCAT (Low-Low Altitude Critical Atmospheric Turbulence) ALL CAT Low Level Turbulence (0-1000 feet) Clear Air Turbulence (CAT) Gust Velocity Statistics Low Level Turbulence Model Meteorology (Turbulence) Turbulence Forecasting						

## INSTRUCTIONS

1. **ORIGINATING ACTIVITY:** Enter the name and address of the contractor, subcontractor, grantee, Department of Defense activity or other organization (corporate author) issuing the report.

2a. **REPORT SECURITY CLASSIFICATION:** Enter the overall security classification of the report. Indicate whether "Restricted Data" is included. Marking is to be in accordance with appropriate security regulations.

2b. **GROUP:** Automatic downgrading is specified in DoD Directive 5200.10 and Armed Forces Industrial Manual. Enter the group number. Also, when applicable, show that optional markings have been used for Group 3 and Group 4 as authorized.

3. **REPORT TITLE:** Enter the complete report title in all capital letters. Titles in all cases should be unclassified. If a meaningful title cannot be selected without classification, show title classification in all capitals in parenthesis immediately following the title.

4. **DESCRIPTIVE NOTES:** If appropriate, enter the type of report, e.g., interim, progress, summary, annual, or final. Give the inclusive dates when a specific reporting period is covered.

5. **AUTHOR(S):** Enter the name(s) of author(s) as shown on or in the report. Enter last name, first name, middle initial. If military, show rank and branch of service. The name of the principal author is an absolute minimum requirement.

6. **REPORT DATE:** Enter the date of the report as day, month, year, or month, year. If more than one date appears on the report, use date of publication.

7a. **TOTAL NUMBER OF PAGES:** The total page count should follow normal pagination procedures, i.e., enter the number of pages containing information.

7b. **NUMBER OF REFERENCES:** Enter the total number of references cited in the report.

8a. **CONTRACT OR GRANT NUMBER:** If appropriate, enter the applicable number of the contract or grant under which the report was written.

8b, 8c, & 8d. **PROJECT NUMBER:** Enter the appropriate military department identification, such as project number, subproject number, system numbers, task number, etc.

9a. **ORIGINATOR'S REPORT NUMBER(S):** Enter the official report number by which the document will be identified and controlled by the originating activity. This number must be unique to this report.

9b. **OTHER REPORT NUMBER(S):** If the report has been assigned any other report numbers (either by the originator or by the sponsor), also enter this number(s).

10. **AVAILABILITY/LIMITATION NOTICES:** Enter any limitations on further dissemination of the report, other than those

imposed by security classification, using standard statements such as:

- (1) "Qualified requesters may obtain copies of this report from DDC."
- (2) "Foreign announcement and dissemination of this report by DDC is not authorized."
- (3) "U. S. Government agencies may obtain copies of this report directly from DDC. Other qualified DDC users shall request through \_\_\_\_\_"
- (4) "U. S. military agencies may obtain copies of this report directly from DDC. Other qualified users shall request through \_\_\_\_\_"
- (5) "All distribution of this report is controlled. Qualified DDC users shall request through \_\_\_\_\_"

If the report has been furnished to the Office of Technical Service, Department of Commerce, for sale to the public, indicate this fact and enter the price, if known.

11. **SUPPLEMENTARY NOTES:** Use for additional explanatory notes.

12. **SPONSORING MILITARY ACTIVITY:** Enter the name of the departmental project office or laboratory sponsoring (paying for) the research and development. Include address.

13. **ABSTRACT:** Enter an abstract giving a brief and factual summary of the document indicative of the report, even though it may also appear elsewhere in the body of the technical report. If additional space is required, a continuation sheet shall be attached.

It is highly desirable that the abstract of classified reports be unclassified. Each paragraph of the abstract shall end with an indication of the military security classification of the information in the paragraph, represented as (TS), (S), (C), or (U).

There is no limitation on the length of the abstract. However, the suggested length is from 150 to 225 words.

14. **KEY WORDS:** Key words are technically meaningful terms or short phrases that characterize a report and may be used as index entries in cataloging the report. Key words must be selected so that no security classification is required. Identifiers, such as equipment model designation, trade name, military project code name, geographic location, may be used as key words but will be followed by an indication of technical context. The assignment of links, rules, and weights is optional.